

STRUCTURES AND TECHNIQUES FOR
IMPLEMENTING AND PACKAGING
COMPLEX, LARGE SCALE
MICROELECTROMECHANICAL SYSTEMS
USING FOUNDRY FABRICATION PROCESSES

DISSERTATION

John Henry Comtois, Major, USAF

AFIT/DS/ENG/96-04

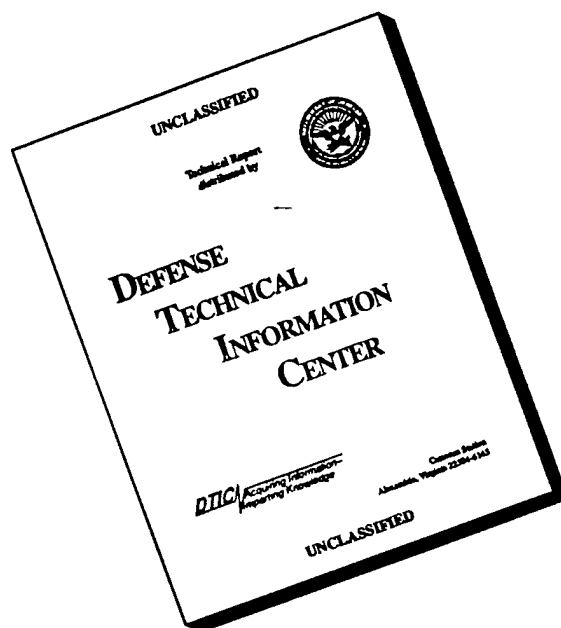
DTIC QUALITY INSPECTED 3

The views expressed in this dissertation are those of the author and do not reflect the official policy or position of the Department of Defense or the U.S. Government.

Approved for public release; distribution unlimited.

19960718 113

DISCLAIMER NOTICE



THIS DOCUMENT IS BEST QUALITY AVAILABLE. THE COPY FURNISHED TO DTIC CONTAINED A SIGNIFICANT NUMBER OF PAGES WHICH DO NOT REPRODUCE LEGIBLY.

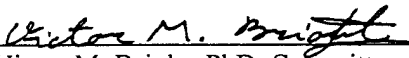
AFIT/DS/ENG/96-04

Structures and Techniques For
Implementing and Packaging Complex,
Large Scale Microelectromechanical Systems
Using Foundry Fabrication Processes

John H. Comtois, B.S.E.E., M.S.E.E.

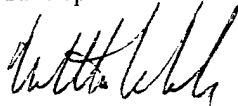
Major, USAF

Approved:




Victor M. Bright, PhD, Committee Chairman
AFIT Department of Electrical and Computer Engineering

8 May 1996
Date



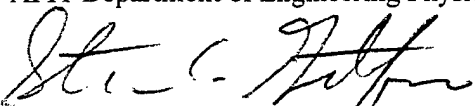
Matthew Kabrisky, PhD, Committee Member
AFIT Department of Electrical and Computer Engineering

8 MAY 96
Date



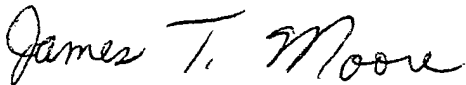
Paul H. Ost diek, PhD, Lt Col, USAF, Committee Member
AFIT Department of Engineering Physics

8 May 96
Date



Dr. Steven C. Gustafson, PhD, Committee Member
University of Dayton, Department of Electro-Optics

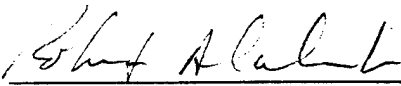
8 May 96
Date



James T. Moore, PhD, Lt Col, Dean's Representative
AFIT Department of Operational Sciences

8 May 96
Date

Accepted:



Robert A. Calico, Jr.
Dean, Graduate School of Engineering

AFIT/DS/ENG/96-04

**Structures and Techniques For
Implementing and Packaging Complex,
Large Scale Microelectromechanical Systems
Using Foundry Fabrication Processes**

DISSERTATION

Presented to the Faculty of the Graduate School of Engineering
of the Air Force Institute of Technology
Air Education and Training Command
In Partial Fulfillment of the Requirements for the Degree of
Doctor of Philosophy

John Henry Comtois, B.S., M.S.
Major, USAF

12 May 1996

Approved for public release; distribution unlimited.

Table of Contents

	Page
Acknowledgments	vii
List of Figures	ix
List of Tables	xv
List of Acronyms	xvi
Abstract	xvii
1. Introduction	1-1
1.1 MEMS Applications	1-2
1.1.1 Military Space Cost Savings	1-3
1.2 Purpose and Impact of this Research on the MEMS Community	1-5
1.3 Evolution Of This Research	1-8
1.4 Organization of This Document	1-10
2. MEMS Fabrication	2-1
2.1 MEMS Fabrication Process Categories	2-1
2.1.1 Bulk Silicon Micromachining	2-2
2.1.2 Surface Micromachining	2-7
2.1.3 High Aspect Ratio Microstructures	2-13
2.2 Process Selection	2-16
2.3 Foundry Fabrication Processes and Example Devices	2-18
2.3.1 CMOS-Based MEMS	2-19
2.3.1.1 Etch Gauges	2-23
2.3.1.2 Suspended Heating Resistors	2-26
2.3.1.3 Thermal Actuators	2-27
2.3.2 MUMPS	2-28
2.3.2.1 Etch Gauges	2-35
2.3.2.2 Fabrication Test Structures	2-38
2.3.2.3 MUMPS Design Techniques	2-45
2.3.2.3.1 Bossing	2-45
2.3.2.3.2 Forming Topological Features	2-49
2.3.2.3.3 Breaching the Silicon Nitride Layer	2-53
2.3.2.3.4 Stacked Polysilicon Structures	2-56
2.3.2.4 MUMPS Fabrication Problems	2-58
2.3.3 LIGA	2-60
2.3.3.1 Etch Gauges	2-63
2.3.3.2 Fabrication Test Structures	2-64
2.3.3.3 Fluidic Components	2-67
2.4 Familiarization Benefits	2-69

Table of Contents (Cont.)

	Page
3. High Force Actuators.....	3-1
3.1 Actuators for MEMS	3-1
3.2 Actuator Types.....	3-2
3.2.1 Piezoelectric Actuation	3-3
3.2.2 Hydraulic and Pneumatic Actuation	3-4
3.2.3 Electromagnetic Actuation.....	3-6
3.2.4 Electrostatic Actuators.....	3-7
3.2.4.1 Rotary Electrostatic Motors	3-13
3.2.5 Thermal Multi-Morph Actuators	3-15
3.3 Need for a New Actuator	3-19
3.4 Lateral Thermal Actuator.....	3-20
3.4.1 Actuator Development.....	3-22
3.4.1.1 Prior Practice.....	3-22
3.4.1.2 Early Research	3-24
3.4.1.3 Characterizing Early Actuators.....	3-27
3.4.2 Final Actuator Design Test Results	3-29
3.4.2.1 Current versus Deflection	3-31
3.4.2.2 Back-bending Characteristics	3-33
3.4.2.3 Repeatability and Reliability	3-35
3.4.2.4 Effects of Actuator Geometry.....	3-35
3.4.2.5 Maximum Operating Frequency	3-38
3.4.2.6 Force Testing	3-40
3.4.2.6.1 Force Test Beam Geometry	3-41
3.4.2.6.2 Initial Force Tests	3-43
3.4.2.6.3 Improved Actuator Force Tests	3-45
3.4.3 General Design Considerations.....	3-51
3.4.4 LIGA Thermal Actuators.....	3-55
3.4.5 Alternative Structures	3-57
3.4.5.1 Compliant Micromechanisms.....	3-57
3.4.5.2 Vertical Actuators.....	3-59
3.4.5.3 Circular Actuators.....	3-63
3.4.5.4 Externally Heated Actuators.....	3-64
3.4.6 Actuator Arrays.....	3-66
3.5 Comparison With Other Actuators	3-71
3.6 Conclusions.....	3-74
4. Wiring Systems.....	4-1
4.1 Substrate Wiring	4-2
4.1.1 CMOS MEMS	4-2
4.1.2 LIGA	4-5
4.1.3 MUMPS.....	4-5

Table of Contents (Cont.)

	Page
4.1.3.1 MUMPS Substrate Wiring Crossovers	4-7
4.2 Hinged Wiring	4-11
4.2.1 Hinged Devices	4-11
4.2.2 Wiring to Hinged Plates	4-14
4.2.3 Hinged Wiring to Sliding Structures	4-17
4.2.4 Hinge Wire Development	4-19
4.2.5 Improved Hinged Plate Contacts	4-25
4.3 Improved Hinges	4-27
4.4 Applications	4-30
4.4.1 Thermal Bimorph Actuator	4-30
4.4.2 Off-Die Grippers	4-31
4.4.3 Grounding Hinged Covers	4-34
4.4.4 Hinged Thermal Actuator	4-35
4.5 Conclusions	4-38
5. Large System Examples	5-1
5.1 Complex Devices	5-4
5.1.1 Mechanical Limitations of MEMS	5-4
5.1.2 Example Devices	5-7
5.1.2.1 Mechanical Relay Switches	5-7
5.1.2.1.1 MUMPS Relays	5-8
5.1.2.1.2 LIGA Relays	5-13
5.1.2.2 Motors	5-16
5.1.2.2.1 LIGA Ratchet Motor	5-16
5.1.2.2.2 MUMPS Stepper Motors	5-18
5.1.2.3 Positioning	5-24
5.1.2.3.1 X-Y Positioning	5-24
5.1.2.3.2 Rotational Positioning	5-26
5.1.2.3.3 Micro Interferometers	5-28
5.1.2.3.4 Modulating Retroreflectors	5-29
5.1.2.4 Self-Assembled Structures	5-36
5.2 Whole Die Systems	5-40
5.2.1 Floorplanning	5-41
5.2.2 Example Systems	5-47
5.2.2.1 LIGA Switch Array	5-47
5.2.2.2 CMOS Tactile Stimulator Array	5-49
5.2.2.3 MUMPS Spatial Light Modulator	5-53
5.2.2.3.1 Hexagonal Mirror Design	5-54
5.2.2.3.2 Hexagonal Array Design	5-57
5.2.2.3.3 Cover Plate Design	5-60
5.2.2.3.4 Fabrication Results	5-62

Table of Contents (Cont.)

	Page
5.2.2.3.5 Micromirror and Array Improvements	5-65
5.2.2.4 MUMPS Holographic Data Storage Mirror Array	5-75
5.2.2.4.1 First Holographic Mirror Array Design.....	5-75
5.2.2.4.2 Second Holographic Mirror Array Design	5-79
5.2.2.4.3 Third Holographic Mirror Array Design	5-85
5.2.2.4.4 Toward Larger Mirror Arrays.....	5-87
5.3 Conclusions.....	5-91
6. Packaging Systems	6-1
6.1 Die Interconnect Techniques	6-5
6.1.1 Wirebonding	6-5
6.1.2 Flip Chip	6-7
6.1.3 Direct Metal Deposition.....	6-9
6.1.4 Polymer Wiring.....	6-11
6.2 Multichip Module Processes.....	6-13
6.2.1 MCM-L (Laminated) Technology	6-13
6.2.2 MCM-C (Cofired) Technology	6-14
6.2.3 MCM-D (Deposited) Technology.....	6-16
6.2.4 High Density Interconnect (HDI) Process	6-18
6.3 Integrating Micromachines With Electronics	6-21
6.3.1 Electronics on the MEMS Die	6-22
6.3.2 Electronics with the MEMS Die	6-24
6.3.3 Pre- Versus Post-Release	6-26
6.4 Package Testing	6-27
6.4.1 MEMS Test Die	6-28
6.4.1.1 CMOS MEMS Test Die.....	6-29
6.4.1.2 MUMPS Test Die	6-31
6.4.1.3 Polymer Wiring MUMPS Test Die	6-35
6.4.2 Chemical Compatibility Testing.....	6-36
6.4.2.1 HDI Materials Compatibility Tests.....	6-37
6.4.2.1.1 EDP Etch of HDI Samples	6-39
6.4.2.1.2 Hydrofluoric Acid Etch of HDI Samples	6-41
6.4.2.1.3 EDP Test With Diamond-Like Coating.....	6-42
6.4.2.1.3.1 Sample 2, 0.95 μm DLC	6-44
6.4.2.1.3.2 Sample 2, 2.3 μm DLC	6-45
6.4.2.1.3.3 Sample 3, 0.95 μm DLC	6-47
6.4.2.1.3.4 Sample 3, 2.3 μm DLC	6-47
6.4.2.1.3.5 Sample 4, 0.95 μm DLC	6-48
6.4.2.1.3.6 Sample 4, 2.3 μm DLC	6-49
6.4.2.2 MMS MCM-D Etch Testing.....	6-50
6.4.2.2.1 TMAH Etch of MMS Substrate.....	6-51

Table of Contents (Cont.)

	Page
6.4.2.2.2 HF Etch of MMS Substrate	6-54
6.4.2.3 Photoresist Compatibility Testing	6-54
6.4.2.3.1 EDP Photoresist Test	6-55
6.4.2.3.2 HF Photoresist Test.....	6-56
6.4.2.3.3 2-Propanol Photoresist Test.....	6-57
6.4.2.3.4 TMAH Photoresist Test.....	6-58
6.4.3 Full Packaging Test	6-58
6.4.4 Polymer Wiring Test.....	6-61
6.5 Conclusions.....	6-63
7. Conclusions.....	7-1
7.1 Packaging Options	7-4
7.2 Comparison of Foundry MEMS Processes.....	7-5
7.3 Future Directions	7-7
Appendix A MEMS Die Layouts	A-1
A.1 CMOS MEMS Die Plots and Device Listings.....	A-1
A.1.1 Testchip3 Die	A-3
A.1.2 Traychip1 Die	A-5
A.1.3 Traychip2 Die	A-7
A.1.4 CMOS4 Die	A-9
A.1.5 CMOS Packaging Test Die.....	A-10
A.2 MUMPS Die Plots and Device Listings	A-12
A.2.1 MUMPS3 Die	A-15
A.2.2 MUMPS4 Die	A-17
A.2.3 MUMPS5 Die	A-19
A.2.4 MUMPS6 Die Number 2	A-21
A.2.5 MUMPS6 Die Number 3	A-23
A.2.6 MUMPS6 Hexagonal Mirror Array 1	A-24
A.2.7 MUMPS7 Die Number 1	A-25
A.2.8 MUMPS7 Die Number 7	A-27
A.2.9 MUMPS7 Hexagonal Mirror Array	A-28
A.2.10 MUMPS7 Devices re-fabricated on the MUMPS8 run	A-29
A.2.11 MUMPS8 Die Number 1	A-30
A.2.12 MUMPS8 Die Number 2	A-32
A.2.13 MUMPS8 Die Number 3	A-33
A.2.14 MUMPS8 Die Number 4	A-34
A.2.15 MUMPS8 Holographic Array Number 1	A-35
A.2.16 MUMPS9 Die Number 5	A-36
A.2.17 MUMPS9 Holographic Die Number 2	A-38
A.2.18 MUMPS10 Die Number 1	A-39

Table of Contents (Cont.)

	Page
A.2.19 MUMPS10 Holographic Die Number 3, 3a.....	A-41
A.2.20 MUMPS11 Die Number 3	A-42
A.2.21 MUMPS12 Die Number 4	A-44
A.3 LIGA Die Plots and Device Listings	A-46
A.3.1 LIGA2, Short Die.....	A-47
A.3.2 LIGA3 Die	A-49
Appendix B Hardware and Software Support	B-1
B.1 Computer Aided Design Layout Tools	B-1
B.1.1 Magic Technology File for MUMPS	B-4
B.1.3 Cadence Technology File for MUMPS.....	B-7
B.1.3 Cadence Technology File for LIGA.....	B-14
B.2 Test Hardware	B-18
B.2.1 Reflux Container for EDP Etching.....	B-18
B.2.2 Patch Panel And Signal Generator Boost Amplifier	B-20
B.2.3 Three Channel Power Interrupter/Sequencer	B-21
B.2.4 Weight Balance Force Tester	B-24
B.2.5 Vacuum Pick	B-25
B.2.6 Test Die Holders.....	B-26
Appendix C Vita, Patent Applications, Publications.....	C-1

Acknowledgments

This research consumed much time beyond 'normal duty hours', time which came in large part from my family, who have been wonderfully patient with my frequent absences. My irreplaceable wife Susan performed duties beyond the pale keeping up with our four children: Chris, Ian, Elizabeth, and John Alexander (J'Alex), aged 6, 4, 3, and 1, especially during the academic phase. A wife such as this, and all these cute and bright kids, are the best reward.

I owe much of the success for this project to the free rein I was given by my research advisor and committee chairman, Dr. Victor Bright, who not only encouraged a wide-ranging research effort and provided many publication opportunities, but who also fostered a companionable atmosphere for all the MEMS students. You can have your office back now. I would like to thank the other MEMS students who helped create the sort of amiable atmosphere that makes events like all-weekend CAD layout sessions not just a job, but an adventure: Lt. Tray Read, Lt. Mark Phipps, Lt. Adrian Michalicek, Capt. Brian Freeman, Lt. Rich Kuhns, Capt. Darren Sene, Lt. Rob Reid, Maj. Dave Burns, and Maj. Bill Cowan.

I am also grateful to Dr. Steven Gustafson of the University of Dayton Research Institute, a research committee member, for providing real-world problems to solve, which gave me the confidence that this work was not just an academic exercise. I would like to thank Lt. Col. Paul Ostdiek, a committee member, and Lt. Col. James T. Moore, the Dean's representative, for their careful reading and useful comments on the final dissertation draft. The last committee member, Dr. Matthew Kabrisky, I would like to thank for the many hours of discussion on a wide range of topics, mostly not MEMS; you have been an inspiration to me of what a Doctor of Philosophy can be.

My sponsor, Mr. James Lyke of the Air Force's Phillips Laboratory, provided the funds and initial direction for this research, as well as contacts with General Electric for packaging. This type of research would not have been possible without the foresight of Dr. Ken Gabriel of DARPA in supporting the foundry fabrication processes.

There are many others who also provided direct support for this research effort: Mr. Charlie Powers for budgeting, lab technicians Bill Trop and Chris O'Brien, who were the first to see many of the new MEMS devices operate for the first time, and Mr. Larry Callahan from Wright Labs, who helped me resurrect the ball bonder. I would especially like to thank the VLSI computer support folks, Mr. Russell Milliron and Mr. Greg Richardson, for their help and humor throughout this CAD-intensive effort.

Many people outside of AFIT also helped this effort along. Jennifer Peltier, Wes Hansford, and John Walker of the Information Sciences Institute really came through with the multi-chip module design when the CAD software proved to be incompatible. Glenn Forman and Richard Saia of the General Electric Corporation were very generous in showing and explaining the HDI packaging process, taking on the design of a test package, and providing sample materials. I would also like to thank Dr. Kris Pister and Richard Yeh of the University of California, Los Angeles, for the exchange of ideas on MEMS and the camaraderie at conferences. A truck-load of thanks is due to Karen Marcus, Dave Koester, and Allen Cowen at MCNC for their patience and valuable 'user-friendly' support with the MUMPS process.

Finally, I would like to thank my parents, Wilfred and Marie Comtois, for providing me throughout my life with the love, support, and examples of living that allowed me to reach this point in my career. I hope I can provide for my four children what you provided for your ten.

List of Figures

	Page
Figure 2-1. Miller indices of cubic crystal planes.....	2-2
Figure 2-2. Identifying flats of a silicon wafer	2-3
Figure 2-3. Differences between isotropic and anisotropic etch of {100} silicon	2-6
Figure 2-4. Square pits anisotropically etched into a {100} silicon wafer	2-6
Figure 2-5. Stiction holding a large surface-micromachined spiral down	2-10
Figure 2-6. Surface micromachined polysilicon electrostatic motor	2-11
Figure 2-7. Surface micromachined polysilicon cantilever.	2-11
Figure 2-8. Curling of surface micromachined cantilevers.....	2-13
Figure 2-9. Copper gear made in deep UV electroplating process	2-15
Figure 2-10. Nickel gears made in the LIGA process.....	2-15
Figure 2-11. Layout for a suspended cantilever in a CMOS MEMS process.....	2-20
Figure 2-12. Optical micrograph of incompletely released glass cantilevers	2-22
Figure 2-13. Cantilevers of Figure 2-12 broken away to show progress of etch. ...	2-22
Figure 2-14. CMOS MEMS test die, 'Testchip3'	2-24
Figure 2-15. CMOS MEMS open square etch gauge, incompletely etched	2-25
Figure 2-16. Suspended heating resistor	2-27
Figure 2-17. Arrays of heat actuated multimorph cantilevers.	2-28
Figure 2-18. Materials and layer thicknesses of the MUMPS process	2-30
Figure 2-19. Illustration of an electrostatic micromirror	2-33
Figure 2-20. Photograph of test die fabricated in the MUMPS4 process	2-35
Figure 2-21. Etch gauge from MUMPS3.....	2-37
Figure 2-22. Layout drawing of an etch gauge with thermal actuation	2-37
Figure 2-23. Structures for investigation of interactions of MUMPS layers	2-39
Figure 2-24. Structures of Figure 2-23 after etches in HF and KOH.....	2-41
Figure 2-25. Nitride hole in a MUMPS die after 30 minute etch in KOH	2-42
Figure 2-26. Structure for determining minimum width of <i>poly2</i> flexures	2-43
Figure 2-27. Cross-section of a <i>Poly2</i> plate crossing 2 μm wide <i>poly0</i> wires.....	2-44
Figure 2-28. Tower structure made from all the MUMPS layers	2-44
Figure 2-29. Options for bossing <i>poly1</i> and <i>poly2</i>	2-46
Figure 2-30. Electrostatically actuated tilting beam mirrors.....	2-47
Figure 2-31. Hinged <i>poly1</i> plate with <i>dimple</i> -bosses for stiffness.....	2-47
Figure 2-32. Piston mirrors with and without <i>poly0</i> wire stubs under flexures.....	2-48
Figure 2-33. Toothed pawls formed in <i>poly2</i> by conforming to <i>poly1</i>	2-50
Figure 2-34. Fold-up mirrors with a ratcheting slider.....	2-51
Figure 2-35. <i>Poly1</i> former used to create a cup in a <i>poly2</i> plate.....	2-53
Figure 2-36. Center post, tilting 'cloverleaf' mirrors.....	2-55
Figure 2-37. Structures formed by the stacked <i>poly1/poly2</i> technique.....	2-57
Figure 2-38. Hinged mirror plate built with stacked <i>poly1/oxide2/poly2</i>	2-58
Figure 2-39. Stringers of <i>poly2</i> following the topology of the underlying <i>poly0</i> ...	2-59
Figure 2-40. Underside of a failed hinged plate.....	2-60

List of Figures (Cont.)

	Page
Figure 2-41. Mask for the 'short' LIGA die.	2-63
Figure 2-42. Timing gauge for LIGA partial undercut etch	2-64
Figure 2-43. Layout drawing of a test grid structure from the LIGA process	2-65
Figure 2-44. Mask drawing of the axle clearance test cell.....	2-66
Figure 2-45. Test spring structure.....	2-67
Figure 2-46. Vortex fluid amplifier	2-68
Figure 2-47. SEM micrograph of a flip-over bimorph actuator.....	2-71
Figure 3-1. Piezoelectric multi-axis actuator	3-4
Figure 3-2. Bulk micromachined silicon microvalve design	3-5
Figure 3-3. Air table, air passages and inlet port	3-6
Figure 3-4. Electromagnetic actuator fabricated in the LIGA process	3-7
Figure 3-5. Cross-sectional drawing of the Digital Micromirror Device™	3-10
Figure 3-6. Drawing of a folded-beam electrostatic comb drive resonator	3-11
Figure 3-7. Electrostatic wobble motor fabricated in electroplated copper	3-14
Figure 3-8. Multi-morph thermal actuator fabricated in CMOS MEMS.....	3-17
Figure 3-9. Weight-balance force tester.....	3-19
Figure 3-10. Basic layout of a 'heatuator' thermal actuator	3-21
Figure 3-11. Schematic of thermal actuator with dimensional labels.....	3-23
Figure 3-12. Polysilicon beam fabrication quality and sag test cell	3-25
Figure 3-13. Early thermal expansion actuator.....	3-26
Figure 3-14. Early thermal actuator attached to a force-measuring spring.....	3-26
Figure 3-15. Test set of the first versions of the thermal actuator	3-28
Figure 3-16. Grippers made with the first version of the thermal actuator.....	3-29
Figure 3-17. Test set of thermal actuators fabricated in 2 μm thick <i>poly1</i>	3-30
Figure 0-1. Deflection versus applied current for 2 μm thick <i>poly1</i> actuator.....	3-32
Figure 3-19. Back bending versus cold-to-hot arm width ratio	3-34
Figure 3-20. Maximum deflection for actuators 100, 150, and 200 μm long.....	3-36
Figure 3-21. Maximum deflection for actuators with widths of 2,3,4 and 5 μm	3-37
Figure 3-22. Maximum achievable deflection versus flexure length.....	3-39
Figure 3-23. Variable diffraction grating.....	3-40
Figure 3-24. Geometry of a bent force testing beam	3-42
Figure 3-25. Three <i>poly1</i> , <i>poly2</i> thermal actuator designs.....	3-46
Figure 3-26. Power versus force for three copies of a P1P2 thermal actuator.....	3-48
Figure 3-27. Input power versus force for the three actuators of Figure 3-25	3-49
Figure 3-28. Portion of an etch gauge layout with thermal actuators	3-54
Figure 3-29. Two sets of four LIGA thermal actuators each	3-56
Figure 3-30. Early version of thermally actuated grippers	3-58
Figure 3-31. Vertical thermal actuator with <i>poly2</i> hot arms	3-60
Figure 3-32. Design of an all- <i>poly2</i> vertical thermal actuator	3-60
Figure 3-33. Vertical thermal actuator with <i>poly2</i> hot arm.....	3-61
Figure 3-34. Thermally raised mirrors on <i>poly2</i> ladder-bridges.....	3-62

List of Figures (Cont.)

	Page
Figure 3-35. Circular thermal actuators fabricated in the MUMPS process.....	3-64
Figure 3-36. Externally heated thermal actuator.....	3-65
Figure 3-37. Ten tethered <i>poly1</i> actuators with an early <i>poly1</i> yoke design.....	3-66
Figure 3-38. Array of five 220 μm long actuators	3-67
Figure 3-39. Unsuccessful attempt to array thermal actuators in series	3-70
Figure 3-40. Two-axis tilting mirror combining motion thermal actuator arms.....	3-71
Figure 4-1. Section of a microprocessor circuit layout.....	4-3
Figure 4-2. Section of the third CMOS MEMS test die	4-4
Figure 4-3. Top and cross-section of a low-resistance MUMPS substrate wire.....	4-6
Figure 4-4. Wiring crossover, with 15 μm wide <i>poly2/anchor2</i> /metal wires.....	4-8
Figure 4-5. High current crossover	4-9
Figure 4-6. Substrate wiring running under a <i>poly2</i> plate.....	4-10
Figure 4-7. <i>Poly0</i> wiring between 50 μm wide <i>poly2</i> mirrors	4-11
Figure 4-8. Fold-up mirror designed with three types of microhinges	4-12
Figure 4-9. Hinged plate attached to a thermal actuator array on the substrate.....	4-13
Figure 4-10. Layout drawing of a flexible hinged wire	4-16
Figure 4-11. Hinged wire contacting a hinged plate.....	4-17
Figure 4-12. Flip-over wiring connecting a sliding wire with substrate wiring	4-18
Figure 4-13. Flip-over switch fabricated on the MUMPS7 run.....	4-20
Figure 4-14. Pull-spring made of <i>poly1</i>	4-21
Figure 4-15. Test cell for flexible wires.....	4-22
Figure 4-16. Hinge plate caught under the hinge staple	4-23
Figure 4-17. Narrow, 480 x 3.5 μm flexible wires	4-24
Figure 4-18. Contact on a hinged plate for hinged wiring.....	4-26
Figure 4-19. Improved hinge design.....	4-28
Figure 4-20. Hinge pin locating guide	4-29
Figure 4-21. Unassembled flip-over grippers	4-31
Figure 4-22. Slide grippers before assembly	4-33
Figure 4-23. Slide grippers in the extended position	4-34
Figure 4-24. Hinged cover plate grounded with a flexible wire	4-35
Figure 4-25. Thermal actuator on hinged plates	4-37
Figure 5-1. Layout plot of the first die submitted for MUMPS fabrication	5-2
Figure 5-2. Lithograph of a water-powered grain mill, ca. 1750	5-5
Figure 5-3. Loose rotating bearing as fabricated in MUMPS.....	5-6
Figure 5-4. Mechanical relay switch with hinged thermal actuator.....	5-9
Figure 5-5. Mechanical relay with hinged contacts and shorting bar	5-11
Figure 5-6. Close-up of contact area of hinged-contact relay	5-12
Figure 5-7. LIGA latching relay array	5-14
Figure 5-8. LIGA latching relay pushed into position.....	5-15
Figure 5-9. Unassembled ratcheting stepper motor on LIGA2 die.....	5-17
Figure 5-10. First version of a polysilicon ratcheting stepper motor.....	5-19

List of Figures (Cont.)

	Page
Figure 5-11. Surface-micromachined rotary stepper motor	5-20
Figure 5-12. Sample timing cycle for stepper motor actuator control	5-23
Figure 5-13. Surface-micromachined linear stepper motor	5-23
Figure 5-14. Two compact X-Y positioning tables using thermal actuators	5-25
Figure 5-15. Flip-up rotating mirror	5-26
Figure 5-16. Microspectrometer	5-27
Figure 5-17. Partially assembled microinterferometer	5-29
Figure 5-18. Array of tilting mirrors.....	5-30
Figure 5-19. Corner Cube Reflector with actuator arrays.....	5-32
Figure 5-20. Connection from actuator array to hinged mirror plate.....	5-33
Figure 5-21. Adjustable tether for hinged plates.....	5-35
Figure 5-22. Corner Cube Reflector with larger electrostatic tilting mirrors	5-35
Figure 5-23. Fusible links used to adjust spring force	5-37
Figure 5-24. Three vertical thermal actuators arranged to lift a hinged plate.....	5-39
Figure 5-25. Initial design for a motorized hinged plate.....	5-40
Figure 5-26. Compact design for an array of test switches.....	5-43
Figure 5-27. Mechanical interference between 'Pull Spring' devices	5-45
Figure 5-28. Array of LIGA mechanical relay switches.....	5-49
Figure 5-29. Thermal tactile stimulator	5-51
Figure 5-30. Die layout showing thermal stimulator array.....	5-52
Figure 5-31. Evolution of a piston micromirror over four fabrication runs.....	5-56
Figure 5-32. Array of 127, 50 μm wide micromirrors.....	5-58
Figure 5-33. Arrays of test mirrors on the first hexagonal SLM die	5-60
Figure 5-34. Die with two arrays of 127 hexagonal piston micromirrors.....	5-64
Figure 5-35. Second 127-mirror hexagonal SLM die.....	5-69
Figure 5-36. Close-up view of the <i>poly1</i> cover plate flipped over	5-70
Figure 5-37. Corner of the cover plate on the second hexagonal SLM die	5-71
Figure 5-38. Minimum voltage needed to deflect 100 μm hexagonal mirrors	5-72
Figure 5-39. Test structures on the second hexagonal SLM die.....	5-73
Figure 5-40. Single test structure on the second hexagonal SLM die.....	5-73
Figure 5-41. Octagonal piston mirror	5-76
Figure 5-42. First linear micromirror array for the holographic storage project	5-78
Figure 5-43. Section of the first holographic storage mirror array	5-79
Figure 5-44. Rectangular piston mirror for second holographic storage array	5-80
Figure 5-45. Second holographic storage mirror array die	5-82
Figure 5-46. Plot of deflection for 50 x 80 μm rectangular <i>poly2</i> piston mirror	5-84
Figure 5-47. Two variations of piston mirror for third holographic storage array .	5-86
Figure 5-48. Thermally actuated mirrors for large linear arrays.....	5-90
Figure 6-1. Schematic of the ball-bonding technique.....	6-6
Figure 6-2. Electronic die flipped over and soldered to a MEMS die	6-9
Figure 6-3. Cross-section of a generic Direct Metal wiring process.....	6-11

List of Figures (Cont.)

	Page
Figure 6-4. Compressive wiring connecting a die to a printed circuit board.....	6-12
Figure 6-5. Single glob-topped die mounted directly on a printed circuit board....	6-14
Figure 6-6. Memory module fabricated on co-fired alumina substrate	6-15
Figure 6-7. 10-chip memory module fabricated in MCM-D technology.	6-16
Figure 6-8. HDI MCM fabrication process flow	6-19
Figure 6-9. 12-chip memory module fabricated in HDI technology	6-20
Figure 6-10. Die plot and sensor structure of ADXL-50 accelerometer	6-23
Figure 6-11. Sample of cells from the packaging test CMOS MEMS die	6-30
Figure 6-12. Packaging test CMOS MEMS die.....	6-31
Figure 6-13. MUMPS packaging test die	6-33
Figure 6-14. Sample of cells from the MUMPS packaging test die	6-34
Figure 6-15. Cross-section of a portion of a polymer wiring pad.....	6-35
Figure 6-16. MUMPS 10 die layout	6-36
Figure 6-17. Typical HDI simulated packaging sample	6-38
Figure 6-18. HDI material samples after a 62 minute etch in EDP	6-40
Figure 6-19. HDI samples etched in hydrofluoric acid for two minutes	6-42
Figure 6-20. Alumina substrate sample with 2.3 μm DLC coating.....	6-43
Figure 6-21. Alumina substrate and 0.95 μm DLC coating after EDP etch	6-44
Figure 6-22. Alumina substrate and 2.3 μm DLC coating after EDP etch	6-45
Figure 6-23. Alumina substrate and 2.3 μm DLC coating after EDP etch	6-46
Figure 6-24. Plaskon substrate and 0.95 μm DLC coating after EDP etch	6-47
Figure 6-25. Plaskon substrate and 2.3 μm DLC coating after EDP etch	6-48
Figure 6-26. Plaskon substrate and 0.95 μm DLC coating after EDP etch.	6-49
Figure 6-27. Unetched MMS MCM substrate	6-50
Figure 6-28. Etch gauge on the MUMPS 8 die.....	6-52
Figure 6-29. Failure of the polyimide dielectric near a die bondpad	6-53
Figure 6-30. MMS MCM substrate etched in 49% HF for two minutes.	6-54
Figure 6-31. MMS MCM test package before MEMS release etch processing	6-60
Figure 6-32. LCD watch printed circuit board rebuilt for polymer wiring test	6-62
Figure A-1. Third CMOS MEMS test die, 'testchip3'.	A-3
Figure A-2. Traychip1 die.....	A-5
Figure A-3. Traychip2 die.....	A-7
Figure A-4. Fabtest1 tinychip design.....	A-8
Figure A-5. Test die laid out in part for another researcher (CMOS4).....	A-9
Figure A-6. CMOS MEMS packaging test die.....	A-10
Figure A-7. MUMPS3 die, the first MUMPS die designed at AFIT	A-15
Figure A-8. MUMPS4 die number 3	A-17
Figure A-9. MUMPS5 die.....	A-19
Figure A-10. MUMPS6 die number 2	A-21
Figure A-11. MUMPS6 die number 3	A-23

List of Figures (Cont.)

	Page
Figure A-12. First hexagonal mirror array die (Hex1).....	A-24
Figure A-13. MUMPS packaging test die.....	A-24
Figure A-14. MUMPS7 chip 7, Physics department die	A-27
Figure A-15. Second hexagonal mirror array die (Hex2)	A-28
Figure A-16. A MUMPS7 re-fabrication die on MUMPS8	A-29
Figure A-17. MUMPS8, die number1..	A-30
Figure A-18. Top half of MUMPS8, die number 2	A-32
Figure A-19. MUMPS8, die number 3	A-33
Figure A-20. Lower left corner of MUMPS8, die number 4	A-34
Figure A-21. First mirror die designed for holographic data storage (Holo 1).....	A-35
Figure A-22. MUMPS9 die number 5	A-36
Figure A-23. Second mirror die designed for holographic data storage (Holo 2) .	A-38
Figure A-24. MUMPS10 die number 1	A-39
Figure A-25. Third die designed for holographic data storage (Holo 3, 3a).....	A-41
Figure A-26. MUMPS11 die number 3.	A-42
Figure A-27. MUMPS12 die number 4	A-44
Figure A-28. LIGA2 die for 30 μm tall fabrication run.....	A-47
Figure A-29. LIGA3 die for 30 μm tall fabrication run.....	A-49
Figure B-1. Reflux reactor for anisotropic silicon etch using EDP	B-19
Figure B-2. Circuit diagrams for signal generator amplifiers.....	B-21
Figure B-3. Block diagram of the three channel sequencer circuit.....	B-22
Figure B-4. Faceplate drawing for the three-channel sequencer.....	B-24
Figure B-5. Weight-balance force tester for vertically acting MEMS actuators	B-25
Figure B-6. Clamp for holding samples in the scanning electron microscope	B-26
Figure B-7. Die clamp for the probe station vacuum table.....	B-27

List of Tables

Table 1-1. A Sample of Areas of Current MEMS Research.....	1-2
Table 1-2. Launch Costs of Contemporary Space Vehicles [2].....	1-4
Table 2-1. Properties of Materials from the Tenth MUMPS Fabrication Run.	2-31
Table 2-2. Substrate Contact Layer Sequences and Mean Contact Resistance.	2-54
Table 3-1. Characteristics of Ideal Actuators.....	3-2
Table 3-2. Common Microelectromechanical Actuation Methods.....	3-3
Table 3-3. Advantages and Disadvantages of Electrostatic Actuators	3-8
Table 3-4. Advantages and Disadvantages of Thermal Multi-morph Actuators. ...	3-16
Table 3-5. Selected Coefficients of Thermal Expansion	3-17
Table 3-6. Requirements for New Surface-Micromachined MUMPS Actuator.....	3-20
Table 3-7. Voltage, Current and Power for <i>Poly1-Poly2</i> Thermal Actuators.....	3-49
Table 3-8. Back-Bending Force of <i>Poly1-Poly2</i> Thermal Actuators.....	3-50
Table 3-9. Comparison of Recently Reported Lateral MEMS Actuators.....	3-72
Table 5-1. Minimum Dimensions Fabricated on the MUMPS8 Run.	5-74
Table 6-1. Comparison of MCM Processes	6-17
Table 6-2. Comparison Of The GE HDI And MMS MCM-D Processes	6-21
Table 6-3. MEMS Device Categories On MUMPS And CMOS Test Die.....	6-29
Table 6-4. HDI Sample Materials and Simulated Package Materials.....	6-38
Table 6-5. Baking Procedures For Photoresist Etch Tests.....	6-55
Table 7-1. Applications for Techniques and Devices Developed in This Research. 7-3	

List of Acronyms

ADI	Analog Devices Incorporated, Inc.
ARPA	Advanced Research Projects Agency
BiCMOS	Fabrication process combining bipolar and CMOS electronics
CCR	Corner Cube Retroreflector
CMOS	Complementary metal-oxide semiconductor electronic process
DIW	Deionized water
DLC	Diamond-like coating
DM	Direct metal interconnect technique
DMD™	Digital Micromirror Device
EDP	Ethylene, diamine, pyrocatechol and water; silicon anisotropic etchant
FC	Flip chip die interconnect technique
GE	General Electric corporation
HDI	High Density Interconnect multi-chip module process
IBM	International Business Machines, Inc.
iMEMS™	Integrated MEMS, a process combining MEMS and circuitry
IR	Infrared
LPCVD	Low pressure chemical vapor deposition
MCM	Multi-chip module packaging system
MCM-D,L,C	Different types of MCMs: Deposited, Laminated, Co-fired
MEM	Micro-electro-mechanical
MEMS	Micro-electro-mechanical systems
MMS	Micro Module Systems, Inc.
MOCVD	Metallo-organic chemical vapor deposition
MOEMS	Micro-opto-electro-mechanical systems
MOSIS	MOS Implementation Service
PGA	Pin grid array, an electronic die package
PZT	Lead-zirconate-titanate
LIGA	Lithographie, Galvanoformung, Abformung (lithography, electroplating, molding)
LSM	Large Scale MEMS
MCNC	Microelectronic Corporation of North Carolina
MUMPS	Multi-User MEMS ProcesS
PMMA	Polymethylmethacrylate, deep exposure lithography photoresist
PSG	Phosphosilicate glass
RIE	Reactive ion etching
SAW	Surface acoustic wave
SEM	Scanning electron microscope
TI	Texas Instruments, Inc.
TMAH	Tetra-methyl ammonium hydroxide
WB	Wire-bonding die interconnect technique

Abstract

Microelectromechanical Systems, or 'MEMS' is a broad new field of research into devices that range in size from a few microns to a few millimeters. Much of the technology supporting MEMS research is borrowed from the microelectronics industry; so MEMS holds out the promise of batch fabrication of micro-miniaturized machines that can be easily integrated with electronics. This dissertation research investigated structures and methods for implementing and packaging complex, large scale microelectromechanical devices and systems using commercially available foundry fabrication processes. It specifies methods for creating and packaging large, complex MEM systems, allowing the exploration of new MEMS architectures at a higher level than was previously possible at research institutions with minimal in-house fabrication capabilities. Completely new areas of research were created, including hinged wiring and a class of devices powered by arrays of low voltage, high force thermal actuators. Throughout this dissertation, example applications of these methods are presented, including stepper motors and large optical systems for high density holographic data storage and aberration correction in optical communication systems. The research culminates in the successful creation of the first commercially fabricated multichip module integrating foundry fabricated MEMS and electronic die.

1. Introduction

Microelectromechanical Systems, or 'MEMS' is a broad field of research into devices that range in size from microns to millimeters. Much of the technology supporting MEMS research is borrowed from the microelectronics industry; so the field takes advantage of four decades of broad, well-funded research into the properties of silicon, thin film deposition, photolithography, and all of the related technology behind microelectronic fabrication. Thus MEMS research holds out the promise of batch fabrication of micro-miniaturized machines that can be easily integrated with electronics. Millions of identical copies of systems can be fabricated to enhance or replace their macro-world counterparts, with the goal of furthering the development of mechanical and sensor systems much as integrated microelectronics revolutionized the electronics industry.

In a rough analogy with the history of electronics, MEMS has gone through the 'vacuum tube' stage, with the establishment of the usefulness of the field, and has entered the 'discrete transistor' phase, where single microelectromechanical (MEM) devices with integrated electronics are being commercially produced [1]. This dissertation aims to help MEMS into the 'integrated circuit' stage by creating support systems that allow the creation of large, complex systems of MEM devices and electronics. With so much work being done on single MEM devices, fabrication processes, material characterization, and modeling, there has been much less work published on large assemblages of devices and their requirements.

1.1 MEMS Applications

Micromachining is an enabling technology like other machining technologies, so it does not focus on a particular application, as a field like III-V materials might apply mostly to electronic devices. MEMS are being applied to problems in a wide range of fields, from biomedicine to displays to aerospace sensors. Table 1-1 lists just a few of the MEMS research areas recently published.

Table 1-1. A Sample of Areas of Current MEMS Research.

Research Areas	Applications
Biomedical	drug delivery systems, sensors, implantable and disposable pressure transducers
Aerospace	gyroscopes, accelerometers, airflow control
Displays	infrared displays, high definition television
Computers	holographic data storage, optical data processing
Communication	optical switching and modulation
Optics	interferometers, aberration correction, laser combining, beam steering
Chemistry	mass spectrometers, gas sensors, scanning tunneling and atomic force sensing microscopes
Robotics	microrobotic actuators, tactile feedback sensors and stimulators
Fluidics	pumps, valves, flow rate and pressure sensors, fluidic amplifiers
Mechanics	micromotors, actuators, gears, linkages

Most MEMS research is being carried out using proprietary or otherwise non-commercial fabrication processes. This may always be the case for the MEMS field, since device operation is largely determined by material choices and fabrication methods. But as more processes prove their utility in MEMS applications, they are being offered as foundry services. Foundries make it possible for researchers from diverse fields such as those represented in Table 1-1 to more easily attempt a MEMS

solution to their problems. However, with this ease comes a loss of fabrication flexibility available to those researchers who have intimate control over an in-house fabrication process.

1.1.1 Military Space Cost Savings

The following discussion of the possible savings the Air Force could realize in space systems from advanced packaging research for MEMS is paraphrased from information provided by the sponsoring agency at the U.S. Air Force Phillips Laboratories [2].

Space system launch and operational costs are significantly influenced by the weight/complexity tradeoffs inherent in making space vehicles more autonomous. While launch costs are almost solely determined by size and weight, the ongoing operational costs are determined by the amount of ground control a satellite needs to continue its mission. Complex satellites require a large ground crew, with each member costing approximately \$140K/yr in 1994 dollars. Improving a satellite's autonomy would reduce the size of the operational staff; but the required increase in functionality implies an increase in size, weight and power consumption, all of which increase the launch costs. Launch costs for contemporary space vehicles are listed in Table 1-2.

Table 1-2. Launch Costs of Contemporary Space Vehicles [2].

Launch Vehicle	Max Payload (kg) to Low-Earth Orbit	Unit Cost (FY92 \$M)	Cost/kg (\$K/kg)
Titan	17,900	160	8.9
Atlas	5,700	78	13.7
Shuttle	23,090	210	9.1
Delta	3,909	60	15.3
Pegasus	455	9	19.8

Although the launch cost per kilogram is lower for heavier vehicles, economies of scale favor smaller satellites due to lower overall launch costs. These economies have led the Air Force space community to consider “stepping down” its systems so they can be launched using the smaller, more economical vehicles. In parallel to this Air Force effort, NASA is challenged to develop space systems that are smaller, cheaper and faster. Interplanetary systems, such as the Pluto Fast Flyby, are striving to field long distance satellites for under \$200M, with payloads that are significantly smaller than those used in previous planetary missions.

Table 1-2 illustrates that launch vehicle cost savings due to weight reduction can be dramatic. These savings are multiplied when a constellation of satellites is to be launched. Aerospace consultants have remarked that every pound of weight eliminated from the Brilliant Eyes spacecraft design would result in a \$2M savings. Other examples of commercial projects that would realize similar savings are the Motorola Iridium and the Teledesic programs. Studies performed by the U.S. Air

Force's Phillips Laboratory have indicated that MILSATCOM will save 25% of its launch weight simply by using more advanced microprocessors. Clearly, the miniaturization of sensors and actuators can have a profound impact on the size and weight reduction of unmanned spacecraft.

1.2 Purpose and Impact of this Research on the MEMS Community

This research investigates the design and implementation of complex micro-electro-mechanical devices, with the aim to create some of the devices and techniques that experiments and literature reviews revealed were missing elements which were hindering the development of large systems of devices. More specifically, this research investigates ways in which complex MEM systems can be fabricated through commercially available foundry services. The underlying purpose is to make it easier for other researchers to take full advantage of the possibilities these services offer, to create complex systems both on a single die or as a package containing multiple die.

MEMS foundry services are just now becoming available [1,3] either through government sponsorship or by adapting existing microelectronic fabrication processes [4]. The availability of foundry services allows the researcher to concentrate on the design and implementation of MEMS devices and systems without having to expend resources on specifying the complex details of the fabrication process; a task which has been, and still is, a large part of MEMS research.

This research also goes beyond what can be done with any one foundry process to explore the possibility of combining foundry die fabrication processes with

commercially available multichip module fabrication processes. The ultimate goal is to outline methods whereby a research institution with minimal in-house fabrication capabilities can create and package large, complex systems containing MEM and electronic die. Such a capability would allow the exploration of new MEMS architectures at a higher level than is currently possible. The advantages of such an approach have already been well established in the microelectronics industry, where the availability of foundry fabrication has allowed the investigation of electronic systems and higher level architectures to be carried out at any institution that can meet the extremely modest costs. The Air Force Institute of Technology (AFIT) itself is one of the benefactors of the availability of microelectronic foundry services in its long-established VLSI curriculum.

Successes and inventions made during this dissertation research resulted in methods and devices for the creation of large, complex mechanical systems on single die as well as in multiple die packages. As a result of this continuing research effort, the range of the structures that can be built in one of the foundry processes was extended with techniques that exploit that fabrication process. In addition, new wiring schemes were developed that extend the places to which power and signals can be delivered.

A whole new class of devices was invented: devices powered by arrays of low voltage, high force thermal actuators. These thermal devices can be built in a variety of MEMS fabrication processes, both commercial and private. Large optical systems have been created and delivered to users around the country, where they may prove

the utility of large scale foundry fabricated systems for high density holographic data storage, aberration correction in optical communication systems, and beam combining and steering for laser systems. The devices and systems presented in this dissertation bear out the utility of the concepts developed during this research. The following is a partial list of new concepts developed during this research:

Lateral polysilicon thermal actuators - a variety of devices which provide high forces in a compact structure, at CMOS-compatible circuit voltages and currents,

Hinged wiring - a method for creating low-resistance connections to hinged or other structures not fixed to the substrate,

Latching relays - a design concept for low contact resistance microrelays which isolate the signal path from the drive circuitry and maintain their state with no power,

Flexible yokes for actuator arrays - methods for connecting multiple lateral or vertical actuators, thermal or otherwise, to generate high forces and allow greater control of the direction of force application,

Self-assembling MEMS structures - an approach which makes it possible to assemble complex hinged MEMS devices without hand assembly, opening the way for economical batch fabrication of this class of devices,

Design techniques for surface micromachining processes - methods for expanding the design possibilities in the MUMPS surface micromachined polysilicon foundry fabrication process, which could also be applied to other processes,

Packaging systems - tests were carried out to prove the feasibility of packaging MEMS and electronic die in several packaging processes, creating the capability to create complex hybrid systems from foundry-fabricated MEMS and electronic die, in foundry-fabricated multichip modules.

Some of the specific devices created to prove the utility of these concepts are themselves the first of their kind, or are an improvement over existing devices of their type. These devices include linear and rotary stepper motors, modulating corner-cube retroreflectors, mirror arrays for holographic data storage, aberration correction, beam steering and laser power combining, grippers which overhang the die edge for practical applications, self-assembling hinged plates, and a wide variety of thermal actuators.

1.3 Evolution Of This Research

This research originally was conceived as an exploration of packaging issues. Specifically, could foundry fabricated Multi-Chip Module (MCM) packaging be used to marry electronic die with MEMS die, both also foundry fabricated, to create complex, highly functional microelectromechanical systems? Positive results would point the way for educational institutions and industry to create hybrid MEMS applications without first having to invest in MEMS fabrication facilities.

For the packaging tests, foundry fabricated MEMS die were planned which would have a selection of 'generic' MEM devices to use as test vehicles to see how

they could withstand the rigors of packaging, and how the packaging could withstand the rigors of release-etching the MEMS die. Extensive reading in the field led the author to the conclusion that while there were common MEM sub-structures related to the various fabrication processes, such as released plates on flexural suspensions or cantilevered beams, there were no 'typical' MEM devices. Each application had a different device because, unlike electronics, the form of the device was more closely fixed by the function. In electronics, for example, a NAND gate can be implemented in CMOS, bipolar, GaAs, even vacuum tube and electromechanical relay technologies. In MEMS, a piston mirror is best implemented as a surface-micromachined device, and the same structure just cannot be implemented efficiently with other MEMS fabrication techniques.

Die were still needed for packaging tests, though. After several exploratory fabrication runs, two die were designed and fabricated. Instead of trying to capture all of the possible MEMS structures, they contained a sampling of the types of structures that were being investigated at the Air Force Institute of Technology (AFIT) at the time, plus an assortment of devices designed specifically for testing breakage due to handling.

At this point delays in setting up the CAD tools to do MCM design, repeated poor quality fabrication of the test die, and delays in the fabrication of the MCMs themselves left the author free to continue exploring the possibilities of the available MEMS foundry processes. It was in the course of this extra-curricular research that totally new techniques and structures evolved which have since become the core of

this research effort. In effect, the effort shifted from device research in support of packaging tests, to packaging tests supporting the furtherance of research into large systems of devices.

1.4 Organization of This Document

This document is organized into seven chapters. The first chapter is this introduction, an overview of the research effort: how it developed and the reasons why it was a useful undertaking. The second chapter provides background material for the rest of the dissertation. It explains MEMS fabrication processes, with emphasis on the foundry processes explored for this research. The following chapters describe the research performed, detailing the main contributions and how they fit into the MEMS field.

The third chapter describes various MEMS actuators, the class of devices that allow MEMS to affect their surroundings rather than just passively sense it. It details the development, testing and applications of the thermal actuator developed during this research, and compares it with the other actuators to show how it complements existing capabilities and improves on them. The fourth chapter discusses the wiring techniques developed to enable the design of large systems in the specific foundry fabrication processes used for this research.

The fifth chapter shows how the various new devices and techniques can be brought together to actually create large, complex devices and systems. Examples include stepper motors, hinged structures, and complex optical systems. These

include optical systems which cover an entire die and which have been shipped out to other institutions for integration into their research efforts. These latter systems, and the many publications resulting from this research, show how this dissertation effort has already started to spread its results throughout the MEMS community.

The sixth chapter describes the initial research into multi-chip module packaging, especially the chemical compatibility testing that lays the groundwork for what will be a continuing effort in this area. The chapter ends with two full scale packaging experiments; though because of delays in procuring the packages they represent only preliminary, but fully successful, full scale tests.

Chapter seven wraps up with concluding remarks on the research effort and what it points to as useful follow on efforts. References are listed at the end of each chapter, and because of the many acronyms used in this field a list of them is included at the front of the dissertation.

Appendix A lists the many die and devices that resulted from this research effort. Die plots are shown along with a list of the major devices contained on the die and what their purpose is. Appendix B lists the CAD program technology files and other items created by the author while assisting in the creation the MEMS research infrastructure at AFIT, and in assisting other AFIT students to complete their Master's degrees. Appendix C contains the author's vita and lists the patent applications and publications that resulted from this research effort.

Chapter 1 References:

1. R. Howe, "Polysilicon integrated microsystems: technologies and applications," *Proc. Transducers '95/Eurosensors IX*, Stockholm, Sweden, Vol. 1, pp. 43-46, 25-29 June 1995.
2. J. Lyke, "A brief white paper supporting the case of electronics miniaturization approaches for space systems," Phillips Laboratory Applied Systems Branch, PL/VTEE, Kirtland AFB, NM, 1994.
3. D. Koester, R. Mahedevan and K. Marcus, *Multi-User MEMS Processes (MUMPS) Introduction and Design Rules*, rev. 3, Oct 1994, MCNC MEMS Technology Applications Center, 3021 Cornwallis Road, Research Triangle Park, NC, 27709.
4. J. Marshall, M. Gaitan, M. Zaghloul, D. Novotny, V. Tyree, J. Pi, C. Pina, and W. Hansford, "Realizing Suspended Structures on Chips Fabricated by CMOS Foundry Processes Through the MOSIS Service," U. S. Department of Commerce, National Institute of Standards and Technology, NISTIR 5402, June 1994.

2. MEMS Fabrication

MEMS have been created with a wide variety of manufacturing processes, but all of the processes depend in some way on the photolithography techniques developed for the microelectronics industry to define small structures. Regardless of how they are created, all MEMS are formed from two basic sets of materials - the ones that form the machinery, the 'structural' materials, and the ones that are removed to release the machinery, the 'sacrificial' materials. The various MEMS processes differ in what these materials are and how they are deposited, patterned and removed. Thus micromachining differs from macromachining in that only rarely are piece parts made in different fabrication processes and then joined to create an individual MEM device. One of the promises of micromachining is the possibility of creating entire systems in large volume batch fabrication processes, resulting in a low cost per system, similar to the manufacturing success of the microelectronics field.

This chapter describes some of the common MEMS process categories in general terms; details of specific fabrication processes are available in the references. Next, processes used for this research are discussed, including examples of devices tried in order to become familiar with those processes.

2.1 MEMS Fabrication Process Categories

MEMS processes fall into three basic categories or combinations of those categories: bulk micromachining, surface micromachining, and high aspect ratio micromachining [1]. General characteristics of these categories which are important

to the subsequent explanation of the foundry processes used in this research are explained in this section.

2.1.1 Bulk Silicon Micromachining

Bulk micromachining processes are unique to MEMS fabrication. Since they have no familiar microelectronics counterpart, some details are presented in this section. Bulk etch processes use single silicon crystals as the structural material, and take advantage of the differing etch rates in the different crystal directions to produce the device geometries [2]. So in these processes both the sacrificial and structural materials are the bulk silicon crystal. To explain the bulk etch process further, Miller indices are used to define the crystal planes. The Miller indices are shown in Figure 2-1, and standard orientations of cut silicon wafers are illustrated in Figure 2-2.

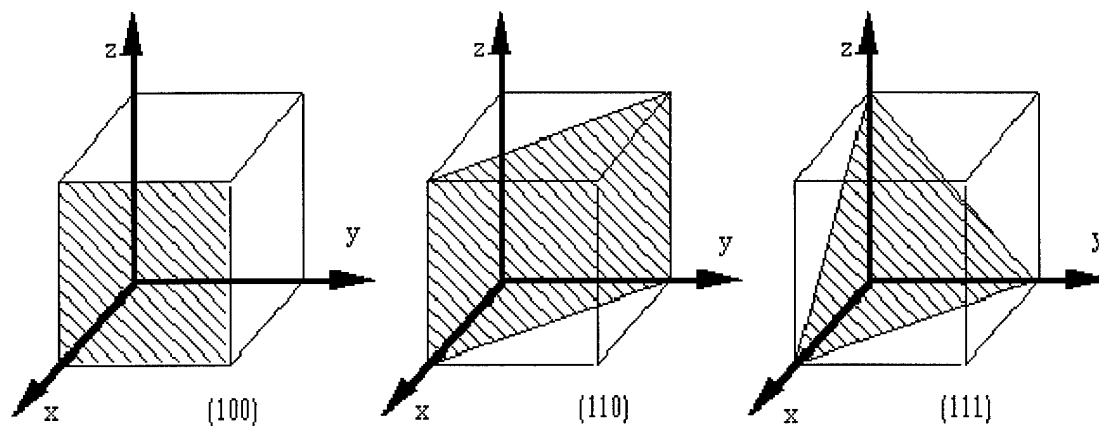


Figure 2-1. Miller indices of cubic crystal planes.

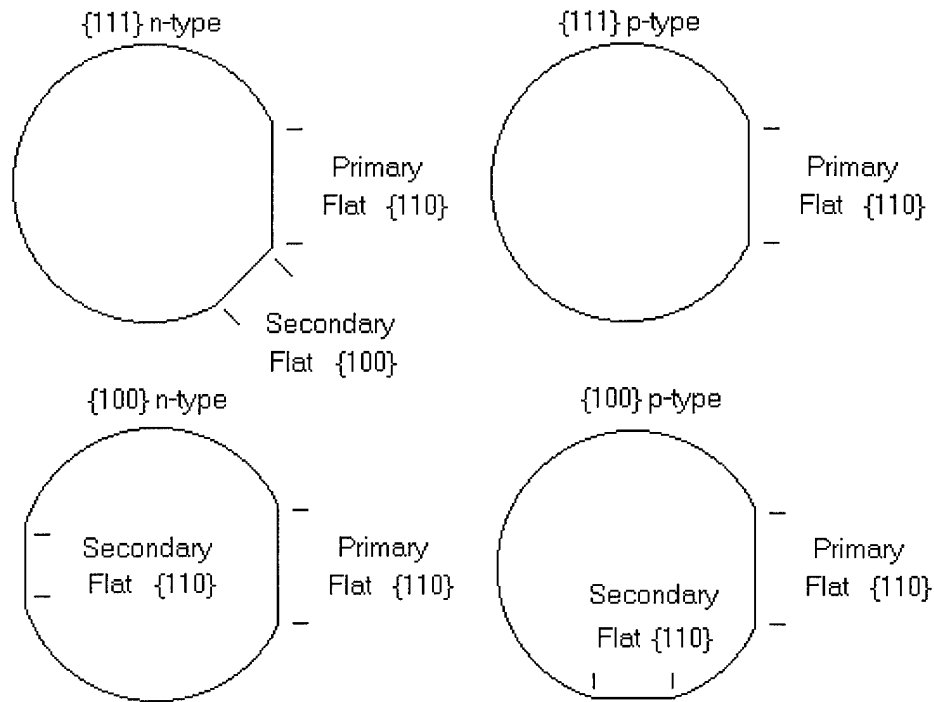


Figure 2-2. Identifying flats of a silicon wafer [after 3].

In microelectronics, etches are performed to open via holes between thin insulating layers for electrical contacts. These films are not crystalline and so the etch proceeds at the same rate in all directions, or isotropically. In single crystal silicon, the atoms are spaced more closely in some crystal directions than others. In particular, the $\langle 111 \rangle$ direction has the least space between atoms, while the $\langle 100 \rangle$ direction has the most space. Anisotropic etching solutions etch along these crystal directions at different rates. Anisotropic etchants include ethylene-diamine pyrochatecol and water (EDP) which etches in the $\langle 100 \rangle$ direction 35 times faster than in the $\langle 111 \rangle$ direction, and potassium hydroxide (KOH) with an etch ratio of 400:1 for the same directions [2]. This selectivity causes the $\{111\}$ planes to act as etch stops while the etch proceeds in other directions.

To form a device feature, the bulk crystal material is covered with a mask layer. This mask pattern forces the final shape of the structure to be revealed as the etch progresses. It is the combination of the mask pattern and the anisotropic etch properties of the bulk material that forms the geometry of the released structure. Because the same bulk material is both the sacrificial and the structural material, and geometries are determined largely by the anisotropic etch properties of the crystal, only a limited number of shapes is possible.

Figure 2-3 illustrates the bulk etch process. In this simple example, a square mask opening is aligned to the $\{110\}$ oriented flat of a $\langle 100 \rangle$ wafer. The etch proceeds in all exposed directions, but fastest in the $\langle 100 \rangle$ direction (straight down). At the boundary of the pit, where four $\{111\}$ planes intersect the four sides of the mask opening, the etching solution cannot get around the edges of the $\{111\}$ planes to reach a faster etching surface, so the etching slows down there, and these $\{111\}$ planes are gradually exposed as the etch proceeds. The etch virtually stops when only those four $\{111\}$ planes are left exposed. Figure 2-3b compares the isotropic etch normally used in microelectronic circuit fabrication with the anisotropic etch used for bulk micromachining, shown in Figure 2-3c.

Thus the combination of square mask opening and anisotropic etch of the crystal planes results in a square inverted pyramidal pit. If the etch is allowed to go to completion, the pit will bottom out into a perfect point. Figure 2-4 shows a series of different sized square mask openings in which the exposed silicon substrate has been

completely etched, leaving only exposed {111} planes. This structure is used to gauge the etch rate in the $\langle 100 \rangle$ direction.

Since there is some slow etching in the $\langle 111 \rangle$ direction, there will be a slight undercutting of the mask edges. To reduce this undercutting, a heavy p-type (boron) diffusion can be placed around the mask opening which further slows down the etch process [4]. Such doping can also be used to define thin structures that are impervious to the etchant and yet are part of the bulk material. In this way membranes or suspended structures can be formed directly in the bulk material instead of in a thin layer of a different material on the surface.

Some of the chemicals used in bulk etches are incompatible with electronic circuitry. KOH is one of the most selective anisotropic etchants for silicon, but it also strongly etches aluminum, the most common conductor used for integrated circuits; so even a brief etch will destroy any exposed aluminum wires or bond pads. EDP etches aluminum slowly, so only a short etch is compatible with CMOS circuitry, but this allows some limited types of MEMS devices to be integrated with standard electronic circuitry.

Another anisotropic silicon etchant is tetra-methyl-ammonium-hydroxide (TMAH). This etchant is compatible with CMOS circuit fabrication processes and is less toxic than EDP. TMAH etches aluminum, but by dissolving silicon in it, the aluminum etch rate can be reduced [5,6]. TMAH was not available for most of this dissertation research effort, but was available for testing against packaging materials and for preliminary etch tests on MEMS die.

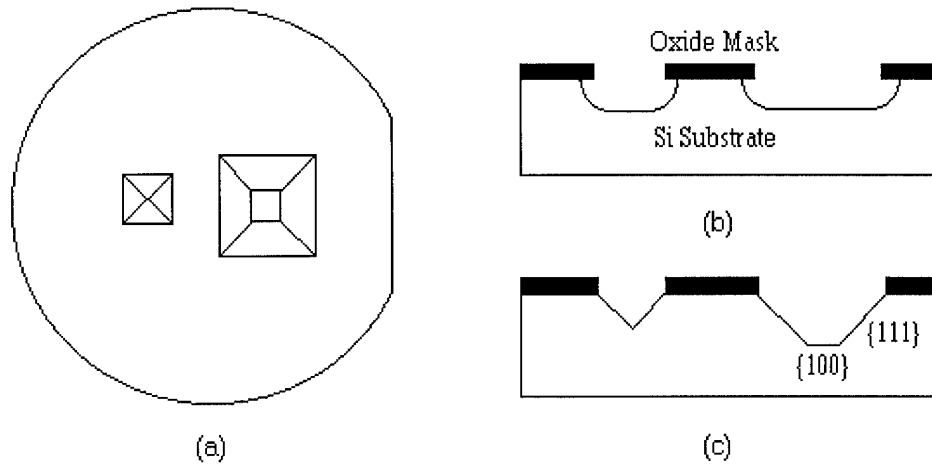


Figure 2-3. Illustration of the differences between isotropic and anisotropic etch of $\{100\}$ silicon wafer with similar masks: (a) mask alignment parallel to the primary wafer flat; (b) profile of isotropic etch; (c) profile of anisotropic etch showing crystal plane directions [7].

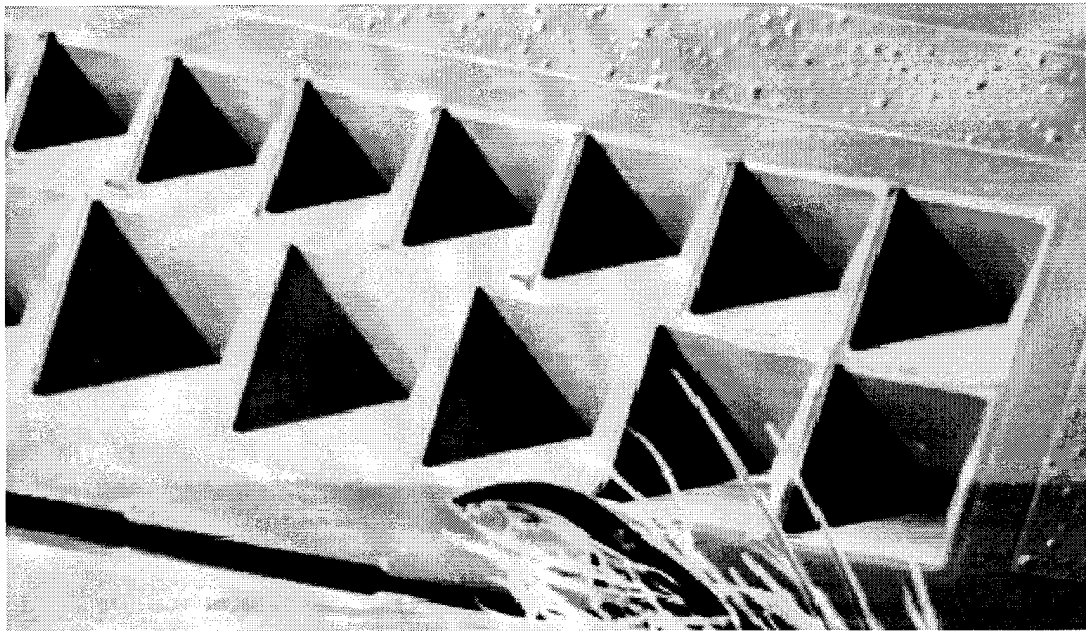


Figure 2-4. SEM micrograph of square pits anisotropically etched into a $\{100\}$ silicon wafer, with the tip of an ant's foot for scale. The largest pit is $55\ \mu\text{m}$ square.

Another fabrication technique often used in conjunction with bulk micromachining is direct wafer bonding. In this process two highly polished surfaces are joined molecularly without adhesives. This allows cavities etched in different wafers to be joined to form more complex structures such as pump or valve chambers. Many of these processes require heat and high electrostatic potentials to form a solid bond. The high temperatures are incompatible with diffused electronic devices. Electrostatic potentials can also destroy the field effect devices used in CMOS circuitry. Wafer bonding thus has limited application for integrating MEMS and electronics together in a single device, so wafer bonding is not used in this research.

2.1.2 Surface Micromachining

This category of MEMS fabrication processes is the one that borrows most heavily from the microelectronic fabrication techniques that have been developed over the past four decades. In this MEMS process thin films of material are deposited, a photoresist is applied, exposed, developed and hardened to pattern the device features, and the unwanted material is removed. The photomask is then removed and the next thin film layer can be applied. Many layers of structural and sacrificial material are built up in this way to produce the final device. After all of the layers are completed, a final release etch is performed which removes the sacrificial material, releasing the remaining structures so they can move freely to perform the 'mechanical' functions of the micro-electro-mechanical device.

There are many variations on this technique using different materials for the structural, sacrificial and masking layers. Each thin film material is chosen for its mechanical or etching properties. In many cases the structural material of one technique is the sacrificial material of another technique. The materials most often used are those also used for microelectronics fabrication. These include polycrystalline silicon (polysilicon or just poly), silicon nitride, silicon dioxide, metals like gold, copper or aluminum, and polyimides. Other materials have been tried, piezoelectric materials, for instance, but the majority of surface micromachined devices use common microelectronic materials because of the low cost and availability of fabrication equipment.

As with the materials, the fabrication equipment is the same as used in the microelectronics industry. Methods for depositing the thin film layers include Metal-Organic Chemical Vapor Deposition (MOCVD), Low Pressure Chemical Vapor Deposition (LPCVD) and sputtering, all of them identical to microelectronic processing. Patterning the deposited films is done by etching, or mask lift-off for metal films. The equipment is often pushed to its limits, however, especially with film thicknesses. Thicker is usually better for surface micromachined MEMS layers; but the deposition and patterning processes take longer and become less controllable. Also, the thicker layers lead to extreme topologies which limits the achievable resolution of the lithography, and can cause coverage problems for successive layers.

Device feature etching falls into two general categories: wet and dry etching. In a wet etch, the etchants selectively dissolve the structural or sacrificial layers as

desired. Often the only control on the progress of the etch is to perform it under environmental conditions where the etch rate is known, and to time the etch to reach the desired profile. Dry etching is typically done by reactive ion etching (RIE), where the material to be removed is bombarded by energetic ions in a reactive gas which then combines with the material and carries it off. RIE is capable of forming straight-walled cuts into the etched material, rather than the rounded features and undercutting of the mask that typically result from a wet etch, as shown in Figure 2-3. Thus RIE is most often the etch used to pattern surface micromachined MEMS, and a wet etch is used for the final sacrificial release.

New release etch methods are being developed to solve one of the most common fabrication problems with surface-micromachined MEMS. The problem is 'stiction', or the collapsing of large, loose structures onto die, where they remain firmly stuck due to electrostatic or Van Der Waals forces between the structure and the die surface, as seen in Figure 2-5. The structures are primarily pulled down by capillary forces as the final etch rinse liquid is evaporated during the drying process. To avoid this, light alcohols like methanol or 2-propanol that have a lower surface tension are used for the final rinse; but processes which avoid evaporative drying altogether are being developed.

In one of these processes, the etchant is displaced with another liquid that can be dry etched or sublimed away, allowing no capillary forces to develop [8]. The latest developments are in surface treatments to prevent stiction even if the structures are pulled down [9, 10]. A final method for preventing stiction is to form small bumps or

'dimples' on the bottom sides of the released structures to reduce the surface area and thus the Van Der Waals forces, so that the restoring spring force of the bent structure is sufficient to pull it off the substrate.

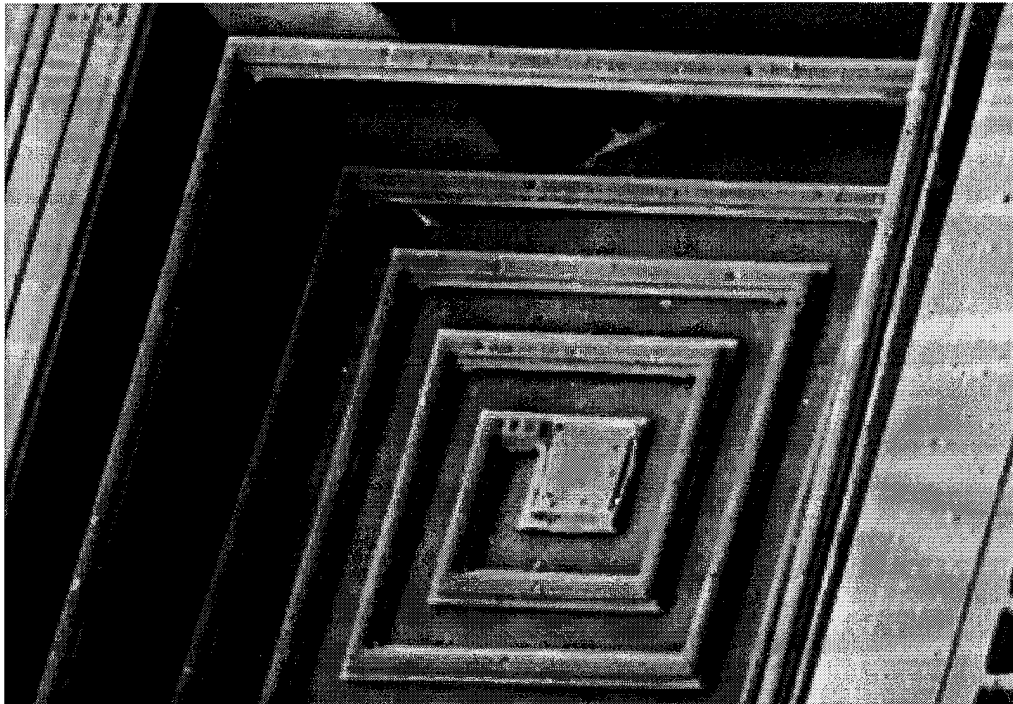


Figure 2-5. Stiction holding a large surface-micromachined spiral down in a bulk-etched silicon pit. The pit is 300 μm across.

A common feature of surface micromachined devices is their flatness, similar to microelectronic circuits. The structural layers are never more than a few microns thick. This is the result of a fabrication process that descends directly from microelectronic processes, where the ability to photolithograph ever finer features is more important than making the structures thicker. Two surface micromachined polysilicon devices are shown in Figure 2-6 and Figure 2-7. These examples show

the general look of surface micromachined devices with their thin layers and extreme topologies.

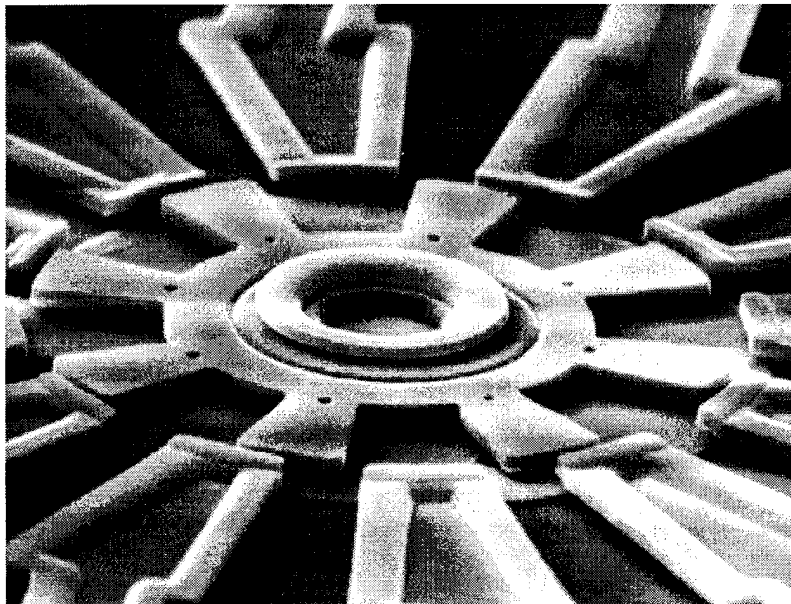


Figure 2-6. Example of surface micromachined polysilicon electrostatic motor, rotor diameter is $100\ \mu\text{m}$ [11].

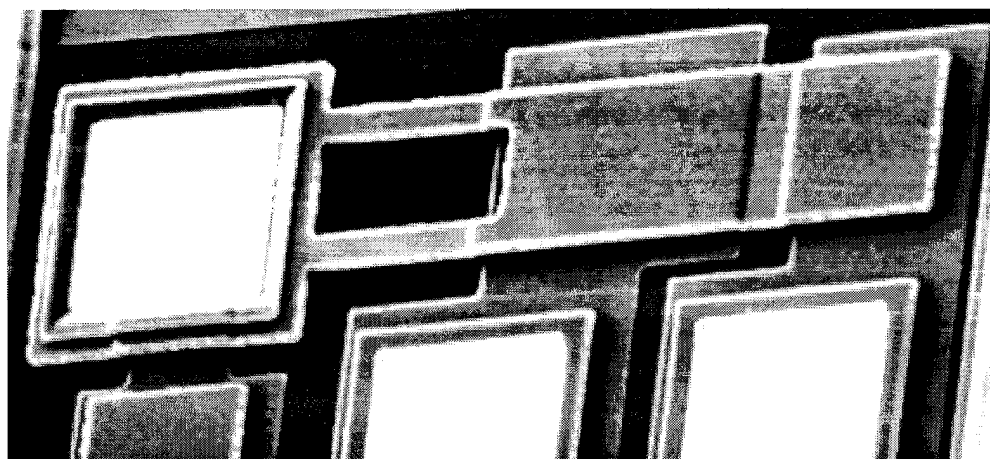


Figure 2-7. Example of surface micromachined $25 \times 100\ \mu\text{m}$ polysilicon cantilever.

Since the surface micromachining fabrication methods mentioned so far are the same as those used in microelectronics, it would seem that integrating MEMS and electronics should pose few problems. But in microelectronics, the structures remain embedded in passivation layers, the same layers that are etched away when releasing some MEMS structures. Embedded like this, the microelectronic structures are not distorted by the residual stress gradient inherent in vapor-deposited layers. An important fabrication step usually required in thin film MEMS processes is a high temperature anneal to remove this stress gradient. If the structural layers are not annealed, the stress gradient will cause them to curl once the sacrificial layers are removed.

Figure 2-8 shows curling of this type caused by the residual stress in released, non-annealed cantilevers. Unfortunately, the temperatures needed for the anneal step are too high for standard semiconductor devices to survive. This is often true of the polysilicon based MEMS processes, where anneal temperatures of up to 1100°C are used [12]. At these temperatures, the carefully planned doping profiles needed for efficient active semiconductor devices are diffused away.

Despite these incompatibilities, compromises can be made to allow the fabrication of both MEMS and electronic devices on the same die. Usually this involves using a lower anneal temperature that does not completely relieve the stress. Perhaps the most sophisticated of these processes is 'iMEMSTM' commercialized by Analog Devices Incorporated (ADI). In the iMEMSTM process, polysilicon MEMS structures can be fabricated on the same die with BiCMOS (bipolar and CMOS)

devices [13]. This makes the process complex, however, and the MEM structures are restricted to a small, isolated area on the die.

The *iMEMS*[™] process is currently limited to two polysilicon MEMS layers, so the types of micromachined devices which can be realized are limited. ADI has commercialized their process, and MEMS accelerometers containing all of the control, process and interface circuitry on the same die are now on the market [14]. ADI also offers the process as a foundry service [15].

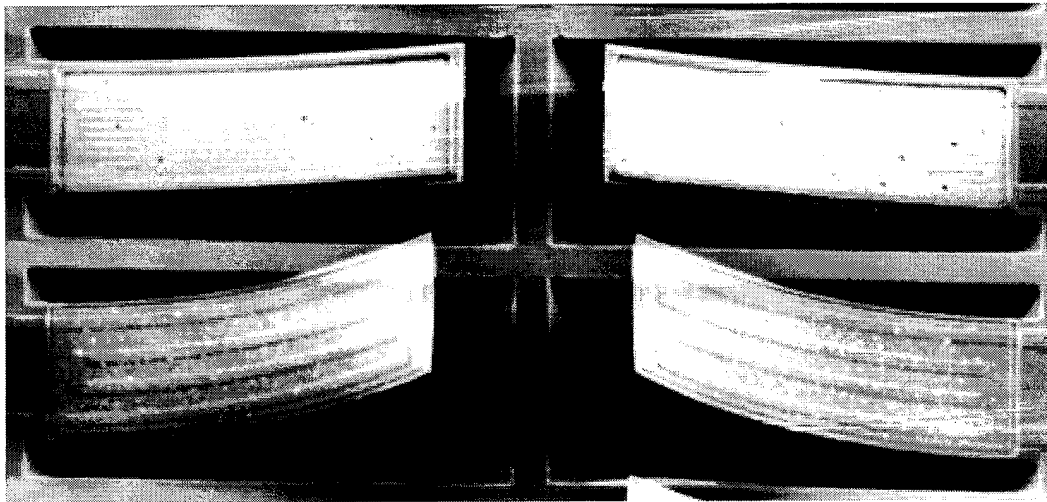


Figure 2-8. Curling of surface micromachined cantilevers caused by residual stress gradients in the thin film layers.

2.1.3 High Aspect Ratio Microstructures

MEMS devices can be fabricated in metal using batch processes instead of conventional machining. These processes use electroplating to build up thick metal structural layers, and several different methods have been tried [16,17,18]. Because

electroplating can build material up much faster than the thin film deposition processes mentioned above, it is practical to reach thicknesses over 200 μm , depending on the lithography techniques used.

A typical electroplated MEMS process starts with a metal plating base sputtered onto an insulating substrate or sacrificial layer. A photoresist or other polymer layer is then applied whose thickness depends on the imaging depth possible with the exposure source. After exposure, the photomask is developed and cured, leaving open pits with metallic bottoms. These pits are then filled with electroplated metal. After the photomask is removed, the metal structures can be used as they are, or they can be released by removing the sacrificial material underneath.

A major difference between the electroplated MEMS fabrication processes is the method used to expose the photoresist. Some processes use ultraviolet (UV) energy to achieve deep exposures, up to 50 μm , in thick photoresist layers. However, they do not require the specialized equipment like a synchrotron or X-ray masks; they can be carried out using common cleanroom facilities [17].

In the LIGA process (LIGA is a German acronym for lithography, electroplating and molding) the photoresist is exposed to synchrotron X-ray radiation. This is a high-energy photon source which allows very deep exposure of the photoresist. LIGA process therefore allows metal thicknesses over 300 μm [19]. The photosensitive polyimide resists used in these electroplating processes allow sharp sidewall formation, as can be seen in Figure 2-9 and Figure 2-10.

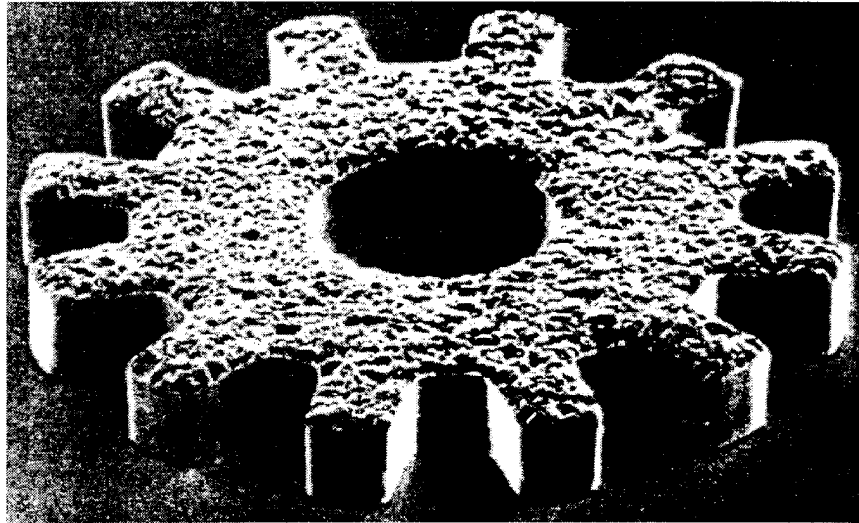


Figure 2-9. Copper gear made in a deep UV exposure and wet electroplating process; the gear is 300 μm in diameter and 45 μm thick [17].

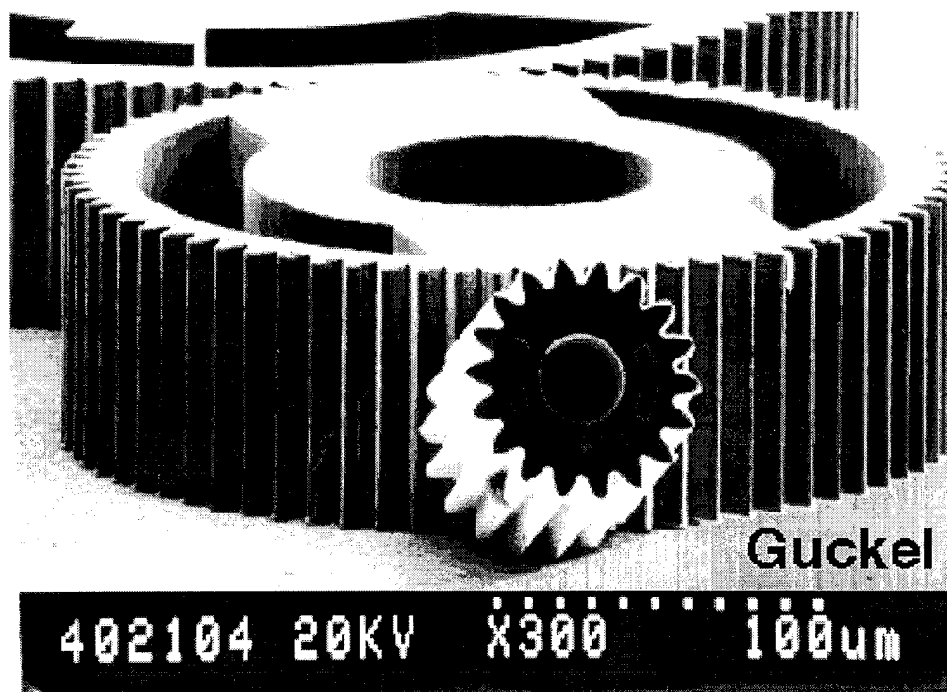


Figure 2-10. Nickel gears made in the LIGA process [20].

2.2 Process Selection

The three foundry processes used in this research were selected on the basis of capability, availability and cost. Foundry processes were required for this research, as AFIT lacks the fabrication equipment necessary to make a complete MEMS die. Versions of each of the three basic MEMS processes described above are available through foundries. At the start of this research there were four processes accessible from AFIT. The Microelectronic Corporation of North Carolina (MCNC) offered a LIGA process through the University of Wisconsin, and also offered the Multi-User MEMS ProcesS (MUMPS), a surface-micromachined polysilicon process. The MOS Implementation Service (MOSIS) offered a CMOS MEMS process from the Orbit foundry. This process had been modified to allow a limited class of bulk-etched MEMS devices to be fabricated in a post-fabrication etch [4]. Also available was the *iMEMS*[™] process mentioned in the previous section.

The CMOS MEMS process was originally considered for in-depth investigation, and some preliminary test die were delivered; but the funding for all MOSIS contracts was suddenly withdrawn by ARPA, leaving no funds for fabrication. Fabrication and etching problems also caused many of the CMOS MEMS devices to fail. Even when the CMOS devices were usable, the restrictions imposed on MEMS device design made the process of limited interest.

The MUMPS process had been used three times when the process choices were made. It had proven to be a reliable and functional process. It was also the least expensive, and the one most representative of the majority of MEMS research being

published at the time. It became the main process used throughout this research. The fact that the MUMPS process is not compatible with electronics made it the driving technology for integrated system development via higher level packaging.

The LIGA process was also offered only once, due to delays caused by a change in the metallurgy, which required development of new polishing techniques [21]. At the beginning of this research the process was not considered for full exploration, since the questions of delivery timeliness and device functionality could not be assessed. It turned out that this forecast was accurate; only one LIGA run was completed, and none have been run since. However, the LIGA process is unique to MEMS, so it received some consideration, especially since it offers metal-on-metal electrical contacts for relays, an advantage that makes it a desirable process to investigate for systems such as micro-switching arrays.

The iMEMSTM process seems to be a good solution for small integrated systems, but the foundry offered to deliver only prepackaged die, and only four of them per die site. The die sites are also expensive, at \$5K per site. So even if unpackaged die could be obtained, the low number of total die made this process uneconomical for the purposes of this research. Surface micromachined MEMS processes were better represented by MUMPS, and any circuitry die needed could be fabricated through MOSIS. For these reasons the iMEMSTM process was not used. In fact, it was the limitations of combined processes such as iMEMSTM that led to this research, to enable the creation of larger integrated systems.

So although three processes were investigated, only the MUMPS process was fully exploited. Devices from the LIGA and CMOS MEMS processes are presented as they relate to the main topic of each chapter as comparison points.

2.3 Foundry Fabrication Processes and Example Devices

This section describes the three selected fabrication processes and shows examples of test structures to illustrate their capabilities. Most current MEMS research is carried out using proprietary, noncommercial fabrication processes. This may always be the case in the MEMS field, since device operation is largely determined by material choices and fabrication methods. But foundry processes are gaining acceptance in the MEMS research community, as evidenced by the growing number of foundry services being offered.

Foundries make it possible for researchers in diverse fields to attempt a MEMS solution to their problems without having to immerse themselves in the details of the fabrication. However, with this ease of use comes a loss of some design flexibility, since foundry processes are offered to researchers who must use them as defined by the manufacturer. Projects are gathered from the users and combined in a single fabrication run. This keeps the cost low for the researchers since they do not have to buy and maintain fabrication equipment of their own. The tradeoff is that they must work within the confines of the process and design rules. This research shows that these restrictions can be a source of creativity as the designer tries to create structures that are not explicitly allowed for in the published design rules.

2.3.1 CMOS-Based MEMS

The availability of a standard process for creating CMOS-compatible MEMS structures [4] allows researchers who do not have access to an in-house fabrication facility to fabricate and to take advantage of micromachined suspended structures. Two of the most desirable properties of suspended structures are thermal and electrical isolation from the substrate. Thermal isolation allows a resistively heated structure to be brought to incandescence with a relatively small current [22]. A similar non-suspended heater would not be able to reach the same operating temperatures since the substrate would act as a heat sink. Suspended inductors decrease the capacitance of the metal lines to the substrate which allows higher frequencies of operation with lower losses [23]. MOSIS offers a CMOS MEMS fabrication capability from the Orbit foundry.

CMOS MEMS is a combination of the bulk and surface micromachining techniques described in Section 2.1. Surface micromachining is used to pattern the CMOS circuitry as usual, and is also used to pattern the glass layers to form a mask for a bulk etching step. The final anisotropic bulk etching step is performed at AFIT on the completed chips. The glass mask itself becomes the suspended structure, and encased in that glass can be any of the CMOS thin film layers. All of the CMOS circuit layers (except aluminum) must remain enclosed in the glass insulating layers; otherwise the EDP used for the anisotropic bulk etch will attack them.

The Orbit CMOS MEMS process starts with a standard two micron CMOS process. This process has two metal and two polysilicon layers, to which are added

two new drawing layers called OPEN and PSTOP. These are not actually new fabrication steps, but instead are combinations of existing steps that produce new features.

The OPEN layer is used to cut a hole through all of the oxide layers down to the bare silicon. In a normal CMOS process oxide layers are deposited between the wafer surface and each of the polysilicon and the metal layers to provide electrical isolation. When connections between wiring layers are needed, the oxide is masked and a hole is etched to make a via. The OPEN 'layer' merely specifies that all of these cuts be made above one another, which exposes the wafer surface. The PSTOP is merely a re-named boron doping step, of the type normally used to create diffusion resistors. Figure 2-11 shows how the OPEN and PSTOP layers are drawn to form a suspended cantilever.

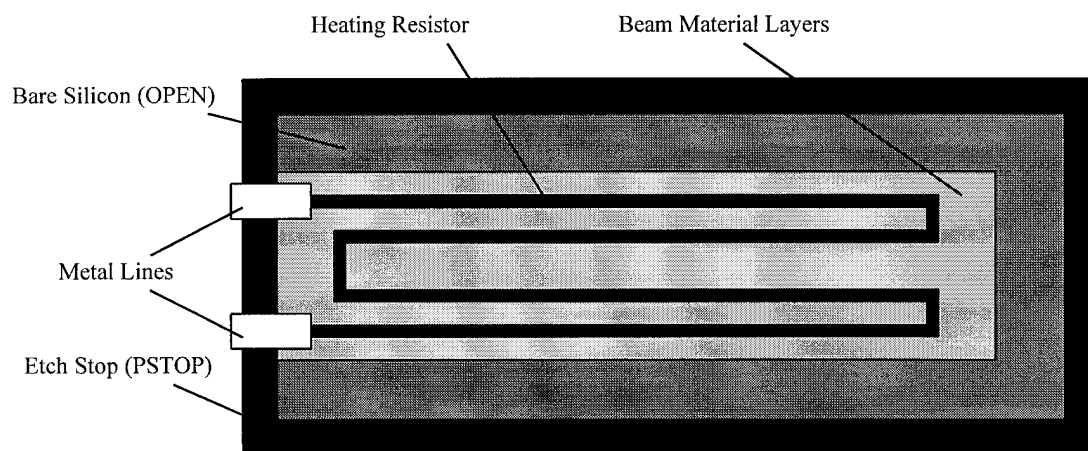


Figure 2-11. Mask layout for a suspended cantilever designed in a CMOS MEMS process [24].

Recall from Section 2.1.1 that the anisotropic etch stops on $\{111\}$ crystal planes, or at a diffused p-type etch stop. This means that any part of the mask that does not form a right angle aligned with the $\{110\}$ wafer flat will be undercut until a final $\{111\}$ plane is reached which does not have an exposed edge at the surface. It is this undercutting which leaves the glass masking structures suspended. Regardless of the shape of the drawn OPEN area, if the etch is allowed to go to completion, the result will be a rectangular, pyramidal pit with a perimeter that just encloses the outside perimeter of the OPEN area. There will be a small amount of undercut at these borders due to the finite etch rate in the $\langle 111 \rangle$ directions. Figure 2-12 and Figure 2-13 show how undercutting results in a suspended structure.

Figure 2-12 is an optical micrograph of incompletely released cantilevers. The light reflects back into the microscope where the silicon is not fully etched from under the cantilever. The bottom of the pit also reflects the light, showing less distinct spots through the glass of the cantilever. Light striking the side walls of the pit is reflected away from the microscope lens. The area left to be etched is clearly outlined by the contrast in the image.

Figure 2-13 shows the cantilevers of Figure 2-12 broken away to clearly show the progress of the etch as it undercuts them. If the etch were allowed to go to completion, the pits would continue to etch down to pyramidal-shaped trenches, and the cantilevers would be completely released.

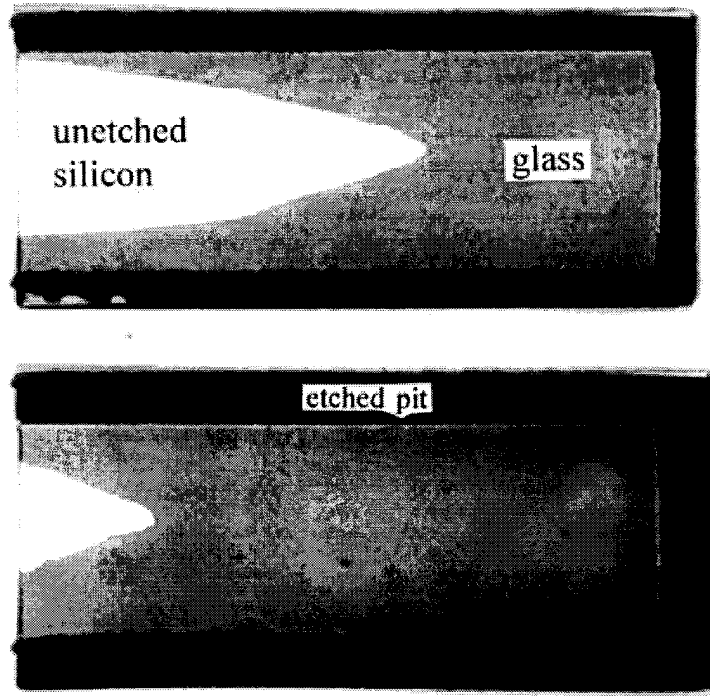


Figure 2-12. Optical micrograph of incompletely released 300 μm long, 100 μm wide glass cantilevers. Light areas are unetched silicon under the cantilevers [25].



Figure 2-13. SEM micrograph of the cantilevers shown in Figure 2-12, broken away to show the progress of the etch under the cantilevers.

While a CMOS-based process obviously allows MEMS and electronics to be fabricated on the same die, the compromises to allow this combination are all made on the MEMS side. Only a few varieties of moving structures can be designed; most of the devices reported on to date involve static structures that take advantage of the thermal and electrical isolation made possible by suspending devices over the bulk etched pit [26, 27]. Vertical and lateral motion is possible by employing the different thermal expansion rates of the structural materials. Example actuators are described in Section 2.3.1.3.

The following devices were designed, built and tested in the course of becoming familiar with the CMOS MEMS process. They are a combination of proven devices and new designs. Test die and lists of the devices on them are listed in Appendix A. Figure 2-14 shows one of the CMOS MEMS test die, 'Testchip3'. A few devices from this and other CMOS MEMS die are described in the following sections to give a general feel for what the process is capable of producing.

2.3.1.1 Etch Gauges

Figure 2-15 shows part of an etch gauge consisting of a set of squares of different sizes. This cell was designed to determine the rate the EDP would etch the bulk CMOS die. The published values for EDP etch rate were for etches performed at 115°C [4]. For safety reasons it was decided that the EDP etches would be performed in a double-boiler setup, so that a known temperature could be maintained even with the inaccurate controls of a standard laboratory hotplate, and there would be no

danger of overheating the etching mixture as long as there was water in the double boiler. Boiling water surrounding the reflux container maintained a constant temperature of around 95°C for the etch. The double boiler reflux container setup is described in Appendix B.

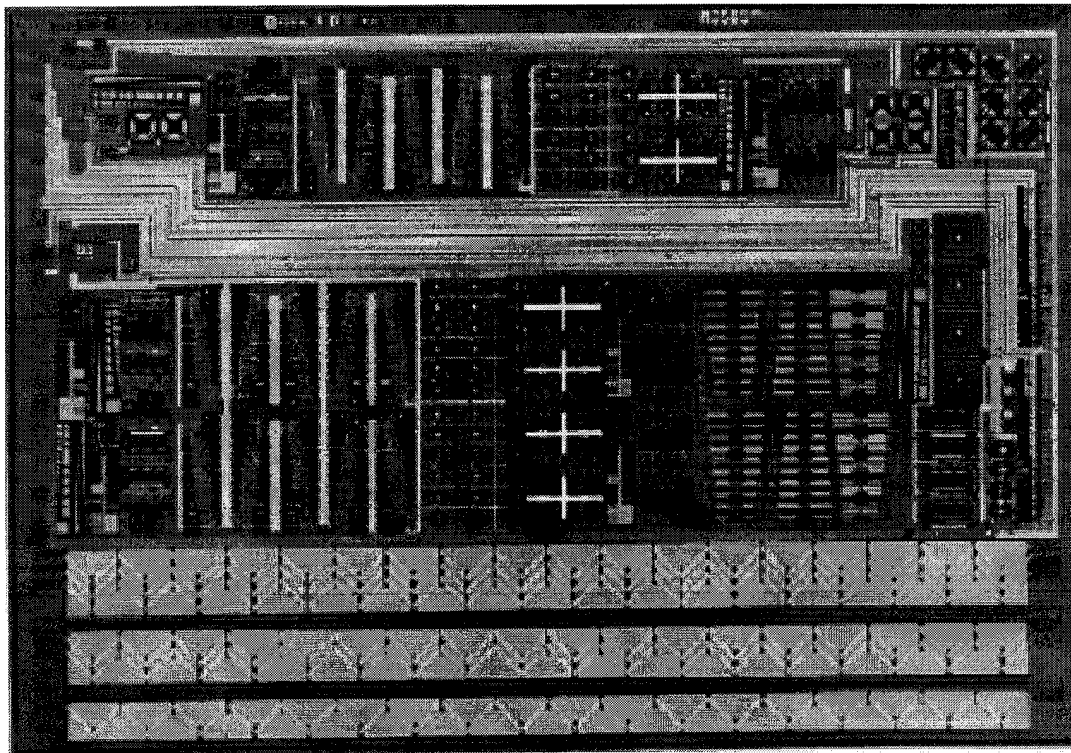


Figure 2-14. Photomicrograph of the a CMOS MEMS test die, 'Testchip3'. The die dimensions are 4.3 x 6.8 mm.

In this etch gauge, all of the pits will etch into the wafer at the same rate, so the pits with smaller openings will bottom out first. This is easily observed under even low magnification, due to the high reflectivity of the bottoms of the incompletely etched pits. The high reflectivity allows the gauge to be read even while the chip is covered with rinse water. Under the optical inspection microscope, the incompletely

etched pits have a white dot in the center due to light reflecting straight back into the microscope from the flat bottom of the pit. Completely etched pits appear dark, since the light reflects off the sloped walls and away from the microscope lens. This eliminates the need to go through the alcohol rinse and drying phase every time the gauge is to be read, and reduces the risk of collapsing delicate structures.

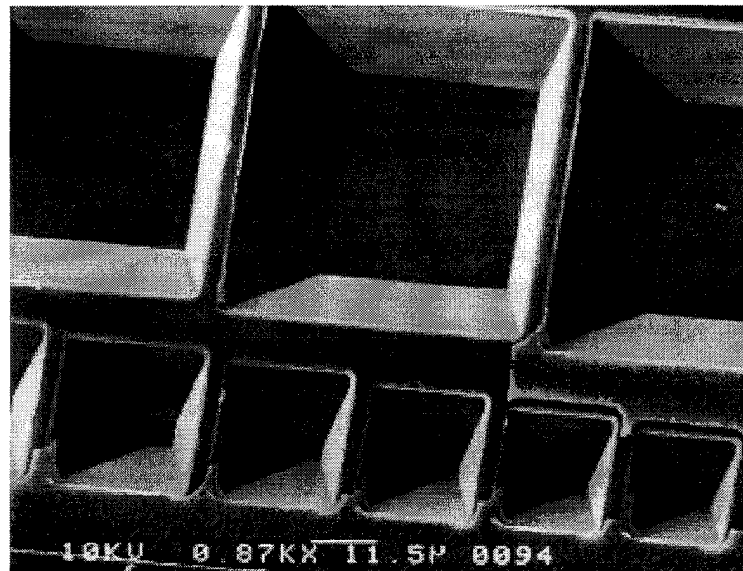


Figure 2-15. Portion of a CMOS MEMS open square etch gauge. Incompletely etched squares have flat bottoms. The large square at the center top is 61 μm wide.

This gauge can be used to determine the etch rate, but it does not make a good etch progress monitor for suspended devices. The reason is that an uncovered pit will etch more evenly than a similar sized pit under a suspended device, since the pillar of silicon under the device cannot be etched from the top. To monitor the etch of a specific suspended device a new method was developed.

A device-specific etch gauge consists of just the glass part of the device, i.e. the same open area patterns are laid out, but no circuit elements are drawn on the suspended glass. As the silicon etches under the gauge, the progress of the etch can be seen through the glass. Figure 2-12 is an example of a device-specific etch gauge used for cantilever-based devices. In that photo, the unetched silicon appears as light colored triangles under the glass, while the etched areas appear dark, as can be seen in a comparison with Figure 2-13, an SEM micrograph of the same pair of devices.

2.3.1.2 Suspended Heating Resistors

This category of device is one of the most common for MOSIS CMOS MEMS devices [26, 27]. To realize a suspended heater, the OPEN areas are defined so that as the pits etch they will overlap and join together. The result is a larger pit whose outer perimeter just encloses all of the constituent pits. Figure 2-16 shows the most basic suspended heater device. This device consists of a polysilicon meander resistor encased in glass and suspended over a large pit. A glass square left suspended by a similar arrangement with four open areas is termed a "trampoline" [4].

The suspended heating element is thermally isolated from the substrate, so a current of a few tens of milliamperes is sufficient to make the resistor glow yellow hot; although such thermal output cannot be sustained for long before the resistor burns out. Infrared (IR) displays use arrays of similar heat sources as pixels to generate a thermal scene [27]. For IR displays the device does not need to be heated as much, so it will last much longer.

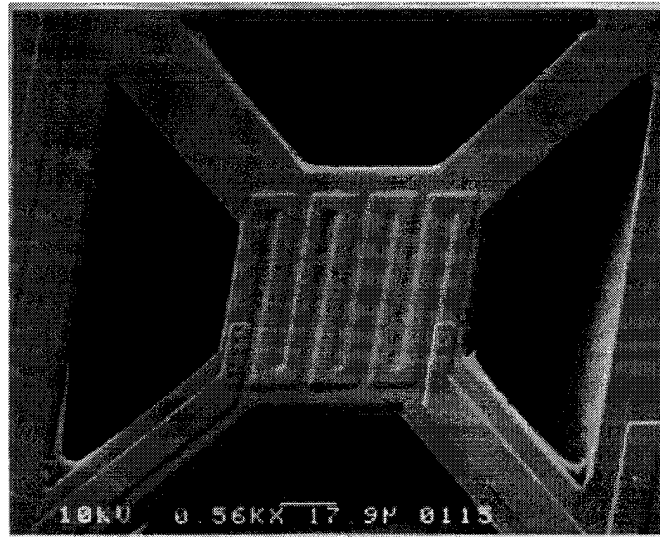


Figure 2-16. Suspended heating resistor, suspended square is 60 μm across.

2.3.1.3 Thermal Actuators

The layout of a suspended cantilever actuator design is shown in Figure 2-11. If the device is drawn with layers of polysilicon (levels 1 or 2) and metal (levels 1 or 2) in the glass, it is possible to cause the cantilever to bend by heating it. A polysilicon resistor heats the structure, and the different coefficients of thermal expansion for the metal, polysilicon, and glass cause the lever to curl. Cantilevered thermal actuators of this design are shown in Figure 2-8. These structures have been studied extensively at AFIT [24,28]. Figure 2-17 shows arrays of heat actuated cantilevers. The initial curl of the released cantilevers is caused primarily by the stress gradient of the second metal layer.

Limited lateral motion can also be thermally produced in CMOS MEMS structures like the spiral shown stuck down in Figure 2-5. In that actuator, thermal

expansion causes the spiral to unwind slightly, allowing controlled positioning of the central plate.

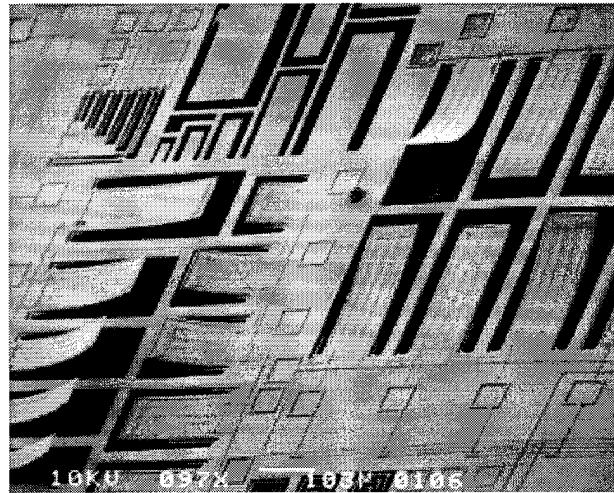


Figure 2-17. Arrays of heat actuated multimorph cantilevers. Cantilevers at the center right are $350 \times 100 \mu\text{m}$ [24]. The array at the top center is a device-based etch gauge.

2.3.2 MUMPS

Many devices were tried in each of the three processes described in this chapter, but the largest variety was done in MUMPS. MUMPS is an ARPA-sponsored foundry process specifically intended to provide an inexpensive alternative to custom MEMS processes; this encourages the designer to try many different ideas due to the low cost [29]. The intention is that the process should be cheap enough and fabrication runs scheduled often enough so a researcher can go through several design cycles quickly. This makes it economical to try a variety of ideas, and provides more opportunities to refine a working idea and characterize the results.

The MUMPS die are 1 cm^2 , and MCNC delivers 15 die per die site. MUMPS is not intended to be a production process, but it is representative of the broad class of surface micromachining polysilicon processes in which a large portion of current MEMS research is being carried out.

In keeping with this philosophy, over 250 MUMPS devices were designed in the course of this research. Some of them were intended only as one-time tests of fabrication layer interactions, and others were discarded as not feasible, as familiarity with the properties and limitations of the MUMPS process increased.

Figure 2-18 depicts the ordering of the MUMPS layers, drawn roughly to scale, showing that MUMPS is a 3 layer polysilicon surface micromachining MEMS process. This is sometimes referred to as a '2.5' layer process, since the lowest polysilicon layer is not releasable. Fabrication starts with a heavily n-doped ($\approx 10^{22}/\text{cm}^3$) $\langle 100 \rangle$ silicon wafer, which forms a conductive ground plane to prevent charge build-up or 'charge mirroring' under electrostatically operated devices. MEMS devices are insulated from the wafer with a $0.6\text{ }\mu\text{m}$ silicon nitride layer, deposited by LPCVD.

The structural polysilicon, or '*poly*' layers, and sacrificial phosphosilicate glass (PSG), or '*oxide*' layers, are deposited over the entire wafer by LPCVD. The layers are individually patterned, and unwanted material is removed by RIE before the next layer is deposited. The poly layers are annealed at 1100°C to relieve stress and to make them more conductive by diffusing in phosphorus from the surrounding oxide layers. The high temperature anneals result in very low stress poly layers with

excellent mechanical properties. An important intermediate step is the formation of dimples by a timed etch which cuts $0.75\text{ }\mu\text{m}$ into the $2\text{ }\mu\text{m}$ thick oxide layer. Subsequent layers of poly will follow the topology of the dimple, forming bumps on the underside of the poly structures which help prevent stiction.

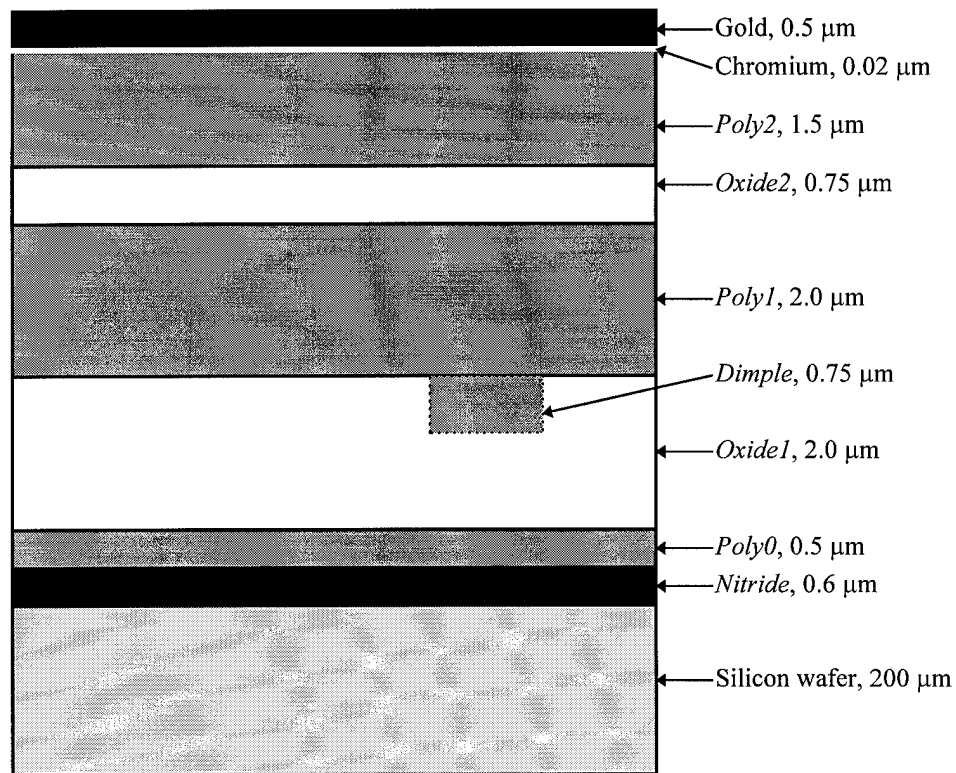


Figure 2-18. Materials and layer thicknesses of the MUMPS process. Layers are drawn roughly to scale, based on the target layer thicknesses. The topology caused by the dimple is not shown here.

Because of the high temperature processing, the Cr/Au metal layers must be deposited last (the chromium is an adhesion layer). The metal layer features are formed by patterned lift-off: a photoresist layer is deposited and patterned, then metal

is sputtered over the entire die. When the photoresist is dissolved, it carries off the metal not attached to other layers.

The releasable polysilicon layers (*poly1* and *poly2*) can be anchored to the silicon nitride, or just *nitride*, by anchor holes cut with RIE through the underlying glass layers before the poly is deposited. These anchor holes are visible in the SEM micrographs as dips in the poly surfaces where the poly has conformed to the topology of the underlying layers. The lowest polysilicon layer, *poly0*, is non-releasable and is used for local wiring and lower electrodes of electrostatically actuated devices. Material thicknesses and properties from the Tenth MUMPS fabrication run are listed in Table 2-1.

Table 2-1. Manufacturer's Reported Properties of Materials from the Tenth MUMPS Fabrication Run.

Material Layer	Thickness (μm)	Stress (MPa)	Resistivity (Ωcm)
poly0	0.4944	1 compressive	1.6×10^{-3}
poly1	1.9720	6 compressive	2.5×10^{-3}
poly2	1.4825	5 compressive	3.3×10^{-3}
metal (Cr/Au)	0.5215	24 tensile	2.96×10^{-6}
silicon nitride	0.5898	37 tensile	-
oxide 1	1.9159	-	-
oxide 2	0.7565	-	-

Figure 2-19 shows a simple device consisting of a metallized mirror with one flexure, anchored to one support post. Note that this design does not use the *poly1* layer, which would be located between the two oxide layers. Figure 2-19a shows a cross-section of the device prior to metallization. After fabrication, the sacrificial oxide layers are etched away with hydrofluoric acid to release the structural poly

layers. Figure 2-19b shows the final structure after the sacrificial material has been removed. Not shown is the topology induced in the *poly2* by the underlying *poly0*.

During RIE etches, the ambient atmosphere in the etching chamber is chosen to specifically etch only the desired layer, and other materials act as etch stops. So when cutting the features into the polysilicon layers, the underlying *nitride* or oxide layers act as etch stops. But there is still some finite cutting into the underlying layers, so the etch is timed to just cut through the thickness of the desired layer, plus some over-etch time to prevent stringer formation in the inside corners, where etching is slower.

MUMPS provides a different mask for the three possible combinations of RIE cuts through the two oxide layers. To cut through the thicker *oxide1* layer there is the *anchor1* mask, so-called because such a cut will result in the overlying *poly1* touching the underlying *poly0* or *nitride*, thus anchoring the *poly1* to the substrate. The *oxide2* layer is patterned using the *poly1-poly2-via* mask, the name is shortened hereafter to just *via*. This etch is timed to only cut through the thinner *oxide2*, and is not guaranteed to cut through both oxide layers.

The *anchor2* cut is timed to cut through both oxide layers at the same time. When the *poly2* layer is deposited over an *anchor2* cut, it conforms to the topology, leaving the *poly2* anchored to the underlying *poly0* or *nitride*, as illustrated in Figure 2-19. The *anchor2* cut will not cut through any intervening *poly1*, though the etch is long enough to partially erode the *poly1*.

Though it may seem possible to replace the *anchor2* cut with a combination of *anchor1* and *via* cuts, this is not recommended because the over-etch needed to

prevent stringers will erode the underlying *nitride* or *poly0*. Two exposures to an etch will completely remove either of those two thin layers. Also, the masks are not guaranteed to be aligned perfectly.

One limitation of this process is that the metal can only be reliably deposited on the uppermost polysilicon layer. This makes running wires more of a challenge since any cross-overs must be built as bridges, and the wire going under the bridge can have no metallization near the bridge. Thus wiring large arrays is difficult and less area efficient than typical metal runs in microelectronic processes.

The polysilicon elements are released in a two minute etch with undiluted (49%) hydrofluoric acid which dissolves the sacrificial PSG layers. Etch holes must be provided for the etchant to undercut large surfaces, so any released structure wider than 80 μm must have holes in it.

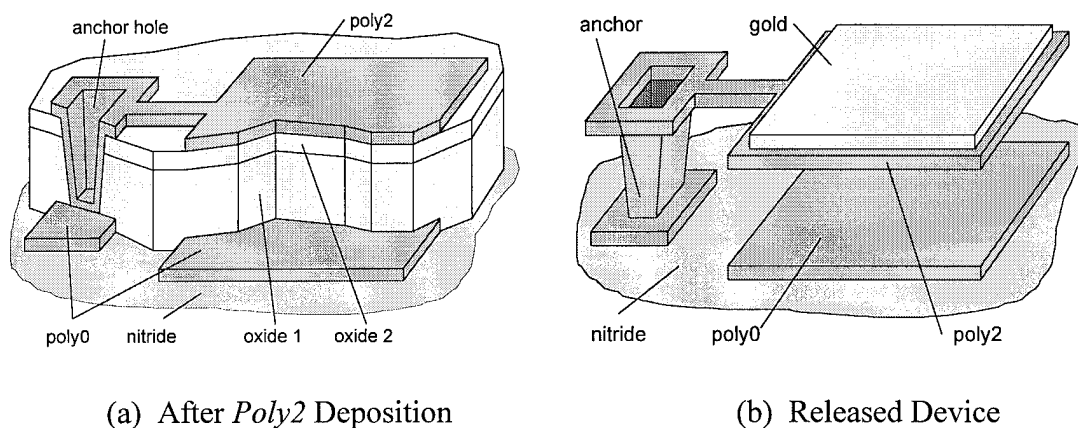


Figure 2-19. Illustration of a simple electrostatically actuated cantilever micromirror device [30]. Thicknesses of the layers and the induced topology are not shown to scale. Note that the MUMPS *poly1* layer, which would be between the oxide layers, is not used in this device.

Thin film layers conform closely to the topology of the previously deposited and patterned layers, so they are not necessarily flat. Unless the designer makes sure a layer is flat where they expect it to be flat by controlling the pattern of the layers beneath it, the induced topology can have detrimental effects on the layer's uniformity, and mechanical properties such as its effective elastic modulus. In extreme cases the topology can trap part of a structure that was intended to move freely.

The MUMPS process is in many ways complementary to the CMOS process. In the CMOS process all of the device elements are encased in glass, thus insulated from each other; this makes it difficult to form MEMS devices such as relays. In the MUMPS process nothing is encapsulated; all of the device elements are electrically connected if allowed to touch, although there is a high resistance due to oxidation of the polysilicon layers.

The following devices were designed, built and tested in the course of becoming familiar with the MUMPS process. They are a combination of proven devices and new designs. Additional devices are listed in Appendix A. Figure 2-20 shows one of the early test die. This die was fabricated on the fourth MUMPS run, and so is referred to as a 'MUMPS4' die. Hereafter, all references to die or devices from specific MUMPS fabrication runs will be made in this way. A few devices from this and other MUMPS die are described in the following sections to give a general feel for what the process is capable of producing.

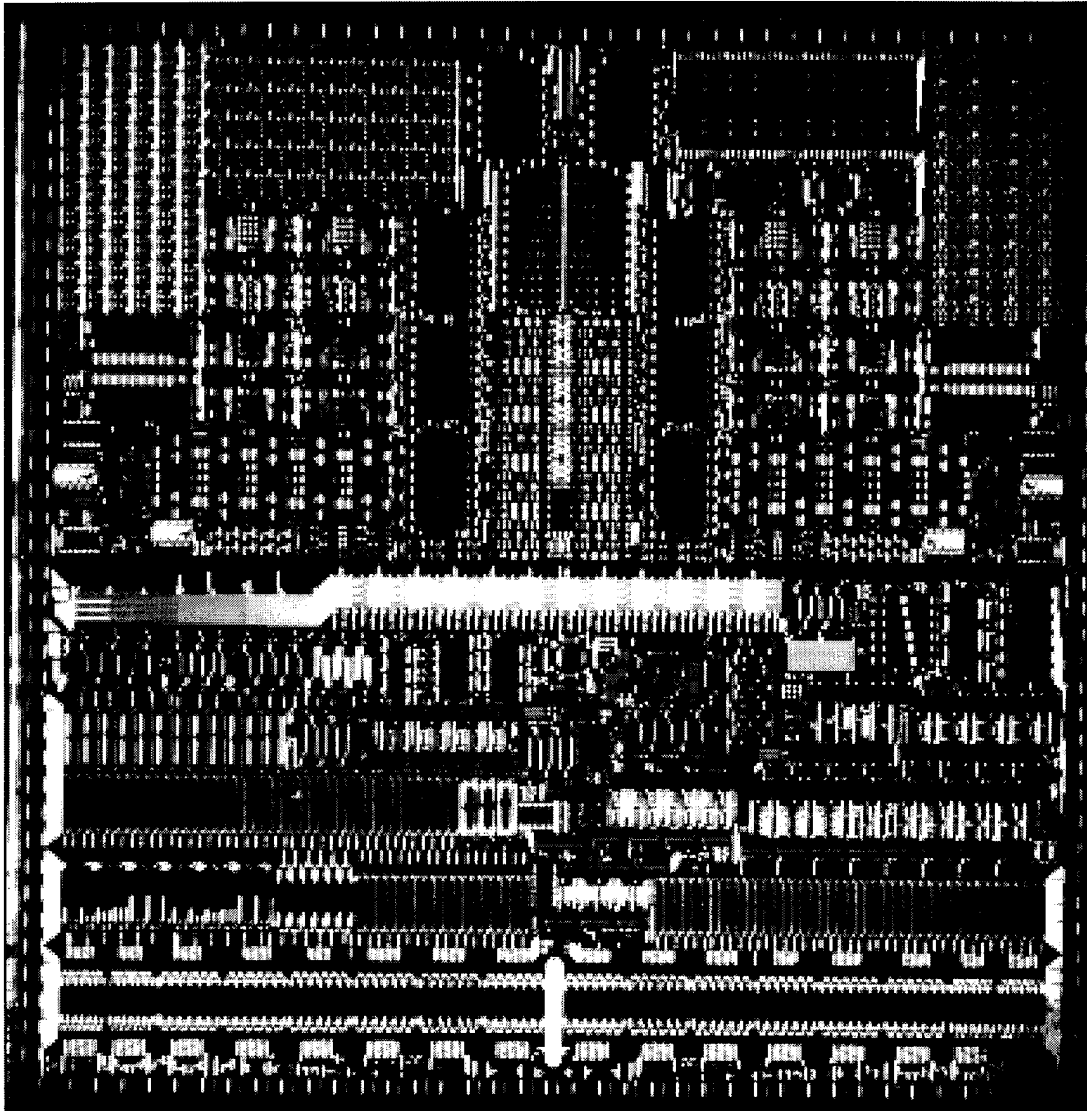


Figure 2-20. Photograph of one of the three test die fabricated in the MUMPS4 process. Die is 1 cm².

2.3.2.1 Etch Gauges

With the success of the etch gauge designs in the CMOS process, a similar design was tested on the early AFIT MUMPS die. In this case, the gauge would be used to indicate when a flat plate of a given size had been completely undercut.

The original MUMPS release recipe called for a 40 minute release in a mixture of buffered HF and alcohol. However, this recipe did not work well because it etched away the aluminum metallization used on the third MUMPS run (MUMPS3). It was clear from experience that the amount of aluminum etching was related to the duration of exposure, at any concentration of HF; so a shorter exposure would be better, whatever the HF concentration. The etch was subsequently modified at AFIT to use just straight (49% concentration) HF in a two minute etch.

This turned out to be a successful approach to preserving the aluminum, and was passed on to MCNC, who then suggested this recipe to all their users. But because of the problems with the original etch recipe, they were already looking for a different metal to use for the next MUMPS run. The metal used for the MUMPS4 run was copper. Copper survived the HF etch well, but oxidized quickly, especially when heated on the 150°C wire bonder table, making it difficult to wire bond to, and also making it a poor choice for reflecting surfaces. MCNC finally chose gold as the metallization, and has been using it from MUMPS5 on.

Figure 2-21 shows an early MUMPS etch gauge, with test squares ranging up from 5 μm on a side to 30 μm on a side in 1 μm increments, then to 50 μm on a side in 5 μm increments. The squares are attached with short 2 μm wide flexures so they can be electrostatically deflected to determine if they are released. A similar gauge had the same squares unattached so they would wash away as they were released, giving a clear visual indication of the progress of the etch, even under low magnification and while still under the rinse water.

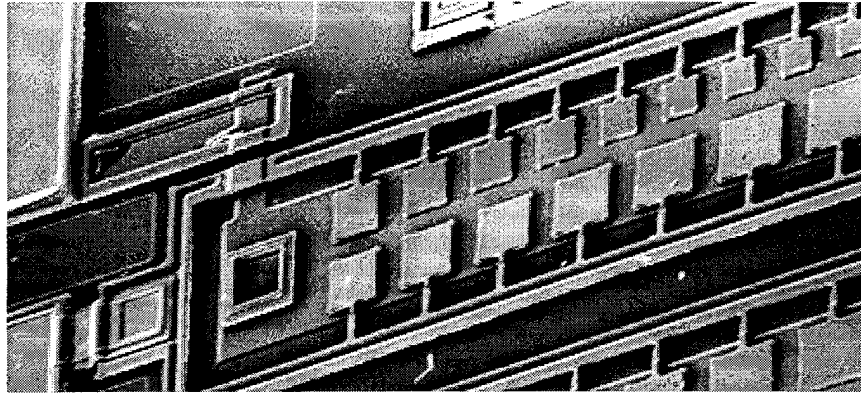


Figure 2-21. Etch gauge from MUMPS3. Square are *poly1*, and the largest square is 50 μm on a side. Most of the squares are stuck down in this picture.

These early gauges had squares too small for the two minute etch procedure, and the loosened squares would often float over and get stuck in other structures on the die. Figure 2-22 shows the design of a practical etch gauge based on the thermal actuator discussed in Chapter 3. In this gauge, the test plates are attached to the ends of the thermal actuators. When the plate is freed by the release etch, it can be waved back and forth by the actuator, clearly indicating the progress of the etch.

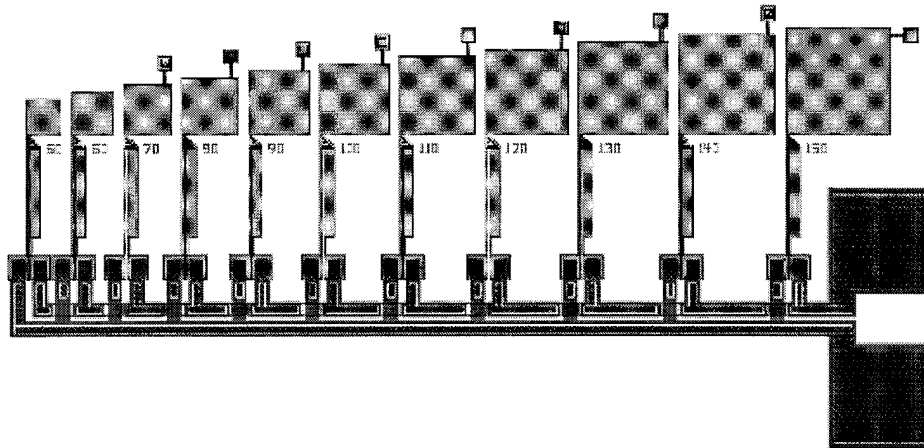


Figure 2-22. Layout drawing of a *poly1* etch gauge with thermal actuation to indicate release. Power applied to the two pads drives all the actuators simultaneously. Largest square is 150 μm on a side.

This gauge meets the desired requirement of visibly indicating the etch progress under low magnification, but it has not been tested under water. However, it can be actuated remotely through bond or probe pads, and could be designed to indicate the state of the etch by a change in capacitance.

2.3.2.2 Fabrication Test Structures

This is a class of structures used for checking how well the fabrication process can match the drawn designs. This tests the published design rules to see how far they can be pushed in various situations, usually to see how compactly a device can be drawn and still function. Test cells like these offered a wealth of fabrication information which led to new design approaches to take advantage of peculiarities in the fabrication process.

Figure 2-23 shows an unetched cell containing structures in the various MUMPS layers in different combinations and widths, to determine the interactions between the MUMPS layers and the minimum possible drawn geometries. Dimensions of this one cell will be given in detail.

In this cell, there is a concentration on the properties of metal lines: this was an investigation into the possibility of drawing metal lines that were not on *poly2* supports, in an attempt to increase the density of metal wiring on a die. This was not a success, since cutting all the layers down to the *nitride* inevitable caused the *nitride* to be eroded away in the RIE etches. Also, the metal exhibits very poor step coverage, breaking off at the steps, especially at *poly2*. This prevents the metal from being used to wire

directly to hinged structures, since it does not survive the step getting from the substrate to the hinged plates.

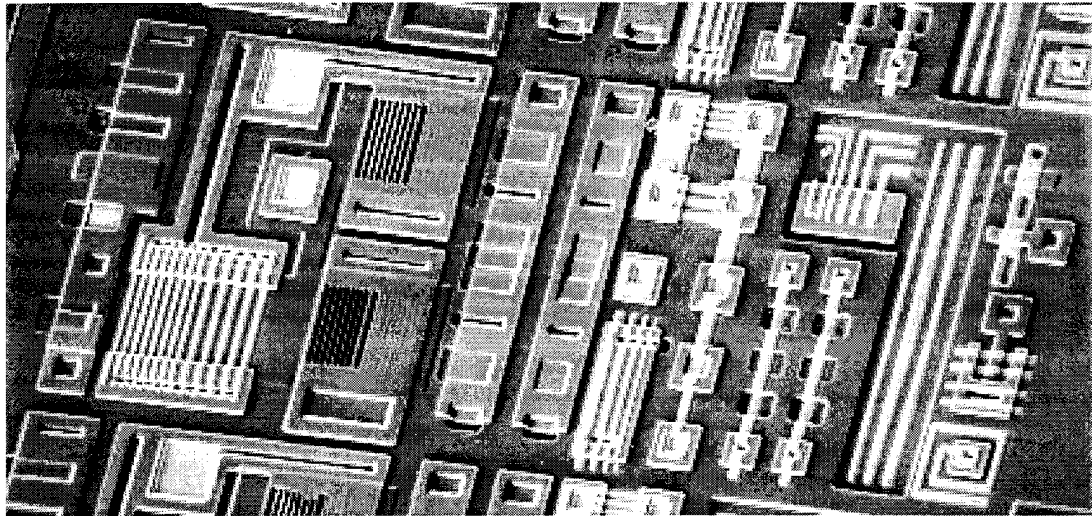


Figure 2-23. An unetched test cell containing a variety of structures for investigations into the interactions between the MUMPS layers. See the text and Figure 2-24 for details about these structures.

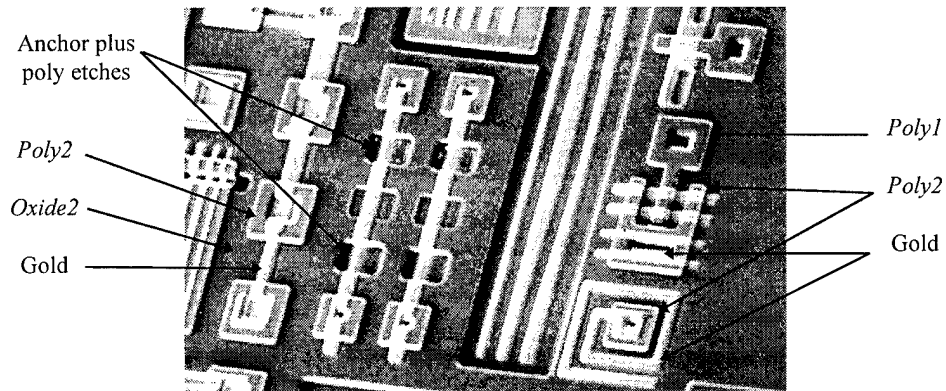
In the right half, from right to left, the cell contains: a 3 μm wide metal spiral suspended from a *poly2* pillar, a 3 μm metal line suspended from a *poly2* support over a *poly1* finger and 2 μm metal lines on *poly2*; a 6 μm metal line anchored by an *oxide2* cut, passing over *poly1* finger; 2, 3 and 4 μm metal lines laid directly into an *anchor2* trench, and some 4 μm metal lines passing over all the oxide cuts and suspended by *poly2* pillars. Next are 1, 2, 3 and 4 μm metal L's with 1, 2, 3 and 4 μm gaps, laid in an *anchor2* trench, and also partly over *poly2*; then 4, 6, 8 and 10 μm metal lines on *poly2* pillars, with 1, 2 and 3 μm metal lines with 1, 2 and 3 μm gaps going to the left to another pair of *poly2* pillars with 12 μm metal lines between them. Finally, in the right

half, there are 1, 2, 3 and 4 μm metal lines on top of and slightly overlapping a *poly2* pillar.

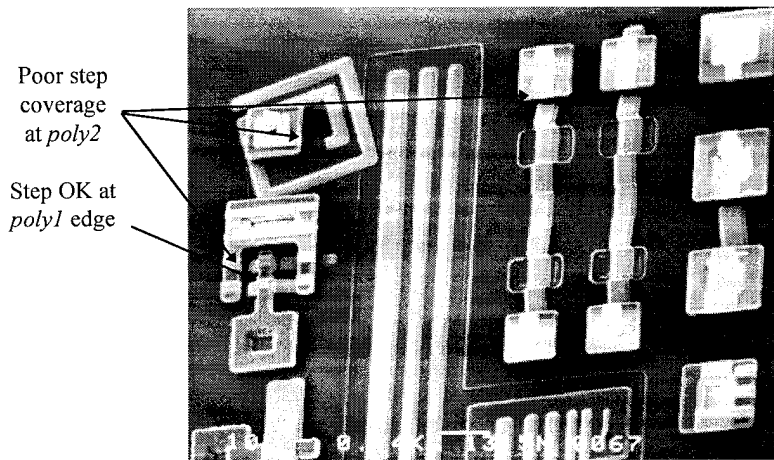
In the center there are tests of the *poly2* topology: two plates of *poly2* are drawn over top of oxide cuts, *poly0* and *poly1*. One of the plates is fully over the underlying test layers and one overlaps them for a cross-sectional view. To the left of these *poly2* plates are grids drawn with smaller lines/spaces than design rules allow: 2 μm /1 μm and 1 μm /2 μm in *poly1* and *poly2*, over *poly0* plates. There are also metal grids: 3 μm line/space and 2 μm line/space, over a *poly0* plate. On the far left is a topology test for the *poly1*. A *poly1* plate is drawn over *anchor1*, *dimple* and *poly0*.

Figure 2-24 shows a series of etch results on the cell shown in Figure 2-23. Figure 2-24a shows a close-up of the lower right corner before any etching; the metal is sitting atop poly and oxide. Figure 2-24b (shot from the reverse angle) shows the area after the normal release etch in HF; note that the metal did not cover the steps at the edges of the *poly2*, and either fell down or washed away. The *nitride* has been visibly damaged in areas where anchor cuts were followed by removal of the overlying poly.

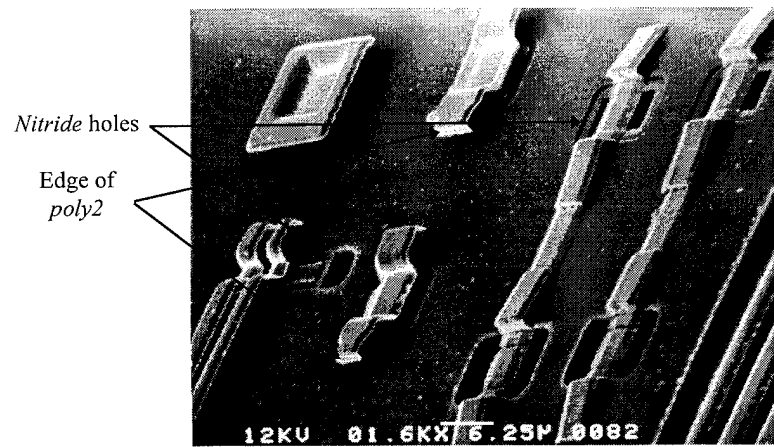
Figure 2-24c shows the area after an etch in KOH for 30 minutes at room temperature. The etch mixture was 44g KOH in 100 ml of deionized water. The KOH has removed all of the poly, leaving only gold, oxide, and *nitride*. This diagnostic technique reveals holes in the *nitride* caused by repeated exposure during RIE etches of the overlying layers. Where the *nitride* has been breached, the KOH etches into the substrate leaving a pit.



(a)



(b)



(c)

Figure 2-24. Portion of test cell of Figure 2-23: (a) unreleased; (b) after a normal 2 minute release etch in HF (note: this figure is taken from the reverse angle); (c) after a 30 minute etch in KOH.

Figure 2-25 shows a close-up of a damaged nitride area after the die has been etched in KOH. The KOH anisotropically etches the exposed bulk silicon under the *nitride*. The whitish area around the opening shows the extent of the *nitride* undercutting. As a test tool, the KOH etch can reveal if a design caused a short to the substrate through the *nitride*. The KOH etch can also show if a structure was incompletely released, by revealing any oxide left on the die.

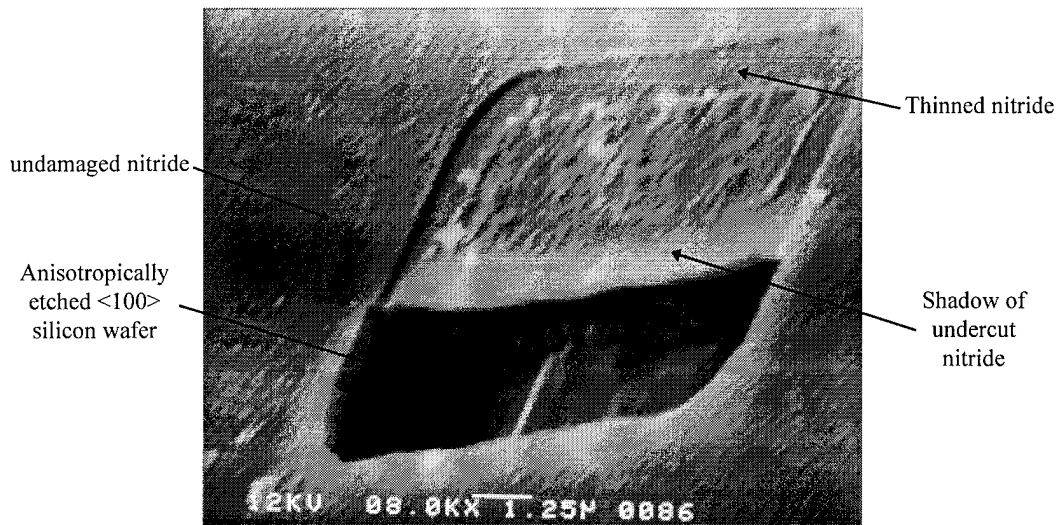


Figure 2-25. *Nitride* hole in a MUMPS die after 30 minute etch in KOH. Before the KOH etch, the hole was cut through the *nitride* by a combination of an *anchor2* and *poly2* RIE etches. The thinned *nitride* is from just an *anchor2* etch.

Figure 2-26 shows a test cell designed to determine the minimum width of a *poly2* flexure for piston mirrors. Narrower flexures are less stiff, so lower drive voltages can be used. This test cell indicates that 1.5 μm widths can be fabricated, but MCNC only guarantees 2 μm minimum *poly2* widths, so the designer would be taking a chance by using a thinner flexure. Similar test structures were used to

determine the minimum spacing from the edge of the gold to the edge of the *poly2*. The published design rules list the spacing as 3 μm , but experience from test cells show that this can be reduced to 1 μm or even a little less. This is important for getting a high percentage of coverage for optical arrays.

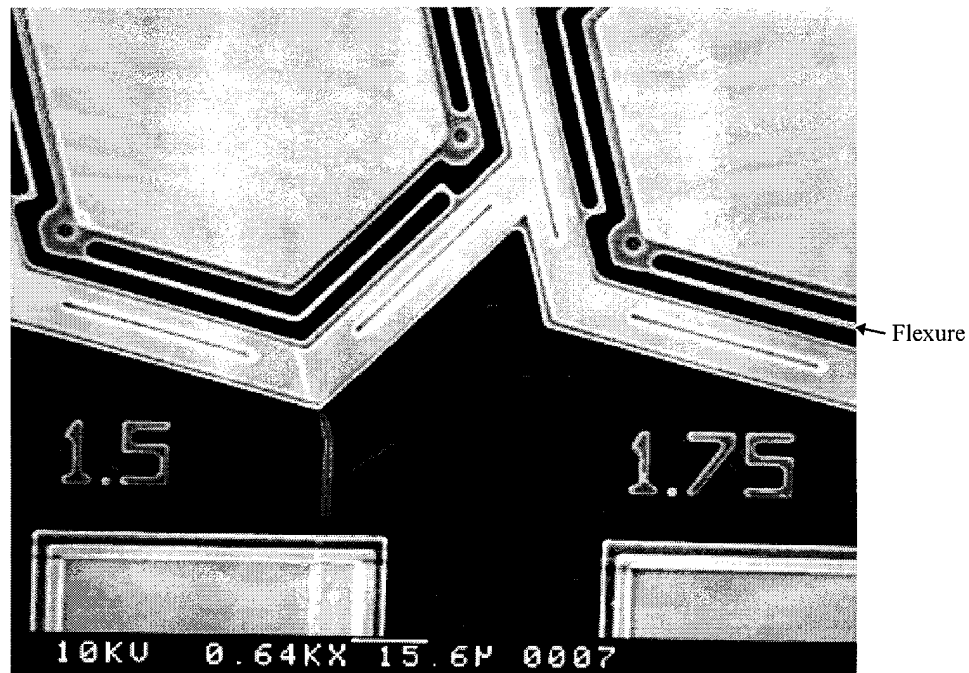


Figure 2-26. Test structure for determining minimum width of flexures drawn in *poly2*. Width is indicated by *poly0* labels.

Test arrays were also used to determine the minimum spacing between anchors and *poly0* wires for compacting the design of mirror arrays. Figure 2-27 shows a cell drawn to represent a cross-section of a mirror array. Structures like these were drawn to avoid having to actually section and polish a die. This structure was used to determine the minimum possible spacing between *poly0* wires and *poly2* anchors, to minimize the space lost to address wiring in a large mirror array.

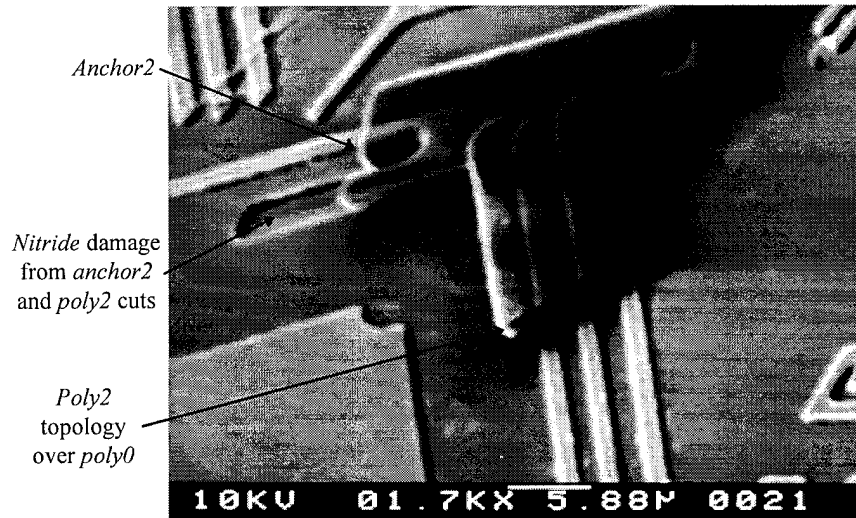


Figure 2-27. Drawn cross-section of a *Poly2* plate crossing 2 μm wide *poly0* wires and near an *anchor2*.

Figure 2-28 shows a tower made from all the MUMPS layers. This structure is both a fabrication test structure and a cross-section test. It has also been used in functional devices as a support for overlying cover plates, since it represents the tallest possible structure that can be built in the MUMPS process.

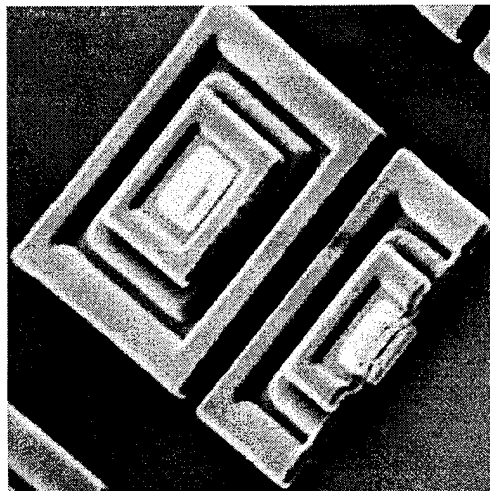


Figure 2-28. Tower structure made from all the MUMPS layers. This is the tallest structure that can be made in the MUMPS process; the top is 7.25 μm above the level of the *nitride*.

2.3.2.3 MUMPS Design Techniques

Designs which seem feasible at the layout stage may fail during the fabrication or release stages because of process interactions or layer topology. The topologies which result from the fabrication of surface-micromachined thin films can be detrimental to many designs. However, topological design can offer new opportunities for the MEMS designer. The design techniques presented in this section take advantage of the topology and the process steps described above to form features that can not be directly drawn as simple design items. These techniques include methods for using conformal layer topologies to shape structures for guide rails or bossing, or to obtain closer tolerances than the design rules would seem to imply.

It is capabilities such as these that extend a foundry process beyond its design rule restrictions. The techniques can be turned around and used with custom MEMS fabrication processes. In these cases the seeming restrictiveness of using a foundry process actually forces greater creativity.

2.3.2.3.1 Bossing

A boss is a protrusion added to a surface. In the designs described here, a boss is a shape impressed in the structure by the conformation of the thin film layers. In machining, bosses are often used to stiffen a thin plate. Some common examples are the ridges on a tin can and corrugated roofing. In micromachining bossing is similarly used to stiffen selected portions of a structure, such as stiffening a sensor

diaphragm [31]. Bossing can take the form of a rise or a depression in the surface which causes the polysilicon plate to resist bending out of the plane of the die. Bossing a beam or diaphragm also alters its effective modulus of elasticity, and can be used to change the resonant frequency of a device.

In surface-micromachined polysilicon, bosses must be formed in the topology of the polysilicon thin film as it conforms to the previously deposited and patterned layers. Any drawn features that affect the topology of overlying layers can be used to form bosses in those overlying layers. Figure 2-29 shows the (a) *poly1*, and (b) *poly2* test structures from the layer test cell shown in Figure 2-23. These poly plates illustrate some of the bossing possibilities, with several options to provide more ways to control the bossing style and depth. Notice that the upper layer, *poly2*, has more options for up and down bossing than the lower *poly1* layer. Not shown is the upward bossing of *poly2* that is possible using *poly0* or *poly1*.

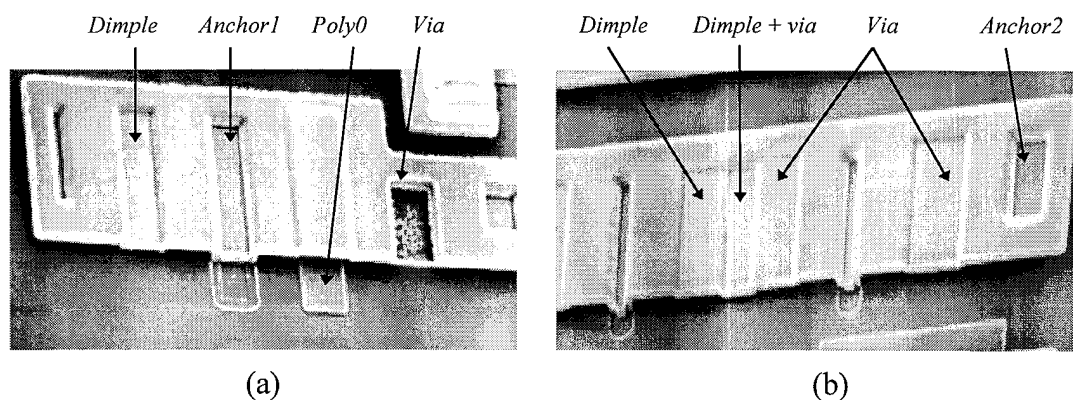


Figure 2-29. Options for bossing *poly1* and *poly2*. The hole in the *poly1* was formed during the RIE etch of the overlying *poly2*: the *via* cut left the *poly1* unprotected by *oxide2*.

Figure 2-30 shows two electrostatically actuated tilting-beam mirrors, one with and one without bossing. After the release etch, the unbossed beam was slightly bent, and the mirrored end was pulled down flat, while the bossed beam withstood the release without sticking down. The bossing of the *poly2* beam is formed by a 2 μm *poly1* beam anchored under it by a 3 μm tether. This tether prevents the *poly1* beam from washing out and getting into some other device, and it does not affect the operation of the tilting beam. Another application is stiffening hinged plates as shown in Figure 2-31. The bosses in the *poly1* plate were formed in the *dimple* layer.

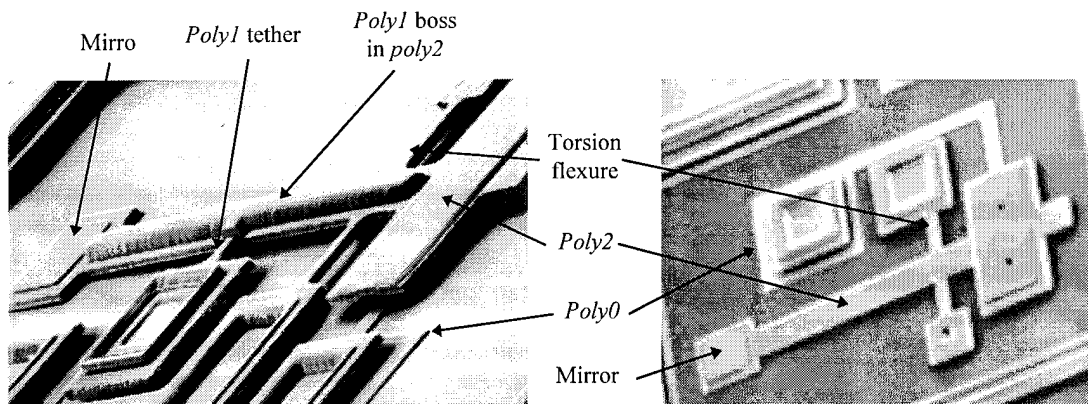


Figure 2-30. Electrostatically actuated tilting beam mirrors. The beam on the left has a 2 μm wide *poly1* former under it which is tethered to a probe pad/anchor. The torsion flexures on both beams are 3x15 μm , and the overall lengths are 155 μm for the bossed beam and 135 μm for the unbossed beam.



Figure 2-31. Part of a hinged *poly1* latching plate with *dimple*-bosses for stiffness.

Since bossing is a result of the conformal effects of thin film deposition it can be hard to avoid, especially in closely packed arrays of devices where there are wires running between the outer devices to power the inner devices of the array. Care must sometimes be taken to prevent the bossing caused by these wires from adversely affecting any structures.

Figure 2-32a shows a 50 μm wide hexagonal piston mirror design with a *poly0* address line that runs under only one of the flexures. This caused a difference in the effective modulus of elasticity between the distorted and undistorted flexures, so the mirror tilted slightly when deflected. To eliminate this effect, *poly0* wire stubs can be run under all of the flexures, to give each of them the same topology, as shown in Figure 2-32b. For the 62 μm wide square piston mirror, the tilt was less than the ± 2 nm error of the test equipment at 316 nm of deflection [32].

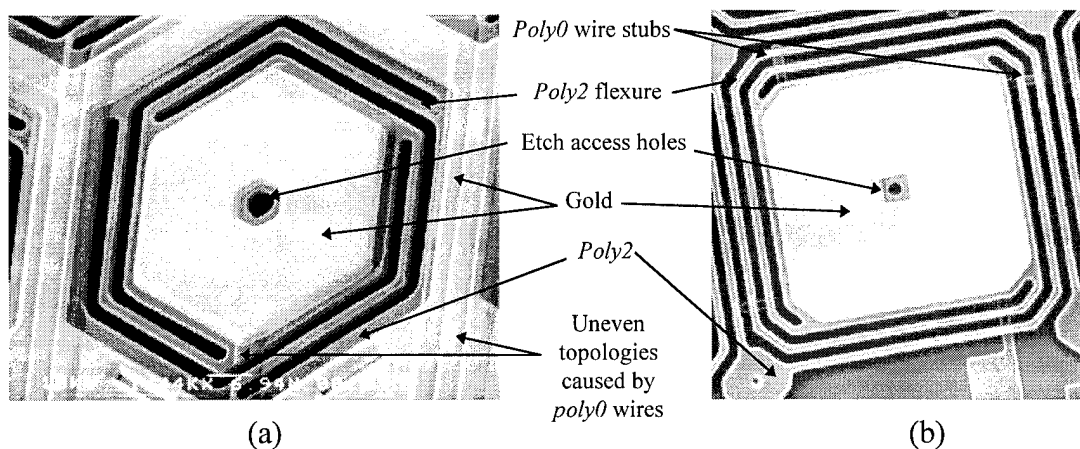


Figure 2-32. Piston mirrors (a) without *poly0* wire stubs and (b) with *poly0* wire stubs under the flexures. The *poly2* hexagonal mirror is 50 μm wide from corner-to-corner across the center, the square mirror is 62 μm on a side. The flexures on both mirrors are 2 μm wide with 2 μm gaps.

2.3.2.3.2 Forming Topological Features

A technique related to bossing is the formation of features such as gear teeth by the conformity of the polysilicon layers. As an example, a pawl which engages a toothed rack in a linear motor could be designed in the same polysilicon layer as the rack, but the designer must adhere to the design rule for spacing between these two features. In the MUMPS process this spacing is 2 μm . Stair-stepping of the drawing when transferred to the mask, and over-etching during the polysilicon patterning step, will cause the two sets of teeth to be fabricated with a slightly different geometry than drawn during layout, so they may not engage perfectly.

As an alternative, the pawl teeth can be made to fit exactly to the rack teeth and be placed as close as the thickness of the *oxide2* layer by having them formed during the fabrication process instead of drawing them explicitly. Figure 2-33 shows a section of a linear stepper motor which uses this approach. In this design, the pawls were drawn as simple rectangles of *poly2* that overlapped the *poly1* rack. The teeth in the rack were explicitly drawn out. When the *poly2* was deposited over the *poly1*, the pawl teeth were automatically formed to the exact shape of the *poly1* teeth, and with a closer spacing of 0.5 μm , the thickness of the *oxide2* layer. This design has the added advantage that the overlapping pawl edge prevents the *poly1* rack from bending up out of contact with the pawl teeth when large forces are transmitted through the rack.

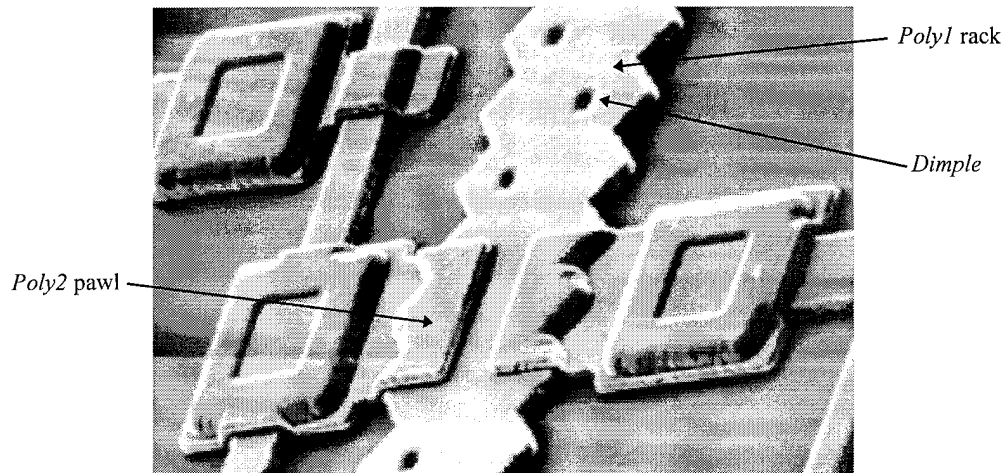


Figure 2-33. Toothed pawls formed in *poly2* by conforming to the underlying *poly1* structure. This linear stepper motor rack has 10 μm tooth spacing.

A common device sub-component that can be formed by topological design is the guide rail. Sliding parts can be guided by a rail which keeps them in the plane of the die. One problem with designing guide rails is that they will conform to the sliding part they are supposed to guide if that part is drawn in place along the rails. The result is that the part can be unintentionally trapped by the guide rail when it conforms around the slider. Figure 2-34 shows two approaches to solving this problem. If the sliding part can be any length, then it is best to draw it overlapping the guide rail on both ends, or just the end in the direction the slider has to move, as with the guide rails on the left in Figure 2-34 .

If the sliding part must be drawn separately from the guide rails, one way to obtain the desired topology is to use a sacrificial structure which is mechanically removed before the device is assembled or operated. In this process a sacrificial polysilicon former induces the desired topology in the overlying layers.

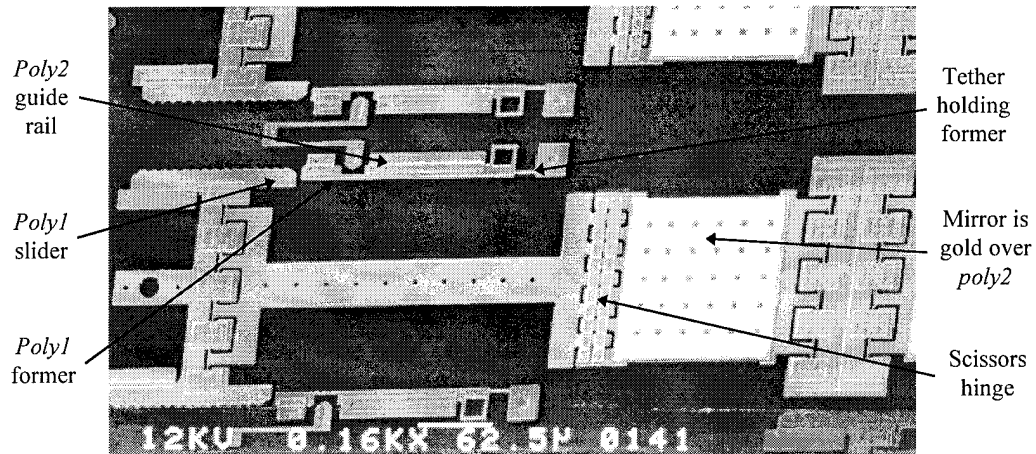


Figure 2-34. Fold-up mirrors with a ratcheting slider which indicates the position. Forcing the slider to the right causes the scissors hinge to fold up and sets the mirror angle. *Poly1* formers are used to give the guide rails the proper topology. The formers are anchored to posts by $2\ \mu\text{m}$ wide tethers.

Figure 2-34 shows how a *poly1* former is used to induce the proper topology in the *poly2* guide rail. The guide is formed so it is the proper height and width to accept the slider on the left. Since this technique is similar to the lost-wax technique used to make castings, it has been termed the ‘lost-poly’ technique; however, the *poly1* former is not melted away as in the lost-wax process, but rather must be mechanically removed.

The *poly1* former can wash out during the release etch, but in some cases it is desirable to ensure that the former stays in place during the release etch so it does not become lodged in another structure. In these cases the former can be tethered by thin flexures which can be easily broken off, or it can be held in place by fusible links which are melted free by passing a current through them [33]. The former can also be removed with an actuator. This can make the process more automated for batch processing.

Thermal actuators which permanently deform in a controllable manner are useful in this application, since they have the force to free the former from any residue that might be left after the release etch, and they can maintain their deflected position without power applied, as will be seen in Chapter 3. In all cases, a space must be left for the former to be moved into, which can affect the design of the device or the placement of neighboring devices.

This design technique can be used when mating parts need to be fabricated apart from each other. Figure 2-35 shows a cup formed at the end of a folded flexure spring which is intended to trap the end of the bossed *poly1* sliding beam coming through the *poly2* slide bearing from the left. The *poly1* former is attached to the spring anchor by a short tether which is broken off after the release etch.

As Figure 2-35 shows, the former does not have to be the same shape as the mating part. Since the former is drawn separately, the tolerance between the two mating parts can be set to any number within the $0.25\text{ }\mu\text{m}$ step size of the mask grid. The designer must also consider the narrowing of the polysilicon parts during the RIE patterning. On the sixth MUMPS fabrication run, the side-etch of the parts was $0.175\text{ }\mu\text{m}$; so the tether in Figure 2-35, which was drawn $2\text{ }\mu\text{m}$ wide, was fabricated $1.65\text{ }\mu\text{m}$ wide.

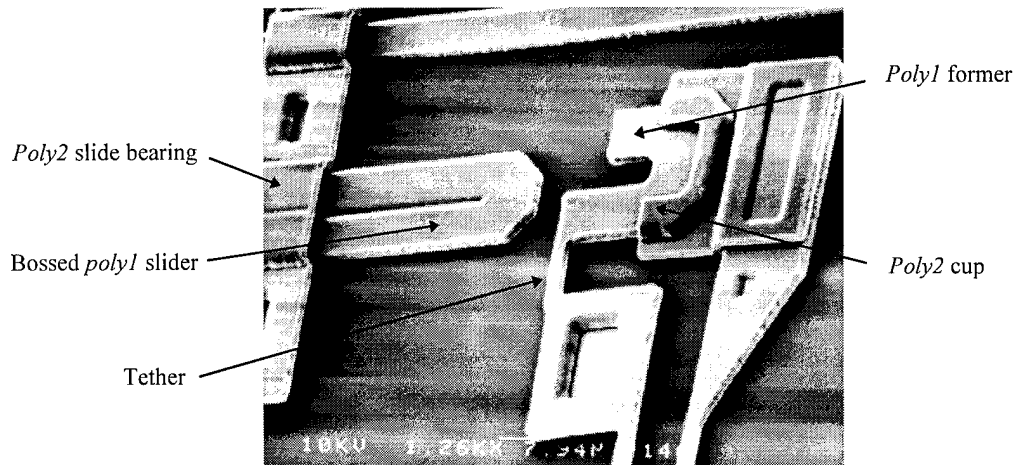


Figure 2-35. *Poly1* former used to create a cup in a *poly2* plate to capture the bossed *poly1* slider moving across from the left. The slider is 16 μm wide. The short, 2 μm wide tether on the former must be snapped off the anchor post to slide the former aside.

2.3.2.3.3 Breaching the Silicon Nitride Layer

The *nitride* layer in the MUMPS process is not patternable, but by a combination of design choices, the *nitride* layer can be breached. Cutting through the *nitride* would ordinarily be a design flaw, because it would cause a structure to become shorted to the substrate. But there are several applications where cutting through the *nitride* is required. One application is to make electrical contact to the silicon wafer so it can be used as a ground plane or so it can be biased for designs with electrostatic actuation. These contacts usually take the form of a wire-bonding pad.

As previously mentioned, underlying layers can be cut through if exposed to repeated RIE etches; therefore, the substrate contacts are formed by specifying combinations of oxide and polysilicon cuts which will also cut through the *nitride* to

expose the silicon wafer below. The *poly2* then makes electrical contact with the wafer, and gold can be applied to the *poly2* to make the contact a probe or bond pad. Three MUMPS layer sequences were investigated to see which gave the lowest contact resistance. Pairs of contacts with 35 μm square *nitride* cuts and 50 μm center-to-center spacing were measured for pad-to-pad resistance through the wafer.

Table 2-2 lists the sequence of MUMPS mask layers that were specified to form the pads, along with the mean contact resistance for four sets of identical pads. The measurements for each pad type were within $\pm 3 \Omega$ of each other. The 5.5 Ω resistance of the test setup, measured by placing the probe points on the same pad, has been subtracted from the contact resistances listed in Table 2-2. The $\langle 100 \rangle$ oriented silicon wafer has a resistivity of 0.5 $\Omega\text{-cm}$ [12]. These test contacts were fabricated on the MUMPS5 run.

Table 2-2. Substrate Contact Layer Sequences and Mean Contact Resistance.

MUMPS Layer Sequence	Mean Contact Resistance
<i>via/anchor2/poly2/gold</i>	no contact made
<i>anchor1/anchor2/poly2/gold</i>	40 Ω
<i>anchor1/via/poly2/gold</i>	28 Ω

Another situation where *nitride* cuts are useful is to provide a common electrical ground for isolated devices in a large array. If there is no room for a common connection to be run in a polysilicon layer, the devices can all be shorted to the wafer through *nitride* cuts. The wafer provides the common connection.

For example, Figure 2-36 shows a *poly2* cloverleaf mirror based on an earlier aluminum mirror design [33]. These mirrors require a common ground contact to the center post; but without a *nitride* cut, a *poly0* wire has to be run in between the mirrors, which decreases the optical efficiency of the array. The topology of the *poly2* flexures and mirror surface is also adversely affected. A *nitride* cut can be incorporated into the post's anchor cut to provide a substrate connection, making the substrate the common ground for an entire array, and leaving the routing channels around the mirror free for *poly0* address wires.

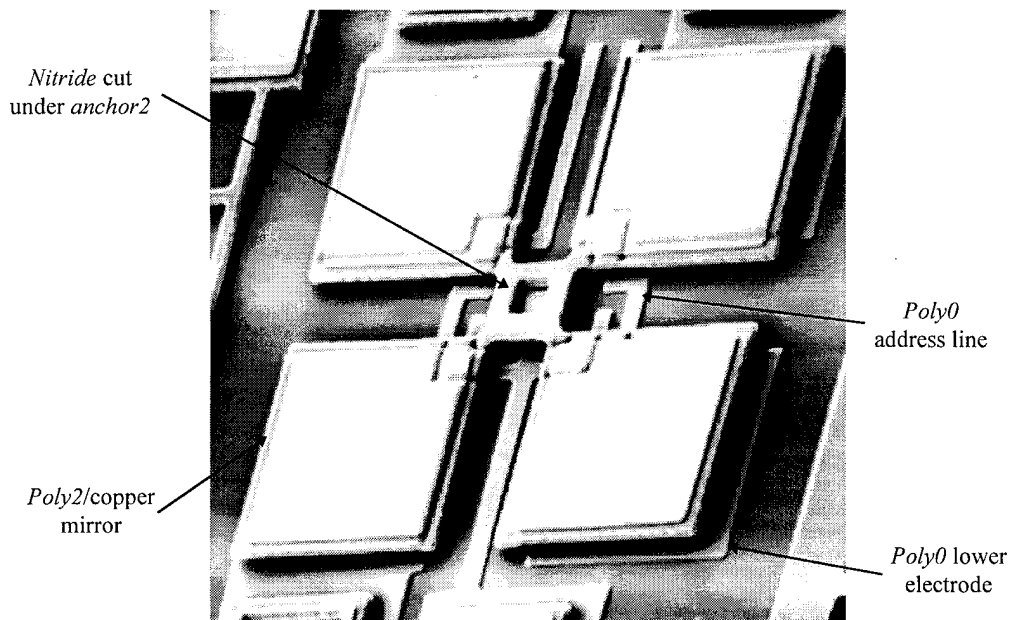


Figure 2-36. Center post, tilting 'cloverleaf' mirrors, after [34]. The mirrors are 50 μm square, and the *poly0* wires are 5 μm wide.

In the mirror of Figure 2-36, the pair of 5 μm wires running in from the top of the SEM micrograph go to the lower mirrors, passing under the inside corners of the

upper two mirrors. The ground line running up from the bottom of the micrograph has wire stubs on it to force the lower two mirrors to have the same topology as the upper two mirrors, so all the mirrors have matching mechanical and optical characteristics.

2.3.2.3.4 Stacked Polysilicon Structures

One consequence of the over-etch time used to remove stringers during poly RIE patterning steps is that the etch duration is long enough to also pattern any other poly layers left exposed by oxide cuts. The 150% over-etch of the *poly2* layer is sufficient to completely cut through any *poly1* exposed under the *poly2* by a *via* cut through the intervening *oxide2*. So 3.5 μm tall stacked *poly1/poly2* structures can be built with the standard MUMPS process, using the *poly2* design rules.

Figure 2-37 shows structures formed with the stacked *poly1/poly2* technique. Figure 2-37a shows the CAD drawing, and Figure 2-37b shows the fabricated structure. The area is drawn first as a *poly1* layer overlapped 5 μm all around by a *via* layer. The features are drawn in *poly2*. If the structure is to be anchored, *anchor1* must be used. All *poly1* that is covered by *via* but not covered by *poly2* will be etched away during the *poly2* over-etch. The resulting structure can be used the same way that a single releasable polysilicon layer can be. Since the structure is made of *poly1* and *poly2*, it can be drawn with attachments to those layers, so the stacked devices can be incorporated in hinged designs, actuators or any suspended structure.

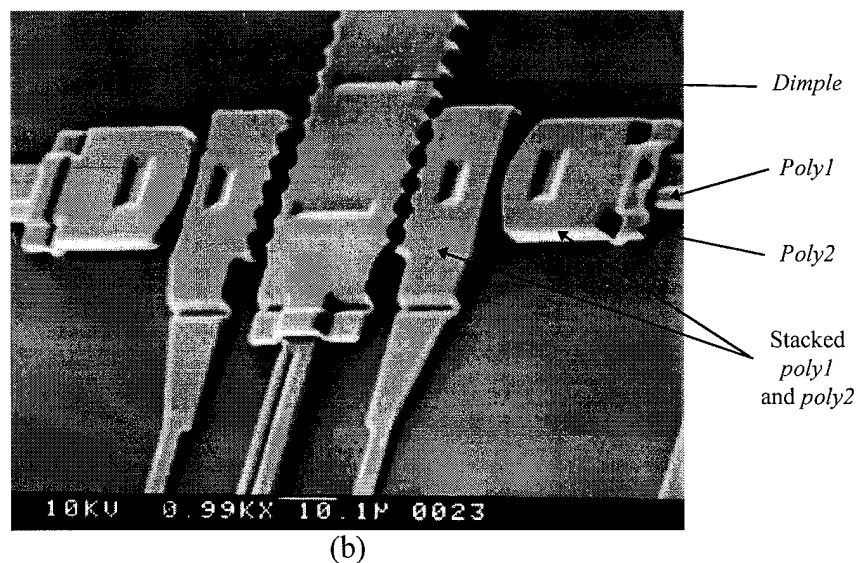
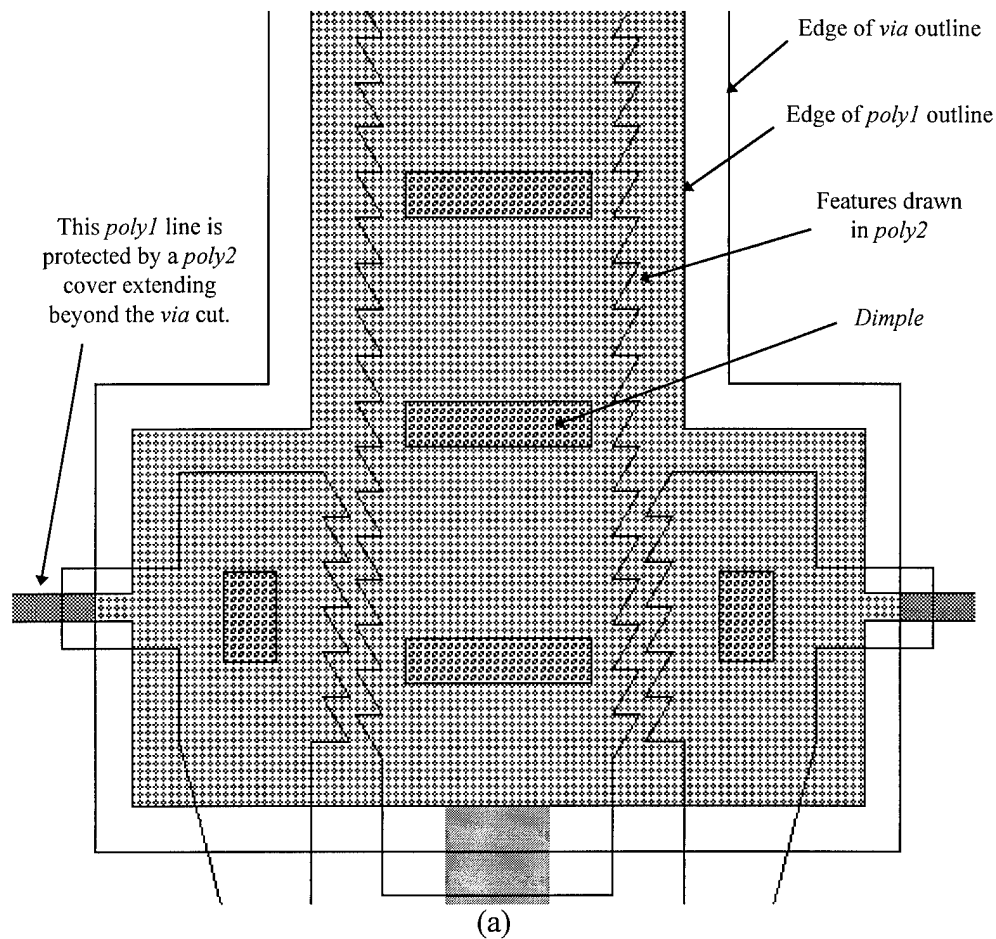


Figure 2-37. Structures formed by the stacked *poly1/poly2* technique: (a) is the CAD drawing, showing the proper placement of the *poly1* and *via* overlaps; (b) shows the fabricated structures.

Another way to stack layers to make a thicker, stiffer structure is to trap the *oxide2* between the *poly1* and *poly2*. This is done by placing an unbroken *via* ring around the area where the *oxide2* is to remain. This prevents the etchant from reaching the *oxide2*, leaving it unetched and trapped between the polysilicon layers. If an etch hole is needed in the expanse of *poly1/oxide2/poly2*, it can be formed like the stacked *poly1/poly2* structures by drawing a *via* with a *poly2* hole in the center. When the *poly1* hole is etched, the over-etch will cut through the *poly1* also. Figure 2-38 shows a portion of a hinged mirror built with stacked *poly1/oxide2/poly2*, with etch holes made as described above.

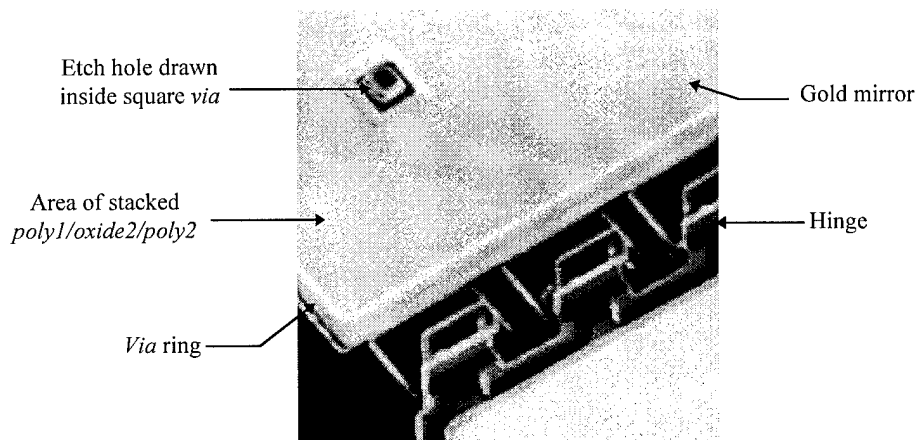


Figure 2-38. Portion of a hinged mirror plate built with stacked *poly1/oxide2/poly2*. Etch hole is drawn as a *poly2* hole over a *via*.

2.3.2.4 MUMPS Fabrication Problems

MUMPS is a new process which went through several evolutionary steps during the course of this research. The search for an ideal metal was mentioned earlier in

Section 2.3.2.1. There were also fabrication problems. On the MUMPS7 and MUMPS8 runs, the RIE etch process for the poly had drifted, and was leaving ragged lower edges on the side walls and heavy stringers, as seen in Figure 2-39. These stringers were especially problematic for electrostatically actuated devices, as they would shift over and short the charged polysilicon layers together, destroying the device. Stringers remain an intermittent fabrication problem.

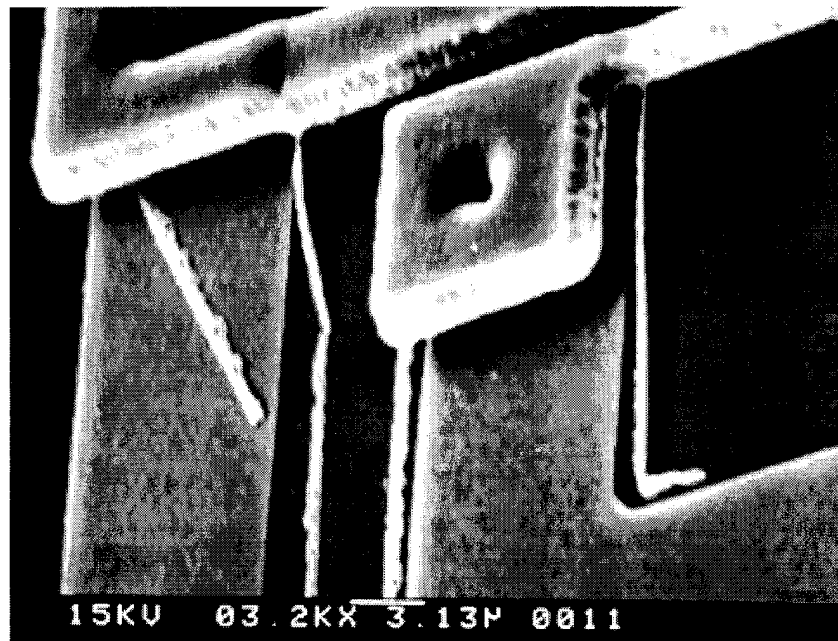


Figure 2-39. Stringers of *poly2* following the topology of the underlying *poly0*.

Another stringer-related problem was hinge failure. A combination of the ragged side walls and poor step coverage of the second oxide led to a joining of the *poly2* and *poly1* where the two layers crossed. This caused shorted devices and prevented hinge pins from rotating. Figure 2-40 shows a failed hinge.

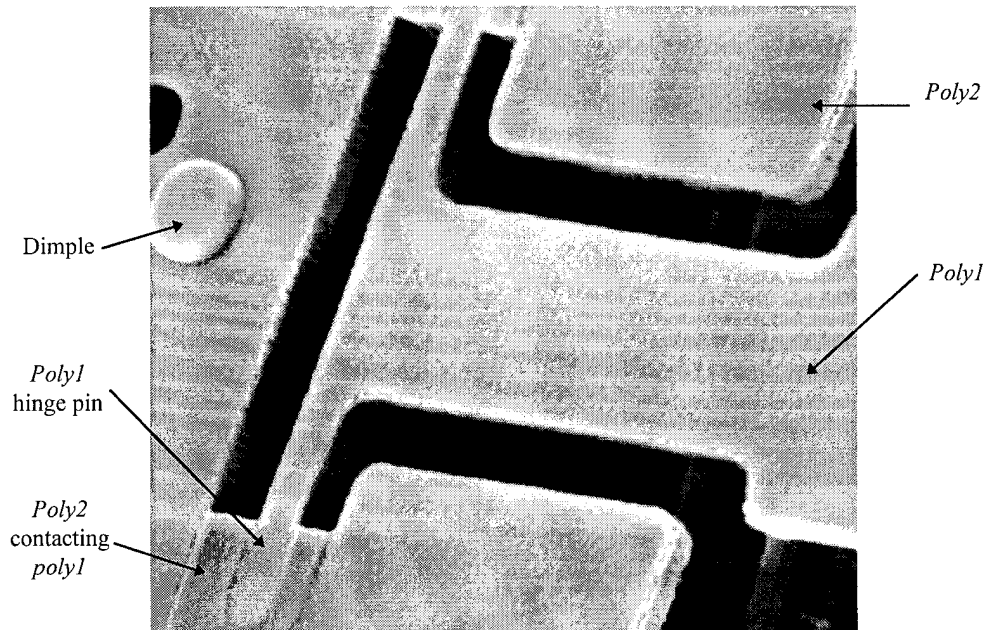


Figure 2-40. Underside of a failed hinged plate. The *poly1* hinge pin is connected to the overlying *poly2* hinge plate due to insufficient *oxide2* coverage and rough *poly1* side walls. The circular structure on the left is the underside of a dimple.

2.3.3 LIGA

LIGA fabrication produces electroplated metal structures patterned with a single mask. The LIGA designs submitted to MCNC are fabricated in the University of Wisconsin's LIGA process [20]. In this process, a silicon substrate has a 1 μm oxide layer grown on it, upon which is sputtered a 500 nm layer of titanium and then a 20 nm layer of nickel for an electroplating base. This base is coated with a layer of polymethylmethacrylate (PMMA) photoresist which is exposed through a single mask to X-rays produced by a synchrotron. The resist is then developed, leaving cavities in the remaining resist with nearly vertical walls. These cavities are then filled with electroplated metal.

Two process variations are offered, 'short' and 'tall'. In the short process, the nickel-iron structural material is grown to a height of $30\text{ }\mu\text{m} \pm 5\text{ }\mu\text{m}$. In the tall process pure nickel is grown to about $200\text{ }\mu\text{m}$ and then milled back to a height of $150\text{ }\mu\text{m} \pm 5\text{ }\mu\text{m}$. Because of the extreme height in the tall process, the designs are restricted to having a length-to-width aspect ratio of no more than 10:1. This turned out to be less of a design constraint than otherwise expected. The only other design rule is a $5\text{ }\mu\text{m}$ minimum line and space restriction; however, the mask making process allows increments of $0.1\text{ }\mu\text{m}$, creating very smooth curves and allowing close tolerances for assembled parts. Only five $5 \times 6\text{ mm}$ die are delivered per die site.

The MCNC LIGA design rules make no explicit provision for the partial release of structures, i.e. no anchors are made through the oxide. However, a partial underetch of the plating base or the oxide layer can release thinner structures while leaving wider structures attached to the substrate. The design philosophy for this dissertation research was to have any part that is less than $30\text{ }\mu\text{m}$ wide be completely undercut and thus released, while wider parts remain attached to the substrate.

For example, axles used for rotating devices are drawn $50\text{ }\mu\text{m}$ across, while the wheels have no parts wider than $25\text{ }\mu\text{m}$ across. The partial release is accomplished by etching away the titanium between the nickel parts without excessive titanium undercut, and then using a timed etch of the underlying oxide using an etch gauge cell as a guide to achieve a $15\text{ }\mu\text{m}$ undercut.

The design rules stressed the need for the devices to be separated by $50\text{ }\mu\text{m}$, although MCNC was not clear on what constituted a 'device'. Therefore, an array of

switches was considered a single device so they could be packed closely together. No fabrication problems were caused by the device density on the die. This device spacing restriction is probably due to the desire to guarantee functional designs through conservative design rules. This restriction may make it difficult to design whole-chip systems without the aid of external packaging to bring electrical connections to the interior of the die.

The following devices were designed, built and tested in the course of becoming familiar with the LIGA processes. They are all new designs or adaptations of designs from other processes including fabrication test structures, fluidic components, actuator test arrays, accelerometers, tactile stimulators, and microrelay switches designed for a Master's research project [35]. Two LIGA chips were designed, one in each of the tall and short variations offered by MCNC.

Figure 2-41 shows the mask for the 'short' test die. No perimeter bond pad frame was provided because too much of the already small die would be taken up by wiring to interior devices, and the wire runs would exceed the 10:1 aspect ratio required for the "tall" chips. Devices that need to be probed for electrical tests have probe pads that also serve as anchor points for the partial release process. For this reason, most of the probe pads are large enough to be wire bonded.

Some of the devices are assembled from parts that are completely released during the 'partial' release etch step. Extra copies are made of those parts to account for loss due to mishandling the small pieces.

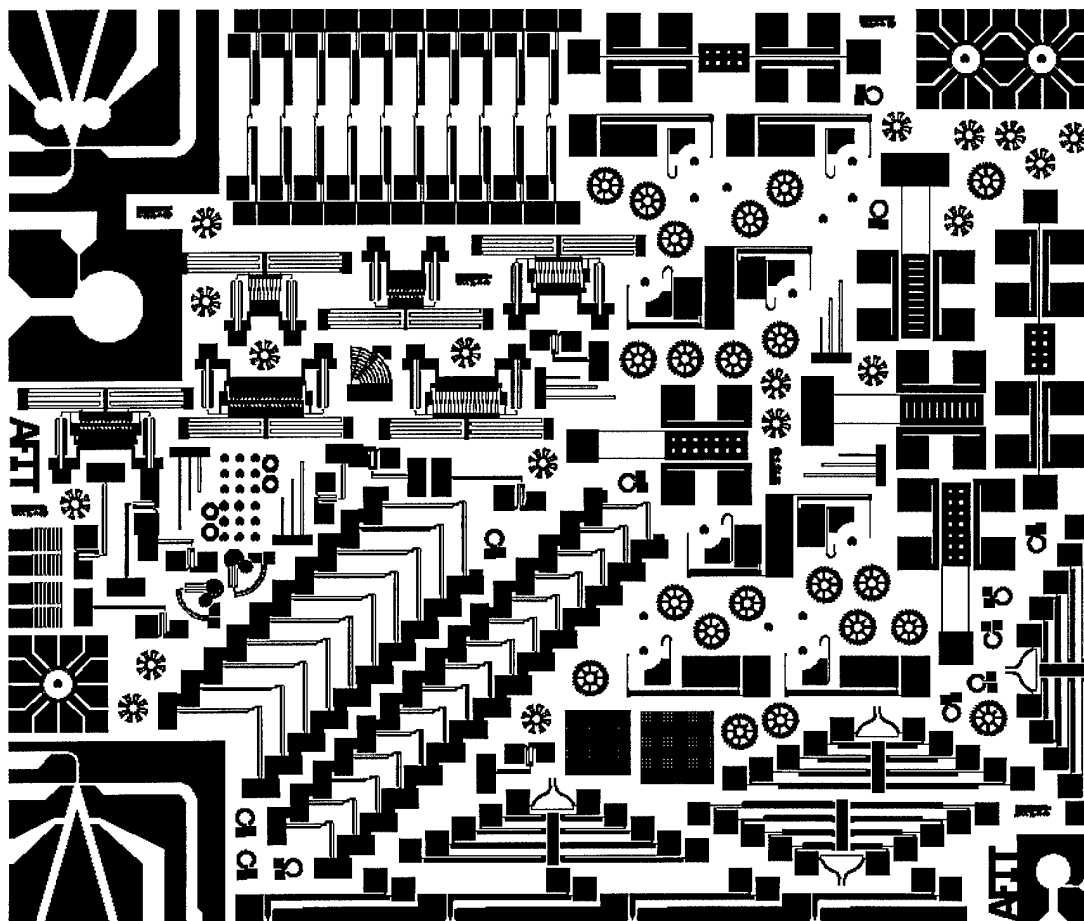


Figure 2-41. Mask for the 'short' LIGA die. The die is 5 x 6 mm, and the devices are $30 \pm 5 \mu\text{m}$ tall.

2.3.3.1 Etch Gauges

The proper release of the LIGA devices requires a carefully timed etch to achieve total undercutting of structures under $30 \mu\text{m}$ wide, while leaving structures $50 \mu\text{m}$ or wider still attached to the substrate by a pillar of oxide. This is achieved by observing the release of the round and square features from the etch gauge shown in Figure 2-42. When the $30 \mu\text{m}$ features are released, a $15 \mu\text{m}$ undercut of all metal

features on the die should be achieved. The etch must be slow enough so that the release can be observed and stopped in time.

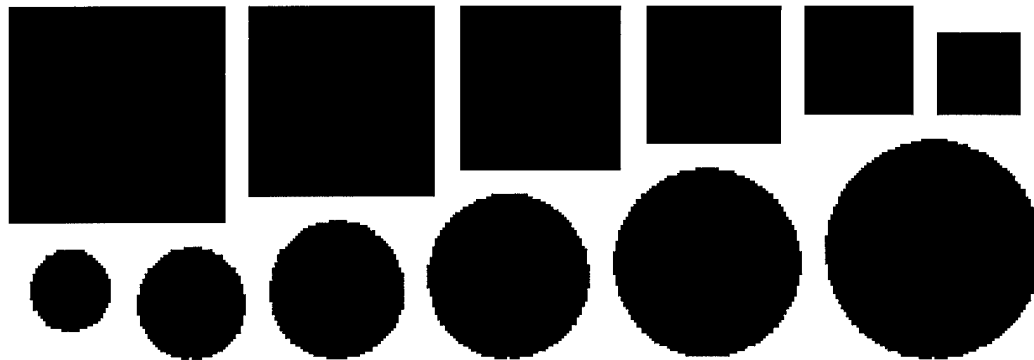


Figure 2-42. Timing gauge for LIGA partial undercut etch. This gauge consists of arrays of square and round posts in sizes ranging from 15 to 40 μm in 5 μm increments. The etch should be stopped when the 30 μm features wash free.

2.3.3.2 Fabrication Test Structures

As with the other foundry processes, simple devices and basic shapes were drawn on the initial die just to see how they would be fabricated. Besides the etch gauge, there were also grid shapes, comb actuators, and springs. Figure 2-43 shows one of the grids tried in the LIGA process. Several grids were tried, with holes 8, 10, 12, 14 μm across surrounded by 10 μm walls. Since all of the features of the grids are less than 30 μm across, the grids get fully released, so they can be retrieved from the etch or rinse liquids and used as parts of other structures, such as electro-hydro-dynamic pumps [36].

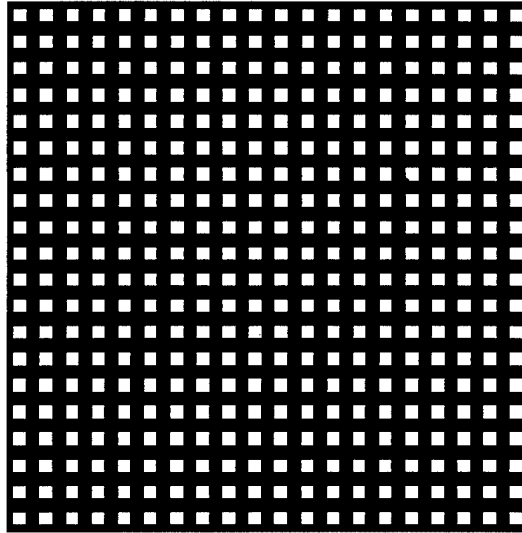


Figure 2-43. Layout drawing of a test grid structure from the LIGA process. Grid is 400 μm square with 10 μm holes.

Another test structure was used to determine the drawn dimensions that would result in the minimum usable clearance between a wheel and axle. This cell comprises a set of 9 axles with increasing diameters and two releasable test 'wheels'. The wheels are octagonal to make them easier to pick up and place with tweezers. The idea is to try a wheel on each of the axles and see how close the tolerance can be drawn while still allowing for free rotation. It will also yield information on how much over-size the axle must be drawn to get an acceptable press-fit for assembling structures permanently. It may also be feasible to heat the tweezers (and thus the wheel that is picked up) to get a tight fit by thermal contraction when the wheel cools down after placing it on the axle.

The wheels are 90 μm wide octagonal toroids with a (drawn) 51 μm diameter round center hole. The axles range in size from 47 μm to 51 μm by 0.5 μm steps. This was intended to be the first cut at a fit, the next in this series of test cells would refine

the clearance by using axles that vary in size by the minimum allowed 0.1 μm . That was not tried here due to the limited space on the die. The CAD drawing of the axle test cell is shown in Figure 2-44.

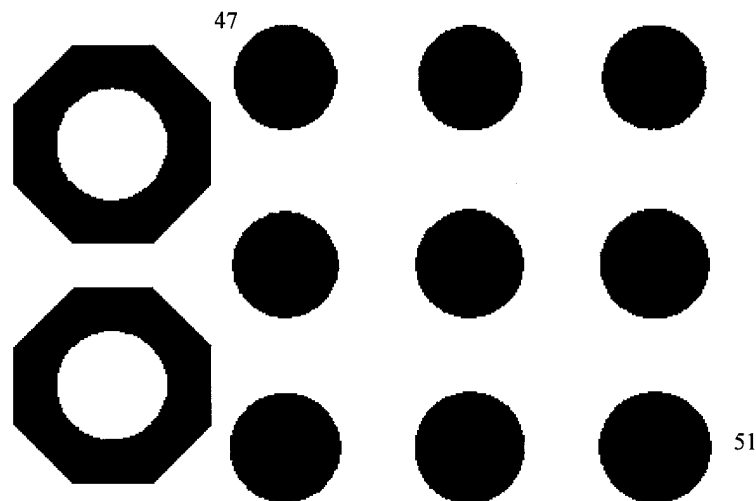


Figure 2-44. Mask drawing of the axle clearance test cell. Octagonal test 'wheel' is 90 μm wide, axles diameters range from 47 to 51 μm by 0.5 μm increments, as indicated by the numbers labeled on the drawing.

The 'moving spring' cell is typical of the 'filler' cells placed on die in every fabrication process. Cells such as these are for trying odd notions just to fill in the spaces around the main test cells. In this cell, a folded, serpentine spring is attached to two anchor/probe pads. The idea is to see if it expands magnetically or thermally when current passes through it, and failing that, to see how springy nickel is at this scale. This structure is also a test of the quality of the fabrication at the minimum design dimensions. Figure 2-45 shows the spring design, which consists of 8 turns per side, each one 125 x 5 μm with 5 μm gaps.

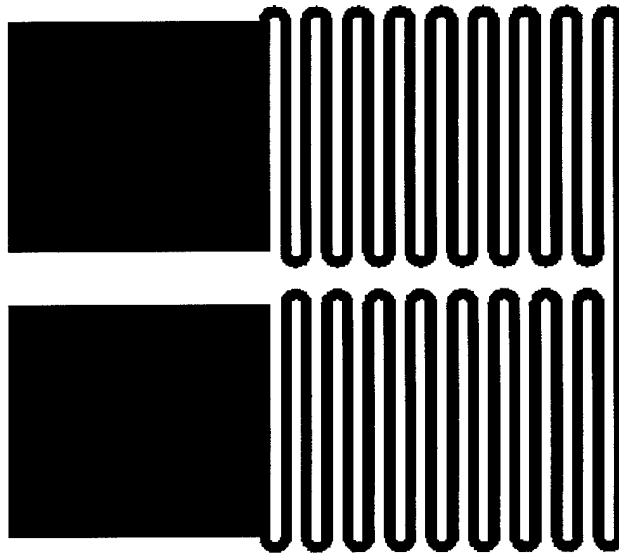


Figure 2-45. Test spring structure, spring has 8 turns per side, each one $125 \times 5 \mu\text{m}$ with $5 \mu\text{m}$ gaps.

2.3.3.3 Fluidic Components

Figure 2-46 shows an example of the fluidic components tried for the first time in the LIGA process. The design for this device, and the others visible in the corners of the die layout in Figure 2-41, is intended mainly to test fluid connections to a LIGA die. They were not drawn as scaled version of any particular macro-device. The vortex amplifier concept is simple enough, however, that this device should exhibit some effect on the fluid flowing through it.

This is a three-port device. The port leading radially into the circular chamber is the input or flow source, the smaller port leading in circumferentially is the control port, and the output port (which must be formed in the cover plate) is a hole above the center of the circular chamber. The source fluid flows from the input port, goes straight across

to the center of the circle and up the output port. When a control flow is introduced, it forces the source flow to take the path around the circumference of the circular chamber, increasing the impedance to the flow.

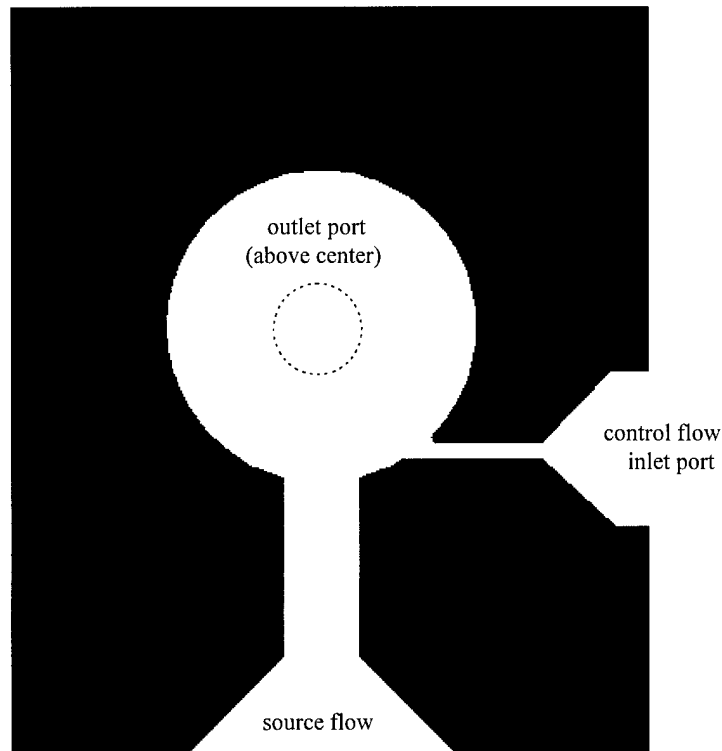


Figure 2-46. Vortex fluid amplifier: chamber diameter is 200 μm , inlet port is 50 μm inside and 170 μm at the edge of the chip, control port is 10 μm across on the inside and widens to 100 μm at the chip edge.

Only one LIGA run was completed during the course of this research, so the process has not been fully investigated, although initial results from these die indicate that the process can make significant contributions to large MEMS systems, especially in the area of large, high fidelity or high current switching arrays, to be described in

Chapter 4. These arrays would fulfill some of the size and power requirements for space applications outlined in Chapter 1.

2.4 Familiarization Benefits

To make best use of the three chosen foundry processes in the time available, the capabilities and limitations of each one had to be quickly determined. In pursuit of this goal, many devices and test structures were tried; the underlying philosophy being that the easiest, quickest way to learn a process is to first try everything imaginable and see what comes of it. After such an immersion an experienced feel for the process is developed, so when a specific design must be drawn, less time is wasted on unworkable approaches. One result is that now the new designs tried mostly work, whereas early on they mostly didn't work.

This approach had benefits besides quick familiarization. In the case of CMOS MEMS, it allowed the establishment of design rules where none were specified. For MUMPS, it became obvious the originally specified design rules were overly conservative, and that in several instances they could be pushed to get closer tolerances, better metallization coverage, etc. With the experience gained, such variations were made with confidence, and the fabrication results justified the changes. Another benefit that arose directly out of pushing the design rules was that 'accidental' fabrication flaws led to the development of layout techniques that expanded the range of devices beyond what the design rules could specify directly, or even what the design rules seem to imply is possible. In particular, the bossing and

poly1/poly2 stacking techniques were developed from what were initially design failures.

The virtues of this broad approach soon became apparent, not only for the in-depth knowledge of the processes gained in a short amount of time, but also the synergy that developed, allowing the creation of new devices. A good example of this synergy is the 'flip-over bimorph actuator', shown in Figure 2-47. This device is an actuator which works on the bimorph thermal expansion principle commonly seen in thermostats, and is operated in a flipped over position.

This actuator combines three different investigation lines: hinged devices, *poly2*/gold bimorphs, and gold-on-gold contacts, to be discussed more in Chapter 4. The use of bimorph structures was already established with the CMOS MEMS process [24], and the effect had already showed up in the MUMPS process as a failure mechanism on a test version of a lateral thermal actuator, where having the gold on top caused the actuator to bend into the substrate and jam. The gold-on-gold contact had been suggested to another researcher for use in MUMPS microrelays [33]. These two ideas, combined with the surface-micromachined hinge idea from UCLA [37] were combined in the final design. The cell was intended to be a filler cell between the main designs. But this offhand combination of ideas turned out to be successful, and can now be added to the repertoire of actuators that can be used in future research.

It is the ease of using a foundry process that makes possible the wide-ranging device research such as this simple example, or the more extensive works described in

later chapters. By concentrating on adapting an existing process to achieve a desired structure rather than trying to devise ways to change the process to get the structure, new devices, applications, and methods are developed which can be turned around and used with custom processes as well.

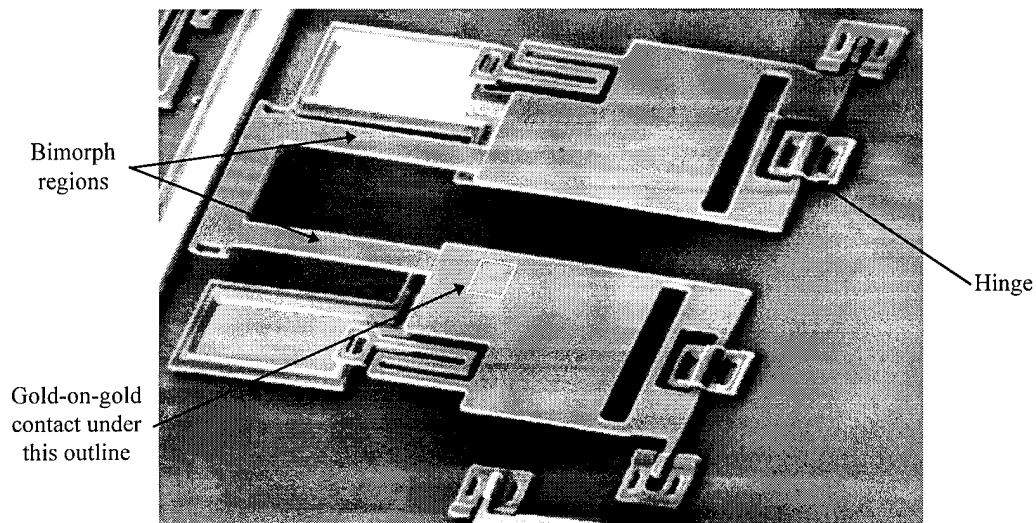


Figure 2-47. SEM micrograph of a flip-over bimorph actuator. The 'U' shaped actuator flipped over to the left has two $100 \times 8 \mu\text{m}$ *poly2*/gold bimorph legs; the gold is underneath so the legs curl upwards. The white outline shows the location of the gold-on-gold electrical contact underneath one of the hinged *poly1* support plates.

All of this experience was gained for the purpose of finding solutions to the needs outlined in Chapter 1, to reach the goal of making Large Scale MEMS (LSM) using the available foundry processes. The most immediate need for this and other research at AFIT was a high-force actuator which would be compatible with foundry fabricated CMOS electronic die.

REFERENCES:

- 1 H. Jerman, "Recent trends in silicon micromachining technology," *Proc. SPIE Micromachined Devices and Components*, vol. 2642, Austin, TX, pp. 3-8, 23-24 October 1995.
- 2 K. E. Petersen, "Silicon as a Mechanical Material," *Proc. I.E.E.E.*, vol. 70, pp. 420-457, May 1982.
- 3 S. M. Sze, *Semiconductor Devices - Physics and Technology*, John Wiley & Sons, New York, 1985.
- 4 J. Marshall, M. Gaitan, M. Zaghloul, D. Novotny, V. Tyree, J. Pi, C. Pina and W. Hansford, "Realizing Suspended Structures on Chips Fabricated by CMOS Foundry Processes Through the MOSIS Service," U. S. Department of Commerce, National Institute of Standards and Technology, NISTIR 5402, June 1994.
- 5 A. Merlos, M. Acero, M. Bao, J. Bausells and J. Esteve, "TMAH/IPA anisotropic etching characteristics," *Sensors and Actuators*, A37-38, pp. 737-743, 1993.
- 6 E. Steinsland, M. Nese, A. Hanneborg, R. Berstein, H. Sandmo and G. Kittilsland, "Boron etch-stop in TMAH solutions," *Proc. Transducers '95/Eurosensors IX*, Stockholm, Sweden, pp.190-193, 25-29 June 1995.
- 7 T. Jenkins, J. Comtois and V. Bright, "Bulk etching of silicon for micromachining," *Proceedings of the National Educators' Workshop: Update 1992, Standard Experiments in Engineering Materials Science and Technology*, NASA, pp. 39-51, Nov. 1994.
- 8 F. Kozlowski, N. Lindmair, T. Scheiter, C. Heiroid and W. Lang, "A novel method to avoid sticking of surface micromachined structures," *Proc. Transducers '95/Eurosensors IX*, Stockholm, Sweden, pp. 220-223, 25-29 June 1995.
- 9 Y. Yee, K. Chun and J. Lee, "Polysilicon surface modification technique to reduce sticking of microstructures," *Proc. Transducers '95/Eurosensors IX*, Stockholm, Sweden, pp. 206-209, 25-29 June 1995.

-
- 10 M. Houston, R. Maboudian and R. Howe, "Ammonium fluoride anti-stiction treatments for polysilicon microstructures," *Proc. Transducers '95/Eurosensors IX*, Stockholm, Sweden, pp. 210-213, 25-29 June 1995.
 11. Information available from the MCNC World Wide Web home page, WWW url: <http://www.mcnc.org>
 - 12 D. Koester, R. Mahedevan and K. Marcus, *Multi-User MEMS Processes (MUMPS) Introduction and Design Rules*, rev. 3, Oct 1994, MCNC MEMS Technology Applications Center, 3021 Cornwallis Road, Research Triangle Park, NC, 27709.
 - 13 Information available from the ARPA/iMEMS World Wide Web home page, WWW url: <http://nitride.eecs.berkeley.edu:8001/>
 - 14 F. Goodenough, "Airbags boom when IC accelerometer sees 50 G," *Electronic Design*, Aug 8, 1991.
 15. Information available from the Analog Devices/UC Berkeley ARPA iMEMS World Wide Web home page, WWW url: <http://nitride.eecs.berkeley.edu:8001>
 - 16 H. Guckel, T. Christenson and K. Skrobis, "Metal micromechanisms via deep x-ray lithography, electroplating and assembly", *Journal of Micromechanics and Microengineering*, Vol. 2, pp. 225-228, 1992.
 - 17 A. Frazier and M. Allen, "High aspect ratio electroplated microstructures using a photosensitive polyimide process," *Proc. Micro Electro Mechanical Systems '92*, Travemunde, Germany, pp. 87-92, Feb 1992.
 - 18 M. Putty and K. Najafi, "A micromachined vibrating ring gyroscope," *Proc. Solid State Sensor and Actuator Workshop*, Hilton Head, NC, pp. 213-220, 1994.
 - 19 M. Harmening, W. Bacher, P. Bley, A. El-Kholi, H. Kalb, B. Kowanz, W. Menz, A. Michel and J. Mohr, "Molding of three dimensional microstructures by the LIGA process," *MEMS '92*, Travemunde, Germany, pp. 202-207, 4-7 February 1992.
 - 20 Information available from the MCNC World Wide Web home page, WWW url: <http://www.mcnc.org>, also mailed to LIGA users.

-
- 21 Communication with MCNC, MCNC MEMS Technology Applications Center, 3021 Cornwallis Road, Research Triangle Park, NC, 27709.
 - 22 J. Marshall, M. Parameswaran, M. Zaghloul and M. Gaitan, "High-level CAD melds micromachined devices with foundries," *Circuits and Devices*, pp. 10-17, Nov. 1992.
 - 23 J. Chang, A. Abidi and M. Gaitan, "Large suspended inductors on silicon and their use in a 2 μ m CMOS RF amplifier," *I.E.E.E. Electron Device Letters*, vol. 14, pp. 246-248, May 1993.
 - 24 B. Read, V. Bright and J. Comtois, "Mechanical and optical characterization of thermal microactuators fabricated in a CMOS process," *Proceedings SPIE Micro-machined Devices and Components*, Vol. 2642, pp. 22-32, 23-24 October 1995.
 - 25 J. Comtois, T. Jenkins and V. Bright, "Micromachining of Suspended Structures in Silicon", *Proceedings of the National Educators' Workshop: Update 1992, Standard Experiments in Engineering Materials Science and Technology, NASA*, pp. 52-64, Nov. 1994.
 - 26 J. Suehle, R. Cavicchi, M. Gaitan and S. Semancik, "Tin oxide gas sensor fabricated using CMOS micro-hotplates and in-situ processing," *IEEE Electron Device Letters*, vol. 14, pp. 118-120, Mar 1993.
 - 27 M. Parameswaran, R. Johnson, M. Gaitan and R. Chung, "Commercial CMOS fabricated integrated dynamic thermal scene simulator," *IEEE IEDM*, pp. 29.4.1-29.4.3, 1991.
 - 28 B. Read, "Silicon based microactuators for telerobotic tactile stimulation," Master's Thesis, Air Force Institute of Technology, Wright-Patterson AFB, Ohio, AFIT/GE/ENG/94D-25, Dec 1994.
 - 29 First MUMPS User's Group Meeting, Chicago, IL, Organized by the MCNC MEMS Technology Applications Center, Research Triangle Park, NC, presentation material and notes, Oct. 21, 1994.

-
- 30 J. Comtois, V. Bright, S. Gustafson and M. Michalicek, "Implementation of hexagonal micromirror arrays as phase-mostly spatial light modulators," *Proc. SPIE Microelectronic Structures and Microelectromechanical Devices for Optical Processing and Multimedia Applications*, Vol. 2641, pp. 76-87, 23-24 October 1995.
 - 31 Y. Zhang and K. Wise, "An ultra-sensitive capacitive pressure sensor with a bossed dielectric diaphragm," *Technical Digest, Solid State Sensor and Actuator Workshop*, Hilton Head, SC, pp. 205-208, 1994.
 - 32 M. Michalicek, V. Bright and J. Comtois, "Design, fabrication, modeling, and testing of a surface-micromachined micromirror device," *Proc. 1995 ASME International Mechanical Engineering Congress and Exposition*, San Francisco, CA, 12-17 Nov. 1995.
 - 33 G. Fedder and R. Howe, "Thermal assembly of polysilicon microstructures," *Proc. IEEE Workshop on Micro Electro Mechanical Systems*, Nara, Japan, pp. 63-68, 1991.
 - 34 R. Boysel, "A 128x128 frame-addressed deformable mirror spatial light modulator," *Optical Engineering*, vol. 30, no. 9, pp. 1422-1427, 1991.
 - 35 M. Phipps, "Design and development of microswitches for micro-electro-mechanical relay matrices", Master's Thesis, Air Force Institute of Technology, Wright-Patterson AFB, Ohio, AFIT/GE/ENG/95J-02, June 1995.
 - 36 G. Fuhr, R. Hagedorn, T. Muller, W. Benecke and B. Wagner, "Microfabricated electrohydrodynamic (EHD) pumps for liquids of higher conductivity," *J. of Microelectromechanical Systems*, Vol. 1, No. 3, pp. 141-146, September 1992.
 - 37 K. Pister, M. Judy, S. Burgett and R. Fearing, "Microfabricated hinges," *Sensors and Actuators A*, vol. 33, pp. 249-256, 1992.

3. High Force Actuators

This chapter discusses the uses of actuators in MEMS. A review of current research in micromachined actuators highlights the need for a new class of actuators to make large mechanical systems a reality. Requirements for the new actuator are listed which set it apart from other actuators. The evolution of the new actuator is described, with test data showing how it meets the requirements specified for it. Example devices are used throughout to characterize the new actuator and to illustrate the variety of forms it can take. These actuators, both singly and in various combinations, have the attributes needed to help fulfill the overall goal of this research, which is to make increased design complexity possible in a foundry-based MEMS fabrication environment, thus enabling higher functionality.

3.1 Actuators for MEMS

The Merriam-Webster dictionary defines a machine as “a combination of mechanical parts that transmit forces, motion, and energy one to another or to some desired end (as for sewing, printing or hoisting)”. Therefore, if a system is to be *electro-mechanical*, it must have moving structures. Actuators, as the name implies, are the features of a device or system which act on its physical surroundings in a mechanical way, moving to perform this transmission of forces, motion, and energy. So although the features of a micro-system might be formed by micromachining

methods, unless it moves in some way the result is a 'MES' (microelectronic system), and not a MEMS (microelectromechanical system).

With actuators, a system can be built that transports, positions or otherwise moves parts of itself or parts of the environment it is operating in. Depending on its function, a system may need a variety of actuators to interact with its surroundings, as with a mechanical pump for the delivery of drugs in an implantable system, or a mirror array that modulates a light beam. Ideally, actuators would have the attributes listed in Table 3-1, depending on the application.

Table 3-1. Characteristics of Ideal Actuators.

low power consumption	large deflections
high force per unit volume	simple construction
reliable, repeatable operation	fast cycling
simple mechanical interface	design flexibility
simple drive and control circuitry	process compatibility

Different applications would, of course, require different combinations of features: perhaps a slower actuator would suffice if it took up less space or was compatible with the rest of the fabrication process used to build the system, or perhaps a fast actuator is needed which might require the designer to use complicated drive circuitry.

3.2 Actuator Types

Because of the obvious importance of actuators to microelectromechanics, there has been detailed research in a wide variety of actuators and actuation schemes.

Some of the basic actuation methods are listed in Table 3-2. Each of these actuation methods has been tried in a variety of forms. Examples of electrostatic and thermal actuation are described in Sections 3.2.4 and 3.2.5, since those were the only actuation methods that could be employed with the available foundry processes.

Table 3-2. Common Microelectromechanical Actuation Methods.

piezoelectric
hydraulic/pneumatic
electromagnetic
electrostatic
thermal expansion

This dissertation research focuses on methods available through foundry processes and which require minimal post-processing, so actuation methods that require special materials or fabrication steps are outside the scope of this research. They represent areas of major research efforts, though, so a brief description of each actuation method is given, along with examples drawn from the most recently reported research. These examples illustrate the incompatibility of these types of actuators with the available foundry processes.

3.2.1 Piezoelectric Actuation

Piezoelectric actuators are the topic of much research because they are capable of high forces and can be batch fabricated. Piezoelectric actuation is being investigated for rotary motors [1], cantilever actuators [2], and multi-angle

microrobotic actuators[3], such as the one shown in Figure 3-1. There are of course many other applications since actuators are such a basic component.

This area of MEMS has the added advantage of being able to draw on the design and fabrication techniques developed for Surface Acoustic Wave (SAW) devices. However, piezoelectric actuation requires the deposition of thin films of piezoelectric materials such as lead-zirconate-titanate (PZT), which is not yet offered as a fabrication step in a foundry process. Piezoelectric actuators also require high voltages, which makes them incompatible with the available CMOS electronics.

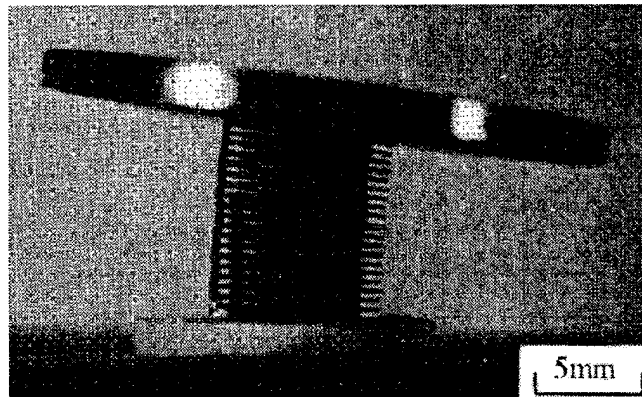


Figure 3-1. Piezoelectric multi-axis actuator. The 8mm diameter actuator shaft is composed of stacked discs of piezoelectric and dielectric materials. A 100 V drive causes it to lengthen by 200 μm . Three sets of actuators per disc allow tilt in any direction around the central axis [3].

3.2.2 Hydraulic and Pneumatic Actuation

Hydraulic actuation may be a possibility using the available LIGA foundry process, but is outside the scope of this research. Hydraulic actuation is used mainly

in microvalves [4] and micropumps [5], which to date have been best constructed in specialized bulk fabrication and wafer bonding processes. Figure 3-2 shows a typical bulk micromachined silicon microvalve for controlling gas flows.

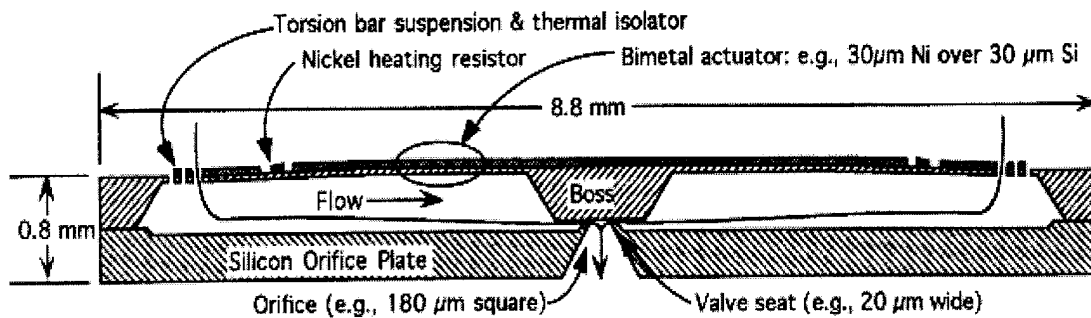


Figure 3-2. Bulk micromachined silicon microvalve design from [4].

Some fluid logic devices have been built as part of the exploratory research, but primarily as an example of the design possibilities using the LIGA process. The connection of tubing and other necessary system components is left for following researchers. One example of a pneumatic device has been fabricated in the MUMPS process, an air table and associated tubing and connections, shown in Figure 3-3. This device represents the first exploratory steps in establishing pneumatics as an option for the MUMPS process at AFIT. It was added to the MUMPS10 die because the stacked *poly1/poly2* design technique seems to hold promise for making connecting structures that are sturdy enough to attach external components such as tubing. It is also a test to see if on-die microtubing can be etched out and then resealed, or if resealing is even necessary.

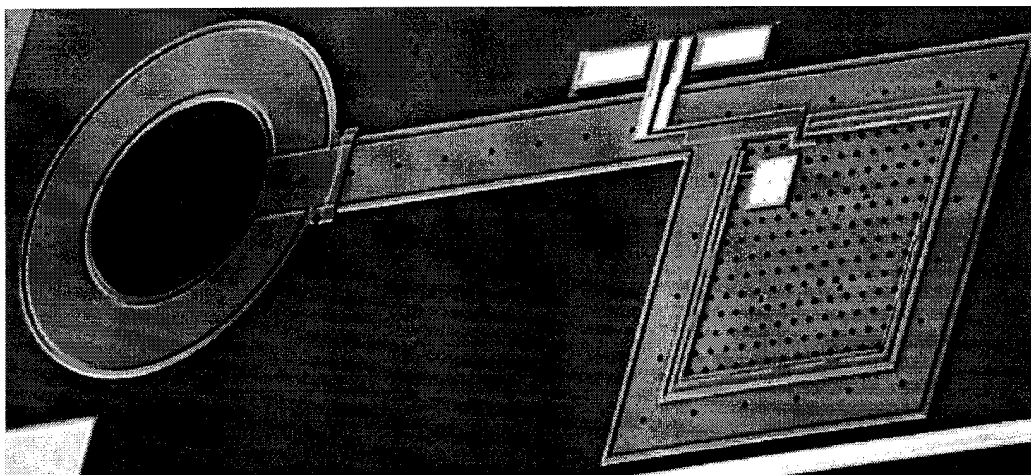


Figure 3-3. Air table, air passages and inlet port. Table area is square, $200\text{ }\mu\text{m}$ on a side in the active area, inlet port inside diameter = $150\text{ }\mu\text{m}$, outside diameter = $300\text{ }\mu\text{m}$. The $4\text{ }\mu\text{m}$ square air holes are spaced $16\text{ }\mu\text{m}$ center-to-center.

3.2.3 Electromagnetic Actuation

Electromagnetic actuation is one of the most common in macro-systems, in the form of electric motors. Electromagnetic devices do not scale down well, and they are difficult to realize in surface micromachining processes because the planar nature of these processes does not allow the creation of efficient multi-turn magnetic windings around suitable metallic cores. External activation of thin magnetic films has been tried for generic actuators [6] and even flying robots [7]; but practical applications have yet to be established.

Electromagnetic actuators have mostly been the purview of electroplated metal processes [8] which provide the thickness and materials necessary to make efficient electromagnetic motors. Even more efficient devices make use of hand-wound coils because of the added complexity of and limited number of turns possible with planar

fabrication processes [9]. Figure 3-4 shows a magnetic linear actuator with planar coils that must be wire-bonded to complete the coils, which form only a few turns.

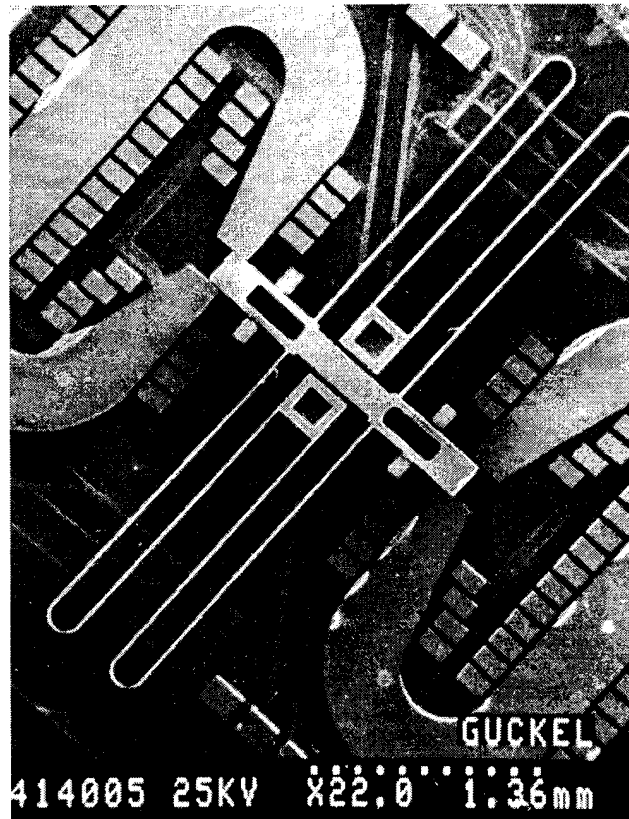


Figure 3-4. Double-sided electromagnetic actuator fabricated in the LIGA process, from [8]. The magnetic coils (rectangular posts) have not yet been completed by joining their tops with wirebonds. Curved springs span approximately 4.6 mm, and the spring/shuttle combination must added by hand after release.

3.2.4 Electrostatic Actuators

Electrostatic actuation is currently the most commonly used microelectromechanical actuation scheme because it does not require exotic materials or complicated structures. Electrostatic actuators are easy to fabricate in a variety of

processes. The force is generated by coulombic attraction or repulsion between two structures charged to different potentials. Electrostatic actuators in general have the advantages and disadvantages listed in Table 3-3.

Table 3-3. Advantages and Disadvantages of Electrostatic Actuators.

Advantages
Simple designs
Compatible with a wide variety of fabrication methods
High frequency and acceleration
Low power consumption
Can achieve rotary motion
Disadvantages
Large area needed for large forces
High bias or drive voltages
Drive circuitry not compatible with standard integrated electronics
Lateral actuators require thick layers with straight side walls
Higher forces or lower voltages require closer tolerances
Require feedback control for linear operation

Surface-micromachined electrostatic actuators come in two varieties, lateral and vertical. Vertical actuators can generate higher forces in a smaller area than lateral actuators because thin film fabrication processes naturally lend themselves to creating the large facing surfaces needed to generate sufficient electrostatic force. However, those same fabrication methods also limit the distance that vertical actuators can move, so vertical electrostatic actuators find application mainly in optical devices where small deflections suffice. Vertical electrostatic actuators were among the earliest MEMS actuators [10]; and have been implemented as bending beams, plates

that move in a purely vertical motion (pistoning) and plates that tilt around torsion suspensions.

Perhaps the best example of a torsional actuator is the Texas Instruments Digital Micromirror Device™ (DMD™). Figure 3-5 shows a cross-section of the DMD™, revealing its surface-micromachined construction and electrostatic actuation features. This device has been incorporated into a 1280 x 1024 element array, 25 x 21 mm in size, and is being commercialized for projection display systems [11].

Piston micromirrors are elements in the large systems designed as part of this dissertation research, and are discussed in detail in Chapter 5. Bending beams clamped at both ends are also finding optical applications as electrostatically collapsible planar gratings for diffractive color displays [12], and movable mirrors are used in Fabry-Perot cavities for optical modulation [13].

Lateral electrostatic actuators take two basic forms, interdigitated combs and gap-closing structures. Gap-closing structures are similar to vertical electrostatic actuators, just turned perpendicular to the plane of the die. The basic comb-style actuator configuration, along with a parallel motion suspension to keep the combs separated, was established in early research of surface-micromachined MEMS actuators [14], and an example is shown in Figure 3-6. The interdigitated comb structure increases the facing areas of the capacitor structure, so it is suitable for surface-micromachined devices fabricated with thin layers. Lateral actuators generally work best in a high aspect ratio micromachining process, such as LIGA, so enough facing area can be built.

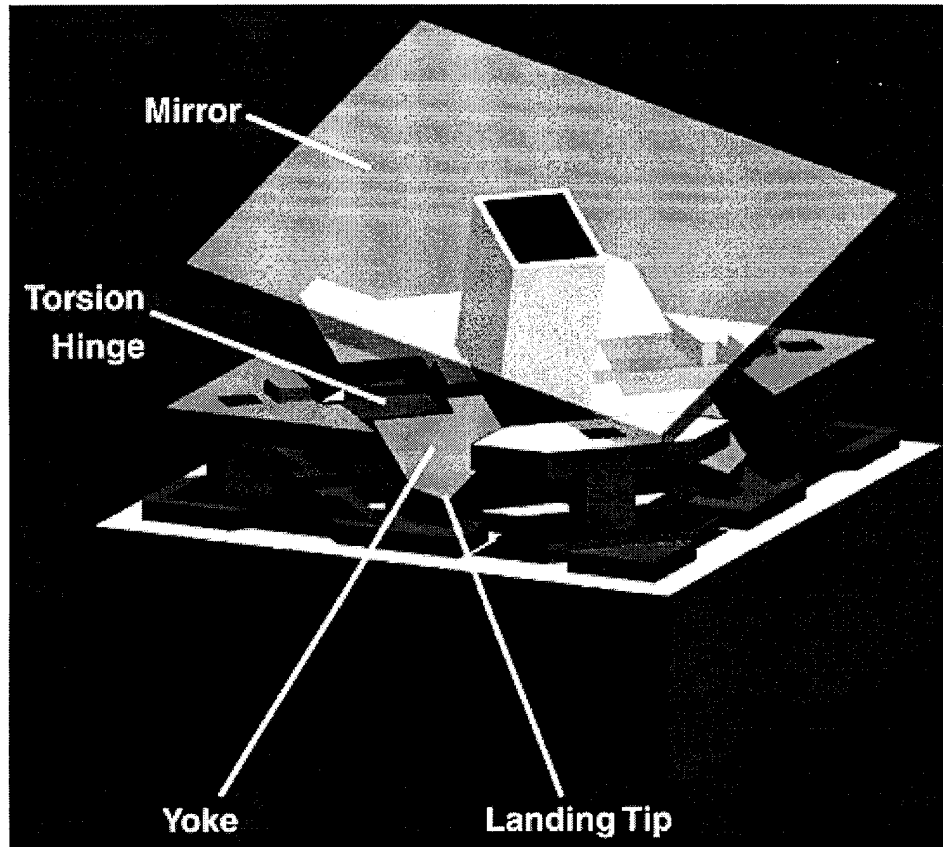


Figure 3-5. Cross-sectional drawing of the Digital Micromirror Device™ [15].

Lateral electrostatic actuators are commonly used to drive resonant structures. They are being investigated for use in vibrating ring gyroscopes [16] and as mechanical filters for electronic signals [17] because of the high Q 's obtainable. A folded-beam electrostatic comb drive resonator is used by MCNC as a test structure on the MUMPS die. The layout drawing of the MCNC resonator is shown in Figure 3-6. This resonator, fabricated in the 2 μm thick MUMPS *poly1* layer, has a nominal resonant frequency of 26 kHz. The resonant frequency of these devices is monitored for fabrication quality control [18], since the frequency is affected by fabrication-dependent parameters like polysilicon thickness and stress gradient.

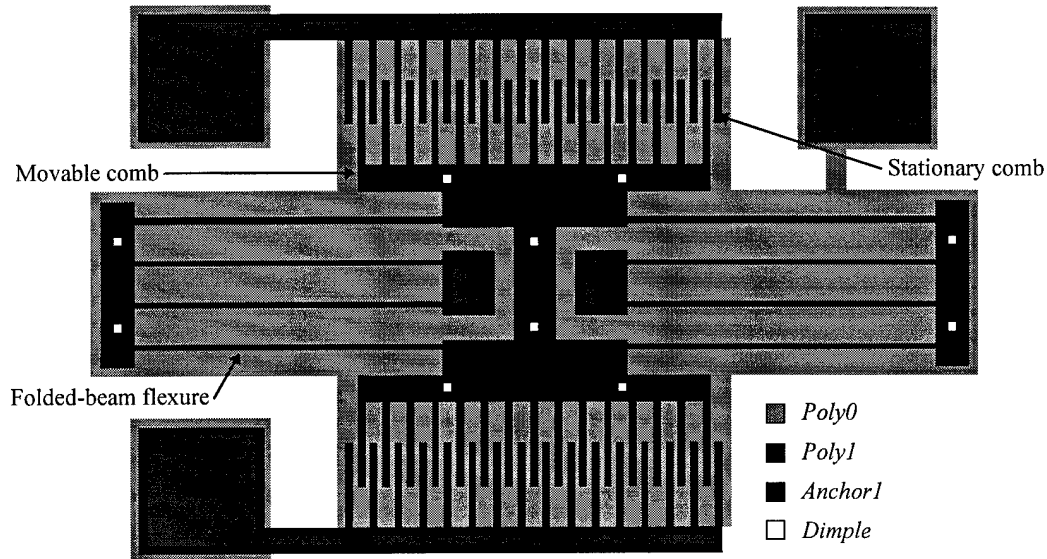


Figure 3-6. Layout drawing of a folded-beam electrostatic comb drive resonator. Comb fingers are 40 μm long, 3 μm wide with 3 μm gaps and a 20 μm initial overlap. This is the MCNC test comb placed on every MUMPS die.

Coulombic attraction is strongly dependent on the gap between the charged bodies. Equation 3-1 gives the electrostatic force F between two parallel plates of area A separated by an air gap (permittivity ϵ_0) of distance d and driven at voltage V . As seen in the squared distance term of the denominator, such actuators are non-linear. They are also unstable when the gap has closed more than about 1/3 [19], unless some form of feedback control is employed [20].

$$F = \frac{\epsilon_0 A V^2}{2d^2} \quad (3-1)$$

Attractive forces on a capacitive structure act to increase the capacitance, and the two mechanical ways to achieve this increase in an air gap capacitor with movable plates are to decrease the gap or increase the area. Electrostatic vertical actuators and gap-closing lateral actuators move to decrease the gap, and the area remains constant.

In these devices the initial gap sets the maximum controllable deflection distance. Alternatively, comb drives can increase the achievable deflection because the gap between the charged plates cannot decrease; the flexure constrains the motion to be parallel with the comb fingers, as seen in Figure 3-6. The only way for this structure to increase the force is to increase the active area by pulling the movable fingers into the static fingers. The force increases with deflection, but in a linear fashion, and the total deflection distance is set by the length of the comb fingers, which the designer can control.

To get more force from electrostatic attraction, Equation 3-1 dictates several approaches, most of which are problematic for MEMS fabrication. First, the gap can be made smaller. This severely limits the deflection achievable by a vertical actuator, and for lateral actuators requires more precise and expensive photolithography techniques. Second, increasing the area is a useful option for vertical actuators until the sag in the structure becomes significant. For lateral actuators, adding more area means adding comb fingers, or making the fingers taller. High aspect ratio MEMS fabrication processes such as LIGA are thus quite suitable for comb actuators; but for surface-micromachined processes the only option is to add more comb fingers. Increasing the die area that the actuator occupies can be a disadvantage, limiting this approach.

The last option for increasing the power of electrostatic actuators is to increase the drive voltage, and voltages between 50 and 100 V are common. A recently reported 'high force' electrostatic actuator has 20 μm tall, 2 μm wide copper comb

fingers with 2 μm gaps, it covers 1mm^2 of die area and is driven at 60 V, achieving 200 μN of force [21]. For many optical applications, where the actuator is itself the only part to be moved, the voltages can be much lower [12].

3.2.4.1 Rotary Electrostatic Motors

One interesting aspect of electrostatic actuation is that it can be used to produce rotary motion. Two basic types of rotary electrostatic motors have been developed, salient pole and wobble motors [22]. In the previous chapter, Figure 2-6 showed a surface-micromachined polysilicon salient-pole motor with an eight-pole rotor and 12-pole stator. The stators are charged and discharged in a circulating pattern, and the charged rotor poles follow the changing stator charges around.

Figure 3-7 shows an electroplated copper wobble motor [23]. Wobble motors are similar to salient pole motors in that the rotor is induced to rotate by charges circulating around stator poles; but in the case of the wobble motor the rotor is built with a center diameter larger than the hub diameter, so one edge is closer to the stators. Given the square dependency of force on gap distance seen in Equation 3-1, whatever edge is closest to the stators will be much more strongly attracted to them, keeping the rotor off center, and this closer edge follows the stator charges around [24].

Wobble motors generally run slower than salient pole motors due to the gear reduction set up by the difference in hub and rotor diameters, which act like a

planetary gear set, but without teeth. This lack of teeth results in slippage when the load increases, so the effective gear ratio can vary with load; but the rolling motion of the rotor around the hub reduces wear compared to the sliding motion of the rotor in a salient pole motor.

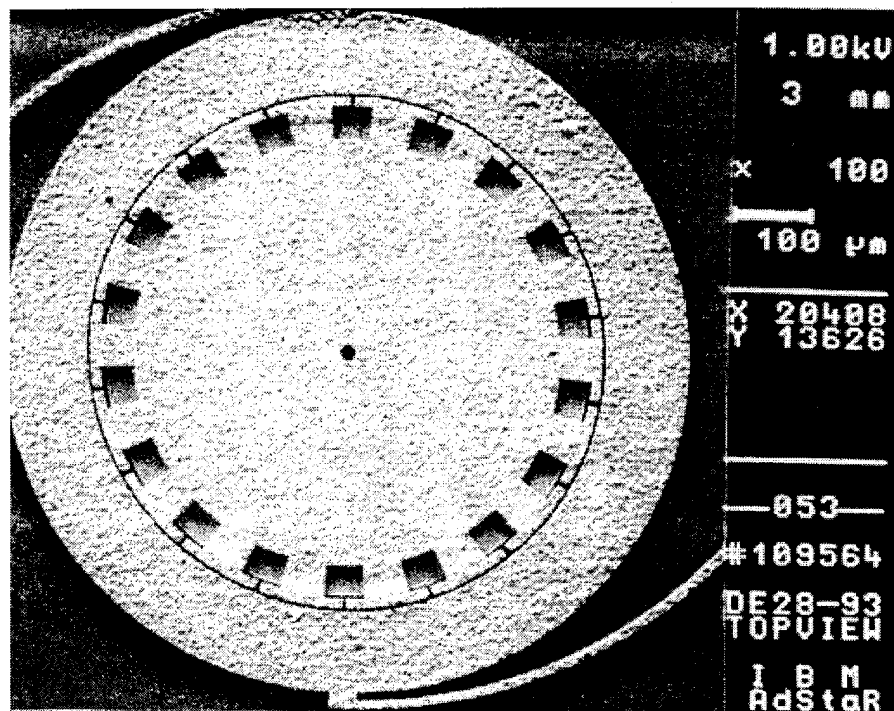


Figure 3-7. Electrostatic wobble motor fabricated in 20 μm tall electroplated copper, from [23].

One basic problem with either of these motors is that the rotor is completely surrounded by the stator. This leaves no free edge for connecting to other mechanisms, which is a serious problem due to the two-dimensional nature of most MEMS fabrication processes. So the rotor itself must carry the features that need to

be rotated, such as mirrors for a scanner [25] or recording media for a data storage device [23].

One other electrostatic motor variant has been developed which uses 90 degree opposed comb drives and a crank mechanism to turn a gear [26]. This leaves an edge of the gear free to connect to other mechanisms through a gear train, but because of the low force per unit area of surface-micromachined polysilicon comb drives, this motor takes up many square millimeters of space, making it impractical for complex systems needing several motors. Also, because of the limited, 17 μm deflection of the actuators the crank throw is small, so the cranked gear has a small diameter.

3.2.5 Thermal Multi-Morph Actuators

Larger forces than those obtainable from electrostatic actuators can be achieved by harnessing thermal expansion. However, thermal actuators are much slower than electrostatic ones since the charges in an electrostatic actuator can be moved almost instantaneously. With thermal actuators, the heat generation in the device and the subsequent removal of that heat take much longer than discharging a plate. Bi- or multi-morphic actuators in general have the advantages and disadvantages listed in Table 3-4.

Most of the research in thermal actuators has been adapting bimorph or multi-morph structures to micromachining methods. These actuators exhibit a characteristic curling motion because the force is distributed across the active, heated area, and they

are clamped at one end. Such actuators can achieve large out-of-plane deflections which are desirable for applications like tactile stimulators for telerobotics [27] and microflaps for airflow control [28].

Table 3-4. Advantages and Disadvantages of Thermal Multi-morph Actuators.

Advantages
large deflections
high forces
low drive voltages
simple drive circuitry
relaxed photolithography requirements
Disadvantages
curling motion
no lateral actuation
multi-layer construction can be complicated
medium to high power consumption
slow actuation cycles

Figure 3-8 shows a thermal multi-morph actuator designed in the Orbit CMOS MEMS process. The beam structure is composed of the four glass layers used in the standard CMOS process. The actuator is heated by a serpentine polysilicon resistor which is located between the bottom two glass layers. The resistor is visible in the photograph because the glass layers over it have conformed to its topology. There is also an aluminum second level metal layer located between the upper two glass layers. The resistor heats the cantilevered beam, and the difference in the coefficient of thermal expansion between glass and aluminum causes the beam to curl down. The beam's initial upward curl, seen in Figure 3-8, is caused by the stress gradient in

the aluminum. Table 3-5 lists the thermal expansion coefficients, showing that aluminum's coefficient is 58 times that of silicon at a given temperature.

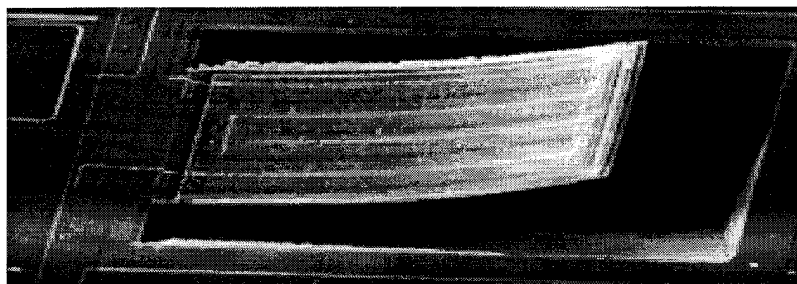


Figure 3-8. Multi-morph thermal actuator fabricated in a CMOS MEMS process. The actuator is $300 \times 100 \mu\text{m}$ and is made of layers of aluminum and glass, with a $2.6 \text{ k}\Omega$ polysilicon heating resistor.

Table 3-5. Selected Coefficients of Thermal Expansion [29].

Material	Coefficient of Thermal Expansion ($10^{-6}/\text{K}$)
Aluminum	23
Silicon Dioxide	0.4

A weight-balance force tester was designed and built for another researcher to determine the capabilities of the actuators under loaded conditions [30]. The force tester, shown in Figure 3-9, consists of a balance arm on knife-edge bearings, a counterweight, a replaceable probe tip, and a weight cup for adding weight on the probe tip side of the balance arm. The probe tip has a diameter of approximately $5 \mu\text{m}$. During device testing, a weight is placed in the weight cup and the probe tip is placed on the actuating device. Weights can be added to vary the force on the microelectromechanical beam while it is operating. The weights are short lengths of

stripped 40 gauge wire-wrap wire, and force at the probe tip is calibrated by placing the tip on a weight scale. The overall error associated with the weight-balance force tester is ± 2 mg, which was the accuracy of the scale used to calibrate the weights. The deflections of the beams under weight loads were measured using the indexed focus control of the probe station microscope.

Unloaded deflections of up to 40 μm were obtained with under 35 mW of input electrical power for 300 μm long, 100 μm wide cantilever beams driven by a 2.6 K Ω heating resistor. The beams actuated under loads of up to 15 mg. The maximum operating frequency for these beams was 149 Hz at an input power of 1.55 mW. The beams continued to operate elastically after 2.5 million cycles, showing no change in deflection behavior [30].

Also tested in that study was the time required to heat and cool the cantilever beam. Results using a microscope-based laser interferometer showed heating and cooling times of 3.3 ms and 3.35 ms, respectively. This beam therefore would have a maximum full-deflection operating frequency of 149 Hz. Above this frequency the beam will not have enough time to heat or cool and so will not completely deflect.

As this section shows, traditional multimorph thermal actuators can provide high forces, but the trade-off is slower response time, high power consumption per unit volume, and a curling motion that is not easily adapted to driving other mechanical structures. These actuators also require more layers and different materials than electrostatic actuators, leading to a more complex fabrication process.

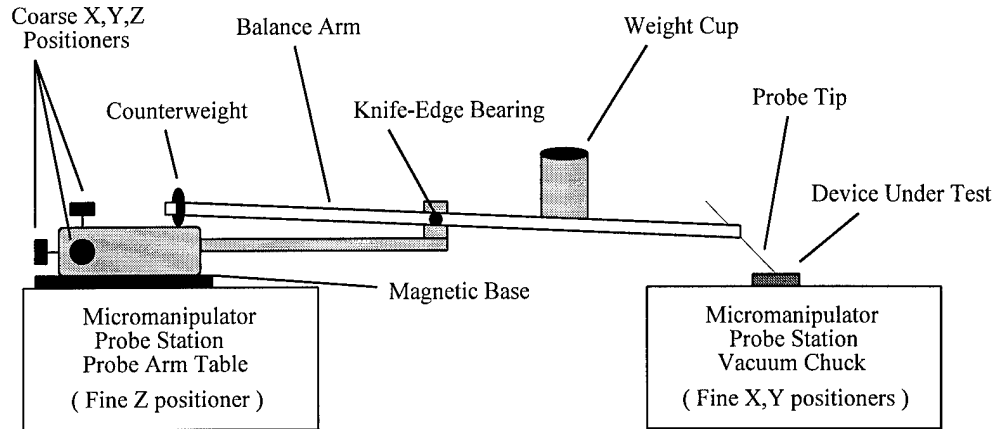


Figure 3-9. Weight-balance force tester. The tester comprises a probe point clamped to a 10 inch aluminum knitting needle which rests on a knife-edge bearing attached to a probe station manipulator base. Weights are short sections of stripped 40 gauge wire.

3.3 Need for a New Actuator

Electrostatic and thermal multi-morph actuators can be fabricated in the foundry processes available for this research. However, thermal multi-morph actuators are most easily fabricated in the CMOS MEMS process and electrostatic actuators in the MUMPS process. Although electrostatic actuation in the vertical direction has found useful applications in practical systems, lateral actuation is required for the larger deflections needed for many large system applications such as positioning optical components.

Lateral electrostatic actuation presented several difficulties. The $2\text{ }\mu\text{m}$ gap between drawn features, imposed by the foundry design rules, necessitates bias or drive voltages well over that which can be supplied by the standard electronic die. The usefulness of integrating MEMS and electronic die in a common package is negated if the MEMS actuators cannot be driven by the integrated electronics.

At CMOS voltages, roughly 3 to 10 volts, the electrostatic comb-drive actuators are not able to generate sufficient force to do much more than move the actuator itself, unless the actuator is made very large. For example, the test resonator put on the MUMPS die by MCNC (shown in Figure 3-6) requires a 50 V bias voltage, on which is impressed the alternating drive voltage, though that can be at CMOS levels.

So MUMPS lateral electrostatic actuators are large, weak, have low deflections, and are incompatible with standard CMOS electronic die. They also have a tendency to twist out of line and short out, though that is a design problem, not a basic problem with electrostatic actuation. The electrical incompatibility and low force are the largest barrier to creating large, integrated systems that can perform useful functions. Clearly, a new type of surface micromachined polysilicon actuator was needed. The desired characteristics of this new device are listed in Table 3-6 in the order of importance to this research.

Table 3-6. Requirements for the New Surface-Micromachined MUMPS Actuator.

Compatibility with standard MOSIS CMOS circuitry
High force per unit area
Robust, compact structure
Easy connection to other structures
Simple layout
Reasonable speed

3.4 Lateral Thermal Actuator

Research for a suitable actuator went through several stages of evolution, described in Section 3.4.1. The resulting device is a lateral thermal actuator,

sometimes referred to as a 'heatuator' for short. These actuators deflect less than a bimorph of the same length, but they deflect in a much more useful way because, unlike bimorphs, they move in the plane of the die, making it simple to connect these actuators to other surface micromachined mechanisms. The active volume is also much smaller, so they can cycle more quickly than the thicker bimorphs, and they require less power.

The new polysilicon actuator has a simple, flexible, and reliable design which has all the desired characteristics of Table 3-6. The only design requirement for achieving motion is to have one arm expand more than the other. So this actuator can take on a large variety of forms, including non-rectangular arms and alternative flexure layouts. A typical actuator looks like the test pointer shown in Figure 3-10. Current passing through the actuator causes the narrow arm to heat and expand more than the wider arm, since the current density is higher in the narrow arm, forcing the actuator tip towards the wider, colder side.

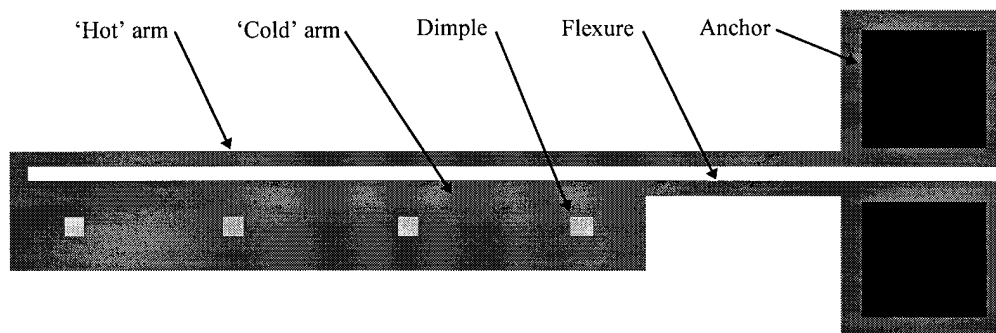


Figure 3-10. Basic layout of a 'heatuator' thermal actuator. Typical dimensions are: narrow 'hot' arm 2 μm wide, 200 μm long; wide 'cold' arm 18 μm wide, 160 μm long; flexure 2 μm wide, 40 μm long. 4 μm square dimples prevent stiction.

The actuator moves laterally in an arcing motion. Typical actuators are 200 μm long, 18 μm wide, and deflect 10 μm at the tip with a drive current of 5 mA at 5 volts, completely compatible with standard CMOS circuitry. The simple design and wide range of viable layout geometries allows this actuator to be fabricated in any MEMS process that includes a releasable, current-carrying layer, which includes most processes.

3.4.1 Actuator Development

The heatuator evolved from a simple thermally expanding beam to a structure that magnifies the expansion in an arcing motion. The final geometry was developed over several fabrication runs which included hundreds of test devices.

3.4.1.1 Prior Practice

The final geometry is patterned after a LIGA-based thermo-magnetic actuator that was published in reference [31], and on observations of thermal expansion in polysilicon beams. The LIGA design is a variation of a similar, purely magnetic LIGA actuator composed of two parallel metal bars with current running through them. In the 'thermo-magnetic' actuator, the parallel bars or 'arms' were joined at one end so the same current would flow through both of them in a 'U' shaped path. One of the arms was made twice as thick for half its length, a geometry that seems to have been chosen to make the actuator easy to model. A schematic of the structure is

shown in Figure 3-11, along with the dimensional labels that will be used throughout the rest of this chapter. Figure 3-11 is not to scale for the original LIGA actuators, which were very long, up to 1 mm.

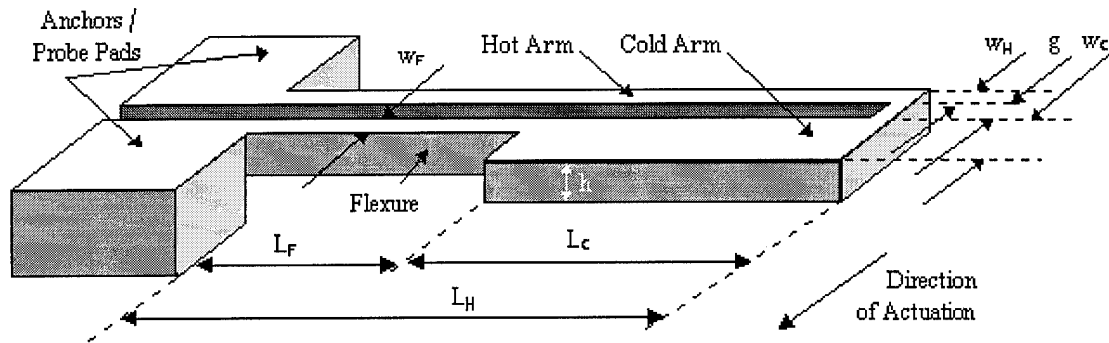


Figure 3-11. Schematic of thermal actuator with the dimensional labels used throughout the rest of this chapter.

The analytical model in Equation (3-2) was developed to describe the motion of this particular actuator geometry [31]. In this equation, ΔT_{BC} is the temperature difference between the arms, α is the coefficient of thermal expansion of the metal, d is the deflection of the tip where the arms are joined, g' is distance between the centers of the arms (not the gap g shown in the figure), and t is the thickness. One important result is that the Young's modulus drops out of Equation (3-2), as it does for any folded beam structure [14], because the actuator arms are constrained on only one side. This eliminates a source of fabrication inaccuracy, since the Young's modulus for thin film polysilicon is process dependent.

But the actuator's special geometry, where in Equation (3-2) $l = L_C = L_F = L_H/2$, $t = w_H = w_F = w_C/2$, while it makes for a simple model, turns out not to be the optimal

geometry for maximum deflection or efficiency. So although the researchers noted that the thermal effects were dominant over the magnetic effects, they apparently did not pursue the device farther. Another problem was that the device, being a variation of a magnetic actuator, was made out of metal. This meant that to generate sufficient ohmic heating, extremely large currents, over 200 mA, were required to operate the device.

$$d = \frac{\alpha(\Delta T_{BC} L_H^2)}{g' \left(0.7707 + 0.3812 \frac{t^2}{(g')^2} \right)} \quad (3-2)$$

3.4.1.2 Early Research

Observations in this dissertation research of the thermal expansion of polysilicon in the MUMPS process began with a ‘filler’ cell on the first MUMPS die, MUMPS3. This cell consisted of long thin poly beams between posts, as shown in Figure 3-12. These beams exhibited a bowing motion when a current was passed through them. The beams expanded thermally, and since they were constrained on both ends, they bowed in the center. It was drawn mostly to see how long thin beams would fabricate and how much they would sag when released. Probe pads were used as the anchor posts because it was convenient to do so, and it was thought the beams might glow usefully, or at least interestingly, if a current was passed through them, as had been observed in suspended polysilicon lines on a prior CMOS MEMS die.

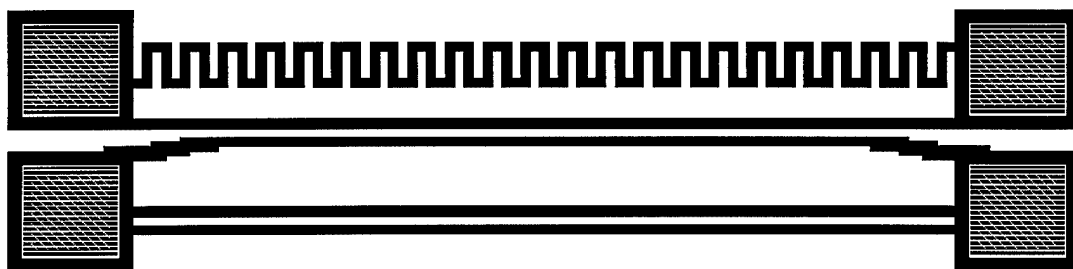


Figure 3-12. Polysilicon beam fabrication quality and sag test cell. The beams are 2 μm wide and 174 μm between probe pad anchors.

On the next MUMPS die (MUMPS4), attempts were made to harness this bowing motion in actuators called 'line drives'. These devices were mainly attempts to increase the observed bowing motion and measure it with a scale. It was not clear from observations if electrostatic forces were playing a part in the motion of the beams, though it seemed to be mostly thermal, based on the weak operation of other electrostatic devices on the MUMPS3 die and the low voltages involved.

Two sizes of 'line drives' were built, as shown in Figure 3-13. Because of the scales attached at the centers of the beams, the beams bowed into an 'S' shape rather than in a single curve. So the scale did not measure the deflection of the bowing, instead it just twisted and jammed in its guide bearing. If the beams had been drawn in a shallow 'V' shape, they may have bowed as planned, but the VLSI layout tool in use at the time allowed only 'Manhattan geometries', making angled lines and rounded objects difficult to draw. Also, no dimples were added, so the beams tended to sag and stick to the die surface, as seen in Figure 3-13.

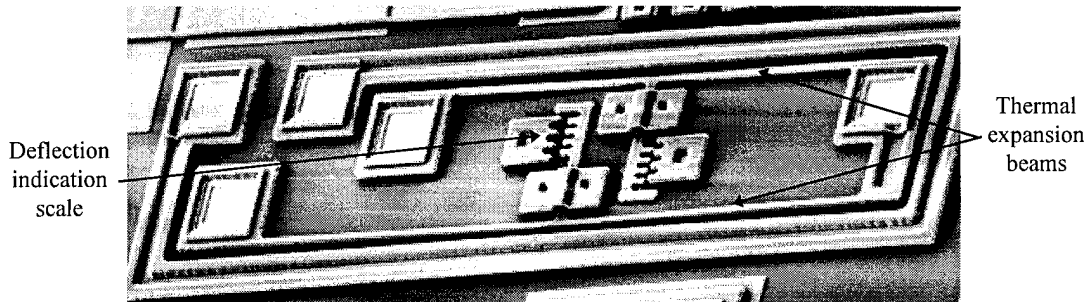


Figure 3-13. Early attempt to harness thermal expansion in a useful actuator. The longer beam is $256 \times 2 \mu\text{m}$, the shorter beam is $160 \times 2 \mu\text{m}$. Beams are stuck down.

Initial attempts were also made to use the LIGA-type actuator structure similar to Figure 3-11. It was adapted as a way to harness the thermal expansion of the polysilicon beam exhibited in the earlier experiments. But the original LIGA design dimensions were not used since it was felt that a cold arm that was wider over more of its length would heat less, resulting in more difference in expansion between the arms and thus a greater deflection. The first version of the actuator, fabricated on the MUMPS4 run, is shown in Figure 3-14. This particular actuator is attached to a folded spring flexure and vernier scale which was intended to measure deflection and force.



Figure 3-14. Early thermal actuator attached to a force-measuring spring and vernier scale. This actuator is $120 \mu\text{m}$ long, and the flexure on the wide arm is $10 \mu\text{m}$ long. The actuator arms have widths of 3 and $9 \mu\text{m}$.

3.4.1.3 Characterizing Early Actuators

In addition to the force testing structure shown in Figure 3-14, actuators with various dimensions were laid out to observe the effects of different lengths. There were two sets of actuators, one in *poly1* and the other in *poly2*, each set with two groups of seven actuators. Except for the length, all of these actuators had the same dimensions, including 3 μm wide hot arms and flexures, and all the flexures were only 10 μm long. These dimensions were later shown to result in structures that were too stiff. The actuators still exhibited some movement, though, so it was felt that they were perhaps too short. Since they were still a peripheral research item at this point, they were repeated with little modification on MUMPS5; they were just made longer.

At the end of each set of MUMPS4 test actuators was a lever arrangement intended to multiply the deflection of an actuator. This levering showed some promise, so it was repeated on each end of the MUMPS5 sets, as seen in Figure 3-15. The actuators each have a topologically-formed cup on the lever to help keep the lever aligned with the actuator, and to reduce the amount of deflection lost in bringing the actuator into contact with the lever.

Figure 3-15 shows most of a MUMPS5 *poly2* test set, including the end of an adjacent set, showing both types of multiplying arms. These test actuators all have flexures that are only 10 μm long. The shorter actuators (on the left in the SEM micrograph) have arm widths of 3 and 8 μm and lengths from 100 to 160 μm in 10 μm

increments. The longer actuators have arm widths of 3 and 6 μm and lengths from 150 to 210 μm in 10 μm increments.



Figure 3-15. Test set of the first versions of the thermal actuator. Actuators are 100 to 210 μm long. Two types of deflection multiplying pointers are shown attached to actuators at the top.

Also on MUMPS5 was a thermally actuated gripper to demonstrate a possible use for the actuators, shown in Figure 3-16. Making grippers seems to be a traditional thing to do with new MEMS actuators to demonstrate a use for them.

The actuators built into all these structures were early, non-optimal designs: the cold-to-hot arm width ratio is too low at 3:1, and the flexure was too short and wide (10 μm x 3 μm). So although these actuators worked, they had disappointingly small deflections. The gripper design worked the best because the deflection of the actuators was doubled by the length of the gripper arms. But most importantly, the

grippers closed fully at 5.5 volts without overheating the actuator arms, showing that the actuators would be compatible with CMOS circuitry.

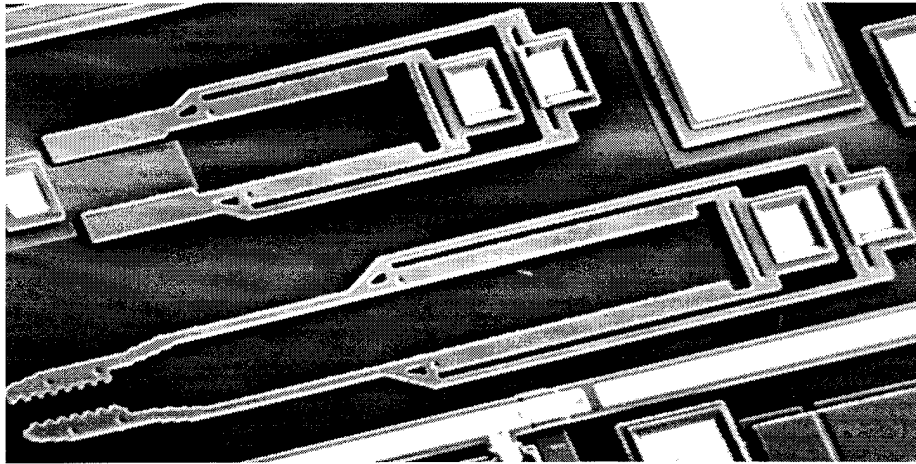


Figure 3-16. Grippers made with the first version of the thermal actuator. The bottom grippers are $390\text{ }\mu\text{m}$ long, and close fully $12\text{ }\mu\text{m}$ with an applied voltage of 5.5 V. The upper pair of actuators is arranged as a variable capacitor with a *poly0* lower plate.

Investigation of the actuators continued into the MUMPS6 run, where 204 variations of these actuators were laid out to determine the optimum length, width and flexure dimensions. The test results from these actuators led to the final design, which is more along the dimensions of the actuator shown in Figure 3-10.

3.4.2 Final Actuator Design Test Results

Given the promising results from MUMPS4 and MUMPS5, and the disappointing results from this and other research using lateral electrostatic comb drive actuators, serious consideration was given to finding the best geometry

'heatuators' on the MUMPS6 run. To determine the characteristics of a rectangular thermal actuator, 17 test sets, each containing 12 rectangular polysilicon test actuators, were designed and fabricated on the MUMPS6 run. Dimensions of the arm widths, flexure length, overall length, and polysilicon thickness differed from array to array, while within each array only one dimension was varied.

The dimension labels used in this section are the ones indicated in Figure 3-11. In most of the arrays the width of the cold arm, w_c , was varied in 1 μm increments, since varying the current density in the cold arm should have the largest impact on the temperature difference between the arms. Figure 3-17 shows a small section of a test array of *poly1* actuators.

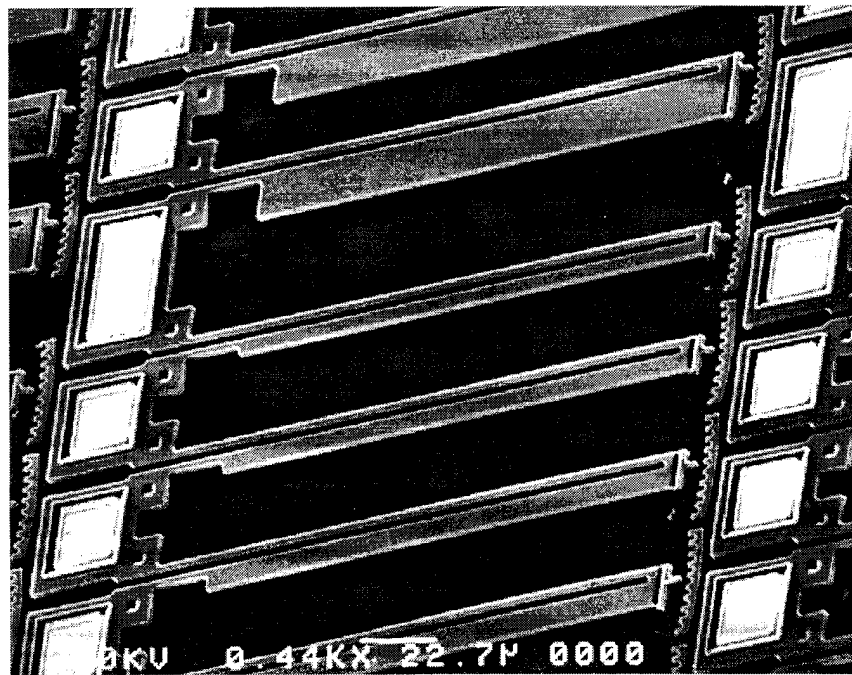


Figure 3-17. Test set of thermal actuators fabricated in 2 μm thick *poly1*. For the actuators shown here, the design dimensions are $w_F=w_H=2\text{ }\mu\text{m}$, $L_H=150\text{ }\mu\text{m}$, $L_F=15\text{ }\mu\text{m}$, and $g=2\text{ }\mu\text{m}$. The narrowest actuator (third from the top) has $w_c=3\text{ }\mu\text{m}$, and the widest (second from the top) has $w_c=14\text{ }\mu\text{m}$.

All of the dimensions reported are the drawn dimensions. The dimensions of the fabricated devices actually come out smaller than the drawn dimensions as a result of slight sidewall over-etching during the RIE process. On the MUMPS6 fabrication run, the polysilicon edge was inside the drawn dimension by $0.175\text{ }\mu\text{m}$; so lines drawn $2\text{ }\mu\text{m}$ wide came out $2\text{ }\mu\text{m} - 2 \times 0.175\text{ }\mu\text{m} = 1.65\text{ }\mu\text{m}$ wide. For the MUMPS10 process, however, the over-etch was much less, at $0.0341\text{ }\mu\text{m}$. This is one dimension that should be checked on each run for accurate test results.

3.4.2.1 Current versus Deflection

The most important characteristics to determine were the compatibility of the actuators with CMOS circuitry, and how far each design could deflect. For each measurement of input electric current versus deflection, the actuator was started at zero deflection, and then deflected to a measured position by adjusting the drive voltage. When the actuator reached the desired deflection, the current through the actuator was recorded, along with the voltage and deflection. This was repeated, increasing the deflection each time, until the actuator began to deform from overheating. Five copies of each actuator were measured, for a total of over 1,020 test sequences [32].

The maximum deflection shown in the following graphs is the maximum deflection before actuator deformation, which means the deflection reported is reversible and repeatable. Deflections were measured using the eyepiece reticule of

the probe station microscope, which limited the accuracy to $\pm 0.5 \mu\text{m}$. A representative deflection versus current characteristic for one actuator geometry is shown in Figure 3-18. No error bars are shown for the deflection readings.

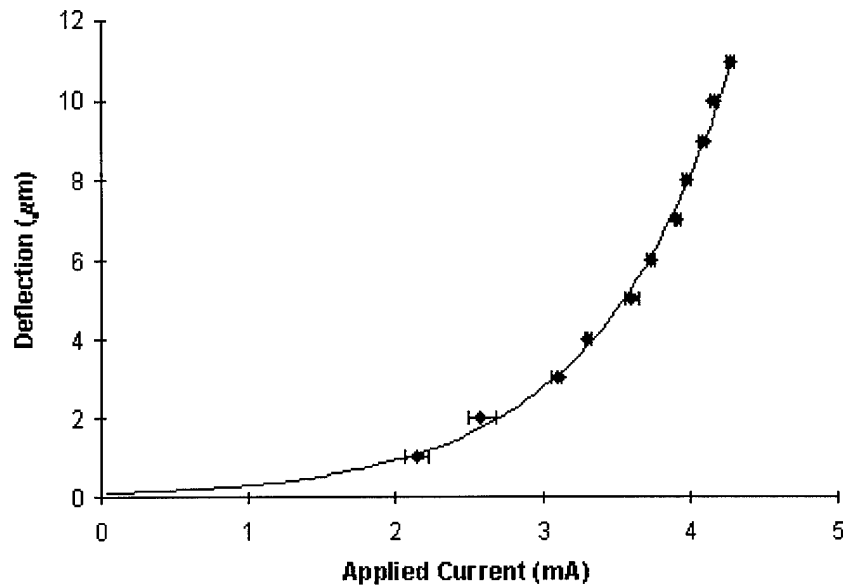


Figure 3-18. Deflection versus applied current for $2 \mu\text{m}$ thick *poly1* actuator [33]. The dimensions are $L_H = 200 \mu\text{m}$, $w_H = w_F = 2 \mu\text{m}$, $L_F = 35 \mu\text{m}$, $w_C = 14 \mu\text{m}$, and $g = 2 \mu\text{m}$. Points show the mean current for five identical actuators. Horizontal error bars indicate one standard deviation in the current measurements. The maximum reversible deflection of $11 \mu\text{m}$ at 4.3 mA was obtained with a drive voltage of 6.7 V , for an input power of 28.8 mW .

Referring to Figure 3-11, the dimensions of the actuator whose characteristics are given in Figure 3-18 are $L_H = 200 \mu\text{m}$ (length of the thinner or 'hot' arm), $L_F = 35 \mu\text{m}$ (length of the flexure at the base of the wider or 'cold' arm), $w_H = w_F = 2 \mu\text{m}$ (flexure and hot arms are the same width), $w_C = 14 \mu\text{m}$ (width of the cold arm), and $g = 2 \mu\text{m}$ (gap between the hot and cold arms). The actuator was made in the *poly1* layer which is $2 \mu\text{m}$ thick. An exponential curve best fits the data, as shown by the solid

trend line in Figure 3-18. Similar exponential results were observed with all the tested actuators. The greatest reversible deflection of any tested actuator was 12 μm at 4.3 mA and 6.0 volts, for a *poly1* actuator with dimensions $L_H = 200\ \mu\text{m}$, $L_F = 40\ \mu\text{m}$, $w_H = w_F = 2\ \mu\text{m}$, $w_C = 14\ \mu\text{m}$, and $g = 2\ \mu\text{m}$.

3.4.2.2 Back-bending Characteristics

These actuators will briefly deflect farther than the maximum deflections shown in the graphs, but then hot arm begins to deform and shrink in length, and the actuator moves backwards from the maximum deflection. When the current is removed, the actuator is left permanently back-bent from the zero position. Measurements were taken of this back-bending effect since it occurred with all of the tested actuators. If not taken to extremes, this back-bending did not cause the actuators to be unusable. Figure 3-19 shows the increase in maximum achievable back-bending versus cold-to-hot arm width ratio for actuators of three different lengths.

As expected, more back-bending can be achieved with longer actuators since there is more hot arm length to shrink; but back-bending also shows a dependence on the arm width ratio similar to the relationship seen next in Figure 3-20 for maximum achievable forward deflection, for reasons that have not been determined. As Figure 3-19 indicates, back-bending is less predictable than forward deflection, especially for large backwards deflections, and gets less predictable as the actuators get longer.

This unpredictability is a result of the mechanism that causes the back-bending, which is the permanent deformation of the hot arm.

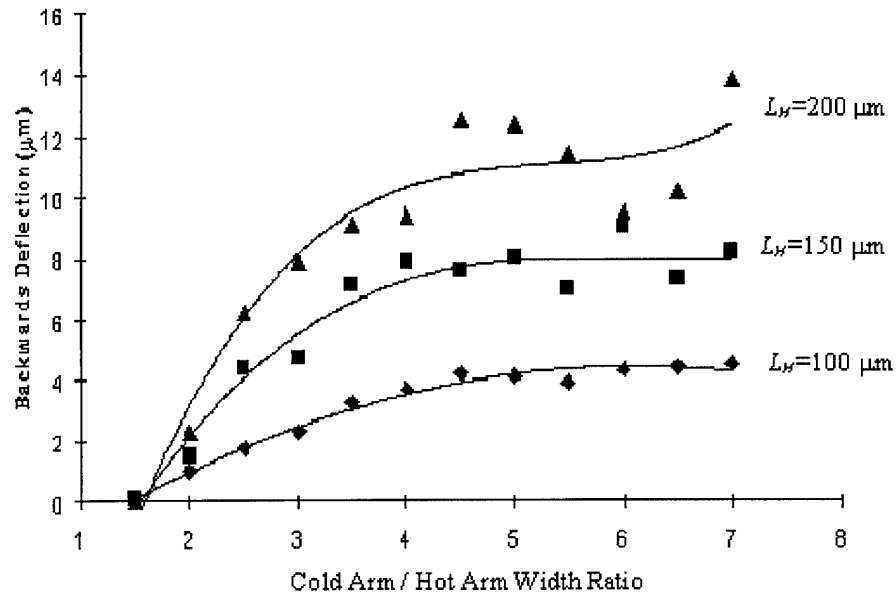


Figure 3-19. Back bending versus cold-to-hot arm width ratio for 100, 150, and 200 μm long *polyI* actuators [33]. The fixed dimensions are $w_H = w_F = 2 \mu\text{m}$, $L_F = 15 \mu\text{m}$, and $g = 2 \mu\text{m}$. The symbols indicate the mean value of the maximum achieved deflection for five identical tested actuators. The lines fit to each data set are 4th order least-squares polynomial fits created by the spreadsheet software, and are intended only to show the general trend, they are not intended to be a model of the behavior.

Small amounts of back-bending can be reasonably controlled, but as the back bending is increased the predictability is lost. When only slightly back-bent, an actuator can be made to deflect around the original zero deflection point, or the actuator can be set to be used only in the region of 'negative' deflection from its fabricated position.

3.4.2.3 Repeatability and Reliability

In forward deflection the devices exhibited good repeatability, as shown by the error bars on the measurements of the drive current in Figure 3-18. Once an actuator was characterized, any identical copy of it could be set to a particular deflection by setting the voltage. This held true for all the actuator geometries measured.

A reliability test was also performed on one of the actuators. An actuator with dimensions $L_H = 200\text{ }\mu\text{m}$, $L_F = 30\text{ }\mu\text{m}$, $w_H = w_F = 2\text{ }\mu\text{m}$, $w_C = 13\text{ }\mu\text{m}$, and $g = 2\text{ }\mu\text{m}$ was operated continuously for 75 hours with a 50 Hz square wave signal, for a total of 13.5 million actuation cycles. The 5.75 volt (peak) drive signal produced a deflection which snapped from $0\text{ }\mu\text{m}$ to $9\text{ }\mu\text{m}$ and back. A slight lateral bow in the hot arm of less than $0.5\text{ }\mu\text{m}$ was apparent after 60 hours, but no change in maximum deflection was detected after the full test.

3.4.2.4 Effects of Actuator Geometry

Compilations of the data showing how variations in geometry affect the maximum deflection are shown in Figure 3-20 through Figure 3-22. Figure 3-20 shows a comparison of *poly1* actuator performance as a function of increasing cold-to-hot arm width ratio for 100, 150, and $200\text{ }\mu\text{m}$ long devices. The fixed dimensions are $w_H = w_F = 2\text{ }\mu\text{m}$, $L_F = 15\text{ }\mu\text{m}$, and $g = 2\text{ }\mu\text{m}$. This shows the expected result that longer actuators deflect more; but more importantly, it shows the effects of the arm width ratio. The deflection increases dramatically for ratios up to about 4:1, then

increases only slightly from there up to 7:1, where further increases in the cold arm width have little effect. Similar results were found for actuators fabricated in the thinner *poly2*, $h = 1.5 \mu\text{m}$. Thus the actuators with arm width ratios of 7:1 achieved the maximum deflection for an actuator of this design. Actuators with an arm width ratio of 2:1 achieved only about half of the deflection of actuators with the same length but with the 7:1 arm width ratio.

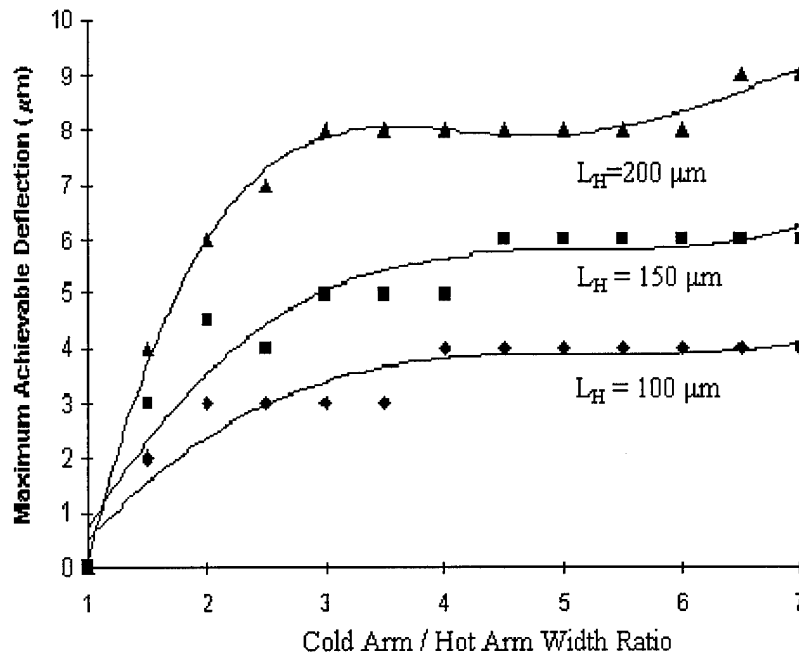


Figure 3-20. Maximum achievable deflection versus cold-to-hot arm width ratio for *poly1* actuators 100, 150, and 200 μm long. Fixed dimensions are $w_H = w_F = 2 \mu\text{m}$, $L_F = 15 \mu\text{m}$, and $g = 2 \mu\text{m}$. The symbols indicate the mean value of the maximum achieved deflection for five identical tested actuators. The lines fit to each data set are 4th order least-squares polynomial fits created by the spreadsheet software, and are intended only to show the general trend, they are not intended to be a model of the behavior.

Figure 3-21 shows the maximum deflection versus cold-to-hot arm width ratio for actuators with different width hot arms and flexures: $w_F = w_H = 2, 3, 4$, and $5 \mu\text{m}$.

These actuators had fixed dimensions of $L_H = 200 \mu\text{m}$, $L_F = 30 \mu\text{m}$, and $g = 2 \mu\text{m}$. Narrower hot arm widths were able to achieve larger maximum deflections, since the stiffness of the flexures increases with width. The flexures were made the same width as the hot arms so they would carry the same current density.

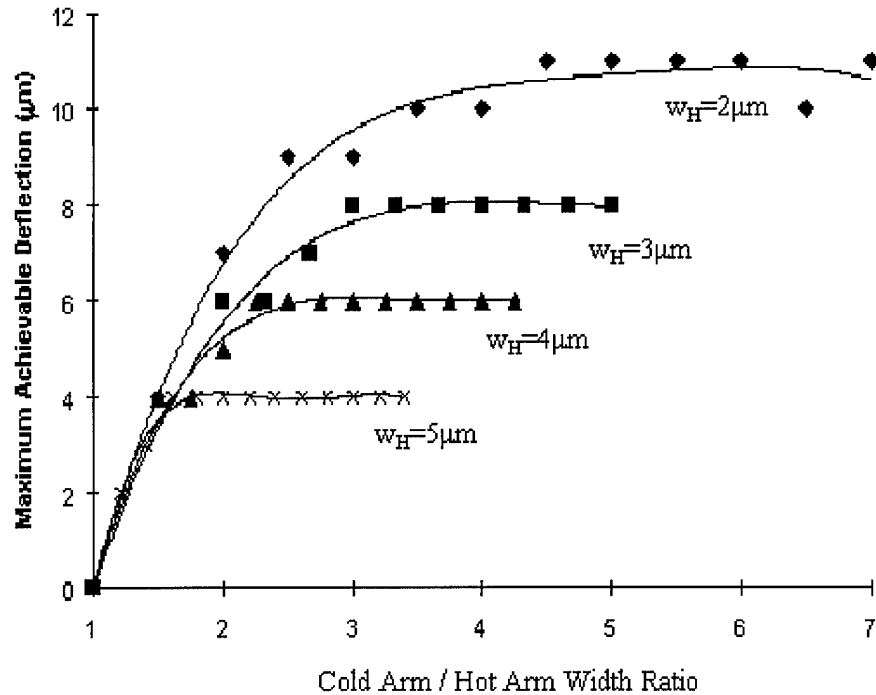


Figure 3-21. Maximum achievable deflection versus cold-to-hot arm width ratio for *poly1* actuators with hot arm and flexure widths of 2,3,4 and 5 μm [33]. The fixed dimensions are $L_H = 200 \mu\text{m}$, $L_F = 30 \mu\text{m}$, and $g = 2 \mu\text{m}$. The symbols indicate the mean value of the maximum achieved deflection for five identical tested actuators. The lines fit to each data set are 4th order least-squares polynomial fits created by the spreadsheet software, and are intended only to show the general trend, they are not intended to be a model of the behavior.

Figure 3-22 shows that the flexure length had less of an effect on the maximum achievable deflection than changes in the cold-to-hot arm width ratio. The results in Figure 3-22 are for actuators with design dimensions of $w_H = w_F = 2 \mu\text{m}$, $w_C = 14 \mu\text{m}$

$L_H = 200\text{ }\mu\text{m}$, and $g = 2\text{ }\mu\text{m}$. The decreased force needed to bend the longer flexures is somewhat offset by their increased thermal expansion, since they act the same as the hot arms. The maximum achievable deflection would go to zero when $L_F = L_H$ and $L_C = 0$, of course. At that point, the actuator will only increase slightly in length as it is heated. The trends indicate that no great increase in maximum deflection can be achieved by trading off cold arm length for flexure length, in the range tested. The poor performance of the earliest actuator designs was due to the dimensions chosen: the flexures and overall length were too short, the hot arms and flexures were too wide, and the ratio of cold to hot arm widths was too small.

3.4.2.5 Maximum Operating Frequency

Tests were performed to determine the maximum operating frequency of these actuators by observing an actuator through the probe station microscope while increasing the drive frequency. Using a 4.82 volt zero-to-peak square-wave driving signal, an actuator with dimensions $L_H = 200\text{ }\mu\text{m}$, $L_F = 35\text{ }\mu\text{m}$, $w_H = w_F = 2\text{ }\mu\text{m}$, $w_C = 14\text{ }\mu\text{m}$, and $g = 2\text{ }\mu\text{m}$ was found to deflect from 0 to $5\text{ }\mu\text{m}$ up to 150 Hz, following the drive signal. This deflection was about half the maximum possible with this actuator geometry due to limitations of the signal generator. From 150 to 300 Hz, the actuator began to stay deflected since there was less time to dissipate the heat from the hot arm. Visible motion ceased at frequencies above 450 Hz, leaving the actuator fully deflected at $5\text{ }\mu\text{m}$.

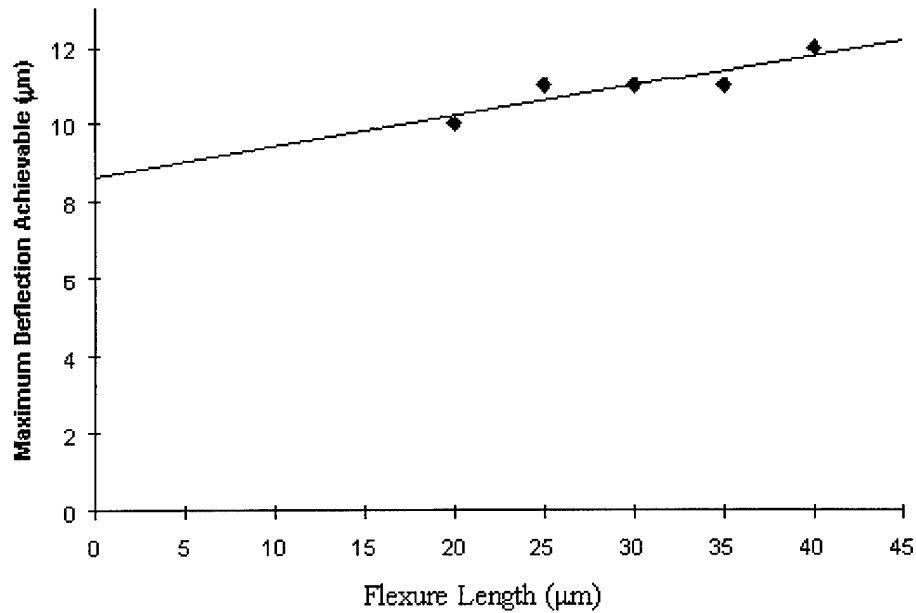


Figure 3-22. Maximum achievable deflection versus flexure length [33]. The fixed dimensions of the actuators are $w_H=w_F=2\text{ }\mu\text{m}$, $L_H=200\text{ }\mu\text{m}$, $w_C=14\text{ }\mu\text{m}$, and $g=2\text{ }\mu\text{m}$. The symbols indicate the mean value of the maximum achieved deflection for five identical *poly1* actuators. The line is a linear fit to show the general trend. Note that the spreadsheet software extends the line to zero, but it is not valid outside the data points.

A more accurate observation was made of the maximum operating frequency with a movable grating incorporating thermal actuators to slide one grating over another, shown in Figure 3-23. The device was designed to shift intensity between the first and second orders as an optical switch. The grating moved $1.75\text{ }\mu\text{m}$ up to a frequency of 1 kHz , where it rolled off, but modulation was still detectable up to 10 kHz [34]. The increased operating frequency of this device compared to single, unattached devices may be due in part to the extra heat loss path down the tethers which join the actuators to the grating, but the flow of heat in these devices has not been determined.

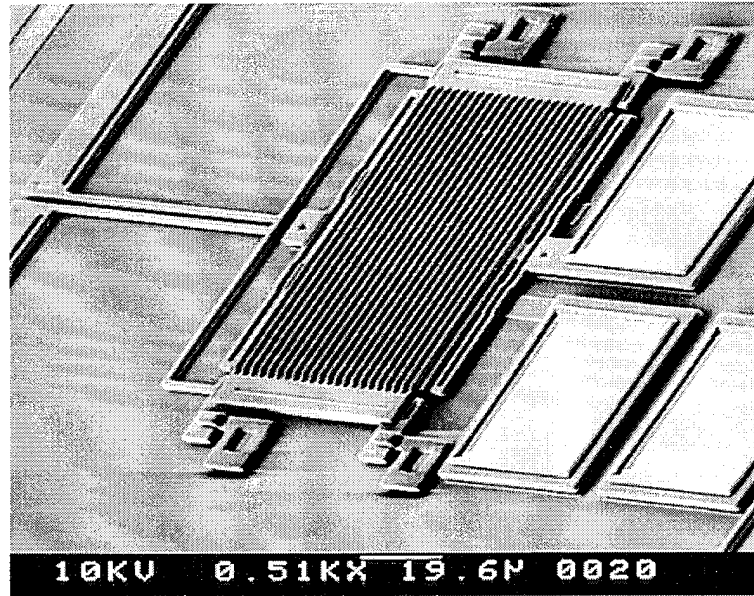


Figure 3-23. Variable diffraction grating, 90 x 120 μm . Both the upper and lower gratings have lines 2 μm wide spaced 4 μm center-to-center. Upper grating is moved laterally over the lower grating by two thermal actuators attached to the left [34].

3.4.2.6 Force Testing

Equation (3-3) shows the deflection versus force relationship of a beam clamped at one end, with the force F applied at a distance L from the clamp [35]. The other variables in Equation (3-3) are the deflection y , Young's modulus E , the width of the beam w , and the height of the beam h . These labels match the direction of bending and dimensional labels of Figure 3-11.

$$y = \left[\frac{L^3}{Ehw^3} \right] F \quad (3-3)$$

Note that the dimension of the arm in the direction of bending (the width, w , in this case for lateral bending) has a $1/x^3$ relationship to deflection, whereas the increase

in deflection due to a change in height is just $1/x$. So making the flexure or hot arm wider in the direction of motion will decrease the deflection of the actuator. Making the beam taller will have a less detrimental effect on the deflection, and would make the actuator stronger since there would be more volume of hot arm material expanding. However, in surface-micromachining processes, while the width is a designed dimension, the height is a process dimension, i.e. the thickness of the deposited layer. So changing the height is not an option for a foundry-fabricated actuator.

3.4.2.6.1 Force Test Beam Geometry

The first force testing device, shown in Figure 3-14, was too stiff and the actuator too small, so the vernier could barely be budged before the actuator burned out. Fortunately, the two deflection multiplying levers at the ends of the test arrays in Figure 3-15 could also be used for force measurements since they incorporated a scale, longer, stronger actuators, and a single flexure designed to be more compliant than the folded spring of the original force tester. The actuator presses on the deflection multiplying arm at some distance from the anchor, and the far end of the arm indicates the deflection against a scale.

The actuator's deflection, as indicated on the scale, does not multiply the deflection at the point of force application by the length ratio. The deflected portion of the beam bends in a curve from the anchor point to the point of force application,

and is a straight line from that point to the tip out by the scale. This means that the pointer arm lies along the line tangent to the curve of the bent beam at the point of force application, and indicates more deflection than the length ratio implies.

Figure 3-24 shows the geometry of a deflected test beam with a deflection-multiplying arm attached past the point of force application.

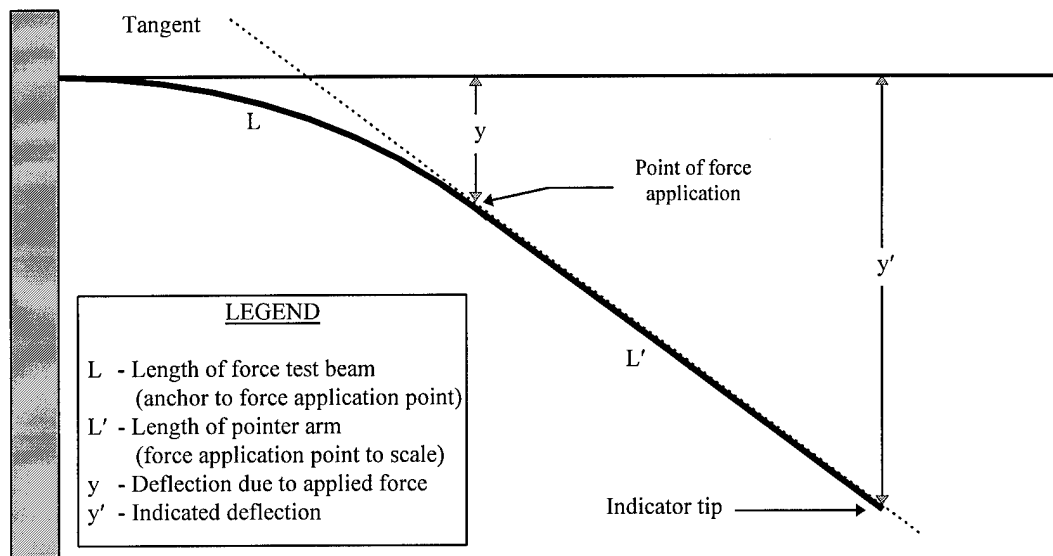


Figure 3-24. Geometry of a bent force testing beam. Beam extends past the point of force application to multiply the deflection. Multiplied deflection is indicated on a scale as seen in Figure 3-25.

The deflection at the indicator tip of the beam is given in Equation (3-4) [35], which has been recast using the notation of Figure 3-24.

$$y' = \left[\frac{F}{6EI} \right] [2L^3 + 3L^2 L'] \quad (3-4)$$

The test beam has a rectangular cross-section, which has inertia, I , given as [35]:

$$I = hw^3/12 \quad (3-5)$$

Substituting for I in Equation (3-4) using Equation (3-5), and re-arranging to get the force, F , as a function of the indicated deflection, y' , yields:

$$F = y' \left[\frac{Ehw^3}{(4L^3 + 6L^2 L')} \right] \quad (3-6)$$

Equation (3-4) is based on Hooke's law for spring force, and is for a linear change in deflection with applied force. Thus Equation (3-6) is only good for situations where the beam deflection versus force is linear. These force test beams are used at small deflections, less than 20 degrees typically, assumed to meet this requirement.

Using Equation (3-6), the factor next to y' is calculated from fixed, known geometrical measurements and the Young's modulus. So it can be pre-calculated for each force test beam geometry and used to convert the observed y' to the force F by a simple multiplication.

3.4.2.6.2 Initial Force Tests

Equation (3-6) can be applied to the devices of Figure 3-15, which were originally designed just to multiply the deflection of the actuator, but can also be used

to determine the force of the actuators. The larger of the two actuators has drawn dimensions of $L_H = 259 \mu\text{m}$, $w_H = w_F = 3 \mu\text{m}$, $L_F = 10 \mu\text{m}$, $L_C = 275 \mu\text{m}$, $w_C = 9 \mu\text{m}$, and $g = 3 \mu\text{m}$. The Young's modulus for polysilicon is taken as $E = 160 \text{ GPa}$ [36].

The width of the flexing portion of the lever arm is taken as $w = 1.65 \mu\text{m}$, based on measured results for similar flexures drawn $2 \mu\text{m}$ wide on the MUMPS6 die. The deposited thickness of the first polysilicon layer is $h = 2.0175 \mu\text{m}$. The length L of the lever from the anchor to the actuation point is $45 \mu\text{m}$, and the length of the pointer portion is $L' = 300 \mu\text{m}$. A maximum deflection of the far end of the lever of $y' = 12 \mu\text{m}$ was attained. This deflection was consistent for 3 tested actuators, and gives an indicated force of $4.33 \mu\text{N}$, using Equation (3-6).

The shorter actuator, with dimensions $L_H = 139 \mu\text{m}$, $w_H = w_F = 3 \mu\text{m}$, $L_F = 10 \mu\text{m}$, $L_C = 155 \mu\text{m}$, $w_C = 9 \mu\text{m}$, and $g = 3 \mu\text{m}$, was also tested. Its multiplying lever had the same w , h , and L dimensions, but $L' = 180 \mu\text{m}$. The actuator deflected the far end of this multiplying arm $8.5 \mu\text{m}$, also consistent for 3 tested actuators. This deflection gives an actuator force of $4.83 \mu\text{N}$, using Equation (3-6), similar to the previous result.

This similarity may indicate that the force test beams are not a significant load on the actuators, and the actuators are just bending as far as they would whether the beams were there or not. These results could also indicate that the force of the thermal expansion does not depend on hot arm length, that only the possible total deflection depends on the length; i.e. there is more hot arm length to expand, though with the same amount of force. In either case, these results were sufficient to show

that the thermal actuators were worth pursuing as a high-force alternative to electrostatic actuators for the MUMPS foundry process. More tests were performed to help analyze these results.

3.4.2.6.3 Improved Actuator Force Tests

The actuators built into the two MUMPS5 structures mentioned above were early, non-optimal designs: the cold-to-hot arm width ratio was too low at 3:1, and the flexure was too short and wide ($10 \times 3 \mu\text{m}$). But these early actuators, even with their non-optimized dimensions, still produced a force much larger than electrostatic actuators, and in much less area, as will be seen later. Newer, optimized designs with purpose-built force testing beams, shown in Figure 3-25, were fabricated on the MUMPS10 run.

These actuators have $220 \times 2.5 \mu\text{m}$ hot arms and $50 \times 2.5 \mu\text{m}$ flexures. They can press in either the forward or back bending direction against a *poly1* force measuring beam. The force measuring beam has $L = 60 \mu\text{m}$ and $L' = 180 \mu\text{m}$. The flexing portion of the beam is drawn at $w = 2 \mu\text{m}$. For the MUMPS10 run, the side wall over-etch was much less than MUMPS6. Features that were drawn $2 \mu\text{m}$ wide were fabricated $1.93 \mu\text{m}$ wide, for an over-etch of $0.0341 \mu\text{m}$ per side wall. The *poly1* thickness on the MUMPS10 fabrication run was $h = 1.9720 \mu\text{m}$.

Entering these values into Equation (3-6) gives a factor of 0.553 N/m to multiply the indicated deflection to get the force needed to achieve that deflection. So

the deflection y' , indicated in μm , times 0.553 yields the force F , in μN , needed to achieve that deflection.

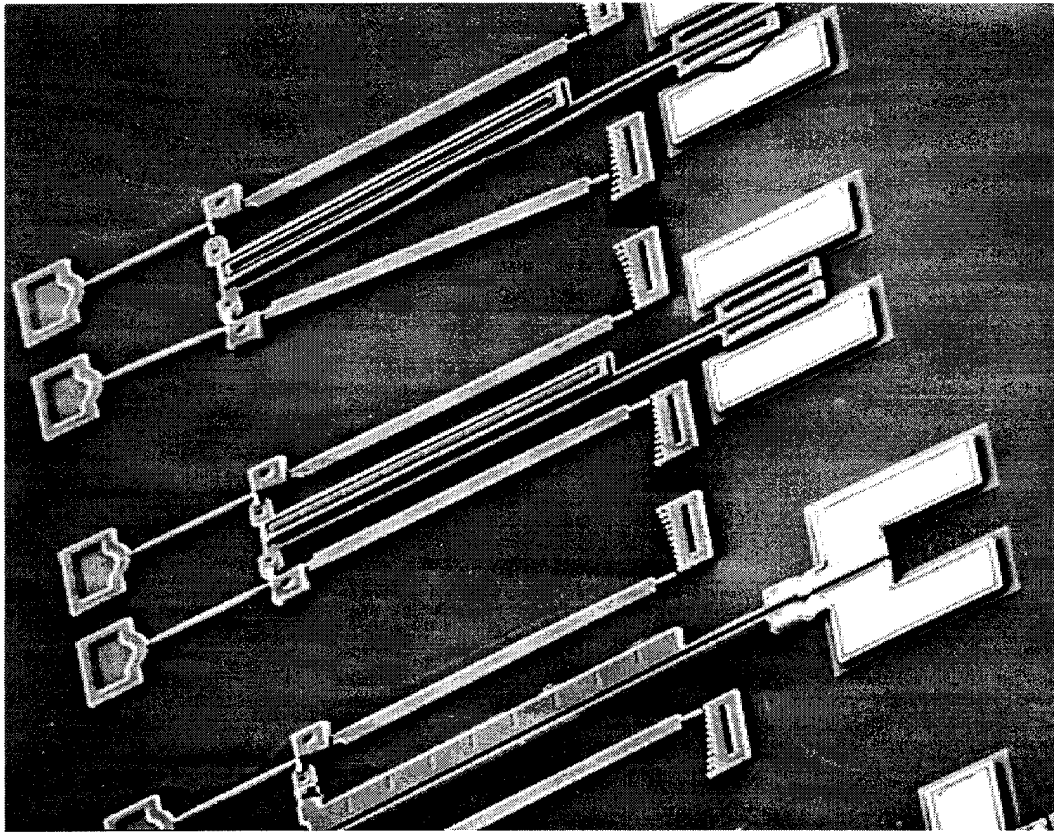


Figure 3-25. Three *poly1*, *poly2* thermal actuator designs. All the actuators are 220 μm long, the hot arms are 2.5 μm wide, and the flexures are 50 μm long. They press against *poly1* force measurement beams on either side.

The actuator designs incorporate additional *poly2* on the *poly1* cold arm to decrease the current density and increase the radiative surface area to increase the temperature difference between the arms. It also makes the actuator stiffer to prevent stiction. The three design configurations are shown in Figure 3-25. The top actuator has a plate of *poly2* anchored to the *poly1* cold arm, this plate has an opening in the

center so the *poly2* appears as a ring. The middle actuator has the same plate without the opening in the center so it has trapped a layer of *oxide2* under the *poly2*, since there is no opening in the anchor ring for the etchant to enter. The entire bottom actuator is a directly stacked *poly1/poly2* construction, including the hot arm. These three types are designated P1/P2, P1OxP2, and P1P2 respectively to keep them separate. The cold arms are 19 μm wide for the P1/P2 and P1OxP2 designs, and 16 μm wide for the P1P2 design, exceeding the 7:1 cold-to-hot arm width ratio specified in Section 3.4.2.4 for maximum deflection.

Figure 3-27 shows a graph of input power versus force for three identical P1P2 actuators. Note that the actuators operate nearly identically until they reach the extreme end of their possible deflection range; they become less predictable where back-bending starts to occur. This is consistent with the results seen for the single, unloaded actuators tested previously, and is consistent with observed operation of all actuators tested.

Figure 3-27 shows the power versus force for the three different kinds of *poly1-poly2* actuators. They show consistent power versus force characteristics despite their different cold arm designs. This indicates that the geometry of the cold arm has little effect on an actuator's operating characteristics, as long as the arm widths meet the 7:1 minimum width ratio determined in Section 3.4.2.4. The actuators have identical hot arm and flexure lengths and widths. This fact and the previous result make it clear that the behavior of these actuators depends mostly on the geometry of the hot arm and flexure.

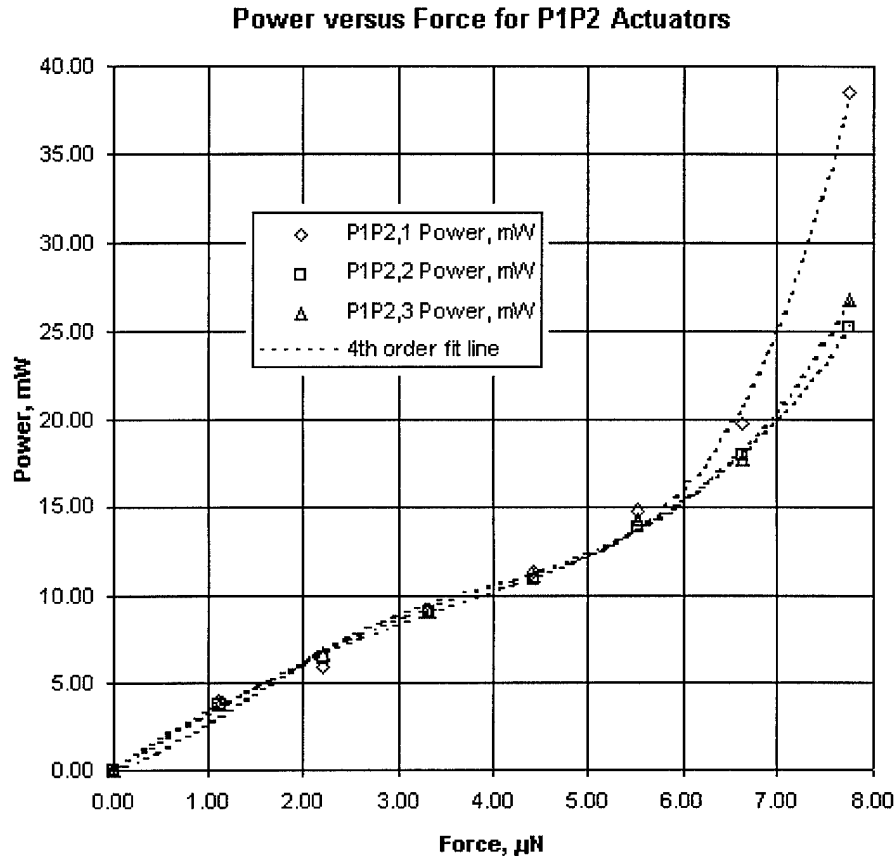


Figure 3-26. Power versus force for three copies of a P1P2 stacked thermal actuator. Input voltage and current at the 3.9 μN point (8 μm deflection) averaged 3.88 V, 2.86 mA; and all the actuators were within 2.5% of this voltage and 0.7% of this current. At higher power the hot arm starts to deform and the deflection characteristic becomes less predictable, but at lower power is consistent between the three copies.

The main difference between these three actuator designs, besides the cold arm styles, is that the hot arm and flexure of the P1P2 actuator is 1.5 μm taller due to its stacked construction. This gives it more cross-sectional area, and apparently more force since it is able to deflect the beam farther before it overheats. However, it takes the same amount of input power to deflect the force test beam a given amount, regardless of the geometry of the actuator doing the pushing. To show this more

clearly, Table 3-7 lists the voltage, current and power for each of the three actuators when they are deflecting the pointer 8 μm , indicating a force of 3.9 μN .

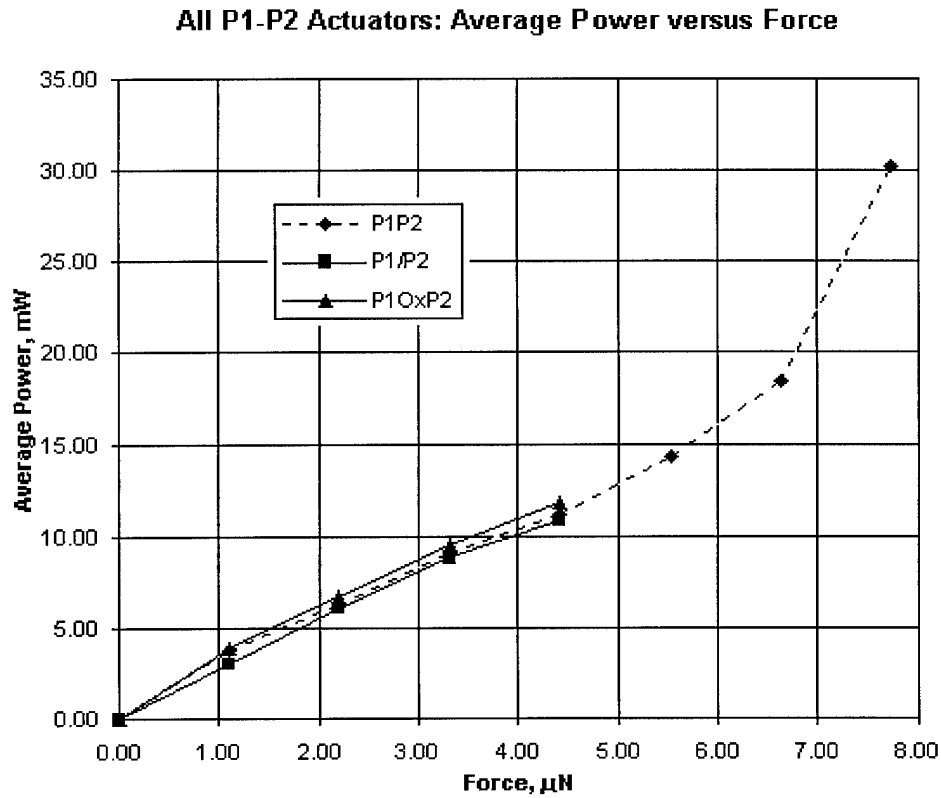


Figure 3-27. Input power versus force for the three actuators of Figure 3-25. Power is averaged over three tests for each actuator type, except the P1OxP2 for which only two were tested.

Table 3-7. Input Voltage, Current and Power for *Poly1-Poly2* Thermal Actuators Producing 4.42 μN of Force on Identical Test Beams.

Actuator Type	Voltage, V	Current, mA	Power, mW
P1/P2	2.94	3.68	10.8
P1OxP2	3.10	3.80	11.8
P1P2	3.89	2.86	11.1

The back-bending forces for the three actuators at rest after being forced into the back-bent state, are listed in Table 3-8. The similarities of these force values mirror the similarities in the forward bending mode. This is also due to the dependence of back-bending deflection on the hot arm and flexure geometries rather than the cold arm design. Also listed is the power that had to be used to force the actuators into the back-bent state. Note the much higher power needed for the P1P2 actuator. Its larger hot arm cross-sectional area allows a higher current to pass before the arm deforms.

Table 3-8. Back-Bending Force of *Poly1-Poly2* Thermal Actuators.

Actuator Design	Force, μN	Power, mW
P1/P2	15.48	40.93
P1OxP2	14.19	40.43
P1P2	12.72	65.65

Unfortunately, the test beams did not stop the actuators from reaching nearly the same maximum deflection that they would have without pressing on the test beams in the forward bending mode. This indicates that the force needed to bend the beams is only a small fraction of the force that the actuators are capable of producing, i.e. the actuators are acting almost as if the force test beams were not there. Although more power is needed to reach the same deflection when pressing on a test beam, stiffer test beams will have to be employed to determine the highest force these actuators can generate. The new test beams can either be shorter or wider. A variety of designs should be tried to bracket the ideal force tester geometry.

One possible drain on the actuator's force is the bowing of the hot arm when pressing against a stiff structure. The hot arm starts to bow rather than push, so the force readings taken above may be the actual force that can be delivered, with the rest of the force lost in the deformation of the actuator itself. Again, further testing with a variety of force test beams would be needed to see what is actually occurring. There may be a variable force delivered depending on the stiffness of the structure being moved.

In back-bending, the actuators can deflect farther when not loaded by a test beam, so the force values listed are the actual force these back-bent beams can deliver with no power applied. In unpowered back-bending, the hot arm is in tension rather than compression, so there is no bowing beyond the permanent warp put into the arm to back-bend it in the first place. However, when a back-bent actuator is powered to move in the forward direction, the same situation applies as with a non-back-bent actuator, and the hot arm still will tend to bow if pressing on a stiff structure.

3.4.3 General Design Considerations

The only requirement to achieve actuation with the U-shaped 'heatuator' structure is to have one arm expand more than the other. The arms do not have to be of equal length, they just have to be joined at the free end and have unequal thermal expansion in order to deflect. So this actuator can take on a large variety of forms, including non-rectangular arms and alternate flexure layouts. There are limits to the

size of the device when fabricated in polysilicon, however. The fact that polysilicon has a higher resistivity than metal allows the actuator to operate in a voltage and current regime more closely matched to IC circuitry ($<10\text{V}$, $<25\text{ mA}$); but the dependence of the resistivity on the actuator dimensions also limits the design space for the device.

Although a longer device is capable of greater deflection for a given current density, the trade-off is that the overall electrical resistance increases with the actuator length. If the resistance becomes too high, sufficient current density cannot be generated in the device before it shorts out from arcing due to high voltage. But, by increasing both the length and the width of each arm the device can be scaled up to larger dimensions to provide more force and/or deflection while keeping the resistance in a region where CMOS-compatible voltages can be used.

Any design change which increases the temperature difference between the hot and cold arms will increase the efficiency of the actuator. Moving the actuator farther from the die surface would help, but bulk etching of the silicon substrate out from under the actuator is difficult in the MUMPS process, and would require that the actuators be protected while the substrate is etched [37]. Hinged actuators can be placed far from the substrate, but these have not been compared with identical non-hinged actuators yet.

One of the sets of test actuators on the MUMPS6 die was designed with a gold layer on the cold arm to reduce the current carried by the polysilicon, but heat conducted from the hot arm resulted in a thermal bimorph action which forced the

free end of the actuator to curl down to the substrate, stopping the motion. Future research should include a more detailed study of the heat flow, or thermal images of the device and its surroundings, to determine optimum methods for increasing the temperature difference between the arms.

Actuator geometry tradeoffs include increasing the flexure length to decrease the amount of force lost in bending the structure. But some of the gain in flexibility is lost as flexure begins to act as a hot arm, resulting in thermal expansion on the cold side. Likewise, the flexure cannot be made thinner than the hot arm because it must carry the drive current; if it is significantly narrower than the hot arm it will overheat and fail before enough heat is developed in the hot arm.

All of the flexing on the cold arm side takes place across the flexure, so increasing the cold arm width has little effect on the stiffness of the overall device. Increasing the ratio of cold-to-hot arm width makes the most significant improvement in actuator deflection versus drive current, up to a point. As Figure 3-20 shows, the benefits of increasing the width ratio taper off quickly after 4:1 for these polysilicon actuators, with almost no improvement after 7:1. Except for possible stiction, though, a wider cold arm is not a detriment, so the cold arm could actually be part of the structure to be moved, as seen in the revised thermally-actuated etch gauge shown in Figure 3-28. This is a more compact version of the etch gauge seen in Figure 2-22.

Increasing the thickness, h , of the overall device will increase the force with little effect on the maximum achievable deflection, since the actuator will expand the same distance for the same starting length, regardless of the height. The stiffness of

the arm is more dependent on the width, a cubic relation, rather than the height, which has a linear relation, as seen in Equation (3-3). This relationship can be seen in Figure 3-27, where the P1P2 actuator, whose hot arm and flexure are composed of both the *poly1* and *poly2* layers fused together, was capable of bending the force test beam much farther than two similar actuators whose hot arms and flexures were *poly1* only. All other dimensions of the hot arm and flexures were identical, most importantly the $2\ \mu\text{m}$ width in the direction of bending.

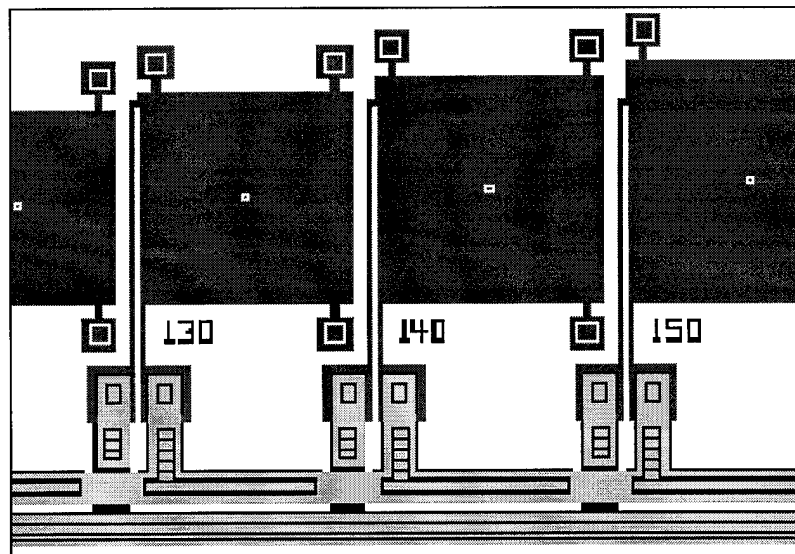


Figure 3-28. Portion of an etch gauge layout with thermal actuators incorporated with the gauge squares. Numbers indicate square size; actuators are identical, with $160 \times 3\ \mu\text{m}$ hot arms and $40 \times 3\ \mu\text{m}$ flexures.

Decreasing the gap, g , between the hot and cold arms would also increase the deflection and decrease the force of the actuator. Although devices were not designed to measure this, one can imagine the gap getting larger and larger, making a very wide U shape, until the expansion of the hot arm only makes the hot arm longer. The

other extreme is where the gap gets smaller until it disappears. This is mechanically similar to a thermal bimorph, but with only a single material there would not be a U-shaped current path, and if there were, perhaps with an extremely thin and slippery insulator, the heat would flow across to the cold arm along the entire length of the now-missing gap, decreasing the temperature difference. So ideally, for maximum leverage and thus deflection, there would be an extremely narrow, electrically and thermally non-conductive gap that would allow the arms to flex without friction.

When these actuators try to move a structure that is too stiff, the hot arm bows out of the plane of actuation, or bows slightly in the plane of actuation. Hold-down guides can help keep the force in the plane of actuation without sinking too much of the heat, but must be placed carefully to avoid inhibiting the motion. One subtle point is that these actuators expand slightly in length as well as move in an arc, so such hold-downs cannot be placed directly at the free end of the actuator. The best solution is to use taller structures, but that option is limited in the MUMPS process. To get more force, rather than making a single large actuator, several actuators can be tethered together and wired in parallel so they can pull in unison, which will be discussed in Section 3.4.6.

3.4.4 LIGA Thermal Actuators

The early actuator geometry tried on MUMPS4 was also tried in the LIGA process to see if geometrical changes could improve the original device. Figure 3-29 shows a test set of thermal actuators fabricated on the LIGA2 run. There are two

groups of four actuators each; one group has smooth sides on the cold arm, and the other has triangular cooling fins (though longer fins would probably have been better). The intent was to see if the increased surface area would help keep the cold arm colder and thus increase the deflection.

Both types of actuators have the following dimensions: the thin arms and the gap are 5 μm wide, the minimum allowed dimension; the thick arms are 20 μm wide, not including the fins; the hot arms range in length from 185 to 635 μm in 150 μm increments with flexures that range in length from 65 to 170 μm in 35 μm increments, respectively. Attached to the end of the array is a compliant gripper mechanism. The gripper has a 220 x 5 μm drive arm, and the flexure placement multiplies the expansion of the hot arm by seven times, from hot arm expansion to gripper tip movement.

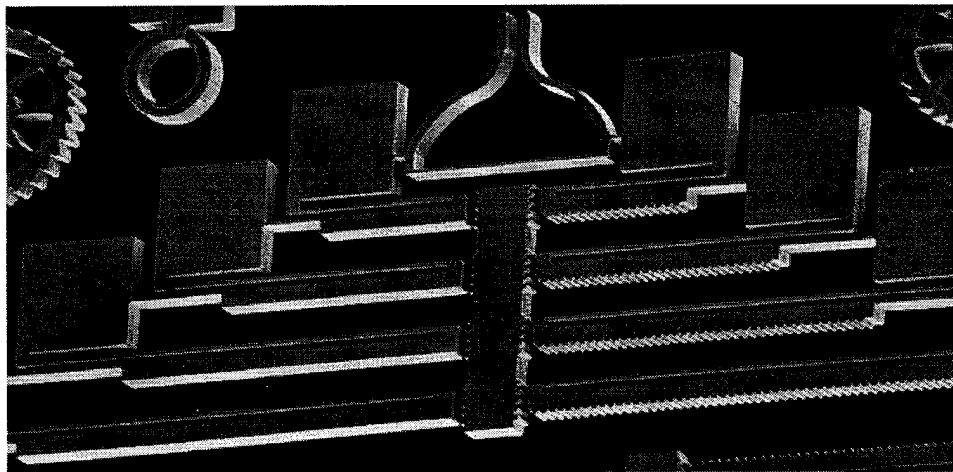


Figure 3-29. Two sets of four LIGA thermal actuators each. The actuators are 185, 335, 485, and 635 μm long with 65, 100, 135, and 170 μm long flexures, respectively. Hot arms, flexures, and gaps are 5 μm wide. A compliant gripper with a single 220 μm long, 5 μm wide hot arm is attached at the top. Also visible are 106 μm diameter actuators with an inner 5 μm wide hot arm and a 5 μm wide, 'finned' outer cold arm. All structures are 30 μm tall.

This set of LIGA actuators represents the older MUMPS4 designs. If another LIGA run is offered, actuator arrays with the 'optimum' geometries described in Section 3.4.2.4 should be tried in the LIGA process and compared with the MUMPS results. One change should be made to the geometry to accommodate the 5 μm minimum design width of the LIGA process, however: the actuators should be overall much larger, with concomitantly longer flexures, or just their flexures should be longer, up to a third of the length of the cold arm.

3.4.5 Alternative Structures

The flexibility of this thermal actuation method was explored by drawing actuators in several different forms and geometries. These include various vertical actuators, circular actuators, and compliant gripper mechanisms. Devices were tried in the MUMPS, LIGA and CMOS MEMS processes.

3.4.5.1 Compliant Micromechanisms

One of the earliest devices was a gripper tried on MUMPS4, shown in Figure 3-30. The design of this gripper does not descend from the 'heatuator' geometry, but rather from the 'line-drive' actuator geometry. Instead of a cold arm and straight flexures, this gripper uses L-shaped flexures which bend in an arc at 90° to the hot arm. The gripper tongs, attached above the flexures, are forced together as the hot arms expand and the flexures rotate.

The gripper shown in Figure 3-30 closes at 5.78 V, 14.7 mA. The current returns through the wider, anchored central arm. The hot arm sections are $107 \times 3 \mu\text{m}$, the flexures are $8 \times 3 \mu\text{m}$, and the gripper tongs extend $60 \mu\text{m}$ from the tops of the hot arms and close $4 \mu\text{m}$.

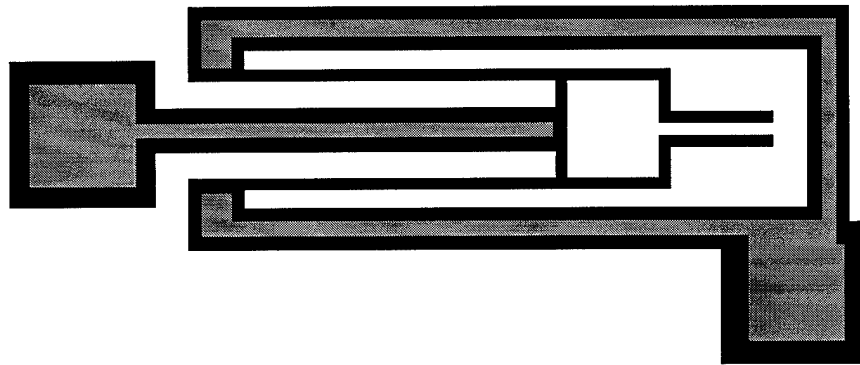


Figure 3-30. Early version of thermally actuated grippers. Hot arms are $107 \mu\text{m}$ long, and gripper jaws close $4 \mu\text{m}$. Overall length is $167 \mu\text{m}$. Jaws close fully at closes at 5.78 V, 14.7 mA

This gripper is an example of a 'compliant micromechanism' since it moves by elastic deformation rather than by hinges [38]. The reference cited here describes a software program for computer-generating an optimum compliant mechanism geometry by telling the program where the force is applied and where the motion should occur. Then, starting with a solid slab of material and the specified boundary conditions, the program determines which parts of the slab should be removed. The program assumes an external force is applied, but could probably be adapted to this situation, where the force is generated within the structure, e.g. with hot arms.

Another compliant gripper design, done in the LIGA process, is shown at the top of Figure 3-29. The operation is similar to the previous gripper design, but in this case there is a single hot arm, and the gripper tongs are at 90° to the hot arm. The current flows only through the hot arm and flexures, there is no wider, cold arm. The design did not prove compliant enough to close fully, however. Longer flexures connecting to the probe pads are needed. This design closed only about halfway before the hot arm deformed.

3.4.5.2 Vertical Actuators

The MUMPS process provides two releasable polysilicon layers, so it is possible to make a thermal actuator which operates in the vertical direction. The first attempt, designed together with another researcher as a way of actuating flipped-over relay arms, is shown in Figure 3-31 [32]. The design keeps the hot arms away from the cold arm by placing them to the side; but this arrangement requires *poly1* formers to raise the *poly2* hot arms high enough over the level of the *poly1* cold arm to cause actuation. These formers have to be removed before the actuator can be operated.

Given the topologies possible by using 'lost poly' formers [37], a similar vertical actuator can be built solely out of *poly2*, and is shown in Figure 3-32. It has self-removing *poly1* formers to make the hot arms higher than the cold arm, which forms the gap *g*. It is also possible to leave the formers in place, if the actuator is to be used strictly in the back-bending mode, i.e. flexing upwards.

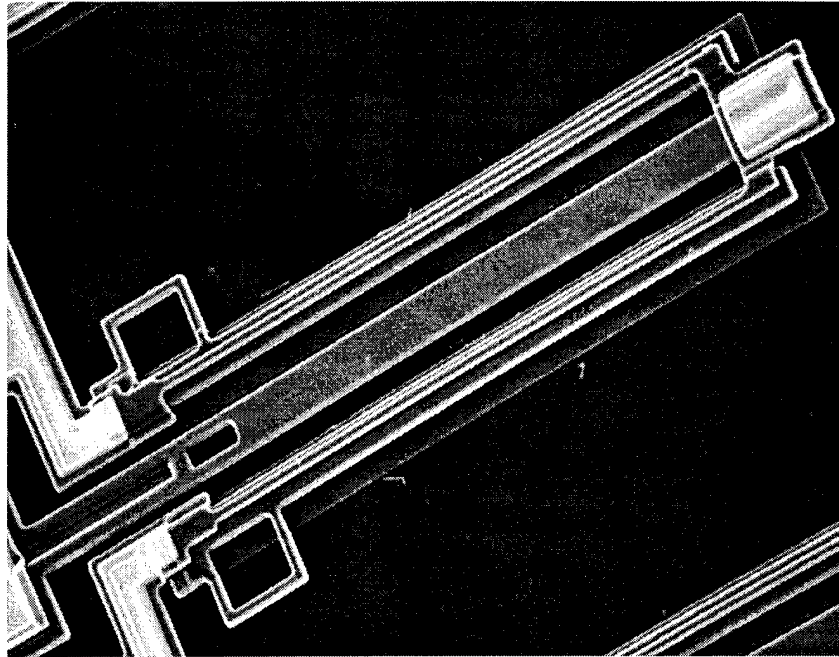


Figure 3-31. Vertical thermal actuator with *poly2* hot arms formed at an elevation above the *poly1* cold arm by *poly1* formers, which must be pulled out manually. Hot arms are $172 \times 4 \mu\text{m}$, cold arm is $160 \times 15 \mu\text{m}$ and attached by two $4 \times 15 \mu\text{m}$ flexures.

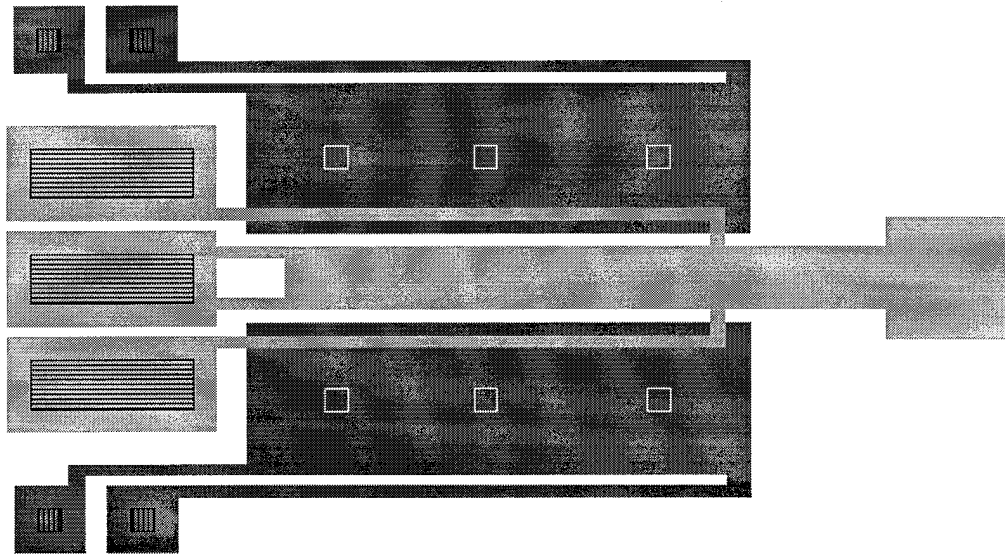


Figure 3-32. Design of an all-*poly2* vertical thermal actuator with self-removing *poly1* formers. Actuator hot arms are $110 \mu\text{m}$ long, *poly1* former/cold arms are $110 \times 33 \mu\text{m}$ and are pulled out by back-bending the attached $120 \times 2.5 \mu\text{m}$ hot arms.

Another geometry is shown in Figure 3-33. This actuator uses a *poly2* hot arm formed above the *poly1* cold arm, thereby using the cold arm as the 'former'. The cold arm is attached with torsional flexures which also pass the current. This actuator is designed to be used in the back-bent mode, and takes 3.68 mA at 6.5V to back bend, resulting in a deflection of 4.5 μm . It has enough force to give an initial lift to a hinged plate, though the exact amount has not been measured. The tip of the actuator in Figure 3-33 is located under a hinged plate, and is intended to give the plate a small initial lift to get it moving in the right direction so a linear motor can raise it the rest of the way.

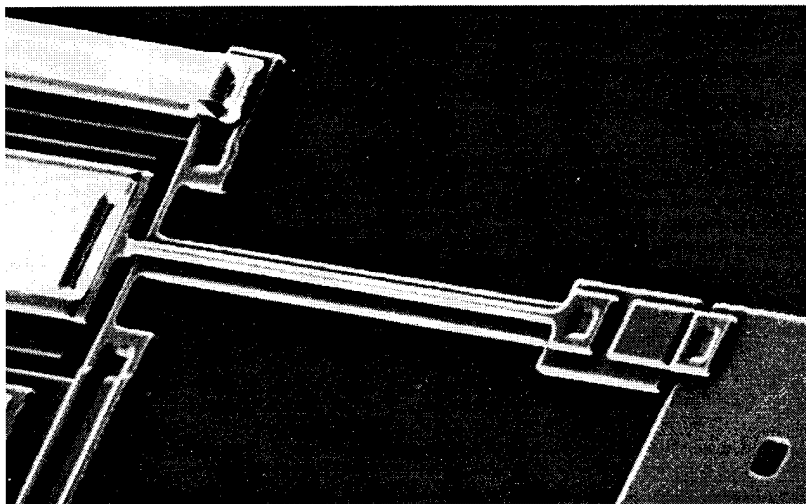


Figure 3-33. Vertical thermal actuator with *poly2* hot arm formed above the *poly1* cold arm. Hot arm is 120 x 3 μm , cold arm is 112 x 8 μm . Cold arm torsional flexures are 10 x 3 μm .

A different type of vertical actuator is shown in Figure 3-34. This actuator descended from the 'line drive' actuator, with the bowing of the *poly2* lines forced

into the vertical direction by the fact that there are two lines tied together in a lattice, making the structure too stiff to bow in the lateral direction. The motion is also forced into the upwards direction by the topology induced in the bridge near the anchors by the underlying *poly0*. Up or down motion was the original intention, with the underlying *poly0* providing an electrostatic force to choose the direction. The topology induced by the *poly0* edge, however, causes the structure to always bow up. This actuator can also be used to give an initial upwards deflection to a hinged plate, but from forward deflection rather than back-bending.

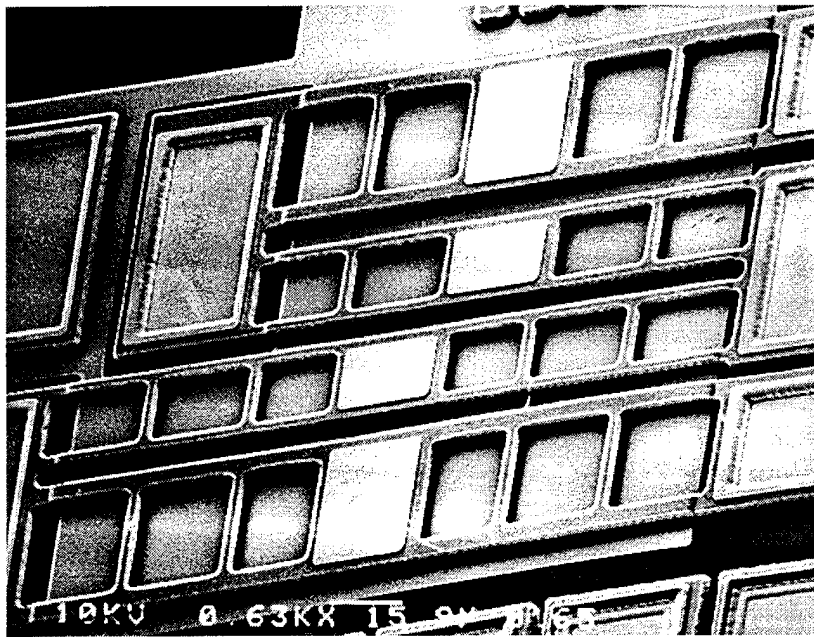


Figure 3-34. Thermally raised mirrors on *poly2* ladder-bridges. Bottom actuator is $180 \times 36 \mu\text{m}$, with legs $5 \mu\text{m}$ wide. Second actuator from the top is $130 \times 22 \mu\text{m}$, with legs $3 \mu\text{m}$ wide.

Devices of this same design made in *poly1* with a *poly2* center supporting a gold mirror were created as an alternative to electrostatically deflected mirrors for a large

linear array. This style of thermal mirror can be made much smaller than piston mirrors and packed more closely together. Their smaller size decreases the drive voltage requirements, unlike the electrostatic mirrors, where a smaller size requires a higher drive voltage. Since most phase-control optical arrays require only small deflections, these mirrors can be operated at low power. The mirrors deflect 2 μm vertically with a 2.75 V, 10.8 mA input. The geometry of the devices can be altered to adjust the drive voltage and current.

As an example of an array application, consider a device using a 600 nm laser which needs mirrors that deflect $\frac{1}{4}$ wavelength. Assuming a linear power versus deflection characteristic (as a first cut, this overestimates the current required), a 0.15 μm deflection should take roughly 2 V and 0.8 mA, or 1.6 mW. On this basis, a linear array of 256 mirrors would require only 0.41 W if all mirrors were actuated simultaneously.

3.4.5.3 Circular Actuators

Circular geometries were also tried by another researcher, but their performance was poor, showing less than 1 μm of deflection [34]. The thickness of the cold arm made it stiffer than the flexure, so it would not uncurl, but at the same time it was not wide enough to stay cool. Also, by drawing the hot arm in a bowed shape to begin with, it was easier for it to just keep bowing rather than force the cold arm flexure to bend. Figure 3-35 shows two circular actuators fabricated in the MUMPS process.

These actuators are 100 μm in diameter, with 2 μm wide inner hot arms and 4 μm wide outer cold arms. The scale markings were a bit optimistic.

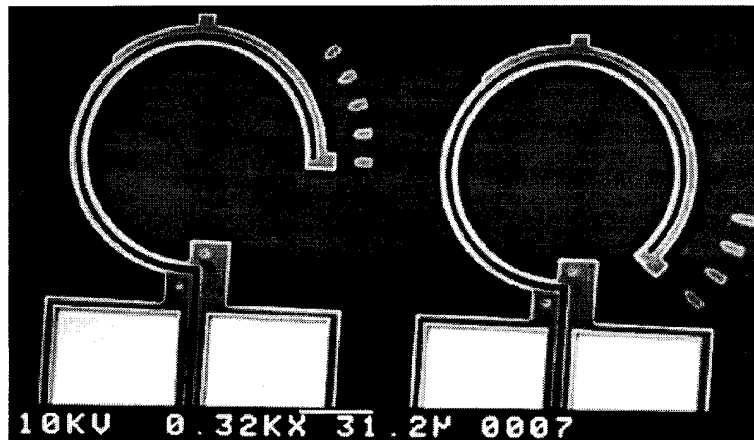


Figure 3-35. Circular thermal actuators fabricated in the MUMPS process. Actuators are 100 μm in diameter.

The LIGA version of a circular actuator also had insufficiently wide cold arms to cause a temperature difference, so these actuators just expanded slightly with no lateral motion. A LIGA circular actuator can be seen in the upper left corner of Figure 3-29. That actuator is 106 μm in diameter with an inner 5 μm wide hot arm and a 5 μm wide, ‘finned’ outer cold arm. Versions of this actuator were put on both the 30 μm thick ‘short’ LIGA die and the 150 μm thick ‘tall’ LIGA die.

3.4.5.4 Externally Heated Actuators

As mentioned in the design considerations of Section 3.4.3, the only requirement to get deflection from this actuator geometry is to have unequal heating

of the two arms. All of the actuators mentioned so far have used internal ohmic heating from a current passing through them; but it is also possible to heat them externally to produce a deflection.

This external heating could be from absorption of optical energy, e.g. a laser beam could be focused on the hot arm, which could have a coating tuned to absorb light at the laser's wavelength. It could be from an exothermic reaction between a chemical coating and chemicals in the environment, or any other heat source. In the test structure shown in Figure 3-36, the external heat comes from a polysilicon heating resistor located just below, but not touching, the hot arm.

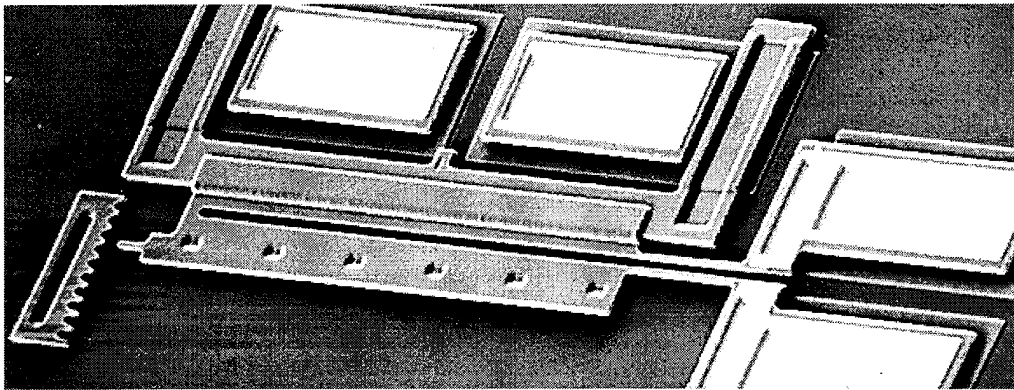


Figure 3-36. Externally heated thermal actuator. Actuator is *poly2*, with two identical $165 \times 14 \mu\text{m}$ arms and $40 \times 2 \mu\text{m}$ flexures. The hot arm is located just above a *poly1* heating resistor which is the external heat source.

This test structure did successfully demonstrate deflection due to external heating; however, it showed two deflections. One was the actuator bending due to differential heating, as expected; and the other deflection was the bowing up of the

heating resistor. The heating resistor bowed up and stopped the lateral motion of the actuator after it had moved only 2 μm .

3.4.6 Actuator Arrays

All of the thermal actuators described so far expand slightly in length as well as move in an arc. Often it is more desirable to have purely linear or rotary motion, or to have more force. The solution is to have two or more actuators act on a common structure in unison to cancel out the arcing motion and/or to combine forces. For example, two actuators were combined to get linear motion in the movable grating of Figure 3-23.

For lateral actuator arrays the 'common structure' was designed in the form of a flexible yoke attached perpendicularly to the free ends of parallel thermal actuators, with flexures to accommodate the arc-like motion. Figure 3-37 shows the first such array which uses a *poly1* yoke with short angled flexures to attach it to the actuators.

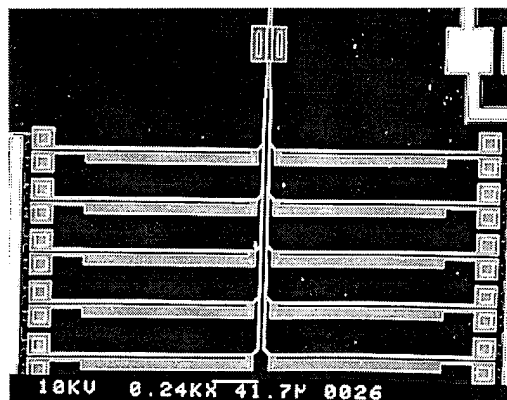


Figure 3-37. Ten tethered *poly1* actuators with an early *poly1* yoke design, feeding through a *poly2* guide bearing. Actuator dimensions are $L_H = 193 \mu\text{m}$, $w_H = w_F = 3 \mu\text{m}$, $L_F = 30 \mu\text{m}$, $w_C = 11 \mu\text{m}$, and $g = 2 \mu\text{m}$. The actuators are wired in parallel to the pads at the upper right.

This initial design seemed too stiff, since the array did not deflect as far as single actuators of similar dimensions. The next version used a *poly2* yoke with longer flexures. *Poly2* was chosen because it is thinner and should therefore be more flexible. However, the flexures turned out to be weak where the *poly2* flexure goes over the edge of the *poly1* actuator, and they required a via attachment to the actuator, which takes up space. The current design uses a yoke with even longer flexures, but fabricated in the same layer as the actuators, usually *poly1*. This design has been standardized as a subcell that forms the yoke arms and wiring automatically when laid end to end. An array of five of these actuators is shown in Figure 3-38.

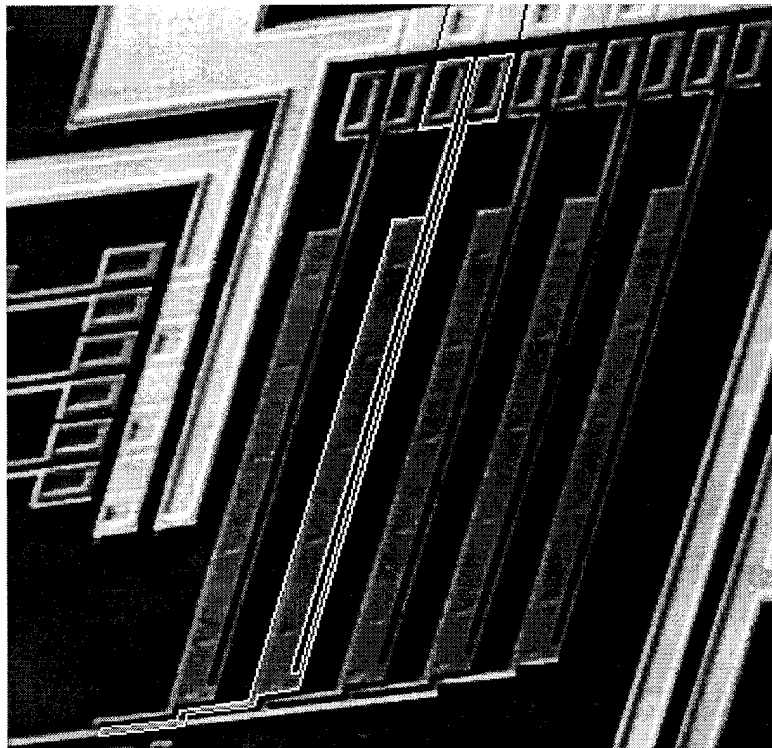


Figure 3-38. Array of five 220 μm long actuators. A single actuator is drawn as a subcell which also contains wiring, a section of yoke arm and the yoke attachment flexure. Hot arms and flexures are 2.5 μm wide. One subcell has been outlined. The wired ends of three other actuator subcells can be seen on the left.

Other options for arraying lateral thermal actuators are possible, but the yoke has proven to be the most compact. However, each actuator could have its own tether, all attached in parallel to a bar, rather than in series as with the yoke design. This would look like the movable grating actuators in Figure 3-23, but with more actuators feeding down to the grating with tethers between the two shown [34]. This uses more space: the actuators must still be placed adjacently as with the yoke, but staggered so there is clearance from the end of each actuator straight over to the bar. However, it could be useful for designs where the force must be spread evenly over a wide structure, since the yoke design concentrates all the force at one point. Such an arrangement could also be used to rotate the bar via unequal heating of the attached actuators.

For extremely large forces, several yokes could be tied together with a bar, in a treed structure which can be made as large as necessary. But the easiest way to increase the force of the yoked arrays is to keep adding actuators to the same yoke. Since each actuator has its own attaching flexure, adding more actuators does not increase the stiffness of the yoke, so more actuators should add force in uniform increments. Arrays of up to 60 actuators on a single yoke have been successfully operated.

One concern with these actuators is that they must be wired in parallel to keep the drive voltage between 3 and 10 volts. The actuators of the arrays shown here are wired in parallel. There was some initial concern over current sharing through so many parallel paths, but the resistance of the polysilicon increases with temperature,

providing built-in current leveling. Any actuator which draws more current will heat more, and as its resistance increases its current draw decreases. Even in arrays of 60 actuators all the actuators heat evenly. This can be observed visually because at the point where the actuators start to permanently deform into a back-bend, they start to glow visibly. All of the actuators in a large array can easily be seen to glow at the same time in the same place for the same length, indicating that they all are heating evenly.

An important consideration for using these arrays is that they work best when they have been given an initial back bend. This allows the actuators to move through their zero position, where the least amount of force is lost in flexing the yoke tethers. Provisions must be made at the point where the array is attached to the driven mechanism to take this initial back-bending into account, though this is not usually a problem. Examples of this will be shown in Chapter 5.

One array idea that did not work was an attempt to arrange the actuators in series mechanically, and therefore also electrically, to add their deflections. The resistance of this combination was too large for a high enough current to pass through it and it eventually shorted out at 140 volts. Even arrays as small as four actuators present too much resistance, and the structure chosen, shown in Figure 3-39, deflected less than a single actuator.

Single thermal actuators have been successfully operated while wired in series of two and three devices, but the resistance soon gets too high for this approach to be

useful. Series-parallel wiring arrangements for large numbers of actuators could be used to control the drive voltage/current characteristics of the ensemble.

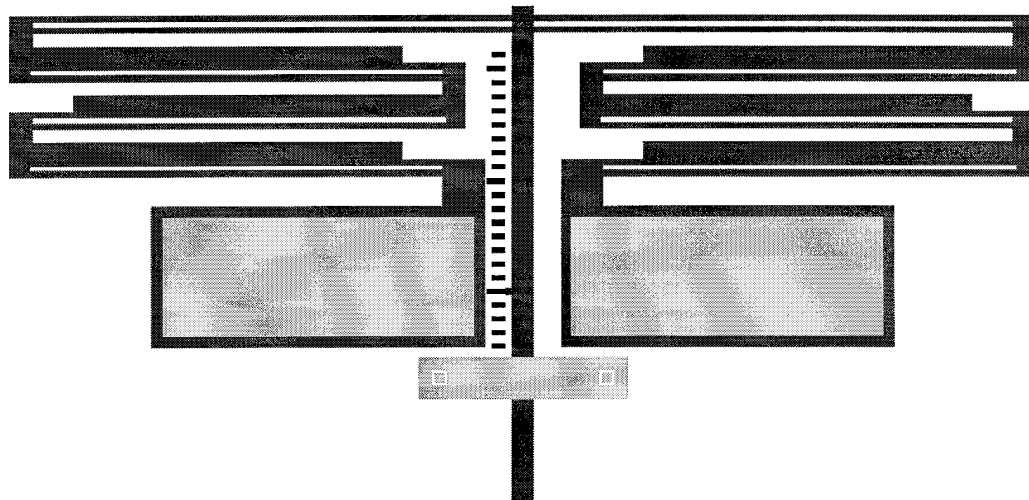


Figure 3-39. Unsuccessful attempt to array thermal actuators in series. The idea was to have the deflections of the elements add to a larger overall deflection. Hot arms are $150 \times 2 \mu\text{m}$. A flexural crossover at the top allows the current to return through the other side. A scale is connected in the center to measure the deflection.

Vertical actuators can be arrayed simply with a bar across their free ends. This works for cases where the arcing motion is acceptable. Or they can be attached to a hinged plate with torsion springs as seen in Figure 3-40. The stiff plate and torsion springs act as the cold arm and flexure for all the actuators. The plate combines the forces of all the hot arms. This device shown in Figure 3-40 is a tilting mirror with *poly1* hot arms hidden underneath. This way the entire *poly2* upper surface can be mirrored for maximum reflectivity. This particular mirror is designed to be tilted on two axes by driving the two actuators separately, but the same basic layout can be used to combine the force of any number of vertical actuators.

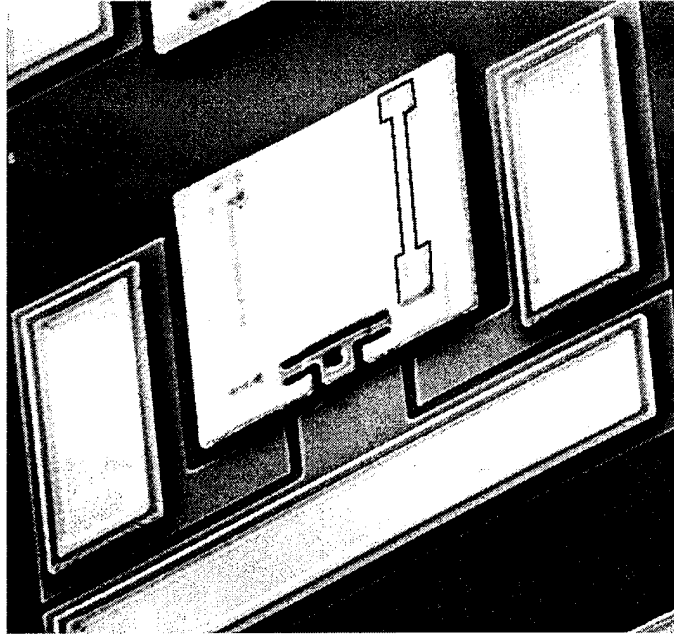


Figure 3-40. Two-axis tilting mirror combining the motion of two *poly1* thermal actuator arms. The covered arms are $35 \times 2 \mu\text{m}$, and their outline can be seen by the topology they induce in the overlying $75 \mu\text{m}$ square gold-mirrored *poly2* plate. One actuator has been outlined for clarity.

3.5 Comparison With Other Actuators

The thermal actuator or ‘heatuator’ is compared here with recently published lateral actuators to illustrate how they complement the capabilities of other available lateral actuators. The comparisons show the heatuators to be smaller, more forceful, and CMOS circuit compatible, the goals of this portion of the research. Since MEMS actuators come in all shapes and sizes, a metric of force per unit area will be used for force comparisons. Area is used instead of volume since the thickness of an actuator fabricated in a surface-micromachined or electroplated metal foundry process is a dimension over which the designer has little or no control.

Table 3-9. Comparison of Recently Reported Lateral MEMS Actuators *

Actuator [reference]	Material layers	Height μm	Force/area mN/mm^2	Drive V	Pwr In mW	Max. Freq. Hz
heatuator, forward	poly	2	1.3	3.3	12.8	1,000
heatuator, backward	poly	2	3.9	7	40.9	1,000
gap closing [39]	poly	2	0.2	35	-	(10K)
comb drive [21]	Cu	20	0.2	60	-	100K
thermal [31]	Ni	25	1.9	(<1)	682	1.3
bimorph [30]	SiO ₂ , Al	3.2,1.2	4.9	6	13.8	149
comb drive [40]	Ni	16	0.86	200	-	40K
electro-mag [8]	Ni-Fe	100	0.02	1.5	450	230

* See text for details of the actuators and numbers presented here. Numbers listed in parentheses are estimates based on results for similar devices; - indicates no data given.

More details on the actuators compared in Table 3-9 are necessary since the actuators have such a wide variety of drive requirements and applications, making a direct comparison difficult and possibly misleading, especially for the input power column. The comb drive and magnetic actuators can be operated in a DC mode or a resonant mode. The resonant modes use less power for large deflections because energy is stored at the resonant frequency in the motion of the shuttle and the bending of the springs. For this reason, the area measurements of those structures include the springs, and not just the area of the actuators. Also, force is dependent on the input power for most of these actuators, especially the thermal ones, so those numbers are even harder to compare. However, these disparities highlight the need for a variety of actuators, so the proper actuation scheme can be chosen for an application.

In Table 3-9, the first heatuator listing is the 'P1/P2' type mentioned in Section 3.4.2.6.3, and the force listed is for maximum forward-bending. The second listing is for the same heatuator in the back-bending mode.

The gap-closing actuator is part of an arrangement for a linear stepper motor, so although the actuator itself can only deflect $2\text{ }\mu\text{m}$, the motor slider moves $40\text{ }\mu\text{m}$. The actuators in this motor have ten $100\text{ }\mu\text{m}$ long gap closing arms, producing a total force of $5.4\text{ }\mu\text{N}$ at 35 V [39]. Like other electrostatic actuator arrays, it can produce a large force, but requires a large area and drive voltage.

The copper comb drive is part of a very large electrostatic array, with the combs arranged in a descending tree structure. The combs have $2\text{ }\mu\text{m}$ gaps, so although the actuator covers 1 mm^2 and is driven at 60 V , it produces only $200\text{ }\mu\text{N}$ of force [21]. This is an example of how weak electrostatic actuators can be. The nickel comb actuator shows more force per area, but it is driven at 200 V . The force at 200 V is reported as $100\text{ }\mu\text{N}$, and the area had to be measured from a photograph of the device, so the force/area figure may be a little off. This actuator was used to drive relay contacts together, and the high voltage was needed because the flexure design was too stiff [40]. Neither of these comb drive actuators would be CMOS circuitry compatible.

The nickel thermal actuator design is copied from the thermo-magnetic actuator that provided the original design idea for the heatuators [41]. The area and power measurements had to be inferred from the paper, which did not relate the force measurements to specific actuator geometries. The actuators mentioned in the paper were very large, 7.4 to 14.8 mm , which may explain their slow speed. Using the dimensions which give the best force per area result, the actuator size is taken as $7.4\text{ mm} \times 0.14\text{ mm}$. The reported force for a 682 mW input is 0.2 gmF , which

converts to 1.96 mN, where 9.8 mN is the force due to gravity from 1 gram. This gives a force/area of 1.9 mN/mm², which seems extremely low given the high power fed to the actuator. This may be due to the non-ideal geometry, based on the results in Section 3.4.2.4 seen for the polysilicon thermal actuators.

The purely magnetic actuator was quite large, 4.6 mm x 3 mm, and 100 μ m tall. This is the actuator shown in Figure 3-4; the measured area is for one magnet plus the folded springs. The device had only 20 turns in the magnet coil, so produced only 280 μ N at 300 mA [8]. This shows how poorly electromagnetic actuators scale down, even in a structure as comparatively large as this. The poor performance is largely due to having only 20 turns in the magnet coil; the magnetic field is weak and poorly confined.

The maximum deflections of all these actuators are not compared because need for a particular deflection is application dependent. As seen in Section 3.2.4, electrostatic actuators have very small deflections, but they can be used in larger structures to increase the lateral deflection, as in a linear motor [39]. Also, larger structures can generally have larger deflections, so to compare deflections is not useful unless the actuators are roughly the same size. In general, though, the thermal actuators have much larger single-actuator deflections than the electrostatic ones.

3.6 Conclusions

The force of thermal expansion is a powerful one, at any scale. In the macro world it is a problem that must be controlled, as with expansion joints in bridges. It is

used for non-adhesive assembly, as with fitting steel tires to cast iron wheels on locomotives, where the tire is heated and expanded, then allowed to cool and tighten onto the wheel. Now in the micro world this force has been harnessed in a new class of actuators. These actuators meet the design goals of high force, large deflection, and flexible design. But possibly the greatest advantage is that these actuators are compatible with the CMOS circuitry which will be used in larger, integrated systems. This is due to the polysilicon construction of these actuators, which gives them an ideal resistivity.

These actuators fill a large gap in the MEMS actuator design space, especially for foundry-fabricated systems where the actuator choices are limited. The tradeoff for high force and large deflections is that these actuators cannot reach the 10's of kHz operating frequencies of the electrostatic actuators, and they use more power.

The high forces possible with these actuators, especially when combined in arrays, allow the creation of large, complex mechanical systems, which is one of the main goals of this dissertation research. The possibilities for large mechanical systems will be explored in Chapter 5, where applications of thermal actuator arrays in stepper motors are explored. However, to make practical use of large numbers of these actuators, wiring networks capable of delivering 10's of mA with low losses across the die are required. This is the next basic structure researched to make possible large integrated systems with foundry processes.

References

1. M. Takahashi, M. Kurosawa and T. Higuchi, "Direct frictional driven surface acoustic wave motor," *Proc. Transducers '95/Eurosensors IX*, Stockholm, Sweden, Vol. 1, pp. 401-404, 25-29 June 1995.
2. S. Lee, R. Ried and R. White, "Piezoelectric cantilever microphone and microspeaker," *Technical Digest, Solid State Sensors and Actuators Workshop*, Hilton Head, SC, pp. 33-37, 1994.
3. T. Idogaki, T. Tominaga, K. Senda, N. Ohya and T. Hattori, "Bending and expanding motion actuators," *Proc. Transducers '95/Eurosensors IX*, Stockholm, Sweden, Vol. 1, pp. 393-396, 25-29 June 1995.
4. P. Barth, C. Beatty, L. Field, J. Baker and G. Gordon, "A robust normally-closed silicon microvalve," *Technical Digest, Solid State Sensors and Actuators Workshop*, Hilton Head, SC, pp. 248-250, 1994.
5. R. Zengerle, A. Richter and H. Sandmaier, "A micro membrane pump with electrostatic actuation," *Proc. Micro Electro Mechanical Systems '92*, Travemunde, Germany, pp. 19-24, February 4-7 1992.
6. J. Judy, R. Muller and H. Zappe, "Magnetic microactuation of polysilicon flexure structures," *Technical Digest, Solid State Sensors and Actuators Workshop*, Hilton Head, SC, pp. 43-48, 1994.
7. K. Arai, W. Sugurawa and T. Honda, "Magnetic small flying machines," *Proc. Transducers '95/Eurosensors IX*, Stockholm, Sweden, Vol. 1, pp. 43-46, 25-29 June 1995.
8. H. Guckel, T. Christenson, T. Earles, J. Klein, J. Zook, T. Ohstein and M. Karnowski, "Laterally driven electromagnetic actuators," *Technical Digest, Solid State Sensors and Actuators Workshop*, Hilton Head, SC, pp. 49-52, 1994.
9. H. Guckel, T. Earles, J. Klein, D. Zook and T. Ohnstein, "Electromagnetic linear actuators with inductive position sensing for micro relay, micro valve and precision positioning applications," *Proc. Transducers '95/Eurosensors IX*, Stockholm, Sweden, Vol. 1, pp. 324-327, 25-29 June 1995.

-
10. H. Nathanson and W. Newell, "The resonant gate transistor," *IEEE Transactions on Electronic Devices*, Vol. ED-14, pp. 117, March 1967.
 11. J. Younse, "Projection display systems based on the Digital Micromirror Device™ (DMD™)," *Proc. SPIE Microelectronic Structures and Microelectromechanical Devices for Optical Processing and Multimedia Applications*, Vol. 2641, Austin TX, pp. 64-75, 24 October 1995.
 12. R. Apte, F. Sandejas, W. Banyai and D. Bloom, "Deformable grating light valves for high resolution displays," *Technical Digest, Solid State Sensors and Actuators Workshop*, Hilton Head, SC, pp. 1-6, 1994.
 13. C. Marxer, M. Gretillat, V. Jaecklin, R. Baettig, O. Anthamatten, P. Vogel and N. deRoos, "MHz opto-mechanical modulator," *Proc. Transducers '95/Eurosensors IX*, Stockholm, Sweden, Vol. 1, pp. 289-292, 25-29 June 1995.
 14. W. Tang, T. Nguyen and R. Howe, "Laterally driven polysilicon resonant microstructures," *Sensors and Actuators*, vol. 20, pp. 25-32, 1989.
 15. L. Hornbeck, "Projection displays and MEMS: timely convergence for a bright future," *Proc. SPIE Microelectronic Structures and Microelectromechanical Devices for Optical Processing and Multimedia Applications*, Vol. 2641, Austin TX, p.2 (abstract only, color reprints available from the Digital Imaging marketing manager, Texas Instruments Inc., P.O. Box 655474, Dallas, TX, 75265), 24 October 1995.
 16. M. Putty and K. Najafi, "A micromachined vibrating ring gyroscope," *Technical Digest, Solid State Sensors and Actuators Workshop*, Hilton Head, SC, pp. 213-220, 1994.
 17. S. Adams, F. Bertsch, K. Shaw, P. Hartwell, N. MacDonald and F. Moon, "Capacitance based tunable micromechanical resonators," *Proc. Transducers '95/Eurosensors IX*, Stockholm, Sweden, Vol. 1, pp. 43-46, 25-29 June 1995.
 18. Information presented by MCNC at the Second MUMPS User's Group meeting, Chicago, IL, Oct 1995. MCNC MEMS Technology Applications Center, 3021 Cornwallis Road, Research Triangle Park, NC, 27709.

-
19. P. Osterberg, R. Gupta, J. Gilbert and S. Senturia, "Quantitative models for the measurement of residual stress, Poisson ratio, and Young's modulus using electrostatic pull-in of beams and diaphragms," *Technical Digest, Solid State Sensor and Actuator Workshop*, Hilton Head, SC, pp. 184-188, 1994.
 20. G. Fedder and R. Howe, "Integrated test-bed for multi-mode digital control of suspended microstructures," *Technical Digest, Solid State Sensors and Actuators Workshop*, Hilton Head, SC, pp. 145-150, 1994.
 21. L. Fan, S. Woodman, R. Moore, L. Crawforth, T. Reiley and M. Moser, "Batch fabricated area-efficient milli-actuators," *Technical Digest, Solid State Sensors and Actuators Workshop*, Hilton Head, SC, pp. 38-42, 1994.
 22. M. Mehregany and Y. Tai, "Surface micromachined mechanisms and micromotors," *J. of Micromechanics and Microengineering*, Vol. 1, pp.73-85, 1991.
 23. L. Fan and S. Woodman, "Batch fabrication of mechanical platforms for high density data storage," *Proc. Transducers '95/Eurosensors IX*, Stockholm, Sweden, Vol. 1, pp. 434-437, 25-29 June 1995.
 24. V. Dhuler, M. Mehregany and S. Phillips, "A comparative study of bearing designs and operational environments for harmonic side-drive micromotors," *IEEE Transactions on Electrical Devices*, Vol. 40, pp.1985-1989, Nov. 1993.
 25. K. Deng, H. Miyajima, V. Dhuler, M. Mehregany, S. Smith, F. Merat and S. Furukawa, "The development of polysilicon micromotors for optical scanning applications," *Technical Digest, Solid State Sensors and Actuators Workshop*, Hilton Head, SC, pp. 234-238, 1994.
 26. E. Garcia and J. Sniegowski, "Surface micromachined microengine as the driver for micromechanical gears," *Proc. Transducers '95/Eurosensors IX*, Stockholm, Sweden, Vol. 1, pp. 365-368, 25-29 June 1995.
 27. B. Read, "Silicon based microactuators for telerobotic tactile stimulation," Master's Thesis, Air Force Institute of Technology, Wright-Patterson AFB, Ohio, AFIT/GE/ENG/94D-25, Dec 1994.

-
28. C. Doring, T. Grauer, J. Marek, M. Mettner, H. Trah and M. Willmann, "Micromachined thermoelectrically driven cantilever structures for fluid jet deflection," *Proc. Micro Electro Mechanical Systems '92*, Travemunde, Germany, pp. 12-18, February 4-7 1992.
 29. W. Riethuller and W. Benecke, "Thermally excited silicon microactuators," *IEEE Transactions on Electronic Devices*, vol. 33, pp. 758-763, June 1988.
 30. B. Read, V. Bright and J. Comtois, "Mechanical and optical characterization of thermal microactuators fabricated in a CMOS process," *Proc. SPIE Micromachined Devices and Components*, vol. 2642, pp. 22-32, 23-24 October 1995.
 31. H. Guckel, J. Klein, T. Christenson, K. Skrobis, M. Laudon and E. G. Lovell, "Thermo-magnetic metal flexure actuators," *Technical Digest, Solid State Sensors and Actuators Workshop*, Hilton Head, SC, pp. 73-75, 1992.
 32. M. Phipps, "Design and development of microswitches for micro-electro-mechanical relay matrices," Master's Thesis, Air Force Institute of Technology, Wright-Patterson AFB, Ohio, AFIT/GE/ENG/95J-02, June 1995.
 33. J. Comtois, V. Bright and M. Phipps, "Thermal microactuators for surface-micromachining processes," *Proc. SPIE: Micromachined Devices and Components*, vol. 2642, pp. 10-21, 23-24 October 1995.
 34. D. Sene, "Design, fabrication, and characterization of micro-opto-electro-mechanical systems," Master's Thesis, Air Force Institute of Technology, Wright-Patterson AFB, Ohio, AFIT/GEO/ENP/95D-03, December 1995.
 35. A. Simon and D. Ross, *Principles of Statics and Strength of Materials*, Wm. C. Brown Company Publishers, Dubuque, Iowa, 1983.
 36. Private communication with the provider of the MUMPS process, MCNC Electronics Tech. Div., 3021 Cornwallis Road, Research Triangle Park, North Carolina.
 37. J. Comtois and V. Bright, "Design techniques for surface-micromachining polysilicon processes," *Proc. SPIE Micromachining and Microfabrication Processing Technology*, vol. 2639, pp. 211-222, 23-24 October 1995.

-
38. G. Ananthasuresh, S. Kota and Y. Gianchandani, "A methodical approach to the design of compliant micromechanisms," *Technical Digest, Solid State Sensors and Actuators Workshop*, Hilton Head, SC, pp. 189-192, 1994.
 39. R. Yeh, E. Kruglick and K. Pister, "Microelectromechanical components for articulated microrobots," *Proc. Transducers '95/Eurosensors IX*, Stockholm, Sweden, Vol. 2, pp. 346-349, 25-29 June 1995.
 40. S. Roy and M. Mehregany, "Design, fabrication, and characterization of electrostatic microrelays," *Proc. SPIE Micromachined Devices and Components*, vol. 2642, pp. 64-73, 23-24 October 1995.
 41. L. Field, D. Buriesci, P. Robrish and R. Ruby, "Micromachined 1x2 optical fiber switch," *Proc. Transducers '95/Eurosensors IX*, Stockholm, Sweden, Vol. 1, pp. 344-347, 1995.

4. Wiring Systems

Wiring becomes a major design concern when many devices in large or complex systems must be connected together or to the outside world. As the number of devices grows, wiring can begin to consume significant amounts of die area. The numbers and types of wiring crossovers can limit the depth of an array or the placement of devices. Wiring limitations become increasingly apparent as the size and complexity of a device grows. A design can become constrained when the system requires more wiring than there is space available, or requires too many connections off the die.

The area consumed by wiring has a major impact on device design and floorplanning. This is especially true for MEMS processes where the wiring must be made in the same layers, and therefore on the same level, as the electromechanical devices. This is the case with two of the three foundry processes used for this research. Cross-talk from the high electric fields used with electrostatic devices, or current carrying capacity to feed thermal actuators can also affect the number and placement of wires and devices within a system. In some cases the appropriate type of wiring is just not available for a device because of how the device is assembled.

This chapter explains the various types of wiring used or developed in this dissertation for connecting together large systems. The development of the large systems themselves and the devices they are composed of is the topic of Chapter 6.

4.1 Substrate Wiring

The most common type of wiring is substrate wiring, which runs along the die surface between devices and bondpads. Each of the three foundry fabrication processes used for this research has different limitations and requirements for such wiring, based on the materials available for creating wires and the order in which those materials are deposited.

4.1.1 CMOS MEMS

The CMOS MEMS process offers the simplest and best substrate wiring options for large systems because it is primarily an integrated microelectronics process, where creating extremely complex systems made of millions of devices is one of the reasons for the process to exist. Figure 4-1 shows a section of an electronic circuit layout; the density of devices and wiring is apparent. This density is possible because the various devices do not have to move, so the wiring can run over them in a solid structure composed of many layers. With MEMS this is no longer true; the devices and wiring must be separated in order for the devices to function, so the advantages of this wiring style are no longer available.

With CMOS MEMS, no special designs are needed for substrate wiring. The wiring is laid out and connected in the same way as in microelectronic circuits. The process makes provision for multiple overlapping wiring layers and their interconnections. Wiring is formed in either of two aluminum layers, and can also be

drawn in the polysilicon layer. Silicon dioxide layers between the metal and polysilicon provide electrical insulation. Connections between layers are made with vias, small circular holes in the oxide between adjacent wiring layers. Vias are provided only between adjacent layers.

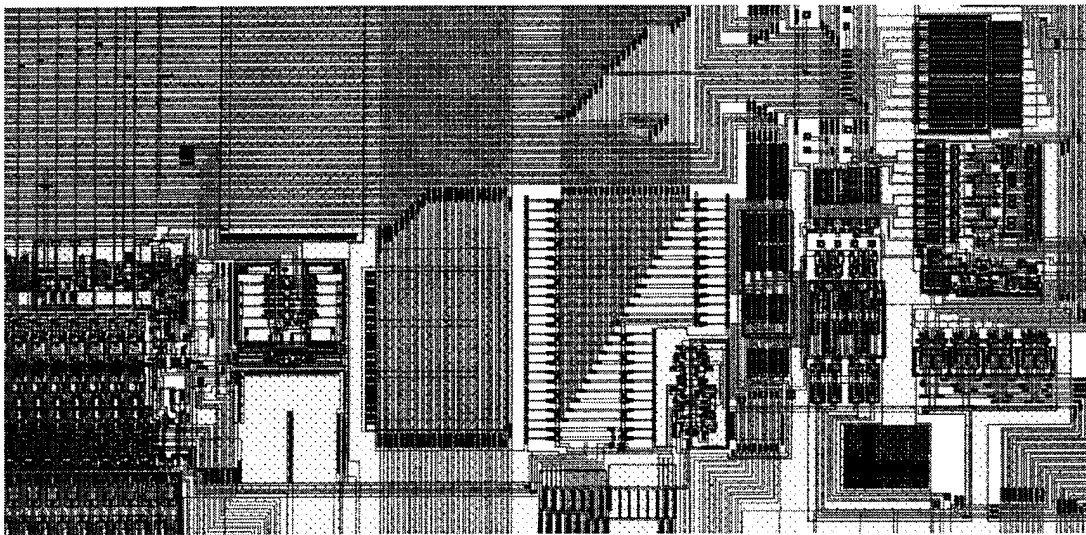


Figure 4-1. Section of a microprocessor circuit layout showing the density of wiring and devices possible when the two can be layered on top of each other [1].

Polysilicon wiring is usually limited to short, low current runs and is used primarily when the two metal layers are already in use in that area. Sometimes polysilicon wiring is used where the vias needed for connections to a metal layer will not fit; polysilicon wiring is then used to route a signal to the device's perimeter where the metal connections are made. This situation rarely arises with MEMS devices; since they are much larger than microelectronic devices, the MEMS designs

do not usually become connection limited. So polysilicon is used primarily as a way to make ohmically heated elements or piezoresistive sensors.

CMOS MEMS designs can take advantage of this wiring simplicity and density on all of the die surface where there will not be open etch pits. The only concern is that wiring does not run too close to open areas where the etchant may penetrate laterally and dissolve it. Figure 4-2 is a CMOS MEMS design; note how the wiring avoids the open areas, but can still be dense elsewhere. The wiring can cross over the pits if sufficient oxide margin is left around them to protect them from the etchant, but as explained in Chapter 1, the anisotropic bulk etching process requires such structures to be non-orthogonal to the underlying $\{111\}$ crystal planes in order to be etched completely under.

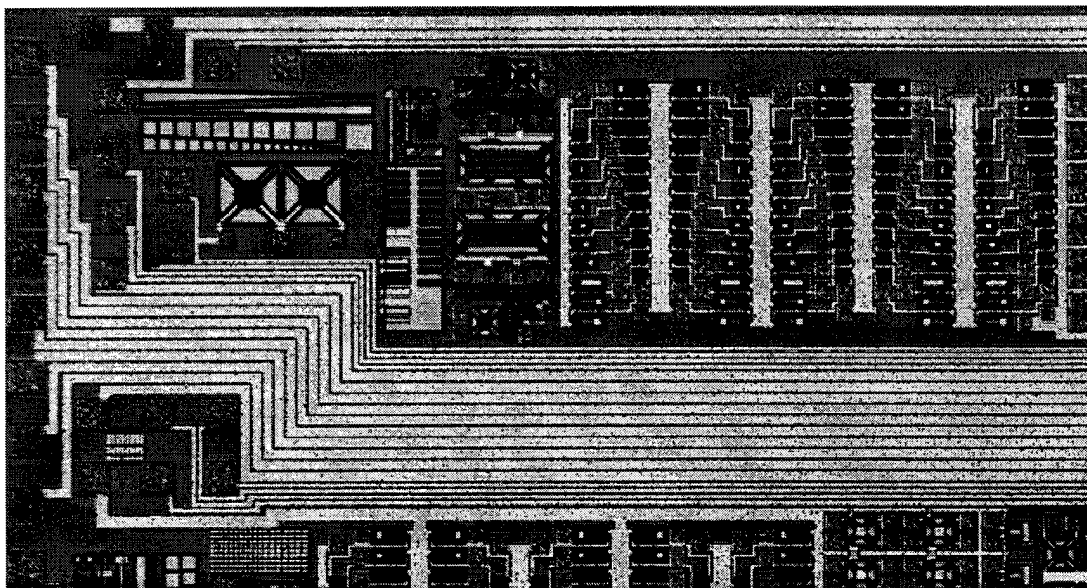


Figure 4-2. Section of the third CMOS MEMS test die showing the density of wiring possible between actual MEMS devices. The wiring runs from bondpads at the left edge of the die to optical devices, not shown, at the right edge of the die.

4.1.2 LIGA

The LIGA process, as offered during this research, has the fewest wiring options. Essentially no provision is made for complex wiring, since there is only one patternable layer. All wiring is substrate wiring, although the release process causes such wiring to detach from the substrate, becoming thin, tall bridges between anchored pads. If electrical crossovers are needed they must be applied manually after fabrication with wirebonds. The wirebonds would preferably be added before the release etch when the pads are still fully supported.

Other published LIGA or electroplated devices have used wiring under the plated structures, as seen in Figure 3-4; but this option was not available on MCNC's second LIGA run. Therefore, all of the LIGA devices tried in this research are unconnected, and can be accessed only by probing or wirebonding. Any connections needed for complex systems must be made off the die at the next level of packaging.

4.1.3 MUMPS

Because of the limitations of the LIGA process and the already complete substrate wiring capabilities of the CMOS MEMS process, most of the research in substrate wiring techniques was done in the MUMPS process. MUMPS provides only one low resistivity material, the gold layer, which must be deposited last. There are no insulating layers since the oxide between the polysilicon layers is etched away in the release process. Only in cases where the structure is made wide and without

etch holes will any oxide be left after the release etch. This means that the only insulator between most released polysilicon layers is an air gap.

Wiring for electrostatic or other low-current devices can be easily drawn in the *poly0* layer; no special provisions are needed, and it can be connected to any other polysilicon layer with anchors. However, polysilicon wiring is too resistive for devices that require some modest amounts of current, such as thermal actuators, or devices that need a low resistance signal path, such as piezoresistive strain gauges. These applications call for the low resistivity that can only be provided by the gold layer.

The fabrication capability tests described in Chapter 2 pointed out the need for metal to be attached only to the uppermost polysilicon layer, *poly2*. To use gold as a wiring layer, a stacked structure must be drawn using the *poly0*, *anchor2*, *poly2*, and gold masks. Figure 4-3 shows top and cross-sectional views of this type of substrate wire.

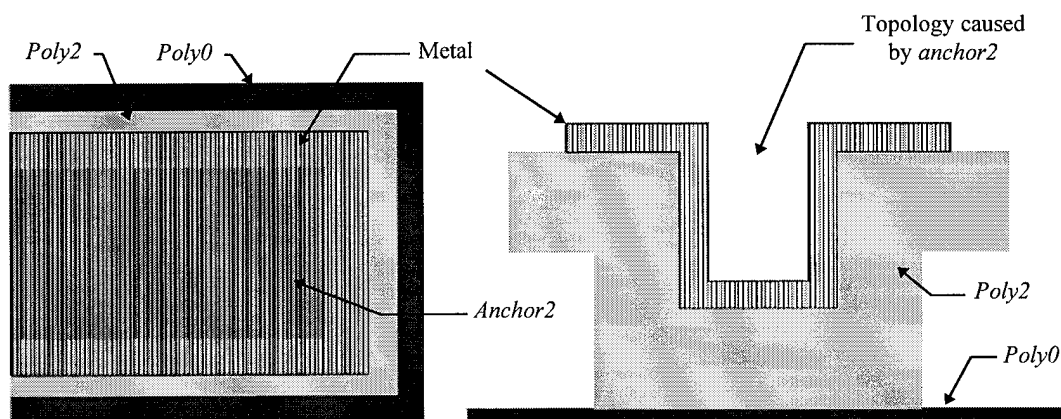


Figure 4-3. Top view and cross-section of a low-resistance substrate wire fabricated in the MUMPS process. The wire consists of metal on a *poly2* support which is anchored to *poly0*.

The *poly2* is needed as a reliable support for the metal layer, and the *anchor2* runs down the length of the wire, attaching it to the substrate. *Poly0* is often run under the *poly2/anchor2/metal* wire to provide a conductance path in case the overlying wire gets cracked or pieces are accidentally broken off. This is especially important when building large numbers of test structures on a single die. Those die often get handled and probed more frequently than die which have only a single purpose device on them, so are more likely to have the tall, exposed wiring damaged.

The minimum specified dimensions of the *anchor2* width, and the minimum distance between the *poly2/metal* and *poly2/poly0* edges force this wire to be at least 14 μm wide, even when the design rules are pushed to the limits explored in Chapter 2. These wires are thus much wider than the 3 μm minimum width possible with the plain metal wires of the CMOS MEMS process. This size, and the fact that wires can not be run over each other for any significant length, means that wiring on MUMPS die takes up much more area than similar wiring on a CMOS die.

4.1.3.1 MUMPS Substrate Wiring Crossovers

The wire described above passes through all the available material layers from the nitride on the substrate up to the final gold layer. This is a problem when there is a need for two wires to cross. Such crossovers must be formed by having the *poly2* and gold of the 'upper' wire continue across the junction, while only the *poly0* is run underneath the other way as the connection for the 'lower' wire. An air gap provides

the insulation between the *poly0* and *poly2* at the crossover, with the *poly2* forming a bridge to carry the gold for the upper wire.

Figure 4-4 shows wiring bus crossovers made in this style. The bus lines cross over or connect to the *poly0* wiring that distributes the signals to local devices. Connections to the *poly0* wires are made simply by running the *anchor2* over the *poly0* wire. The *poly2*/metal wires in Figure 4-4 do not run on *poly0*: this micrograph is from an early die which provided the object lessons for that particular redundancy concept.

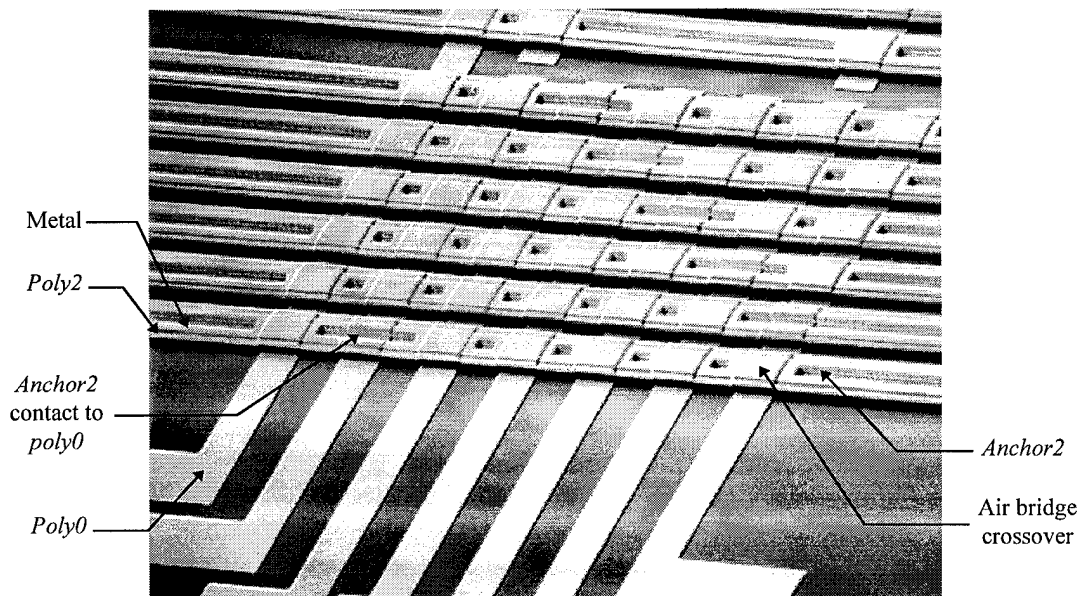


Figure 4-4. Wiring crossover, with 15 μm wide *poly2/anchor2/metal* wires crossing over or connecting to 20 μm wide *poly0* wires running crosswise beneath.

This crossover forces a break in the gold metallization of the underlying wire, so if high currents must be passed on both levels, extra-wide *poly0* must be used for the lower wire. Figure 4-5 shows a high current crossover, which feeds a large thermal

actuator array. If the *poly0* lines are too narrow, they heat the overlying *poly2* bridge enough to melt the gold, causing the upper low resistance path to be broken. The *poly2*, now carrying the full current with no heat sink, then burns through. When designing crossovers, consideration must be given to which path most needs an unbroken metal wire.

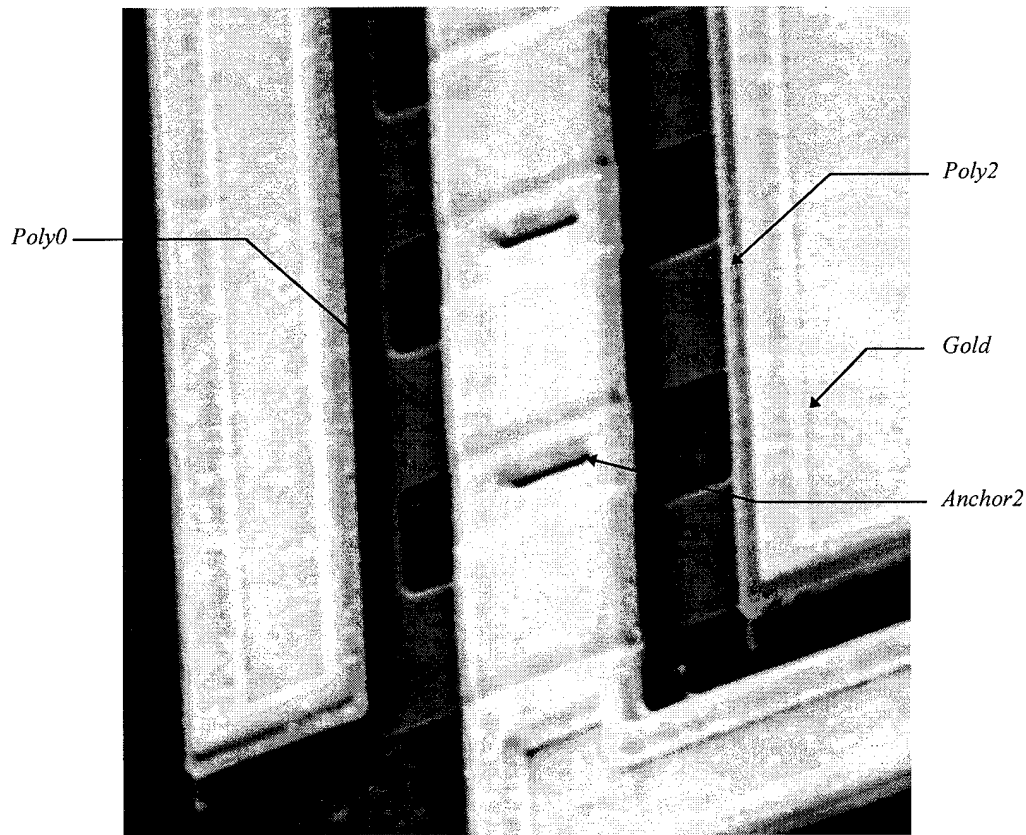


Figure 4-5. High current crossover feeding an array of thermal actuators. *Poly0* wires cross under in three strips to make room for support pillars for the *poly2* bridge. The three *poly0* wires are a total of 48 μm wide, and the *poly2* bridge is 20 μm wide with 17 μm wide gold. Each *poly0* cross-under can pass roughly 90 mA before overheating the *poly2*/gold bridge crossing over it.

MUMPS designs are limited to two levels of non-overlapping wiring, and since the wiring is made in the same layers as the devices being wired, the choices for

wiring large arrays of devices are limited. The only other conductive path available is the substrate under the *nitride* layer, which can only be reached by 'accidentally' cutting through the non-patternable nitride with a combination of RIE etches, as seen in Section 2.3.2.3.3.

The main problem with having the wiring and mechanical features fabricated in the same polysilicon layers is that they generally can not be drawn in the same area on the die. In some cases *poly0* wiring can run underneath a *poly1* or *poly2* structure if it does not have to carry much current. Figure 4-6 shows substrate wiring running up to a *poly2* plate, where the signal wires must run under in *poly0* only. The path of the *poly0* can be seen by the topology it induces in the overlying *poly2* plate.



Figure 4-6. Substrate wiring running under a *poly2* plate. The wiring changes from 16 μm wide *poly0/poly2/gold* to just 8 μm wide *poly0* where it goes under the *poly2* plate. The *poly0* wires travel under the *poly2* plate without touching it.

This wiring solution is not useful if the *poly2* surface must be flat, e.g. for optical reasons. If this is the case, then deep arrays of individually wired devices

must give up area for the wiring runs. Ideally the wiring would run anywhere under the array and not affect its topology, but this is not possible with the MUMPS process, so the wiring must run between devices as shown in Figure 4-7. Trading device area for wiring area limits the efficiency of systems like large mirror arrays which would ideally cover the entire array area with active mirror surfaces.

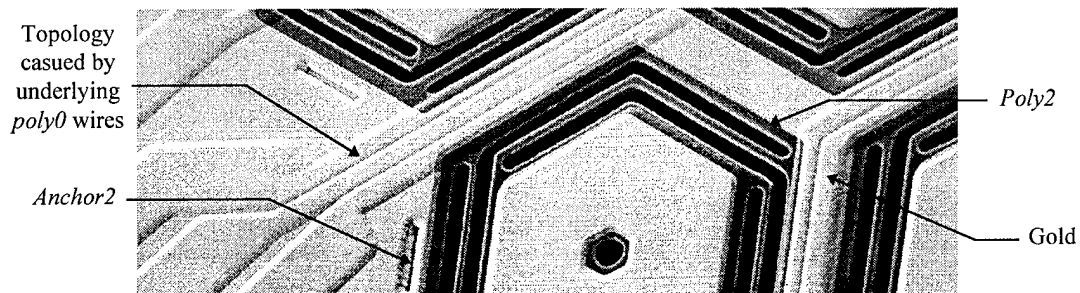


Figure 4-7. 2 μm wide *Poly0* wiring running into a large array between 50 μm wide *poly2* mirrors. Array area is given up for wiring so the devices are not affected by the topology caused by the wiring.

4.2 Hinged Wiring

The other class of wiring developed for the MUMPS process during this research is hinged wiring. Large, complex systems may contain components which are on hinged plates or are slid into position across the substrate during assembly. These devices cannot be reached with standard substrate wiring, so various forms of hinged wiring were developed during this dissertation research to connect to them.

4.2.1 Hinged Devices

Microhinges allow a structure to be assembled by folding up polysilicon plates. The plates are fabricated on the substrate, taking advantage of the dimensional control

of photolithographed features. After the release etch these plates are rotated on hinges and locked into place with a variety of catches [2]. Figure 4-8 shows a folding mirror which uses substrate and scissors hinges. Hinges allow surface-micromachined systems to enter the third dimension, greatly increasing the range of possible system designs.

Fresnel lenses, mirrors and gratings have been built on hinged plates at AFIT [3]. But these are all unpowered, static devices. Much more functionality can be designed if the hinged devices could be moved by microactuators.

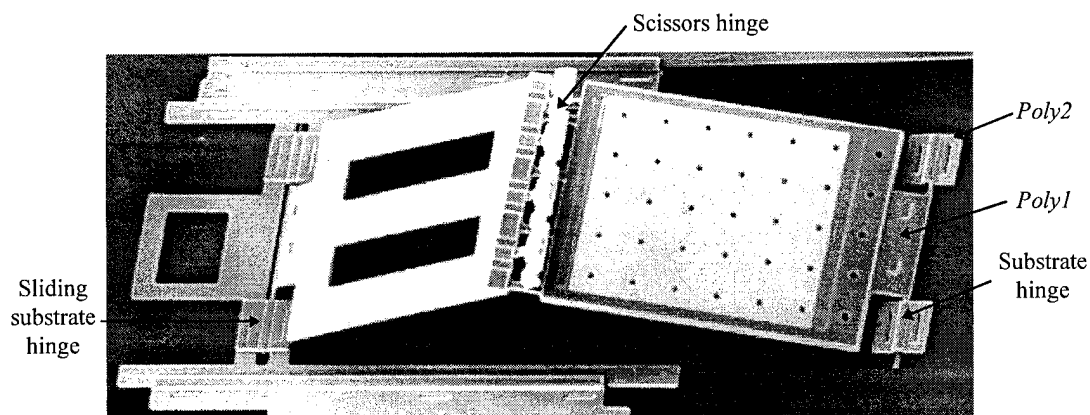


Figure 4-8. Fold-up mirror designed with three types of microhinges [4]. Sliding substrate hinges allow it to rotate off the die, scissors hinges allow it to bend in the middle, and substrate hinges anchor it [2]. Note the looseness of the hinges, especially the scissors hinges.

Two options are available if a design requires hinged features that move. The moving feature can be tethered to an actuator on the substrate [5], as shown in Figure 4-9. This 'fan' device employs one of the thermal actuator arrays described in Section 3.4.6 to wave the plate back and forth. The array is tethered to a slot-and-tab lock that keeps it fixed to the plate but allows the plate to rotate. The plate has three

substrate hinges with $2\text{ }\mu\text{m}$ square hinge pins and is bossed by underlying *poly0* for added stiffness. This is a test device, but in an actual system the plate could carry a variety of optical elements. The actuator array could then be used to position the plate as an initial set-up step after fabrication, or to move the plate as part of the operation of the system.

In the 'fan' device, the actuators remain on the substrate where providing current to them is not a problem. The other option for a moving, hinged structure is to have some type of actuator on the hinged plate. Then a second device could be moved by the actuator which is attached to the plate. This makes it possible to build up a complex structure with even greater design possibilities.

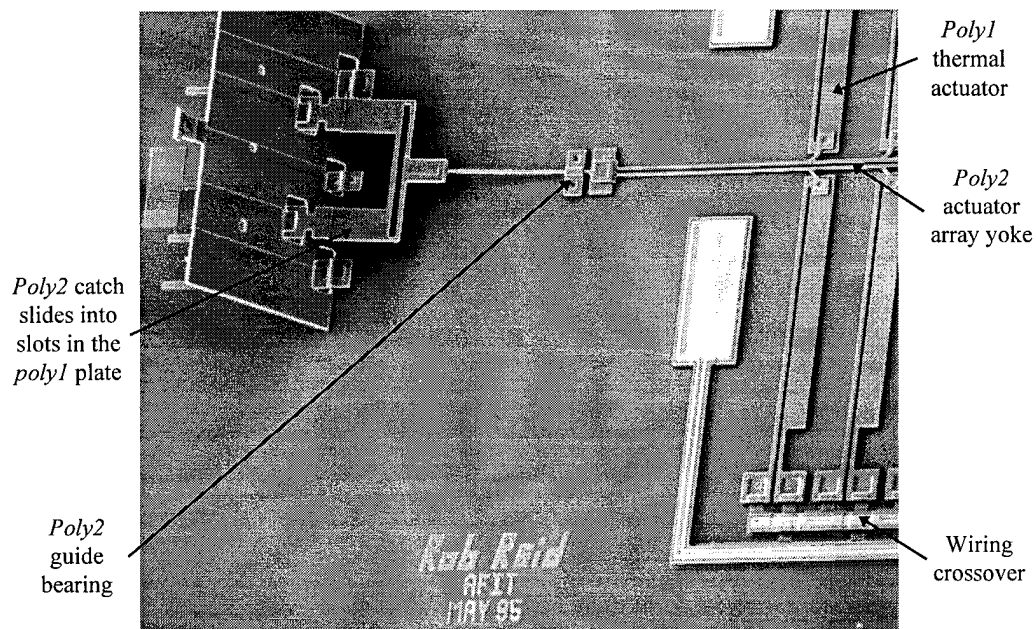


Figure 4-9. Hinged plate attached to a thermal actuator array on the substrate [5]. The array has ten $200\text{ }\mu\text{m}$ long *poly1* actuators that can wave the $110 \times 213\text{ }\mu\text{m}$ plate back and forth about 45 degrees. The *poly1* tether is $103\text{ }\mu\text{m}$ long, $2\text{ }\mu\text{m}$ wide from the yoke connection to the catch connection, and passes under a *poly2* guide bearing.

4.2.2 Wiring to Hinged Plates

Wiring becomes much more complicated when it must be run to devices that are off the substrate on a hinged plate. If the device is an electrostatic actuator [6], then flexible polysilicon wiring is sufficient to operate the device since large currents are not needed. Flexible polysilicon wiring can remain attached to both the substrate and the hinged plate as the plate is rotated. If thermal actuators are put on a hinged plate, however, polysilicon flexures that are narrow enough to bend with the plate without breaking the hinges will be too narrow to supply sufficient current.

For hinged construction to be practical and flexible it will need a reliable, low resistance wiring connection. One problem in the MUMPS process is that all the polysilicon is conductive, so an actuator requires at least two plates to be raised and wired since all actuators have at least two power connections. This assembly step is difficult in practice and would be uneconomical in a high volume production process; although automated assembly using microactuators would solve the problem.

As the MUMPS fabrication test structures in Section 2.3.2.2 showed, the metal layer does not cover the edge of *poly2*. This precludes its use as a wiring mechanism, since it cannot go directly from the *poly2* substrate wire across to the hinged plate. Such a metal line would detach at the *poly2* edges when the plate was rotated into position. Better step coverage for the metal might solve this, but the designer does not control the details of a foundry fabrication process.

The hinged plate wiring solution developed in this dissertation research is a wire that is also hinged. A long, narrow *poly2* flexure with gold on top is hinged at one end so it can be rotated. When it is flipped over, the gold on top faces downward to the die. It can then touch other gold on the top of *poly2* substrate structures or gold on hinged *poly2* structures, forming a gold-to-gold contact. When pressed down and held with a clamp, the spring force of the *poly2* flexure keeps the gold contacts pressed together. Figure 4-10 shows the layout drawing of a hinged wire.

The wire clamp is fabricated in two pieces; one piece is the clamp itself which slides between two guide bearings, and the other piece is a *poly1* former to raise the *poly2* clamp high enough to slide over the wire. The former is removed and the clamp slid back before the wire is flipped into position. The guide bearings then take the upward thrust of the clamp when the wire is flexed. For automated assembly, the clamp sliding operations can be done with thermal actuators, and the hinged wire could be pressed down by a bed-of-nails type automated assembly jig like the ones used for the automated testing of circuits.

To assemble this type of hinged plate wiring, the flexible wire can either be placed and clamped after the plate is erected, or the plate can be erected after the wire is clamped into place. The first option would make it possible to flip up the plate and the wire automatically with microactuators. The second option is easier for hand assembly under the probe station, which has a limited depth of focus, but it would be difficult to raise the plate against the spring force of the clamped hinge wire using microactuators.

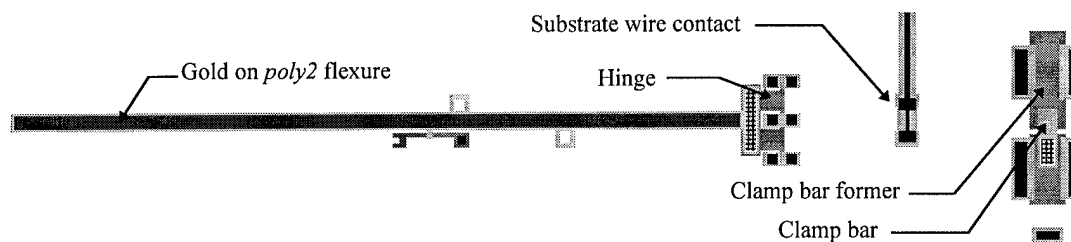


Figure 4-10. Layout drawing of a flexible hinged wire. The wire is fabricated on the substrate, to the left, then flipped over to the right and held down with a sliding clamp. Gold on the top face of the wire contacts the substrate wire to the left of the clamp forming a gold contact on the target device. This flexible wire is $560 \times 13 \mu\text{m}$. The clamp has two sliding parts: a *poly1* former to create the proper topology in the *poly2* clamp bar. The *poly1* former is pulled out before assembly.

Figure 4-11 shows an assembled hinged wire. In this design, the flexural contact on the hinged plate was much too stiff to bend even with the hinged wire pressing against it, although it still forms a low resistance contact. Since the contact did not bend at all, the guide posts on either side did not help in the assembly. Tests on structures similar to this indicate that sufficient current (5 mA) can still be passed through the narrow contact area to operate hinged thermal actuators. Improved contacts are discussed in Section 4.2.5.

The micrograph shows the flexible hinged wire contacting a substrate wire which is located between the clamp and the hinge. The substrate wire is tall enough to force the hinged wire to bend, providing the spring force for the contact. There must be some downward force on all the contacts, otherwise the contact's resistance will be too large or no contact will be made.

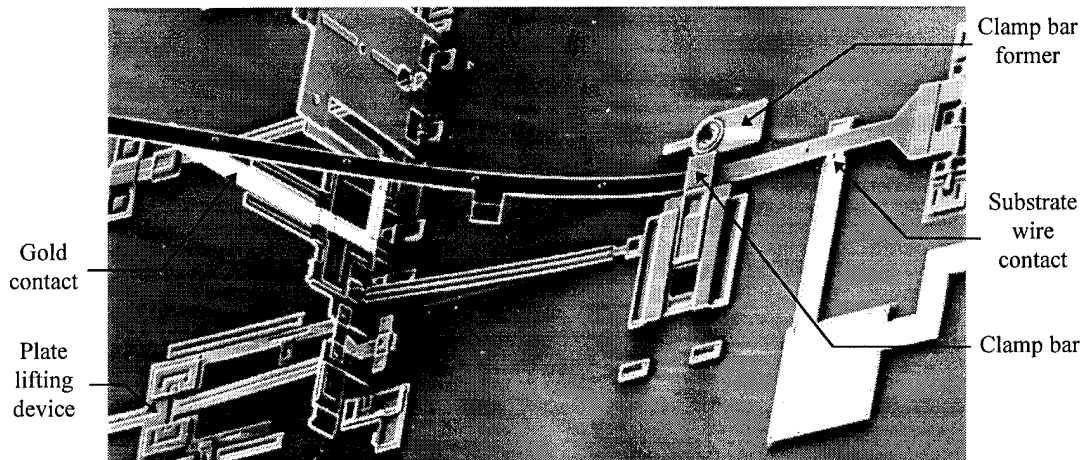


Figure 4-11. Hinged wire contacting a hinged plate. The $13\text{ }\mu\text{m}$ wide *poly2*/gold wire is held in tension by a sliding clamp and makes contact between a wire on the substrate and a gold contact on the hinged plate. Note the *poly1* former for the clamp rotates out of the way in this design. Also, since the hinged plate contact did not bend, the wire is flexed much more than intended.

4.2.3 Hinged Wiring to Sliding Structures

Another class of devices created to meet the research goal of enabling the implementation of large, complex systems was devices that are slid into position after the release etch. Wiring such devices is similar to hinged plates because even though the device is still on the substrate, direct substrate wiring connections cannot be made to it. The solution again uses hinged wiring for gold-on-gold low resistance connections.

Figure 4-12 shows a test structure with two hinged wires flipped over and making contact to a sliding *poly2* beam. The sliding beam is gold plated on top, forming a sliding contact between the ends of the two flipped wires. The other ends of the flipped wires touch cantilevered contacts which run off through substrate wires

to probe pads. This variant of hinged wires has the hinge off to the side so a shorter flexible wire section can be used for compactness. The same sliding clamp scheme is used to hold the hinged wire in tension against the contacts.

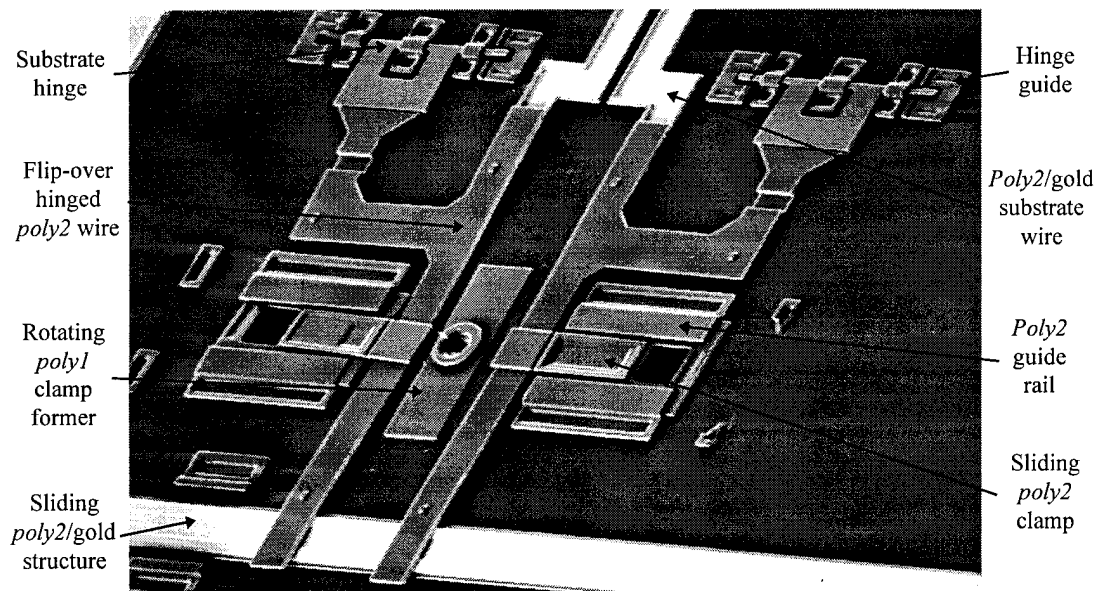


Figure 4-12. Flip-over wiring connecting a sliding wire with substrate wiring. The sections of *poly2* wiring are $255\text{ }\mu\text{m} \times 19\text{ }\mu\text{m}$. The former for the two wire clamps is a single *poly1* plate that rotates out of the way. The resistance through all four contacts of this device was $13.3\text{ }\Omega$.

The device shown in Figure 4-12 was intended to show how the hinged wires could be used to make sliding contacts for slip rings, but the clamp tension is too strong. The *poly2* beam can be pulled under the hinge wires with a probe, but if it is pushed back it will bow up rather than slide, indicating that the contacts would be too stiff for a microactuator to operate a structure with slip rings of this type. A much looser spring tension would be necessary, which might result in higher contact resistance, or a contact resistance that fluctuates widely when the wire is moved. One

solution would be to have the wire lifted while the structure was slid, then placed back down, possibly with vertical thermal actuators.

For this device, the resistance between the probe pads was measured to be 13.3 Ω , an average contact resistance of 3.32 Ω for each of the four contacts in the series. Similar structures average contact resistances of 3.3 Ω to 5.8 Ω . The contact for this wire is 12 μm wide, the width of the gold on the flip-over wiring. However, the length of the contact area depends on the angle at which the wiring strikes the substrate wire or sliding structure, which is variable. For this reason, the substrate wire terminates in a cantilevered contact which will flex to increase the contact area.

4.2.4 Hinge Wire Development

The hinged wire concept grew out of an earlier idea for making a low resistance microrelay contact. Concurrent research into MUMPS polysilicon microrelays showed that poly-on-poly contacts had too much resistance when actuated electrostatically [7]. The concept of hinges led to the development of a flip-over contact that would allow the metal, normally on the top polysilicon layer and facing upwards, to become the bottom-most layer, facing downwards. In that position, it could be used to short two substrate contacts together. The basic idea was used in the design of the switch shown in Figure 4-13.

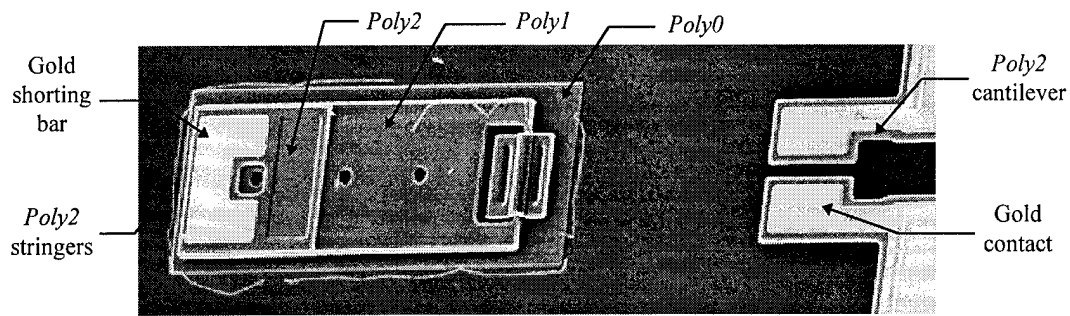


Figure 4-13. Flip-over switch fabricated on the MUMPS7 run. That fabrication run had problems with *poly2* stringers, which can be seen around the *poly0* edges. When the 100 μm long hinged plate is flipped over, the gold shorting bar on the plate makes contact across the two gold pads on the *poly2* cantilevers.

The flip-switch established the fact that the basic flip-over gold-on-gold contact was a workable design, although it worked best when some downward pressure was applied. The pressure could be provided by the restoring force of a bent polysilicon beam. The idea of a long flexible wire came from observations of how much flexing polysilicon beams could withstand before breaking. This was seen in test structures like the pull-spring shown in Figure 4-14, which could be pulled by a probe point to over three times its starting length without breaking.

The original version of this spring on the first MUMPS die illustrated the impact that the polysilicon topology could have on device operation. The *poly1* spring was drawn with *poly2* guide rails intended to let the spring only move laterally. When fabricated, the guide rails conformed to the ends of the leaf springs, trapping each leaf end in a cup. So although the *poly1* was released, it was trapped in position by the guide rail. To move the springs, the guide rails had to be broken away.

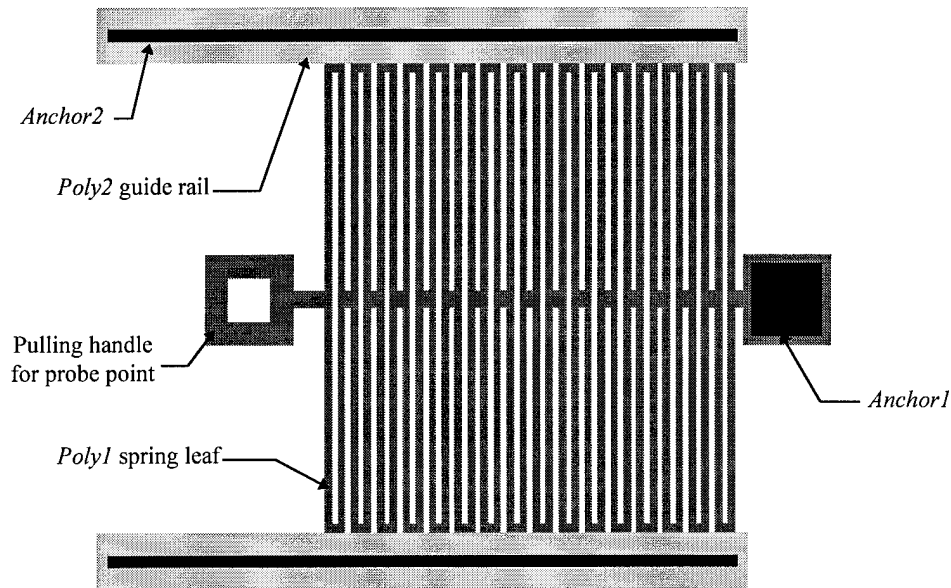


Figure 4-14. Pull-spring made of *poly1*. The spring is 190 μm long, and can be pulled to three times its length without breaking. Each leaf of the spring is 200 x 3 x 2 μm .

Starting with the two concepts of hinged gold-on-gold contacts and flexible polysilicon springs, designs were drawn to test the feasibility of making high current crossovers for substrate wires. The idea was to allow for both wires of a crossover to carry high currents in metal, rather than the lower one having to cross in just *poly0*, as seen in Section 4.1.3.1. One wire would be a standard *poly2*/gold substrate wire, and bowed across it would be a flexible *poly2* wire.

The flexible wire would be flipped upside down so there would be gold-on-gold contacts at either end. One end of the flexible wire would be hinged, and the other end would have some sort of catch to hold it down. This would flex the wire, making it bow upwards in the center, where it could cross several substrate wires without touching them. The flexed wire would make contact to two wires or contacts on

either side of the wires to be crossed over, and would be the spring to press itself onto the gold contacts. Figure 4-15 shows a test cell intended to see which end catch would be the easiest to assemble. All of these catches worked by having some part of the catch tucked under a flanged *poly2* post.

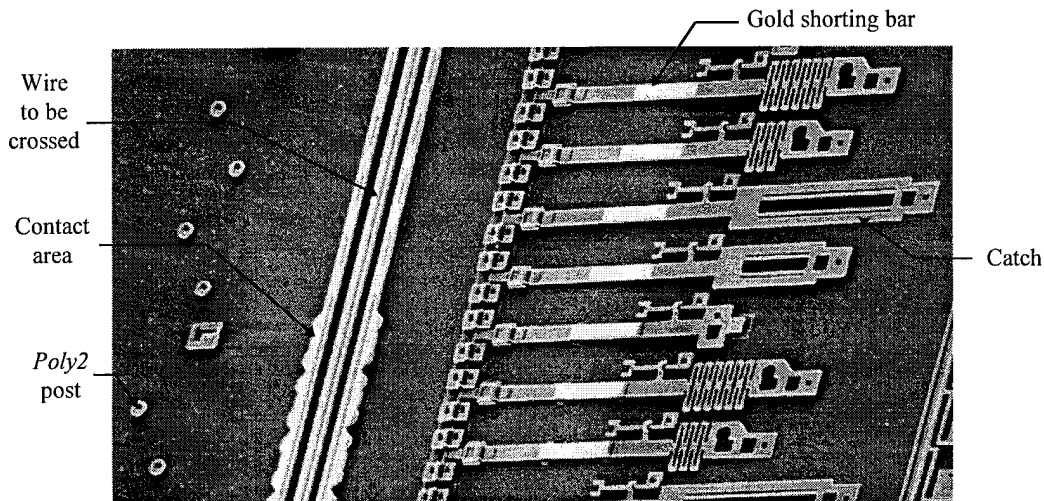


Figure 4-15. Test cell for flexible wires. The flexible wires cross over a substrate wire without touching it, making contact across the outer two wires. This set has flexible wires $150 \times 20 \mu\text{m}$ with a variety of catches at the end, all involving a part that must be tucked under a flanged *poly2* post.

When tested, none of the catch designs were easy to assemble. The catches were too fragile and most broke while trying to latch them. The ones that did manage to stay in one piece did not provide enough spring force to make the gold-on-gold contacts reliable. With the low contact force, the contact resistances ranged from 10Ω to no contact at all. Another major problem with these wires was the hinge design. The $2 \mu\text{m}$ wide hinge pins broke easily if bumped, and the plates holding the hinge pins would catch under the hinge 'staples', as seen in Figure 4-16.

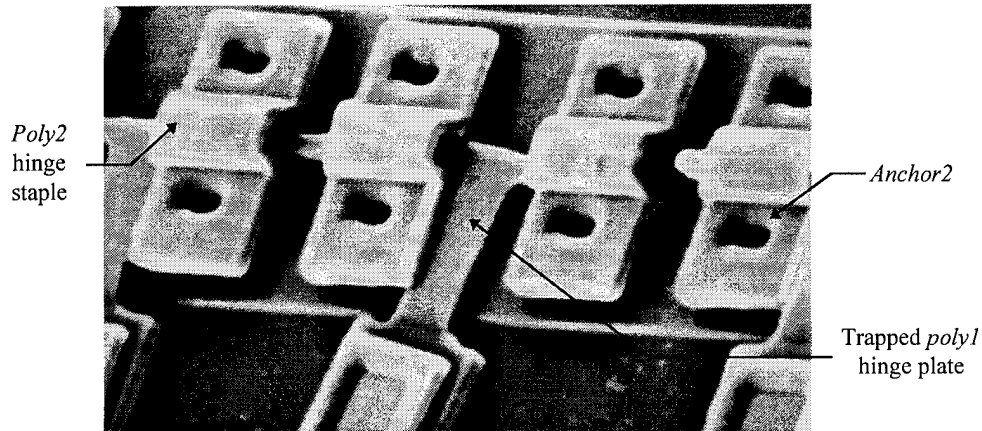


Figure 4-16. Hinge plate caught under the hinge staple. This makes the plate impossible to lift until the hinge pins are re-aligned with the staple.

A better arrangement would be to use the sliding clamp seen in Figure 4-12, and consider one of the wires shown to be half of the crossover. A longer wire with a sliding clamp on both ends has the spring force needed for reliable contacts, and is easier to assemble than the tuck-under catches. With clamps on each end, the bow in the center will form a bridge that can cross as many intervening wires as needed. The spring force is generated at the clamped ends. As seen in Figure 4-12, the clamp forces the wire to bow down between the contacts.

Also on the same die, flexible hinged wires similar to the ones shown in Figure 4-15 were arranged to contact a hinged plate. These wires were made much thinner, since it was thought that the flexing force would otherwise be too strong for the hinge pins and hinged plate catches to withstand. When the wires were tested they were found to be too hard to manipulate with probes because they were too narrow. They could be flipped over onto the hinged plate, but did not have any place for the probe to push down to press the wire in place.

These wires also had catches that were meant to slip under a flanged post. The catches proved extremely difficult to get in place after the hinged plate was raised, since the wire had to be flexed downwards and slid into position. The thin wires also tended to break easily under the probe point. The small hinges are also too loose when released to help direct the wire straight over to the contacts, and the hinged plate would get trapped under the hinge staples. Figure 4-17 shows a set of these wires in the sort of disarray that occurred whenever they were tested.

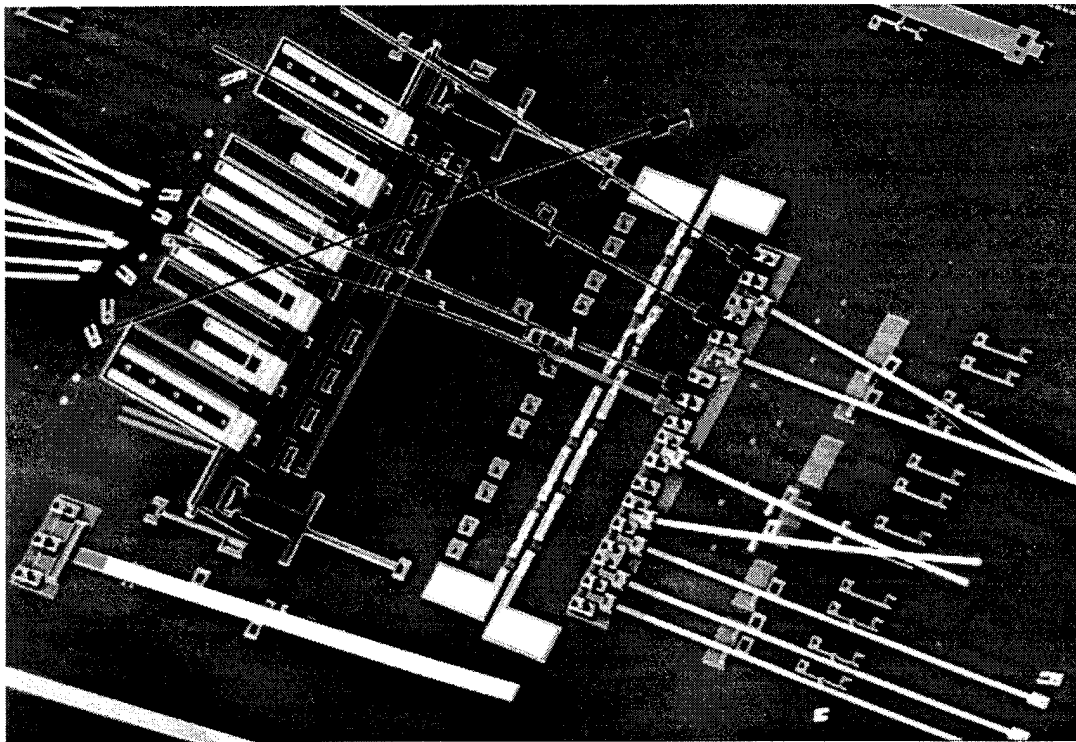


Figure 4-17. Narrow, $480 \times 3.5 \mu\text{m}$ flexible wires proved too small and fragile to be erected with probe points. A poor hinge design also made them difficult to align and flip over.

The test cell of Figure 4-17 was arranged with 6 pairs of wires with 3 types of hinged plate contacts. The signal goes up one flexible wire, across a gold shunt, and

back down another flexible wire. The hinged wires pass the signal to and from the hinged plate from a bus wire on the substrate. These wires were 480 μm long and only 3.5 μm wide with 2.5 μm wide gold on top.

A few wider wires were also laid out just to see if they too could be flexed. These were intended to carry larger currents, although not much hope was held out that the hinged plate could support them. A sliding catch was designed for these wires which was close to the final design. Upon testing, the wires worked well and were the basis for the final version seen in Figure 4-11. The only unfinished design feature is the flexural contact on the hinged plate.

4.2.5 Improved Hinged Plate Contacts

Figure 4-18 shows the concept of an improved flexural contact. The contact plate is between guide posts that ensure correct alignment of the wire to the contact. They also make placing the wire on a raised plate simpler. One possible improvement would be to match the spring force of the contact flexure to the spring force of the clamped hinged wire. This would allow the contact to bend over for more contact surface area, but may result in a flexure that is too narrow to carry sufficient current.

Another option also under investigation is to eliminate the cantilevered contact on the hinged plate altogether. Tests of the metal deposition characteristics indicated that if the metal is drawn so it overlaps the edge of a *poly2* plate, it will break off at

the edge since it does not fully cover the step in the topology. By doing this intentionally, the gold can be run right to the edge of the *poly2* plate. When a hinged wire is flipped over on top of the edge, the gold on the wire can contact the gold at the edge of the hinged plate.

The contact area will be small, but tests on broken cantilever contacts, and the non-flexing contacts like the one seen in Figure 4-11, show that enough current can be passed to power a hinged thermal actuator. The advantage is that the wiring alignment is not as critical, so guide posts are unnecessary. Also, the hinged wire does not have to be flexed as much, making for an overall shorter structure when assembled.

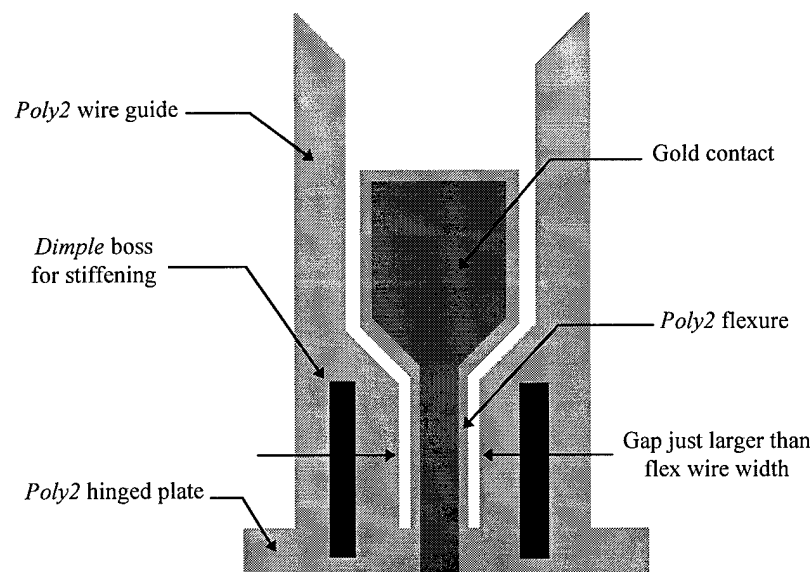


Figure 4-18. Version of a contact on a hinged plate for hinged wiring. Contact has a flexure whose spring force is matched to the hinged wire's force to provide greater contact area. Guides ensure maximum contact overlap and ease of assembly.

4.3 Improved Hinges

A common problem seen in early hinged devices, and especially the hinged wires, was the inadequacy of the hinges themselves. The 2 μm square hinge pins in use were too weak to take much lateral force, and the basic design with a simple hinge pin and 'staples' left too much play in the position of the hinged plate after release.

Two micron square hinge pins had been used up to this point because they were merely copies of the hinges described in the initial paper on the topic [2]. This design had proved adequate for other applications where more hinges were used on each plate. Analyzing the target layer thicknesses for the MUMPS process revealed that the hinge pins could be wider. The thickness of the two oxide layers plus the *polyI* layer was 4.5 μm , (currently 4.75 μm , starting with MUMPS9) so this was the height available to turn the hinge pin.

A test cell was designed to determine the maximum hinge pin width that could be easily rotated. Small hinged plates were built with hinge pins ranging from 2 to 5 μm in 0.5 μm increments. This test cell revealed that plates with pins up to 4 μm wide could be flipped over. Current designs at AFIT use 3.5 μm wide hinge pins.

Pin strength is not the only concern, though. While some hinges did not break at the pin, they did become trapped under the hinge staple, making it impossible to flip them over. This is solved by placing *polyI* wall around the hinges if they are to be flipped up, or around extended pin ends if they are to be flipped over. The walls

can be placed within 2 μm of the hinged plate according to the MUMPS design rules, so any part of the plate that might slide sideways and get caught under the staple is drawn at least 3 μm from the staple. Dimples are added to make the pins and walls non-planar so the pins will not be able to slide under the walls. Figure 4-19 shows the improved hinge design for plates that must be flipped completely over, as with flexible hinged wires.

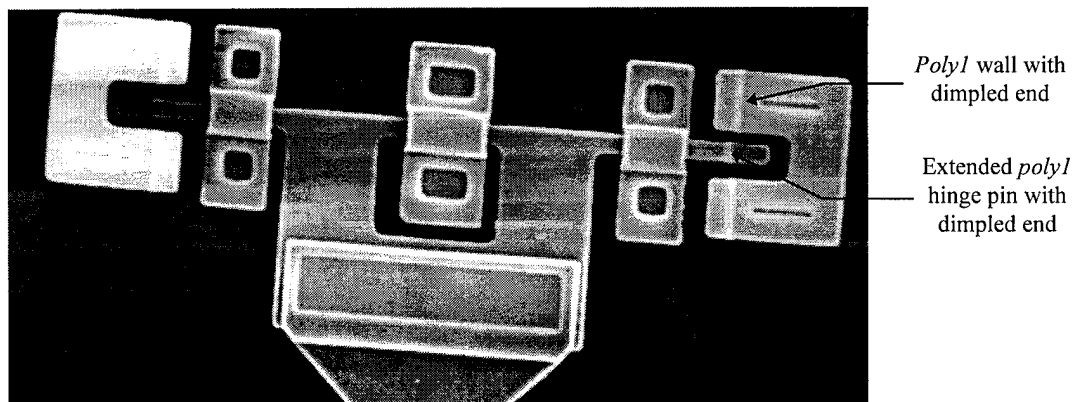


Figure 4-19. Improved hinge design. Hinge pin is 3.5 μm wide, and *poly1* walls have been placed around the hinged pin ends so the plate cannot slide under the hinge staples.

A related problem is keeping the hinged plate located when it is being rotated, otherwise it will have several microns of play as the hinge pin slides about in the large staple opening left by the dissolved oxide. For static devices a solution to this problem is to use a second flip-up plate with a slot to fix the main plate's position. This will not work for hinged plates that must be rotated back and forth during operation. For actuated plates, the lateral hinge pin motion must be constrained along its axis so the plate can still rotate.

One design which could do this is a slide-over guide with a slot that can capture the end of a protruding hinge pin. The slot is just wider than the thickness of the *poly1* plate, so it can locate an extending pin more accurately than just the hinge staple, yet still allow the limited lateral motion needed at the hinge pin axis to accommodate the pin's rotation. The guide can be automatically moved into position with thermal actuators for automated assembly.

Figure 4-20 shows the layout for a hinge pin guide currently in fabrication. In this design, the guide is pushed over to the hinge pin end after the release etch. The portion of the guide which runs under the *poly2* rails is made wider so when it is slid into position, the space left by the dissolved oxide between the guide and the rail anchors is taken up.

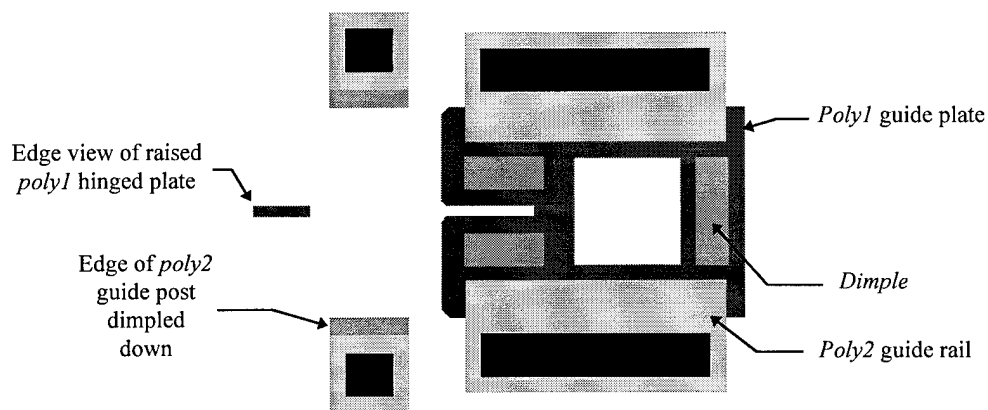


Figure 4-20. Hinge pin locating guide for hinged plates that must be able to rotate. The guide locates the pin so it has less play than it would if constrained by just the hinge staples.

4.4 Applications

A few test applications are described to illustrate how the various wiring techniques can be used for single devices and larger systems. In some cases the applications were made possible by the existence of the wiring technique, and in other cases the wiring technique was developed when the design ran into wiring problems.

4.4.1 Thermal Bimorph Actuator

Figure 2-46 showed a thermal bimorph actuator which combined the gold-on-gold contact with hinged plates to allow upwards vertical deflection. This actuation method could not be usefully employed in the MUMPS process before the flip-over gold-on-gold contacts because the MUMPS process only places gold to top of the *poly2*. When heated, the greater thermal expansion of the gold causes the actuator to bend down. But it could only bend down 2.75 microns, not a very useful actuation direction or distance.

With the flip-over scheme, the bimorph can be built as a hinged plate which, when flipped over, connects to cantilevered gold substrate contacts, also seen in Figure 4-21. With the bimorph inverted, it can curl upwards when heated, with much more deflection possible. The hinged plates carrying the actuator could also be set at any angle and connected with flexible hinged wiring, increasing the designer's choices for applying these actuators.

4.4.2 Off-Die Grippers

Two versions of grippers were tried. One was similar to the flip-over bimorph, with the bimorph section replaced by two lateral thermal actuators. The two actuators required three hinged plates since there are two current paths sharing a common return line. The gripper flips over the edge of the die where the tips are free to actually grip something, rather than being over the die like the demonstration grippers in Figure 3-16. Figure 4-21 shows a set of grippers before assembly, revealing the geometry of the gold contacts.

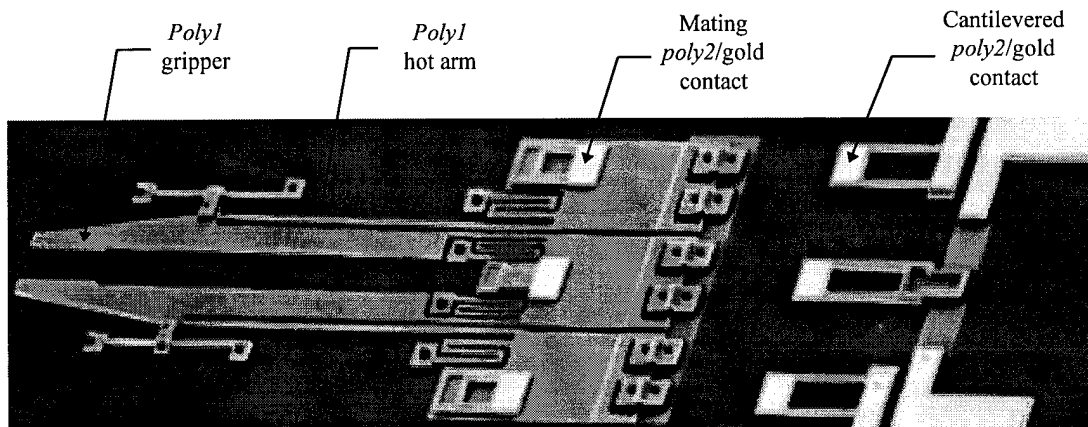


Figure 4-21. Unassembled flip-over grippers. The gripper tips go over the edge of the die where they are free to grip other objects. Cantilevered contacts on the flipped-over plates connect to cantilevered contacts on the substrate to power the 200 μm long thermal actuators.

This version of flip-over grippers was difficult to assemble because the hold-down latches were too small to manipulate easily with probe points, and the older hinge style made it difficult to flip over three plates without breaking the fragile

actuator arms. Updated grippers with the proven slide-catch from the hinged wire design, and improved hinges will make this device more viable.

The other version of off-die grippers are slid into position instead of flipped over. This makes assembly easier since sliding is simpler to do with probes. The design is also more robust than the flip-over grippers, which rely on fragile hinge pins for connection to the substrate. The sliding grippers remain firmly positioned by the guide rails and sliding stops. Power is applied to the thermally actuated arms through flip-over hinged wiring like that of the test structure shown in Figure 4-12.

To aid in assembly, the gripper incorporates lost-poly guide rail formers that can be snapped off after the grippers are extended. There are also two thin tethers between the wiring contacts at the back of the grippers to help slide the assembly out as a single unit; these must be snapped before applying power. Figure 4-22 shows the grippers before assembly, with the hinged wires in their initial position.

Figure 4-23 shows an assembled gripper. After the gripper is slid into position and the *poly1* formers and tethers are removed, the hinged wiring must be flipped over into position and locked down. The *poly1* formers for the hinged wire catches rotate out of the way and remain attached to the substrate.

Sliding *poly1* blocks at the rear are intended to prevent the grippers from being forced backwards. However, it has been found that the clamping force of the flexible hinged wiring is sufficient to hold the grippers against any push that would not otherwise break them. This was fortunate because slots in the sliding blocks were too narrow to pass under their *poly2* guide posts.

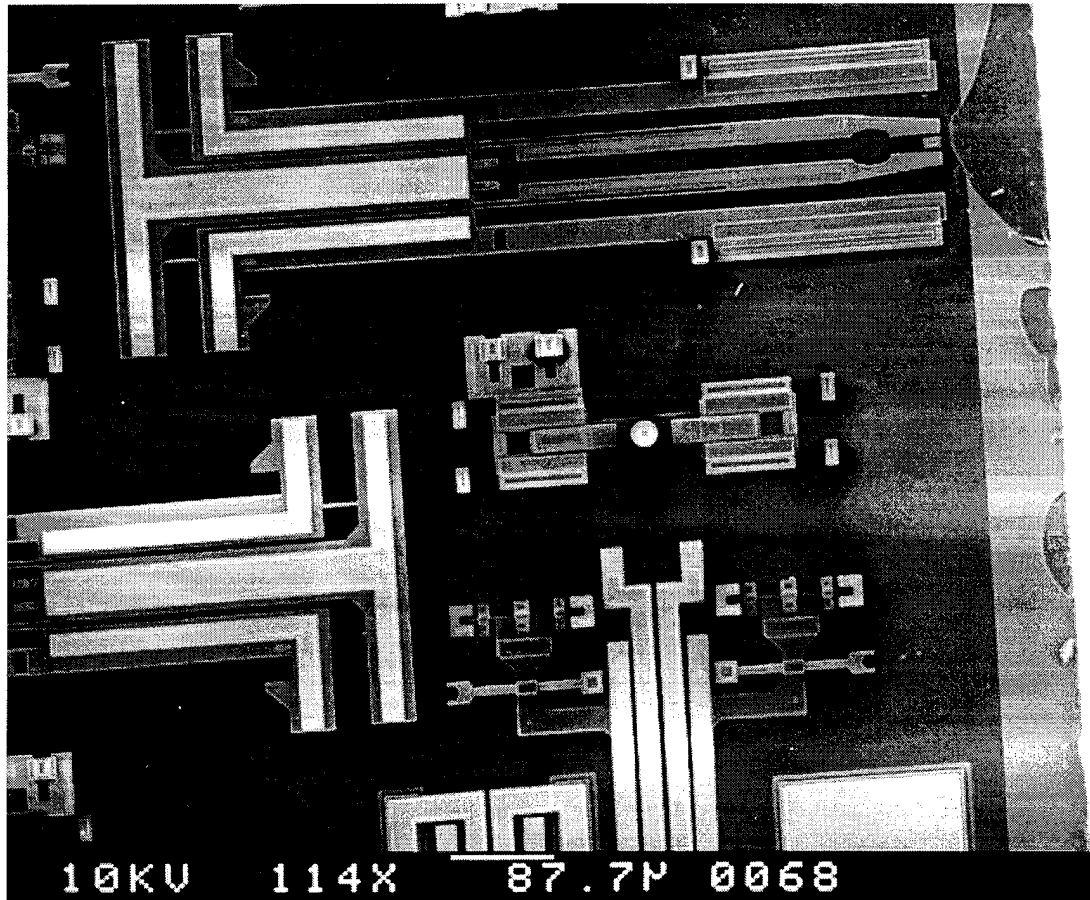


Figure 4-22. Slide grippers before assembly. The three main sliding sections are connected with two thin tethers so they can be slid into place as a unit. Also attached are formers for the guide rails. Overall structure is $730 \times 1410 \mu\text{m}$. The nitride at the die edge was chipped when the wafer diced.

The many assembly steps will have to be automated before such devices can be made practical. All of the sliding can be done with linear stepper motors, and linear motors for raising hinged plates are in fabrication. The various motors will be discussed in Chapter 5. The only part of the assembly that probably cannot be done with microactuators is pressing the flexible wire down so the clamp can be slid over top of it. This might be possible to do with spring-loaded presser feet after the die are packaged.

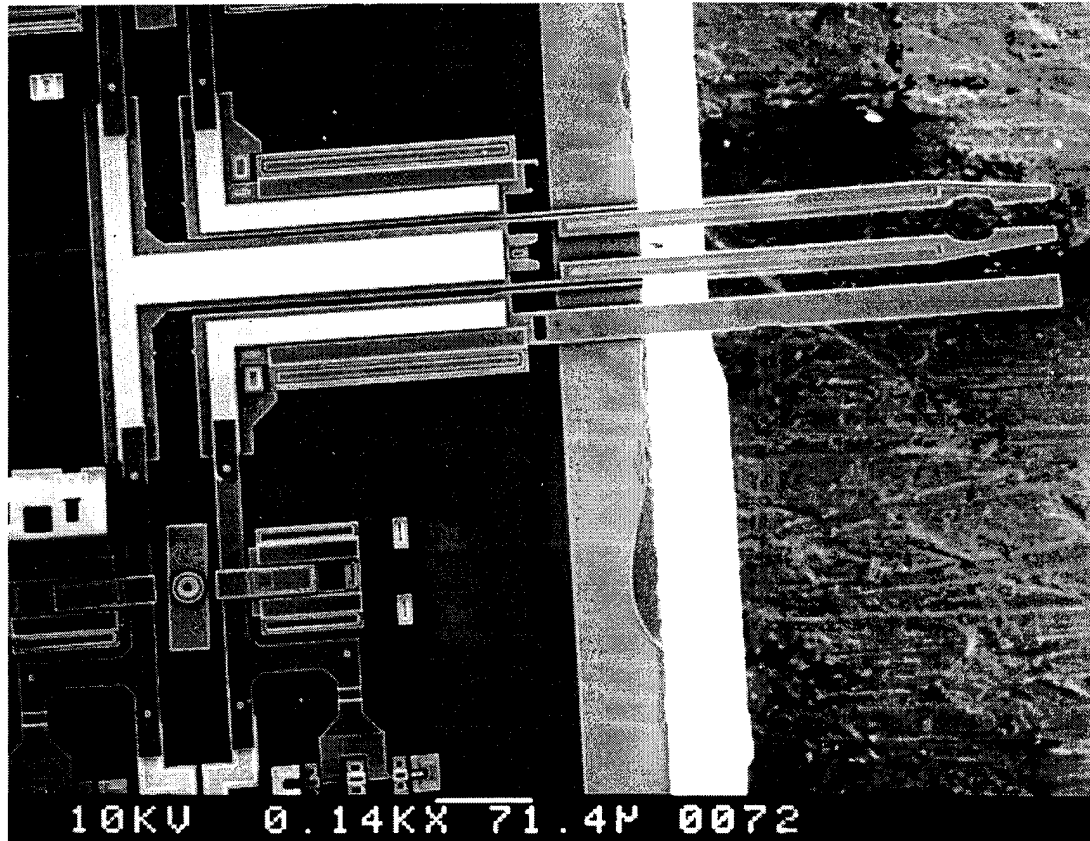


Figure 4-23. Slide grippers in the extended position. One *poly1* former for the *poly2* guide rails has been removed. The tethers between the sections have also been removed. Actuators are $225\text{ }\mu\text{m}$ long with $2.5\text{ }\mu\text{m}$ wide hot arms and flexures. Note that the sliding block at left center above the wire clamp could not be slid into position. The rough area on the right is the SEM die holder below the die. The white margin is the diced edge of the die.

4.4.3 Grounding Hinged Covers

On some mirror arrays, it is desirable to have a flip-over hinged cover plate. The plate prevents stray reflections from non-active areas of the array [8]. For example, one mirror array designed by the author for another researcher had a cover plate which was intended to have an anti-reflective coating so only light whose phase

has been adjusted by the piston mirrors under the plate would be combined at the output [9].

Figure 4-24 shows a portion of a cover plate with a flexible contact and clamp taken from the flexible hinged wire design. This provides a secure ground connection, rather than trying to ground the plate with an unreliable connection through the hinge pins. If the plate is not grounded its charge may affect the operation of the electrostatically actuated piston mirrors under it. This design is currently in fabrication.

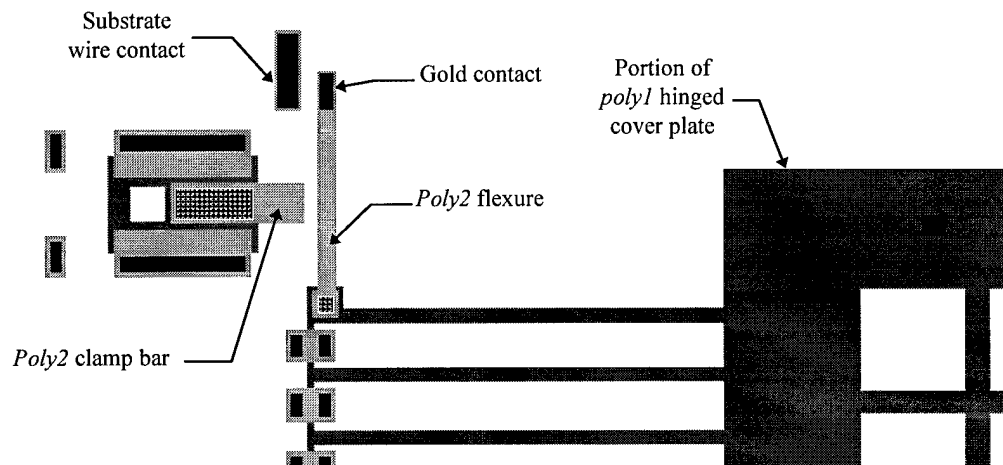


Figure 4-24. Hinged cover plate grounded with a flexible wire based on flip-over wires seen in Figure 4-12.

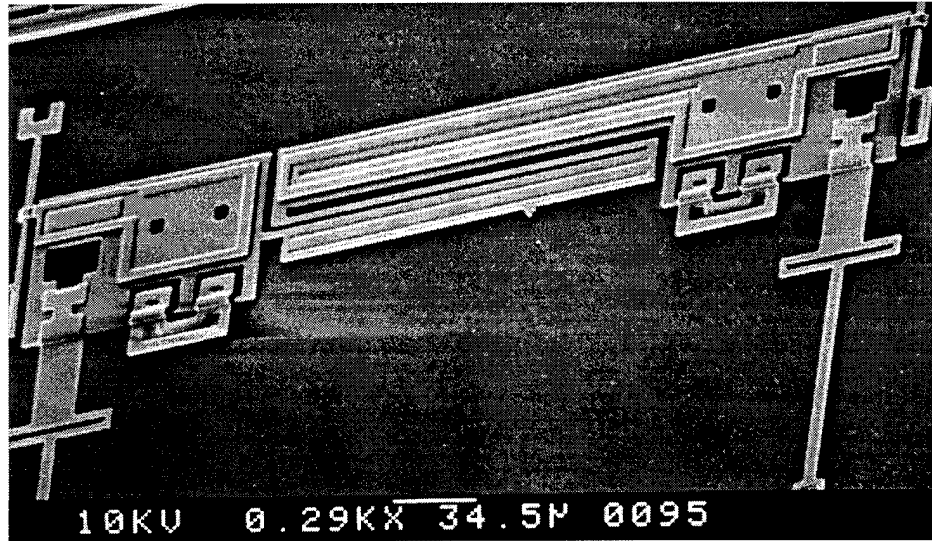
4.4.4 Hinged Thermal Actuator

One of the reasons for developing the flexible hinged wire was to be able to use thermal actuators on hinged plates. The test application was a microrelay, based on

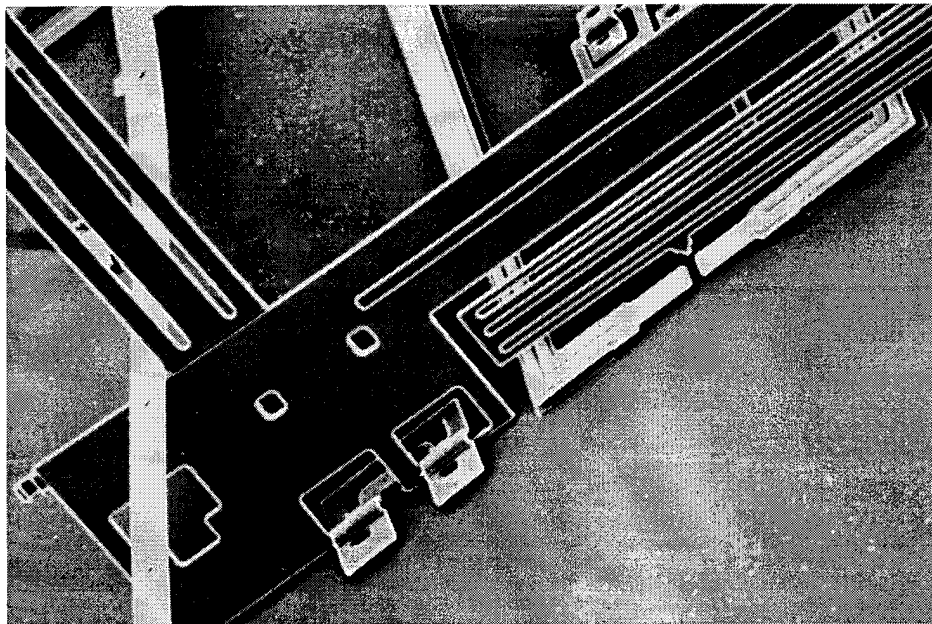
the flip-over switch in Figure 4-13, described in more detail in Chapter 5. But in general, hinged thermal actuators, by allowing actuation in any direction, would greatly expand the range of possible designs for larger systems, one of the author's research goals.

The thermal actuator is mounted on two hinged plates which must be raised together to prevent the actuator from breaking. Future versions should have a third plate which spans the two actuator plates so they can be lifted together easily. Figure 4-25 (a) shows a test cell for practicing lifting the two plates without breaking the actuator; and (b) shows an assembled actuator with a hinged wire set to one side of the intended contact. The cantilevered contact proved to be too stiff to give with the pressure of the flexed wire, making it difficult to assemble the entire structure; but it was found that the gold-on-poly contact made by placing the wire next to the contact worked well enough to power the actuator. That style of contact may not remain viable in the long run as the polysilicon oxidizes, so new gold contacts were designed for the hinged plates, as discussed in Section 4.2.5.

A pair of 560 μm long flexible hinged wires connect the hinged thermal actuator to substrate wires leading off to probe pads. The best way found to assemble this cell, with the wires on the too-stiff contacts, was to clamp the wires in position first, then lift the plates. This was extremely difficult, as the plates would twist due to play in the hinges, and the plates would not always latch upright.



(a)



(b)

Figure 4-25. Thermal actuator on hinged plates, fabricated on the MUMPS9 run.
 (a) Unassembled test cell; *poly1* actuator is 218 μm long and has 626 Ω resistance.
 (b) Assembled actuator; hinged wire is set next to the originally intended contact because those contacts were too stiff.

For one of the structures which was assembled, the resistance between the probe pads was 648 Ω . The resistance of the actuator itself, measured by probing on the

hinged plate before assembly, was 626 Ω . Subtracting this from the total resistance leaves 22 Ω for the contact resistance of the series of four gold-on-gold hinged wire contacts, or an average of 5.5 Ω per contact, consistent with measurements of similar contacts. As seen in Section 4.2.3, the contact area depends on the angle of contact, which can be adjusted by the contact design. The resistance of the gold-on-poly contact was not measured, since it should change as the polysilicon oxidizes, but freshly assembled contacts could pass enough current to operate the actuator and even to burn it out.

4.5 Conclusions

Substrate wiring innovations were unnecessary for the CMOS MEMS process, not possible in the LIGA process, and successful in the MUMPS process. The MUMPS process design capabilities are extended by the development of various forms of flexible hinged wiring. These wires free the designer to move powered devices one step off of the die surface and onto sliding and hinged plates.

To extend wiring of this sort out farther on hinged plates will require that one of the released layers, preferably the lowest one, be an insulator like silicon nitride. It would also require at least two releasable layers above the nitride, so that all of the devices described in this chapter could be built on a hinged plate exactly as they are now built on the substrate, including the normal substrate wiring.

The examples shown in this chapter demonstrate that the wiring designs created in this research do make possible more complex systems and devices. However, to be

fully useful, these wires should be capable of being assembled on a volume production basis. Although sliding parts can be moved with microactuators, there is currently no way to flip the hinged wires over. Suitable actuator systems are being developed for this task and will be discussed in Chapter 5.

REFERENCES:

1. C. McCarty, *Information Art: Diagramming Microchips*, Museum of Modern Art, New York, 1990.
2. K. Pister, M. Judy, S. Burgett and R. Fearing, "Microfabricated Hinges," *Sensors and Actuators A*, Vol. 33, pp. 249-256, 1992.
3. V. Bright, J. Comtois, S. Gustafson and E. Watson, "Realizing micro-opto-electro-mechanical devices through a commercial surface micro-machining process," *Proc. SPIE 1996 International Symposium on Lasers and Integrated Optoelectronics*, San Jose, CA, 27 Jan. - 2 Feb. 1996, Invited Paper.
4. D. Sene, "Design, fabrication, and characterization of micro-opto-electro-mechanical systems," Master's Thesis, Air Force Institute of Technology, Wright-Patterson AFB, Ohio, AFIT/GEO/ENP/95D-03, December 1995.
5. J. Reid, V. Bright and J. Comtois, "Arrays of thermal microactuators coupled to micro-optical components," *submitted to SPIE International Symposium on Optical Science, Engineering, and Instrumentation*, Denver, CO, 4-9 Aug 1996.
6. P. Chu, P. Nelson, M. Tachiki and K. Pister, "Dynamics of polysilicon parallel-plate electrostatic actuators," *Proc. Transducers '95/Eurosensors IX*, Stockholm, Sweden, Vol. 2, pp. 356-359, 25-29 June 1995.
7. M. Phipps, "Design and development of microswitches for micro-electro-mechanical relay matrices," Master's Thesis, Air Force Institute of Technology, Wright-Patterson AFB, Ohio, AFIT/GE/ENG/95J-02, June 1995.
8. J. Comtois, V. Bright, S. Gustafson and M. Michalicek, "Implementation of hexagonal micromirror arrays as phase mostly spatial light modulators," *Proc. SPIE Microelectronic Structures and Microelectromechanical Devices for Optical Processing and Multimedia Applications*, vol. 2641, pp. 76-87, 23-24 Oct. 1995.
9. V. Bright, J. Grantham, C. Christenson and J. Comtois, "Micromirror array control of a phased array laser diode," *submitted to SPIE: Micromachining and Microfabrication '96*, Austin, TX, 14-15 October 1996.

5. Large System Examples

The most useful way to verify that the devices and techniques developed during this research do make larger and more complex systems possible in a foundry process is to try some examples. The basic actuation and wiring problems have been addressed, but designing larger systems also brings to light further problems such as input/output (I/O) limitations and floorplanning. Addressing these basic large system layout problems drew on knowledge gained from prior printed circuit board and VLSI circuitry design and layout experience. The result are MEMS die with a density and number of devices similar to Medium- and Large Scale Integrated circuitry or 'LSI'; leading to the obvious name for this new MEMS level of integration: 'LSM', for Large Scale MEMS.

LSM techniques had been employed from the very first die layout, since the author was engaged at that time with a complex VLSI design project where wasting any die area had to be avoided. The VLSI die layout approach was carried over to the MEMS die, which reflects the same device packing density. The MCNC employees even gave AFIT an informal 'shoehorn' award for the densest die, at the first annual MUMPS User's Group meeting [1]. The AFIT die was just a black square when MCNC made a plot of the entire wafer reticule. Figure 5-1 shows the layout plot of the first die submitted to the MUMPS fabrication process. Note the bilateral symmetry; only half the die had to be drawn.

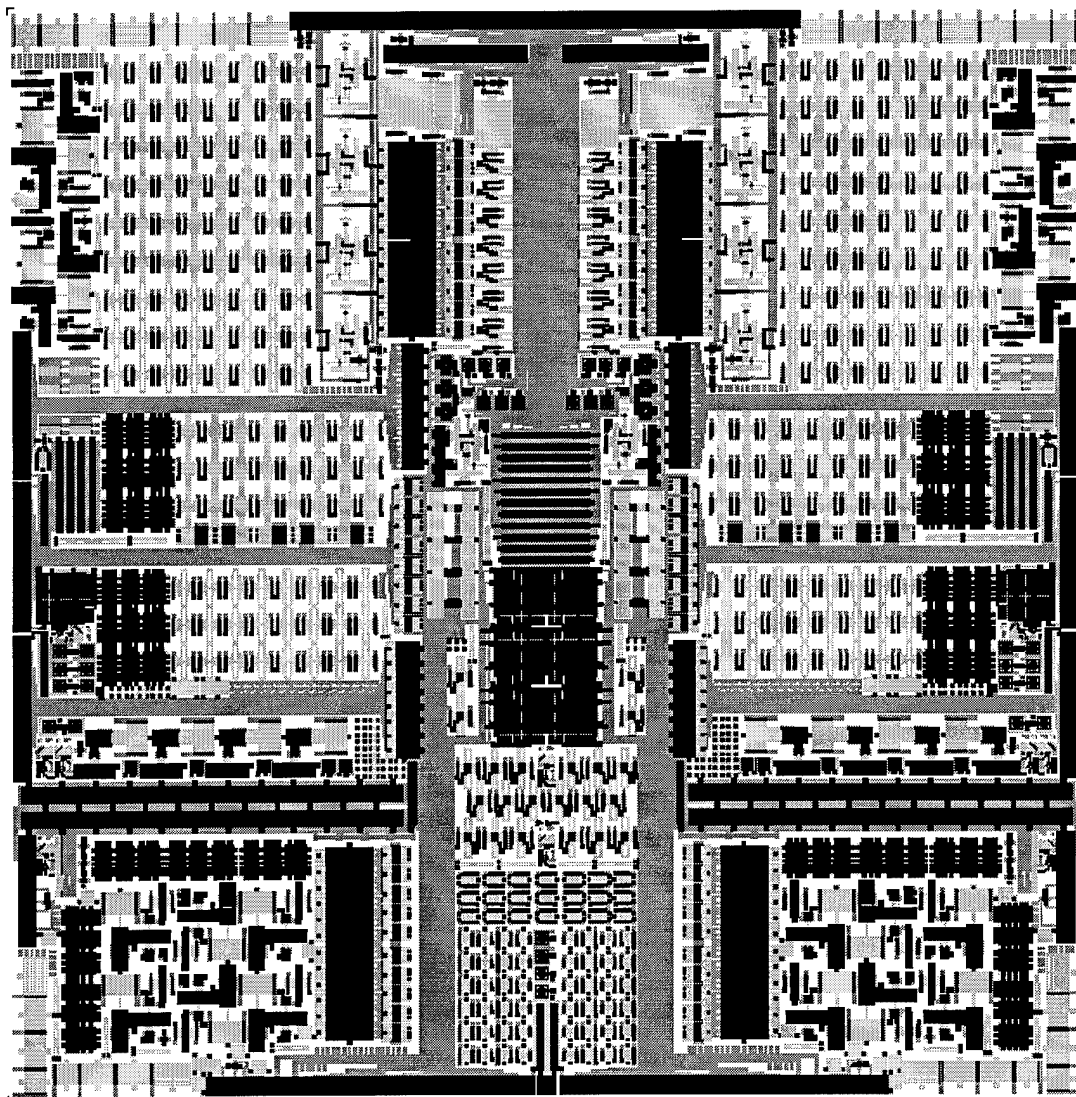


Figure 5-1. Layout plot of the first die submitted for the MUMPS fabrication process, showing density of devices and symmetrical layout. This die was fabricated on the MUMPS3 run.

Almost all subsequent AFIT MEMS die have followed this same layout philosophy, which has advantages beyond maximizing the device count. Dense packing itself brings to light layout problems such as mechanical interference between adjacent devices, wire routing problems, and I/O limitations. Partitioning

the die into halves or quarters allows separate researchers to have a section of the die that they can design without concern for the overall floorplan. Their sections can then be quickly assembled for the final design, in a smaller subdivision of the multi-user concept.

The early MEMS die, though extremely dense, were composed of mostly unrelated devices. To truly test the ideas developed during this research, several large systems were tried by the author and other researchers. These were practical systems rather than just generic layouts, because many practical problems are inadvertently avoided if the system does not have some fixed goal. For example, if a device in a generic 'system' does not *have* to be in a specific place, it is a natural inclination not to put it there, and all of the wiring and placement problems never appear.

This chapter describes a few of the more complex devices and systems developed in this dissertation research effort. The largest two of these systems cover an entire die. Their development is followed through several stages to illustrate how they evolved and what knowledge was gained from each design iteration.

This sample contains a mixture of developed and speculative devices. All of the latter are in currently fabrication, but are expected to work *perfectly* (of course) upon release. However, experience shows that often the first iterations are 'information dense' in failure modes. The speculative designs are included here to illustrate possible applications of the devices and techniques developed in the preceding chapters, and not necessarily as devices designed for a specific application.

5.1 Complex Devices

The devices described in this section are either complex themselves, or are necessary components for still larger and more complex systems. With MEMS, as with macro-machine design, more complexity is not a good thing if the function can be accomplished with a simpler device. Complexity itself is not the goal, but systems that incorporate more functionality generally require more parts. When a large, mechanically complex MEMS design is developed, the limitations of the MEMS fabrication process on making precision mechanical parts must be considered.

5.1.1 Mechanical Limitations of MEMS

One characteristic of surface micromachined devices that must be kept in mind when designing complex mechanical systems is the extremely poor tolerance, as a percentage of the overall device dimensions, compared with macromachines [2]. This is why the most successful micromachines so far have used flexural suspensions and motions, since these eliminate the concern with tolerances of parts sliding or rotating about one another. Quoting from reference [2]:

“Many impressive and useful micromachines have been designed and built ... but these devices typically involve the use of simple mechanical flexures. While micromachines are impressive for their size, their relative accuracy (in parts per million) is two orders of magnitude lower than is typically achieved by precision macromachines. Indeed, it is interesting to note that if one were to look at a picture of a typical micromachine, one might be inclined to compare its mechanics to those of macromachines from the early 1700s.”

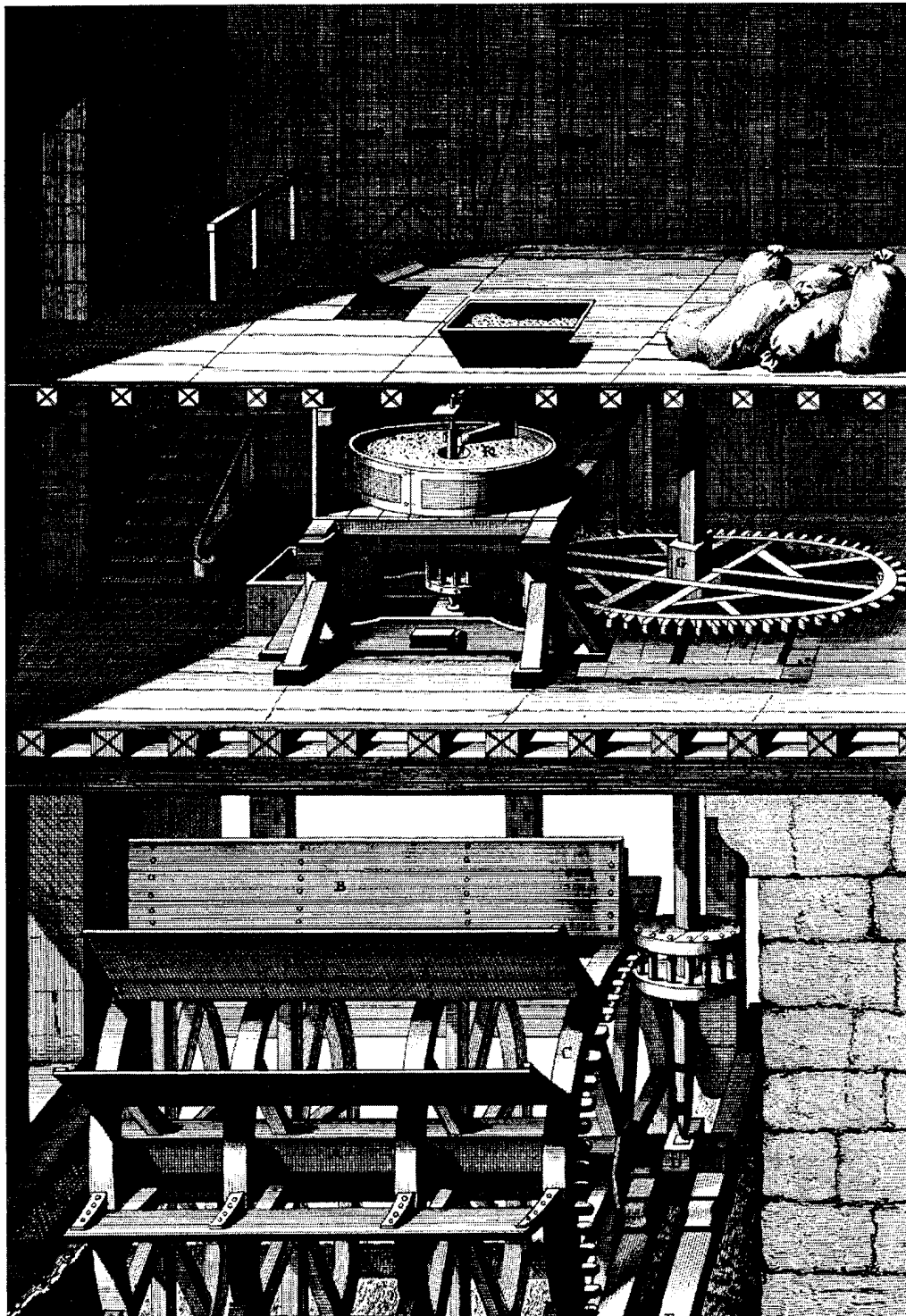


Figure 5-2. Lithograph of a water-powered grain mill, ca. 1750 [3]. Current micromechanical structures are on the same order of precision.

Even before coming across this reference, the looseness of MEMS machinery was a key point kept in mind; in fact, a book of Italian lithographs of 18th century machinery was kept around as a reminder and reference for possible machine designs [3]. An example of one of these designs is shown in Figure 5-2. It is interesting to note that the bearings on this wooden device probably had closer tolerances than the rotating bearings on current MEMS devices.

In surface-micromachined devices, the poor tolerance is due to the thickness of the sacrificial layers between the structural layers that make up the moving parts. Figure 5-3 shows a cross-sectional drawing of a rotating wheel and hub before and after release. The thicknesses of the *oxide1* and *oxide2* layers are the source of the play in this bearing, 1.5 μm laterally (0.75 μm on each side of the hub) and 2 μm vertically for the current MUMPS process.

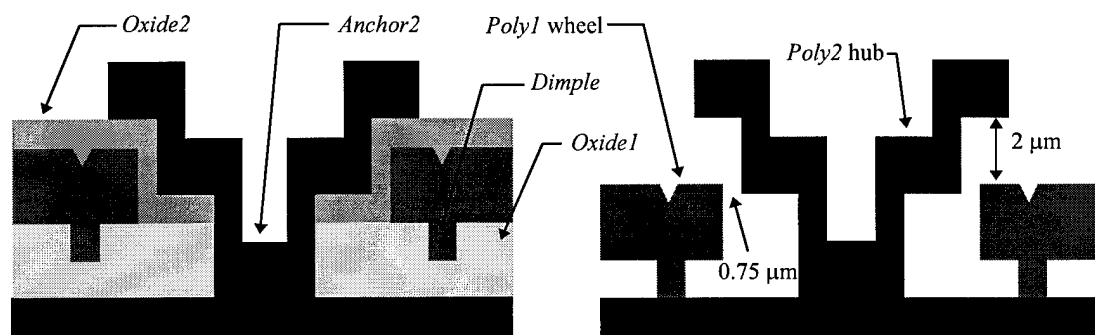


Figure 5-3. Illustration of a loose rotating bearing as fabricated in the MUMPS surface micromachining polysilicon process. Not drawn to scale.

Closer tolerances can be achieved in the LIGA or even the MUMPS process by fabricating the wheel and hub separately; but the device then has to be hand-assembled, and the wheel is not held to the substrate by a cap on the hub. For the MUMPS process, a hinged cap could be used, but the parts would still have to be hand-assembled. Wafer bonding can provide a way of capping close-tolerance bearings, but that takes the design outside the capabilities of currently available foundry fabrication processes.

5.1.2 Example Devices

So far, simple devices have been used to explain various topics, such as characterizing the thermal actuators and illustrating the variety of forms they can take. This section describes in detail some larger, more complex devices. These devices were chosen because they can be basic components of still larger systems.

5.1.2.1 Mechanical Relay Switches

One application for larger MEMS devices is mechanical relay switches. Using fabrication processes that incorporate a conductive metal layer, it is possible to make switch arrays with low contact resistance. Such arrays would be radiation-hardened, have little series resistance and would be small enough to be packaged with circuit die. They could perform functions such as switching in backup circuits in redundant processor arrays or similar electrical system configuration tasks that don't require

high operating speeds but do require a low-resistance contact that is electrically isolated from the relay drive circuitry.

5.1.2.1.1 MUMPS Relays

One of the first MEMS research projects at AFIT was an investigation of microrelay switches [4]. As detailed in Section 4.2.4, one of the contributions to that research was the idea of flipping a gold-on-*poly2* plate over on top of gold contacts. The basic concept, shown in Figure 4-13, was the only MUMPS design which formed a low resistance contact. All of the various *poly-to-poly* contact schemes had high contact resistance, possibly due to the formation of native oxide on the polysilicon surfaces when exposed to air.

Since that initial research was completed several new techniques were developed, warranting another look at MUMPS-based microrelays. The two relays shown in this section are by no means the last word in relays. They are large and hard to assemble, but their testing led to many improvements for future hinged-wire devices.

With the newly established technique of wiring to hinged plates, two possible variations of a hinged relay were tried. The first design used a switch similar to the one in Figure 4-13, with a flip-up thermal actuator to press it down against the contacts. An adjustable *poly1* bar under the switch plate sets the pivot point for the switch, so the shorting bar-to-contact distance can be adjusted. Once the optimum

setting of the pivot is determined, future relays can use a fixed post. The switch plate has flexures for the return spring force. Figure 5-4 shows the relay before assembly.

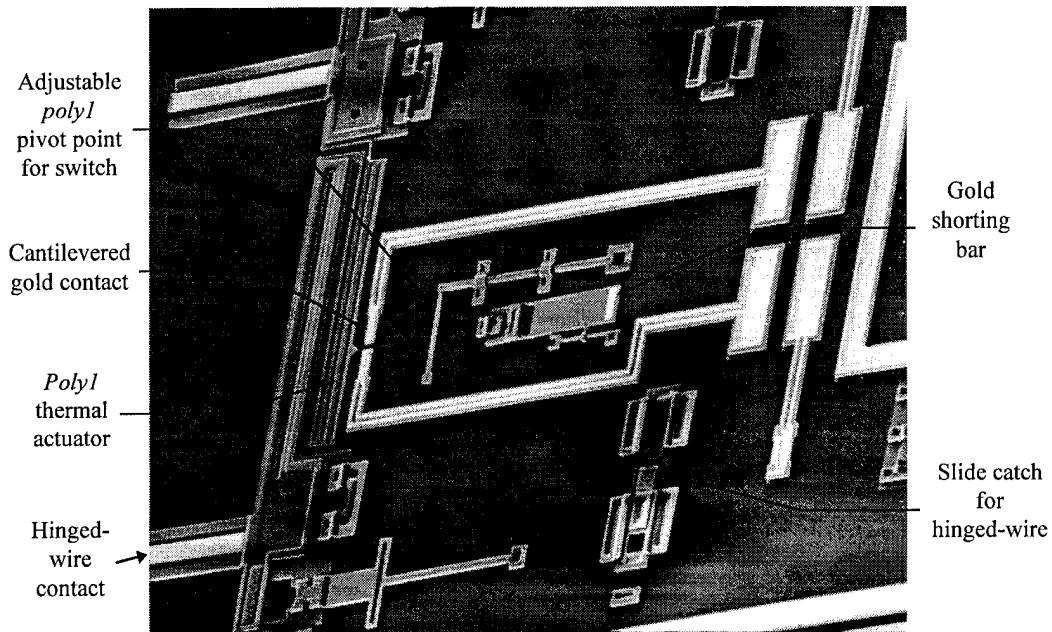


Figure 5-4. Mechanical relay switch with hinged thermal actuator. The switch must be flipped over onto the L-shaped *polyl* return spring, the hinged thermal actuator flipped up, and its wires attached. The loose hinges make this difficult to achieve.

To assemble the relay, the switch must be flipped over, and the actuator's two plates raised at the same time with the hinged-wires in place. The actuator was difficult to assemble, but usually set up properly, although the catches did not hold it perpendicular to the substrate. The main failure point was the switch. The loose and weak early hinge design, and too-small lifting jack, made it difficult to get any of these into place without snapping them off. The long hinged-wire contacts also proved difficult to arrange, and did not bend with the hinged-wire. An assembled

hinged thermal actuator is shown in Figure 4-25b, from a relay whose switch snapped off. However, even if the switch did flip over easily, the overall manual effort to get the entire device assembled makes it a poor candidate for a mass-produced device. It also takes up a large area on the die because of the hinged wires. Testing of the hinged actuator showed that wires can carry enough current to easily operate and back-bend the actuator. If sufficient current passes through the wires, though, the heat and the bimorph action causes them to press down on the hinged plate, which could cause it to move out of position. This and other tests of this device resulted in the following list of improvements for a future attempt at this design:

- Improved hinges on switch, actuator plates, and wires
- Stacked *poly1/poly2* back-bending thermal actuator
- Updated, shorter hinged-wires with improved slide catches
- Fixed pivot point for the switch
- Improved contact on hinged plate for hinged-wire
- Helper plate for lifting both actuator halves at the same time
- Stronger latches with the proper angle for the actuator plates.

The other option tried for a hinged relay has the contacts and shorting bar on hinged plates, and the actuator on the substrate. This makes it easier to power the actuator, which moves the shorting bar plate in the same manner as the 'fan' of Figure 4-9. The design does not eliminate the hinged wires, though, so the overall device

still takes up a large area and must still be painstakingly hand-assembled. Figure 5-5 shows this variation of the hinged relay, and Figure 5-6 shows a close-up of the contact area.

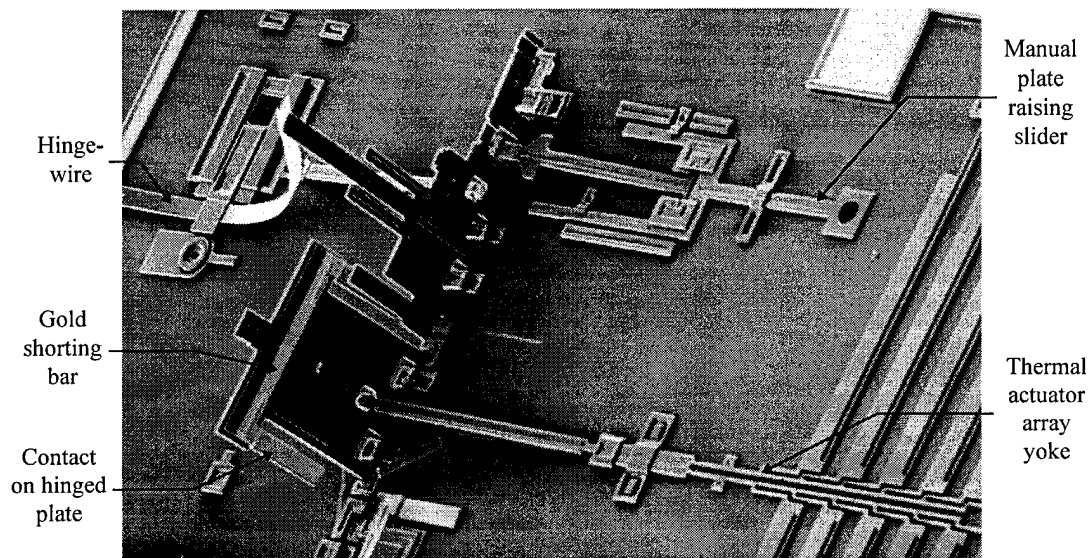


Figure 5-5. Mechanical relay with hinged contacts and shorting bar. Array has ten standard 220 μm long *polyI* actuators. Note the stiff hinged-wire contact which does not bend under pressure from the hinged-wire.

This relay also unfortunately had the stiff hinged-wire contacts which were difficult to assemble. Results from the flip-over wiring used with the sliding grippers indicate that the contact force of the flexed hinge wire is sufficient even at extremely low angles, so these extra-tall contacts are unnecessary, the contact can be much lower on the hinged plate, which will make it easier to assemble.

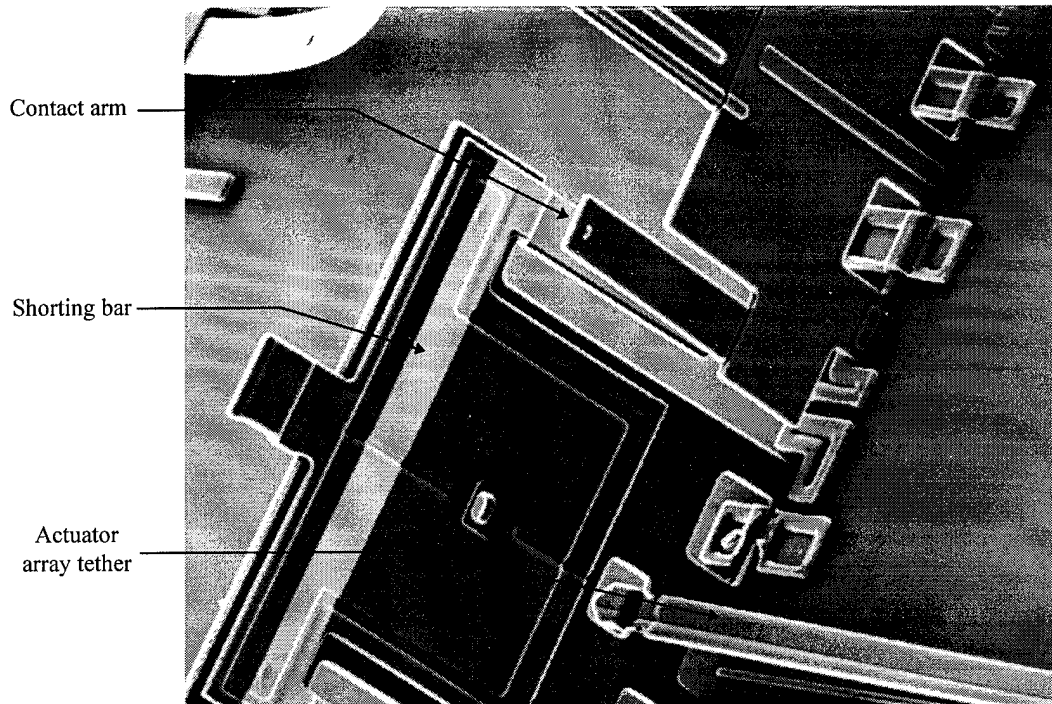


Figure 5-6. Close-up of contact area of hinged-contact relay. The thermal actuator array pulls the plates into contact via the tether which runs off the photo at the lower right corner.

Testing of this structure also led to a list of improvements for the next revision:

- Improved hinged-wire contacts, much lower on the plate.
- A smaller array of 6 actuators would have enough force
- No guide bearing is needed on the array yoke
- The hinged plate catch should be closer to the wire contact point
- The hinged wire can be narrower since it does not power the actuator
- The shorting bar can be a straight, stiff bar centered on the contact arms.

These relays were both large, roughly 0.5 mm x 1.5 mm, mostly due to the hinged components. Overall they demonstrate that each separate device works: the

wiring, the actuators, and the gold-on-gold contacts; but they also demonstrate that these relay designs are area-consuming and difficult to assemble by hand. The improvements listed above should lead to more compact and durable designs which are easier to assemble. But these two relay designs in general are good only as demonstrations of design techniques that might best be applied elsewhere, and so are not being pursued farther by the author.

5.1.2.1.2 LIGA Relays

A more compact and useful relay can be built in an all-metal fabrication process such as LIGA. This eliminates the need for large hinged plates to bring metal layers into contact. An all metal process allows the actuator to be operated laterally, more in keeping with a surface-micromachining approach, and thus requiring no manual assembly.

The relay, shown in Figure 5-7, is designed to isolate the signal circuit through the switch from the drive circuit which closes the switch. The relay is a latching design, i.e. it remains closed after the drive power is removed. The contact arms press together when closed, so they will not be subject to intermittent opens when mechanically shocked. After latching or unlatching, the actuators pull away from the relay contacts, leaving the switched circuit isolated from the drive circuit.

To close the switch, the left actuator pushes up the side of the switch with the cup, which pushes past the other half whose tapered pin end clicks into the cup. The

actuator is then turned off, and bends back and out of contact with the switch. To open the switch, both actuators are turned on, and they push both halves of the switch up and out of contact. The left actuator is then turned off first, allowing the cup side to return to rest without engaging the pin half of the switch. The switch could also be disengaged by using only the right actuator, and pushing until the left contact arm snapped open. The switch arms have wedges on them to slightly magnify the motion of the actuators, which in turn have round tips that slide along the wedges when pushing the arms.

The relays built on the first LIGA run had non-optimized actuators which could not move the contact arms far enough. However, the switch arms latch as designed when pushed with a probe, as seen in Figure 5-8. The contact is less than 1Ω for the $30\text{ }\mu\text{m}$ tall nickel-iron switches.

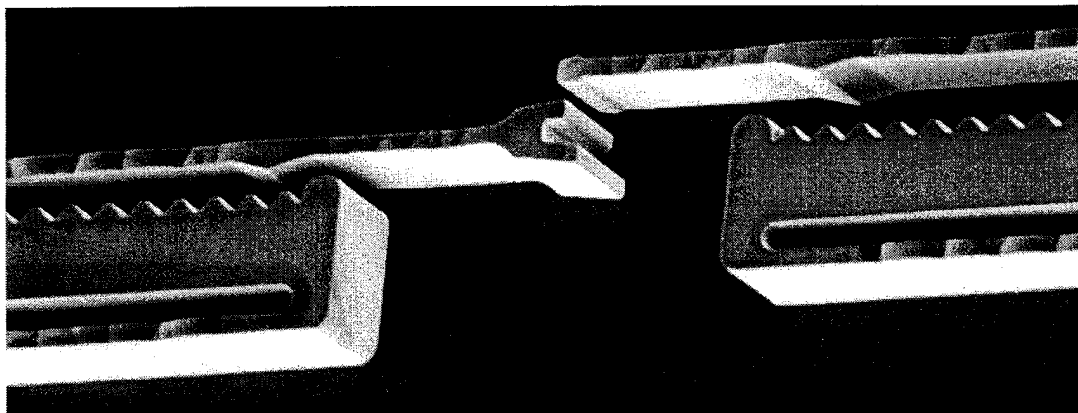


Figure 5-7. LIGA latching relay array. The thermal actuator on the left latches the relay, both actuators can be used to unlatch it, or the right one can do it alone. This relay is built in $30\text{ }\mu\text{m}$ tall nickel-iron. Relay arms are $5\text{ }\mu\text{m}$ wide and $325\text{ }\mu\text{m}$ long.

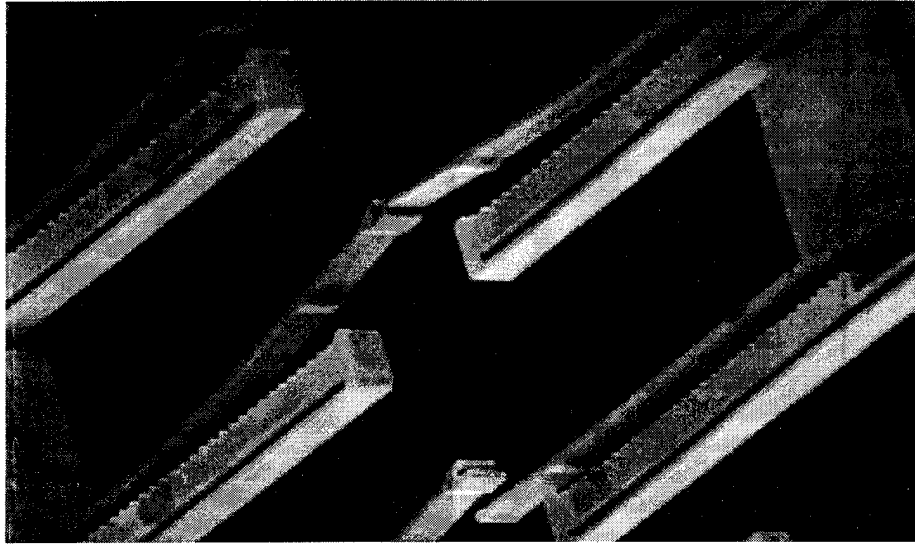


Figure 5-8. LIGA latching relay pushed into position for contact resistance measurements. The actuators are too short to deflect the contact arms this far, but the latching mechanism works as designed, and contact resistance is less than 1Ω .

An advantage of this design is that the actuators do not provide the contact force, as other MEMS-based electrostatic microrelay designs do [5,6]. These relays remain either closed or open with the power off. The force needed to make a low resistance contact comes from the contact arms bowed against each other.

A similar structure could be built in stacked *poly1/poly2* MUMPS layers, but the contact resistance and the resistance of the polysilicon contact arms would not make a low resistance switch. One way to make such a switch would be to use the MUMPS process to create the actuators and associated circuitry, then use an electroless nickel plating step to form the contact arms. This would be one step beyond a plain foundry fabrication approach, though. Other processes that include metal coatings, such as the SCREAM process [7], though not a foundry process, could also be used to make thermally actuated lateral latching relays.

5.1.2.2 Motors

Many practical applications, especially mechanically complex ones, require more deflection or more complicated motions than can be provided by one actuator or a single array of actuators. One such system, articulated microrobotic arms, was recently explored [8]. To determine the forces needed to move the proposed arms, hinged plates were attached by tethers to sliding pull-rings with integral force measurement springs. By manually pulling on the rings with a probe, it was found that forces up to 43 μN were needed to overcome friction in the movement of the hinged plates and the sliding pull-rings.

Thermal actuator arrays can meet this force requirement, but they must be incorporated into a more complex structure to achieve the longer deflections needed for a practical microrobotic system. The device that best fits this and other mechanical applications is a stepper motor. The high force per unit area of thermal actuators makes such micro-motors practical, and their circuit-compatible drive requirements ensure that devices based on them can be easily integrated into larger systems.

5.1.2.2.1 LIGA Ratchet Motor

Stepper motor design started with a ratcheting motor laid out for the LIGA2 die, shown unassembled in Figure 5-9. This motor has a single large actuator that moves a flexible arm which in turn pushes the ratchet wheel one tooth for each actuation. On the return stroke the arm slides backwards over the ratchet teeth, so a passively

sprung pawl is used as a 'mechanical diode' to keep the wheel moving in only one direction. The motor is simple in terms of parts count, but cannot be driven in reverse.

The rotor is fabricated separately, and must be manually placed on the axle. The rotor is 200 μm across, however, so it can be easily handled with tweezers. Drawing the rotor separately allows a 1 μm axle/rotor bearing tolerance. If the motor were drawn in place, the minimum gap of 5 μm allowed by the design rules would have to be left around the hub. This would create a total play of 10 μm in the bearing.

Testing shows that this mechanical arrangement works well if the actuator is pushed with a probe; but like all the other LIGA thermal actuators on this die, the one attached to this motor is an early design which did not have sufficient deflection to move the wheel an entire tooth. An assembled motor is shown in Figure 5-9.

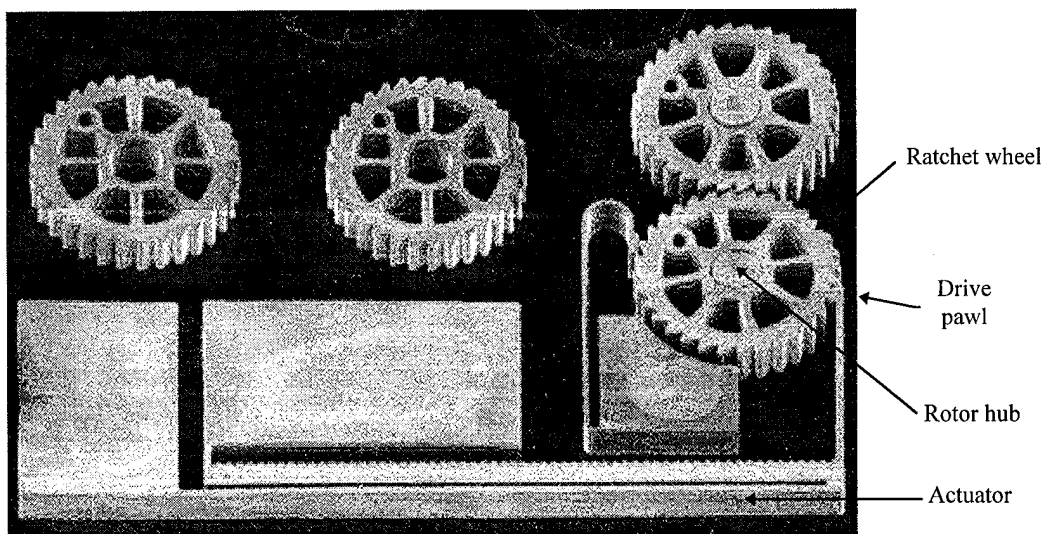


Figure 5-9. Unassembled ratcheting stepper motor on the 30 μm thick LIGA2 die. The motor hub is 50 μm in diameter and the rotor, several of which are visible, is 200 μm in diameter with 64 teeth. The single actuator has a 660 x 5 μm hot arm.

The advantage of this general motor layout, with a separate actuator moving a toothed wheel via a pawl, is that it leaves most of the wheel's perimeter free to transmit power to a device located next to it, such as a train of gears, as seen in Figure 5-9. This motor design thus has a great advantage over an electrostatic micromotor, where the rotor is totally surrounded and cut off from lateral contact by the stator poles. This advantage made it desirable to try the same motor design in the MUMPS process.

5.1.2.2.2 MUMPS Stepper Motors

The first attempt to transfer the LIGA stepper motor design to the MUMPS process was a quick and direct transfer of the LIGA mask drawing to the MUMPS *poly1* layer. The few small changes included a new *poly2* hub similar to the drawing in Figure 5-3, dimples under the rotor, and topologically formed pawls. The resulting motor is shown in Figure 5-10.

This motor's actuator would have suffered the same shortcomings as the LIGA actuator except it had a different fault that made it deflect even less. In an attempt to lower the resistance of the single large actuator, and also possibly lower the ohmic heating of the cold arm, a copy of a *poly2*/gold substrate wire was placed on the cold arm. Instead of increasing the deflection, though, the gold and polysilicon formed a thermal bimorph. Heat conducted from the hot arm caused the cold arm to deflect downward and scrape against the substrate, stopping the lateral deflection. As with

the LIGA motor, the rest of the mechanism functioned fine when the actuator was pushed with a probe.

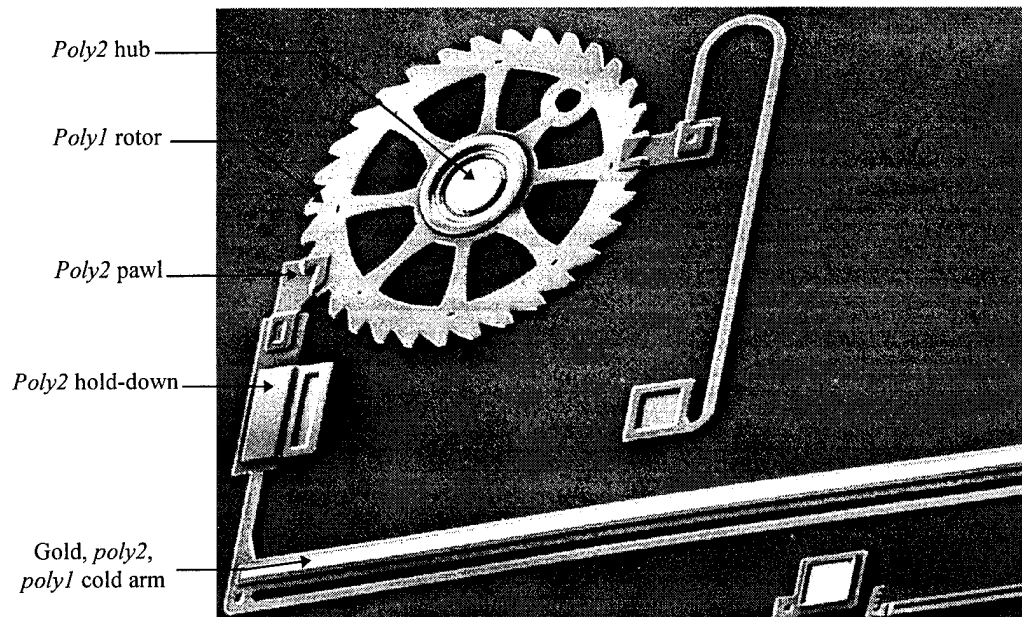


Figure 5-10. First version of a polysilicon ratcheting stepper motor. This design is a copy of the LIGA motor seen in Figure 5-9. *Poly1* rotor is 200 μm across.

The next version of the motor dispensed with the single actuator and ratchet approach. Instead, the newly invented thermal actuator array was attached to a more flexible pawl arm, and the pawl was pressed against the rotor by a second actuator array set at 90 degrees to the main array. This motor is shown in Figure 5-11.

The actuators in the new motor are operated from a slightly back-bent position. More deflection is possible from the main array if it travels through its initial zero deflection position. The drive pawl is sized to allow variation in the amount of back bend. By back-bending the pusher array to place the drive pawl in contact with the

rotor, the pawl can be left in the engaged position as a brake when no power is applied.

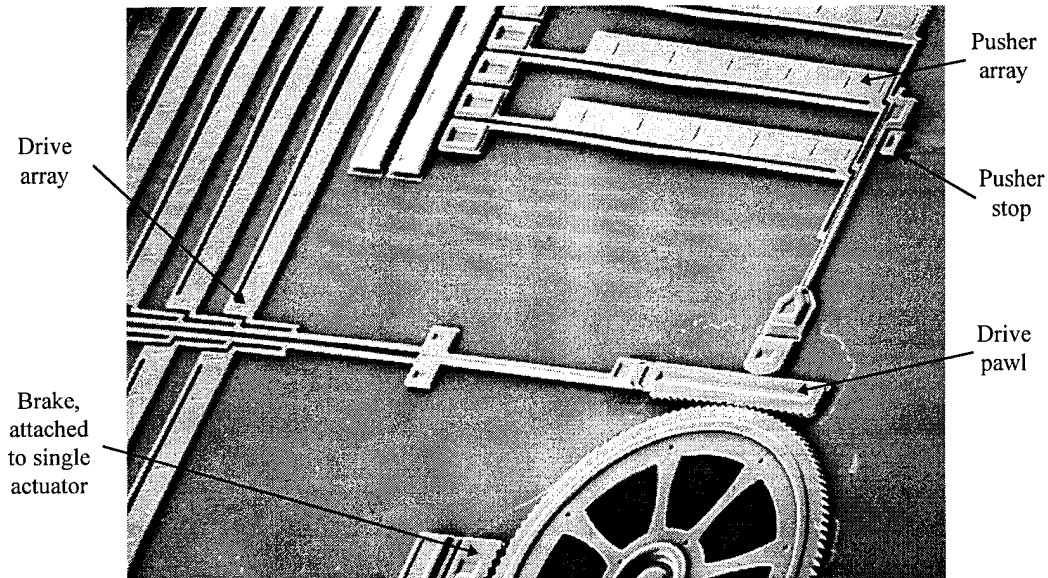


Figure 5-11. Surface-micromachined rotary stepper motor with 200 μm diameter rotor. The drive array consists of ten actuators and the pusher array consists of three. All the actuators are the same standard 220 μm long design; the SEM micrograph was taken at an angle of 45 degrees which foreshortens the horizontal features. The rotor teeth and pawls are made of stacked *poly1/poly2*. The actuator arrays are set to their back-bent operating position which leaves the drive pawl engaged when unpowered.

Unlike the ratchet motor, the drive arm is not constantly in contact with the rotor. Having the drive pawl pushed into contact with the rotor eliminates the need for a passive pawl to prevent backwards motion when the drive array retracts. By timing the action of the two arrays properly, the rotor can be driven in either direction. The motor design does incorporate a third, single actuator which can act as a brake. This braking pawl allows precise positioning to be maintained when the drive pawl is disengaged, if there is a force on the rotor from attached machinery. The

third actuator may not be needed if the rotor itself is the driven mechanism, where the device to be rotated is mounted on the rotor.

A stop is placed on the pusher array to keep it from pressing the drive pawl too hard against the wheel, which can cause the drive pawl to pop out of position. The stop also makes it simpler to set the pusher pawls in their initial back-bent position, since there is more tolerance for a slightly over-bent array. For the same reason the stop allows a wider variation in the drive voltage for forward-driven pusher arrays.

The latest variation of the motor incorporates a hold-down to help prevent the drive pawl from possibly jumping out of place. One other design feature which improves the durability of the motor is a pillar of trapped oxide in the center of the hub which makes it much stronger. Small hubs with just *anchor2* in the center have been found to be too easy to detach from the substrate.

The new motor design thus brings together several of the techniques developed throughout the research effort, each solving a basic design need. Besides the actuator arrays that make the whole idea possible, the stacked *poly1/poly2* fabrication technique is used for the mating faces on the rotor and drive pawl. This replaces the original topologically formed pawl which has more of a tendency to ride up over the rotor. High current substrate wiring is also used to feed power to the actuator arrays, and bossing is used to stiffen the drive array yoke.

Many variations of this motor have been tried, with different numbers of actuators, different styles of rotor teeth, even no rotor teeth. One alternative has the pushing pawl attached directly to the drive pawl with a flexible tether. Other

variations include actuator arrays that work in the forward or back-bending modes. All the variations tried have worked, so the basic scheme is quite flexible.

More actuators can be arrayed for driving the rotor. Early test motors included 60 actuators in the drive array which could be separated from the yoke to determine the minimum number of actuators needed to make the motor move. It turned out that single actuators could make the motor operate, though it was no trouble operating the motor with 60 drive actuators. Additional sets of actuators can be arranged to drive the rotor in sequence if more even force application is required.

Electrostatic actuators could be used in a similar pawl-driven motor, but as discussed in Chapter 3, the arrays of comb drives needed to produce sufficient force would be extremely large; but if sufficient deflection can be obtained they might operate faster. Gap closing actuators do not have enough deflection for the toothed versions of this motor, but may have the force to operate a motor of this type with a 'smooth' rotor face, which is actually slightly rough from the RIE etch.

A digital control circuit was built to investigate the timing of the actuators. The circuit is described in Appendix B. It allows the turn on and turn off times for each array to be programmed separately at any of 256 time divisions per cycle. A typical cycle is shown in Figure 5-12. This graph includes the operation of the third actuator which brakes the rotor while the drive pawl is being repositioned.

Figure 5-13 shows a linear stepper motor. This motor has the same actuator movement as the rotary motor, except the rotor has been replaced with a sliding rack. This variation of the linear stepper motor has two sets of opposing actuators for

higher force and less friction. There is also a version with a single set of drive and pusher actuators that push the drive pawl and rack against a stationary wall to engage.

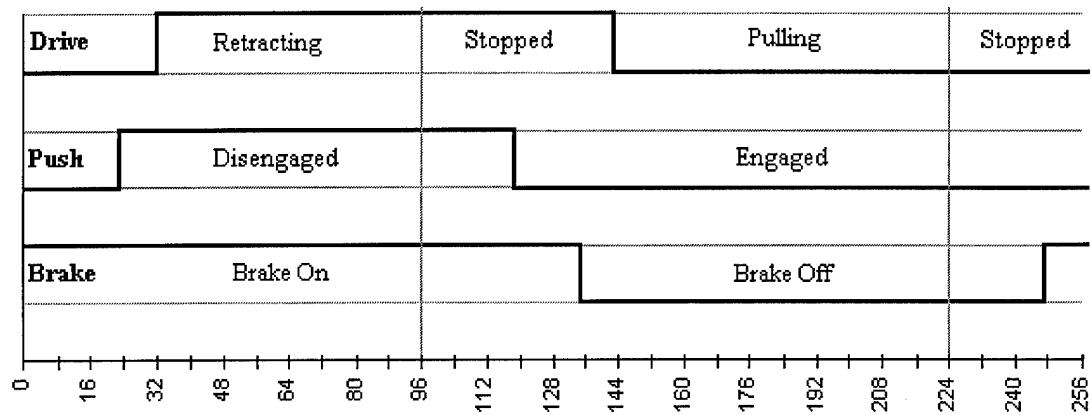


Figure 5-12. Sample timing cycle for stepper motor actuator control. The timing circuit controls relays which can be turned on and off once per cycle at any of 256 divisions.

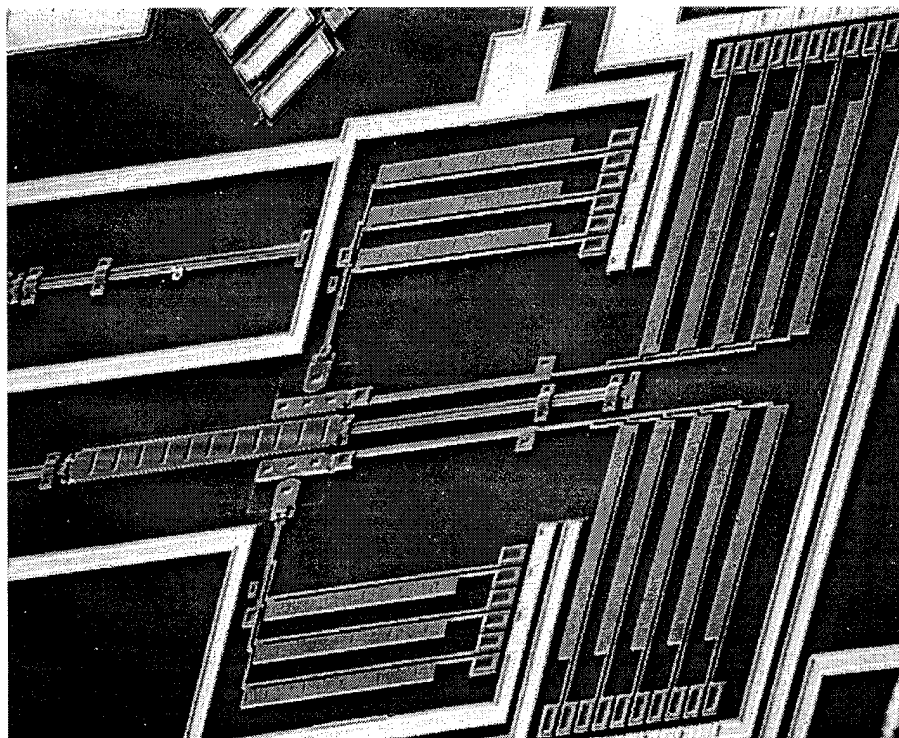


Figure 5-13. Surface-micromachined linear stepper motor. All actuators are $220\text{ }\mu\text{m}$ long, and the sliding rack is $250\text{ }\mu\text{m}$ long, and can be operated in either direction.

5.1.2.3 Positioning

An important application for actuators is the positioning or fine-adjustment of components. With the variety of actuation techniques made available by this research, the devices to be adjusted can be located on the substrate, above the substrate, even over the edge of the die. The types of devices to be adjusted or positioned can be unlimited: robotic appendages or slide-out sensors, for example.

Much of the MEMS research effort at AFIT has involved the positioning of optical components. An example of an optical positioning application that could be adapted to actuator control would be hinged mirror positioning. A linear motor such as the one in Figure 5-13 could be coupled to a slide-up angled mirror of the type shown in Figure 4-8. Such an arrangement would allow the angle of the mirror to be adjusted electro-mechanically, instead of manually as currently designed.

The following examples show some of the devices and systems designed by this and other researchers that have involved positioning by actuators developed as part of this research. These applications show actuators being used to position a mechanically connected element, or an actuator being used to move a sub-component as a fundamental part of the operation of the system.

5.1.2.3.1 X-Y Positioning

The typical device used to demonstrate a fine positioning application of actuators is the X-Y translation table. Uses for X-Y translation tables include

positioning of optical components and scanning, or atomic force microscope tips [9,10]. Figure 5-14 shows two simple X-Y translation tables with their small 'tables' connected directly to the actuators.

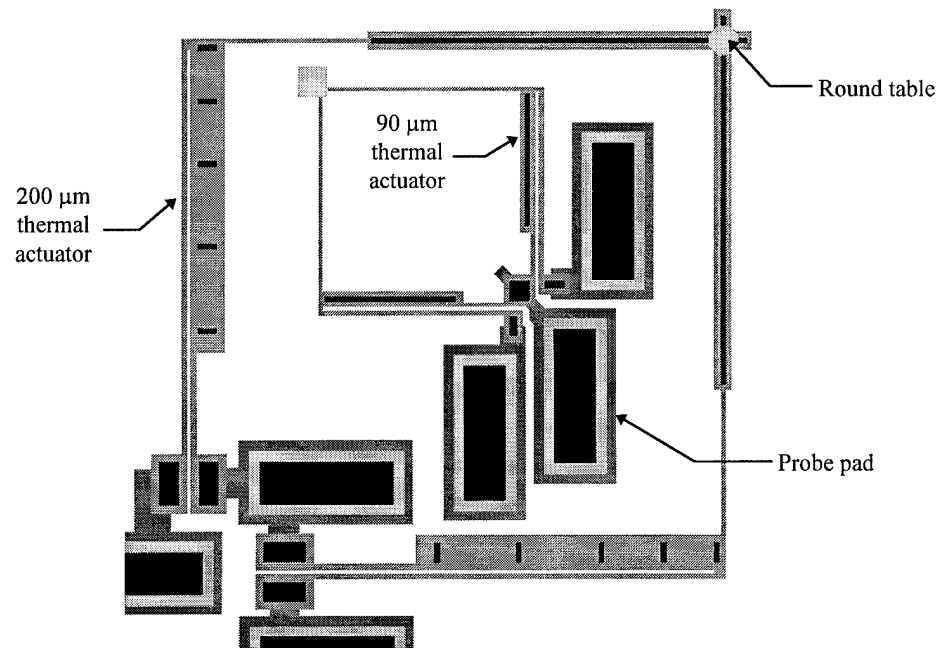


Figure 5-14. Layout drawing of two compact X-Y positioning tables using thermal actuators. Larger actuators are 200 μm long, smaller ones are 90 μm long. The nested layout saves die are on the test chip, it is not necessary for operation of the tables.

The devices are in fabrication on the MUMPS11 run. The table will move in an arc when one set of actuators is operated, so one actuator does not control purely X motion and the other only Y motion. By controlling both sets of actuators in unison, however, the center of the table can be placed anywhere in its range of positions, about 10 μm square for the larger table, based on deflection tests of similarly sized thermal actuators.

5.1.2.3.2 Rotational Positioning

Rotational positioning of components is an important application that the stepper motors described in Section 5.1.2.2 can perform. Figure 5-15 shows a flip-up hinged mirror attached to a rotating table. The table is moved by actuator arrays in the same motion used in the rotary stepper motor shown in Figure 5-11. The devices described here are being fabricated on the MUMPS11 run. They are expected to work as well as the motor design they are based on.

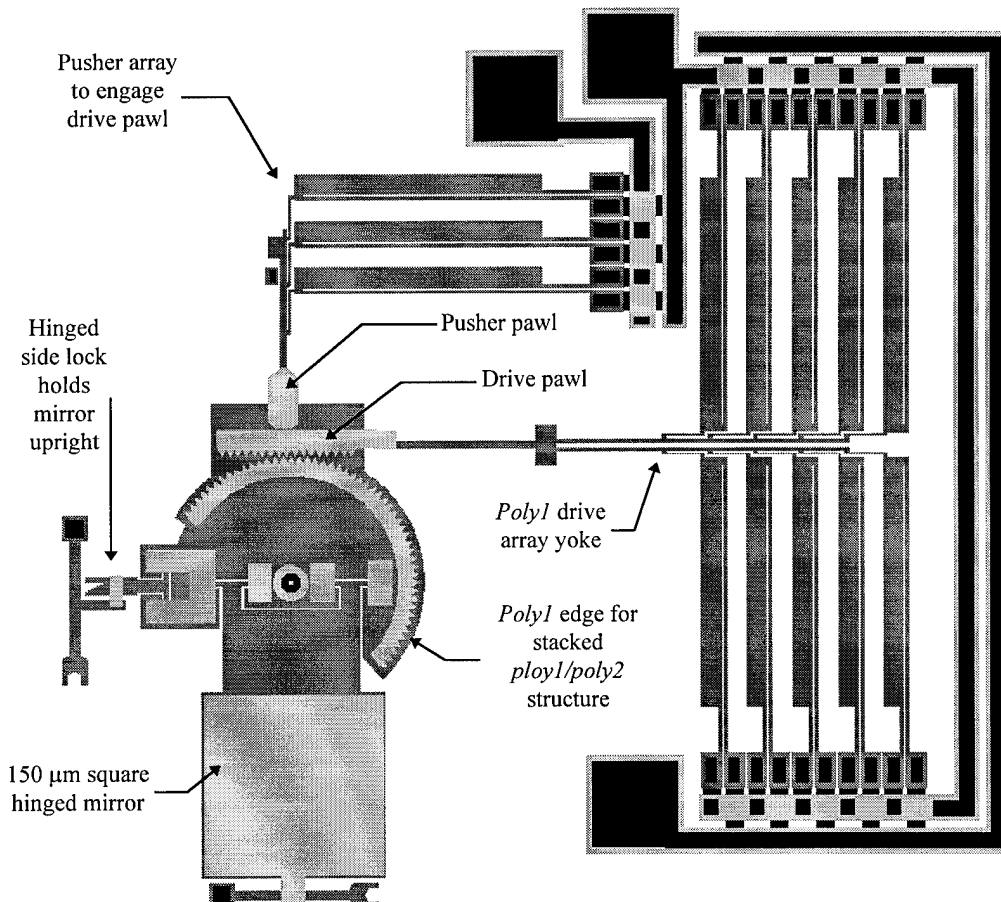


Figure 5-15. Flip-up rotating mirror. Rotating table is 200 μm in diameter and is driven stepper-motor fashion by the arrays of 220 μm actuators. Mirror is 150 μm square.

A spectrometer, shown in Figure 5-16 was designed as a mechanical demonstration system to show a rotationally positioned device 'in use'. A spectrometer uses a rotating grating to diffract different wavelengths from the source to the output aperture. A flip-up, rotating grating is the key component in this system. The rotational positioner is identical to the one shown in Figure 5-15, with the mirror replaced by a $185 \times 200 \mu\text{m}$ grating having $2 \mu\text{m}$ lines and $2 \mu\text{m}$ spaces. Other components added on to make a 'system' are angled mirrors to couple the light perpendicularly on and off the die to and from the grating. The mirrors allow different diffraction angles to be used.

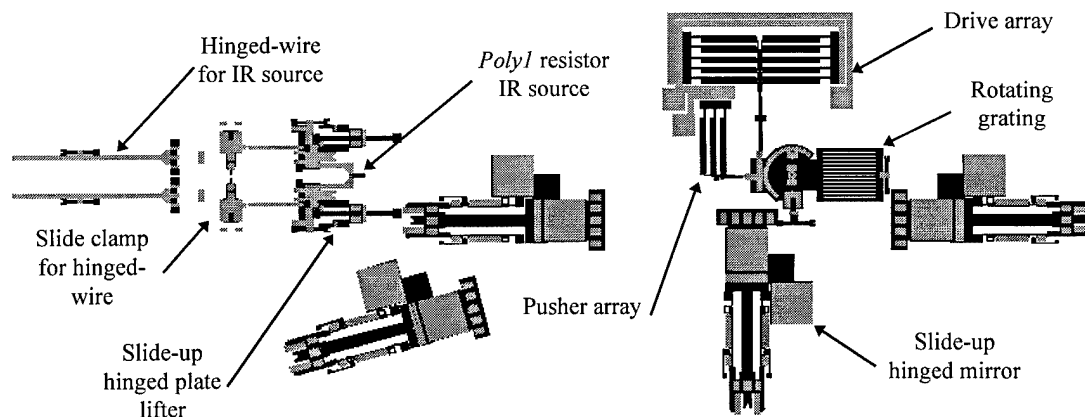


Figure 5-16. Microspectrometer designed to demonstrate an application of a rotationally positioned optical component, in this case a $185 \times 200 \mu\text{m}$ grating in place of the mirror on the rotational positioning motor of Figure 5-15. Slide-up mirrors make optical connections perpendicular to the die surface. Mirrors are set at 0° , 15° and 90° to the grating. A hinged *poly1* resistor acts as an alternate infrared light source.

An infrared source was also added to the example spectrometer layout. The source is a hinged polysilicon resistor which is powered through hinged-wires. So conceivably the spectrometer could be used to determine the spectrum of a

polysilicon infrared source at different drive voltages, though it is only intended to be a mechanical demonstration system.

5.1.2.3.3 Micro Interferometers

A system designed with an actual application in mind is the interferometer shown in Figure 5-17. This system is intended to modulate an optical signal [13]. The signal comes into the interferometer from an optical fiber or is coupled in from above with tilted mirrors. A grating is used to split the incoming signal, and the energy diffracted into the ± 1 orders is fed down two optical paths. One path has a fixed mirror and the other has a mirror that can be moved with thermal actuators. There is a hinged plate to block the zero order energy passing straight through the grating. A second grating recombines the energy which now interferes with itself constructively or destructively depending on the position of the movable mirror.

In the figure the interferometer is partially assembled. The fixed mirror has not been raised so the rest of the interferometer components can be seen. The input (or output, the design is bi-directional) grating is attached with a tether to the blocking plate so both can be raised at the same time. The moving mirror is attached to a pair of thermal actuators by tethers on either side. One of these tethers can just be seen running off at the upper right corner of the picture. The overall size of the interferometer is $172 \times 400 \mu\text{m}$.

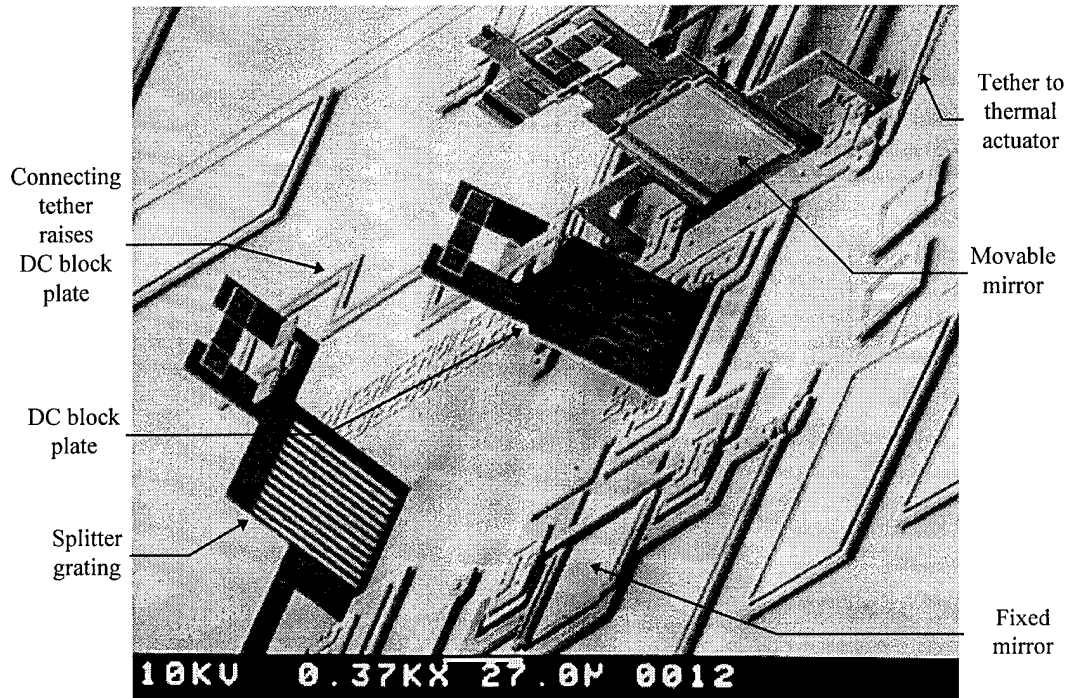


Figure 5-17. Partially assembled microinterferometer [13]. The grating on the left is the beam splitter. The plate marked 'DC BLOCK' blocks the zero order energy coming straight through the grating. The raised mirror behind the block is attached to two thermal actuators, not shown. The stationary mirror is not raised, and the second grating is not visible. All optical components are roughly $50\text{ }\mu\text{m}$ square.

5.1.2.3.4 Modulating Retroreflectors

Another large device designed to modulate a light signal is a retroreflector. A retroreflector is one corner of a cube where all three mutually perpendicular walls are mirrored. Such a mirror arrangement will reflect light back in the direction of its incoming path, and is commonly used in roadside reflectors. The device was proposed as a possible remote communication link [11], though no design specifics were given. The development of practical devices has gone through several stages and is still ongoing.

Corner Cube Retroreflector (CCR) designs take advantage of hinged plates, which are flipped up to form two of the mirrors, while the third mirror is on the substrate. The first design used electrostatically actuated tilting mirrors on the substrate as the modulating component. The modulating mirrors for the device, which form the substrate mirror, are shown in Figure 5-18. The rows of the modulating mirrors tilt in unison to change the angle of reflection.

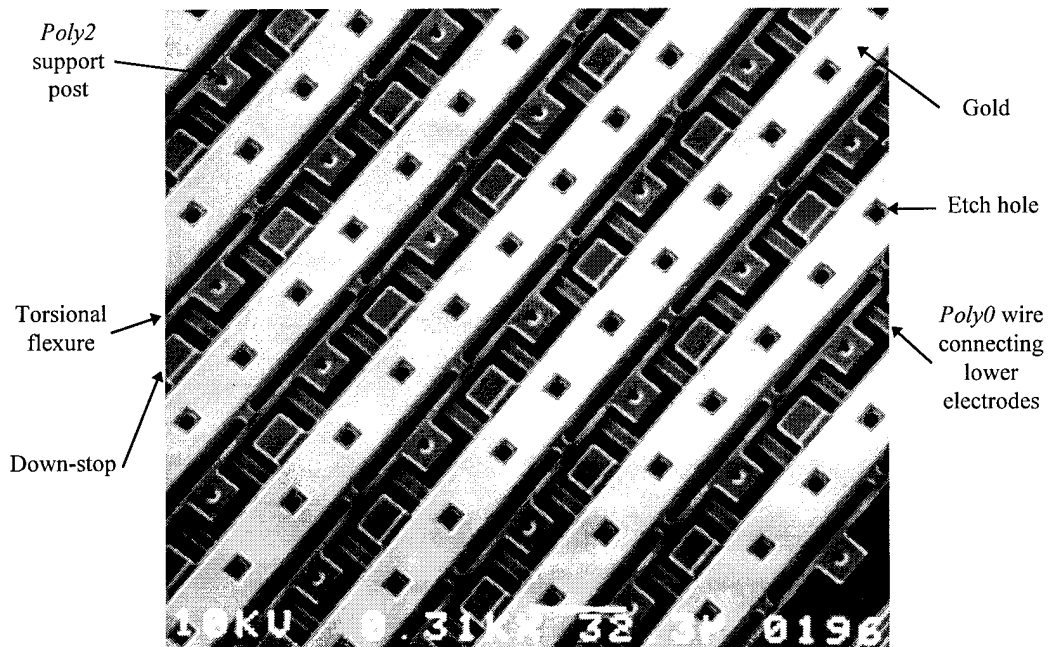


Figure 5-18. Array of tilting mirrors forming the modulating mirror of a Corner Cube Reflector. A unit cell of the array measures $56 \times 30 \mu\text{m}$, with two $2 \times 20 \mu\text{m}$ flexures. The mirrors tilt down at the edge facing the upper left of the figure, and down-stop tabs prevent the *poly2* mirror plates from contacting the *poly0* lower electrodes.

Since surface micromachined layers are thin, large tilting angles are not possible with mirrors anchored to the substrate. Large tilt angles require the mirror to be short in the tilting direction. This decreases the actuator area compared to piston mirrors,

and leaves a large percentage of the array without a reflective surface. Notice that the gold area of the array is less than 50%.

Arrays of tilting mirrors up to 1 mm square have been successfully built and tested. The mirrors of the first test array, on the MUMPS5 run, actuated fully at 27 V. This same type of mirror array could also be used for other optical applications. Rows or sections of rows of an array could be individually actuated to form a multi-directional beam splitter or form a beam steering array.

One problem with this design is that positioning hinged plates to be mutually perpendicular is difficult to do, even with side-plates to hold them in place, because of the looseness of the hinges. Devices with multiple hinged plates are also hard to assemble, with more plates increasing the chances that one will be broken.

The first CCR could not be tested fully because the 166 MPa tensile stress in the metal on the MUMPS8 fabrication run caused the large hinged mirror plates to curl. Also, the *oxide2* coverage problems described in Section 2.3.2.4 prevented the hinges from operating properly. Heavy stringers also prevented the electrostatic mirrors from operating, so the first version did not give many useful results.

The next version needed to have working hinges, with improvements to decrease the play, and a way of adjusting the hinged mirrors besides manually. The development of thermal actuator arrays and the fan device shown in Figure 4-9, made possible a way to adjust the mirrors. The hinged plates can be positioned under actuator control, and also modulated by the same actuator. This allows the substrate mirror to be stationary, so it can be reflective over its entire area.

One problem with using actuators to position the mirrors is that their long tethers would run across each other. The mirrored plates must be rotated up towards the substrate mirror so the gold is facing into the cube corner. The drive tether is fabricated in place on top of the mirror plate so when the plate is raised, the tether slides along and into the keyhole slot. Once in the slot, notches at the end of the tether catch on the plate, trapping the tether in place and allowing it to move the plate in either direction. To prevent the long tethers from intersecting, bellcranks were placed in line with the actuators to turn the tethers 90 degrees. Figure 5-19 shows the second CCR design.

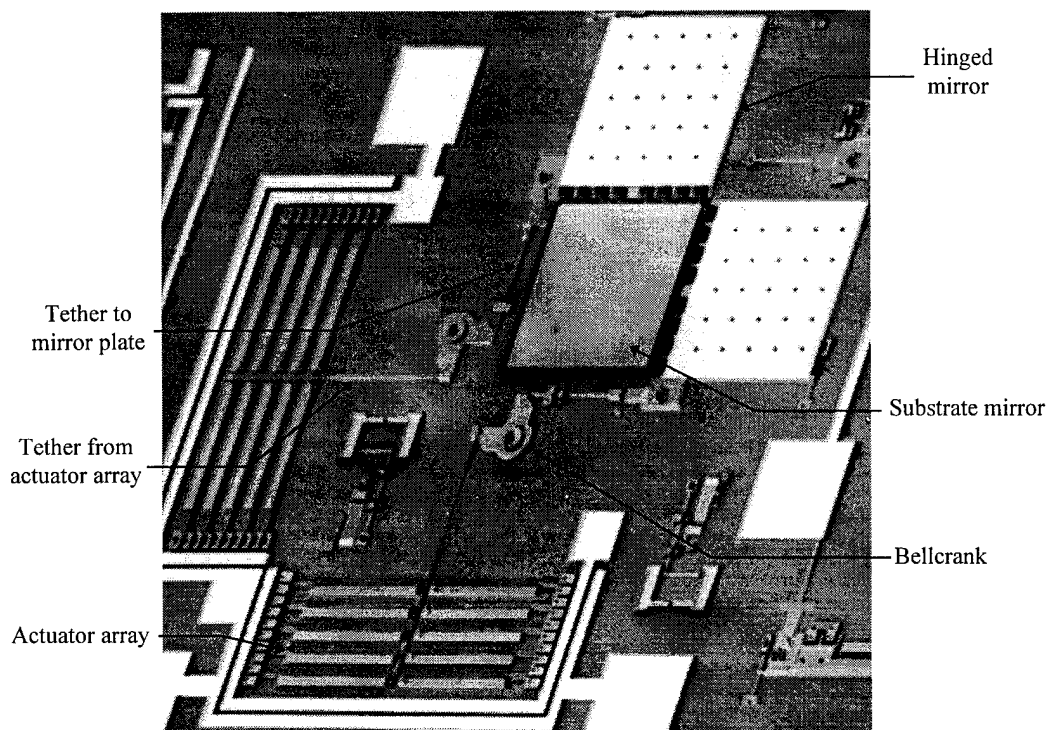


Figure 5-19. Corner Cube Reflector with actuator arrays to position and modulate the hinged plate mirrors. Mirrors are $300\text{ }\mu\text{m}$ square, and each is driven by an array of ten $200\text{ }\mu\text{m}$ actuators. Bellcranks on the drive tethers eliminate mechanical interference.

To counter possibly high metal stress, the hinged plates had to be made stiffer, though the high stress on the MUMPS8 run was unusual. The next version of the CCR had hinged plates made of *poly1*, *poly2* and trapped *oxide2*, as described in Section 2.3.2.3.4. This combination forms the thickest structure that can be released.

On this design, the guide bearings near the bellcrank did not allow sufficient lateral motion of the tether as the bellcrank rotated; so to actuate a mirror, the bearing had to be broken off, usually to the detriment of the enclosed tether. The basic idea of using a bellcrank to change the angle of actuator deflection worked well, though. The next design had only one hinged mirror actuated, eliminating the need for the bellcranks. The passive mirror is positioned perpendicularly to the substrate by a locking plate, with the improved hinges to increase the positional accuracy. Figure 5-20 shows the tether attachment of the third CCR design.

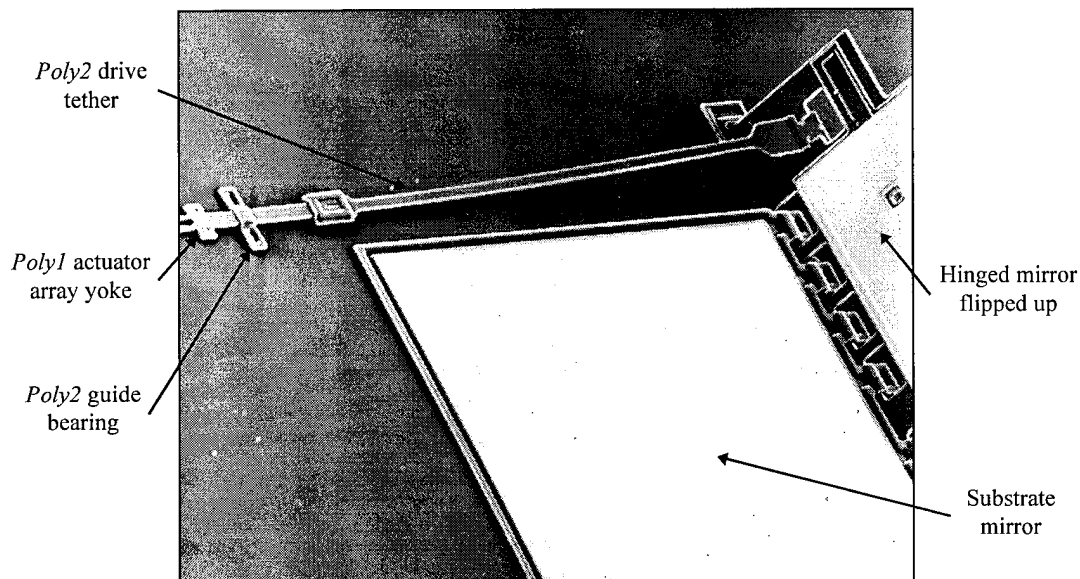


Figure 5-20. Connection from actuator array to hinged mirror plate on the third CCR design. Hinged mirrored plate is $290 \times 275 \mu\text{m}$ and is made of *poly1*, trapped *oxide2*, and *poly2*, for extra stiffness to prevent curling due to metal stress.

With all the connection, hinge and stress problems taken care of, the CCR could be assembled and tested, revealing a new problem. The actuator arrays are used in the back-bent mode so greater deflections can be achieved, but the amount of initial backbend is variable, as the test results of Section 3.4.2.2 showed. This variation must be dealt with at the point where the actuator array connects to the driven structure.

With the stepper motors, the back bend variation was easily accommodated by making the toothed drive pawl longer, since it does not matter which set of teeth engage the rotor or slider. For hinged plates, the drive tether locks into place, as seen in Figure 5-20, so the degree of backbending sets the initial angle of the hinged plate. If the deflection is too great, then the plate cannot be brought into perpendicularity. The solution used for the next CCR design, in fabrication on the MUMPS11 run, was to provide more notches on the drive tether, as shown in Figure 5-21. After the actuator array is back-bent, the best notch to use can be selected.

Thermal actuation is slow, so another electrostatic CCR was also laid out, using the mirrors of the CCR shown in Figure 5-19. New tilting mirrors were designed to actuate at a lower voltage; they are wider and have longer torsional flexures. This also gives them a larger percentage of reflective area over the array. The unit cell for this new tilting mirror array is $50 \times 90 \mu\text{m}$. Figure 5-22 shows the layout plot of the third CCR with tilting electrostatic mirrors to replace the thermal actuators of the CCR shown in Figure 5-20. This CCR is also in fabrication on the MUMPS11 run.

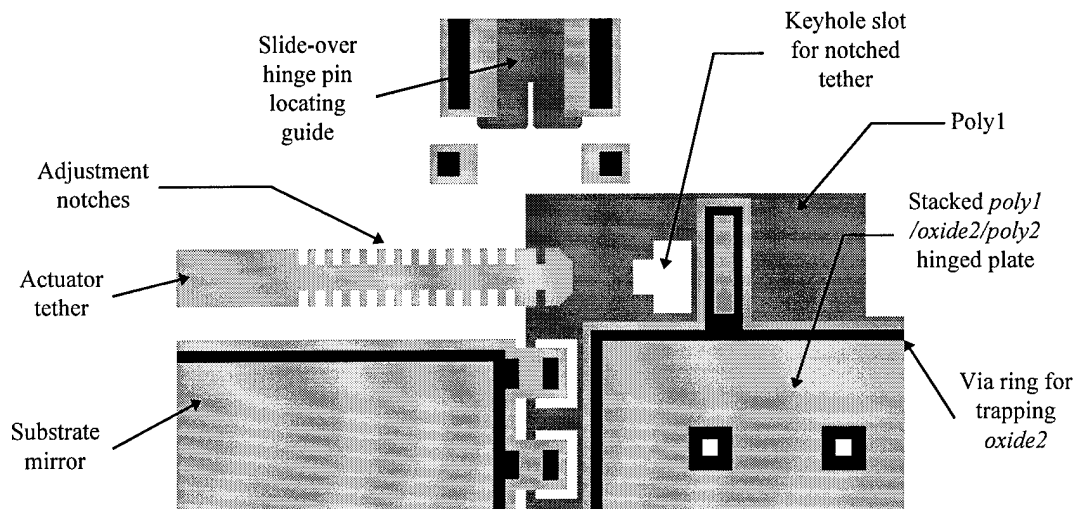


Figure 5-21. Adjustable tether for hinged plates. Fourteen notches provide a choice for setting the initial angle of the hinged plate. The proper notch is selected by lifting the tether and moving the plate after the actuator array is back-bent and the plate is raised.

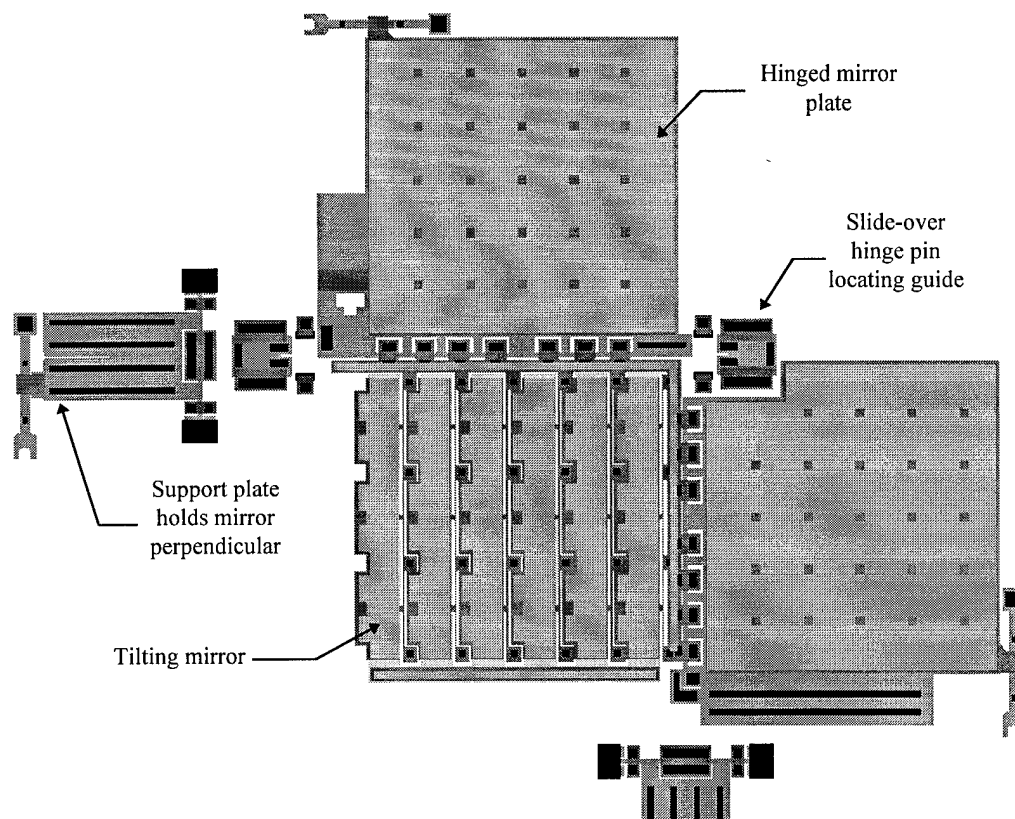


Figure 5-22. Corner Cube Reflector with larger electrostatic tilting mirrors.

One problem to be addressed in future thermally actuated CCR designs is the attachment of the drive tether on one side of the mirror. Testing showed that the mirror plate tends to rack in the hinge staples and gets out of perpendicularity when operated. A solution would be to run the drive tether through the middle of the substrate mirror, so the hinged mirror could be driven at the center. Some of the substrate mirror area would have to be given up for the better actuator attachment. Slide-over positioners should also help the hinged plate stay in line with the hinge staples.

For the adjustable tether design, the hinged plate can be held temporarily in the upright position by a second plate, like the ones seen in Figure 5-22. These support plates could also be used for shipping the device, if the plates could be raised and disengaged under actuator control.

5.1.2.4 Self-Assembled Structures

Perhaps one of the most useful positioning applications would be the self-assembly of MEMS devices. Most assembly of microelectromechanical components is currently done by hand using a probe station. This is a time-consuming process which results in many broken devices. Another published method of assembly is actually a method for controlled disassembly by melting fusible links [12]. It has found use mainly in adjusting the force of multi-leaf springs and releasing parts of large structures which are temporarily tethered to survive the release process. Figure

5-23 shows a fusible link used to adjust a spring's force by releasing more leaves of the spring.

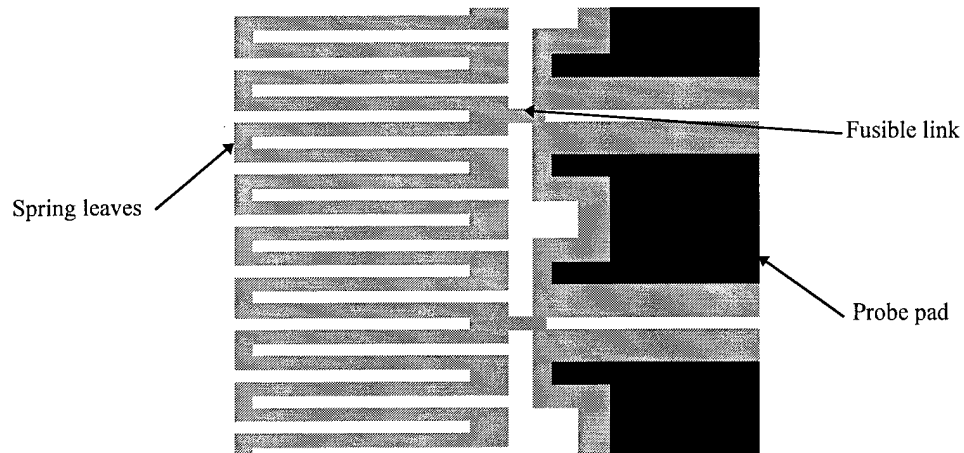


Figure 5-23. Fusible links used to adjust spring force by releasing leaves of a multi-fold spring. Current passed through the probe pads melt the links and releases the spring leaves.

Some of the devices developed during this research have features which are formed topologically. One common assembly step is the removal of the *polyl* formers after such a device is released. Examples are vertical thermal actuators and devices with guide rails. A vertical actuator designed with self-removing *polyl* formers is shown in Figure 3-32. Back-bending lateral thermal actuators are ideal for this application, since they stay back-bent after the power is removed. The actuator can swing a former out of the way permanently with one application of power to back-bend them.

Another task that would be ideal for motorization is assembling sliding parts. This would be a simple task for a linear motor since there is only sliding friction to overcome. For example, the grippers shown in Figure 4-23 are currently slid into

position by hand. The linear stepper motor design shown in Figure 5-13 is not limited in the distance it can push a toothed rack since the actuators stay in one place. So the only cost would be the extra area needed for the actuators, and the toothed rack could be incorporated into the existing structure.

A more demanding task for linear stepper motors is raising a hinged plate. One problem with this assembly task is overcoming the initial resistance to lifting. Raising hinged plates is like opening a bifold closet door: it can't be opened by pushing solely on the edge. The door must be given an initial bend by pulling on the handle, then it can be opened fully just by pushing on the edge. The farther the initial bend, the greater the leverage, so the easier it is to push open from the edge if there is resistance from the hinges.

Figure 5-24 shows the layout of a structure used to test the lifting capability of vertical thermal actuators. Three vertical actuators are attached to a hinged plate. The purpose is to see which actuators can lift the plate. The closer the actuator is to the hinge, the greater the initial lift. The vertical actuator shown in Figure 3-33 is the outermost actuator of this test structure. Only the outermost actuator, located 175 μm from the hinges, could visibly lift the plate. The actuators are 120 μm long and lift the plate in the back-bending mode, so they only need to be powered once to back-bend them, then they stay deflected.

Research is ongoing to adapt linear stepper motors to the task of raising hinged plates. Figure 5-25 shows the initial attempt. In this design a vertical thermal actuator is used to give the plate the initial lift that bends the hinge, then a linear

stepper motor is used to push the plate the rest of the way up. This design was concurrent with the lift-test design of Figure 5-24, and the vertical actuator was attached optimistically close to the hinges.

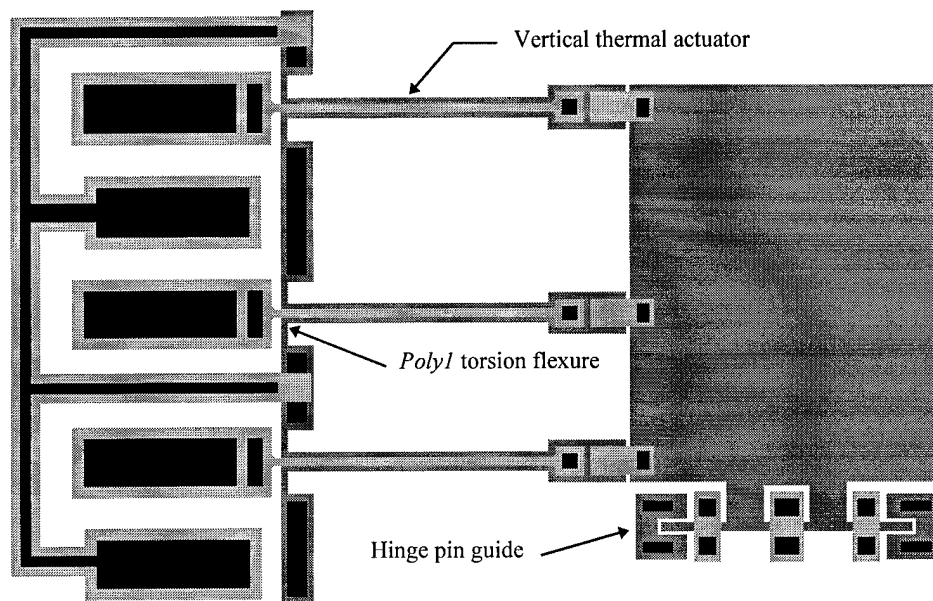


Figure 5-24. Three vertical thermal actuators arranged to lift a hinged plate. The plate is $130 \times 185 \mu\text{m}$, and the $120 \mu\text{m}$ long actuators are placed 30 , 95 , and $175 \mu\text{m}$ from the hinges. Figure 3-33 shows an SEM micrograph of the outermost actuator.

The slide-up lever arrangement designed to assist the manual assembly of hinged devices [13] is adapted to this task by attaching it to a toothed rack, and by altering the end which pushes on the plate so the lever can be completely withdrawn after the plate is raised. If the plate needs to be adjusted after raising, then the pusher arm can be left engaged. A manual pusher of this type can be seen in the upper right of Figure 5-5.

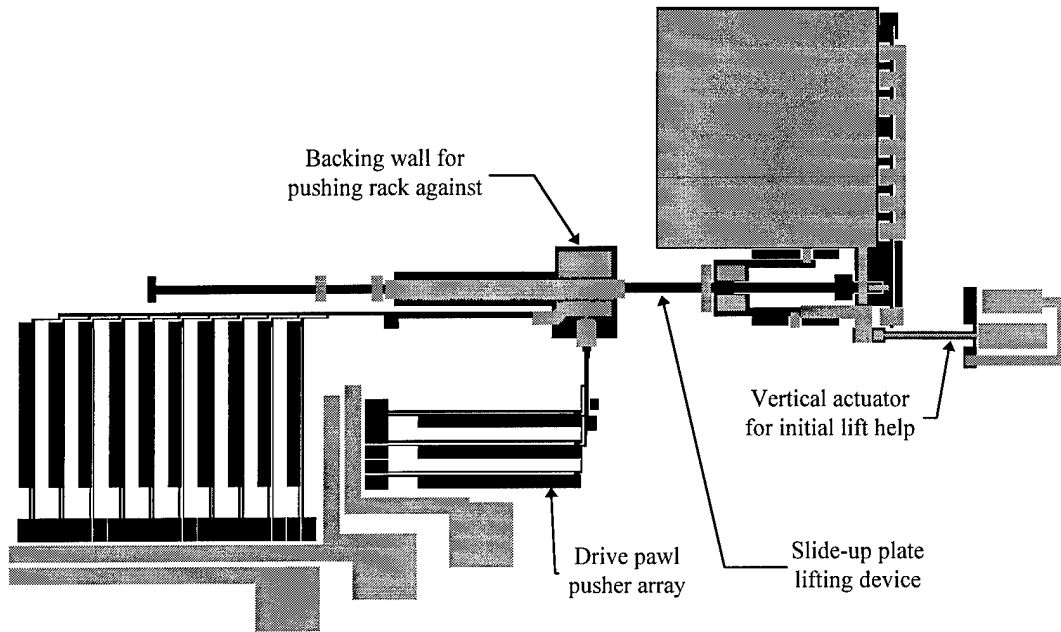


Figure 5-25. Layout of initial design for a motorized hinged plate. For clarity, only the *poly1* and *poly2* layers are shown. The lift motor is a single-sided version of the linear stepper motor shown in Figure 5-13, with ten 220 μm long drive actuators.

In the initial drawing of this device, the subcell containing the pushing pawl was shifted away from the actuator array tether, so it washed away after release. Though the cell could be tested by pushing the drive pawl manually, the tests were not conclusive because it was difficult to set up the proper sequencing of movements. A braking pawl may have to be added to hold the sliding rack into position, as done with the rotating stepper motor in Figure 5-11. Another version is in fabrication on the MUMPS11 run, with the pusher-pawl tip subcell fixed.

5.2 Whole Die Systems

Early in this research effort, opportunities arose that made it possible to try truly large MEMS systems, ones which covered, or could cover, an entire die. These arose

before the development of the thermal actuator arrays, so they served mostly to demonstrate wiring techniques point out the shortcomings of the wiring and packaging. In addition, they also serve as models of the sorts of considerations that must be made when laying out large systems.

5.2.1 Floorplanning

Laying out a large MEMS design is similar in many ways to laying out a VLSI circuit. Concerns include floorplanning, limitations on the number of input/output lines, and accommodating the next level of packaging. MEMS also adds the consideration of keeping the mechanical structures from colliding, a problem not seen with purely electronic designs. Floorplanning a die and deciding how a complex design will be partitioned into subcells can greatly affect the amount of time needed to draw a system or modify it for a later revision.

Floorplanning is similar to making an outline of a large document, like a dissertation. Without a rough idea of where all the major parts are going to go, the layout takes longer and often has to be re-arranged as details come to light that require alterations to the design. Such changes are very time consuming, especially when the wiring is already in place; and all the more so with a process like MUMPS, where each wire is composed of four mask layers. Of course, an initial layout effort starts off more quickly if time is not 'wasted' on floorplanning.

From many observations, and prior experience, a pattern became clear: novice MEMS (and VLSI) layout designers tend to place a device and then wire it, then place another and wire it, etc. This approach is passable for a MEMS test die where most of the devices are not related. On such die, most of the devices have integral probe pads, and are not wired to the bondpads at the perimeter of the chip; they are self-contained and can be piled together like a fieldstone wall. But when there are large numbers of devices to be wired to bondpads, this ad hoc approach quickly uses up a significant portion of the layout area and time. Opportunities to share wires and pads are missed because the layout becomes so irregular that patterns cannot be discerned and used to advantage.

In one case, multiple copies of a single cantilever switch were to be wired to bond pads at the die perimeter, to determine the contact resistance. As devices were placed and wired individually the layout became wiring limited, and ended up with a density of only 3 switches per mm^2 , and used 25 bondpads to drive 24 devices. Since the author was in charge of the overall layout of most of the early AFIT MEMS die, there was an ulterior motive to improve this layout. The more space on the die that could be saved by packing these switches in, the more space would be available for devices associated with this research.

After redrawing, many more switches were packed into less space, and the layout was made regular, allowing quick and reliable layout of control lines. The density of switches for the new layout was 27 per mm^2 . The total device count went from 24 to 216 switches, with 72 of them addressable from the same 25 bond pads,

and the other 144 had probe pads. The increased number of devices allowed 5 different designs to be tried, all in 68% of the original area. Figure 5-26 shows a section of redrawn switches.

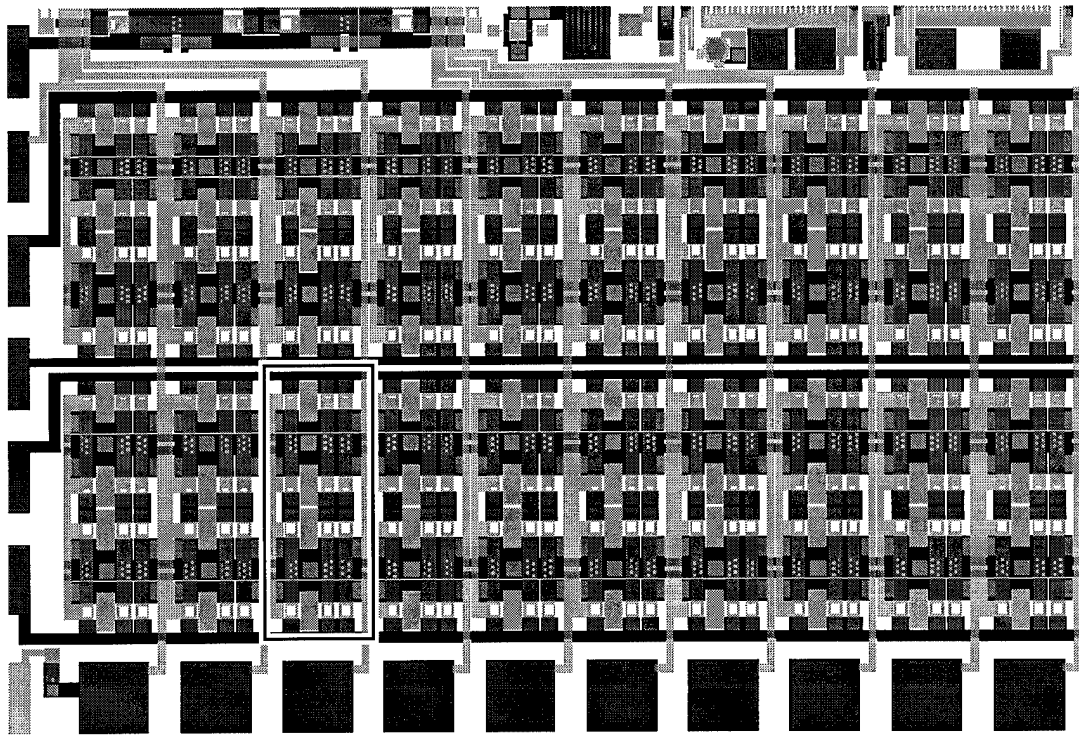


Figure 5-26. Compact design for an array of test switches. Regularity of the layout allows use of a repeated 'unit cell', one of which is outlined in the bottom row.

A major advantage of laying out devices in a regular array is that the wiring can be included in the 'unit cell' of the array. The wiring within the array is then assembled automatically, eliminating the chance of mis-wiring. Only the wiring external to the array has to be hand-wired; and even here, the regularity of the wiring at the edge of the array makes large sections of the external wiring reusable. The elimination of wiring mistakes and the savings in wiring time far outweighs the time

spent planning the unit cell, a point often appreciated in an academic environment where time is always in short supply and is often found after midnight.

Floorplanning also includes deciding how related devices in a system are arranged with respect to each other and to the bond pads. If the organization of the next level of connectivity is known, changes can be made to the layout to accommodate it. These changes include matching the size and spacing of the bond pads to the packaging, and grouping of common signal lines to make circuit board routing less congested. Automated and hand routing of both the die and the circuit board is simpler if signals going to a common destination share adjacent pins on the die package.

If the next level of connectivity is the probe station, then the floorplan can also include the most effective placement, size and orientation of probe pads. For example, if a device needs three probe pads, then the designer should not place them in a row on the same side of the device. This may be the most convenient plan at layout time, but on the probe station, the probes will interfere with one another, or a probe will have to cross over the device, making it harder to observe.

MEMS devices add another twist to the floorplanning problem. The system may include device with sliding, expanding, or hinged parts. These must have a clear path for assembly and operation. The overlap errors occur when parts are laid out in haste, or more often, when a part is placed and later modified. All of the copies are also modified, so unless each one is looked at, possible overlap errors go undetected.

Figure 5-27 shows the result of not planning for the motion of a part. This device stores the energy of the pulled spring, which is released when the latch is moved by a thermal actuator. After the release etch, the spring is to be pulled and latched; the spring energy can be used later by electrically releasing the latch. The spring tether is connected directly to a device to be pulled, to lifting a plate, or drive a toothed rack and rotate a gear train, for example. When viewed as an individual device, these springs were free to move, but when packed onto the die, their motion was blocked by the neighboring cell.

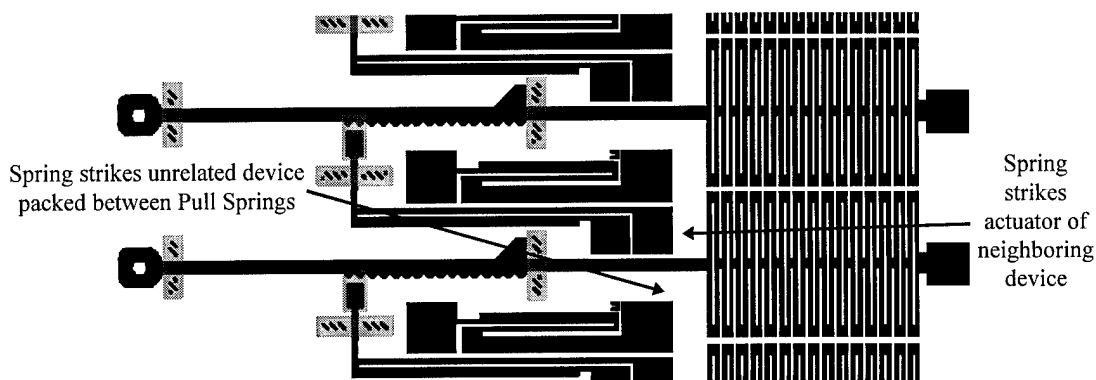


Figure 5-27. Mechanical interference caused by placing 'Pull Spring' devices too close together. The springs cannot be fully extended because they have been placed such that the spring strikes the neighboring device and an unrelated device that was placed between them.

Floorplanning is more than just maximizing the use of die area, arranging components for proper operation, or interface with external wiring. Consideration must also be given to powering and controlling the system. If the devices are power-hungry, then the wire widths have to be adjusted accordingly, but more important,

especially for the MUMPS process, consideration has to be given to which wires take the path with unbroken metallization at a crossover, as discussed in Section 4.1.3.1.

With even slight resistance in the wiring, devices deep in an array might be starved for power as devices closer to the periphery sink the available current. In VLSI designs, even power distribution is achieved by gridding the power lines wherever possible. Such cross-connections prevent any spot in the power grid from getting a lower supply voltage, a phenomenon called 'rail span collapse'. Since MEMS devices like actuators often have only one electrical port, unlike logic circuitry, the only common power rail is the ground. The power source lines are also the control lines. So gridding is less of a necessity with MEMS; but even if just the ground line is involved, and the area consumed by gridding is inconsequential, it should be considered as part of the floorplan, especially if it can be built in as part of a unit cell.

In fabrication processes where wiring can take up a significant portion of the die area, such as the MUMPS and LIGA processes, the number of individual devices may be limited by the area needed for the wiring before it becomes limited by area needed for the devices. But most often the number of devices, especially in MEMS where each device operates independently, is limited by the number of I/O lines than can be run off the die. This is an area where the next level of packaging can provide solutions, especially for MEMS processes that do not allow the reduction of control lines by moving more of the control and addressing circuitry onto the MEMS die.

5.2.2 Example Systems

The systems described next demonstrate the types of large systems that can be created in the three foundry processes. By far the most complex systems could be built in the MUMPS process, which consequently was the process which received the most attention throughout this research. The other two fabrication processes, LIGA and CMOS, received less attention not only because they were less available, but also because they were less capable of making a variety of large, complex MEMS systems. This was due partly to the more limited types of MEMS structures which could be built, and partly the lack of practical applications available for the devices that could be built. The CMOS process, however, was left largely unexplored due to the loss of fabrication funds early in the research.

5.2.2.1 LIGA Switch Array

The LIGA foundry process just does not provide enough wiring or mechanical options to make very complex systems. For the two LIGA process variations available, the most complex systems might possibly involve fluid logic. Some initial devices were built, as seen in Section 2.3.3.3, but the topic was in general outside the scope of this research. Fluid logic is being actively pursued elsewhere, though [14].

A practical system would be an array of mechanical relay switches of the type shown in Figure 5-7. With more effective actuators, these switches can be applied to a variety of configuration switching tasks. Their mechanical nature makes them

radiation hardened, and their latching operation means they maintain their setting without power applied, unlike solid state switches. This makes them ideal candidates for battery-powered devices or situations where power is limited, such as satellites. A batch-fabricated array of micro-relays would also be much cheaper and less space consuming than using individual macro-relays.

For example, some redundant processor systems for space applications use several processors running the same program concurrently, and a majority must 'agree' on all calculations. If the same processor disagrees repeatedly, it is switched out of the circuit and replaced with a backup processor. One failure mode in space is radiation damage. Ionizing radiation can create trapped charges in the gate oxide layer of a field effect transistor, shifting the threshold voltage far enough to render the device useless. Over time, however, this type of damage can self-repair as charges recombine. A processor may thus become operable once again; so the ability to switch it in and out of the circuit could extend the useful life of the overall system [15]. Such a switch would need hundreds of individual, isolated relays.

A test array of these switches was fabricated on the each of the two LIGA die using the mask layout shown in Figure 5-28. This test array does not cover the whole die, but in a system where dozens of connections may have to be made, the whole die would be used. The restrictions of the LIGA process fix the layout so that all of the electrical connections are on either side of the array. This is ideal from a flow-through circuit topology point of view, except that a single row of switches is not wide enough to cover the die, so several rows would be needed. The number of

switches would be restricted by the space needed to turn the wires leading from the inside edges of the rows and run them over to the bondpads on the periphery. Power lines also could not be shared, since this would mean they would have to cross the signal lines, and no crossovers are possible in the available LIGA processes. All of these concerns could be addressed by a packaging system that can run connections to pads inside the periphery. Such a system is explored in Chapter 6.

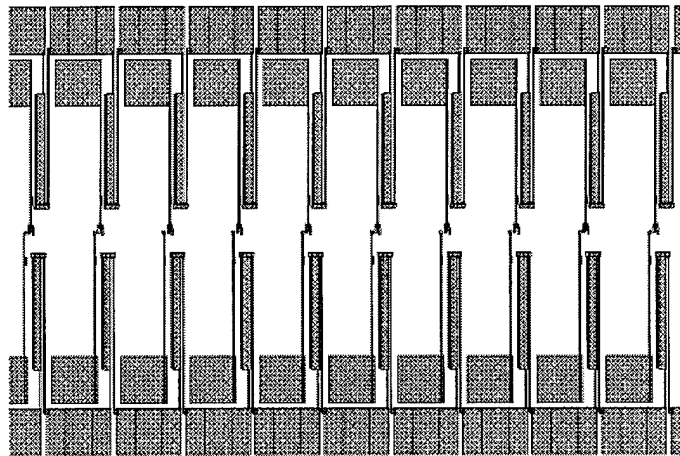


Figure 5-28. Array of LIGA mechanical relay switches of the type shown in Figure 5-7. Probe pads are shared between adjacent thermal actuators, but would have to be split to allow wiring out of the contact arms in a system layout, or contacts would have to be brought in on top.

5.2.2.2 CMOS Tactile Stimulator Array

There has only been one large whole-die system built in CMOS MEMS. The die was designed for packaging tests, and contains a collection of generic MEMS and electronic devices. The devices were important only to show that the die could be packaged without destroying them, and were chosen to represent typical MEMS

device types. No particular purpose was to be ascribed to the individual devices beyond this; but instead of just laying out a die of disconnected devices, the urge to make something that might be useful beyond package testing won out. So the die also contains an integrated system combining an array of MEMS devices and simple decoding circuitry to address them.

The devices in the array are thermal tactile stimulators. The system is supposed to act as a data link to a finger tip, passing information as small points of heat. The devices are spaced far enough apart to be perceived as separate points, a kind of thermal Braille. The idea of thermal stimulation was first proposed by an AFIT student researching MEMS tactile stimulators that pressed on the finger tip [16]. Though the main device of that research was a bimorph actuator, many of the test devices built on the early CMOS MEMS die were suspended resistors like the one shown in Figure 2-16, since it was one of the early, established CMOS MEMS devices and made a good benchmark [17].

Observations made of incompletely released suspended resistors revealed that they can glow visibly almost up to the point where the underlying unetched silicon still touched the suspended structure. So the final thermal stimulator design is intended to be only partially released, leaving a pillar of silicon under the center of the trampoline to make it strong enough to resist touching. The only other change from the device shown in Figure 2-16 is the addition of a short resistor which can be used to monitor the temperature of the device or tell if the trampoline has been broken. The final design is shown in Figure 5-29.

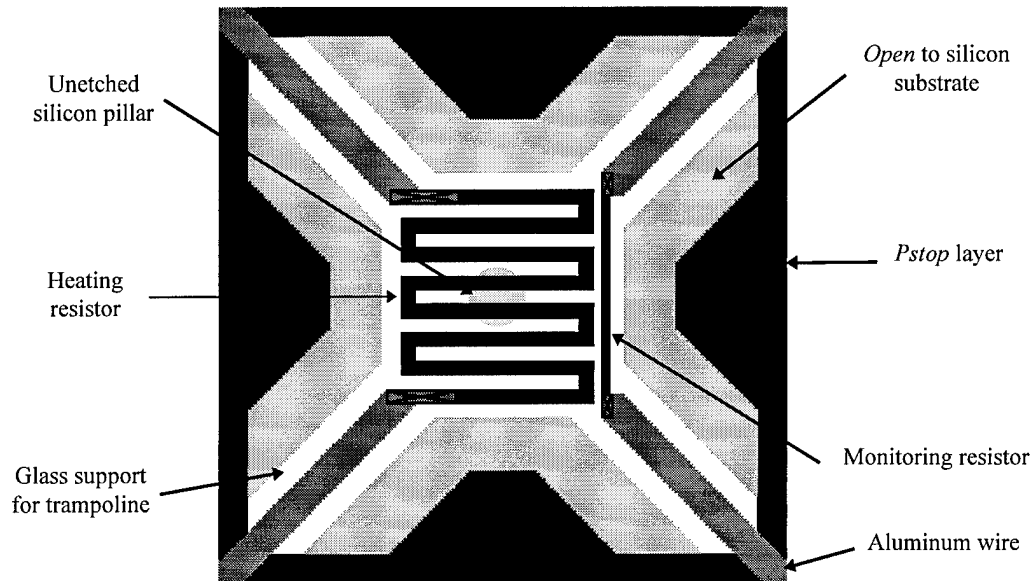


Figure 5-29. Thermal tactile stimulator. Device is $85\text{ }\mu\text{m}$ square, suspended over an $180\text{ }\mu\text{m}$ pit. Main serpentine polysilicon resistor is $5\text{ }\mu\text{m}$ wide, smaller monitoring resistor is $3 \times 70\text{ }\mu\text{m}$. The light gray circle in the center shows where the unetched pillar of silicon touches the underside of the trampoline for added strength.

An 8×8 array of these devices, spaced $500\text{ }\mu\text{m}$ center-to-center was laid out in the center of the die and connected to a pair of 3:8 decoder circuits for addressing each device individually, one at a time. Each row and column has a 3-bit address, so only 6 control lines are needed to address the entire array. The address bits are decoded to drive an N-transistor with a $40\text{ }\mu\text{m}$ wide, $2\text{ }\mu\text{m}$ long gate. The transistor was sized so its on resistance would be insignificant compared the $2.2\text{ K}\Omega$ of the suspended resistor, so it would have more than enough current passing capacity. The die layout of the thermal stimulator array and its associated circuitry is shown in Figure 5-30.

Devices were tested before release and were operational, but after release in EDP most showed open circuits. Test will have to be re-done using TMAH as the

etchant. TMAH is much more selective for silicon over silicon dioxide, and so should be less likely to infiltrate between the glass layers and attack the polysilicon resistors, which is the probable failure. Similar devices on other die survived EDP etching, so either the fabrication was slightly different, or the EDP aged.

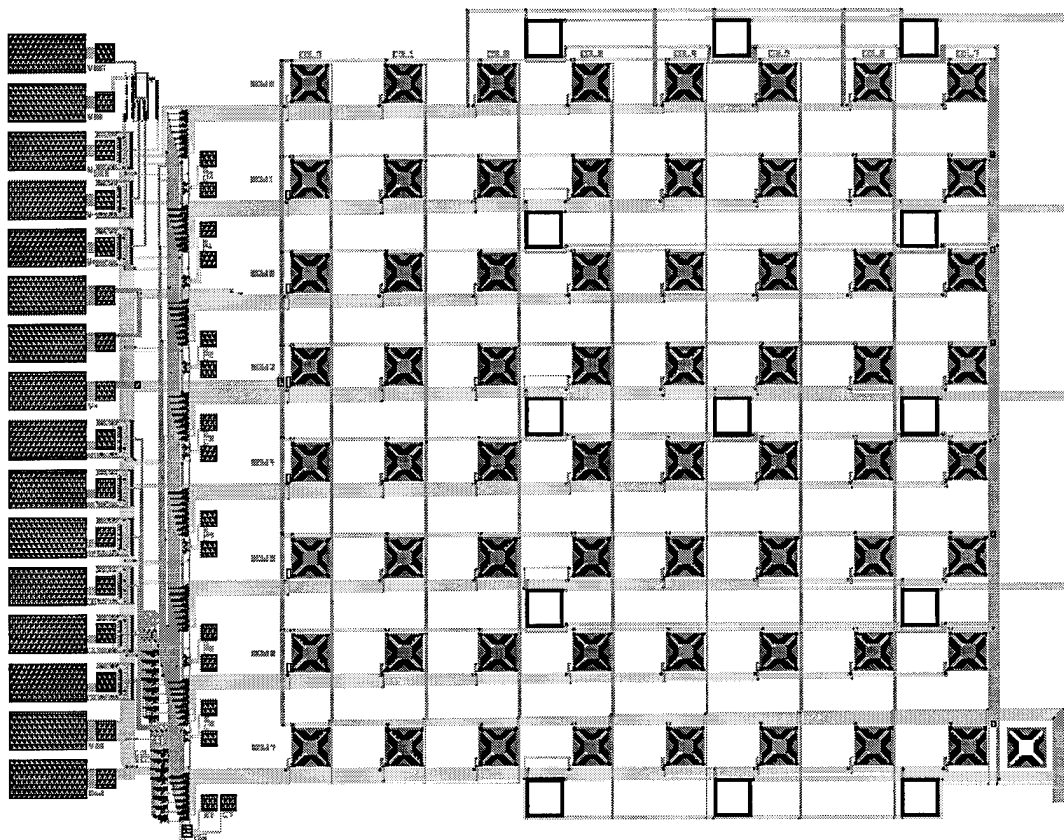


Figure 5-30. Die layout showing only the thermal stimulator array and its addressing circuitry on the left. Array is 3.7 mm square, with stimulators spaced 0.5 mm apart. The empty boxes are the locations of the backup array of stimulators, connected directly to bondpads not shown on the right. In the lower right corner is a blank stimulator with just the glass and open areas, which acts as an etch gauge.

Thermal stimulators have an advantage over moving parts because they are not affected by dust. If these devices, or larger ones if these prove too weak, should

work, then a more complex system, complete with a proper microprocessor style interface could easily be designed. The fact that the device is built in a CMOS process makes integrating it with complex circuitry on the same die simpler.

Although LSM is possible with the CMOS MEMS process, the actual MEMS devices are limited in what they can do, and the materials are not optimized for MEMS structures, so there is not much variety to the LSM designs that can be built. This system shows that for certain applications, designing a large CMOS MEMS system is easily accomplished.

5.2.2.3 MUMPS Spatial Light Modulator

Micromirrors are finding increasing application as components of large MEM systems. Applications of micromirror arrays include active aberration correction for a variety of optical devices such as free space optical communication systems, and optical correlation for non-cooperative target recognition or target acquisition, tracking and pointing [18,19]. The key element in these systems is the array of moving micromirrors, called Spatial Light Modulators (SLMs). The first whole-die MEMS system laid out for this research was a 127 mirror hexagonal array to be used as an SLM for correcting the distortion from another optical element in a communication system [20].

As the first large system with a practical application in mind, this system received more consideration than almost all the others, and its design, modeling and

testing was the topic of a publication [21]. The design went through a major revision, resulting in a second, completely rebuilt array. Both arrays will be described here to show the complete evolution of the final whole-die system. The project for which the die was built is ongoing, so integrated testing of the array in a larger system has not yet been performed.

The design of the 127-mirror array involved balancing the constraints of the MUMPS fabrication process and the limitations of the materials used in that process, with the requirements for an efficient, flexible mirror array architecture. Ideally, each micromirror would have a perfectly flat surface with 100% reflectivity, and have identical, low stiffness flexures for zero-tilt vertical motion at low address voltages. The mirrors would completely cover the array surface with no gaps between them, and would have address wiring that could be extended to any depth and which would not affect micromirror properties. Also, the mirror addressing and drive circuitry would be integrated on-chip, simplifying the electrical and physical connection to the rest of the system. The limitations of the MUMPS foundry process forced tradeoffs to achieve a system that could be successfully fabricated and still meet the requested functionality.

5.2.2.3.1 Hexagonal Mirror Design

The array is hexagonal because its constituent electrostatically actuated mirrors are hexagonal and are arranged in six concentric rings around a center mirror. A

hexagonal mirror design was chosen because it allows the minimum number of flexures for a purely vertical piston-like motion [22]. Hexagons also pack efficiently, maximizing the active surface area of the array. The mirror evolved over several early MUMPS runs from a square piston mirror drawn on the first MUMPS run (MUMPS3).

The hexagonal piston mirror development is an example of the rapid development cycle possible with a foundry process. The evolution of this device from test structure to the final refined version is illustrated in Figure 5-31. The initial piston mirror is shown Figure 5-31(a). Aluminum was used in the early MUMPS fabrication runs, but was later replaced with gold, which is unaffected by the release etch. Initial results were promising, and refinements were made to reduce the drive voltage so the mirror could be used as an element of a practical system.

The main modification was reducing the number of flexures to three, which led to a hexagonal mirror shape [23]. To make the flexures as loose as possible, they have to be made of the thinnest available polysilicon layer, since the stiffness of the flexure has a cubic relationship to thickness. This led to the first design tradeoff: the thinnest MUMPS layer, and therefore the one that makes the most pliable flexures, is *poly2*, also the only layer that can be reliably metallized. So both the flexures and the mirror have to be designed in the same layer. This means that any area taken up by the flexures directly reduces the movable mirrored area of the array.

The first hexagonal mirror design, shown in Figure 5-31(b), has each of the three flexures running along two sides of the hexagonal micromirror, which gives the

greatest length possible for each flexure without overlapping them laterally with more turns. Longer flexures can be made by going around more sides or by folding the flexure back along the same two sides, but these approaches add the width of extra flexures and gaps to the area between neighboring mirrors. The extra flexure length also adds more diffracting edges to the design, increasing stray light generation.

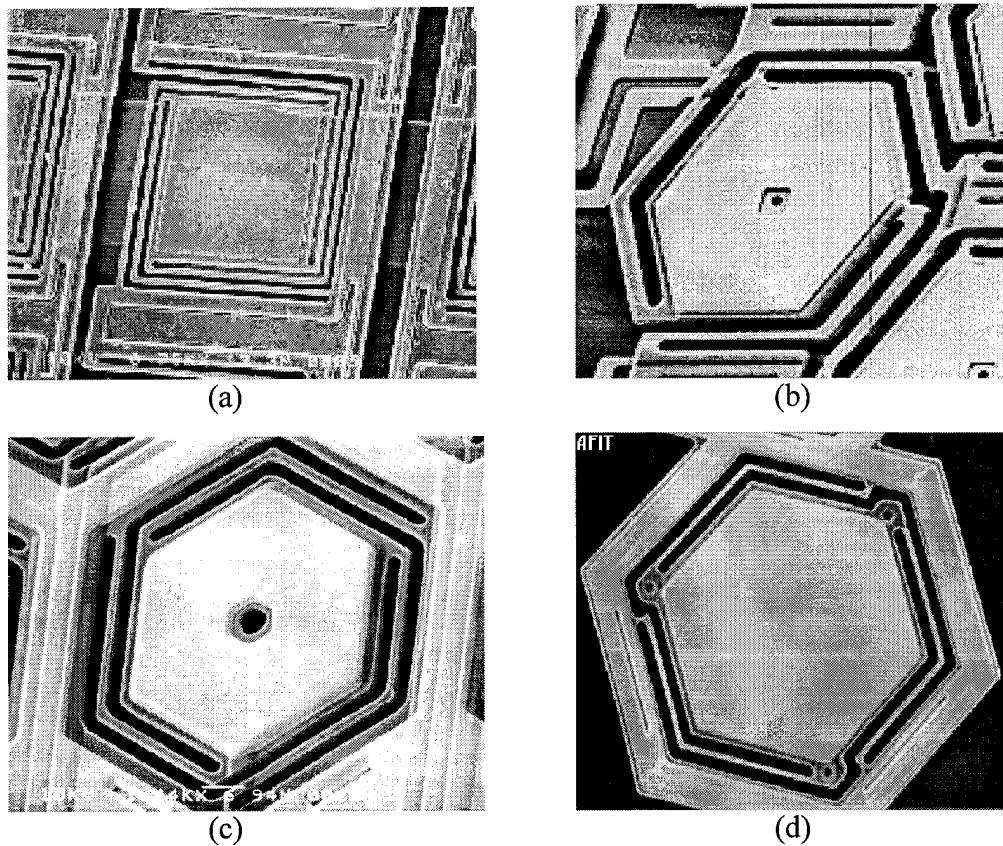


Figure 5-31. Evolution of a piston micromirror over four fabrication runs. (a) 30 μm square mirror with four flexures and aluminum metallization, (b) 60 μm hexagonal mirror with three flexures and copper metallization, (c) 50 μm hexagonal mirror with gold metallization, part of first 127 mirror array, (d) 100 μm hexagonal mirror with gold metallization, part of the second 127 mirror array.

The first hexagonal mirror achieved a reduction in drive voltage, so with the adoption of the Cadence layout CAD tool, the 50 μm version shown in Figure 5-31(c)

was designed. The design rules for the MUMPS process set the minimum dimension for lines and gaps designed in *poly2* at 2 μm , so 2 μm was chosen for the widths of the flexures and the gaps on either side of the flexures.

MCNC's design rules state that etch holes must be placed every 30 μm to guarantee the full release of the *poly2* structures. The desire to have a minimally distorted mirror surface meant the number of etch holes had to be held to a minimum. So only a single 4 μm wide etch hole was considered acceptable, fixing the width of the mirror at a conservative 50 μm .

Detailed testing of this hexagonal mirror [24] indicated the need for some further refinements which are covered in the next section. Figure 5-31(d) shows the final device, which is 100 μm across, with no etch hole. This entire development cycle was completed in only four fabrication runs, which would take less than a year with the current fabrication schedule.

5.2.2.3.2 Hexagonal Array Design

The first array was intended to be a proof of concept, so the size of the array was determined by the size of the available packaging. The largest package was a 145 pin grid array, which limited the maximum possible number of mirrors in the array to 144. The largest regular array of concentrically arranged hexagonal mirrors that fits this package is 127 elements. Figure 5-32 shows a close-up of the array.

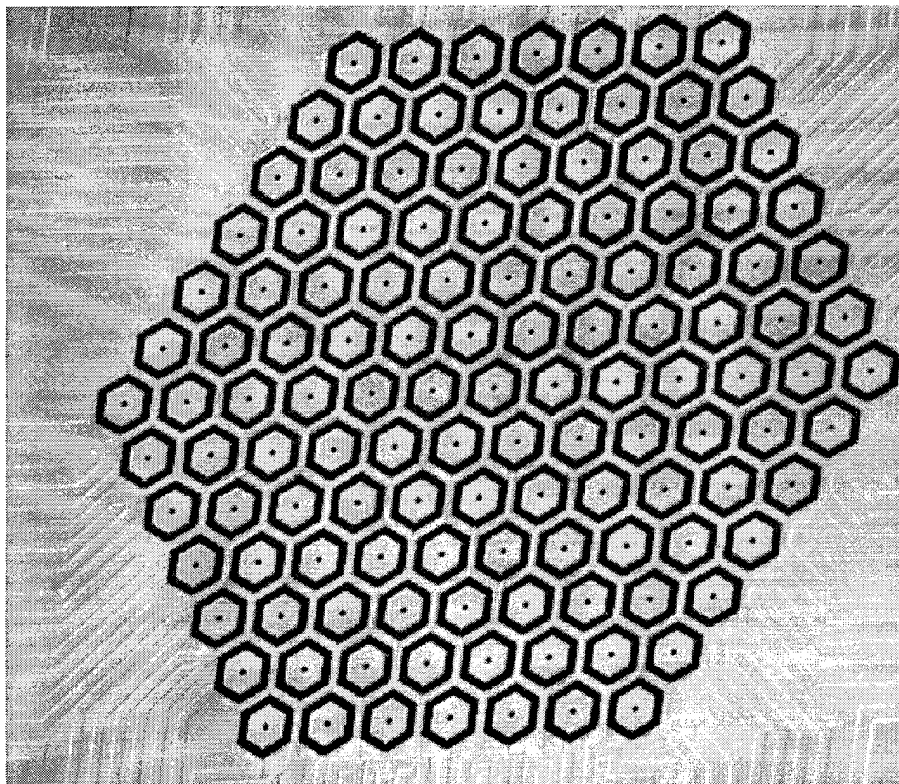


Figure 5-32. Array of 127, 50 μm wide micromirrors. Mirrors are arranged in 6 concentric rings around a central mirror. Each mirror is individually addressable by *poly0* wires whose topology can be seen in the gold-covered *poly2* plate surrounding and supporting the mirrors. Array is 975 μm across the widest part of the hexagon.

Another constraint that was considered when deciding how big the array should be was the tradeoff between active and static mirror areas: to make each mirror individually addressable, a *poly0* wire must be run to the lower electrode of each mirror. These *poly0* wires had to be run between the mirrors so the topology they induced in the overlying *poly2* layer would not affect the flatness of the active mirror surfaces or the uniformity of the flexures. The minimum allowed line/space for *poly0* is 2 μm , so 4 μm is added to the space between the mirrors for each additional minimum width address line. Hand-drawn wiring tests showed that a circular array of

127 mirrors in 6 concentric rings needs at most three *poly0* wires between mirrors to address every mirror in the array, including the center one, while at the same time leaving some of the adjacent mirror sides free for anchors.

Providing each mirror with an anchor for each of its three flexures would entail adding 10 μm of dead space between all the mirrors. Instead, all of the mirror flexures were attached to a common *poly2* frame which served several purposes. Besides anchoring the mirrors and saving the 10 μm of space that would otherwise be needed, the frame acts as a cover over the address wires, and can be given a coating of gold to increase the reflectivity of the array. Even though the mirrored surface of the frame cannot move, it can provide a strong zero deflection optical reference plane for signal processing. The final design of the support frame allowed a mirror edge-to-edge spacing of 26 μm , and a mirror center-to-center distance of 75 μm . Although each side of every mirror does not have an anchor, there are enough anchors spread around the array to hold the frame securely and prevent it from sagging. Past the edge of the array, the *poly0* address lines were extended as *poly0/poly2*/gold substrate wires to provide a low resistance path to the bondpads.

The resulting 127 mirror array and associated wiring was small enough so that two arrays with 131 bondpads around each array could be fit on the 1 cm square MUMPS6 die. Each array could be pre-tested on a micro-manipulator probe station, the best one wire-bonded out, but the unused one had to be covered over with a piece of paper so the bond wires that passed across it would not sag onto it and short out.

There was also enough room around each array to place four copies of test cells, each containing 44 variations of the hexagonal micromirror. These were designed to test different sizes of mirrors and address electrodes, the need for the etch holes, and different arrangements of down-stops to prevent the mirror from touching the address electrode when fully deflected. The test cell is shown in Figure 5-33.

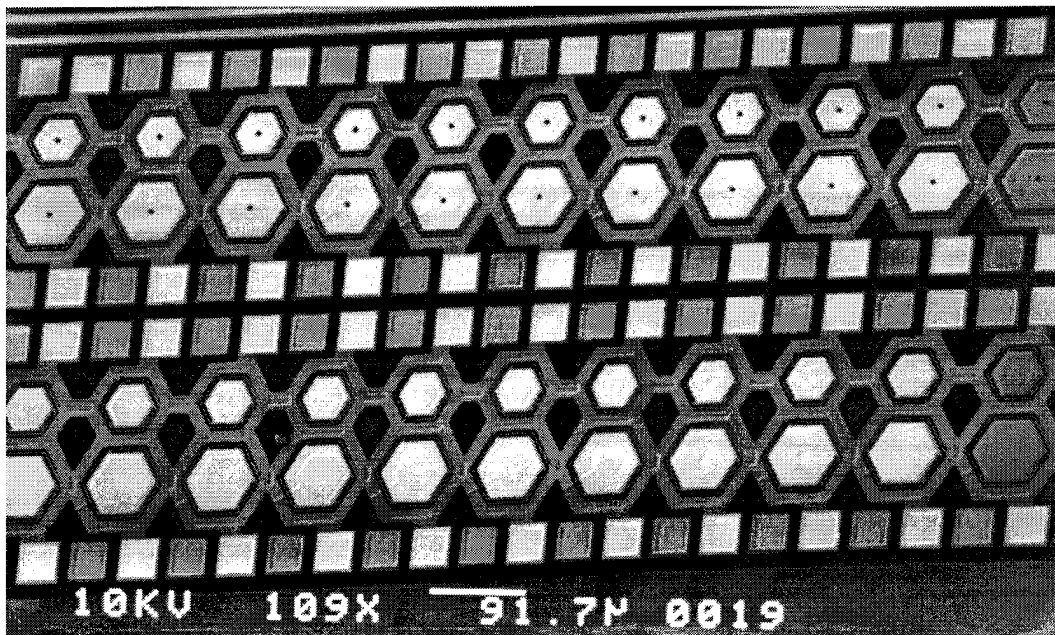


Figure 5-33. Arrays of test mirrors on the first hexagonal SLM die. There are two sizes of mirror, 50 μm and 75 μm , with a variety of different address electrode sizes, down-stop variations, and some without etch holes.

5.2.2.3.3 Cover Plate Design

A cover plate was designed to be placed over the entire array to eliminate light scattering caused by the flexures, wire topology, and mirror anchors, and to improve the overall reflectance of the array. The cover plate has hexagonal holes that expose

only the metallized surface of the mirrors, so when it is in place the incident light sees a flat, reflective plane of which some portions can be moved vertically.

The chip layout had room for eight *poly1* cover plates per array to compensate for losses during handling. The cover plates were drawn without anchors so they would be fully released from the die. The post-processing procedure for the cover plates was to have them wash off the die during the release etch so they could be sputtered with gold and then positioned over the mirror array and glued into place. The support frame around the perimeter of the mirror array was drawn with square locating pins at the corners, corresponding to square holes at the corners of the cover plate.

The glue for the cover plate was to be placed by hand, so to accommodate the inaccuracy of the glue edge, a large margin was left around the array. The glue is a drop of photoresist placed on the die, and a probe point is used to drag the edge of the drop over to the cover plate edge. As the photoresist air-hardens, it flows more slowly, so fairly precise control of the edge can be achieved with a little practice.

To hold up the cover plate, the *poly2* mirror support frame was extended around the array and drawn without etch access holes. The result is that the frame is not completely release-etched underneath. The remaining *oxide1* and *oxide2* anchors the support frame more securely, and also forms a barrier to prevent the possibility of the photoresist creeping under the frame and over to the mirrors by capillary action. Figure 5-34 shows the entire die, note that the wiring takes up a large part of the die area. Spaces between the wires are filled with *poly1* cover plates and test mirrors.

5.2.2.3.4 Fabrication Results

The fabricated die had several flaws that were not anticipated based on the first hexagonal mirror. These flaws made the mirrors in the array non-uniform. The initial hexagonal micromirror design, shown in Figure 5-31(b), was drawn with the Magic VLSI CAD tool, which could only draw rectangles with 1 μm minimum dimensions. So the flexures had to be drawn in stair-step fashion. When the Cadence CAD tool was adopted, the mirrors could be drawn as pure hexagons with angled lines, eliminating the stair-stepping that made the flexures uneven. It was assumed that the underlying mask grid would have 0.1 μm steps, based on the reported mask characteristics of the LIGA process, the previously drawn die. The underlying grid for the hexagonal array was therefore set at 0.1 μm . This assumption turned out to be an error.

Visual inspection of the fabricated micromirrors revealed unevenness in the mirror flexures. The flexure sides were smooth, but the flexure sections that ran in directions parallel to the die edges were 1.65 μm wide, while sections that ran at 60 degree angles to the die edges were 1.99 μm wide. The design width of the flexures was 2 μm .

This unevenness was caused by stair-stepping, or 'fracturing' of the angled lines when translated to the final mask. Due to the orientation of each hexagonal mirror, two of its three flexures are half 1.65 μm and half 1.99 μm wide; while the third flexure, whose halves are both at 60 degree angles to the die edges, is 1.99 μm wide

along its entire length. This uneven width, though slight, results in enough difference in flexure stiffness to cause a 7 nm difference in deflection between the flexure that was 1.99 μm wide along its entire length and the flexures that were 1.99 μm wide along only half their length [21].

A related distortion, a narrowing of the gap between the flexure and the mirror, occurred regularly across the array in every fifth row of mirrors. This indicated an interaction between the underlying step sizes of the design grid and the mask grid. It turned out that the masks were made on a 0.25 μm grid instead of a 0.1 μm grid as originally thought. As the mirror layouts stepped across the array, the flexure sections at 60 degree angles were fractured differently because the vertices of the polygons were snapped to a 0.1 μm grid, not a 0.25 grid. Another distortion that showed up on all the mirrors was a bump in one of the flexures where the poly0 wire goes under the flexure to the address electrode. This topological distortion was expected, however.

All of the mirrors therefore suffered differing degrees of distortion to their flexures; so they were all expected to tilt when they were fully deflected to 316.4 nm. Tilt measurements were taken [24] of a fully deflected 50 μm wide hexagonal mirror whose only flexure distortion was the difference in width due to angular orientation. Measurements taken at each corner where a flexure joined the mirror revealed a 7 nm difference in deflection between the flexure that was 1.99 μm wide along its entire length and the flexures that were 1.99 μm wide along only half their length. The various different distortions led to the design of the second generation array.

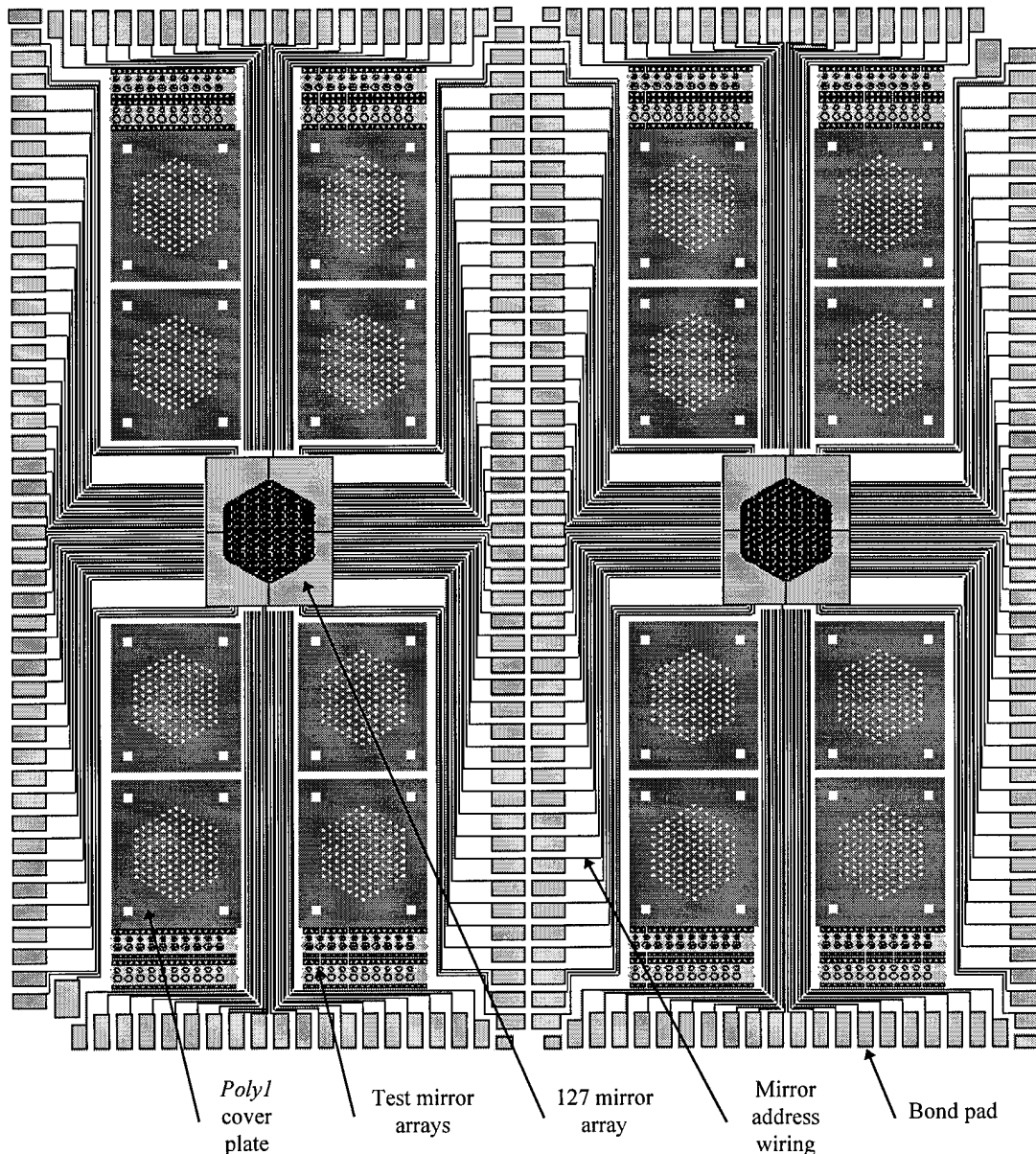


Figure 5-34. Die with two arrays of 127 hexagonal electrostatic piston micromirrors. Each array is $975\ \mu\text{m}$ across, and the micromirrors are spaced $75\ \mu\text{m}$ center-to-center. Each *poly2* micromirror has individually addressed *poly0* electrode underneath. Each array has 8 *poly1* cover plates and its own set of 131 bondpads.

Another feature of the first generation array that did not work out well was the cover plate. Washing the plates off the die during the release etch, and gold sputtering them separately from the rest of the die worked out very well. But it was

too difficult to align and hold the cover in place for gluing using microprobes. The guide pins fabricated into the mirror support frame were too short to hold the cover plate in place, so it could not be held steadily enough to be glued down precisely in position. The arrays that were bonded out for testing therefore did not include cover plates, but instead had to rely on the metallization of the support frame between the mirrors to provide the optical reference plane, which was the backup plan. A vacuum micro-pickup tool was built to place and hold the cover plate, but an improved design for the second generation array eliminated the need for the cover plate to be loose.

5.2.2.3.5 Micromirror and Array Improvements

As a result of the testing, a list of improvements was drawn up for the next revision of the hexagonal micromirror and the 127 mirror array. These improvements were intended to overcome the problems with non-uniform flexure fabrication of each micromirror, to decrease the driving voltage requirements, and to make the cover plate easier to attach and adjust. The following bulleted paragraphs list the improvements made for the second hexagonal micromirror array and the reasons for making them.

- The new mirrors are 100 μm across their widest dimension. This increases the overall size of the 127 mirror array, and increases the percentage of active surface in the array. Larger mirrors also require less drive voltage because of the larger area for electrostatic attraction. The main limitation on making mirrors larger than this

would be the amount of sagging in the center when the mirror is fully deflected; such a distortion may become optically significant. A square *poly2* mirror 62 μm on a side was measured to sag 5 nm in the center when deflected 316.4 nm, 1/2 wavelength of the HeNe test laser [24].

- Results from the test arrays on the first hexagonal SLM die and from test structures on other die indicated that the 30 μm etch hole spacing was too conservative, so the new mirrors have no etch hole. This increases the reflective area of the mirror and eliminates stray light reflections from etch hole edges.

- Dimples are placed at the mirror end of each flexure for down-stops. Stops were not included in the first design to save space, though they were tried on test mirrors. The test mirrors indicate that this is the best location for these stops. The increased size of the new mirrors makes the area given up for down stops less important. Although the dimples are fabricated under *poly1*, the conformity of the thin films results in a useable dimple in *poly2* also, when the *poly1* is removed.

- The entire array is rotated 15 degrees, thus all the flexures are drawn at some multiple of 15 degrees, so there are no lines parallel to the mask grid. All the lines will therefore get stair-stepped similarly on the mask grid, so all the flexures drawn the same width should be fabricated the same width.

- All features are drawn to a 0.25 μm grid to match the mask grid to eliminate cyclical width errors as the mirrors are stepped across the array. Another change made to prevent flexure width variations was to widen the gap on either side of the flexures from the minimum 2 μm to a more conservative 3.1 μm .

- *Poly0* address line stubs are placed under the corners of all three flexures.

One stub is used for the actual address line and the other two stop short of connecting with the address lines under the support frame. This ensures that the flexures all get the same topology. The wider flexure gap means that these stubs can be drawn without having to increase the width of the support frame that runs between the mirrors, to accommodate the 2 μm gap needed between the edge of the stubs and the address lines.

- The new cover plate is attached to the substrate by a long hinge. The cover plate flips over into position on the array. Due to the compressive stress in the *poly1* layer, the cover plate will tend to curl up when it is flipped over, so its center contacts the array first. The cover flattens out as the edges are pressed down. The die will have to be masked when the back side of the cover plate is metallized, but the features to be masked are large, and large margins were left around the array and cover plate, so the required manual processing is simple. Up and down bossing was added to the perimeter of the cover plate, but its size makes the height difference of the boss insignificant.

- The cover plate and mirror array support frame have cross-hair fiducials for fine alignment of the cover plate to the array. Holes are fabricated in the cover plate to allow easier adjustment of the plate with microprobe tips.

- Long tethers from the hinges to the cover plate add flexibility so the plate can lay flat, and form a large enough margin around the cover so that sheets of paper or

plastic can be used to mask the rest of the die when the underside of the cover plate is sputtered with gold.

- A larger margin of the mirror support frame, without etch holes, is left around the array since the die may be in the etch longer, and residual *oxide* is still needed under the frame to prevent the cover plate glue from creeping under the frame to the mirror array by capillary action.

- There is only one array per die. The larger mirrors and the hinged cover plate scheme leave room for only a single hexagonal array and a few test mirror arrays. Larger, $350\text{ }\mu\text{m} \times 175\text{ }\mu\text{m}$, and evenly spaced bondpads will simplify wire-bonding.

The final hexagonal micromirror design is shown in Figure 5-31(d), and the entire die is shown in Figure 5-35. Much of the die is taken up with wiring, though the wires could be spaced more closely together if needed. The bow in the cover plate causes the changing shadow pattern across the array, indicating the center will be pressed down as desired when the cover is glued, so that the entire cover will be held flat against the mirror support frame. Figure 5-36 shows a close-up view of the cover flipped over on top of the array. Note that only the gold-covered surfaces of the mirrors are visible; the rest of the surface is flat except for the *poly0*-formed bosses that space the cover above the mirrors.

Test arrays of hexagonal mirrors on the second die explore minimum spacing between *anchor2* and *poly0* wires, minimum flexure widths, minimum edge overlap for metal to *poly2*, and stacked *poly1/poly2* mirrors for decreased sag. Portions of

these arrays are shown in Figures 2-26 and 2-27. Inspection of these test cells led to a less conservative metal overlap design rule of 1 μm , used on later designs here at AFIT. These and other test structures indicate that 1.5 μm features can be made, but not reliably on every fabrication run, though 1.75 μm features now seem reliable.

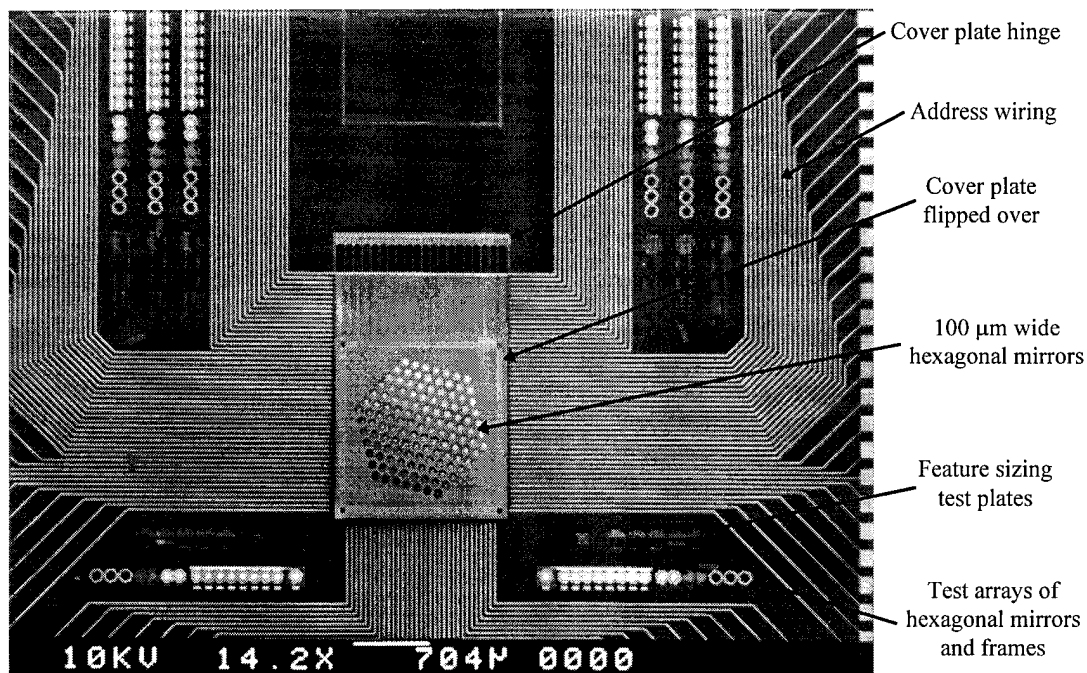


Figure 5-35. Second 127-mirror hexagonal SLM die. The cover plate is flipped over onto the array but not glued down. The individual micromirrors are 100 μm across, and the active area of the array is 1500 μm across.

All of the hexagonal test mirrors fabricated well enough to operate, despite heavy stringers on the MUMPS7 fabrication run which made the main hexagonal array unusable. This may be because the test mirrors' *poly0* wires, where the stringers formed as seen in Figure 2-39, did not run under many *poly2* features. So there was less opportunity for a stringer to short the address lines to the mirror frames.

The mirrors were tested on the probe station to determine the minimum drive voltage needed to make them deflect down fully onto their dimple stops ($1.75\text{ }\mu\text{m}$ of travel), as viewed optically from directly above.

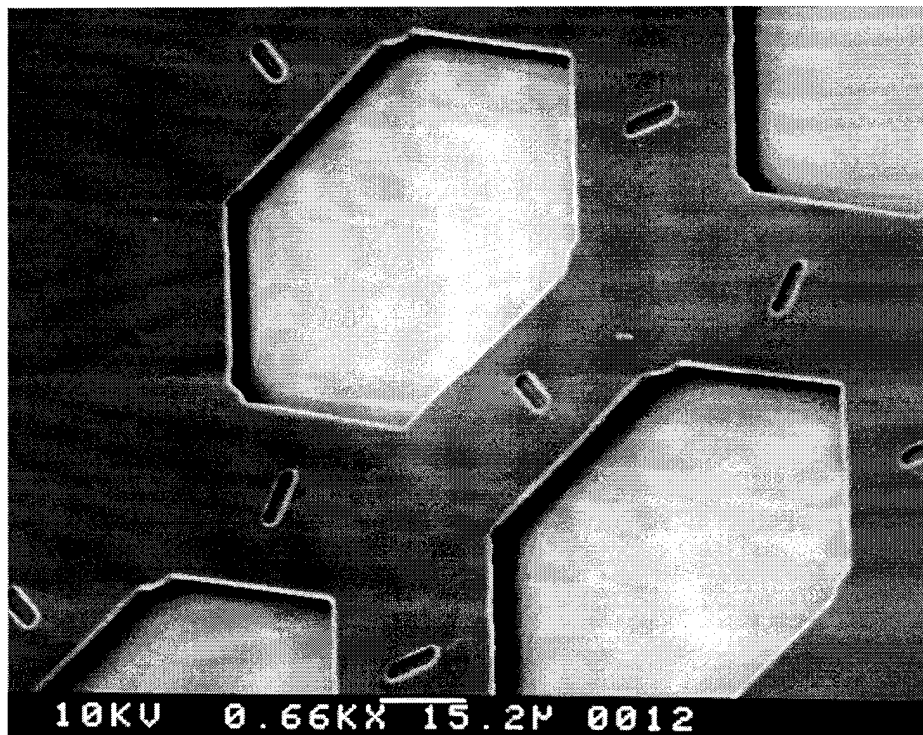


Figure 5-36. Close-up view of the *poly1* cover plate flipped over on top of the second hexagonal mirror array. Only the gold-covered surfaces of the mirrors are visible; the rest of the surface is flat except for *poly0*-formed bosses that space the cover above the mirrors.

Figure 5-37 shows a close-up of a corner of the cover plate after being flipped into place. The length of the hinge made the lateral play in the hinge pins insignificant, so the plate flipped over almost exactly into position. The plate is shown in its initial position after flipping. The substrate wires are *poly0/poly2/gold* up to the edge of the cover plate. They continue on to the mirror electrodes as plain

poly0, but their paths can still be seen by the topology they induce in the overlying *poly2* mirror frame. Figure 4-6 shows an analogous view of the address wires running under the mirror frame on the first hexagonal SLM die.

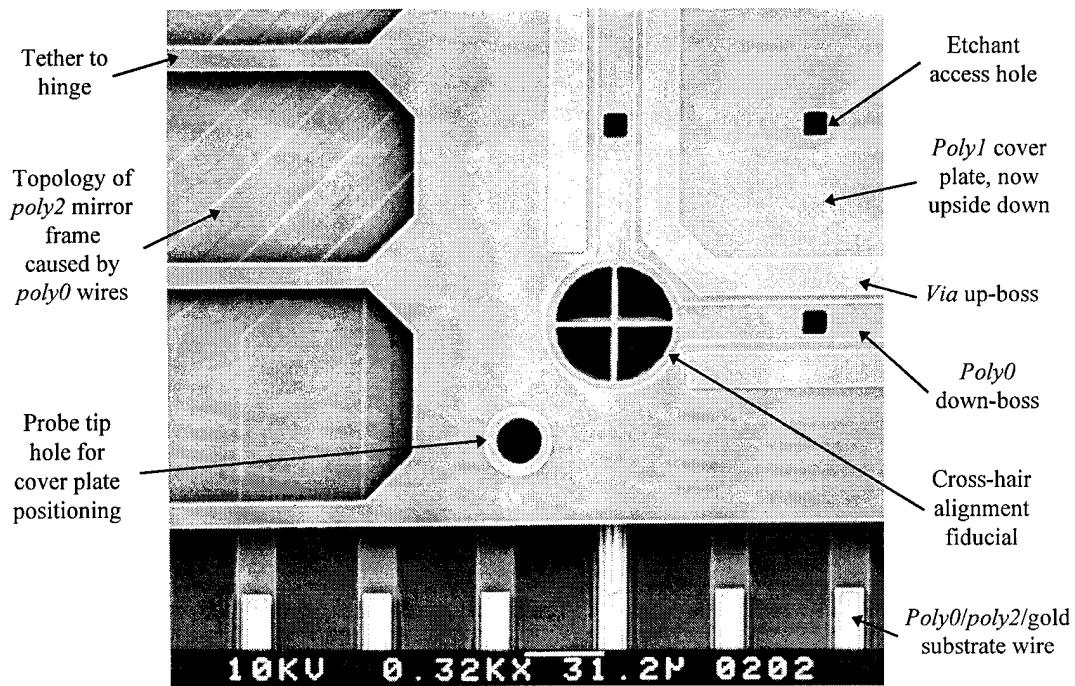


Figure 5-37. Corner of the cover plate on the second hexagonal SLM die. The cover plate is flipped over into almost exact alignment. Fiducial is 50 μm in diameter with 2 μm wide cross-hairs.

The 50 μm hexagonal mirrors in the first SLM had operated at 45 V, with 30 V for the larger 75 μm mirrors in the test array on that die. One of the reasons for going to the larger, 100 μm mirror was to lower the drive voltage even more, to 15 V. The drive voltage versus flexure width results for the 100 μm hexagonal test mirrors are summarized in Figure 5-38.

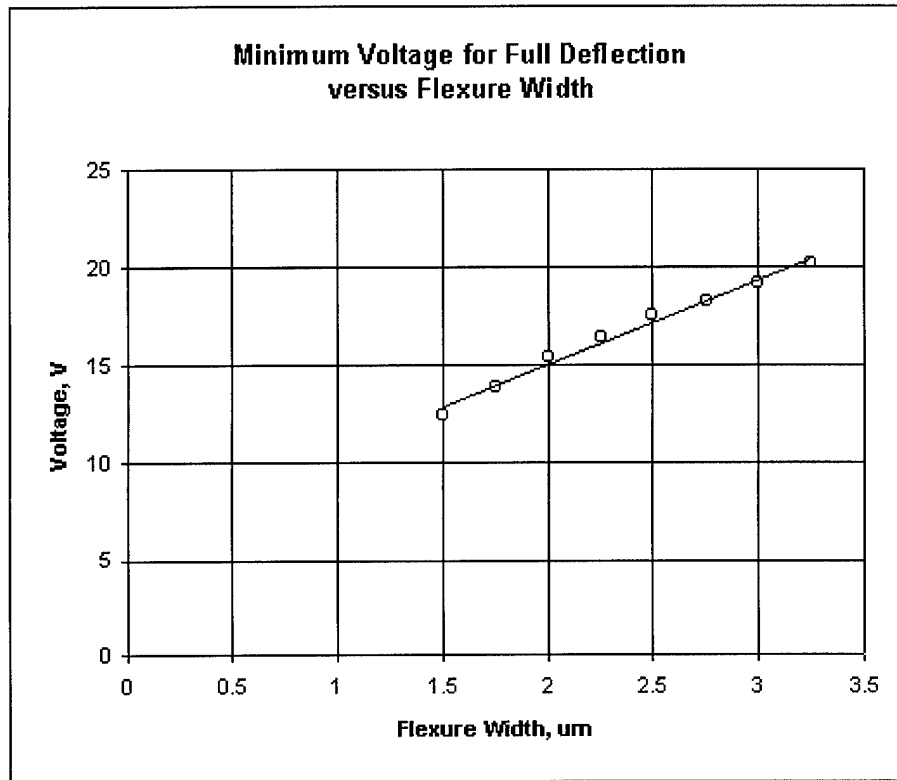


Figure 5-38. Minimum voltage needed to fully deflect 100 μm hexagonal test mirrors with different flexure widths. Full deflection for this test is defined as the mirror moving all the way down onto its dimple stops, a distance of 1.75 μm . Flexures are *poly2*, 1.5 μm thick and 94.5 μm long. Trend line is a linear fit to the data.

The *dimple* down-stops at the inside ends of the *poly2* flexures allowed the 100 μm mirrors to withstand drive voltages up to 52.25V before sagging and shorting to the *poly0* lower electrode. The linear relationship seen in Figure 5-38 reflects the linear dependence of a beam's width to the force needed to deflect it, as seen in Equation (3-3). For the vertical motion of this mirror, the width of the beam corresponds to the variable h in that equation.

Also on this die were structures to test the limits of the design rules for minimum size of the *dimple*, *hole1*, *hole2*, *anchor1*, and *anchor2* features, and bosses formed by *poly0*. Figure 5-39 shows all the test plates, and Figure 5-40 shows a

close-up of the *anchor2* test plate. SEM photos of these plates serve as a visual guide showing how the different sized features can be expected to fabricate.

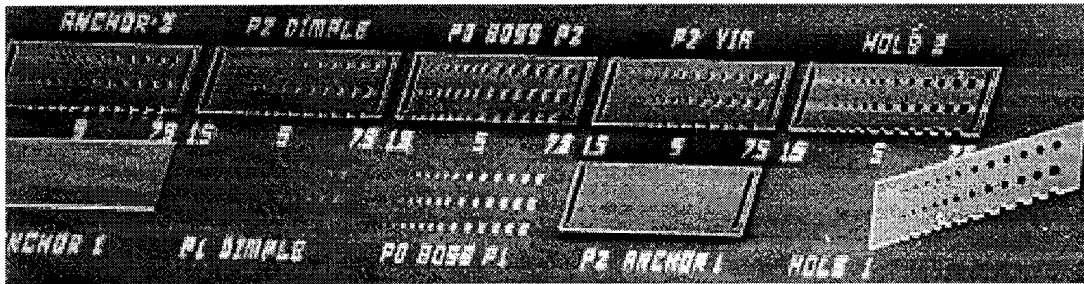


Figure 5-39. Test structures on the second hexagonal SLM die. Plates have the labeled features in sizes from 1.5 to 7.5 μm in 0.5 μm increments. One round and one square set of features are in the center of the plate. A third, square set is drawn overlapping the edge of the plate, so when the plate edge is patterned by RIE it forms a cross-sectional view. The *poly1* plates have washed off because the *anchor1* features were not fabricated on this die in the MUMPS7 run.

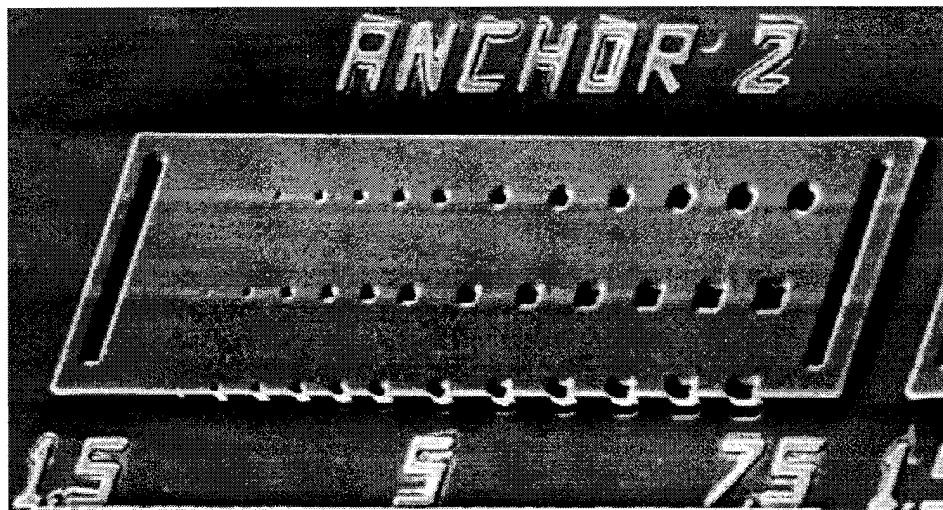


Figure 5-40. Test structure on the second hexagonal SLM die. This *poly2* plate shows *anchor2* features fabricated from 1.5 to 7.5 μm across, in 0.5 μm increments. This plate indicates that *anchor2* can be fabricated solidly down to 3 μm . Notice the heavy stringers around the *poly0* labels.

The minimum feature sizes that can be expected to fabricate, based on these test plates, are listed in Table 5-1. These minimum sizes are less than the minimum widths that MCNC guarantees [25], also listed in Table 5-1, so they should be used with that caveat. The MCNC design rules do not appear to be too far from what this test indicates the minimum dimensions can be. However, in densely packed designs it is often important to get all features as close together as possible. This is especially true in mirror arrays, where space lost to anchors, for example, directly detracts from optical efficiency.

Table 5-1. Minimum Dimensions Successfully Fabricated on the MUMPS8 Run.

Interacting Masks or Material Layers	Minimum Observed Width, μm	MCNC Design Rule Specifications, μm
<i>Poly0</i>	1.5	2
<i>Poly0 - Poly2</i>	1.5	2
<i>Anchor2 - Poly2</i>	3	4
<i>P1P2Via - Poly2</i>	3	4
<i>Dimple - Poly2</i>	3	not specified
<i>Hole2 - Poly2</i>	1.5	2
<i>Hole1 - Poly1</i>	1.5	2

Situations rarely arise where the features have to be pushed this small, and usually the feature is not an absolute necessity: small bosses on narrow tethers or small dimples on closely packed mirrors. Certainly, a 3 μm anchor should not be required to hold a large plate down, except for cases where it is intended to break free in operation, and usually there are more reliable ways to accomplish this, with fusible links, for example.

Dimples are not specified for the *poly2* layer, though that is where they have been most often needed with mirror designs, which is what prompted this investigation. Once the *dimpled poly2* plate was drawn, however, it was a simple task to copy and change layers to get the other test plates, and there was room on the die going to waste, so they were also built. This is how many of the test structures seen throughout this dissertation came about, as extensions to the main investigations, drawn to fill in the die.

5.2.2.4 MUMPS Holographic Data Storage Mirror Array

The next whole-die system opportunity was also an optical application: the idea was to see if it was feasible to replace a slower liquid crystal matrix used to encode the data in a holographic data storage system [26]. With the experience gained from the hexagonal mirror array designs and drawings, this system was extremely simple to design and draw.

5.2.2.4.1 First Holographic Mirror Array Design

At first, no number of mirrors was specified, so 80 μm wide octagonal mirrors were chosen, for several reasons. The octagonal shape was used so the mirrors could be packed along the main diagonal of the die, to get the longest possible linear array. The hexagonal mirrors were not re-used because they don't pack closely at 45 degrees. The spot shone on each mirror was assumed to be round, so regular

octagons of the largest releasable diameter were used. 80 μm was chosen as a conservative size which could be released fully without etch holes. The octagonal shape has no 30 degree angles like the hexagons, each of the four flexures would have the same length of 90 and 45 degree sections, so they would deflect vertically. Address line stubs were also used to ensure flexure uniformity.

Figure 5-41 shows the layout plot of a single 80 μm mirror, which was drawn as just a quarter, then copied around to make up the entire mirror. 133 mirrors of this size can be arrayed along each main diagonal of a 1 cm^2 MUMPS die, as seen in the layout plot of the die in Figure 5-42.

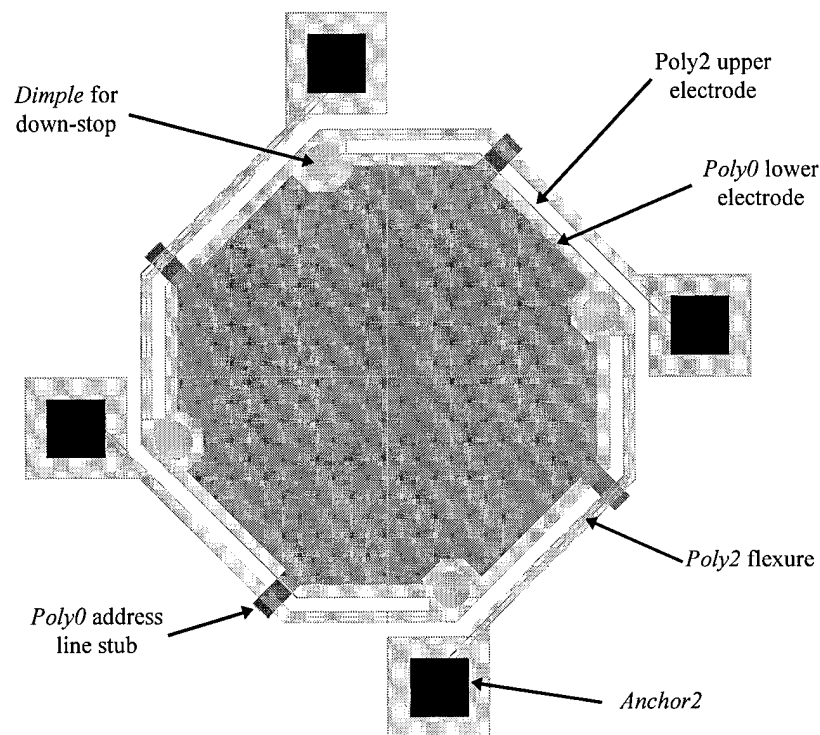


Figure 5-41. Octagonal piston mirror. The mirror is 80 μm across, and the flexures are 2 μm wide, 62 μm long. Address line stubs are used to give all the flexures the same topology. Only $\frac{1}{4}$ of the mirror is drawn, then copied around to make the entire mirror; the edge lines of the quarter subcell can be seen crossing the mirror layout.

Since the mirrors are regular octagons, they can be arrayed on both diagonals, forming a large X on the die. The two arrays share one set of bondpads, resulting in two test arrays that only have to be bonded out once. This was a major concern after the experience of wire bonding the first hexagonal SLM die. On good days the wire bonder would run for 50 or more bonds, but on bad days it might only do 2 before breaking the wire, requiring finicky re-threading of the 1 mil gold wire.

So time that could be saved at the bonding stage would be worth any amount of extra drawing time. Therefore, each bond pad runs to two mirrors through a network of substrate wires that covered the entire die in a grid, as seen in Figure 5-42. The entire die is symmetrical, so only half had to be drawn, plus some small details around the center mirror which is shared by both arrays, and at the corners, where the MCNC test resonator had to be accommodated. In the spaces between the wires, arrays of octagonal mirrors were laid out to test different mirror shapes and flexure lengths.

Figure 5-43 shows a section of the first holographic storage mirror array layout, illustrating how the mirrors are stacked and wired. Each address line connects to the lower electrode of two mirrors, one in each of the arrays that run along the main diagonals of the die. The die is symmetrical, so only half of it had to be drawn; therefore every other mirror is either a feed-through mirror for an address line or the terminal mirror on the address line.

The first array was fabricated on the MUMPS8 run, which came back with high metal stress and heavy stringers. These flaws made the main array and most of the

test mirrors unusable. While the first die was in fabrication, though, another die was being designed which superseded it, but built on the experience gained with this first die, especially the wiring style.

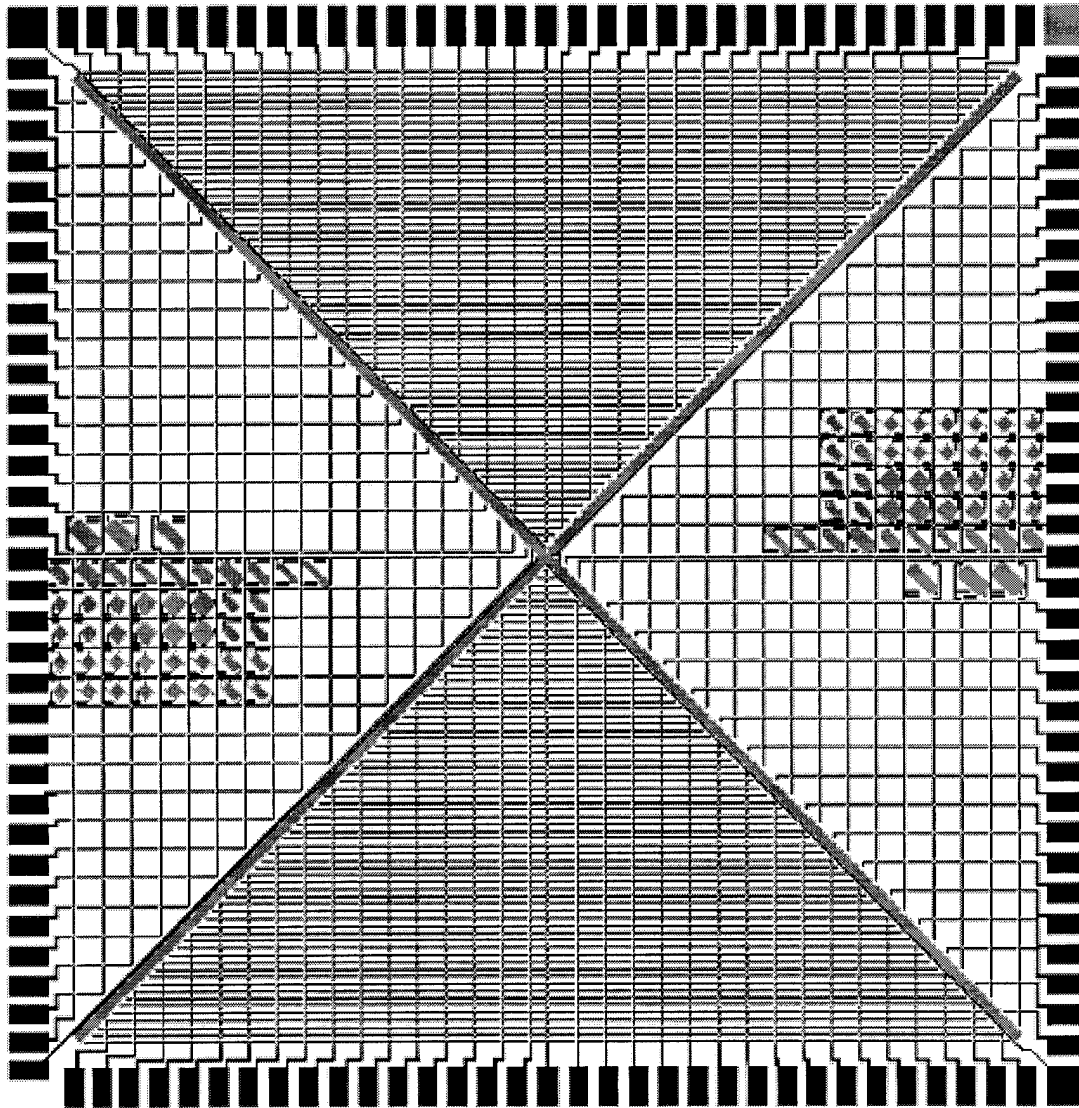


Figure 5-42. First linear micromirror array for the holographic storage project. This die was a feasibility test for making such a large array in the MUMPS process. The 1 cm² die has two 133 mirror arrays of 80 μ m wide octagonal piston mirrors running down the main diagonals. Each pad addresses one mirror of each array. On the left and right sides are test mirrors of various sizes and flexure lengths, worked into the spaces between the address wires.

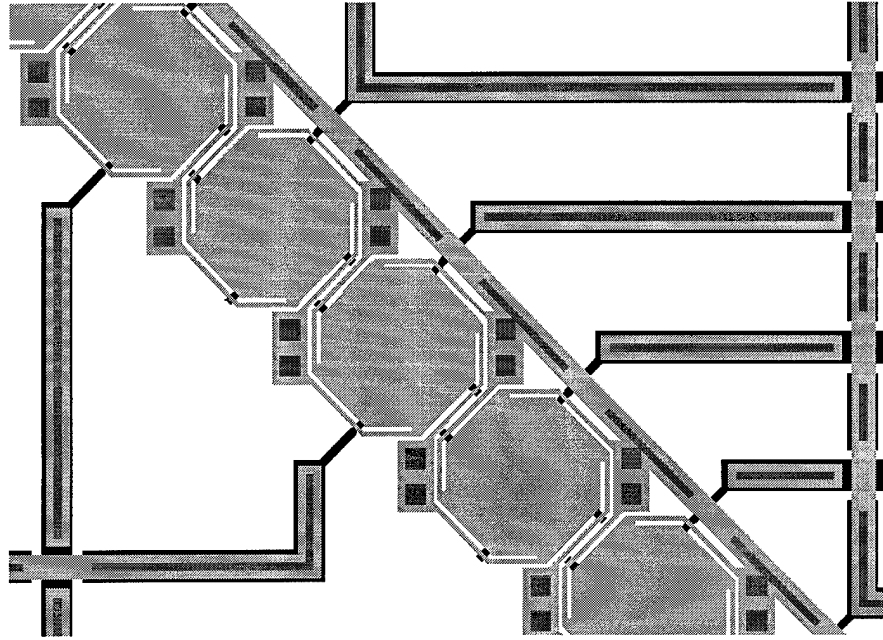


Figure 5-43. Section of the first holographic storage mirror array layout showing how the mirrors are stacked and wired. Each address line connects to the lower electrode of two mirrors, one in each of the arrays that run along the main diagonals of the die. The die is symmetrical, so every other mirror is either a feed-through mirror for an address line or the terminal mirror on the address line.

5.2.2.4.2 Second Holographic Mirror Array Design

The second die was designed because more information was available on what was required of the mirrors. The mirrors in the array were to be placed as close together as possible, and their shape did not matter. The total number of mirrors needed was 256. To accommodate this many, the fundamental design of the mirror was changed. Originally, for lack of better information, it was assumed that the light would hit each mirror as a spot, so the mirror was made close to circular, and the flexures were placed all around the outside. But to fit 256 mirrors in a row would require that no space in the array be lost to flexures and their attendant gaps.

The new mirrors were made as $50 \times 80 \mu\text{m}$ rectangles. This allowed the use of all rectangular features, which are much simpler to draw and manipulate than non-rectangular ones. The mirrors were laid out rectangulary on the screen, then rotated 45 degrees after all the features were drawn. The flexures were run to the corners of the rectangle on the sides facing out from the array, so any additional space needed by the flexures would not add to critical dimension, in the direction of packing. With no constraint on the width of the array, the mirror and flexures could be made as long as needed, to ensure a lower drive voltage, but not so long that the mirror would sag. The new rectangular design is shown in Figure 5-44.

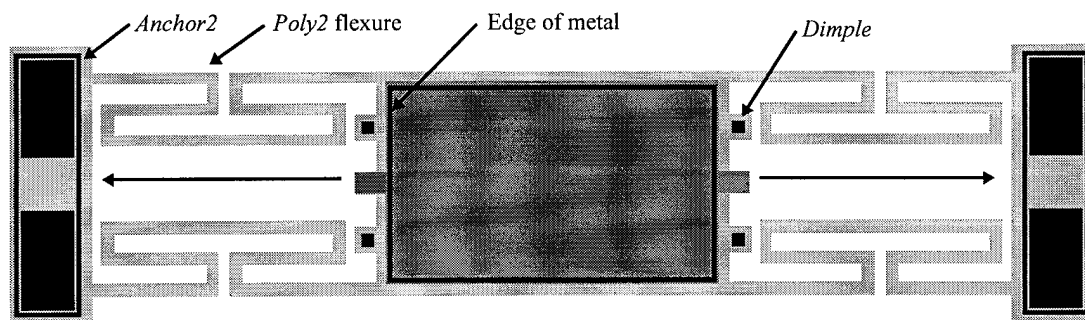


Figure 5-44. Rectangular piston mirror for the second holographic storage array. The mirror's *poly2* upper electrode is $50 \times 80 \mu\text{m}$. The four $2 \mu\text{m}$ wide *poly2* flexures are $188 \mu\text{m}$ long. Dimples at the mirror sides prevent the mirror from shorting when fully deflected. Address line can run under the *poly2* anchor/ground rail between the *anchor2* on either side, as indicated by the arrows.

These mirrors cannot be arrayed along both diagonals as with the octagonal mirrors of the first die, because the center mirror cannot be shared. So the second holographic storage array die has only a single array. The mirrors are still drawn as a $\frac{1}{4}$ cell which is copied around to form the entire mirror. The die was also drawn as

two identical halves. The half-cell was drawn with only every second mirror in place, and their associated address wires and bond pads. The whole die was then formed by copying the half-cell and rotating it 180 degrees. The mirrors of the second half then filled in the spaces between the mirror of the first half, filling out the array.

The mirror cells form a rail down either side of the array which anchors the mirrors, thus connecting all the *poly2* upper electrodes to a common ground. These rails have four connections to bondpads, providing redundancy for this important connection since it is easy to accidentally break the tall *poly2* wires when probing the die. The address lines for each individual mirror run from the bondpads to the outside of the frame in standard *poly0/poly2*/gold substrate wires, then continue under the frame between anchors to the *poly0* lower electrode.

Test cells were drawn on the other main diagonal of the array half-cell, so when it was copied, all of the test cells were copied also. The test cells are variations of mirrors that can tilt in any direction as well as piston. The second array is shown in Figure 5-45.

For this design, an analytical model was available to compute the flexure length needed so the mirrors would deflect a given amount at a given voltage [24]. The full model incorporates the effects of cross-talk from neighboring mirrors, ambient temperature, fringing electric fields around the edge of the mirror, and deformations of the mirror surface. However, for mirrors with an edge-to-edge separation of 2 μm , the cross-talk is negligible. Ignoring thermal and fringing effects, which are also minor for mirrors this large, and ignoring sagging of the mirror surface due to

gravitational or electrostatic forces, the address voltage versus displacement model simplifies to Equation (5-1) [21].

$$V = (z_0 - d_f) \sqrt{\frac{2kd_f}{\epsilon_0 A}} \quad (5-1)$$

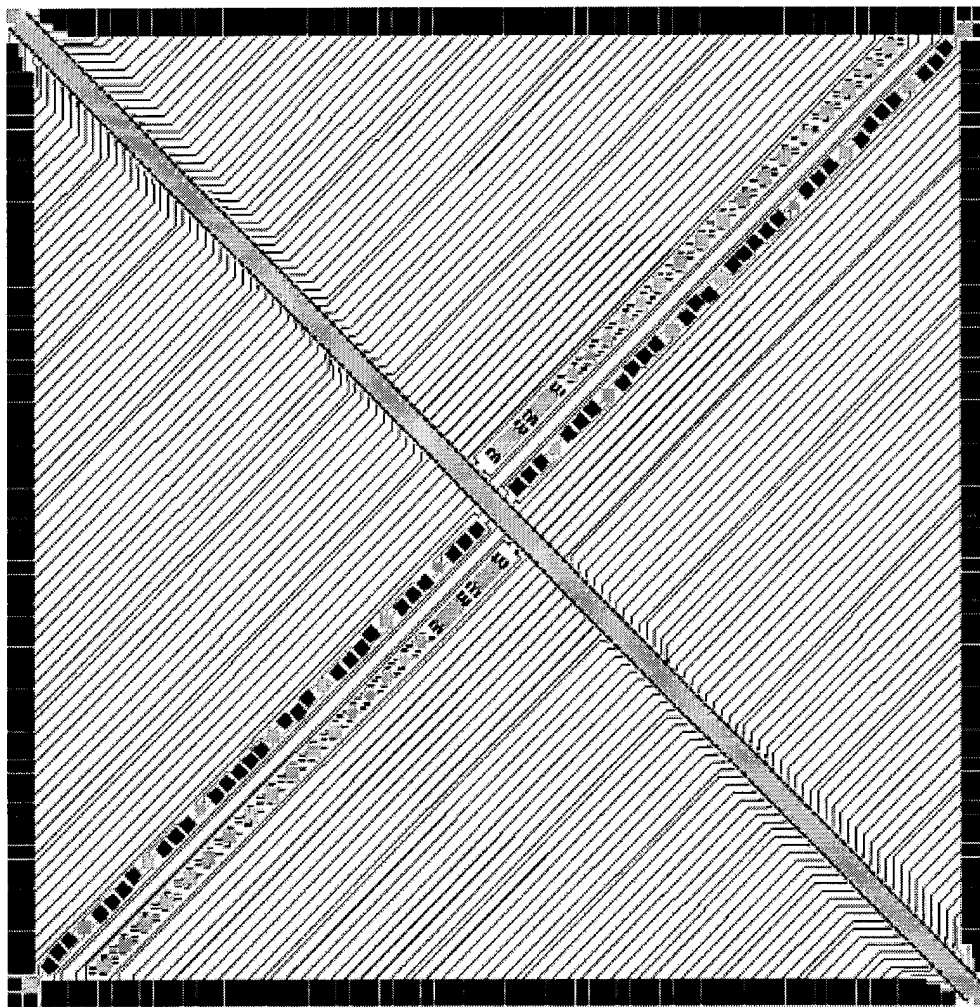


Figure 5-45. Second holographic storage mirror array die. Array contains 256 mirrors in the main array, running from upper left to lower right. Each 50 x 80 μm mirror is individually addressable from a separate bond pad. Test mirrors run along the other diagonal. Bondpads at the ends of the main array are substrate contacts.

In Equation (5-1), V is the address voltage, z_0 is the resting separation between the bottom of the mirror and the addressing electrode, d_f is the desired downward mirror displacement from this resting position, ϵ_0 is the free space dielectric constant, and A is the micromirror area. The k term, given in Equation (5-2), is a spring constant which accounts for the number and geometry of the mirror flexures. In Equation (5-2), '4' is the number of flexures, and L , w , t , and E are the length, width, thickness, and modulus of elasticity for the flexure beam, respectively. This equation, which is just the basic cantilever force relationship of Equation (3-3), does not account for the bends in the flexures or stresses in the material, just the total length and cross-section.

$$k = 4 \left[\frac{Ewt^3}{L^3} \right] \quad (5-2)$$

For *poly2* piston mirrors with 2 μm wide flexures, Equation (5-1) is plotted in Figure 5-46 for various flexure lengths. The other variables are: $\epsilon_0 = 8.85 \times 10^{-12}$ F/m, $z_0 = 2.75 \mu\text{m}$, $E = 160$ GPa, $t = 1.5 \mu\text{m}$, and $A = 3.5 \times 10^{-9}$ m², the area of the *poly0* addressing electrode which is 46 x 76 μm .

For the second mirror design, the target drive voltage was 12 V for a 400 nm deflection. Figure 5-46 indicates a flexure length of at least 160 μm would be required. The lengths as actually drawn were 188 μm . They were made slightly longer because the flexures have bends which increase their stiffness, but the available model could not take this into account, though these modifications were

added later [13]. The flexures face each other across the mirror, so the mirror cannot rotate slightly as it goes down, as the spiral-armed hexagonal or octagonal mirrors can, which also increases the force needed. Testing shows that this mirror design deflects all the way down at 18.5 V, but no data has yet been taken on the voltage needed to deflect just $0.4\text{ }\mu\text{m}$ to compare with the prediction.

The second holographic storage mirror array is currently being integrated into a test system to evaluate its performance as a phase modulator. Even while the second revision is being tested, a third revision was designed to take advantage of advances in microlens fabrication, and to look into the possibility of operating the mirrors in a binary fashion to make their deflection independent of the drive voltage, as long as the voltage is high enough to deflect them fully.

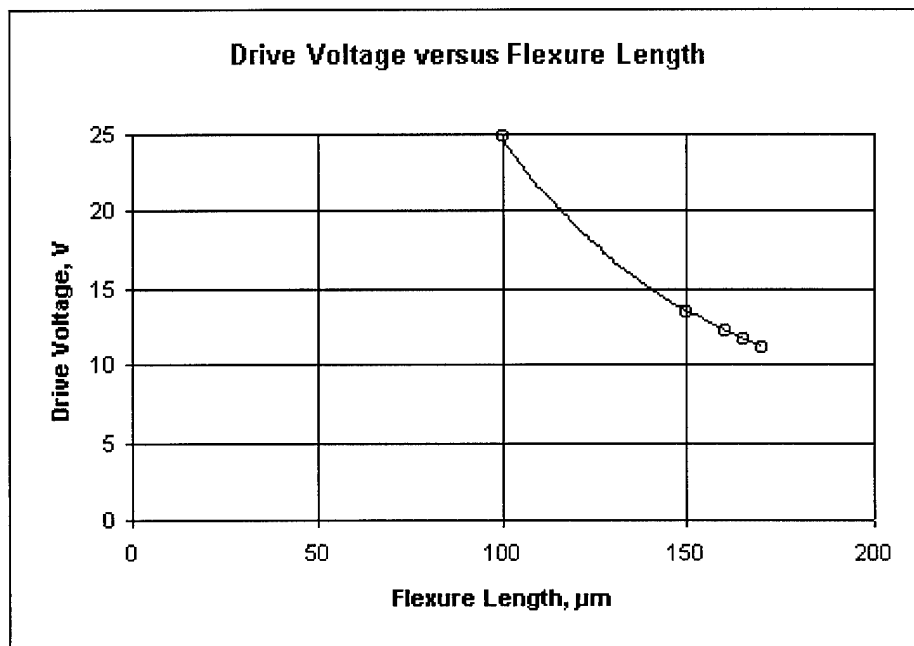


Figure 5-46. Plot of Equation (5-1) for the $50 \times 80\text{ }\mu\text{m}$ rectangular *poly2* piston mirror of Figure 5-44.

5.2.2.4.3 Third Holographic Mirror Array Design

To capture more of the incident light falling on the array a plan was made to place a microfabricated lenslet array over the mirrors. One side effect of the lenses is that the spot size focused on the mirrors will be only 3 μm , much smaller than the 50 μm width of the current mirrors. Rather than jump right in and make an array with more and smaller mirrors, it was decided to just make the metallized portion of each mirror smaller. So for the third revision, the mirrors are 10 μm diameter circles in the center of the existing *poly2* upper electrode. This will eliminate the chance of the mirrors being warped in case the metal stress was high again. Not changing the number of mirrors also made it very simple to modify the design, since only parts of the one mirror subcell had to be changed.

There are two variations of the third revision mirror design, involving the down-stops and their placement. The first variation uses the regular dimples for down stops, but places some closer to the smaller mirrored circle to reduce sag. The other revision uses *poly1* posts to limit the travel of the mirror plate to 0.75 μm . This will enable it to withstand higher maximum drive voltages, but that was not the primary consideration.

The main idea is to use the mirror in a binary mode, where the mirror is either undeflected, or fully deflected at 0.75 μm . This eliminates the problem of calibrating the mirror drive voltage to deflect the mirror some desired amount, such as $\frac{1}{4}$ of the wavelength of the laser being used. The drive voltage can be any voltage higher than

the one that drives the mirror fully down on its stops, so there can be a wide error margin instead of none.

For a binary mirror, it would be best if the exact amount of downward deflection could be designed, so that the deflection were exactly $\frac{1}{4}$ wavelength of the laser, for example, but that is not possible in the MUMPS process, so this is just a proof of concept design. It would be the thickness of the *oxide2* layer which sets the deflection distance of this type of binary mirror. Figure 5-47 shows the two mirror variations for the third revision.

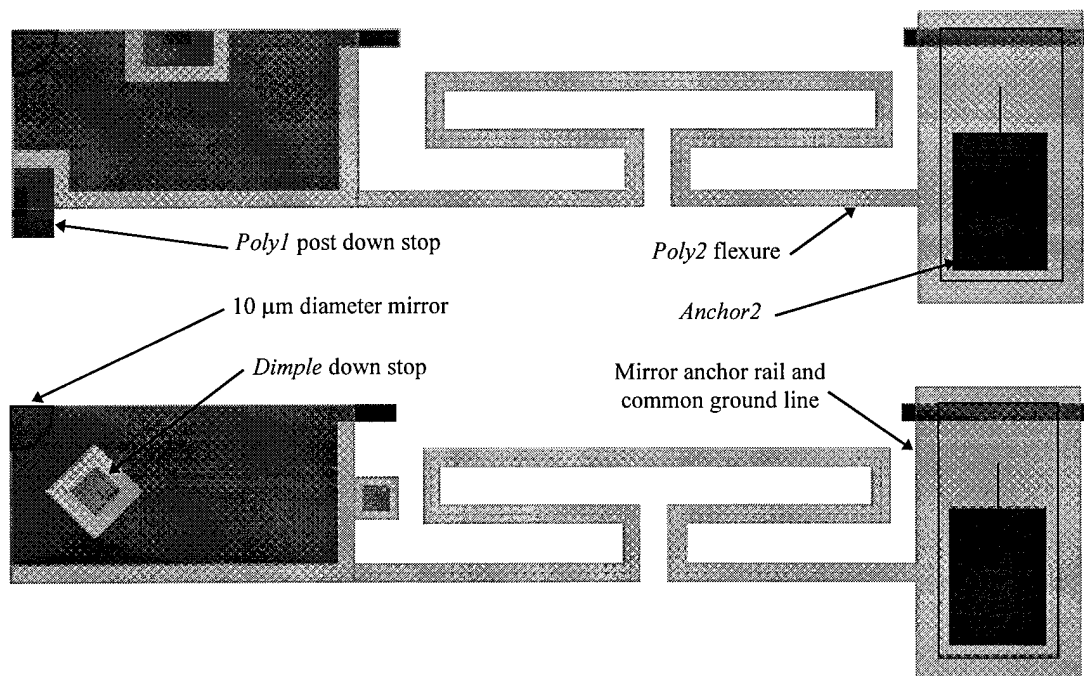


Figure 5-47. Two variations of the piston mirror for the third holographic storage array. These are the $\frac{1}{4}$ subcells; four of these are copied around to form the entire mirror, which has the same general outline as the mirror in Figure 5-44.

The rest of the die is unchanged except for the addition of standoff posts for the lenslet array. These posts are incorporated into the *poly2* ground rails that run down either side of the mirror array. The rails are the anchors for the mirror flexures, the common ground line, and now the support for the lenslet array also. The posts are formed with small squares of *poly1* suspended under the regular *poly2* rail by vias. The *poly0* address lines pass under the posts, which are located between the *anchor2* areas of the rail.

The posts add 2 μm of height to the rail to keep the bottom of the lenslet array substrate from touching the piston mirrors. The thickness of the lenslet substrate should therefore be sized for the proper focal length, since that length cannot be set by the posts, which are already as tall a structure as can be made in the MUMPS process.

5.2.2.4.4 Toward Larger Mirror Arrays

One reason for not having more mirrors in the array is the limitation on the number of bondpads that can be fit around the perimeter of the die. Large bondpads have been used on AFIT die because they have to be manually wirebonded, and the larger, rectangular pads allow for several retries if needed. A 250 μm center-to-center spacing is normally used, though this was reduced to 150 μm to accommodate the 256 mirror array. Even at a denser 80 μm pitch, only 496 pads could be fit in a single row around the perimeter.

An increase in the number of individually addressable mirrors would require a different connection besides wirebonding, or getting more of the address circuitry onto the die so fewer off-die connections are needed. The latter is not an option for MUMPS, so a denser connection technology would be needed. The High Density Interconnect (HDI) technology, to be discussed in Chapter 6, allows wiring to be brought directly over a die. For die connections spaced every 150 μm across the 1 cm^2 MUMPS die, HDI could connect over 4,000 pads.

Realistically, electrostatic mirrors would probably have to be at least 20 μm wide to keep the drive voltage low, unless they were made very wide and used in a binary fashion, so the sag would not affect them. So a more practical upper limit on electrostatic piston mirrors in a linear array on a MUMPS die is 640; still more than can be adequately handled by wirebonding.

A mirror that might allow denser packing than this was fabricated as a test device on the third holographic mirror array die. This mirror is a thermally actuated device that can be made much narrower than electrostatic devices because its operation does not require the large actuator area of the electrostatic piston mirrors.

The thermal mirror is based on the ladder-bridge vertical actuator shown in Figure 3-34. The layout drawing of the mirror array test cell version is shown in Figure 5-48. A *poly0* plate under the mirrored center of the actuator bridge bosses the bridge up, giving it a tendency to bow upwards instead of downwards as the beams expand.

These thermal mirrors have the same advantages and disadvantages over electrostatic piston mirrors that the lateral thermal actuators have over electrostatic comb drives. They use more power and move more slowly, but they are much smaller and use much lower drive voltages. This means that many more can be packed onto a diagonal array, and they can be driven with standard CMOS circuitry.

These mirrors were tested on the probe station and observed to move vertically about 1.5 to 2 μm at 2.75 V and 10.8 mA. At 3 V and 11.5 mA the gold gets hot enough to melt, but for the smaller deflections needed for phase optics, these extreme temperatures would not be approached. As an example, consider a 600 nm laser and a mirror that needs to move $\frac{1}{4}$ wavelength, or 150 nm. Assuming a linear relationship for the voltage and current versus deflection characteristic, which actually overestimates the power based on the curves found for the lateral thermal actuators, then interpolating from the results given above, this particular mirror design would require only 0.21 V at 0.81 mA, or 167 μW , to move 150 nm. For a 512 mirror array, the total power drain would be only 85 mW if all the mirrors actuated simultaneously.

These mirrors could be made as narrow as desired, down to 5 μm at an extreme, and still have some gold on them. However, the operating voltage of the mirror would depend on the resistance of the wire supplying the current as well as the resistance of the actuator itself, so substrate wires with gold on them would have to be used, which makes the minimum width 10 μm . Any lengths of plain polysilicon wire in the address lines would have to be the same for all the mirrors.

The length and width of the actuator and its legs can be used to design for a specific operating voltage range to match the drive circuitry. The only other unknown at this time is the effects of thermal cross-talk, but this can be measured with the existing laser interferometer used for the electrostatic mirror tests [13].

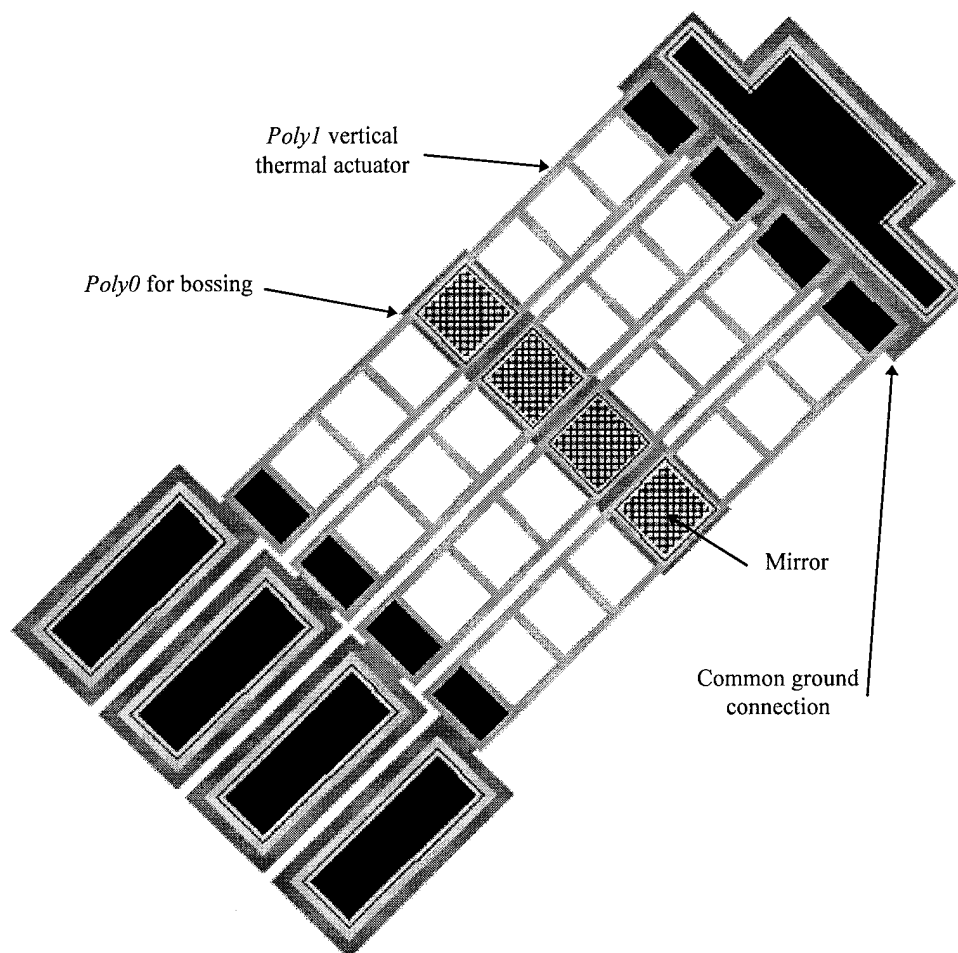


Figure 5-48. Thermally actuated mirrors for large linear arrays. These actuators can be made in *poly1* or *poly2*, with different lengths and widths to adjust the operating current and voltage or mirror size and spacing.

5.3 Conclusions

The devices and systems presented in this chapter bear out the utility of the concepts, devices and techniques developed during this research for enabling the design of practical, large and complex MEMS structures. Even though the devices themselves were sometimes poorly designed or fabricated or quickly superseded, the basic techniques used could be transferred easily to the newer designs. The thermal actuators provide the force needed to operate large devices, and the substrate wiring has the capacity and flexibility to deliver current for those actuators whether they are on the substrate or on a hinged plate.

The large optical arrays demonstrate that factors beyond the design rules and material properties need to be considered when moving from single micro-opto-electro-mechanical (MOEM) device designs to large arrays of devices. Specifically, the mask-making process, process uniformity, on-chip wiring, and packaging considerations become important as the designer moves to large arrays of devices. Systems that require some manual assembly benefit from any steps taken to make the assembly process more precise. Very large released structures must take into account the bowing of the material due to the residual stress, even if the stress is extremely low.

In a surface-micromachining process such as MUMPS, considerable die space must be allowed for wiring large numbers of devices. As the devices get smaller, the wires and number of bondpads begin to limit the size of arrays that can be built. The

solution to the limitation in wiring and connections on the die of the LIGA and MUMPS processes cannot currently be solved by integrating the drive and control electronics onto the die. For these foundry processes, the solution must come from the outside in the form of denser packaging of the MEMS die with their associated electronic control die, the topic of the next chapter.

References

1. First MUMPS User's Group Meeting, Chicago, IL, Organized by the MCNC MEMS Technology Applications Center, Research Triangle Park, NC, presentation material and notes, Oct. 21, 1994.
2. H. Slocum, "Precision machine design: macromachine design philosophy and its applicability to the design of micromachines," *Proc. Micro Electro Mechanical Systems '92*, Travemunde, Germany, pp. 37-42, February 4-7 1992.
3. Gabriele Mazzotta, L' Architettura Della Macchine, Foro Buonaparte 52-20121 Milano: G&R Associati, Plate XLIX, 1983.
4. M. Phipps, "Design and development of microswitches for micro-electro-mechanical relay matrices," Master's Thesis, Air Force Institute of Technology, Wright-Patterson AFB, Ohio, AFIT/GE/ENG/95J-02, June 1995.
5. J. Drake, H. Jerman, B. Lutze and M. Stuber, "An electrostatically actuated micro-relay," *Proc. Transducers '95/Eurosensors IX*, Stockholm, Sweden, Vol. 2, pp. 380-383, 25-29 June 1995.
6. J. Jason and M. Chang, "A surface micromachined miniature switch for telecommunications applications with signal frequencies from DC up to 4 GHz," *Proc. Transducers '95/Eurosensors IX*, Stockholm, Sweden, Vol. 1, pp. 384-387, 25-29 June 1995.
7. K. Shaw, Z. Zhang and N. MacDonald, "SCREAM I: a single mask, single-crystal silicon process for microelectromechanical structures," *Sensors and Actuators A*, Vol. 40, pp. 63-70, 1994.
8. R. Yeh and K. Pister, "Measurement of static friction in mechanical couplings of articulated microrobots," *Proc. SPIE Micromachined Devices and Components*, Vol. 2642, Austin TX, pp. 40-50, 23-24 October 1995.
9. P. Indermuhle, V. Jaeklin, J. Brugger, C. Linder and N. deRoosj, "AFM imaging with an XY-micropositioner with integrated tip," *Sensors and Actuators A*, Vol. 46-47, pp. 562-565, 1995.

10. V. Jaeklin, C. Linder and N. DeRooij, "Novel polysilicon comb actuators for XY-stages," *Proc. Micro Electro Mechanical Systems '92*, Travemunde, Germany, pp. 147-149, February 4-7 1992.
11. K. Brendley and R. Steeb, Military Applications of Microelectromechanical Systems, RAND report to the Office of the Secretary of Defense, United States Air Force, United States Army, RAND, Santa Monica, CA, 1993.
12. G. Fedder and R. Howe, "Thermal assembly of polysilicon microstructures," *Proc. IEEE Workshop on Micro Electro Mechanical Systems*, Nara, Japan, pp. 63-68, 1991.
13. D. Sene, "Design, fabrication, and characterization of micro-opto-electro-mechanical systems," Master's Thesis, Air Force Institute of Technology, Wright-Patterson AFB, Ohio, AFIT/GEO/ENP/95D-03, Dec 1995.
14. R. Furlan and J. Zemel, "Comparison of wall attachment and jet deflection microfluidic amplifiers," *Proc. IEEE MEMS-96 Workshop*, San Diego, CA, pp. 372-377, 11-15 Feb. 1996.
15. Private conversation with J. Lyke of the Applied Microelectronics Branch, Space Electronics Division, Space Missile Technology Directorate, Phillips Laboratory, Kirtland AFB, NM.
16. B. Read, "Silicon based microactuators for telerobotic tactile stimulation," Master's Thesis, Air Force Institute of Technology, Wright-Patterson AFB, Ohio, AFIT/GE/ENG/94D-25, Dec 1994.
17. J. Marshall, M. Parameswaran, M. Zaghloul and M. Gaitan, "High-level CAD melds micromachined devices with foundries", *Circuits and Devices*, Vol. 8, No. 6, pp. 10-17, November 1992.
18. R. Boysel, J. Florence and W. Wu, "Deformable mirror light modulators for image processing," *Proc. SPIE*, Vol. 1151, pp. 183-194, 1989.
19. L. Hornbeck, "Deformable mirror spatial light modulators," *Proc. SPIE*, Vol. 1150, pp. 86-102, 1990.
20. Proposal # R-8864, Deformable Mirror Devices, prepared by S. Gustafson in response to Department of the Air Force, Wright Laboratory, Wright-Patterson AFB, OH, RFP # F33615-92-R-1120, 15 October 1992.

21. J. Comtois, V. Bright, S. Gustafson and M. Michalicek, "Implementation of hexagonal micromirror arrays as phase mostly spatial light modulators," *Proc. SPIE Microelectronic Structures and Microelectromechanical Devices for Optical Processing and Multimedia Applications*, vol. 2641, pp. 76-87, 23-24 Oct. 1995.
22. S. Gustafson, G. Little, T. Rhoadarmer, V. Bright and J. Comtois, "Minimally Connected Piston Micromirror Light Modulator, Revision A," U.S. Patent Application No. 60/003,358 filed 7 September 1995.
23. V. Bright, J. Comtois, S. Gustafson and E. Watson, "Realizing micro-opto-electro-mechanical devices through a commercial surface micro-machining process," to be published in *Proc. SPIE 1996 International Symposium on Lasers and Integrated Optoelectronics*, San Jose, CA, 27 Jan. - 2 Feb. 1996, Invited Paper.
24. M. Michalicek, V. Bright and J. Comtois, "Design, fabrication, modeling, and testing of a surface-micromachined micromirror device," *Proc. of the 1995 ASME International Mechanical Engineering Congress and Exposition*, San Francisco, CA, 12-17 November 1995.
25. D. Koester, R. Mahedevan and K. Marcus, *Multi-User MEMS Processes (MUMPS) Introduction and Design Rules*, rev. 3, Oct 1994, MCNC MEMS Technology Applications Center, 3021 Cornwallis Road, Research Triangle Park, NC, 27709
26. S. Gustafson and G. Little, "Modulators for phase encoded reference beams in digital holographic data storage systems," *Optical Society of America Annual Meeting*, paper MEEL, 11 September 1995.

6. Packaging Systems

Most sensing applications can be performed more effectively with sophisticated devices that combine more inputs or provide more measurement resolution, in much the same way that currently available micro-controllers provide more functionality in a single package than past generations of simple microprocessors [1,2]. For example, increased control over actuation and measurement has allowed the internal combustion engine to be made more efficient, reliable and environmentally benign, as evidenced by longer service intervals, lower emissions, and more power per volume. Such integrated sophistication is not possible with most foundry fabricated MEMS processes; so given this foundry-based constraint, many potential applications remain untouched for lack of knowledge in combining multiple MEMS devices fabricated in different processes into a single package with advanced electronics.

In microelectronics, the need for combining multiple device die in a single package is increasingly being satisfied with a variety of multi-chip module technologies, both commercially established and experimental [3,4]. In these processes, multiple electronic die are mounted on a common substrate and wired together in a variety of ways to create what are essentially miniature circuit boards. This approach can greatly increase functionality for a given device area, while at the same time increasing performance. These performance increases are mostly the result of removing the parasitic circuit elements that result from interconnect structures of integrated circuit packages and the circuit boards they are mounted on. Reliability

and size advantages are also gained by eliminating one level of connectivity, the level of individually packaged die plugged into a circuit board [4].

Foundry fabricated MEMS should also be able to benefit from MCM technologies, but in an even more significant way. For electronics, an MCM allows a denser packing of devices; for MEMS, an MCM would allow new and unique combinations of different MEMS and electronic die, to provide the processing and control circuitry that cannot be placed directly on many foundry-fabricated and most specialized MEMS die. This would free the designer from having to make compromises either in the electronic or MEMS components, allowing each device to be fabricated in separate, optimized runs. Thus even simple devices that do not require an MCMs increased circuit density or performance would still benefit from the increased design flexibility that MCM packaging allows.

Most MEMS currently use the same single-die packaging as microelectronics, for the same reasons that MEMS fabrication uses the same techniques as microelectronics: the technologies are established, so material properties are well known and the costs are low. There are also a wide variety of electronic packages and applications, covering most of the needs that would also be encountered with MEMS, including optical packaging, high pin count packaging, and thermal relief packaging. Different packages are needed when the MEM devices must interact with the environment more directly by pumping fluids, manipulating objects or measuring pressure.

Pressure sensors, the oldest established commercial MEMS product, have a variety of packages, but the packages are optimized for this application. This is an indication that many MEMS, because of their specialized applications, will be forced to follow the same specialized packaging development route. But for systems where available electronic packaging techniques will suffice, more data must be gathered on how those packaging options can be applied to MEMS.

Examples of the need for integrated packaging of foundry fabricated MEMS die can be seen in some of the devices described in the previous chapters. The whole-die mirror systems are limited not only by the area needed for wiring, but also by the number of connections that can be made to the die. Denser interconnect technology would allow more electrical connections to the die, and thus more optical elements; in lieu of having the control circuitry on the die, which is not possible with the available foundry processes. Given the constraints of using only foundry processes to build up complex systems, MCMs provide the densest packaging options, and achieve nearly the same benefits as having all the devices fabricated on the same die. They also make possible the benefits of having separately fabricated and optimized electrical and mechanical die.

As an example, consider an optical measuring system incorporating the thermally actuated stepper motors described in Chapter 5 for positioning of the optical components. If there are only a few motors and optical sensing elements, the overall system might not need many connections, but would need low noise sensing circuitry, and sequencing circuitry to control the motors. So although an MCM's

dense wiring may not be taken advantage of, the other benefits of small size, low noise, and die integration for a low external connection count may make an MCM package a good economic or system integration choice. In this example, the motors' low drive voltage requirements make their control circuitry an obvious choice to include on an easily and cheaply fabricated commercial CMOS die, along with the low noise amplifying circuitry needed for the sensors, thus keeping the die count low and the die types simple. The sponsor of this dissertation research gives further reasons for research in high density packaging of MEMS, paraphrased here [5]:

One of the biggest challenges to realizing savings from MEMS is devising suitable packaging schemes to take fullest advantage of this miniaturization. Like microcircuits, the density advantage of a MEMS component can be greatly enhanced at the system level through the use of advanced packaging technology. In conventional packaging, single electronic or MEMS die are placed in individual packages, which are then mounted on boards, which in turn are mounted on back planes inside an enclosure. So, while a MEMS design may boast a significant miniaturization advantage, much of this advantage may be eroded by neglecting packaging concerns in the whole system. Not only are conventional packaging approaches inefficient from a size and weight standpoint, but they can also introduce electrical performance penalties due to excessive path lengths and the resulting parasitic resistive, capacitive and inductive elements. Highly integrated packages can also reduce the number of circuit interconnections, increasing the reliability of the overall system. Despite intense research in MEMS and high density packaging, there has been little work done on bringing these two fields together.

For this dissertation research, foundry-fabricated electronic and MEMS die were integrated in MCM packaging. This should allow an institution with no fabrication facilities to design, specify and test highly integrated and functional, commercially manufacturable MEMS. This chapter is a brief introduction to the available technologies and possibilities. For this study, two MCM packaging processes were tried, but only chemical compatibility tests could be performed. This chapter therefore presents packaging types and preliminary packaging results.

6.1 Die Interconnect Techniques

The following sections introduce the interconnection techniques used in this dissertation research and in the test MCMs. All are attempts to make a large number of reliable electrical connections in an automated process. Some emphasis is placed here on the removability of die connected with these techniques. Often, the expense of an MCM or the die in it makes it economical to replace a bad die rather than lose the entire package.

6.1.1 Wirebonding

Wire-Bonding (WB) is the oldest and still most common IC interconnection technique, and is also the most common method for connecting die in MCMs. Gold or aluminum wires are thermocompression/ultrasonically welded to the bondpads of the circuit die and the package lead frame. WB is compatible with MEMS die,

released or unreleased. There are two types of wire bonds, ball bonds and wedge bonds. The difference lies in the mechanism used to compression-weld the wires.

Figure 6-1 shows a schematic of a wire-bond being made by the 'ball-bonding' process. In a ball-bonder, the interconnect wire has a ball of metal formed on the end by an electric spark. The ball is ultrasonically compression-welded by a ceramic capillary tube onto the die pad. When the tube is lifted from the ball, the wire feeds out from the tube, then the other end of the connection is made by the edge of the tube pressing the wire to the package's lead frame pad. When the tube retracts after the second bond, the wire breaks off and a small piece of wire is left exposed at the bottom of the tube. A charged electrode is brought near this wire, and the resulting spark melts the end of the wire into a ball for the next bonding cycle.

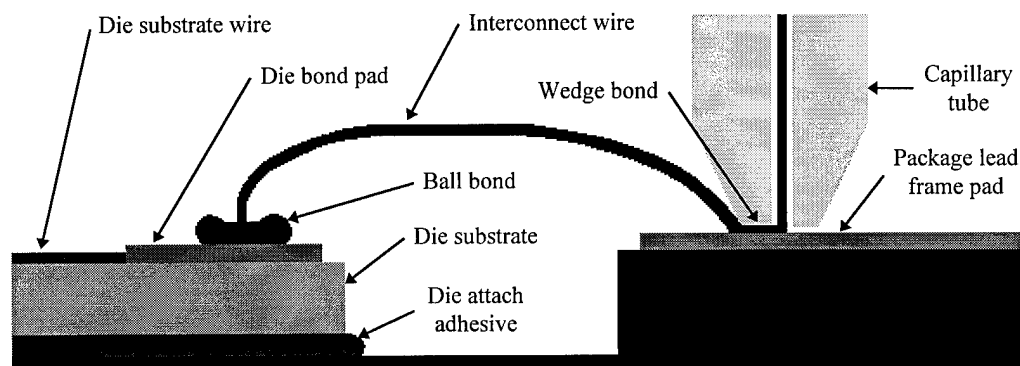


Figure 6-1. Schematic of the ball-bonding technique. The bond wire passes through a capillary tube which presses it onto the pads and applies the ultrasonically assisted compression force. The package can be vacuum clamped to a heated table to aid the bonding process.

The other wire-bonding technique is 'wedge bonding', where a metal tip is used to compression weld both ends of the bond wire, without the need for the ball formation step. Wedge bonding is the method used for most commercial packaging, but ball bonding was the technique used to connect prototype die throughout this dissertation research.

One slight disadvantage of the wirebonding process is that connections are made one after another, because the wire feeds out of the bonding machine in a single stream. Even so, an automated bonder can make these single connections in a blur of motion, making hundreds of connections a minute. Other techniques have been developed to make all die connections in parallel, but these require special masking and fabrication steps and are currently more expensive than wire-bonding, the established connection method.

6.1.2 Flip Chip

The Flip Chip (FC) technique involves placing solder bumps on the die bondpads or on the substrate landing pads; then flipping the die over and reflow-soldering to complete the connection. This technique has been investigated for application to MEMS die [6], and the first commercial foundry-fabricated MEMS flip-chip die are being introduced by MCNC on the MUMPS12 fabrication run [7]. In this initial MCNC process, an electronic die is to be flipped over on top of the MEMS die.

The electronic die is projected to contain these circuits [8]:

- Preamplifiers and buffer amplifiers
- Capacitance measurement circuitry for single and double-ended devices
- Voltage and current references
- Oscillator and clock generator.

Circuits projected for future electronic die designs include:

- Analog-to-digital and digital-to-analog converters
- University of Michigan Standard interface sensor bus
- Resistance measurement circuits.

These circuits are to be built in the Orbit Analog CMOS process, through the MOSIS foundry service. This is same fabricator used for the CMOS MEMS circuits in this dissertation research. This process does not allow the high voltages needed for many of the electrostatic actuators, and is intended for sensing and measuring devices. All interconnections between the electronic circuits must be done through wiring on the MUMPS die, going up and down through solder bump connections. For the capacitance measurement circuit, a reference capacitor must also be built on the MUMPS die. The circuits on the electronics die are laid out as separate cells with their own bond pads.

The pads are 60 to 90 μm in diameter, and the solder bumps are roughly as high as the diameter of the pads. The solder is reflowed at 390°C. The attachment of the electronics die adds approximately 10 MPa of stress load to the MUMPS die; enough to cause a $\pm 0.5\%$ change in resistance of stress measuring piezoresistors [8].

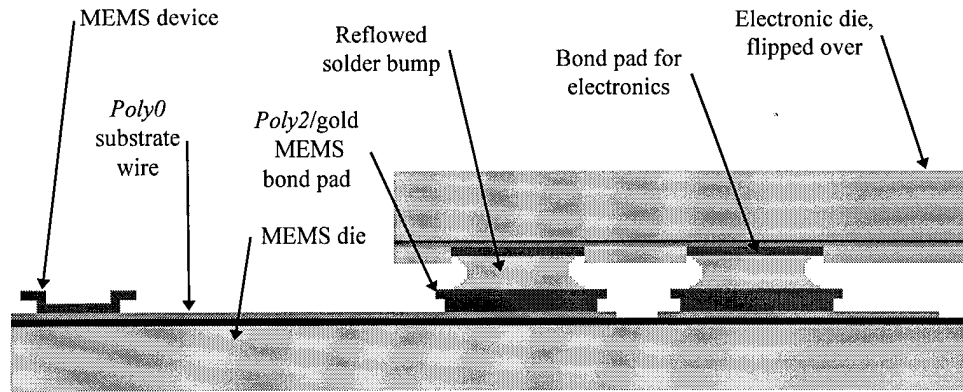


Figure 6-2. Electronic die flipped over and soldered to a MEMS die. In the MCNC process, roughly a quarter of the MEMS die is covered by the electronics die.

One drawback to applying this technique for MCMs is that the die must be inverted, which would limit its application for MEMS die that require connections to an outside environment, such as optical I/O. In the MCNC approach the electronics die does not cover the entire MEMS die, so large areas will still be open facing up. The MEM devices must be released before the flip chip attachment.

6.1.3 Direct Metal Deposition

Another method for interconnecting die is to deposit the wiring as a thin film over the die, a process called Direct Metal deposition (DM). It is 'direct' because there are no bond wires, leads or solder between the die pads and the MCM wiring. Since the wiring is nearly identical to the wiring on the die themselves, the performance of the MCM is similar to that of a large die, with low parasitic circuit elements in the interconnect lines.

In these processes, the die are placed face down on a flat surface and the substrate is glued and clamped; in one process, the epoxy glue becomes the substrate [3]. When the glue dries, the tops of the die are co-planar with the exposed surface of the substrate. This is a necessary step because the wires are patterned photolithographically, so the image plane must be as flat as possible for good resolution and metal coverage. There must be no gaps between the edge of the die and the rest of the substrate or the metal will not cover the steps in the topology [9]. This clamping step would obviously be hard on released MEMS die unless a provision were made to have the released portions over a well, with only the perimeter of the die around the MEM devices being pressed against the surface of the flat, which would require a custom flat to be milled for each module.

After the die are planarized to the MCM substrate, a dielectric coating is applied to insulate them from the wiring, which will be run right over the tops of the embedded die. This step would also be hard on released MEM devices, because the dielectric is often a spin-coated polymer, which would clog any released MEMS. After the dielectric is applied, via holes to the die pads are opened, then a metal film is sputtered or electroplated onto it and patterned. The dielectric coating, via cutting, and metal deposition and patterning steps can then be repeated for as many wiring layers as needed. A schematic of a general process is shown in Figure 6-3.

In DM processes, the need for a planar surface on and between the die means that the die must be formed into the substrate, making this as much a packaging scheme as well as a wiring technique. The DM method has been researched at AFIT,

as a variation of Wafer Scale Integration [9], and a version of it is being offered commercially [10].

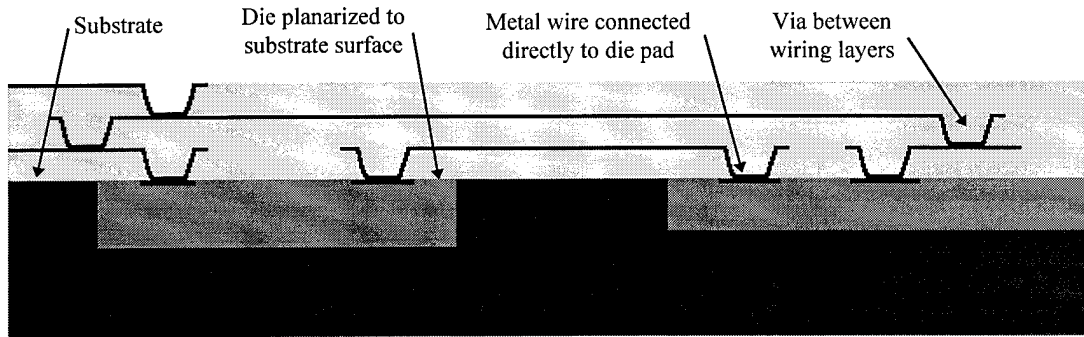


Figure 6-3. Cross-section of a generic Direct Metal wiring process. This illustrates the general principles, and is not meant to represent any particular process.

6.1.4 Polymer Wiring

One alternative wiring method tried as part of this dissertation research is the compressed polymer wiring found in cheap LCD watch displays. In these devices, the conductive pads on the LCD glass package are connected to matching pads on the printed circuit board that contains the rest of the watch's circuitry through a polymer wire array. The wire arrays are a sandwich of conductive strips and insulating rubber. The spacing of the conductive strips is less than the width of the pads, so that the lateral position of the wire is not critical, as long as the two sets of pads are roughly aligned and the polymer wire array is between them. The assembly is clamped to apply pressure to the wiring to ensure good contact. Figure 6-4 shows the wiring arrangement.

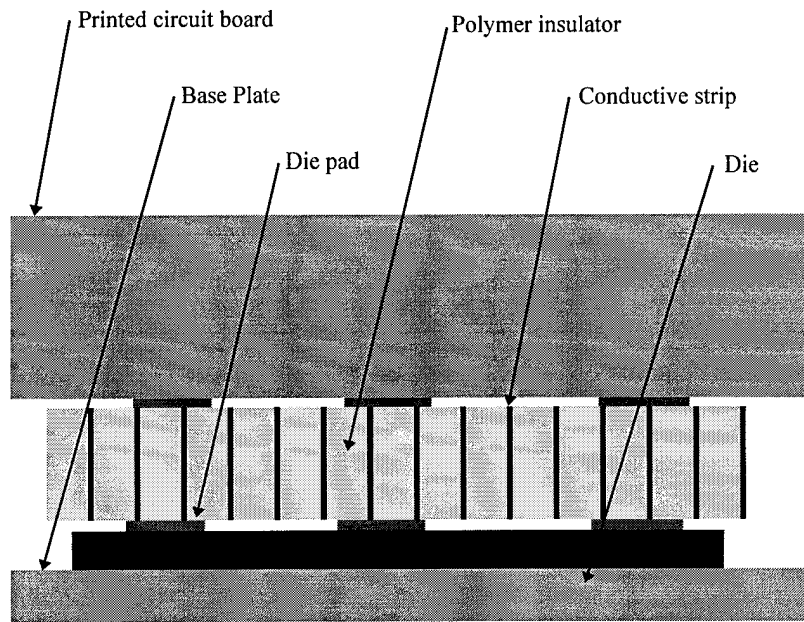


Figure 6-4. Compressive wiring connecting a die to a printed circuit board. The die is clamped between a base plate and the circuit board, trapping the polymer wiring array.

An advantage of this wiring technique for MEMS devices is that it requires no chemicals or heat; it is a totally dry, mechanical process. The polymer wiring connections can run down two sides of the die, leaving the center and two edges free for MEM devices. The drawback is that fewer connections can be made than with the wiring methods described above. But it is simple and inexpensive, and millions of examples have been fabricated and are available for \$2.98 retail. Die mounted this way can be easily removed, making it ideal for situations where the die may need to be replaced, either as a consumable portion of a larger system, or other situations where the die must be interchangeable but a bonded package would be too bulky and expensive.

6.2 Multichip Module Processes

The various types of commercially developed Multi-Chip Module processes are described here to illustrate their advantages and drawbacks for MEMS die packaging. These processes are intended for electronic die, so the problem of releasing a MEMS die after packaging has not been investigated. Two of these processes were chosen in this dissertation for an attempt to package MEMS die with electronic die, and their choice was based on their availability as foundry processes.

6.2.1 MCM-L (Laminated) Technology

This technology is an extension of laminated printed circuit board (PCB) technology. By patterning the conductor lines finely enough on the PCB, a bare integrated circuit die can be mounted directly on the board either face-up for WB connection, or face-down for FC connection. After mounting and bonding, the die is coated in a process called "glob-topping". The die is globbed with an epoxy or other sealant to protect the wirebonds and seal the device from environmental degradation.

Commonly found in inexpensive applications, this MCM process saves money and space by eliminating unnecessary packaging. Examples of this process can be found in many types of consumer electronics such as watches, calculators, and greeting cards that incorporate electronic music boxes. Figure 6-5 shows a toy electronic organ that was incorporated into its own instruction manual before certain unauthorized young researchers investigated it. This organ uses the chip-on-board

technique to eliminate the integrated circuit packaging that would make the organ too bulky and expensive for this application.

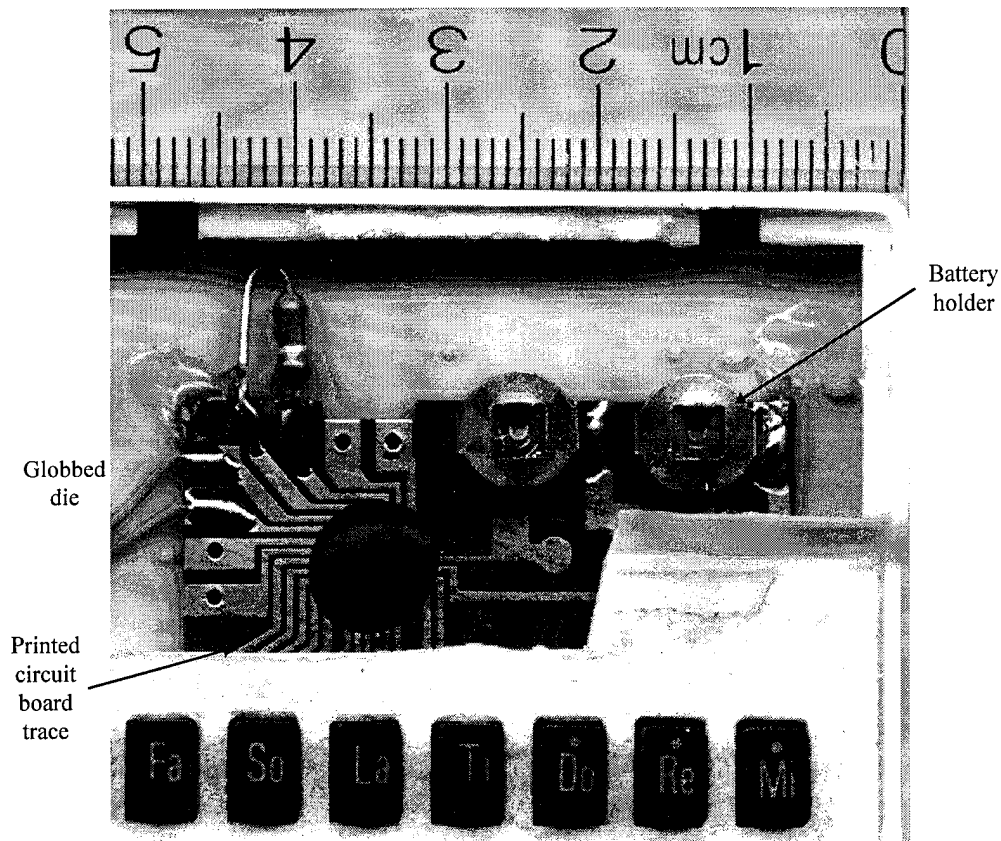


Figure 6-5. Single glob-topped die mounted directly on a printed circuit board, similar to MCM-L packaging. Die is wire-bonded directly to the printed circuit board traces and covered with a drop of black epoxy.

6.2.2 MCM-C (Cofired) Technology

This older technology uses screen printing techniques developed for thick film hybrid circuits. Layers of green (unfired) ceramic tape with holes punched in them for vias are screen printed with pastes of refractory metals to form wires and fill the

vias. These layers are pressed and fired together to form the module substrate [4]. Because of the firing step, refractory metals must be used, and they have higher electrical resistance than thin film deposited metals.

Figure 6-6 shows an MCM-C module. The cofired substrate is alumina, laid up in about 15-20 individual layers of green ceramic tape, each 5 mil thick. It has tungsten wiring with a gold finish on the top layer to increase conductivity and bondability. The die are attached with a polymer to allow for removal, and the connections are WB.

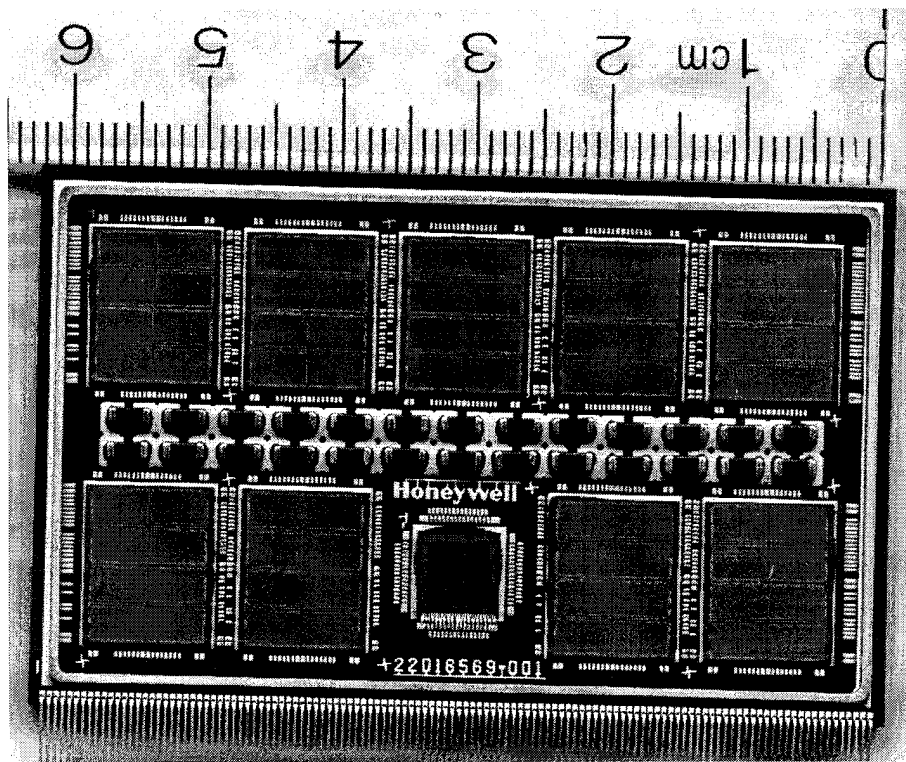


Figure 6-6. Memory module fabricated on co-fired alumina substrate. Module contains nine radiation-hardened 256K memory die and one line driver die. Die are wire-bonded to the substrate with 1.25 mil aluminum wires. Note the large number of pads, each of which must be wire-bonded one at a time.

6.2.3 MCM-D (Deposited) Technology

In this technology, the MCM consists of a substrate on which wiring and dielectric layers are deposited as thin films in the same way as on MEMS or electronic die. Thus very fine line widths and multiple wiring layers are possible. Variations of this technique include different substrate materials (silicon, ceramic, aluminum), different wire metallizations (gold, aluminum, copper), and different dielectrics (polyimide, silicon dioxide). The die are mounted above the substrate wiring and connected with WB or FC techniques. Figure 6-7 shows a 10-chip memory module.

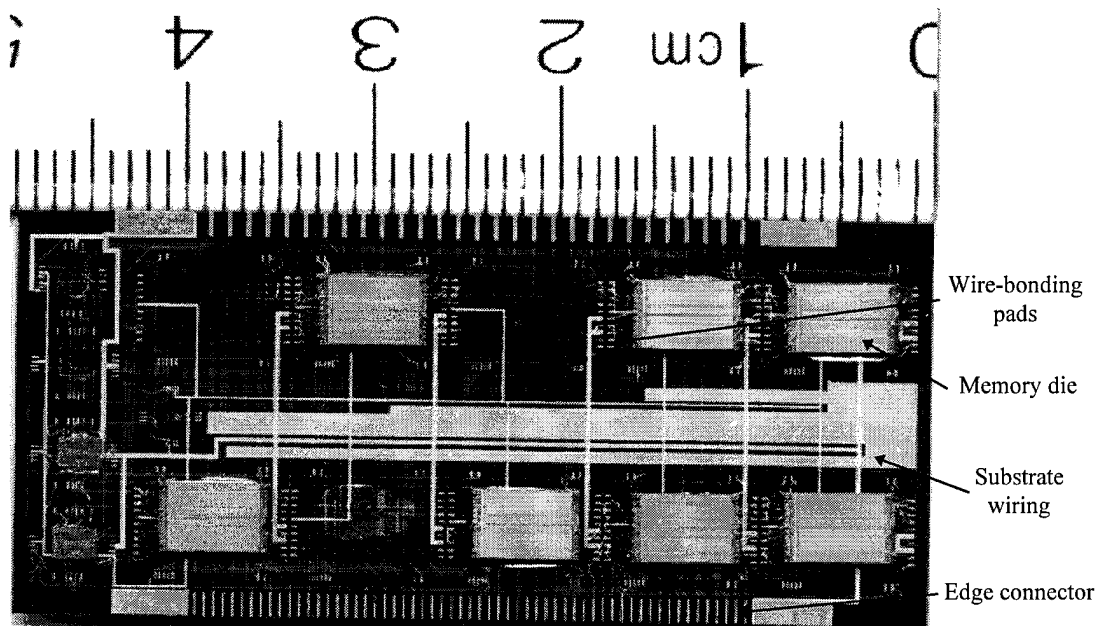


Figure 6-7. 10-chip memory module fabricated in Phillips Laboratory's MCM-D technology. The silicon substrate has $0.5\text{ }\mu\text{m}$ thick oxide dielectric layers and $0.5\text{ }\mu\text{m}$ thick aluminum wiring, which is also used to form edge connector leads. This sample was partially disassembled during testing, and three of the memory die are missing.

In the memory module shown in Figure 6-7, the substrate is silicon with a 0.5 μm oxide insulating layers and 0.5 μm thick aluminum wiring. The die are attached with a polymer glue, which allows for removal of parts for repair. This module was designed by the U.S. Air Force Phillips Laboratory and built and assembled at Sandia National Laboratory [11].

The Information Sciences Institute (ISI) at the University of Southern California, the group which runs the MOSIS integrated circuit foundry service, also offers an MCM service called the MIDAS Foundry Access Service [12]. MIDAS offers access to three MCM fabrication runs from IBM, nChip, and Micro Module Systems (MMS). Each of these companies offer a slightly different process, although all would be classified as MCM-D. The processes provide several wiring layers for power planes and for device interconnection wiring. The key features of each of these processes are listed in Table 6-1 for comparison.

Table 6-1. Comparison of MCM Processes Offered By The MIDAS Service [12].

Property	IBM	nChip	MMS
Substrate material	Alumina	Silicon	Aluminum
Signal/Power wiring layers	3/2	2/1	3/2
Dielectric material	Polyimide	Silicon dioxide	Polyimide
Wiring material	Copper	Aluminum	Copper
Die attach material	Epoxy	not listed	Ablebond 789-3
Die bonding method	WB	WB	WB
Die edge-edge spacing	400 μm	1.81 mm	500 μm
Operating frequency	100-400 MHz	200 MHz	<100-400 MHz>*

* Data not supplied, but claimed by MIDAS to be similar to the IBM process.

6.2.4 High Density Interconnect (HDI) Process

As seen in Section 6.1.3, the DM process makes the wiring, die and substrate a single unit, so a section of substrate with die and wiring would form an MCM if external leads were attached. A commercial process, the 'High Density Interconnect' (HDI) process, was developed by the General Electric Corporation [13] and licensed for production to Texas Instruments, Inc. [14].

In the HDI process, wells are milled into a ceramic substrate so that the die surfaces will be coplanar after they are glued on; then Kapton polyimide sheets are glued over the top, eliminating the problem of filling the voids between the die and the substrate well walls. Via holes are drilled through the Kapton dielectric layers by excimer laser ablation. Only one layer can be drilled per via, and there must be metal under the hole. The glue for attaching the Kapton polyimide sheets is sprayed on before the plastic sheets are pressed down.

Metal for the interconnect wires is deposited over the entire Kapton sheet and then patterned. Titanium and copper are sputtered for a plating base, 4 μm of copper is electroplated on, and then another layer of titanium is sputtered on top of the copper. The metal is patterned in a maskless photoresist etch step. There is also one layer of aluminum wiring deposited on the substrate for backside substrate contacts for the electronic die or as a ground plane. This metal layer also forms the bond pads for the entire MCM package.

Figure 6-8 shows the steps in the HDI manufacturing process.

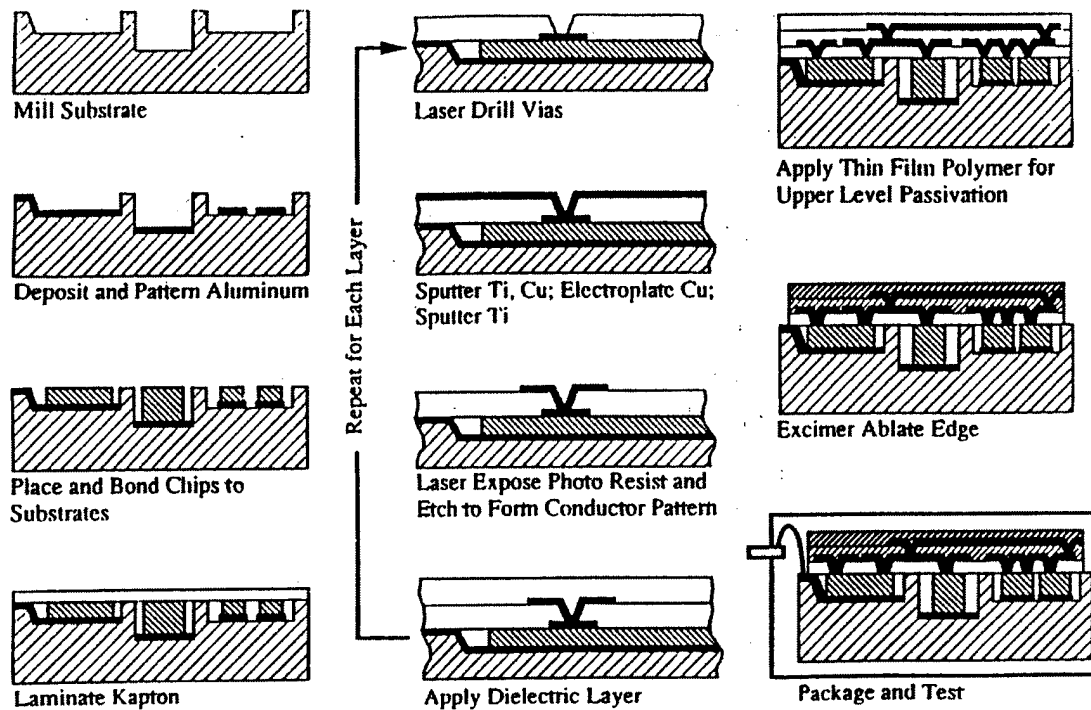


Figure 6-8. HDI MCM fabrication process flow [13].

The wire-patterning photoresist is exposed by a scanned laser beam. This allows the connections to each die to be jogged as needed to match the placement of the die on each individual substrate. The die placement is provided for each module from a database of chip reference point geometries [14]. This adaptive lithography technique eliminates the need for exact die placement and allows a closer pitch for the signal lines since less provision has to be made for misregistration of the wiring layers.

The HDI packaging process allows for repair: the plastic overlays can be peeled off and new ones fabricated, and the glue holding the die down can be softened with locally applied heat. The DM metallization has been removed and replaced on die

pads as many as 11 times with no measurable loss of performance [10]. Figure 6-9 shows a 12-chip memory fabricated in a four layer HDI module [15].

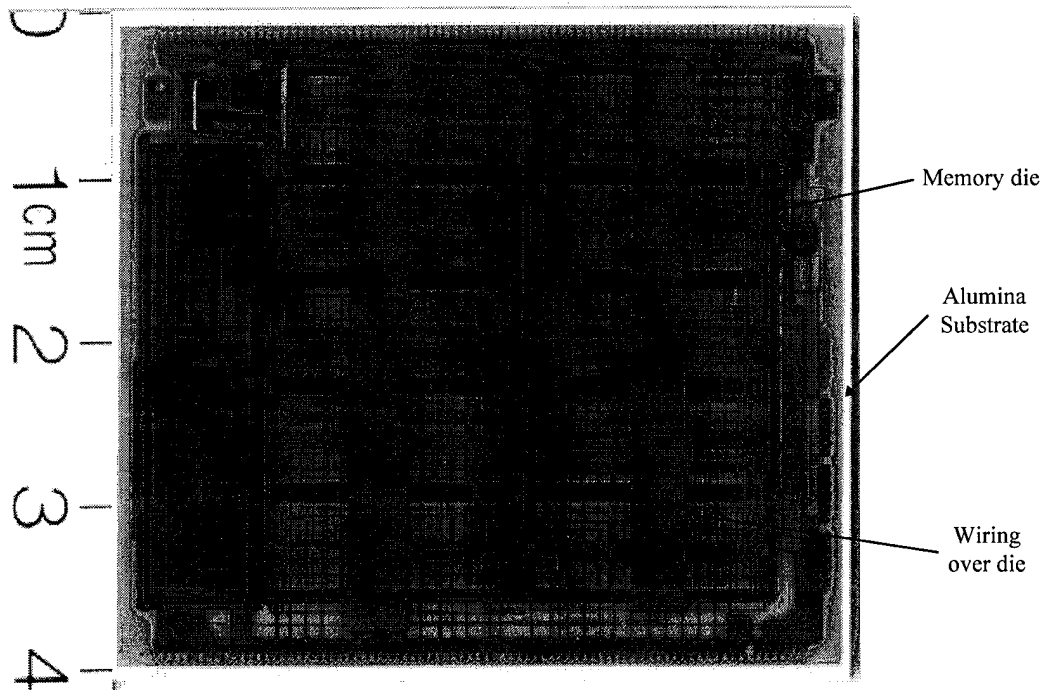


Figure 6-9. 12-chip memory module fabricated in HDI technology. The die sit in wells milled into the white alumina substrate. Electroplated and patterned copper wiring is formed on Kapton sheets which are glued over the die. Vias between layers are cut by an excimer laser [15].

Table 6-2 compares the HDI process to a typical MCM-D process. The major difference is the operating frequency, which is much higher for HDI packages. But this one number indicates the great advantage DM has over WB for die interconnects: its nearly eliminates parasitic circuit elements, especially inductance, that are introduced by wire bond wires.

Table 6-2. Comparison Of The GE HDI And MMS MCM-D Processes [10,13,14].

Property	HDI	MCM-D
Substrate material	Alumina	Aluminum
Signal/Power wiring layers	4	3/2
Dielectric material	Kapton	Polyimide
Wiring material	Ti/Cu/Ti	Copper
Die bonding method	DM	WB
Die edge-edge spacing	375 μm	500 μm
Operating frequency	>1 GHz	100-400 MHz

6.3 Integrating Micromachines With Electronics

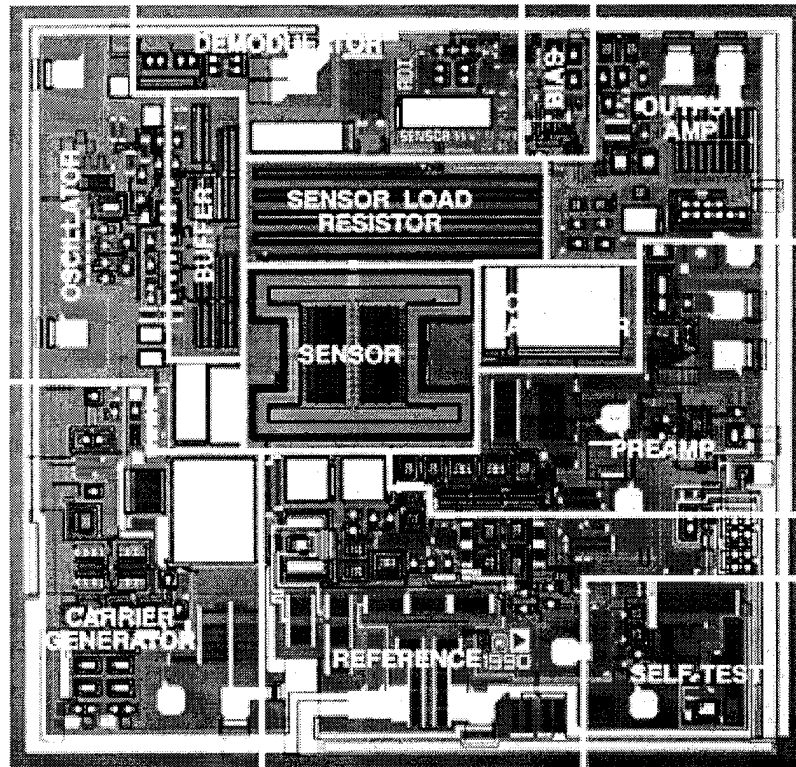
As shown in the preceding chapters, the fabrication processes for MEMS and electronic die use the same techniques of photolithography, deposition and etching, but with different temperature and exposure profiles. This makes forming both types of devices on a single die difficult, forcing compromises to be made on either the MEM or electronic side, or both. Polysilicon MEM structures work best when annealed to reduce the stress gradient that results from the deposition process, and active electronics with carefully planned impurity diffusion profiles cannot withstand the temperatures needed in the anneal process. The etchants used to release polysilicon MEMS devices remove the passivation layers or pad metallization on the electronics die. Electronics die can be handled in ways that would destroy released MEM devices, with vacuum pick-and-place equipment, for example. However, some progress has already been made in integrated processes.

6.3.1 Electronics on the MEMS Die

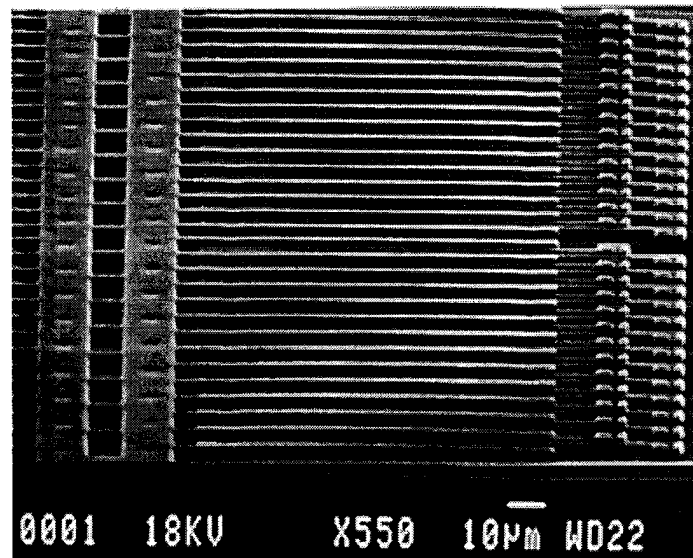
There is one commercial process which combines MEM and electronic devices on a single die, the 'iMEMSTM' process offered by Analog Devices, Inc. [16]; developed with the University of California, Berkeley under an ARPA contract. This process provides a central area for two-level polysilicon MEMS surrounded by BiCMOS electronics. This process requires that the MEM devices be in a separate well, and special masking and processing steps are needed to ensure the electronics survive the MEM device processing. This process represents the state of the art in integrating surface-micromachined polysilicon MEM and electronic devices.

This process has produced the first commercial surface-micromachined product, the ADXL-50 accelerometer, which is being used for triggering air bags in automobiles and is available for sale [17]. The integrated die contains the MEM sensor, drive and sense electronics. The die plot and an SEM micrograph of the comb-finger sensor are shown in Figure 6-10.

This process is also offered on a foundry basis but was not chosen as part of this dissertation research because it is an established process. Also, the delivered die are small and only come as already-packaged single die, unsuitable for MCM testing. The area of the die available for MEM devices is small, and the MEMS process is limited to 2 levels of polysilicon, with no metallization. The small die size and even smaller mechanical area on the die limit the complexity of the systems that can be produced.



(a)



(b)

Figure 6-10. (a) Die plot of an ADXL-50 commercially produced surface-micro-machined accelerometer. Note that the MEMS sensor area is only a small portion of the die. (b) Half of the ADXL-50 accelerometer MEM sensor structure. This device has a suspended polysilicon proof mass with 100 μm long comb fingers for capacitive feedback controlled positioning and sensing of the proof mass [16].

In the iMEMS[™] process the electronic and MEM devices can not be interspersed as needed. The MEM devices are restricted to a particular area, and so far only single mechanical devices have been integrated. So this process is currently limited to small scale, though sophisticated, MEMS.

6.3.2 Electronics with the MEMS Die

Better methods are needed to integrate MEM and electronic devices besides trying to put them both on the same die. Separately fabricated die would eliminate the complications and compromises necessary for total MEMS integration, but this leaves open the problem of connecting the two types of devices on a large scale with easily fabricated, low-noise wiring. MEMS may not reach widespread use until designers who do not have their own MEMS fabrication capability can specify complex, commercial-grade MEMS on a foundry basis, as currently possible with custom electronic die. MCM integration is one way to achieve this, given the types of foundry fabricated MEM and electronic die available.

One method, not involving MCMs, was the MCNC flip-chip method discussed in Section 6.1.2, but that is the only method currently available in a foundry process, and as of this writing the first production run has not been completed. The other method is the CMOS MEMS method; but as already discussed, while CMOS MEMS makes for excellent electronics and integration, the types of MEM devices that can be fabricated are extremely limited. The rest of this chapter will discuss initial research

into using foundry fabricated MCMs to integrate electronic die with MEMS die, rather than on MEMS die. CMOS MEMS die will be included mainly because those die also represent standard CMOS electronics.

Surface-micromachined or electroplated MEMS die do have electronic components on them, but only the passive ones that result from the devices' geometry, such as resistors and capacitors, or inductors for MEMS processes with metal layers. Thus current MEM devices are integrated only in the sense that any physical object has electronic properties. They are not integrated in the 'integrated circuit' sense since they lack the active circuit amplifiers needed for sensing and control. For example, a microrobotic arm built with current MEMS technology would not have the feedback and drive circuitry integrated into it, bringing it to the point of integration where it would require only a power source and an instruction word for operation.

Control is not distributed throughout current MEM systems, just the actuators and sensing elements. For something like an optical or accelerometer array, this is all that may be needed; but for a complex system, it might be better to have fewer control and sense lines running across a die, for less cross-talk, power loss, and area loss. While MCM integration may bring the electronics close enough to the MEM devices to operate as if they were located on the same die, even MCM integration will fall short of the ultimate integration where the electronic and MEM devices can be placed on a single die in any arrangement. But as a first step, MCM integration may bring

about the level of sophistication that makes MEMS useful for complex systems, rather than just sensors.

6.3.3 Pre- Versus Post-Release

With a combination of dissimilar die, and the need for a release etch of the MEM devices, there arises the question of chemical compatibility between the release process and the packaging and other die. Should the MEMS die be released before assembly, adding the need for extremely careful handling, or should they be released after packaging, entailing the protection of incompatible elements during the release etch? Ideally the MEM device should be released as close to the end use as possible to avoid the rigors of packaging, shipping and harsh storage environments. But even if release can only be put off until the last manufacturing step, several opportunities for breakage will have been avoided.

One of the questions faced in this part of the dissertation research was whether to release the die before or after they were packaged. If there are multiple MEMS die types, then the problems are compounded as the die might not be compatible with each other's release processes, or one or the other may not be compatible with the electronic die or packaging. The answer is 'it depends'. If all the materials used in the die and MCM fabrication processes are compatible with the release etch, then post-release is better from a handling, storage and shipping point of view. If the materials are not chemically compatible, then ways must be found to package pre-

released die, or to isolate the releasable die with dams or masks when etching. So chemical compatibility tests form the bulk of the research done in this area so far.

6.4 Package Testing

It would be difficult to foresee all of the problems that might come up when integrating different die with different processing needs into the same MCM, without a particular application in mind. So an attempt was made to incorporate the two most widely different MEMS die available in two widely different MCM technologies.

The two processes tried were the MMS MCM-D process offered by ISI, the same group that offers the MOSIS CMOS MEMS process. Initially the IBM process was chosen for the MCM-D packaging test for MEMS die, but this was shifted to the similar MMS process when software for designing the IBM substrates was found to be out of date for the newer version of the Cadence drawing tool used at AFIT. See Table 6-1 for the details of these processes.

The other MCM was to be the commercially available HDI process offered by Texas Instruments. However, through efforts of the sponsor an opportunity arose to work directly with General Electric (GE), the developer of the HDI process, to help further refine the process for MEMS applications. So the overlay process used was similar to the commercially available process, only slightly modified. Specifically, the alumina substrate has been replaced with a material called 'Plaskon', an aggregate plastic material that is easier to mill the die cavities into. Also, changes were made to

accommodate fragile components [18]. GE had developed a 'tent' modification wherein the Kapton plastic was run over a cavity that held fragile suspended microwave components, a situation similar to that encountered with MEMS devices. This idea can be used to provide a cover over devices that must be protected during the etch of another device in the package.

As of this writing, the HDI packages have not been fabricated, because they were added onto a fabrication run for a different project, and that other project has been delayed. The MMS MCMs were received too late to perform any in-depth testing of how the packaging might affect the operation of the MEMS devices, but some preliminary tests were done on the chemical compatibility of the packaging materials with the MEMS etchants then currently in use. So the results presented in the following sections are only preliminary.

6.4.1 MEMS Test Die

In order to try the MCM packaging, MEMS test die had to be provided. Rather than just use MEMS die already on hand, special test die were fabricated that contain a variety of MEMS devices. A die was designed for the MUMPS and CMOS MEMS processes. The devices included on these die are intended to represent the various sorts of MEMS structures that might be encountered in an actual application. They are not intended to form a complete system when connected together, though the

CMOS MEMS die has a complete system on it, the thermal stimulator array described in Section 5.2.2.2.

The following two sections describe briefly the devices contained on the die and the classes of devices they are intended to represent. Table 6-3 lists general categories of MEMS devices appearing on the two test die. This table also highlights the limitations of the CMOS MEMS process when compared to the MUMPS process.

Table 6-3. MEMS Device Categories Included On MUMPS And CMOS Test Die.

Device Category	MEMS Processes	
	MUMPS	CMOS
Suspended Heaters	MUMPS	CMOS
Vertical Actuators	MUMPS	CMOS
Horizontal Actuators	MUMPS	--
Electrostatic Combs	MUMPS	CMOS
Piston Mirrors	MUMPS	--
Hinged Plate Assembly	MUMPS	--
Lost Poly Assembly	MUMPS	--
Pads and Wires	MUMPS	CMOS
Rotating Devices	MUMPS	--
Breakage Detectors	MUMPS	CMOS
Pad Continuity	MUMPS	CMOS

6.4.1.1 CMOS MEMS Test Die

The CMOS MEMS die contains a collection of MEM devices that were fabricated on previous runs, some new devices put on the die because there was room for them, and a few purpose-built MEM devices. There is a selection of electronic devices gathered from other AFIT projects to serve as example electronic circuit layouts, including analog-to-digital converters and operational amplifiers. Added to

these were some purpose-built electronic layouts: the addressing circuitry for the thermal stimulator array, and ring counter circuits built for the sponsor for testing HDI packages.

Several examples of the MEM devices on the die are shown in Figure 6-11, and Figure 6-12 shows a photo of the entire die. This photo should be compared with Figure 5-30, which shows just the thermal stimulator arrays extracted from the rest of the die drawing. There are 71 pads, a number which was chosen to nearly match the available 64 pin DIP packages.

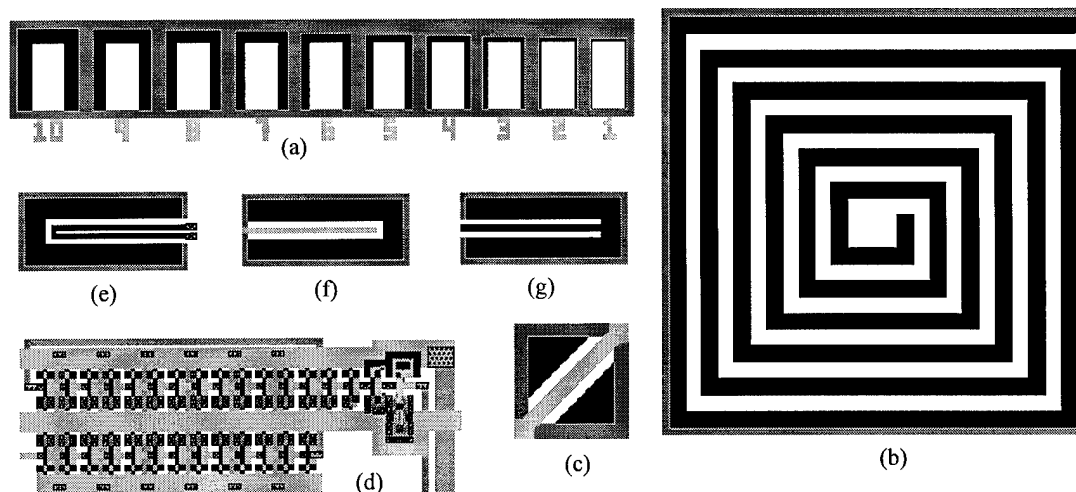


Figure 6-11. A sample of cells from the packaging test CMOS MEMS die: (a) test cell to determine minimum *open* width design rule; (b) all-glass etch gauge for a large spiral actuator; (c) diagonal suspended metal line for breaking or fusing a power bus; (d) chain of 30 inverters for an externally completed ring counter (31st inverter is the output pads driver, not shown); (e) breakage monitoring cantilever with 'U' shaped polysilicon resistor; (f) breakage test cantilever with aluminum strip to prevent broken end from detaching; (g) cantilever with polysilicon line open at the end to monitor etchant intrusion, also a possible etch gauge.

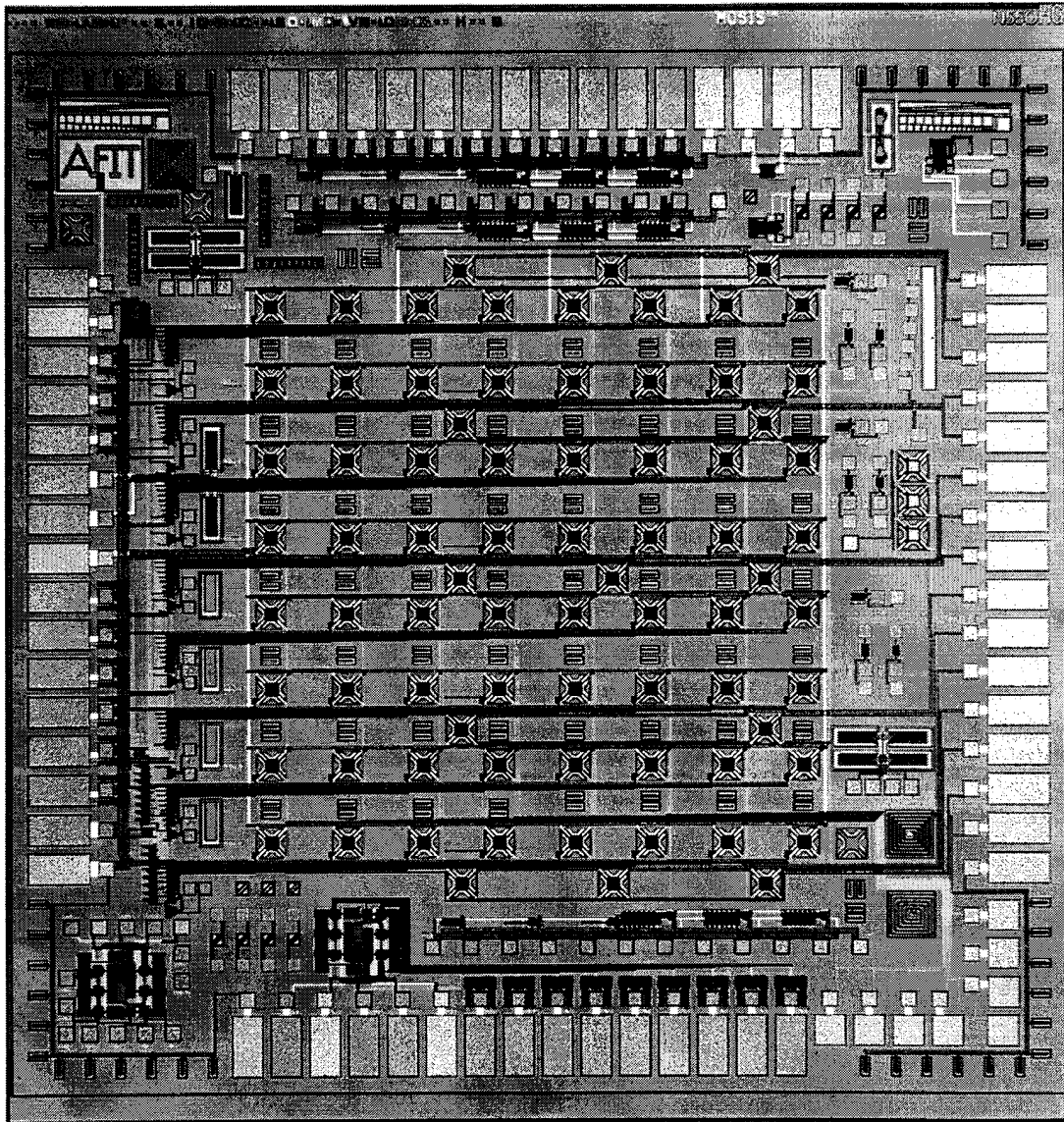


Figure 6-12. Packaging test CMOS MEMS die. The active die area is 6800 x 6700 μm . The layout is dominated by the thermal stimulator arrays in the center, and their addressing circuitry on the left. The corners contain small cantilevers to test for breakage caused by handling.

6.4.1.2 MUMPS Test Die

The MUMPS die contains a collection of MEM devices that were fabricated on previous runs, and many purpose-built devices. Many of the purpose-built devices

were intended to test if the die was operable even if it could not be observed, by changes in resistance or capacitance. The die was designed early in the dissertation research and the devices it contains are older designs. So although it includes many classes of MEMS structures, several of the newest devices developed during this dissertation research are not represented such as the thermally driven stepper motors, mirrors, and self-assembling structures.

Unfortunately, the two MUMPS runs, MUMPS7 and MUMPS8, on which this die was fabricated, both had serious fabrication flaws as described in Section 2.3.2.4. These flaws prevented most of the devices from operating, especially the hinged and electrostatic devices. The design was subsequently built on the more successful MUMPS9 run, but those die were delivered too late for inclusion in the MMS MCM packages, though some were sent to GE for inclusion in the HDI package.

Figure 6-13 shows a composite photo of the die taken at GE for the purpose of accurately measuring the locations of the bond pads. The main features of the die are indicated. There are 144 bond pads, which matches the number of pins on the largest available package, a 144 Pin Grid Array (PGA) package. A single die can then be mounted in a PGA package for testing. Figure 6-14 shows a sample of the types of devices included on the MUMPS packaging test die.

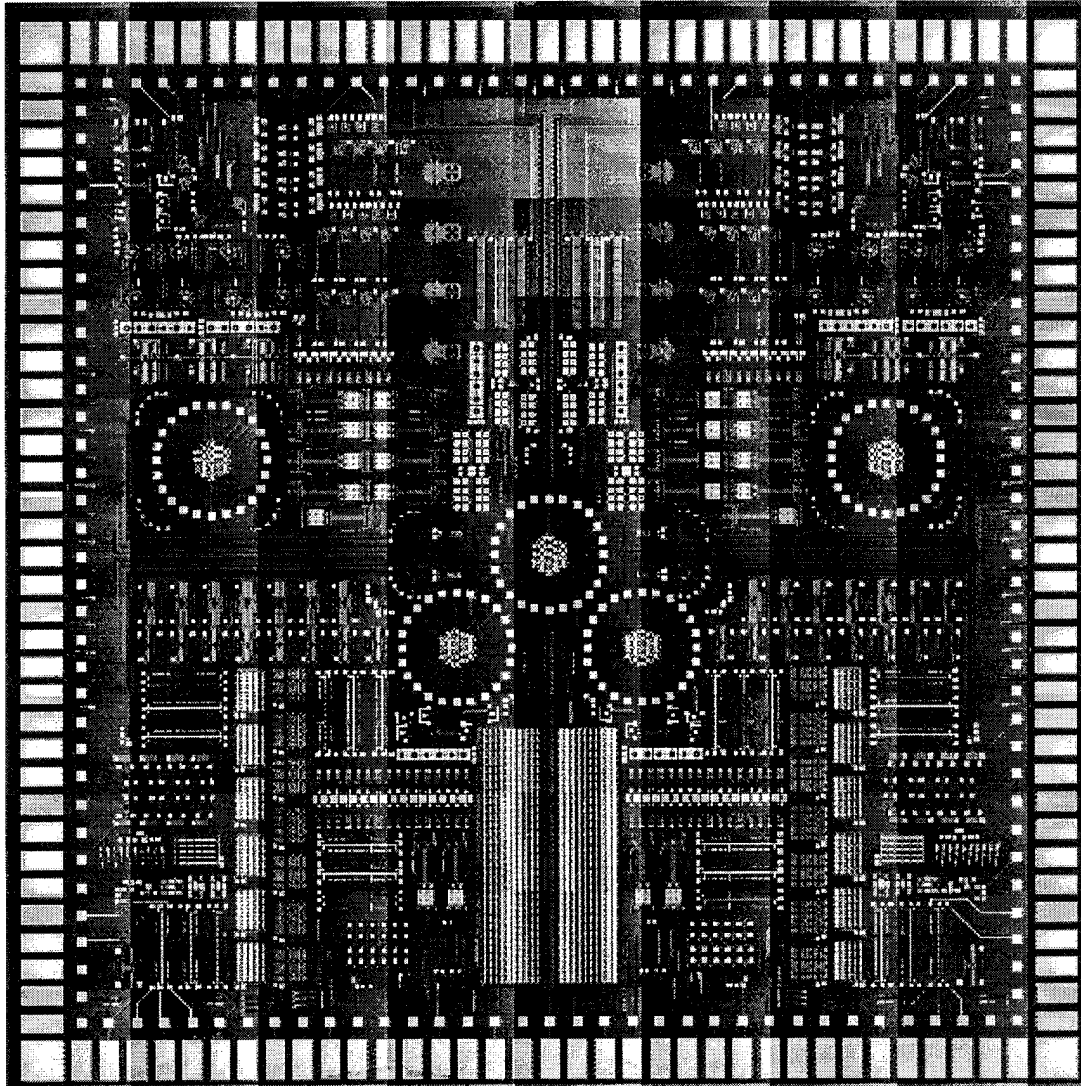


Figure 6-13. MUMPS packaging test die. The die is 1 cm^2 . The layout is bilaterally symmetrical and contains a variety of general MEM structures including mirrors, breakage monitors and thermal actuators. The inner row of pads can be used for DM bonding, the outer, larger pads are for WB.

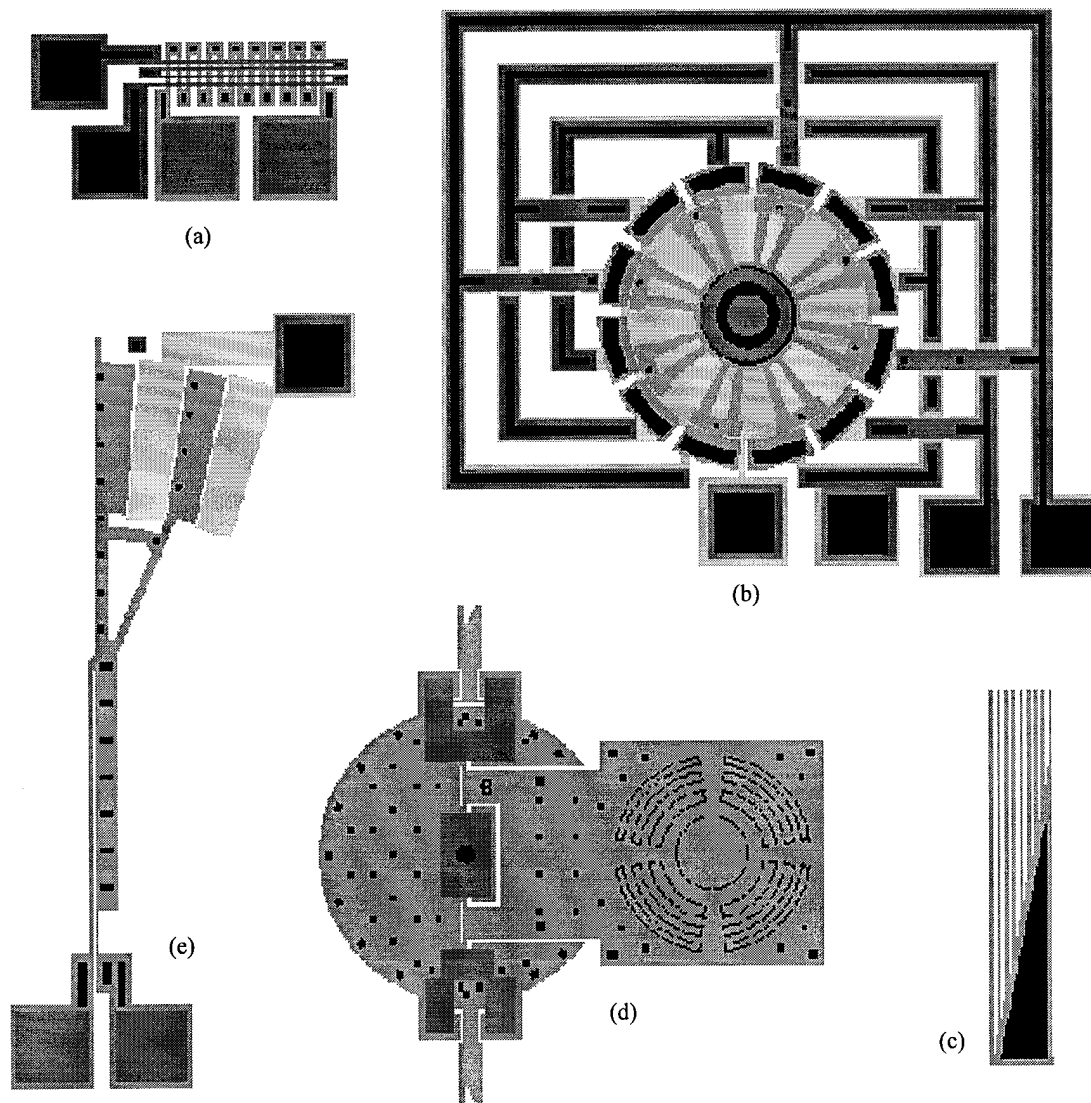


Figure 6-14. A sample of cells from the MUMPS packaging test die: (a) crossed polysilicon resistors for monitoring release condition by thermal gradient measurement; (b) electrostatic motor; (c) 2 μm wide fingers for breakage and stiction monitoring; (d) hinged, rotating Fresnel lens; (e) thermally actuated variable capacitor.

6.4.1.3 Polymer Wiring MUMPS Test Die

The MUMPS10 die was designed with two rows of special pads designed to accommodate the polymer wiring scheme described in Section 6.1.4. The rest of the die contains the usual mix of new devices, some of which are connected to the pads. There are also wires between pads in the same row and between pads in opposite rows for pad-to-pad continuity tests. Figure 6-15 shows a cross-sectional view of a portion of the 0.5 x 1 mm polymer wiring pad. The topology of these pads was designed such that the uppermost surface which contacts the polymer wiring is only the gold layer. Figure 6-16 shows the MUMPS 10 die which has a row of 8 polymer wiring pads running down each side. This number of pads matches the number and spacing of contact pads on the printed circuit board (PCB) of the LCD watch purchased for the test.

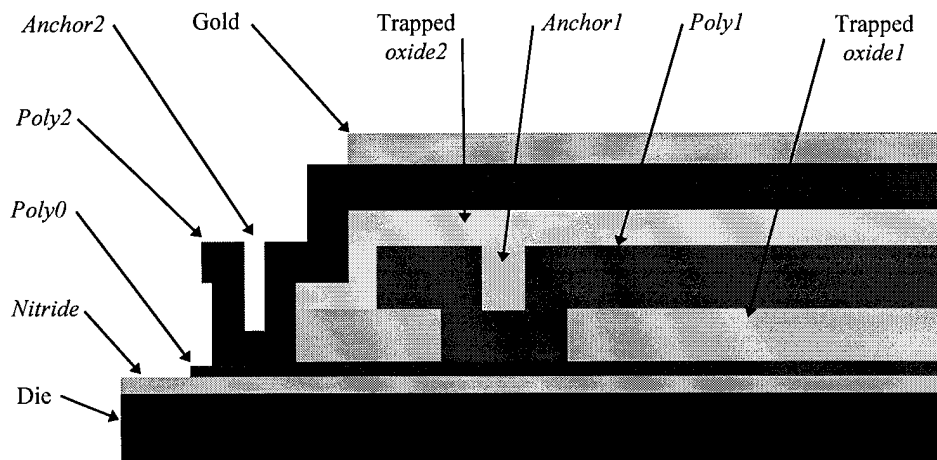


Figure 6-15. Cross-section of a portion of a polymer wiring pad. The *poly1* layer is used to boss the central *poly2* portion of the pads to ensure that the uppermost gold layer is the only surface to contact the polymer wire. Contacts are made at the corners of the pad to the *poly1* former to prevent it from building up a charge.

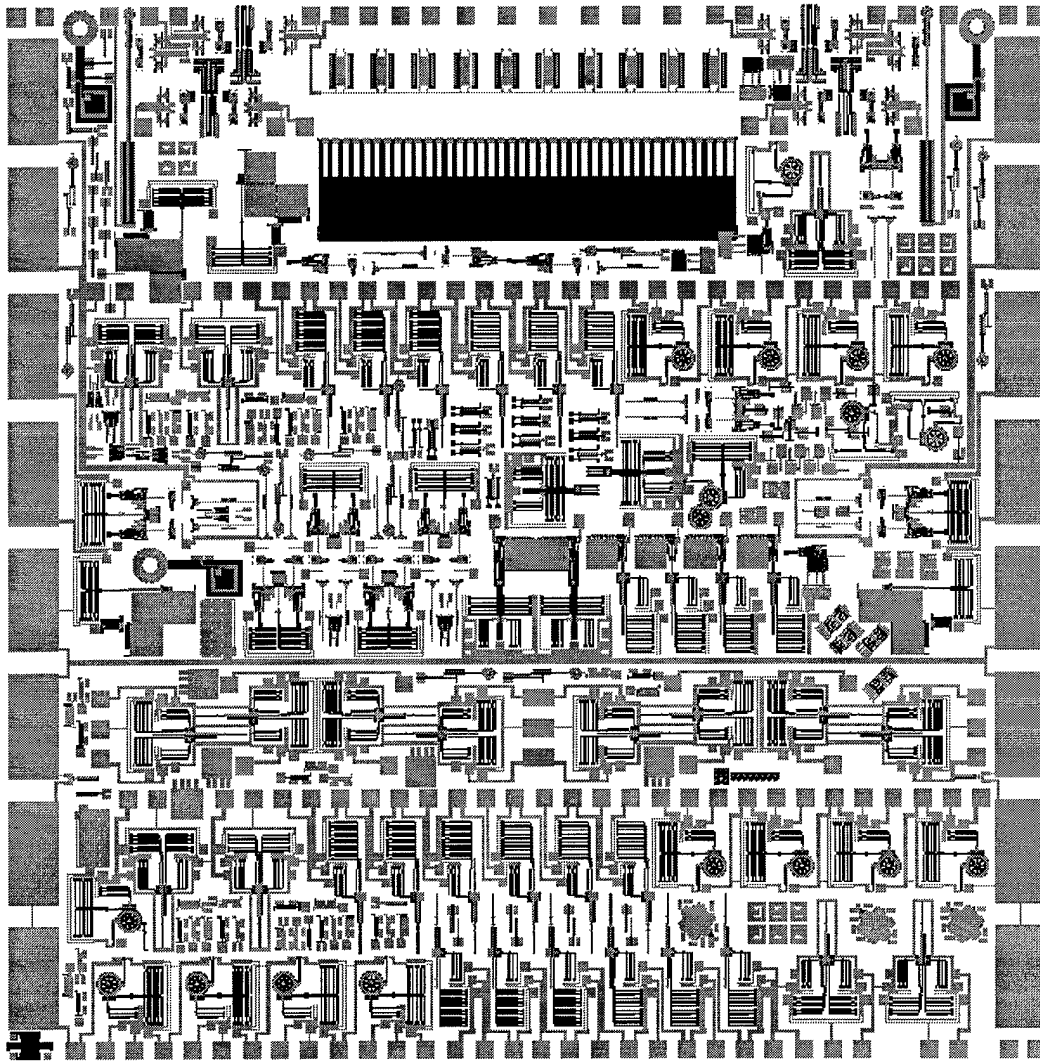


Figure 6-16. MUMPS 10 die layout showing the polymer wire bond pads down the sides. Each pad is 0.5 x 1 mm. The rest of the die contains the usual assortment of test structures including stepper motors, corner cube reflectors, test actuators, and piston mirrors.

6.4.2 Chemical Compatibility Testing

Before committing die to MCM packages, tests were conducted to see how well the packaging materials can withstand the etchants used to release the MEM devices. Testing consisted of exposing the materials to the same etch sequence used to release the MUMPS and CMOS MEMS die, as listed below.

MUMPS Release Process

1. Remove protective photoresist layer in 3 minute acetone rinse/swirl,
2. Rinse in deionized water (DIW) for 5 minutes,
3. Dip in HF for 90-150 seconds,
4. Rinse in DIW for 5 minutes,
5. Rinse in 2-propanol for 5 minutes,
6. Dry the die on the warm glass dish.

CMOS MEMS Release Process (EDP)

1. 10 second dip in 10% HF to remove any native oxide on OPEN areas,
2. Rinse in DIW for 5 minutes,
3. Etch in EDP in reflux container at 95°C, observing etch gauges at 15 minute intervals:
 - 3a. pull die out of EDP and rinse for 1 minute in DIW,
 - 3b. observe die while it is under a drop of DIW so it does not dry out,
 - 3c. return to EDP etch if needed, else:
4. Rinse in DIW for 5 minutes,
5. Rinse in 2-propanol for 5 minutes,
6. Dry the die on the warm glass dish.

CMOS MEMS Release Process (TMAH)

Same as for EDP, but etch is at 85°C.

6.4.2.1 HDI Materials Compatibility Tests

For the HDI chemical compatibility testing the GE Corporation sent samples of materials and assemblages of materials which simulated actual packages. All of the simulated packages consisted of substrates roughly 1.5 cm square with Kapton layers

laminated on top with two glues used at the GE prototyping fabrication lab: Ultem, SPI epoxy, and a polyimide. Details of the material and deposition were not given. These samples had a trench ablated down the middle with an excimer laser to expose the edges of the laminates and the substrate. Figure 6-17 shows a schematic of a typical Plaskon sample. The sample types are listed in Table 6-4.

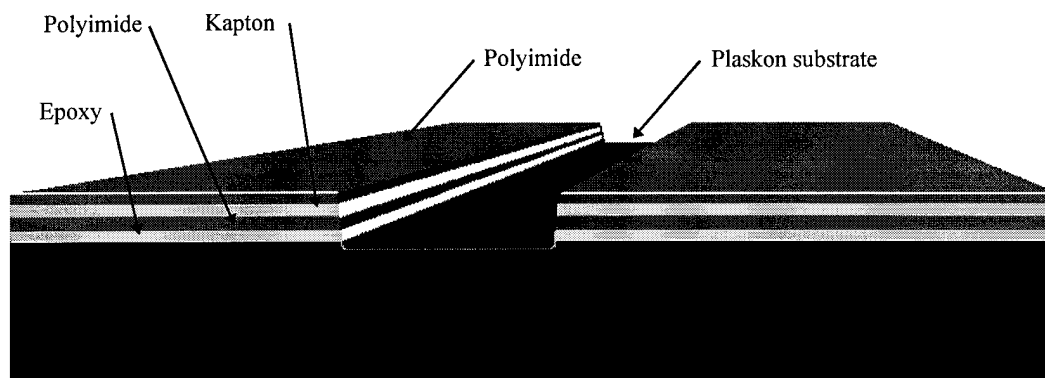


Figure 6-17. Typical HDI simulated packaging sample. Drawing is not to scale, the laminates are much thinner than shown. Samples are roughly 1.5 cm square, 4 mm thick, with a 5 mm wide trench cut with an excimer laser.

Table 6-4. HDI Sample Materials and Simulated Package Materials.

1. Plain Plaskon substrates
2. Alumina substrate / Ultem / Kapton / SPI epoxy / Kapton
3. Plaskon substrate / SPI epoxy / polyimide / Kapton / polyimide
4. Plaskon substrate / SPI epoxy / Kapton / SPI epoxy
5. 0.5 mil Kapton sheet

The samples were tested to see if they survive the standard etches used for the MUMPS and CMOS MEMS die. SEM micrographs were taken of unetched and fully etched samples. It was difficult to discern the different laminate layers in the SEM

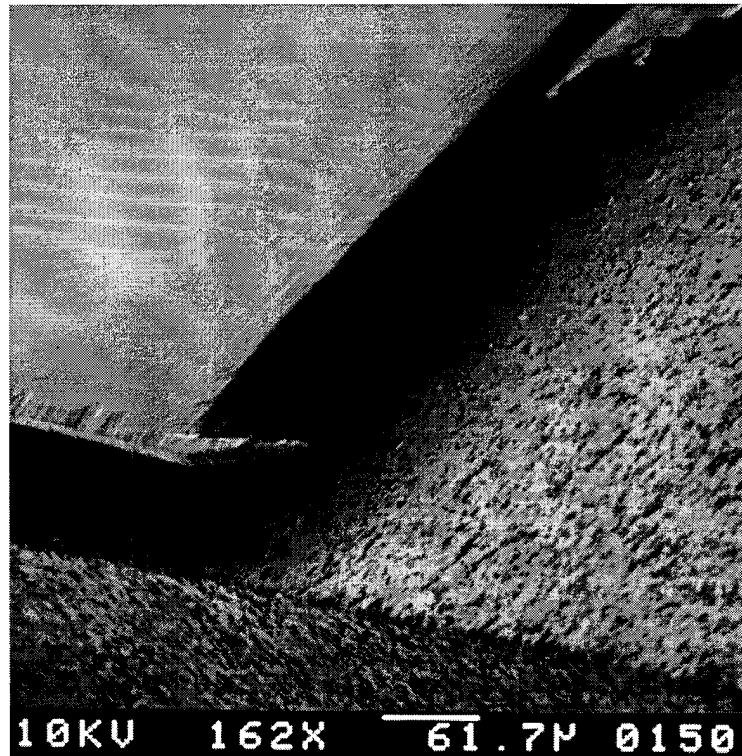
images, but damage was easily seen when it occurred. The following sections summarize the test results.

6.4.2.1.1 EDP Etch of HDI Samples

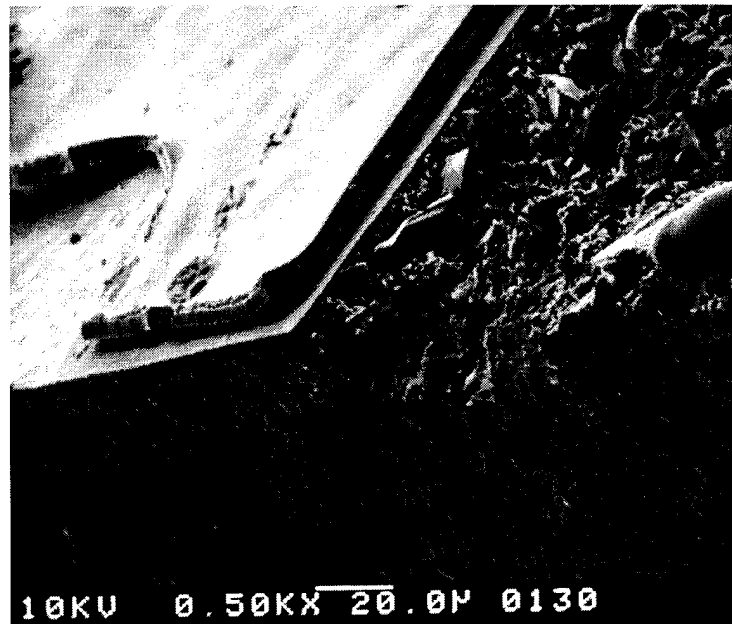
The EDP etch was timed by observing one of the CMOS MEMS die that contained an etch gauge and some of the same structures included on the packaging test die. The CMOS MEMS die was etched in the same container along with one copy of each of the five HDI samples listed in Table 6-4. The total EDP etch duration was 62 minutes, and post-etch rinsing followed the full procedure listed in Section 6.4.2. Figure 6-18 shows etched samples 2 and 4 listed in Table 6-4.

The samples were SEM photographed after the entire etch, but were observed twice during the etch, at 21 and 38 minutes. Detrimental effects were observed on all the samples except the plain Plaskon substrates. Closer observation in the SEM showed that the EDP does not affect Plaskon or the ceramic substrates, but attacks all the other materials, including Kapton. The EDP dissolved the polyimide and softened the Kapton. These effects began almost immediately, since by the first visual inspection at 21 minutes the laminates were already beginning to peel at the edges.

These results indicate that EDP etching will not work with any of these types of laminates. The damage starts early enough in the process that there is no chance that a shorter etch time will be enough to release even the smallest MEM devices. However, the CMOS MEMS die are the most robust when released. So it may still be possible to package them in HDI modules if handled carefully.



(a)



(b)

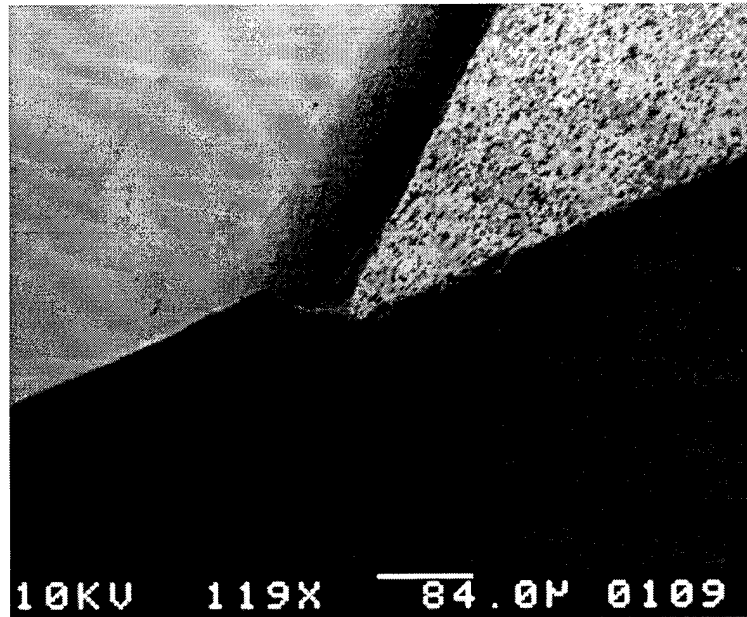
Figure 6-18. HDI material samples after a 62 minute etch in EDP: (a) alumina substrate, (b) Plaskon substrate; corresponding to Table 6-4 entries 2 and 4, respectively. In both cases the dielectric layers delaminated. The rough surface of the Plaskon trench was caused by the excimer laser ablation.

6.4.2.1.2 Hydrofluoric Acid Etch of HDI Samples

The HF etch was also done according to the procedure listed in Section 6.4.2, except that the initial rinse in acetone was not performed; this is because any protective photoresist on the MUMPS die must be removed prior to packaging them. The two minute etch was done on each sample individually. No MUMPS die were etched because the etch time for MUMPS die was already well established. Figure 6-19 shows etched samples corresponding to the samples shown in Figure 6-18.

The HF had a small effect on the alumina sample laminates, but this occurred only on one side of the trench; so this may be due to the extreme bevel on that side of the trench. HF does not seem to affect the laminates on the two samples with the Plaskon substrate, though the Plaskon was affected slightly. Whereas the EDP etch seemed to have no effect on the Plaskon, the HF seems to etch one of its components, or it loosens one of the types of grains enough that some grains fall out, as seen in Figure 6-19b.

The results of this experiment show that HF etching is possible for HDI-packaged die. The HF does not damage the ceramic substrate or the Kapton, at least not during the two minute etch needed to release the MUMPS die. This is a useful outcome since the MUMPS die or surface-micromachined polysilicon MEMS die like them are the main reason for going into MCM packaging in the first place, i.e. to mate them with non-MEMS circuit die in a single package. The non-MEMS die will be protected by layers of Kapton, and so they will be unaffected by the HF etch.



(a)



(b)

Figure 6-19. HDI samples etched in hydrofluoric acid for two minutes: (a) alumina substrate, (b) Plaskon substrate; corresponding to Table 6-4 entries 2 and 4, respectively. The peeled edge in (b) is from dicing, not etching. Note that some grains have fallen out of the Plaskon aggregate.

6.4.2.1.3 EDP Test With Diamond-Like Coating

After the initial etching tests, a follow-up experiment was also performed to determine if a diamond-like coating (DLC) could be used to protect the laminates

from the EDP. This material is used as a capacitor dielectric; it is non-conductive and can be deposited pinhole free. The DLC can be removed with an oxygen plasma etch after the MEMS release etch. GE engineers felt it should make a good protective coating for the EDP etch, but were concerned about the adhesion of the DLC; so they wanted a quick yes or no result on the resistance of the DLC to EDP etching.

For this experiment sample types 2, 3 and 4 from Table 6-4 were coated with 0.95 and 2.3 μm thick DLC coatings, for a total of six sample types. Details of the DLC composition and deposition were not released. The samples were all etched simultaneously in EDP at 80°C for 1 hour. Figure 6-20 shows an etched DLC sample in the SEM clamp. The following paragraphs give a brief summary of each of the sample types.

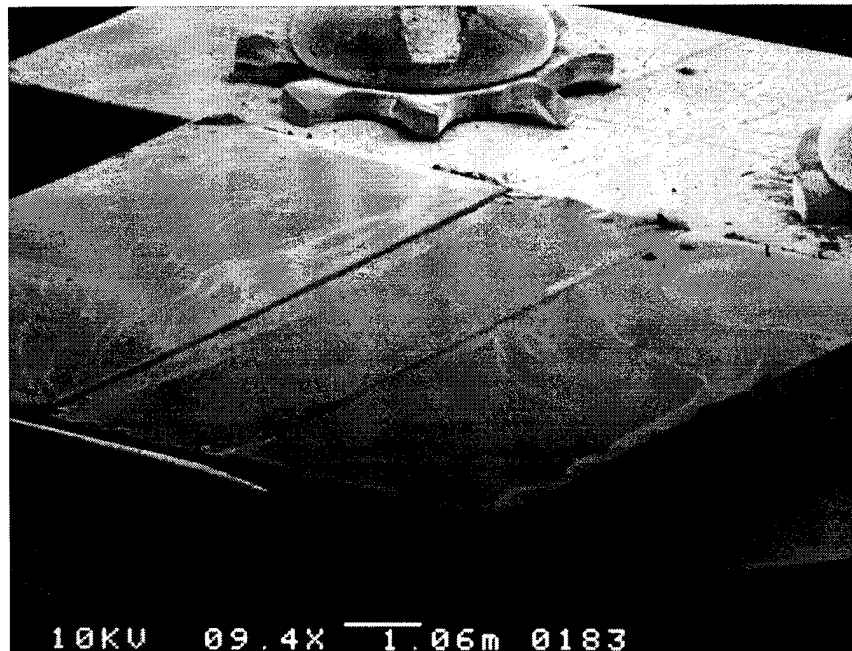


Figure 6-20. Alumina substrate sample with 2.3 μm DLC coating, mounted for SEM examination. The DLC coating was intended to protect the laminate from the EDP etch, but has cracked and failed along the outside edges and trench edges.

6.4.2.1.3.1 Sample 2, 0.95 μm DLC

The DLC covered the top edge of the trench sidewall, but failed at the lower edge, allowing the EDP to get under the laminate. The DLC cracked on the ceramic surface also; so although the ceramic was not affected by the EDP, this shows that 0.95 μm of DLC cannot protect even a slightly rough surface. The laminate surface away from the edges seemed to be unaffected, but in the previous experiments the EDP affected the Kapton chemically, bleaching it and making it more brittle after it dried, but left it smooth. As with all the samples, the DLC cracked at the sharp edges of the sample.

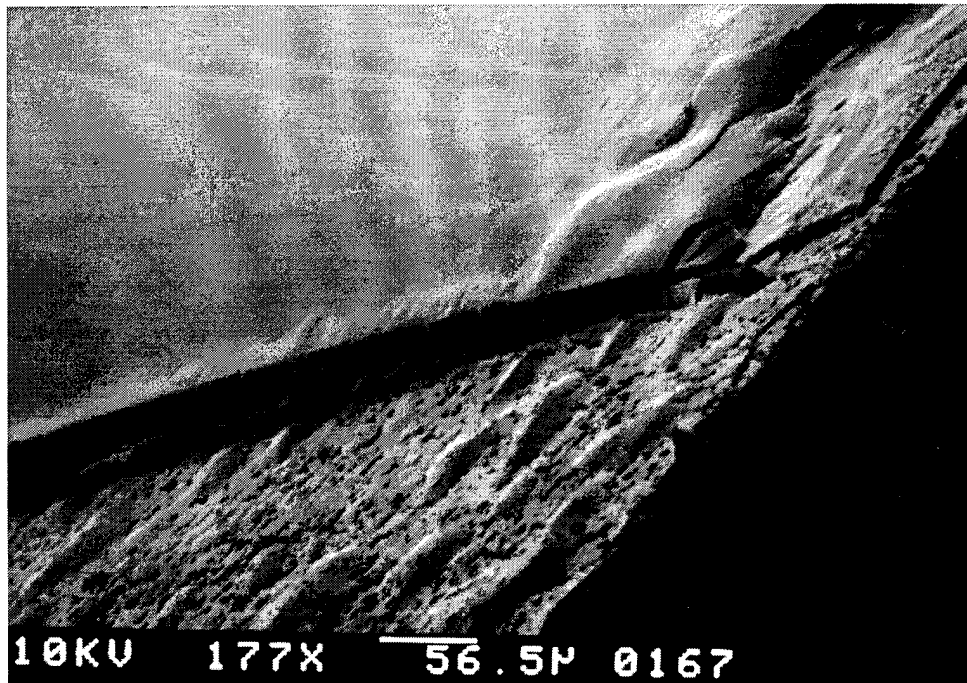


Figure 6-21. Sample with alumina substrate and 0.95 μm DLC coating after EDP etch for one hour. The DLC is bubbled and cracked on the trench floor, but smooth over the top of the laminate.

6.4.2.1.3.2 Sample 2, 2.3 μm DLC

The top of the laminate seemed to be protected after the EDP etch, but the dry sample is a little misleading, the laminate was curled up after the etch but went back down as the sample dried, mostly along the diced edges; so it looked flat when inspected in the SEM, as seen in Figure 6-20. The DLC seems to have covered the top of the trench sidewall but failed at the bottom, leaving ripples along one sidewall as shown below in Figure 6-22. Failure of the DLC caused delamination of the Kapton sheet during the etch on many samples, though the Kapton laid flat again on the sample shown in Figure 6-22 after the sample was dried.

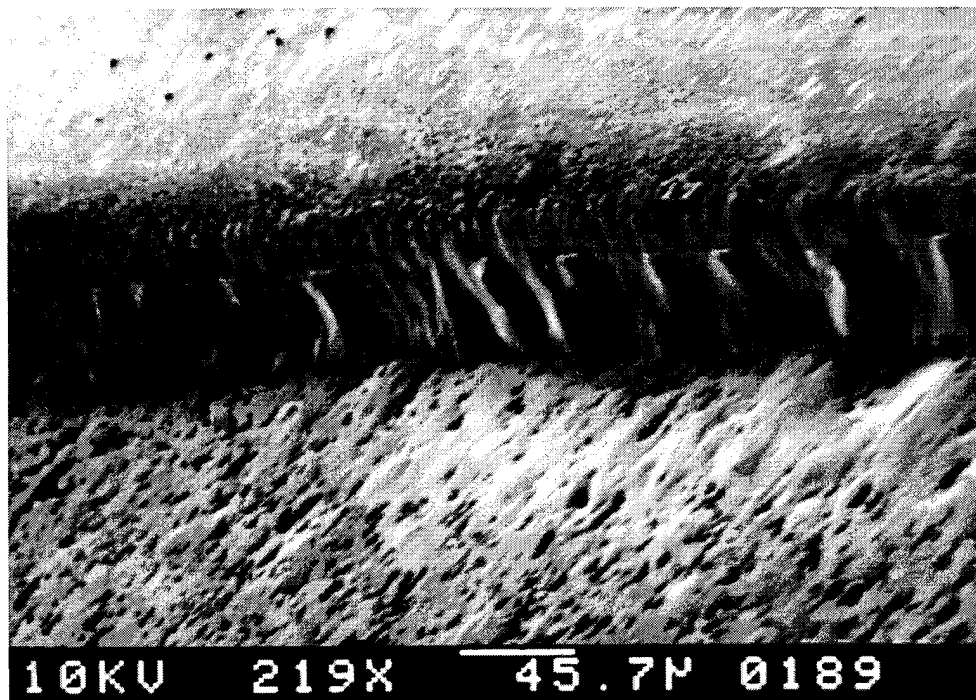


Figure 6-22. Sample with alumina substrate and 2.3 μm DLC coating after EDP etch for one hour. The DLC is bubbled and cracked at the trench floor, leaving a rippled edge that let the EDP reach the laminate. The laminate was curled up when just removed from the etch, but laid back down after drying.

The wall on the opposite side of the trench was ablated differently, leaving a ramp of material that forms a smoother transition from the trench bottom to the sidewall. The DLC covered this feature well, no breaks in the DLC were seen, as shown in Figure 6-23. This coverage prevented the EDP from penetrating this area of the sample, and the DLC on this side of the trench was not observed to be curled up immediately after removal from the etch.

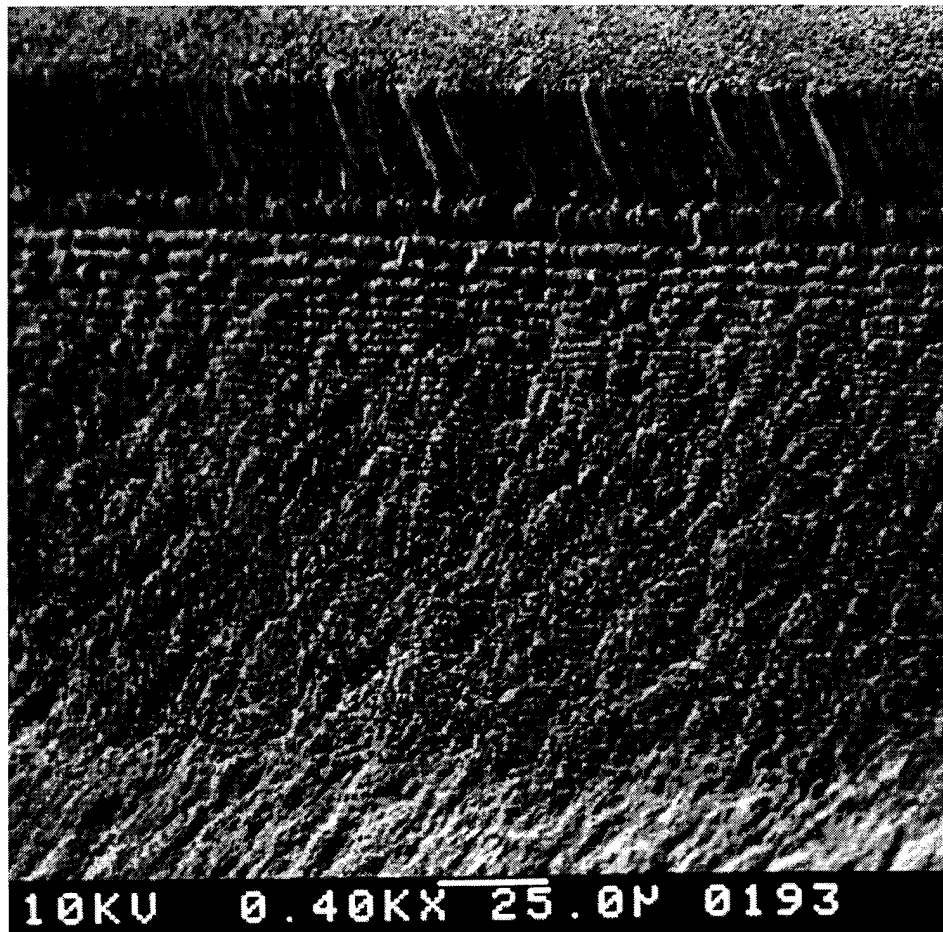


Figure 6-23. Sample with alumina substrate and 2.3 μm DLC coating after EDP etch for one hour. A ramp of material left by the laser ablation was well-covered by the DLC, protecting it from the EDP.

6.4.2.1.3.3 Sample 3, 0.95 μm DLC

On all the Plaskon samples, the DLC surface was very rough in the trench, which was not covered well by 0.95 μm of DLC. After the etch in EDP the DLC was cracked along the bottom of the trench wall, and at the sample edges, as seen in Figure 6-24.

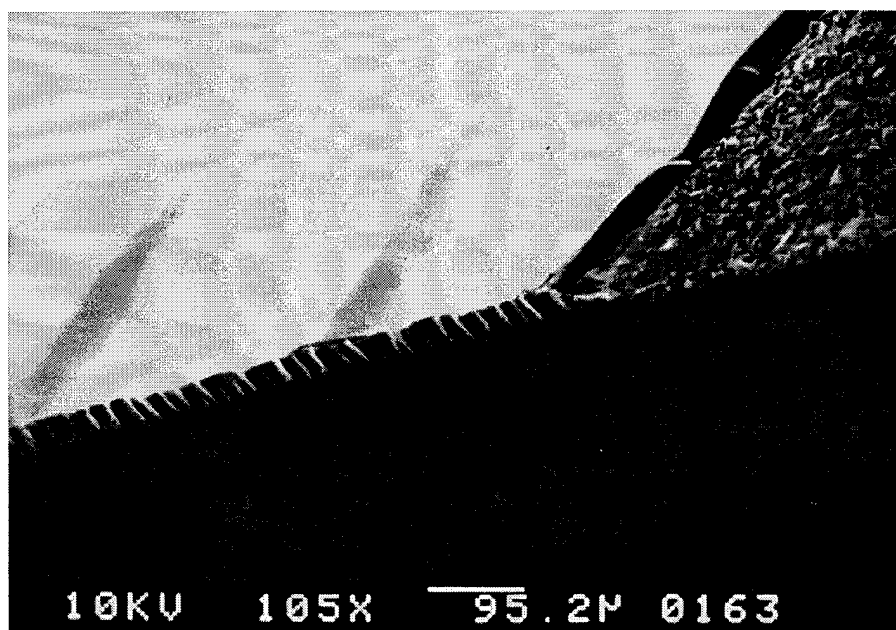


Figure 6-24. Sample 3, with Plaskon substrate and 0.95 μm DLC coating after EDP etch for one hour. The Kapton has delaminated around all the edges. It was curled up when still wet, but laid back down after drying.

6.4.2.1.3.4 Sample 3, 2.3 μm DLC

This sample showed the best results overall. Examination showed the DLC removed from the trench bottom after the EDP etch. The DLC covered the step at the top edge of the laminate very well, but cracked at the bottom, although no

delamination was observed on the sample immediately after removal from the etch or after drying. There were pinholes on the laminate surface, and the DLC failed around all the outside edges. So although the ablated trench edge was protected, the overall sample failed. Figure 6-25 shows a clean section of the sample, at the trench edge and away from the outside edges.

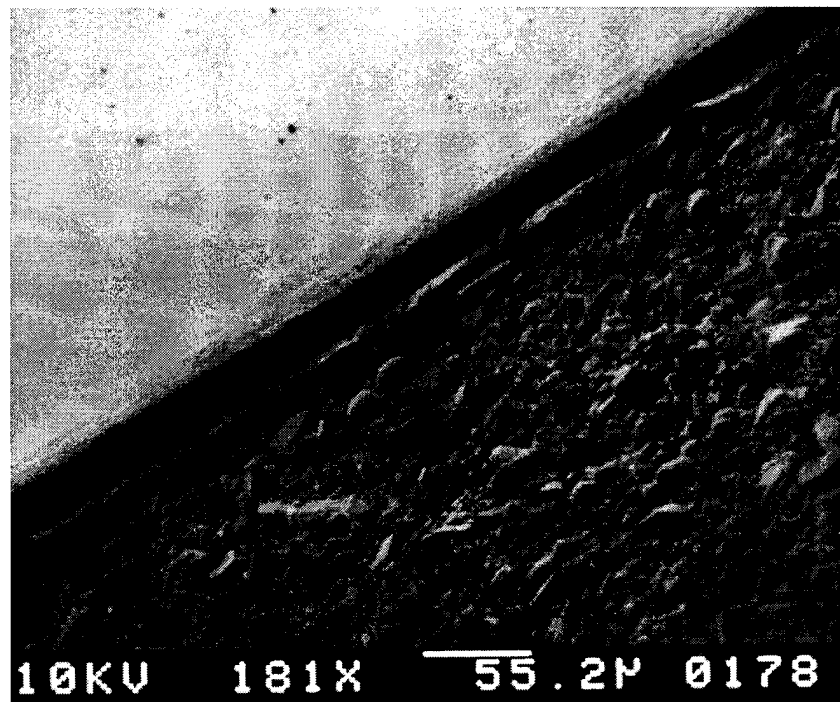


Figure 6-25. Sample 3, Plaskon substrate and 2.3 μm DLC coating, after EDP etch for one hour. The Kapton was protected at the top edge of the trench wall, but cracked at the bottom trench side walls, though no delamination was observed when the sample was still wet from the etch.

6.4.2.1.3.5 Sample 4, 0.95 μm DLC

On these samples the Plaskon substrate surface in trench was very rough, and the DLC did not cover it completely. The laminate peeled up from the diced edges of

the sample and from the trench edges. The surface of the laminate away from the edges also showed damage from cracks which allowed the EDP through.

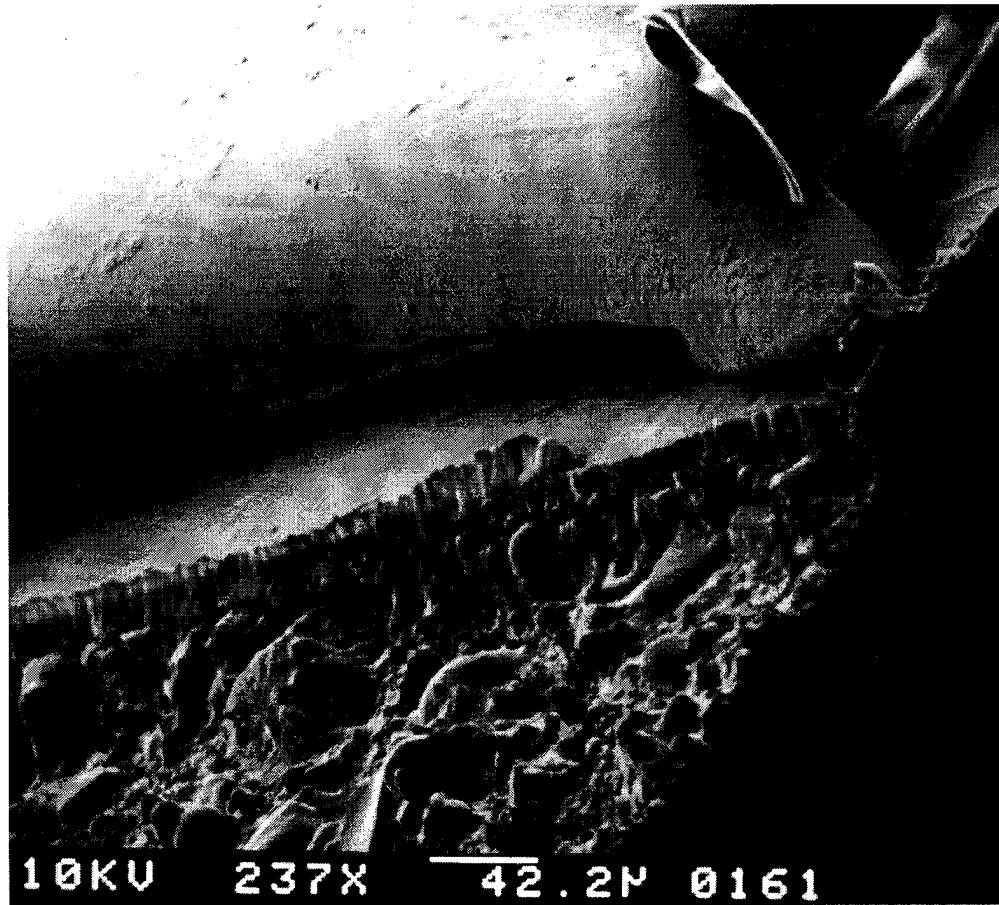


Figure 6-26. Sample 4, Plaskon substrate and 0.95 μm DLC coating, after EDP etch for one hour. The DLC coating failed entirely and the Kapton delaminated.

6.4.2.1.3.6 Sample 4, 2.3 μm DLC

The thicker DLC did not cover the trench floor well enough to protect the laminate on this sample also. The EDP penetrated the DLC and peeled the laminate, similar to the results seen in Figure 6-26. The surface of the laminate also shows

evidence of pinholing; the EDP got through the DLC and attacked the laminate, cracking the DLC further.

6.4.2.2 MMS MCM-D Etch Testing

Substrates without die were received from the MMS MCM process and were subjected to the MEMS release etch procedures. Figure 6-27 shows an unetched substrate at the edge, with bond pads and a wire buried under a polyimide layer. These substrates have an aluminum base plate and polyimide dielectric layers, as listed in Table 6-1.

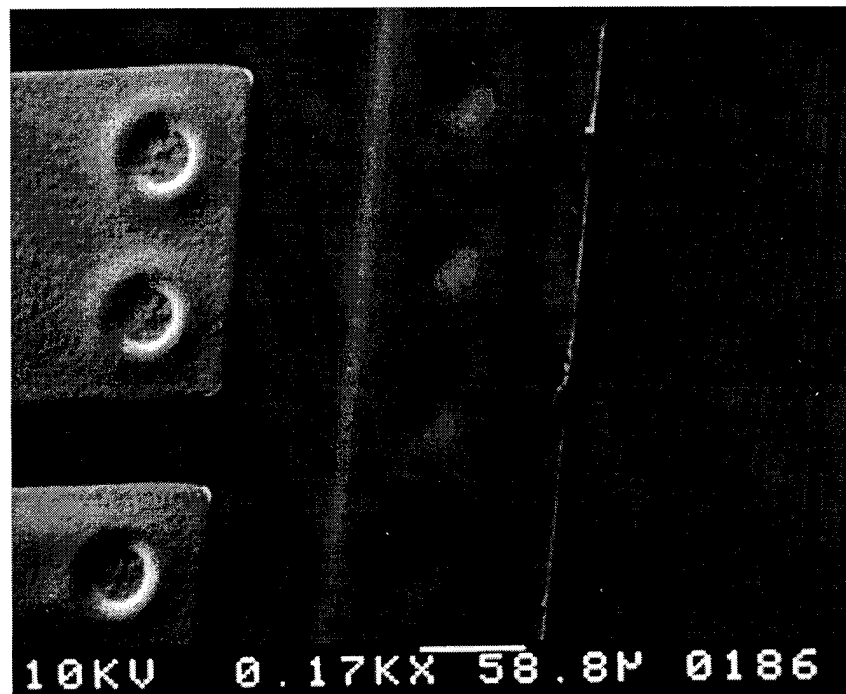


Figure 6-27. Unetched MMS MCM substrate. This view shows the sawed edge of the aluminum base plate on the right, with bond pads on the left and a wire buried under a polyimide layer, in the center of the micrograph.

6.4.2.2.1 TMAH Etch of MMS Substrate

For these samples, TMAH was available for the CMOS MEMS etch. The TMAH was diluted to a 10% strength with DIW for a faster etch that would be reasonably clean. The etch rate at this concentration and at a temperature of 84°C was reported as 1 µm/min [19]. EDP was not tried, as the HDI results showed the polyimide would not survive unprotected in that etchant.

Preliminary etches were performed on a CMOS MEMS and a MUMPS8 die which had bulk etch gauges. The gauge on the MUMPS8 die showed a 41 µm deep etch completed at 85 minutes, for an etch rate of 0.48 µm/min up to this observation. This is less than expected for the concentration used, half the etch rate given in the reference. The depth of a completely etched pit, d , is calculated from the width of the pit, w , using Equation (6-1); where 54.7° is the angle of the {111} planes from the horizontal surface of the die.

$$d = \frac{w}{2} \tan(54.7^\circ) \quad (6-1)$$

Figure 6-28 shows the etch gauge from the MUMPS8 die. The 70 µm wide pit is completely etched, indicating 58 µm depth after 115 minutes of etching, for an etch rate of 0.51 µm/min over the entire etch. This includes the 6.3 µm underetch of the nitride around the edges of the pit. The rough side walls in the smaller gauge squares are a result of the squares being too close together. For those pits, the walls between squares have been undercut, and are starting to join and etch straight down. This

creates the rough surface, which is also seen at the incompletely etched bottoms of the largest two squares.

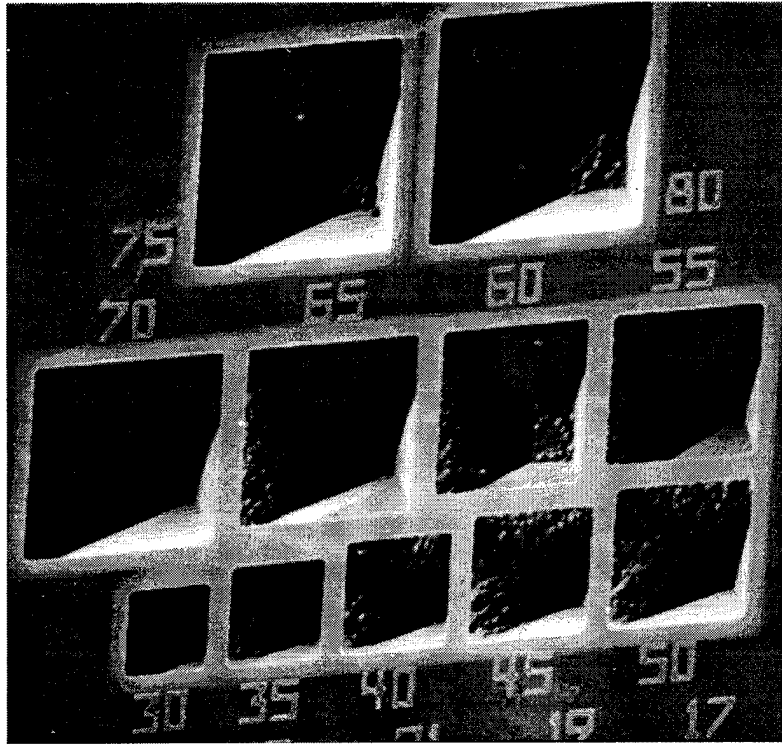


Figure 6-28. Etch gauge on the MUMPS 8 die, *poly0* labels indicate the drawn pit width. The completely etched 70 μm wide pit indicates a 58 μm depth, including the width of the pit etched under the nitride opening. The underetch appears as the light-colored margin around the pit openings. The larger two pits are not yet complete as can be seen by their rough bottoms. The smaller pits also show roughness, but this is due to their side walls being breached under the nitride and starting to etch down, most clearly seen between the 30 and 35 μm pits.

An MMS substrate was etched in the 10% strength TMAH mixture at 85°C. At ten minutes a visual inspection revealed bubbling near the die bond pads, so the etch was stopped. Inspection in the SEM showed that cracks had formed at many die bond pads, and the dielectric laminate was bubbling up, as shown in Figure 6-29. All of the

failures near bond pads were similar to this, possibly due to the topology of the dielectric at this feature.

The MUMPS8 die etch rates indicate an etch duration of 90 minutes at this concentration is needed to achieve MEM device release. The MMS substrate will probably fail in the TMAH etch long before the die are released. Also, the TMAH etches the aluminum substrate, even when silicon is dissolved in the mixture [18]. A 10% TMAH solution was saturated with dissolved silicon. Test die placed in the solution showed no etch rate on the gauge after 37 minutes at 85°C, but all the aluminum was removed from the exposed bond pads. This indicates that any MMS substrate aluminum wiring exposed by the polyimide failure would be subject to etch by the TMAH.

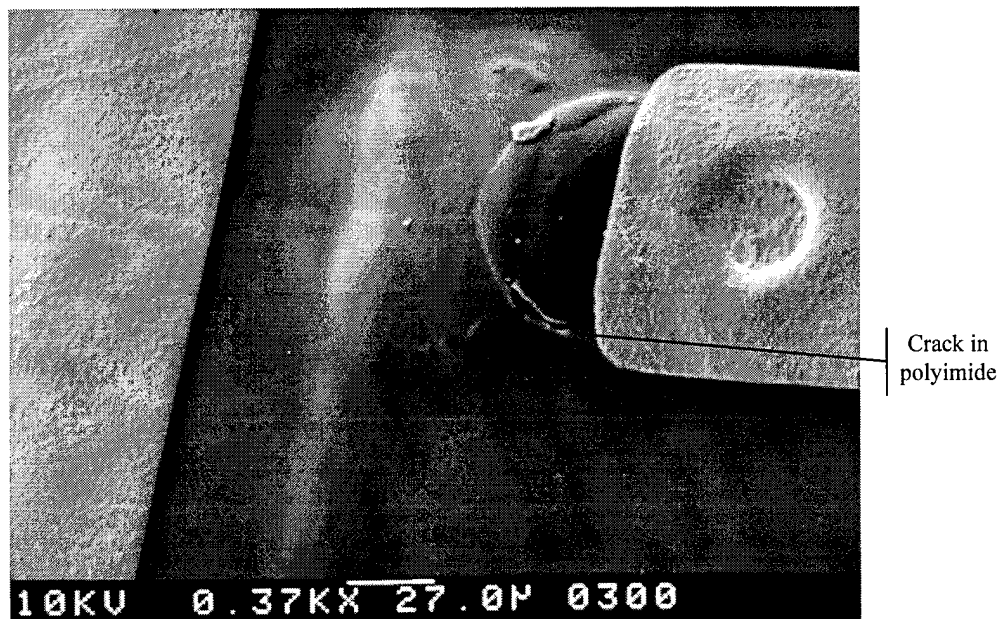


Figure 6-29. Failure of the polyimide dielectric near a die bondpad. The dielectric has split, allowing the etchant to penetrate and bubble the laminate. The underlying wiring is aluminum, so this would also be etched destroyed by the TMAH.

6.4.2.2.2 HF Etch of MMS Substrate

An MMS MCM substrate was also etched in HF for two minutes. The HF seems to have had little or no effect on the MMS materials as it did with the HDI materials. Some bubbles were observed to form in the open metal areas where the die are to be attached, but as Figure 6-30 shows, no visual change in any of the materials occurred. These results corroborate with the more detailed HDI materials testing and indicate that the MMS substrates would also easily survive the release etch needed for surface micromachined polysilicon MEM devices.

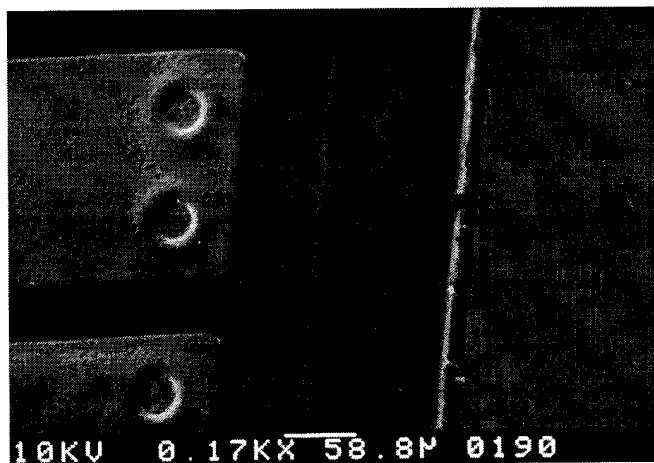


Figure 6-30. MMS MCM substrate etched in 49% HF for two minutes. This view shows the sawed edge of the aluminum base plate, with bond pads and a wire buried under a polyimide layer. These materials show no change from their unetched state, as seen by comparison with Figure 6-27.

6.4.2.3 Photoresist Compatibility Testing

Because neither foundry fabricated MEMS die is compatible with the other's release etch chemistry, one die must be protected while the other die is etched. The

tests on HDI and MMS materials indicate that none of the coatings available for the tests could withstand the anisotropic silicon etch, especially since that etch step is so long. However, most of the materials were resistant to the brief HF exposure, despite the high concentration of the acid.

The Kapton, polyimide, and epoxies were all resistant to the HF release etch procedure. Another common material that could be used for encapsulation is photoresist. The available photoresists were also subjected to the same set of chemical compatibility tests to determine if they could play a part in the overall packaging and release procedure.

6.4.2.3.1 EDP Photoresist Test

This test was to determine if the photoresist could be used to protect the aluminum pads which are etched by EDP. Four CMOS test die were coated with the photoresists available for laboratory use, Waycoat HR-200 negative photoresist, and Shipley S1350-J positive photoresist. The test die were coated with these materials and baked according to the hard and soft bake procedures listed in Table 6-5.

Table 6-5. Baking Procedures For Photoresist Etch Tests.

Photoresist	Soft Bake Procedure	Hard Bake Procedure
Shipley S1350-J	20 minutes at 70°C	20 minutes at 90°C
Waycoat HR-200	20 minutes at 65°C	20 minutes at 135°C

These die were placed in the EDP etchant at 95°C to see if the aluminum pads under the photoresist coatings were protected from the etchant. At 17 minutes into the etch, the die were pulled out for inspection. The two HR-200 photoresist samples were completely destroyed, the two S1350-J photoresist samples were still in place. At 30 minutes, the S1350-J was still in place, but the aluminum pads underneath were discolored, indicating the resists did not completely protect the die. After a full 54 minute etch duration, indicated by the etch gauges on the die, the soft baked S1350-J was completely removed. The hard-baked S1350-J washed off in the rinse, even though it was still in place when pulled out of the etchant.

6.4.2.3.2 HF Photoresist Test

This test was to determine if the photoresists could be used to protect a CMOS die while a co-packaged MEMS die was release etched in HF. A glass cover slide was used to represent the CMOS die, since the dielectric on those die is glass, and actual die did not have to be used since their etch gauges were not needed. The glass slide was covered with a drop of each photoresist and soft baked at 65°C for 20 minutes. Only soft-baked samples were used, because soft-baked photoresists can be removed with a wet rinse in acetone, while the hard-baked S1350-J photoresist must be plasma ashed in an oxygen atmosphere.

The full two minute HF etch was performed, followed by a five minute DIW rinse. The glass slide not covered by either photoresist was completely dissolved,

since it was etched from both sides. The S1350-J resist protected the glass, but became brittle and flaked off when touched. Thinner sections of the S1350-J did not protect the glass, indicating that the HF had penetrated it. The HR-200 resist was unaffected, and completely protected the glass, even at the thinnest sections of resist.

6.4.2.3.3 2-Propanol Photoresist Test

Part of the current MEMS release procedure is a final rinse in 2-propanol which drives out the DIW. The lower surface tension of the 2-propanol helps prevent released parts from being pulled down as it evaporates, as described in Section 2.1.2. To determine which photoresist could withstand this final rinse step, the same procedure as used for the HF test was repeated with a 5 minute soak in 2-propanol.

The samples were inspected after drying them on a warm hotplate (roughly 60C), also part of the release procedure, as listed in Section 6.4.2. The S1350-J positive photoresist, which partially dissolved in the 2-propanol, was still softened after being dried. The HR-200 negative photoresist was slightly softened, but did not dissolve at all. This slight softening is not a problem, since the photoresist is for protecting the die during the HF etch. The 2-propanol rinse step is used for both the MUMPS and CMOS rinse steps, and does not affect either die. The only concern is that the photoresist does not dissolve during the rinse step and leave residue on the released MEMS die. These tests indicated that HR-200 is sufficient to protect an electronics die during the entire HF release and 2-propanol rinse process.

6.4.2.3.4 TMAH Photoresist Test

For the TMAH test, a glass cover slide was again coated with the HR-200 and S1350-J photoresists and soft baked at 60°C for 20 minutes. The test slide was placed in the 10% TMAH solution for 15 seconds. The S1350-J immediately began dissolving. This was expected, since TMAH is a positive photoresist developer. The HR-200 negative photoresist was also softened and delaminated from the slide, but did not dissolve. This test indicates that, as with the EDP, neither of these resists can be used during the TMAH anisotropic silicon etch.

6.4.3 Full Packaging Test

The results of all the chemical compatibility tests indicated that it should be possible to perform a partial test on the assembled MMS MCM substrates. The HR-200 photoresist can be used to protect the CMOS MEMS die while performing the full release procedure for the MUMPS die. A test on a ceramic IC package showed it would be discolored by the HF release procedure, but the gold wirebonds and pads were unaffected. So all of the MMS MCM materials that would be exposed to the HF are unaffected by a two minute exposure.

Since both the tested anisotropic silicon etchants, EDP and TMAH proved harmful to the polyimide packaging materials, the CMOS MEMS die would have to be treated as just an electronics die and not released. Figure 6-31 shows a fully

assembled MMS MCM containing the CMOS MEMS and MUMPS test die shown individually in Figure 6-12 and Figure 6-13, respectively.

Following the procedure used for the photoresist etch tests, the CMOS MEMS die was glopped with HR-200 photoresist out to a distance of roughly 5mm from the die edges. The MCM was then soft baked for 20 minutes at 60°C and run through this release procedure:

- etch in 49% HF for two minutes, fifteen seconds,
- rinse in DIW for 5 minutes,
- rinse in 2-propanol for 5 minutes,
- dry on a warm hotplate at approximately 50°C.

The released package was tested on a probe station to determine if the CMOS die was protected and all the MUMPS devices were released. The HR-200 showed some thinning at the sharp corners of the CMOS MEMS die, but the HF did not appear to have penetrated, as the die was unetched. The MUMPS die did show evidence of residue at the corners. However, residue with this same appearance was also present on other die from the eighth MUMPS run. This test did not make clear if the residue was from the die or from some other material in the package, but no materials were observed dissolving in either the HF etch or the rinse steps. No tests were performed on the die adhesives, however, and a few small bubbles were observed near the die edges during both the HF and 2-propanol steps.

The MUMPS devices were all properly released, except for the residue in the corners. Several of the thermal devices, including ones with residue, were successfully operated both at their own probe pads, and from the pads on the MCM substrate. This indicates that the wirebond connections were unaffected. So this preliminary test indicated that the MMS substrates can be indeed be used to package foundry fabricated MEMS and electronic die together in a MCM.

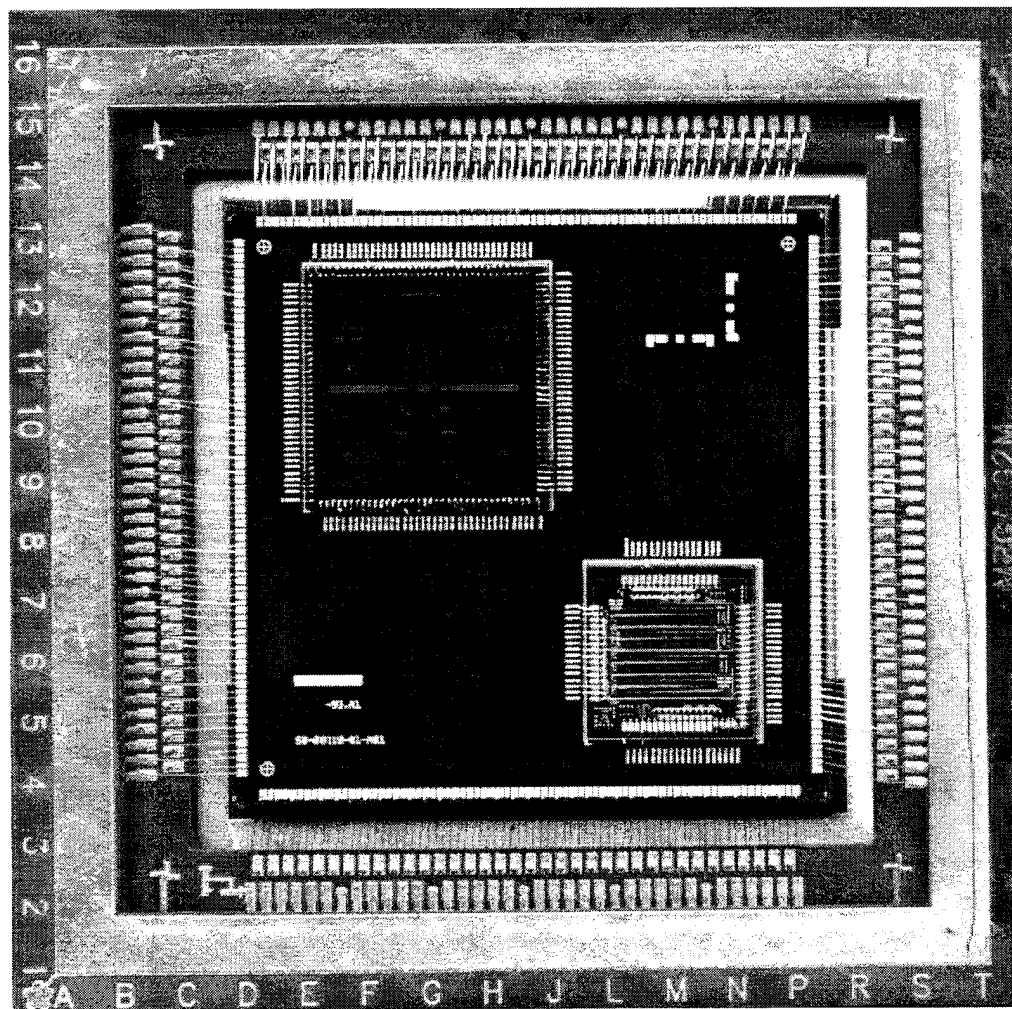


Figure 6-31. MMS MCM test package before MEMS release etch processing. MMS substrate is mounted in a 192 pin grid array package. The MUMPS (upper left) and CMOS MEMS (lower right) test die are attached and wire-bonded to the substrate, which in turn is wire-bonded to the PGA.

6.4.4 Polymer Wiring Test

For testing the polymer wiring concept for MEMS, an LCD watch was disassembled for parts. By coincidence, a MUMPS chip is just as wide as the LCD displays used in the cheap watches seen selling in stores for about \$2. This made the 'test fixture' easy to assemble. The polymer wire strip was used as is, the traces on the printed circuit board were cut where they run under the epoxy glob over the clock die, and 40 gauge wire-wrap wire was soldered to the traces, as shown in Figure 6-32.

Given the stacked structure of the polymer wiring, a larger pad area will lower the resistance as more resistive connections are added in parallel. A resistance in the range of a few to several tens of kilohms is sufficient for LCD applications because an LCD display, like electrostatic MEMS devices, depends on a voltage to operate and does not draw continuous current.

Measurements of the test setup through the two wire traces, the polymer wire, and across two connected pads on the test die showed a resistance of 2.5 K Ω per contact. Contact resistance measurements are sensitive to the contact pressure, one of the reasons for assembling the device with screws. Variations in the contact resistance between assembled devices may be unacceptable in some applications.

This contact resistance is sufficient for electrostatic MEMS operations. The resistance is on the order of the resistance of thermal actuators, so this connection would not be good enough for driving those devices at high currents. Contact resistance could be a benefit for electrostatic operations, because it would not allow

sufficient current to pass in case the electrostatic device shorts between electrodes, either due to an excessive drive voltage or mechanical shock, thus preventing the thin mechanical flexures from overheating and deforming. However, this much resistance would need consideration in MEMS sensing applications.

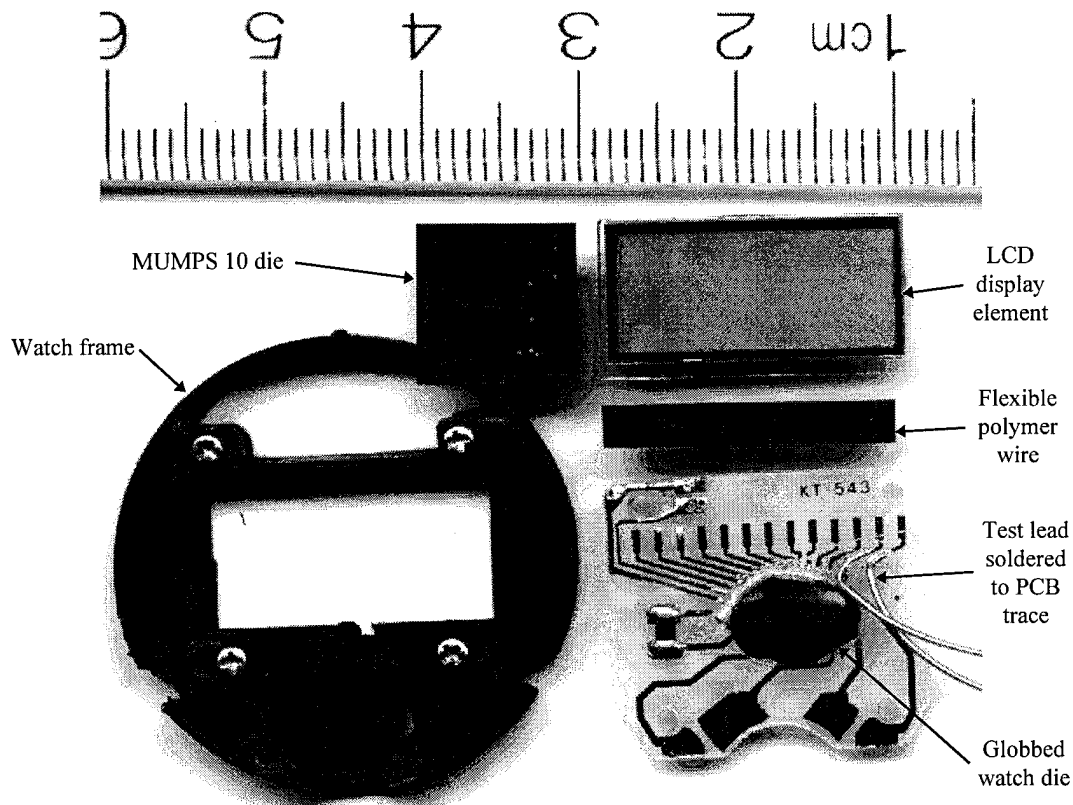


Figure 6-32. LCD watch printed circuit board rebuilt as test bed for the polymer wiring test. The section of polymer wire is shown alongside the board; the black color of the dielectric polymer in this wire hides the conductive traces, which are also dark. On the left is the framework that holds the LCD display or MEMS die. An unreleased MUMPS 10 die is placed next to the LCD display element to show their coincidentally similar widths.

Reliability tests could not be performed to measure the change in resistance due to environmental factors, this initial test is just a proof of the concept. However, the

reliability of this connection for electrostatic operations can be inferred from the fact that millions of LCD watches are manufactured for under \$1 wholesale and operate for years under non-laboratory conditions.

6.5 Conclusions

The flexible polymer wiring scheme is sufficient in some limited MEMS applications, especially for electrostatically actuated devices. However, the high resistance of the polymer wiring, and more importantly, the lower density of interconnections, limit its range of application. The mechanical connection with all contacts made at once makes this a cheap and easy-to-use packaging method for systems where 20 or fewer connections to electrostatic devices are needed. This is especially true if it is anticipated that the MEMS die will have to be swapped out regularly, as in a testing situation or in an environment where the MEM devices will be degraded. This also makes a very inexpensive packaging where this type of connection is appropriate, as seen by its current LCD watch mass-market applications.

Chemical compatibility tests indicate that CMOS MEMS die will have to be released before packaging in either of the commercial MCM processes. This is not a great limitation, though, for two reasons. First, CMOS MEMS can already be integrated with circuitry on the same die, so they are less likely to need MCM packaging. Second, they are more robust, so if they are to be packaged in MCMs

they should be better able to withstand mounting and bonding after release. They would still have to be protected from the HF release etch of any surface-micromachined MEMS die if packaged together. Any purely electronic die would also have to be protected, but they could be encapsulated, either temporarily or permanently, since they have no moving parts.

Both of the commercial MCM processes contain materials that can withstand a two minute etch in HF. The successful release etch of the MMS MCM is a useful result, since surface-micromachined MEMS like the MUMPS die often have no electronics on them, and so would benefit the most from the lower noise connections and higher interconnect line count available in MCMs.

References:

1. J. Dybowski, "Embedded techniques," *Circuit Cellar INK, The Computer Applications Journal*, No. 52, pp. 76-82, November 1994.
2. Intel MCS-80/85 Family User's Manual, Intel Corp. 3065 Bowers Ave, Santa Clara, CA 95051, pp. 4-2 - 4-3, October 1979.
3. A. Laskar and S. Blythe, "Epoxy multichip modules: a solution to the problem of packaging and interconnection of sensors and signal-processing chips," *Sensors and Actuators*, A-36, pp. 1-27, 1993.
4. J. Lyke, "Multi-chip module technology for military systems," *Relevant Papers in Advanced Packaging: a compilation*, Phillips Laboratory, Applied Systems Branch, PL/VTEE, Kirtland AFB, NM, 1991.
5. J. Lyke, "A brief white paper supporting the case of electronics miniaturization approaches for space systems," Phillips Laboratory, Applied Systems Branch, PL/VTEE, Kirtland AFB, NM, 1994.
6. K. Marcus, D. Koester and V. Dhuler, "MEMS infrastructure: multi-user access and smart MEMS," *Government Microcircuit Applications Conference*, pp. 207-210, 1993.
7. Information available from the MCNC World Wide Web home page, WWW url: <http://www.mcnc.org>.
8. Information obtained at the Second Annual MUMPS User's Group Meeting, Chicago O'Hare Airport Hilton Hotel, 27 October 1995.
9. G. Takahashi and E. Kolesar, "Silicon-hybrid wafer-scale integration achieved with multilevel aluminum interconnections," *Proc. IEEE National Aerospace and Electronics Conference (NAECON)*, Dayton, Ohio, pp. 17-22, May 1989.
10. J. Lyke, "Two- and three-dimensional high performance, patterned overlay multi-chip module technology," *Relevant Papers in Advanced Packaging: a compilation*, Phillips Laboratory Applied Systems Branch, PL/VTEE, Kirtland AFB, NM, 1991.
11. Sample and information provided by J. Lyke, Phillips Laboratory Applied Systems Branch, PL/VTEE, Kirtland AFB, NM.

-
12. Information available from the MOSIS World Wide Web home page, WWW url: <http://info.broker.isi.edu/1/mosis>
 13. W. Daum, W. Burdick, R. Fillion, "The GE ICs first multichip module technology," *Relevant Papers in Advanced Packaging: a compilation*, Phillips Laboratory Applied Systems Branch, PL/VTEE, Kirtland AFB, NM, 1991.
 14. *Texas Instruments MCM Foundry User's Guide version 4.0*, Texas Instruments, Inc., Dallas, Texas.
 15. Sample HDI module and information provided by U.S. Air Force Phillips Laboratory.
 16. Information available from the Analog Devices/UC Berkeley ARPA iMEMS World Wide Web home page, WWW url: <http://nitride.eecs.berkeley.edu:8001>
 17. F. Goodenough, "Airbags boom when IC accelerometer sees 50 G," *Electronic Design*, Aug 8, 1991.
 18. Private communication from Richard Saia of the General Electric Corporate Research Center, Schenectady, NY.
 19. O. Tabata, R. Asahi, H. Funabashi, K. Shimaoka, and S. Sugiyama, "Anisotropic etching of silicon in TMAH solutions," *Sensors and Actuators A*, Vol. 34, pp. 51-57, 1992.

7. Conclusions

This dissertation research investigated structures and methods for implementing and packaging complex, large scale microelectromechanical devices and systems using foundry fabrication processes. This was accomplished through the design, fabrication, and testing of complex microelectromechanical devices and systems, and an investigation of foundry fabricated packaging options. By achieving this goal, this research provides new ways for research institutions with minimal in-house fabrication capabilities to create and package large, complex MEM systems using the commercially available foundry services. In doing so, this research expanded the knowledge in the areas of designing large MEM device arrays and packaging compatibility with MEMS. It also created completely new areas of research in hinged wiring and high force thermal actuator arrays, areas in which a review of the literature and experience gained in the design and fabrication of MEM devices indicated new approaches were needed. Through these achievements, this dissertation helps advance research in the MEMS field in general.

The devices and systems presented in this dissertation bear out the utility of the concepts, devices and techniques developed during this research. Some of these devices and ideas are now being tested at other research institutions: the University of California, Los Angeles, (thermal actuator arrays), Stanford (holographic mirror arrays), University of Dayton Research Institute (hexagonal spatial light modulator), and the U.S. Air Force Wright Laboratories (beam steering mirror arrays). Since

most of these techniques and devices have been presented by the author at conferences, meetings, and in publications, further applications are likely.

Table 7-1 lists some of the devices and techniques developed in this dissertation research, along with application areas. Hundreds of different devices and components and dozens of die layouts were designed and tested, then improved or superseded to reach the goals of this research and create the devices listed in Table 7-1. These results support the author's initial research approach and design philosophy: that the easiest, quickest way to learn a fabrication process is to first try everything imaginable and see what comes of it. After such an immersion an experienced feel for the process is developed, so when a specific design must be drawn, less time is wasted on unworkable approaches.

It is important to continue fabricating process test structures and 'wild ideas'. In this dissertation research effort the small, and sometimes not so small, investment in die area and design time has always been rewarded with new or reinforced knowledge of what is and what is not possible to create. This is especially true if the structures seemingly have nothing to do with the 'primary' research effort, because that is when new possibilities are discovered. A good example is the MUMPS stacked *poly1/poly2* technique, which was first noticed as a design 'failure' of an exploratory thermal emitter design, but later proved instrumental in the design of successful mechanical structures such as the stepper motors.

Table 7-1. Applications for Techniques and Devices Developed or Investigated in This Dissertation Research.

Techniques And Devices	Application Areas
Hinged wiring method for surface micromachining processes	Metal-to-metal low resistance connections to hinged and sliding structures, method to make low resistance contacts in microrelays
Thermal actuators and arrays	Devices requiring compact, high force actuation at low voltages and frequencies
Latching relays	Switches with isolation of the signal lines from the drive circuit, stay on or off without power being applied
Thermal and electrostatic tilting mirrors	Optical beam steering, scanning
Stacked <i>poly1/poly2</i>	Surface micromachining technique for creating structures with a higher aspect ratio than with the individual polysilicon layers
Thermal stepper motors	Rotary or linear positioning of MEM structures, self-assembly of MEM structures
Mirror array cover plates	Method for reducing stray reflections from mirror arrays for increased optical efficiency
Thermal mirrors	Low frequency (< 1 KHz), close packing mirrors for linear arrays
Large mirror arrays	Spatial light modulators for aberration correction, optical communication, holographic data storage, optical beam steering
MCM packaging for MEMS	Method to use foundry process to package surface micromachined MEMS with electronic die
Polymer wire packaging	Inexpensive method for packaging MEM devices so they can be easily replaced
Overhanging grippers	Ways to place grippers into position off the die where they can be used effectively
Topological design for bossing and the 'lost poly' technique	For forming surface-micromachined structures by taking advantage of the topology that usually is a detriment to device design

7.1 Packaging Options

The packaging tests performed to date indicate that most commercial multi-chip packaging methods can be adapted for surface micromachined MEMS die. Methods like MCM-D, -C, or -L can be adapted through the protection of HF-sensitive portions, as proven by the successful release of a MUMPS die in a foundry-fabricated MCM-D package. Tests also indicate that the more sophisticated High Density Interconnect or other dielectric overlay/direct metal wiring processes would be even more amenable to MEMS insertion. These processes protect the non-MEMS die as a matter of course by overlaying them with HF resistance materials as part of the wiring fabrication.

Test modules containing MUMPS and CMOS die are currently in fabrication at GE Corporation to test the HDI process. Though they won't be delivered in time to be part of this dissertation, the research results from releasing the MUMPS die and testing the package will have important implications for the agency sponsoring this research, the U.S. Air Force Phillips Laboratory. These packaging methods may provide a pathway for meeting the goals for smaller and cheaper spacecraft as outlined in Chapter 1.

The flexible polymer wiring scheme is a way to package MEM devices inexpensively and simply, with obvious implications for mass-marketed MEM devices, as evidenced by its current application for LCD watches. This completely dry, mechanical packaging and assembly method can be used in applications that

require up to a few tens of die connections, though the high resistance of the polymer wiring used for this test limits its application to voltage driven devices as opposed to devices like thermal actuators that need a current supply. The method can be applied right here at AFIT in test setups for electrostatic MEM devices.

CMOS MEMS remain a challenge for packaging since none of the test packages proved resistant to the anisotropic etchants needed to release CMOS MEMS devices. However, the CMOS MEMS devices have proven to be generally more robust than the surface micromachined devices, so perhaps they could withstand being packaged after release.

7.2 Comparison of Foundry MEMS Processes

In a comparison of the three foundry fabrication processes used in this dissertation research, the most flexible and functional is the MUMPS surface micromachining process. The other two processes, LIGA and CMOS MEMS, provide too few releasable structural layers to create very complex devices. The greater flexibility and the ability to pack devices more closely together allow the MUMPS process to be used for truly large scale MEM designs such as spatial light modulators and other optical arrays.

However, the LIGA and CMOS MEMS processes have advantages that make them better choices for specific applications. The CMOS MEMS process has the obvious advantage of being completely compatible with CMOS electronic circuitry, so if a MEM system does not depend on large motions or dense packing, it can take

advantage of the availability of electronics on the same die. Experience with the Orbit CMOS fabrication process indicates that the MEMS features remain secondary considerations in this primarily electronic process, as evidenced by several fabrication runs ruined by glass left in the *open* areas.

The withdrawal of ARPA funding for CMOS fabrication runs cut short the wide-open experimentation in the CMOS MEMS process that was undertaken at the beginning of this research. However, the author feels that the same unbridled experimentation that was tried in the MUMPS process could also be applied to the CMOS MEMS process, with the same benefits accruing in experience being gained and new design techniques being developed.

Fewer conclusions can be drawn about the LIGA process, since only one run was completed during the course of this research. While its single releasable layer places it at a disadvantage when trying to create complex mechanical structures, its metal structures are natural candidates for electromagnetic devices. Such devices have already been extensively explored by many other researchers; however, the latching relay applications, first explored in this research, are also promising.

Although the thermal actuator developed in the MUMPS process had its origins in a LIGA thermo-magnetic device, there have been very few applications of LIGA thermal actuators. Their high current demands and low voltage operation are a drawback to powering them from standard integrated circuitry; but if more LIGA runs are offered, these devices should be explored further. Special effort should be made to create arrays of thermal actuators.

The structures and techniques created during this dissertation research were intended to explore and extend the range of devices and systems that could be built in foundry processes, where the designer controls only the dimensions of the features laid out in foundry specified material layers. But imagine what could be done if designers did have some limited control over the fabrication process. They could specify three or more polysilicon layers, allowing truly flexible hinged structures. They could have refractory metal runs encased in nitride layers under the polysilicon, or layers which are planarized so they don't affect the overlying polysilicon structure topology. There could be releasable non-conductive layers, so that hinged actuators would not need to be raised on fragile, separate plates, and complex wiring could be put on hinged structures to power devices far from the substrate. ARPA and the foundries it supports are even now developing programs to bring these additional benefits to MEMS researchers.

7.3 Future Directions

As the previous paragraph indicates, MEMS research is a topic of continuing interest to the author. Large research projects are never completely finished, and this one leaves some questions to be further explored, and poses new ones. Some research threads that were started during the exploratory phases of this research are listed in the following paragraphs. The continuing evolution of devices developed during this research could provide the basis for future AFIT class projects and theses.

The latching relay structures could be built in any fabrication process that has at least a single releasable structural layer. MUMPS versions of such relays have been submitted for fabrication. One possible way to decrease the contact resistance of switches made in the MUMPS process is to make the mating parts of the relay in electroless nickel, attached to polysilicon actuator arrays. The standard gold wiring can be used to run the signals to bond pads.

Thermal mirror arrays have also been submitted for fabrication. Studies need to be made of their uniformity, current versus deflection, and frequency response characteristics. Thermal cross-talk between closely packed devices may also be a concern. As seen in Chapter 5, these devices could make possible a low-voltage, high density mirror array that is directly compatible with standard CMOS circuitry and which operates at frequencies up to several kilohertz.

Ideally, all MEMS designs would be completely batch manufacturable, but to date, hinged devices have had to be hand assembled using a microprobe station. The linear thermal motors show promise of having enough force to make sequenced self-assembly of complex hinged devices a reality. Devices intended to prove this concept are also in fabrication.

The holographic data storage array is an ongoing and highly visible project involving ARPA, industry, and academia. Refinements to the mirror arrays would provide good introductory projects for a MEMS class, since the devices are straightforward electrostatic mirrors. Other mirror-based projects that are providing

material for AFIT research are the diode power combining mirror array, and beam steering piston and tilt mirrors.

Hinged wiring is a proven concept invented during this dissertation research, but it is far from completely refined. Versions of wiring for hinged plates currently in fabrication include placing the hinged plate contact lower, and creating a contact on the hinged plate from overlapped gold which covers the edge of the *poly2*.

If funding is available for CMOS MEMS fabrication, or better bulk etching techniques become available, the thermal stimulator array research should be revisited. These arrays could serve not only as tactile thermal input devices, but also as low resolution infrared displays. The design also provides a head start for students interested in exploring CMOS MEMS devices attached to CMOS circuitry.

If arrays of thermal actuators prove viable in the LIGA process, then they should of course be applied to the latching relay design. The extremely low contact resistances exhibited by the existing devices indicate that this is definitely a promising direction to take in microrelay research, and one that is of interest to the sponsoring organization.

Many other new devices and concepts were invented and explored during the course of this research. The device designs, SEM micrographs and descriptions, along with this dissertation, remain behind to be mined for ideas and used by follow-on researchers.

Appendix A

This appendix contain plots of all the die designed in whole or in part during this dissertation research. These plots show the variety and number of die that were designed, fabricated, and tested to gain the knowledge and experience needed to complete this dissertation. Many of the devices on these die did not become a direct part of this dissertation research, but all provided design and test experience.

The die are grouped by MEMS technology and arranged by fabrication sequence. The CAD layout drawings are used to illustrate the die, except for the third CMOS test die, for which a scanned micrograph provided a better view. Micrographs that exist of other die are used in the main body of this dissertation, and are referred to. The CAD layouts, as used here, show a reduced number of drawing layers to keep the features recognizable.

The separate sections on each foundry service start with a brief history of all the die, including any changes or problems with the fabrication runs. For the MUMPS die, a listing of the reported thin film properties provided by MCNC is included for the fabrication runs completed to date. Also included after each die plot is a list of the major device subcells on the die, each with a brief explanation of what the device is or what it was supposed to accomplish. The location of a copy each listed device is indicated on the die plot with lettered callouts. These lists show only major cells or device types; each die may contain many individually designed sub-devices or versions of the listed device. Many of the die were put together by the author from subcells designed by other researchers. On the die that contain a mix of researchers' devices, the author's own devices are indicated on the plot or in the caption.

A.1 CMOS MEMS Die Plots and Device Listings

Research into CMOS MEMS started off with two bad fabrication runs. On the first run, testchip1, the drawings were not properly translated to the CIF file, with the

result that the glass was not removed from the *open* features. On the second attempt, testchip2, the design was sent to the wrong fabricator, who interpreted the *open* features as pads and put aluminum in those areas. The third attempt, testchip3, was successful and resulted in well-fabricated die. Since the first two test chips were nearly identical to each other and contain the same devices as the third chip, only the third chip is shown here. The major difference between the designs is that the third die has some devices at one edge of the die which are connected to pads at the other edge of the die.

The fourth CMOS MEMS run, traychip1, was fabricated successfully, but showed evidence of incomplete glass removal at the edges of the *open* areas. On the fifth run, traychip2, glass covered nearly the entire *open* areas, leaving the MEMS structures unreleasable. The 'fabtest1' die, which was intended to be fabricated as a MOSIS 'tinychip', was incorporated into the traychip2 design instead.

The next run by the author was the packaging test die, called ATCM02 for 'Assembly Test Chip - MEMS', and it was the second assembly test chip, the other one being a MUMPS design. This design was fabricated twice, and both fabrication runs were successful. The 'cmos4' die was only partly laid out by the author, and was also fabricated successfully, with only small fringes of glass in the *open* areas.

A.1.1 Testchip3 Die

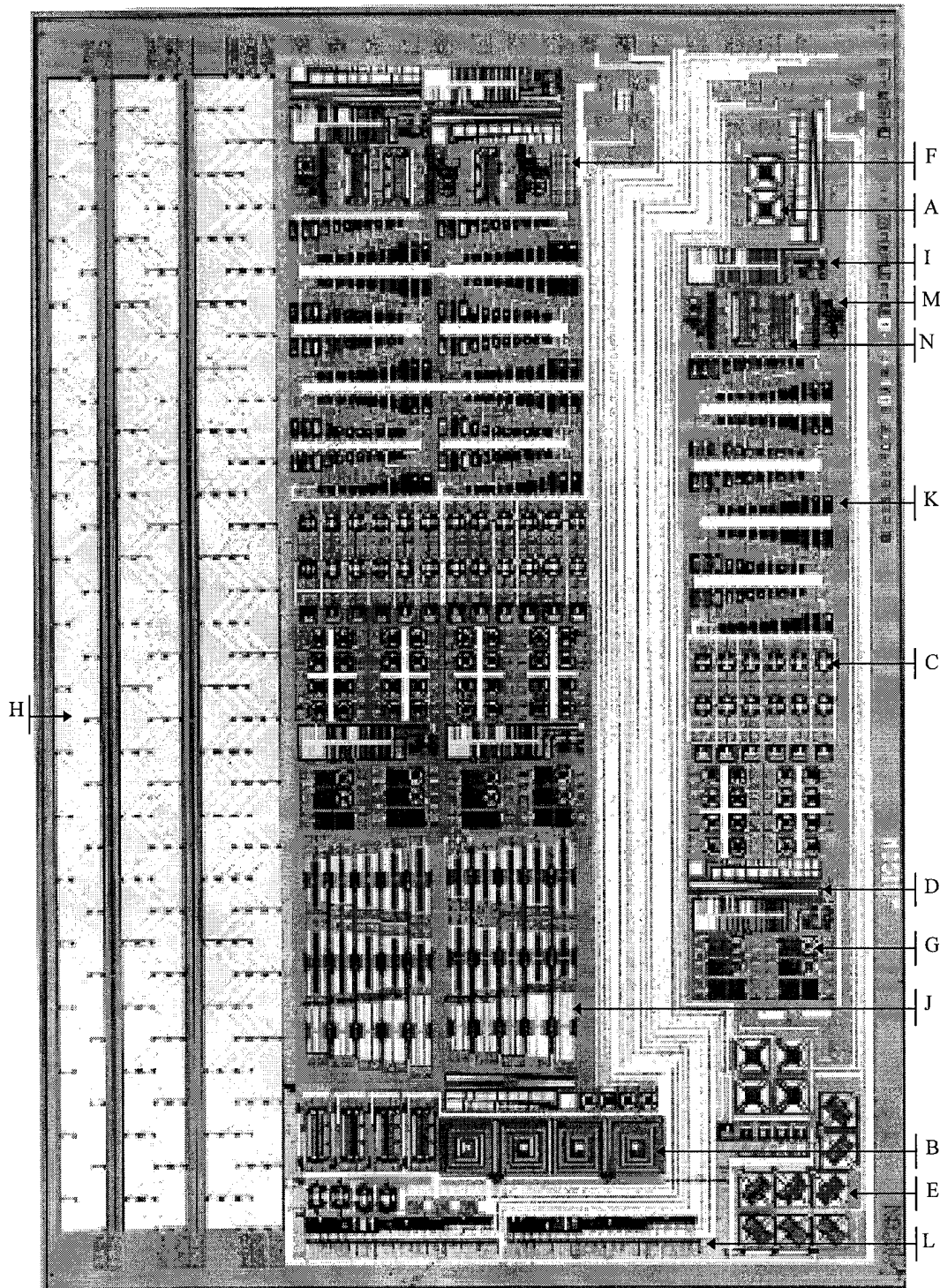


Figure A-1. Third CMOS MEMS test die, 'testchip3'.

A. Irpixel	suspended heating element
B. big_spiral	large spiral actuator with a mirror at the center
C. defrm_mirror	thermally tilted mirrors
D. etchdepthtest	etch gauge with a series of open squares
E. flex_mirror	suspended mirror with heating elements to curl it
F. fuselink	suspended metal link to act as a fuse
G. inductors	suspended spiral inductors
H. inductortest	large zigzag inductors for another researcher
I. layer_test	various materials in cantilevers, bridges over <i>open</i> areas
J. mech_filter	failed attempt to make a suspended polysilicon device
K. mirror_levers	thermal bimorph actuator cantilevers in many sizes
L. nswitch	nmos switch for controlling polysilicon heaters
M. ringctr_stage	inverter stage for a ring counter circuit
N. var_xformer	side-by-side flat coils, one of which is moved thermally

A.1.2 Traychip1 Die

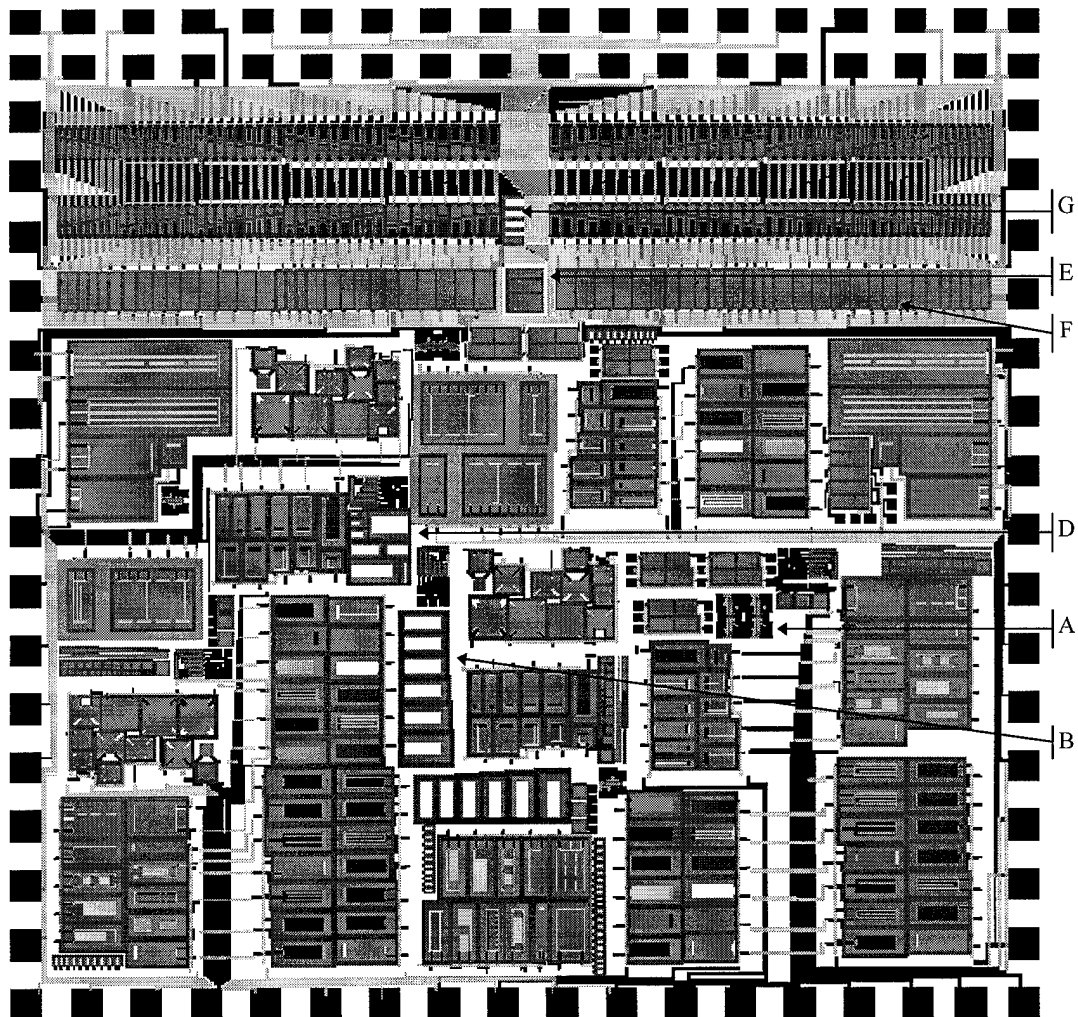


Figure A-2. Traychip1 die, the author's devices are mostly in the dense arrays at the top third of the die. Devices in the lower half are bimorph thermal actuators and test gauges for determining the minimum *open* width design rule.

- A. IRpixel_tiny8 minimum size suspended heating resistors
- B. opentest test cell to determine *open* width design rules
- C. defrm_mirror4 another thermally tilted suspended mirror
- D. etchtest an etch gauge with glass cantilevers
- E. risers bridges with mirrors in the center, bowed thermally
- F. snakes various sized zigzag thermal actuators
- G. snakes_gauge glass-only version of 'snake' cells for etch timing

A.1.3 Traychip2 Die

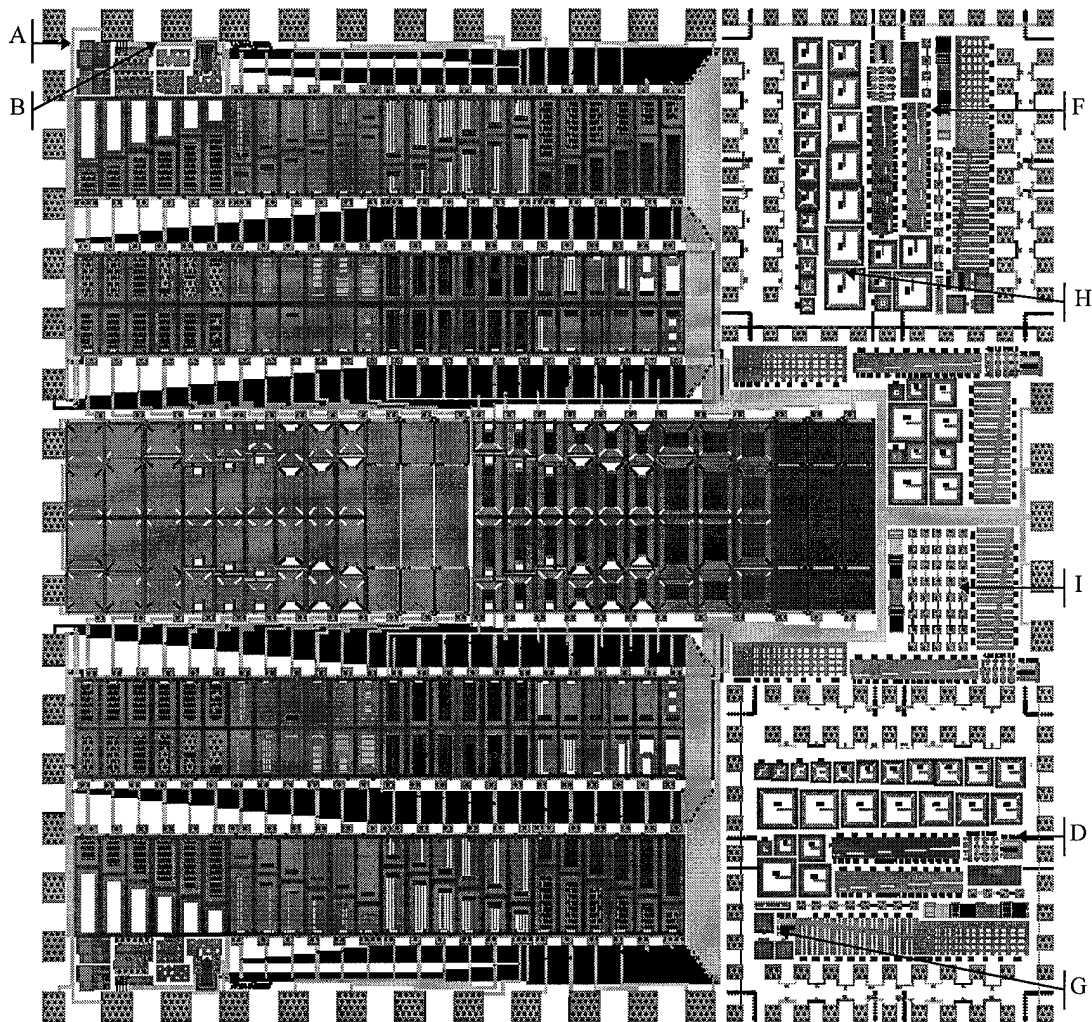


Figure A-3. Traychip2 die. The sections in the upper and lower right corners are a die layout intended for a smaller die but fit onto this one. A close-up of that die layout is shown in Figure A-4.

- | | |
|------------------|--|
| A. NEWS_cell1 | cell designed for a paper on anisotropic bulk etching |
| B. NEWS_cell2 | cell designed for a paper on etching suspended structures |
| C. fabtest1 | tinychip design shown in Figure A-4 |
| D. incursionTest | device to measure etchant incursion sideways through glass |
| E. m1m2test | test to determine etch rate of exposed metal layers |

- F. pstopGauge open square etch gauge with *pstop* in the *open* areas
- G. speckles *open* areas speckled with glass squares for etching pyramids
- H. squareTest Large suspended squares with scales for etch timing
- I. wireTest test to determine current carrying capacity of wiring layers

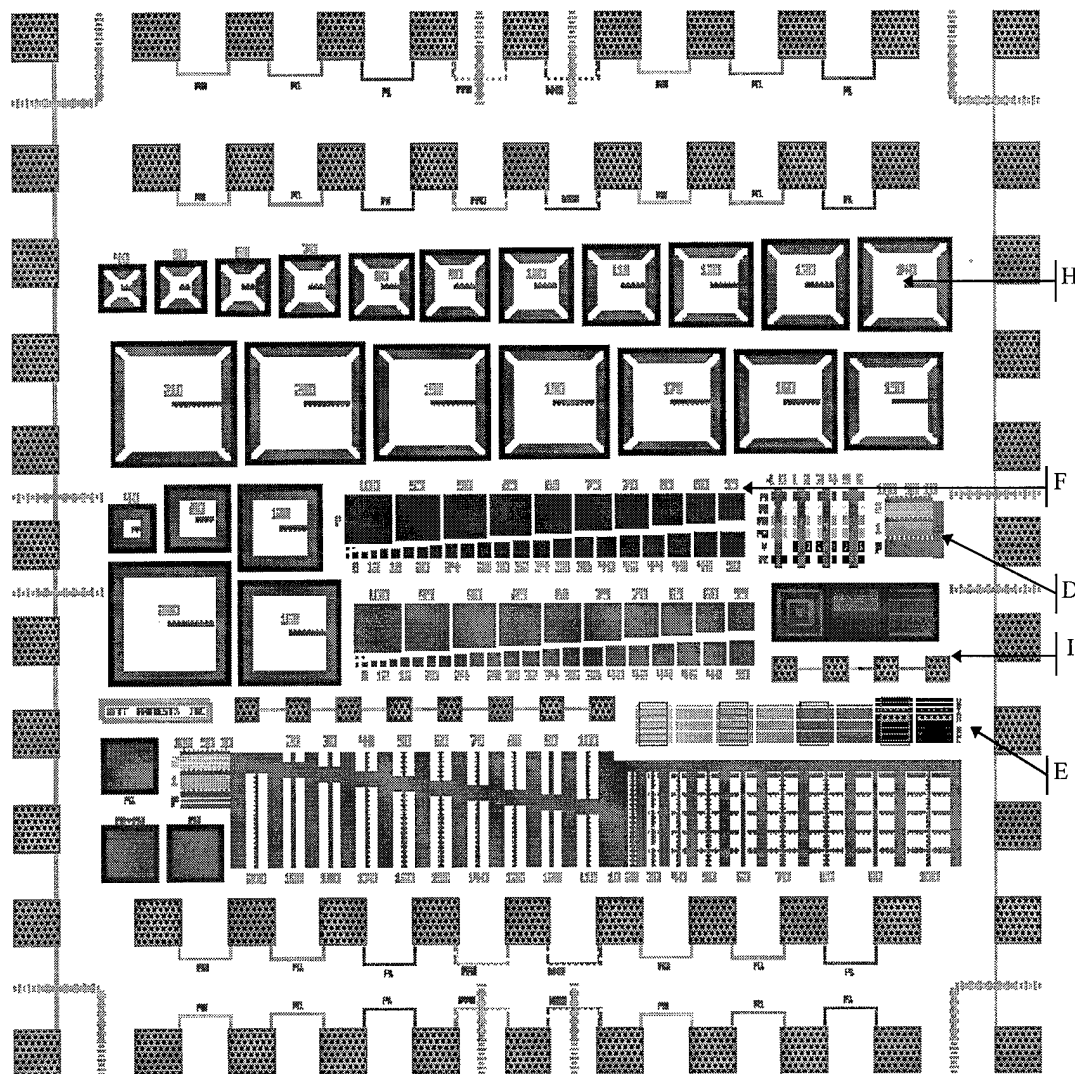


Figure A-4. Fabtest1 tinychip design. This chip design contains test structures to determine design rules and etch rates of suspended and embedded structures and the die edges.

A.1.4 CMOS4 Die

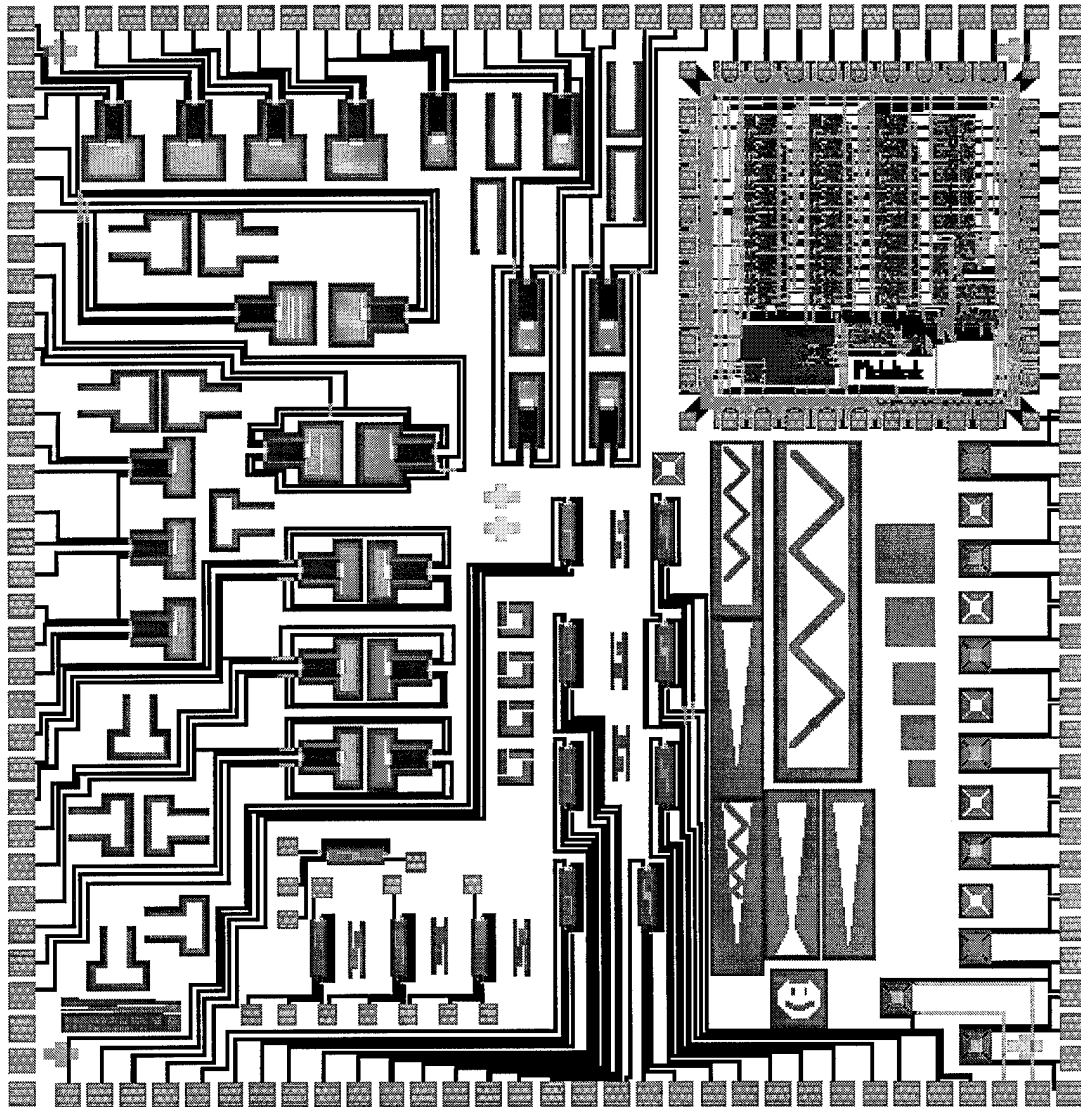


Figure A-5. 'CMOS4' die laid out in part for another researcher. Upper right corner is a tinychip design of electronic circuits for a second researcher. The author's designs are the large zigzag and triangular glass cantilevers for testing long etch durations.

A.1.5 CMOS Packaging Test Die

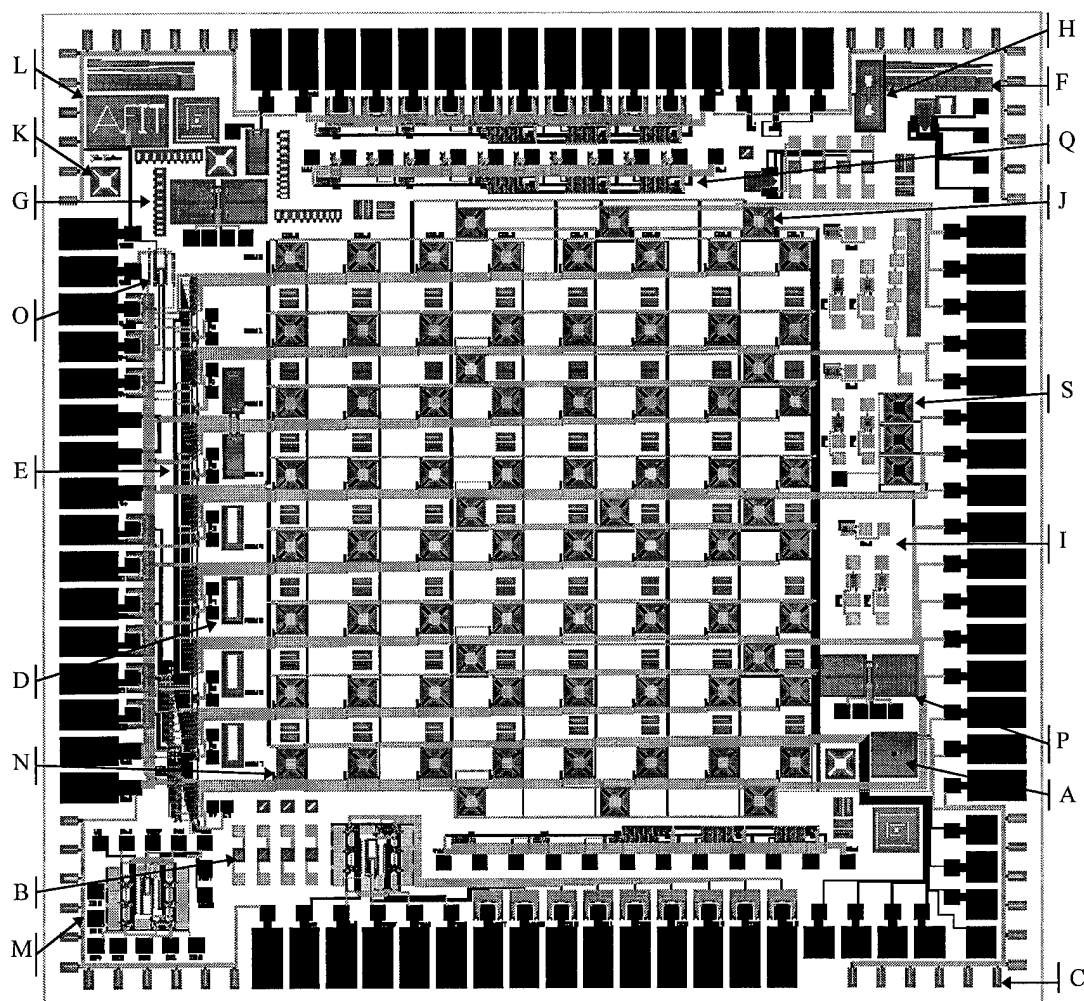


Figure A-6. CMOS MEMS packaging test die. The center of the die contains an array for thermal tactile stimulation. On the left is addressing circuitry for the stimulator array, on the bottom are generic electronic circuits, on the right and top are ring counter circuits. In the corners are breakage monitoring structures and generic MEM devices. A micrograph of this die is shown in Figure 6-12.

A. big_spiral	large spiral thermal actuator
B. break_fuse	suspended glass bridge with metal wire running through
C. break_test	small cantilever with polysilicon resistor along its length
D. cant_gauge	glass etch gauge for cantilever cell
E. decoder_3-8	decoder circuitry for selecting thermal stimulator cells
F. etchdepthtest	open square etch gauge
G. opentest	minimum <i>open</i> width test cell
H. hands	hand-shaped thermal bimorph cantilever actuators
I. hdickt	ring counter circuits attached to HDI bond pads
J. heatstim-85-180	suspended heating resistor with breakage monitor resistor
K. heatstim_gauge	plain class etch gauge for thermal stimulator design
L. move_logo	AFIT logo attached to thermal bimorph actuator
M. newdac2	digital-to-analog converter circuit
N. nswitch	40 μm wide gate transistor to turn on thermal stimulators
O. opamp2	operational amplifier circuit
P. piezo3	4 suspended cantilevers in Wheatstone bridge config.
Q. ring_ctrs	chains of inverters wired as whole or partial ring counters
R. susp_hdi_pad	HDI pad designed to be bulk etched underneath

A.2 MUMPS Die Plots and Device Listings

The MUMPS designs started with the third fabrication run offered by MCNC, and the MUMPS die are numbered by fabrication run. The third fabrication run used aluminum for the metallization. The third fabrication run was delivered twice. The first lot had over-etched side walls on the polysilicon structures, so MCNC delivered the backup lot also. Unfortunately the lithography on the backup lot was poor, and many of the minimum width polysilicon features were incompletely fabricated. The result was that devices like mirrors that had long, thin flexures were unusable. The fourth MUMPS run used copper for the metallization, and all subsequent runs have used gold. Reported properties for all the MUMPS runs are in the following tables.

Table A-1. Manufacturer's Reported Properties of Materials from the Third MUMPS Fabrication Run.

Material Layer	Thickness (μm)	Stress (MPa)	Resistivity (Ωcm)
poly0	0.5345	96.6 tensile	-
poly1	1.9685	1.7 tensile	-
poly2	1.5050	15.9 tensile	-
metal (Al)	1.0000	17.9 compressive	-
silicon nitride	0.5144	91.3 tensile	-
oxide 1	2.3233	-	-
oxide 2	0.4924	-	-

Table A-2. Manufacturer's Reported Properties of Materials from the Fourth MUMPS Fabrication Run.

Material Layer	Thickness (μm)	Stress (MPa)	Resistivity (Ωcm)
poly0	0.5207	14 compressive	1.74×10^{-3}
poly1	1.8755	4 compressive	2.95×10^{-3}
poly2	1.4800	9 compressive	2.74×10^{-3}
metal (Cu)	0.5200	73 tensile	2.08×10^{-6}
silicon nitride	0.5169	63 tensile	-
oxide 1	-	-	-
oxide 2	-	-	-

Table A-3. Manufacturer's Reported Properties of Materials from the Fifth MUMPS Fabrication Run.

Material Layer	Thickness (μm)	Stress (MPa)	Resistivity (Ωcm)
poly0	0.5450	10 compressive	2.34×10^{-3}
poly1	2.0175	3 compressive	3.33×10^{-3}
poly2	1.4800	8 compressive	4.00×10^{-3}
metal (Cr/Au)	0.5200	29 tensile	2.96×10^{-6}
silicon nitride	0.4940	113 tensile	-
oxide 1	2.0800	-	-
oxide 2	0.5150	-	-

Table A-4. Manufacturer's Reported Properties of Materials from the Sixth MUMPS Fabrication Run.

Material Layer	Thickness (μm)	Stress (MPa)	Resistivity (Ωcm)
poly0	0.5200	19.7 compressive	1.84×10^{-3}
poly1	2.0220	5.1 compressive	2.58×10^{-3}
poly2	1.5650	5.1 compressive	2.72×10^{-3}
metal (Cr/Au)	0.5540	30 tensile	3.39×10^{-6}
silicon nitride	0.6213	19.2 tensile	-
oxide 1	2.0151	-	-
oxide 2	0.5230	-	-

Table A-5. Manufacturer's Reported Properties of Materials from the Seventh MUMPS Fabrication Run.

Material Layer	Thickness (μm)	Stress (MPa)	Resistivity (Ωcm)
poly0	0.4880	-	2×10^{-3}
poly1	2.0100	8.0 compressive	1.65×10^{-3}
poly2	1.4706	11.1 compressive	1.54×10^{-3}
metal (Cr/Au)	0.5318	21 tensile	3.30×10^{-6}
silicon nitride	0.6049	41.0 tensile	-
oxide 1	2.0400	-	-
oxide 2	0.5281	-	-

Table A-6. Manufacturer's Reported Properties of Materials from the Eighth MUMPS Fabrication Run.

Material Layer	Thickness (μm)	Stress (MPa)	Resistivity (Ωcm)
poly0	0.4696	8.0 compressive	1.5×10^{-3}
poly1	1.9780	10.3 compressive	2.5×10^{-3}
poly2	1.5450	5 compressive	3.3×10^{-3}
metal (Cr/Au)	0.5200	166 tensile	3.50×10^{-6}
silicon nitride	0.5580	133 tensile	-
oxide 1	2.0362	-	-
oxide 2	0.6133	-	-

Table A-7. Manufacturer's Reported Properties of Materials from the Ninth MUMPS Fabrication Run.

Material Layer	Thickness (μm)	Stress (MPa)	Resistivity (Ωcm)
poly0	0.5122	3 compressive	1.5×10^{-3}
poly1	1.9948	3 compressive	2.2×10^{-3}
poly2	1.5048	6 compressive	3.0×10^{-3}
metal (Cr/Au)	0.4923	5 tensile	3.0×10^{-6}
silicon nitride	0.6243	67 tensile	-
oxide 1	2.0008	-	-
oxide 2	0.7598	-	-

Table A-8. Manufacturer's Reported Properties of Materials from the Tenth MUMPS Fabrication Run.

Material Layer	Thickness (μm)	Stress (MPa)	Resistivity (Ωcm)
poly0	0.4944	1 compressive	1.6×10^{-3}
poly1	1.9720	6 compressive	2.5×10^{-3}
poly2	1.4825	5 compressive	3.3×10^{-3}
metal (Cr/Au)	0.5215	24 tensile	2.96×10^{-6}
silicon nitride	0.5898	37 tensile	-
oxide 1	1.9159	-	-
oxide 2	0.7565	-	-

Table A-9. Manufacturer's Reported Properties of Materials from the Eleventh MUMPS Fabrication Run.

Material Layer	Thickness (μm)	Stress (MPa)	Resistivity (Ωcm)
poly0	0.4987	19 compressive	2.0×10^{-3}
poly1	1.9869	4 compressive	2.7×10^{-3}
poly2	1.5154	11 compressive	2.9×10^{-3}
metal (Cr/Au)	0.5340	20 tensile	2.9×10^{-6}
silicon nitride	0.6051	-	-
oxide 1	2.0825	-	-
oxide 2	0.7352	-	-
dimple	0.6650	-	-

A.2.1 MUMPS3 Die

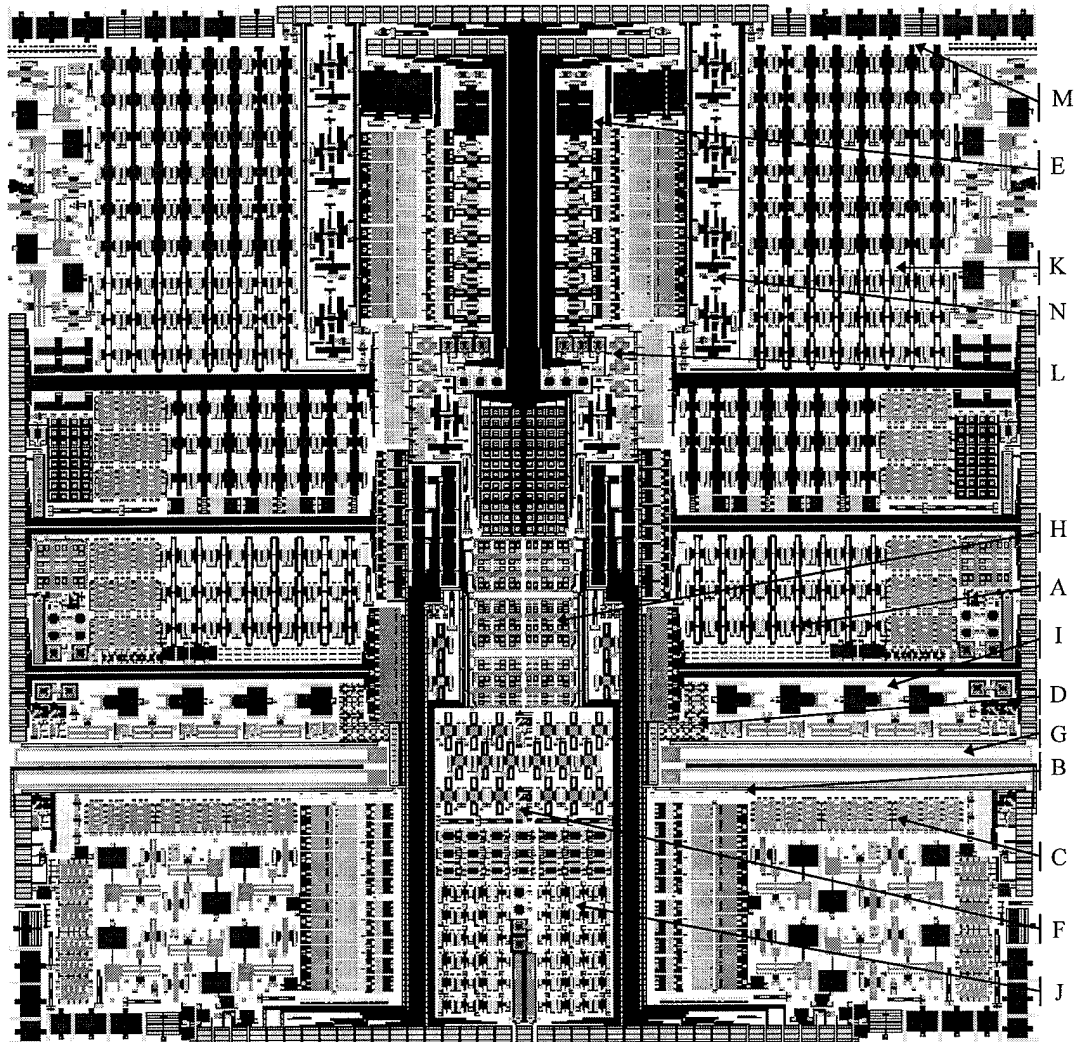


Figure A-7. MUMPS3 die, the first MUMPS die designed at AFIT. Mirror arrays in the center, and the large cantilevers around them designed by another researcher, are connected by wiring buses (wide black lines) to pads at the periphery of the die. The die layout is bilaterally symmetrical except for cells along the center from top to bottom.

A. IRpixel_array	suspended meander resistors in <i>poly1</i> and <i>poly2</i>
B. bridges	long thin suspended beams, early thermal actuators
C. cantilevers	various sizes of cantilevers for another researcher
D. element	spiral resistor heating element, on die and suspended
E. etchgauge	suspended and loose squares of <i>poly1</i> and <i>poly2</i>
F. layer_test	test cell to investigate layer interactions
G. linear_motor1	attempt to make an electrostatic linear motor
H. mush_array	4-leaf cloverleaf mirrors originally called mushroom mirrors
I. plate_pull	electrostatic actuator intended to pull a plate in
J. relay_array	electrostatic comb driven polysilicon relay
K. res_array	electrostatic comb resonators with weights
L. spiral_mirror	large spiral with a square mirror in the center over poly0 plate
M. springs	large springs pulled with a probe point
N. triphammer	attempt to make an electrostatic comb driven stepper motor

A.2.2 MUMPS4 Die

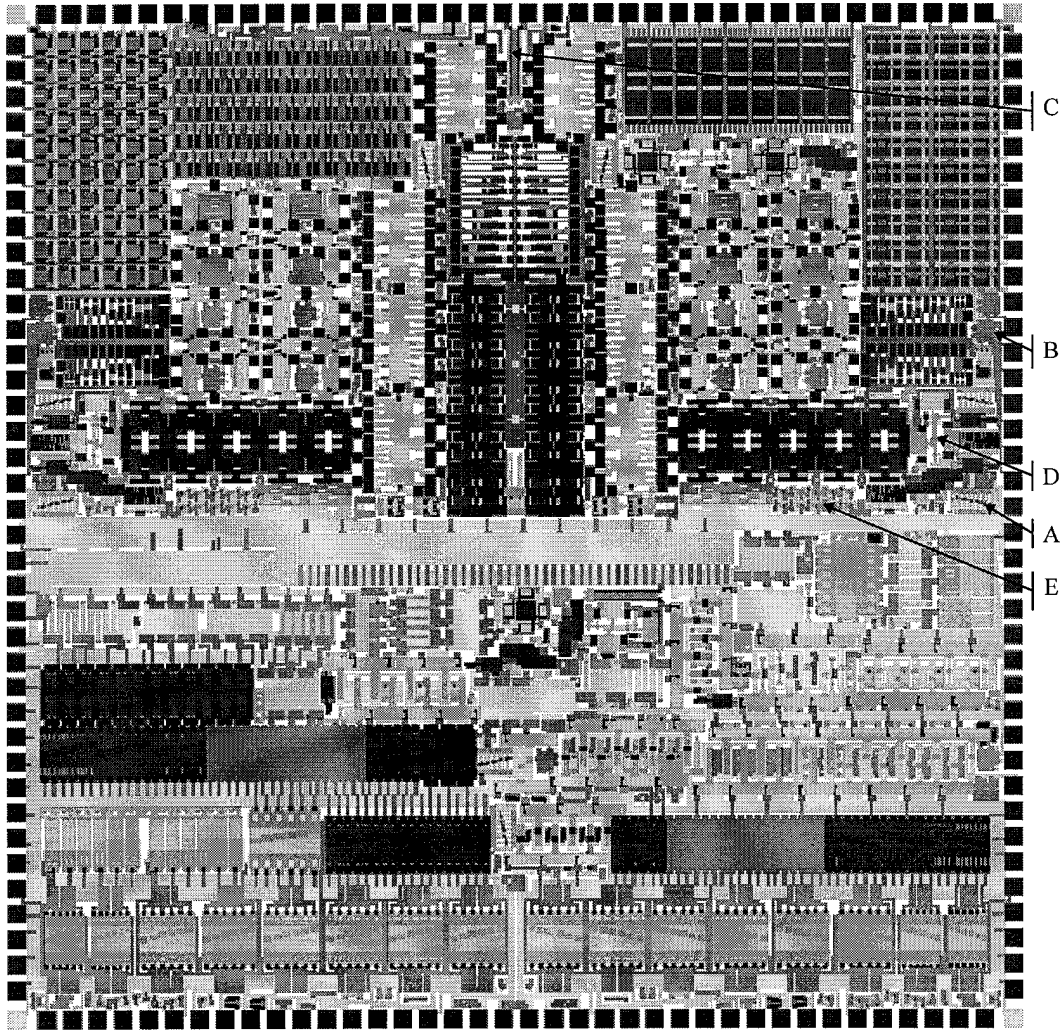


Figure A-8. MUMPS4 die number 3. There were three MUMPS4 die, but they all ended up very similar to this one. They were laid out as a bottom half and two upper quarters. This die has one of each of the upper quarters, and the other two die had two of the same of each of the upper quarters. The author placed and wired the devices in the upper quarters, packed the entire chip design down and interspersed his own devices among those of the other two researchers, whose devices were electrostatic relays (upper quarters) and large cantilevers (lower half). The corner pads are substrate contacts.

Most of these devices are too small to be indicated on a die plot this size, only the lettered devices are indicated. The small devices are fit around the wiring and larger devices over the entire die.

dimple_drive	electrostatically actuated stepper motor attempt
dmd_clone	tilting mirror with two torsional flexures
heat_tilt	tilting mirror driven by single expanding beams
A. heatuators	first version of lateral thermal actuators
B. hm_array	test array of seven hexagonal piston mirrors
line_drives	single-beam thermal actuators
C. linear_motor2	another attempt to make a linear electrostatic motor
lock_mld	device designed to hold a stretched spring electrostatically
mech_mem	memory cell based on the 'riser' actuators below
oxtest	layer interaction test cell
pushpull_gauge	electrostatic comb drives with deflection gauges
risers	thermally actuated ladder devices for vertical motion
D. triphammer2	second attempt at an electrostatic stepper motor
var_blaze	rows of tilting mirrors
vert_heatuators	vertically acting thermal actuators
E. vm_array	square piston mirror array
xyz_table	a too-large electrostatic comb driven positioner

A.2.3 MUMPS5 Die

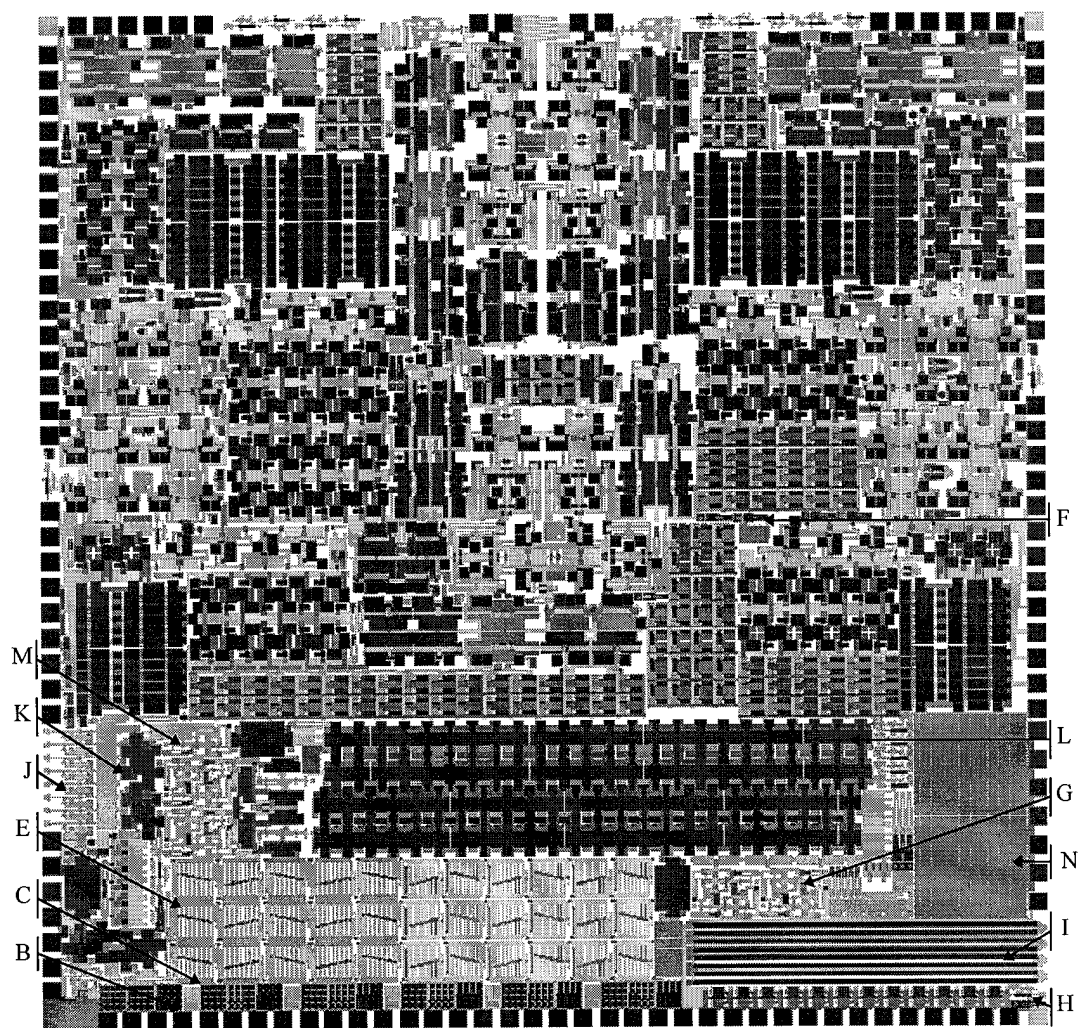


Figure A-9. MUMPS5 die. There was only this one die design submitted to the MUMPS5 fabrication run. The author laid out this entire die also, partly with cells designed by other researchers.

A. IR_P2onP1	infrared source built (accidentally) of stacked <i>poly1/poly2</i> (This cell is too small to see on the plot)
B. bubbles	test cell of <i>poly1</i> and <i>poly2</i> cavities
C. cvm1_array	one of three arrays of mirrors with covered flexures
D. heat_varcap	pair of thermal actuators with capacitor plates on their ends (This cell is too small to see on the plot)
E. heatuators	test arrays of lateral thermal actuators
F. heatweezers	tweezers incorporating a pair of lateral thermal actuators
G. layer_test2	tests of layer interactions
H. lift_n_lock	flip-up devices with flexure hinges
I. lin_trans	linear position sensor, was supposed to have resistive readout
J. pull_store	manually pulled springs with thermal actuator locks
K. pushpull_gauge2	second attempt to measure comb drive deflections
L. res_array	arrays of electrostatic comb drive resonators with weights
M. triphammer3	last try at original style of stepper motor, with thermal drive
N. var_blaze2	very large arrays of tilting electrostatic mirrors

A.2.4 MUMPS6 Die Number 2

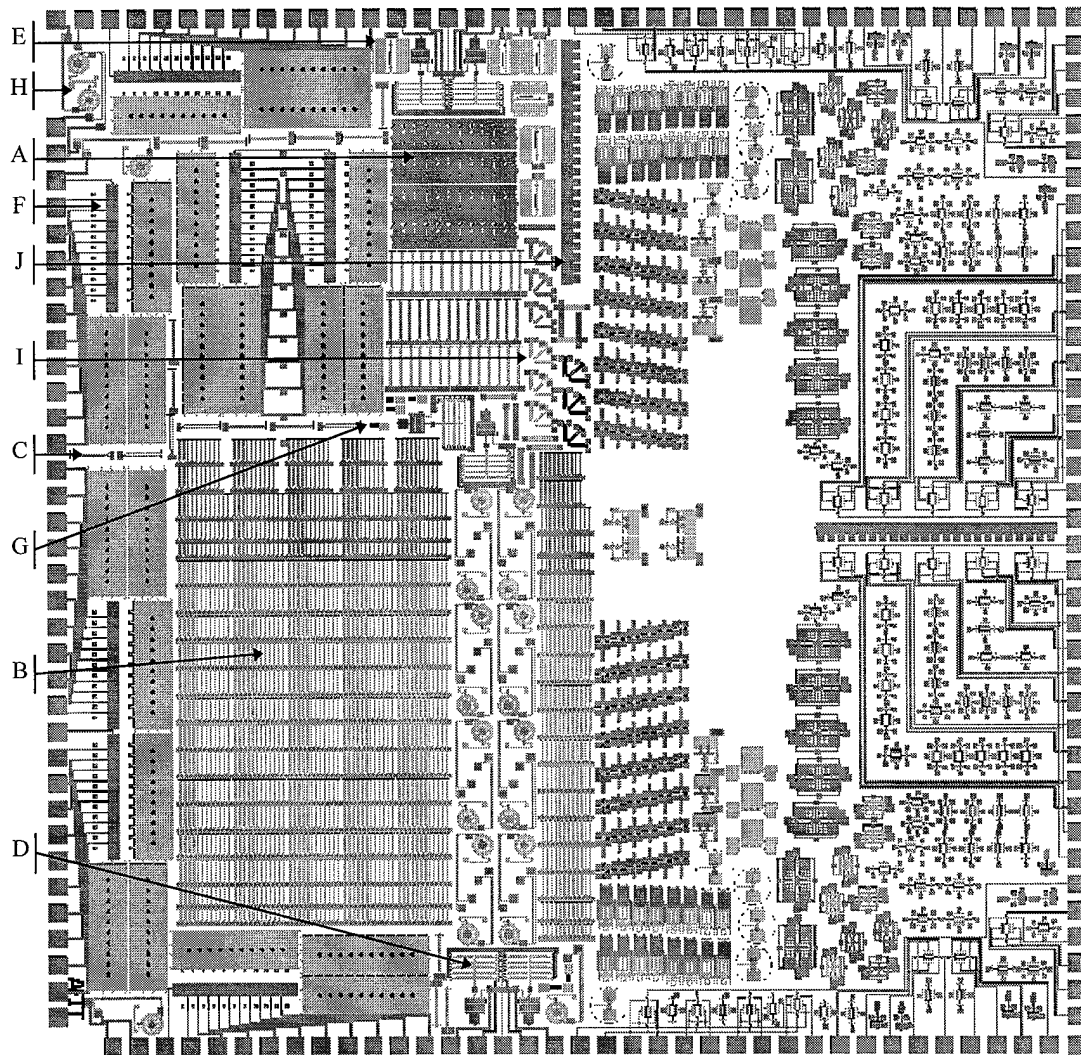


Figure A-10. MUMPS6 die number 2. The author laid out the left half of this die. The blank areas on the right half are another researcher's cells which were changed for a later die and no longer are linked to this plot file. The author's cells are dominated by a large test array of thermal actuators and mirror arrays built for the physics department.

A. UD-hexTest	test piston mirror array from hexagonal array die number 1
B. heat-array	arrays for characterizing lateral thermal actuator geometries
C. heat-ladder	thermal actuator with alternate hot arm design
D. heat-multiPush	thermal actuator array with actuators arranged in series.
E. heat-multiPull	parallel-attached thermal actuator array, this is the first array of thermal actuators that worked, but it was attached to a variable capacitor structure that didn't.
F. linear-mirror	ten piston mirrors with cover plates for laser combining
G. metal-test	test of metal deposition on <i>poly1</i> , <i>poly0</i> , <i>nitride</i>
H. p1-ratchet	copy of LIGA ratchet motor in <i>poly1</i> , did not work
I. stress-test	suspended serpentine piezoresistors in <i>poly1</i> , <i>poly2</i>
J. switch-array	flip over hinged switches with gold-on-gold contacts

A.2.5 MUMPS6 Die Number 3

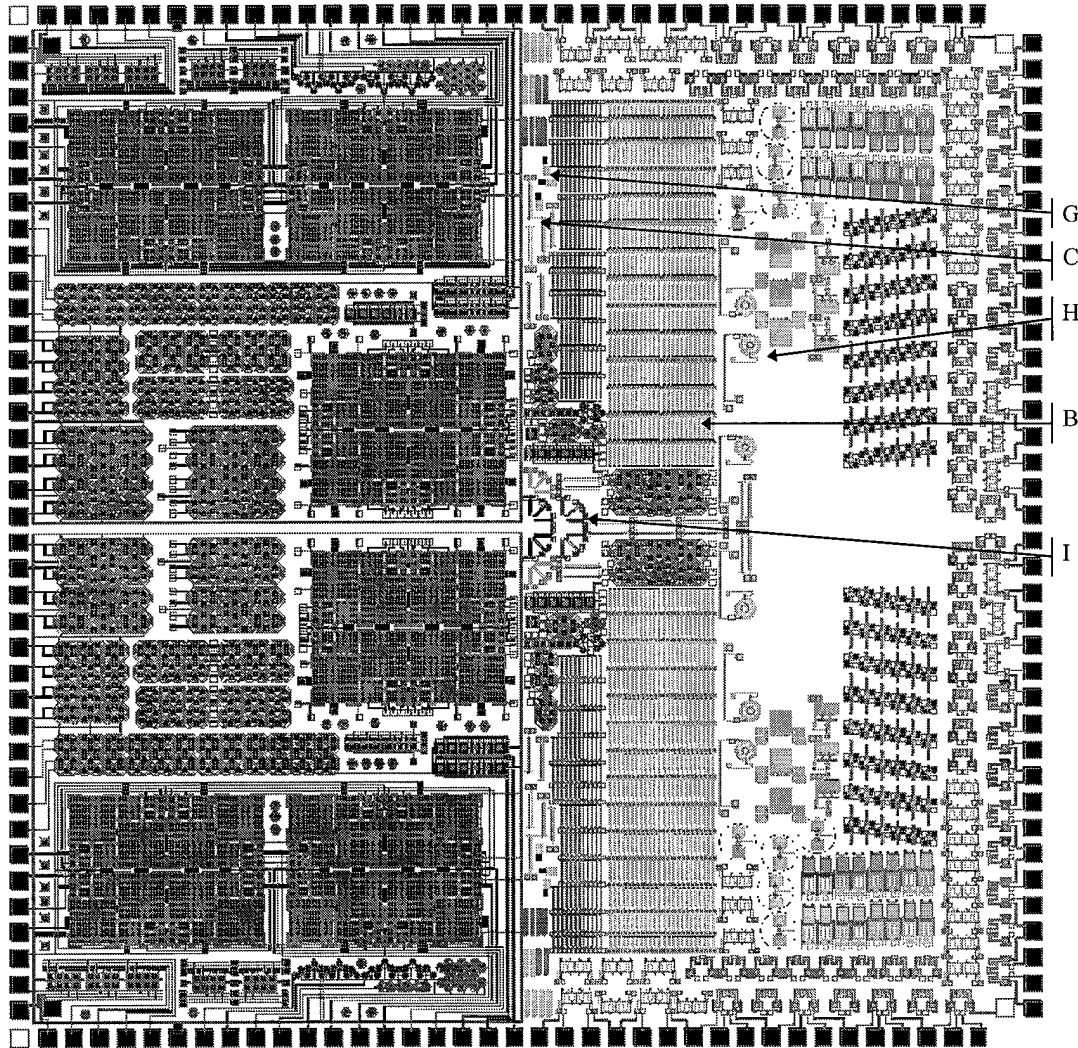


Figure A-11. MUMPS6 die number 3. The author laid out the right half of this die, mostly with cells from other researchers, but leaving room for some duplicates of cells on the MUMPS6-2 die. The blank areas on the right half are another researcher's cells which were changed for a later die and no longer are linked to this plot file. The lettered callouts refer to the cell list on the previous page.

A.2.6 MUMPS6 Hexagonal Mirror Array 1

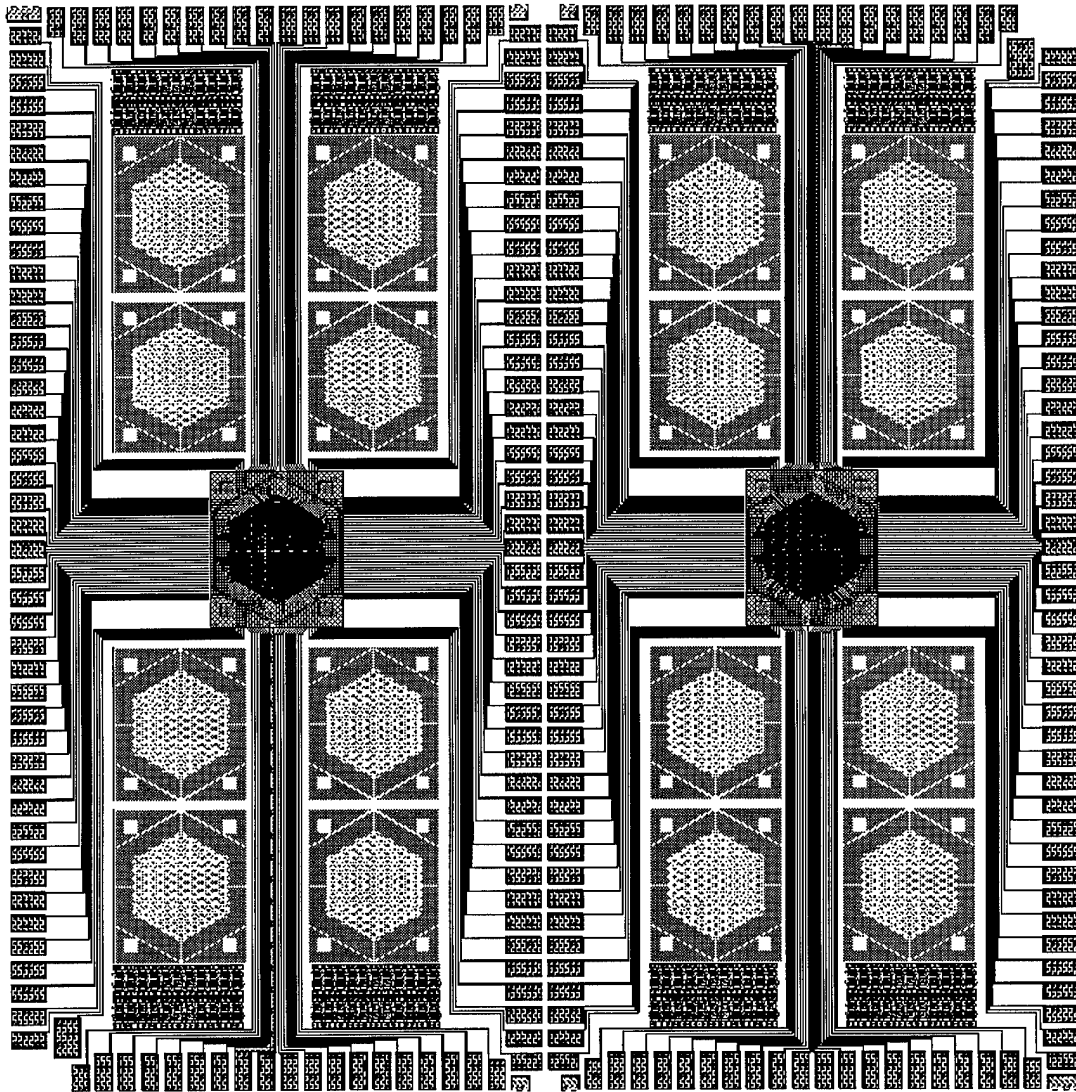


Figure A-12. First hexagonal mirror array die, 'Hex 1'. There are two arrays per die, each containing 129 individually addressable mirrors. Mirrors are 50 μm wide. Address lines run to bond pads; each array has its own set of bond pads. Each array has eight poly1 cover plates, and four identical sets of test mirrors near the bond pads. More information is available in Section 5.2.2.3.

A.2.7 MUMPS7 Die Number 1

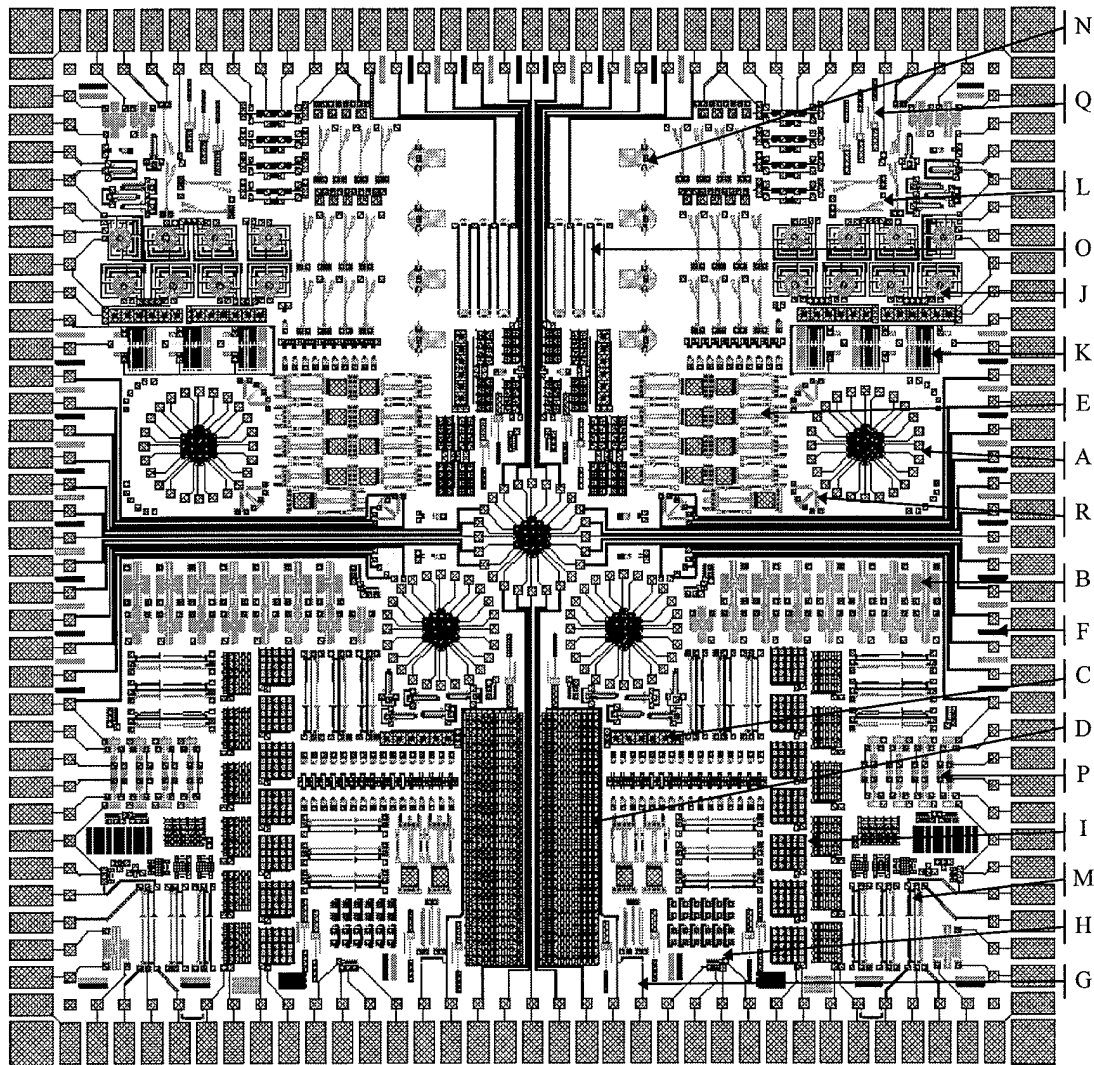


Figure A-13. MUMPS packaging test die. This die contains 'generic' MEMS structures and is intended for testing how well MEMS die can survive different packaging processes. The die contains a selection of mirrors, thermally and electrostatically actuated devices, hinged devices, and breakage monitoring structures. Some copies of the devices are connected to wire- and HDI-bond pads at the periphery; the HDI pads are the smaller, square pads. A SEM micrograph of this die is shown in Figure 6-13. This die was also fabricated on the MUMPS 8 and 9 runs.

A. 19mirror_array	50 μm hexagonal mirrors in a 19-mirror array
B. MCNC_test_cell	electrostatic comb-driven resonator designed by MCNC
C. SquareMirrorArray	Array of square piston mirrors with center flexures
D. VarBlaze	Rows of electrostatic tilting mirrors
E. adj_45deg_	Hinged mirror to be pushed up into position
F. break_test	50-200 μm long, 2 μm wide cantilevers in <i>poly1</i> , <i>poly2</i>
G. coveredHeaters	<i>poly1</i> conductors with <i>poly2</i> covers
H. crossed_resistors	<i>poly2</i> conductors crossing <i>poly1</i> conductors at 90°
I. cvm3_array2	<i>poly1</i> mirrors with <i>poly2</i> covering the flexures
J. electrostatic_motor	salient pole motor with 8 rotor and 12 stator poles
K. force_test	cantilevers with various bosses to test bend strength
L. heat_varcap	variable resistor with lateral thermal actuator
M. heatuator_array	lateral thermal actuators with deflection indicators
N. rot_mir_w_fres	flip-up, manually rotatable Fresnel lens
O. linear_motor3	structure with 'lost poly' formers for assembly tests
P. p1_combcap	tilting capacitors with interdigitated electrodes
Q. slide_probe	manually sliding probe with distance scale
R. straingauge	<i>poly0</i> , <i>poly1</i> , and <i>poly2</i> piezoresistors

A.2.8 MUMPS7 Die Number 7

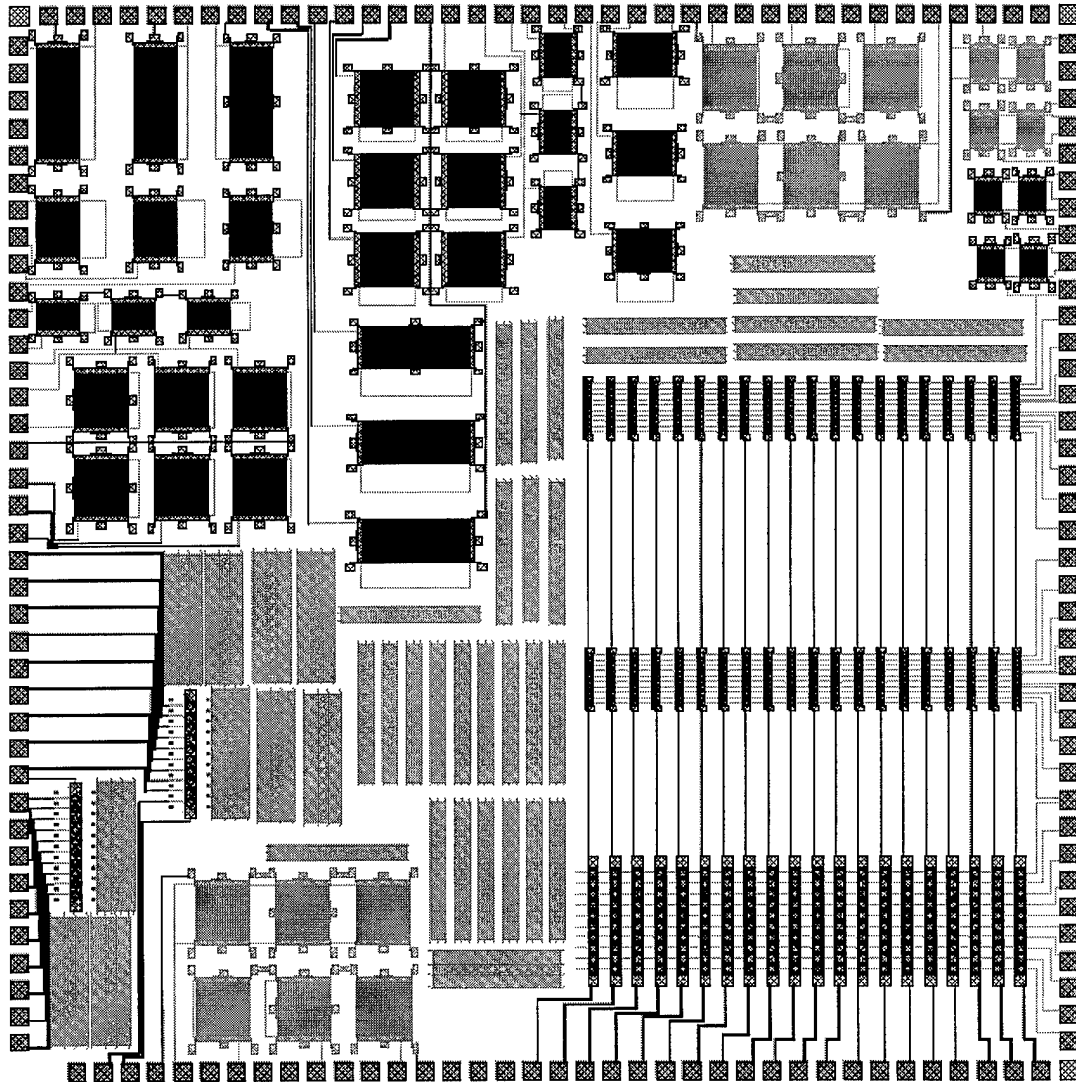


Figure A-14. MUMPS7, die number 7. Electrostatically actuated gratings and piston mirrors designed and drawn for the Physics department. The square structures at the top are gratings in different sizes with various grating line widths and spacings. The black ones are *poly2*, and the gray ones are *poly1*. On the right are three types of small piston mirrors in arrays of 10, all wired to bondpads at the die edges. In the lower left are two arrays of ten 50 μm wide hexagonal mirrors, with *poly1* cover plates filling in the center of the die.

A.2.9 MUMPS7 Hexagonal Mirror Array

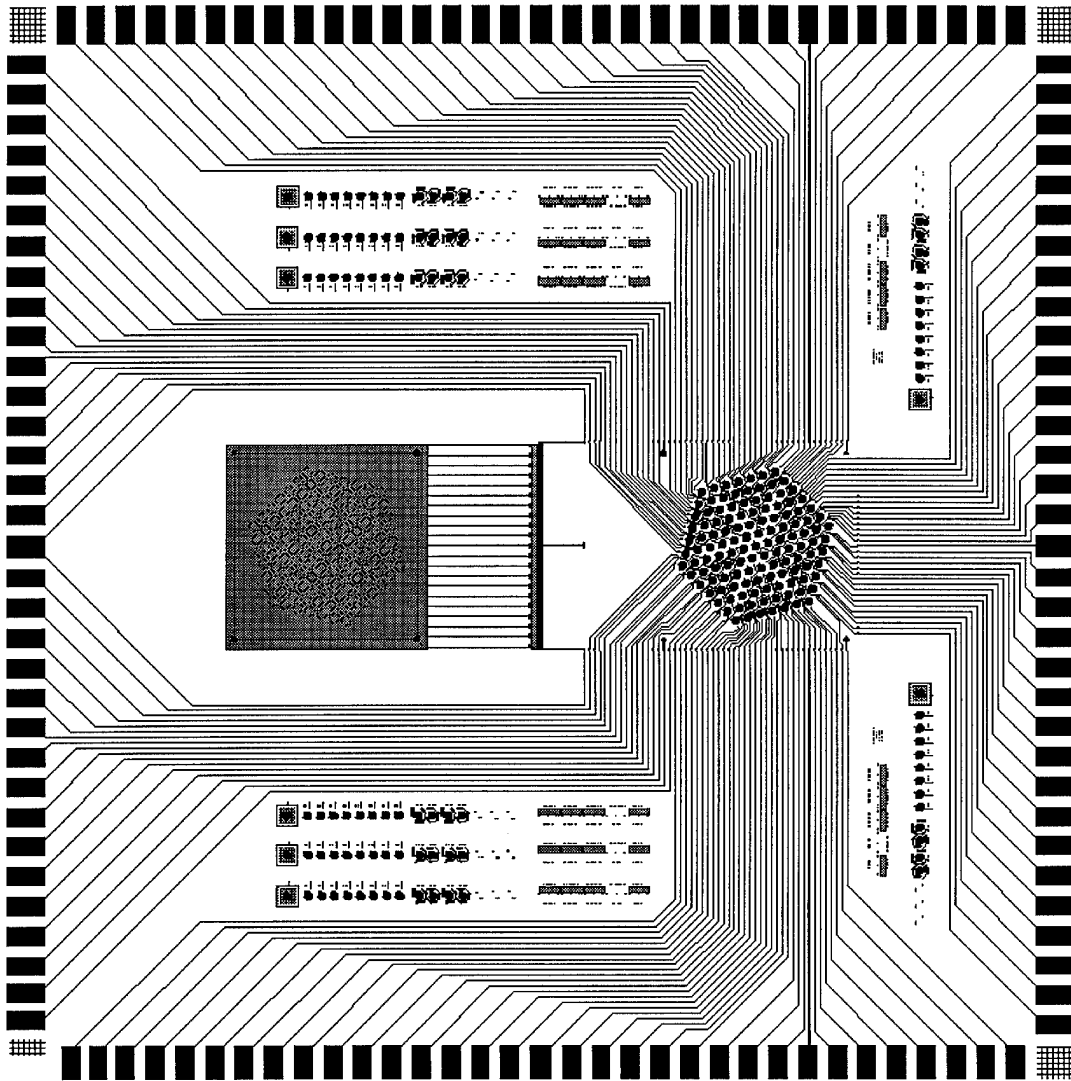


Figure A-15. Second hexagonal mirror array die, 'Hex 2'. There is one array containing 129 individually addressable mirrors. Mirrors are 100 μm wide. Address lines run to individual bond pads. There is a single, hinged cover plate. Arrays of test structures are laid out between the address lines. More information and micrographs are available in Section 5.2.2.3. This die was also fabricated on the MUMPS9 run.

A.2.10 MUMPS7 Devices re-fabricated on the MUMPS8 run

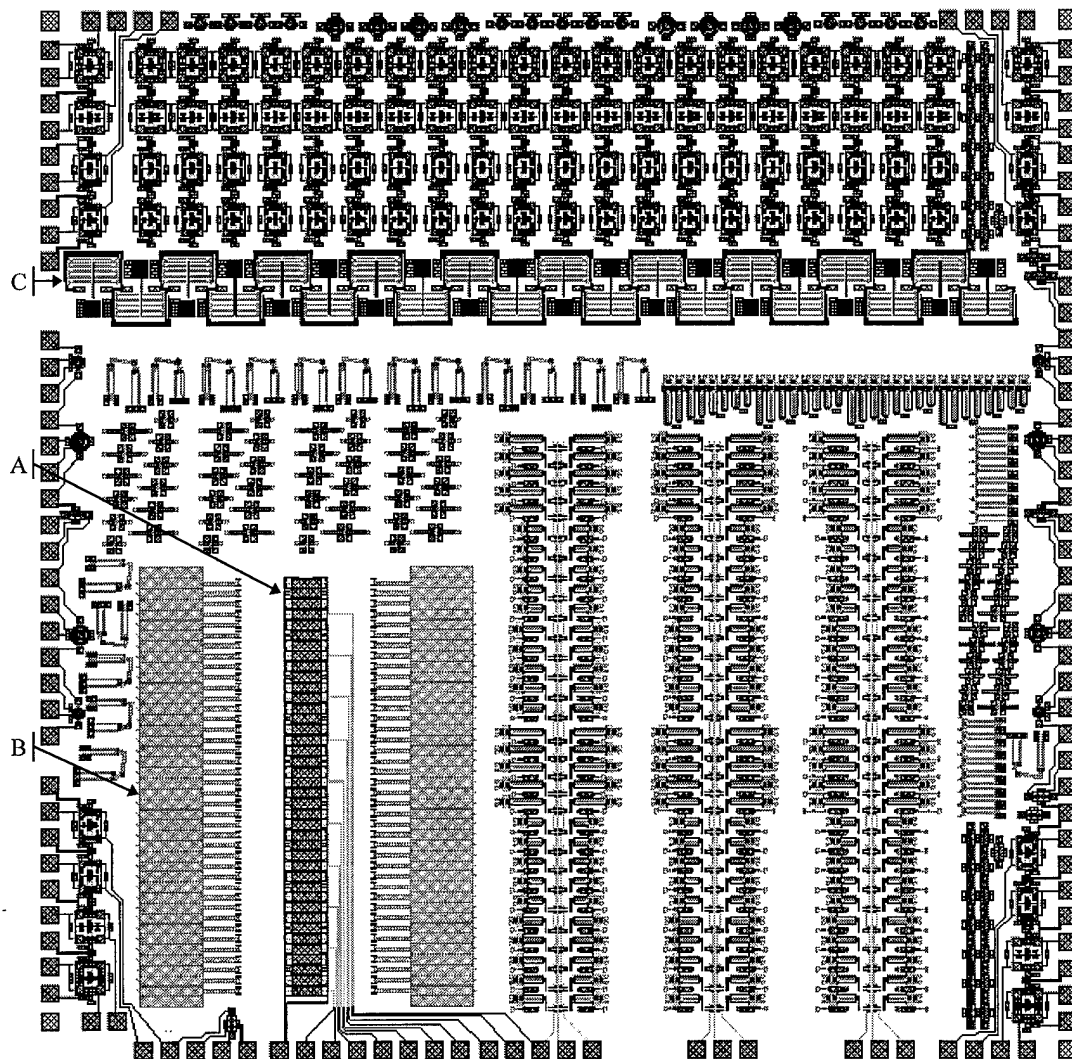


Figure A-16. A MUMPS7 re-fabrication die on MUMPS8. Because of fabrication problems on MUMPS7, MCNC agreed to provide free die sites on the MUMPS8 run, most of which were used to re-run devices from the MUMPS7 run. The author laid out this die with a mix of cell designs from other researchers and his own cell designs. The bulk of the cells are polysilicon switch designs and gyroscopes.

- | | |
|------------------|---|
| A. diodeArray4 | 4 types of rectangular piston mirrors sized to match a linear array of semiconductor diodes, for beam combining |
| B. diodeCover | hinged covers, one side is solid plates, other side has holes to expose mirrors, for selecting different mirror designs |
| C. heatMultiPush | variation of first thermal actuator array, attached to a spring |

A.2.11 MUMPS8 Die Number 1

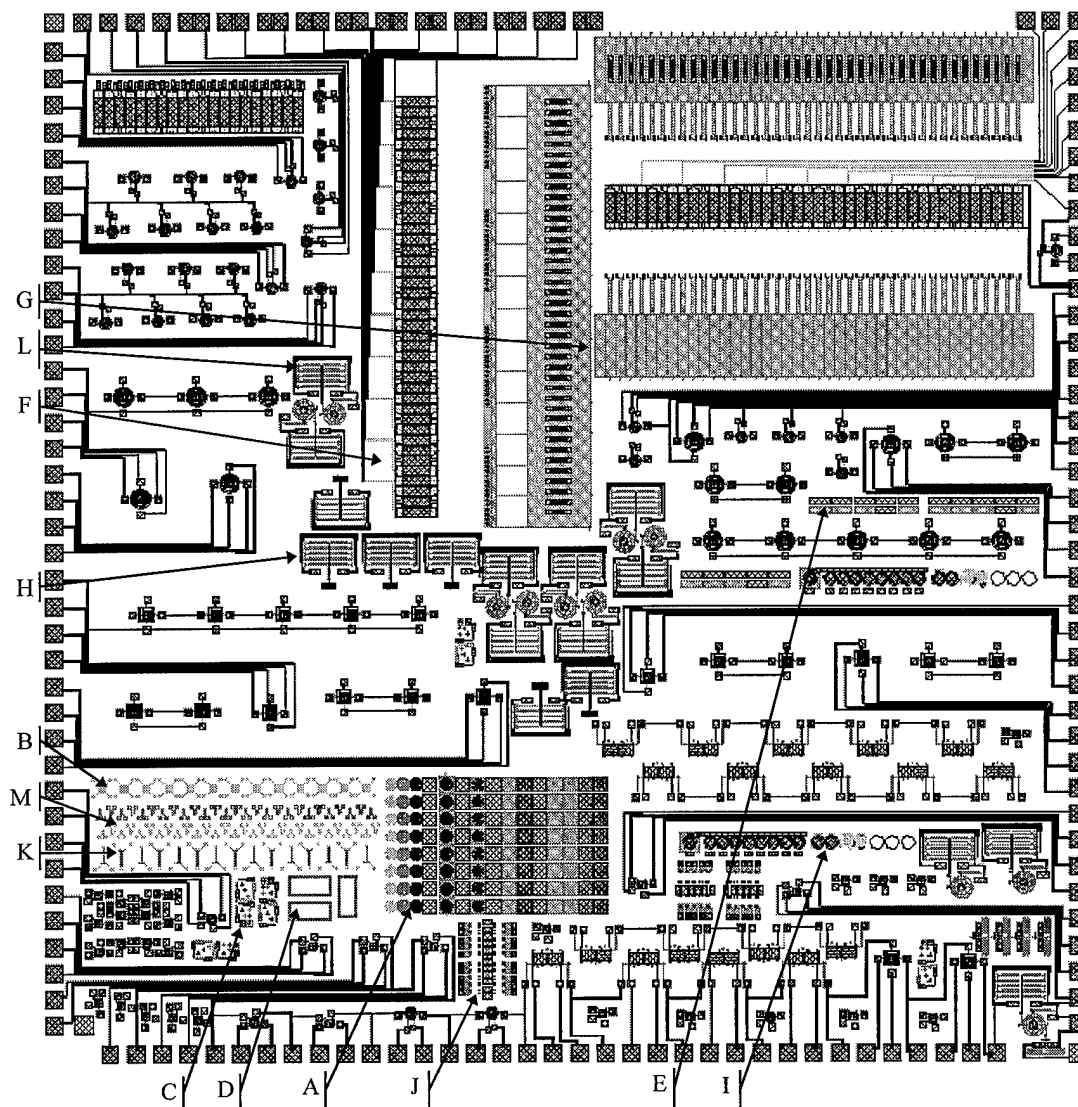


Figure A-17. MUMPS8, die number 1. This die was partially laid out by another researcher, then optimized by the author and filled with the author's cells. This design also contains cells intended to have the die anisotropically etched underneath, similar to the CMOS MEMS die.

A. AngleTest	angled lines in all layers, fabrication test
B. IRpixel2	bulk etch suspended heating resistor
C. alignmentTest	layer alignment fabrication test
D. bulkEtchGauge	open squares bulk etch gauge (cell location shown only)
E. dimple_anch_test	dimple and anchor minimum size fabrication test
F. diodeArray4	piston mirrors for combining laser diode array beams
G. diode_cover	open and blank covers for diode mirror array
H. heatMultiPull	thermal actuator array attached to a spring
I. hexArray2test	hexagonal mirror test cell repeated on this die
J. hingeTest	test to determine maximum hinge pin width
K. mirrorLever	bulk etch suspended thermal bimorph actuator
L. stepMotor2	second design of a thermally actuated ratchet motor
M. susp_heatuator	bulk etch suspended lateral thermal actuator

A.2.12 MUMPS8 Die Number 2

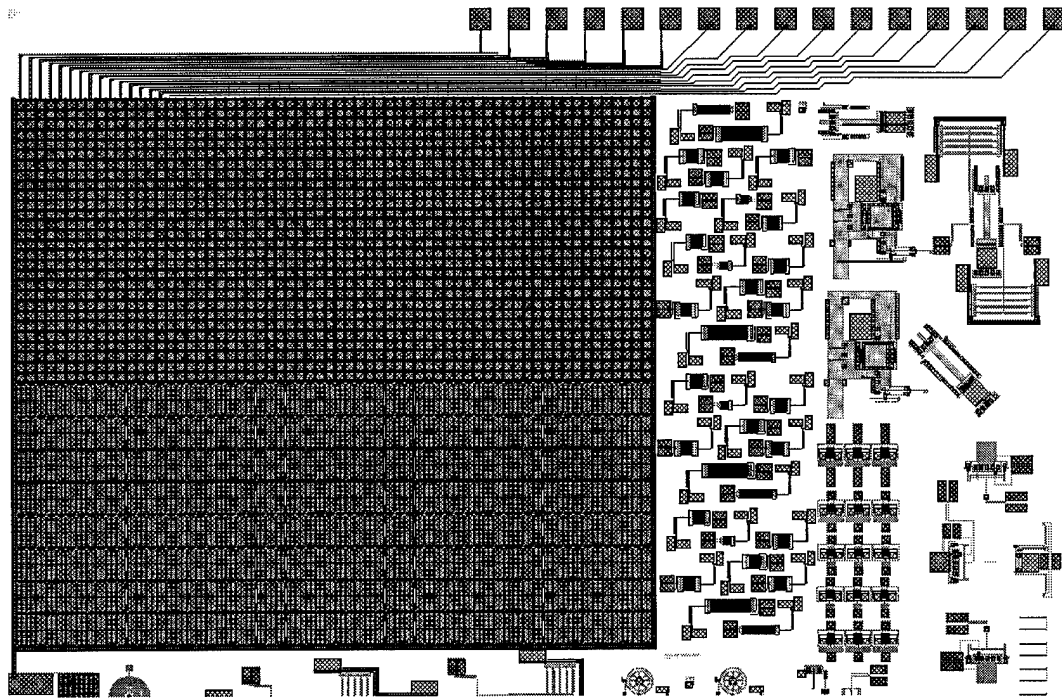


Figure A-18. Top half of a MUMPS8, die number 2, laid out by another researcher which contains two large, densely packed piston mirror arrays designed by the author. These arrays are intended for laser beam steering tests. The mirrors are wired in 4 sets of 16 columns, addressable by column; i.e. the first, second, third, etc. column of each of the four sets is wired to a common bond pad at the top of the die. The top half of the array contains square mirrors, and the bottom half contains rectangular mirrors.

A.2.13 MUMPS8 Die Number 3

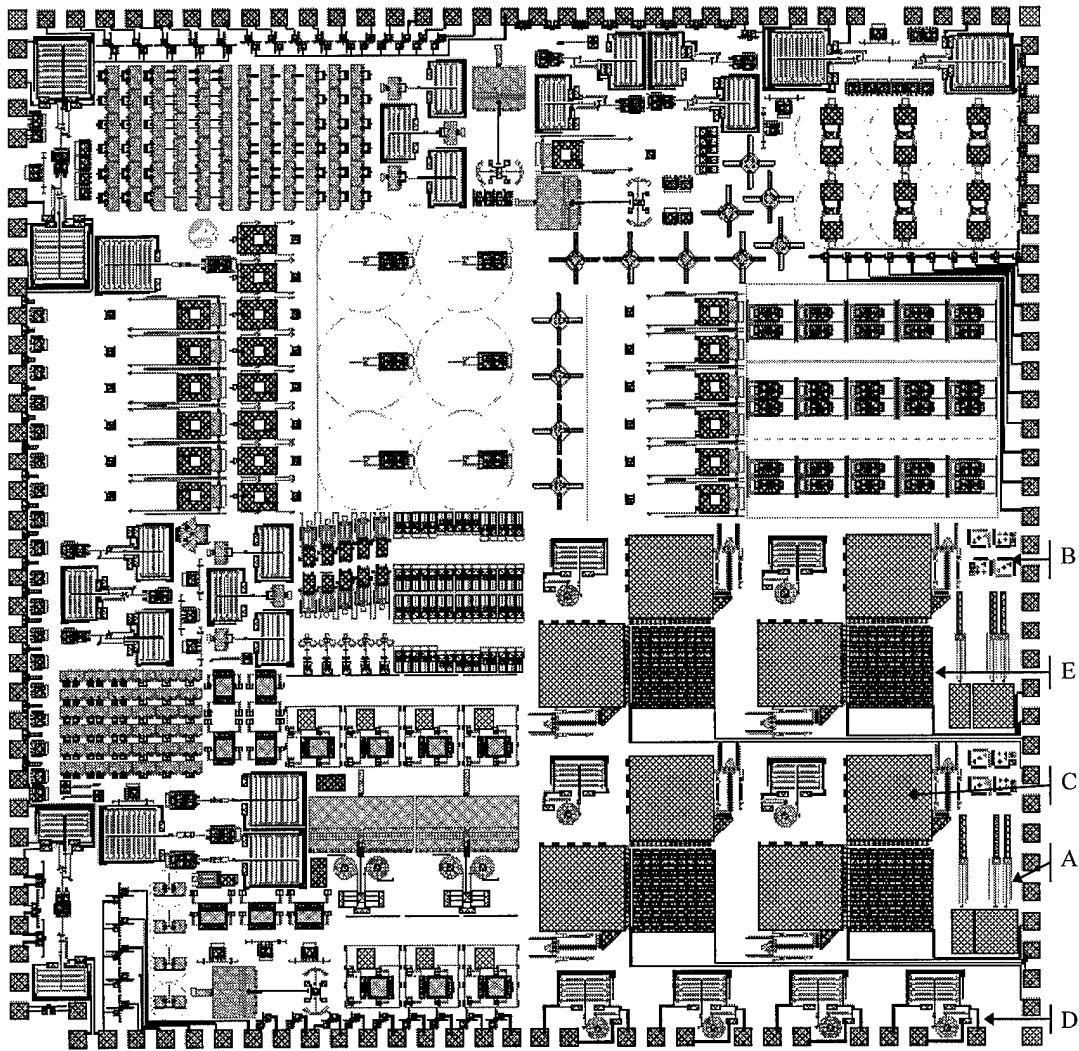


Figure A-19. MUMPS8, die number 3, containing the author's and another researcher's cells, laid out jointly. Other researchers began using thermal actuator arrays on MUMPS8.

- | | |
|--------------------|---|
| A. FeelerEtchGauge | large plates with sliding probe to determine etch depth |
| B. alignmentTest | layer alignment fabrication test |
| C. cornerCube8 | large corner cube retroreflector with 800 μm sq. mirrors |
| D. stepMotor2 | second design of a thermally actuated ratchet motor |
| E. varBlazeCell | electrostatic tilting mirror for active corner cube mirror |

A.2.14 MUMPS8 Die Number 4

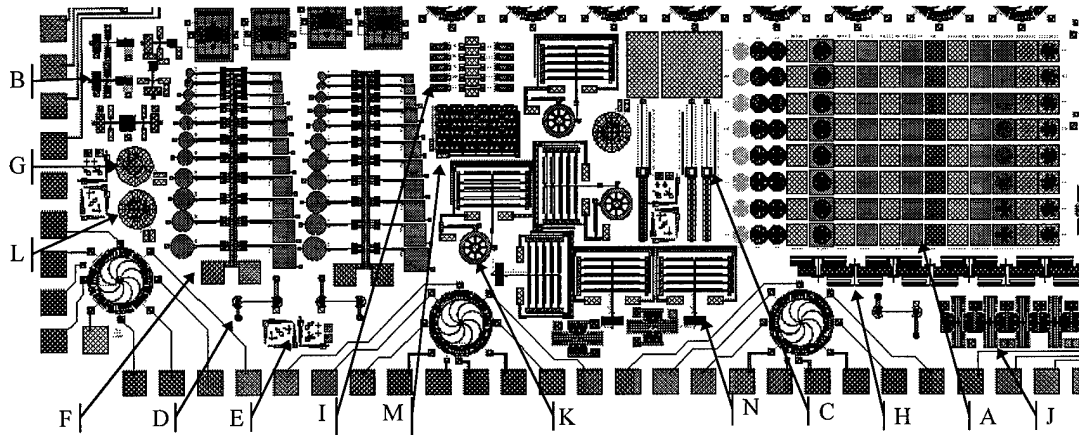


Figure A-20. Lower left corner of MUMPS8, die number 4, laid out by another researcher. Some space was left on the die for the author to fill with his own cells.

A. AngleTest	angled lines in all layers, fabrication test
B. Diff_cap_test	electrostatically tilting comb capacitor structure
C. FeelerEtchGauge	large plates with sliding probe to determine etch depth
D. WattMotion	parallel motion with rotating joints
E. alignmentTest	layer alignment fabrication test
F. etchGaugeLarge	thermally actuated etch gauge with large etch test plates
G. flowerMirror	tilting electrostatic mirror designed for another researcher
H. heatMultiPush	serially connected thermal actuator array with indicator
I. hingeTest	test to determine maximum hinge pin width
J. resonator_weight	electrostatic comb driven resonator with tuning weights
K. stepMotor2	second design for a thermally actuated ratchet motor
L. umbrellaMirror	tilting electrostatic mirror designed for another researcher
M. varBlaze2array	test array of electrostatic tilting mirrors
N. heatMultiPull	lateral thermal actuator array attached to a spring

A.2.15 MUMPS8 Holographic Array Number 1

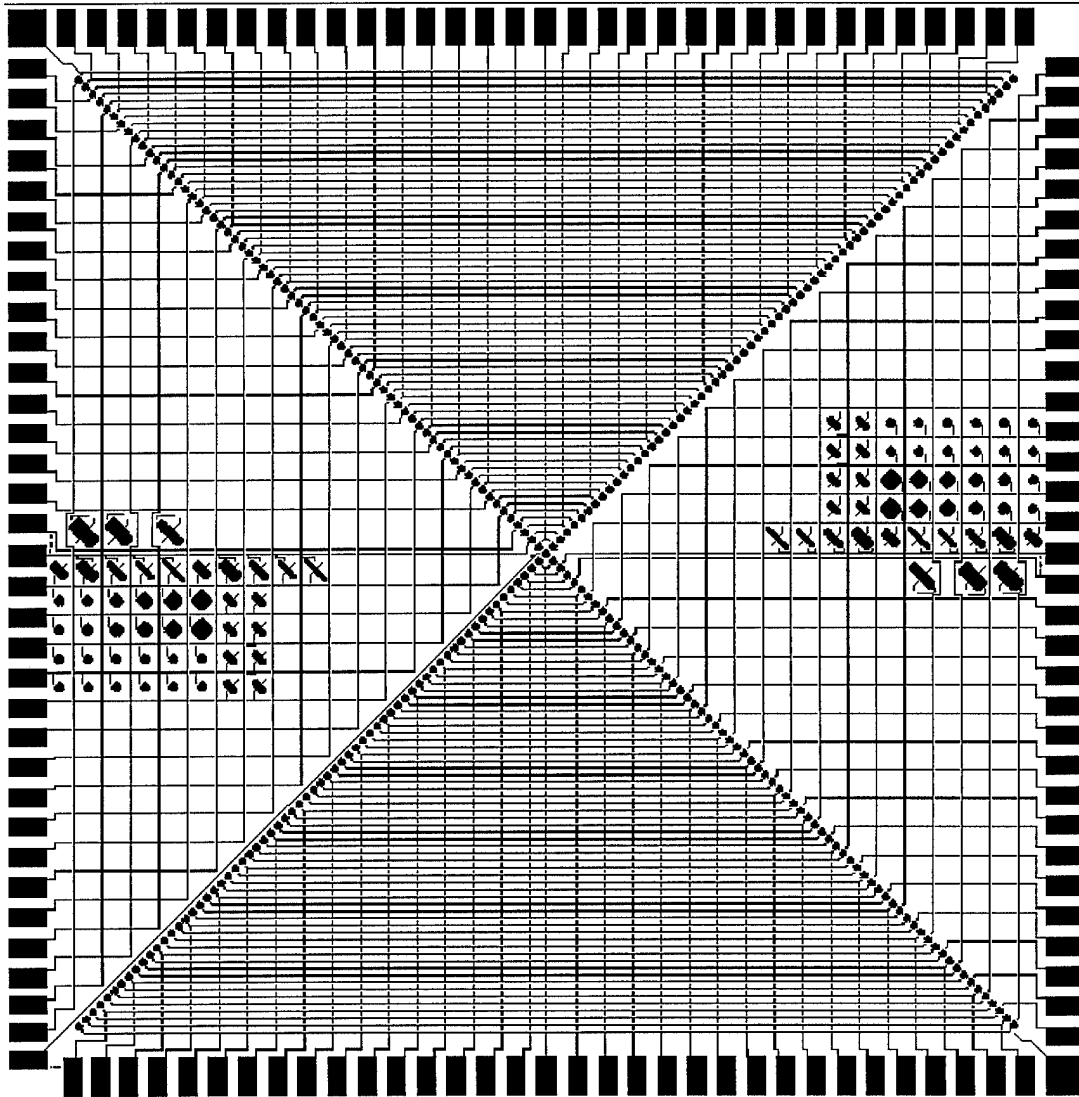


Figure A-21. First die designed for a holographic data storage project, 'Holo 1'. The die contains two arrays of 133 octagonal mirrors, with the center mirror shared by both arrays. Each mirror in each array is individually addressable. Address lines run to bond pads at the die perimeter, and corresponding mirrors in each array share a bond pad. Various sized test mirrors are placed between the address lines on the left and right sides of the die. More information is available in Section 5.2.2.4.1. This die was also fabricated on the MUMPS9 run.

A.2.16 MUMPS9 Die Number 5

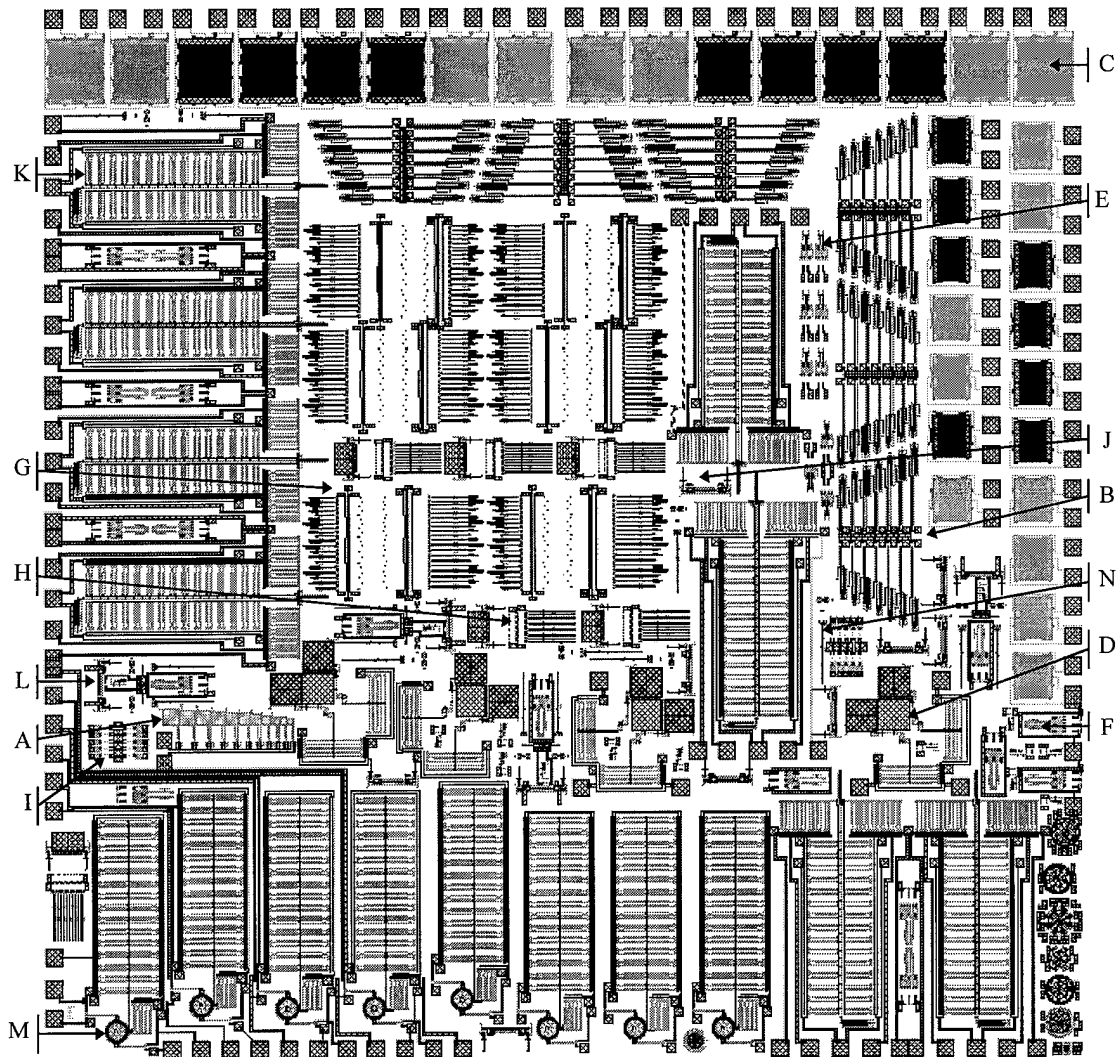


Figure A-22. MUMPS9 die number 5. This die contains only the author's devices, mostly stepper motors with over-large actuator arrays. These are the first stepper motors that operated correctly.

A. EtchGaugeLargeSq	thermally actuated etch gauge with square etch test plates
B. P1P2_array1	test array of different style <i>poly1</i> on <i>poly2</i> thermal actuators
C. P1P2grid	large, electrostatically actuated gratings for the physics dept.
D. cornerCube3	corner cube reflector with thermally actuated hinged mirrors
E. flip_bimorph	flip-over, hinged gold-on- <i>poly2</i> bimorph actuator
F. flip_grip1	flip-over, hinged grippers with lateral thermal actuators
G. flipbus	test of flip-over gold-on-gold wiring and wire hold-downs
H. flipwire_test	test of narrow flip-up hinged wires contacting a hinged plate
I. hingeTest	test of maximum hinge pin width
J. hinge_heatuator	hinged lateral thermal actuator contacted by hinged wires
K. linmot	thermally actuated linear stepper motor
L. relay100_adj	hinged thermal actuator pressing down on a flip-over switch
M. step_rotor	thermally actuated rotary stepper motor
N. wired12_hinge	12 μm wide hinged wire with slide-clamp

A.2.17 MUMPS9 Holographic Die Number 2

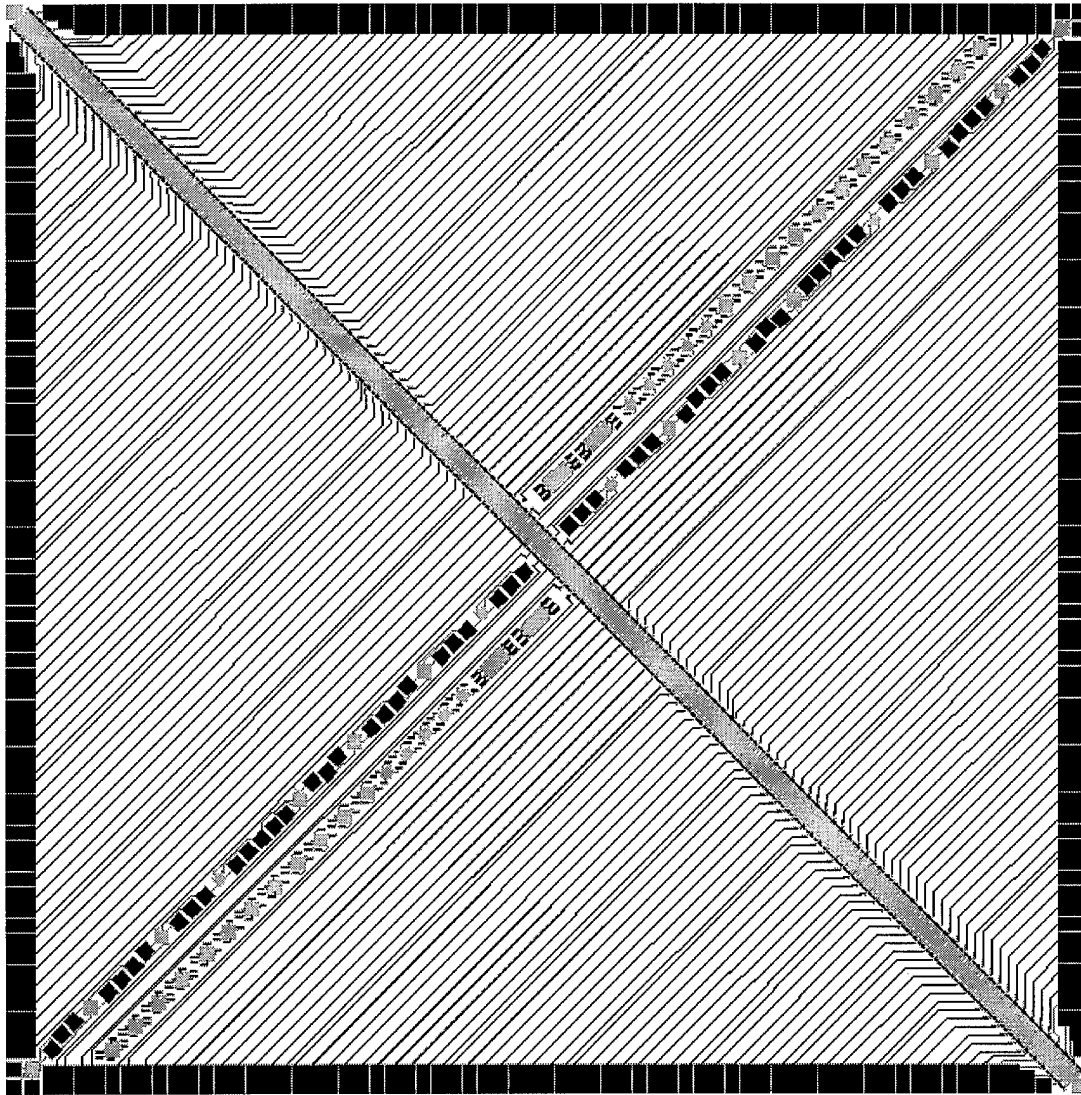


Figure A-23. Second design for the holographic data storage mirror array, 'Hex 2'. This die has a single array of 256 rectangular mirrors, each individually wired to a bondpad at the die perimeter. The main array runs on the diagonal from upper left to lower right, and test arrays of electrostatic multi-axis tilting mirrors run along the other diagonal.

A.2.18 MUMPS10 Die Number 1

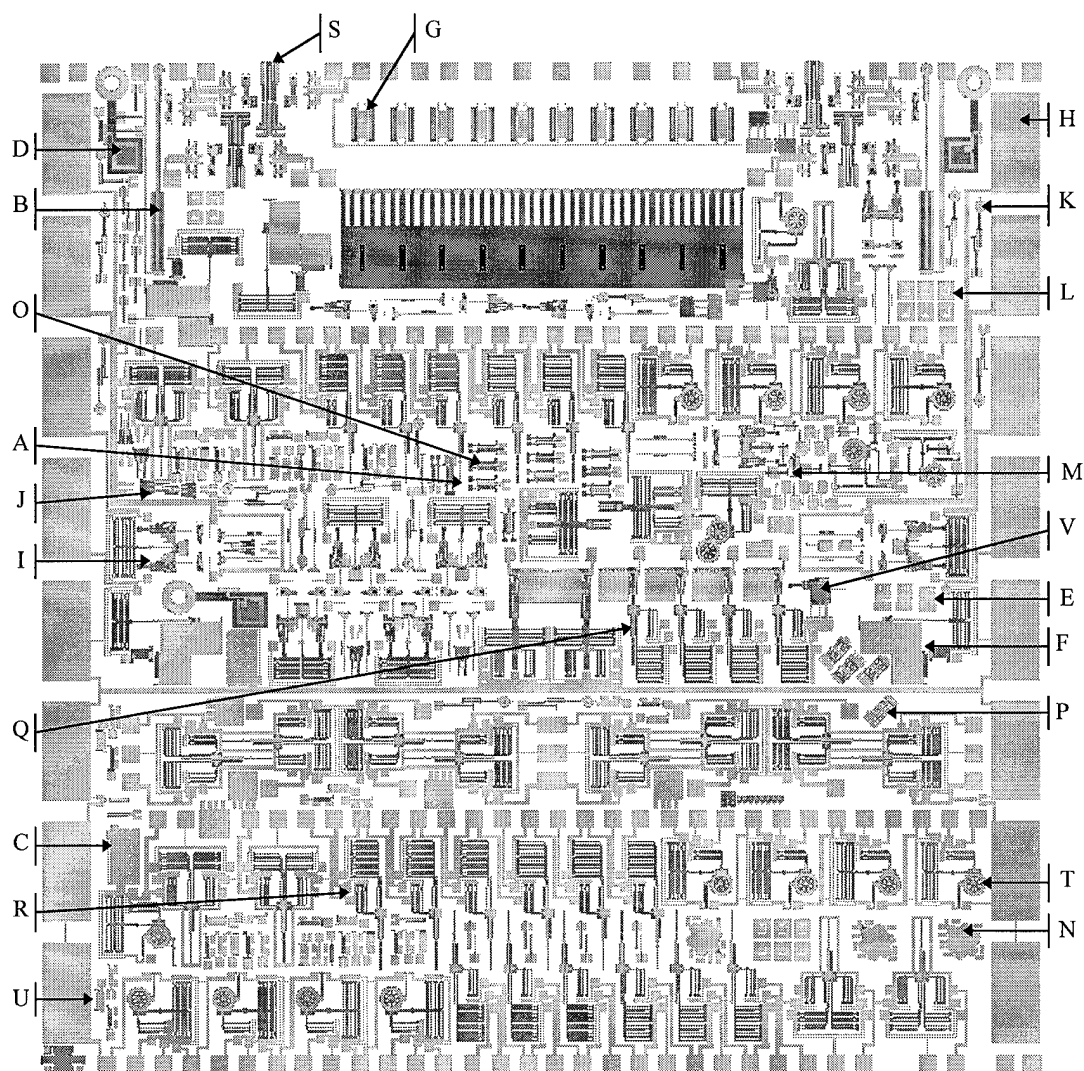


Figure A-24. MUMPS10 die number 1. This die contains only the author's devices. It is arranged with large pads along the sides for testing an alternate die wiring scheme; more information is available in Section 6.4.4.

A. ForceTest_beam	lateral thermal actuator force test beam
B. LinVarCap	linear sliding variable capacitor, sliding gold contact test
C. Square_P2cov	square mirror with <i>poly1</i> flexures covered by <i>poly2</i> plate
D. air_table1	<i>poly1</i> platform with holes for air flow, with plenum, tubing
E. binary_2flex	2-flexured piston mirror for up-or-down-only operation
F. cornerCube300	corner cube reflector, one hinged mirror thermally actuated
G. diodeArray1	revision of diode laser array power combining mirrors
H. flexPad1	bond pad for flexible, conductive polymer wiring
I. flex_relay2	thermally actuated relay with hinged contacts
J. flip_bimorph2	second version of hinged bimorph thermal actuator
K. forceTestAdj	force test beam with adjustable length
L. heat_covMir	thermally actuated tilting mirror with covered actuators
M. heat_pointer	lateral thermal actuator with offset expansion beams
N. hexMirror30cov	hexagonal mirror, <i>poly1</i> flexures covered by <i>poly2</i> plate
O. htr200_P1P1	200 μm long varieties of <i>poly1</i> , <i>poly2</i> thermal actuators
P. liftBridge	vertical actuator with mirror for linear mirror array
Q. liftmotor1	linear stepper motor arranged to lift a hinged plate
R. linmot4_1sided	linear stepper motor with drive pawls on only one side
S. slide_grip1	thermally actuated grippers that slide over the die edge
T. step_rotor	thermally actuated rotary stepper motor
U. underHeat	externally heated lateral thermal actuators
V. vertHeatLift	vertical thermal actuators arranged to lift a hinged plate

A.2.19 MUMPS10 Holographic Die Number 3, 3a

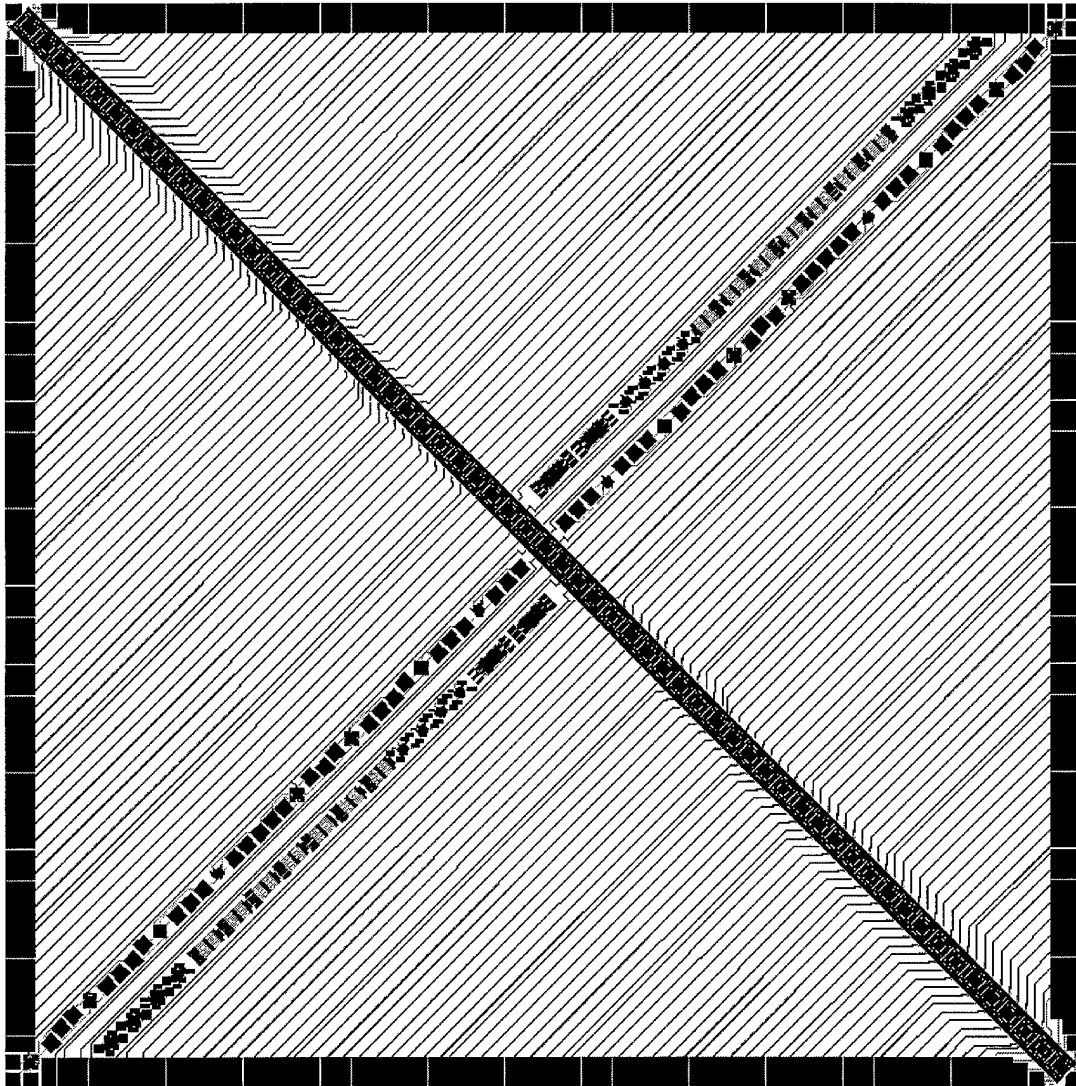


Figure A-25. Third design for the holographic data storage mirror array, 'Holo 3, 3a'. This die has a single array of 256 rectangular mirrors, each individually wired to a bondpad at the die perimeter. The main array runs on the diagonal from upper left to lower right, and test arrays of electrostatic multi-axis tilting and thermally actuated vertical mirrors run along the other diagonal. Two versions of this die were fabricated, one with dimples for the mirror down-stops (Holo 3), and one with *poly1* posts (Holo 3a). The difference cannot be seen at the scale of these plots, so only one die is shown. Both die have the same test cells on the opposite diagonal.

A.2.20 MUMPS11 Die Number 3

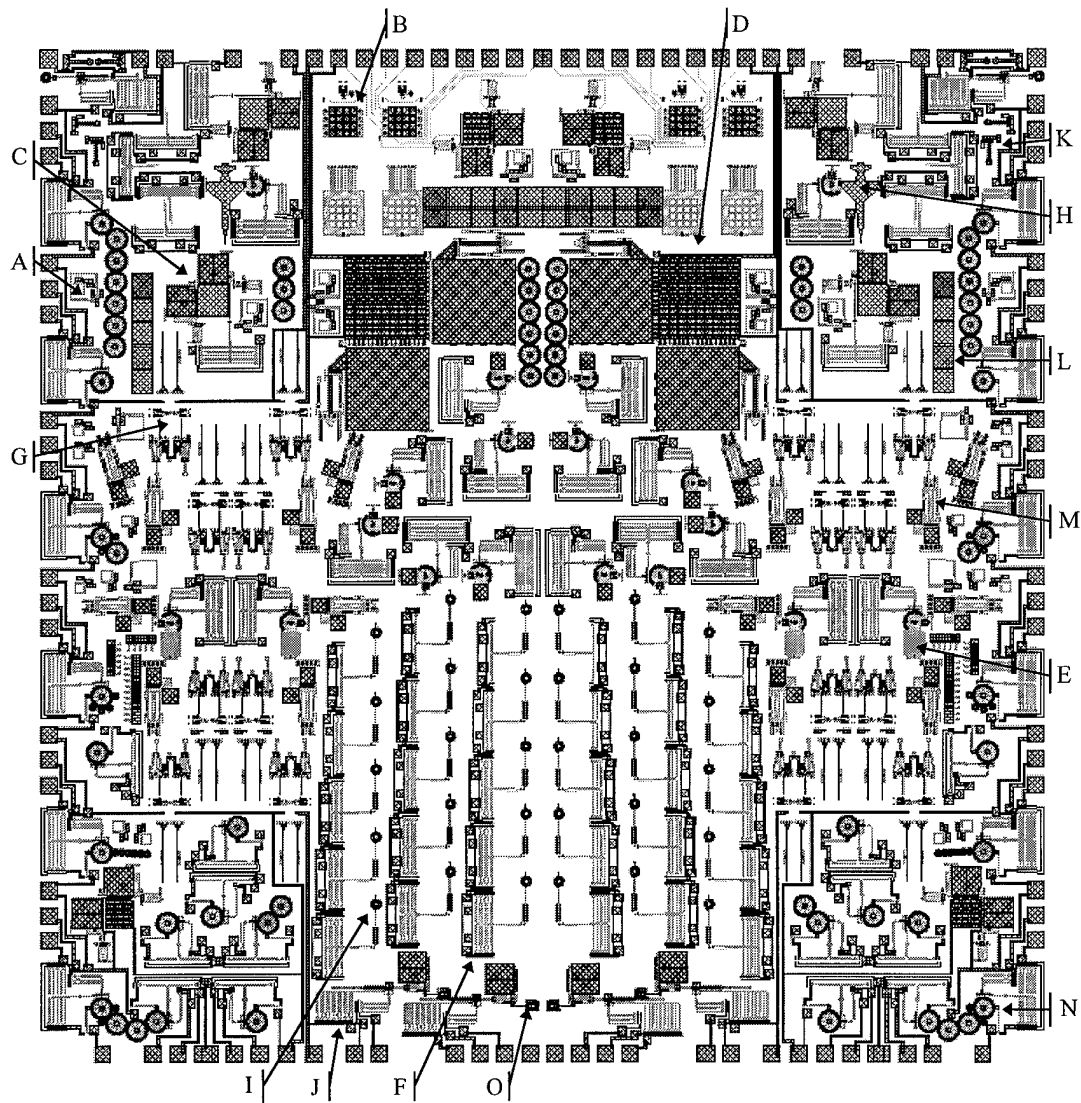


Figure A-26. MUMPS11 die number 3, which contains only the author's devices.

A. XYtables	two sizes of thermally actuated X-Y positioners
B. binary60sq_array16	array of 16 square piston mirrors with a grounded cover
C. cornerCube300	CCR with adjustable thermal actuator array
D. cornerCube800	electrostatically actuated CCR with 800 μm sq mirrors
E. flip-rot200	thermally rotated platform for flip-up optical components
F. heatuator-arrays	arrays of lateral thermal actuators for force testing
G. hingedIRsource	flip-up heating resistor with hinged-wire connections
H. jet-logo	AFIT MEMS logo shaped like an F-16, flips up and rotates
I. lateral_force_tester	second design of adjustable force test beam
J. liftMotor2	version of hinged plate lift motor from MUMPS 10, fixed
K. longtilt	electrostatic tilting mirror with torsion flexures
L. mirgrating	different types of fixed gratings with gold plating
M. slide-up-mirror	adjustable-angle hinged mirror
spectrometer:	built up of adjustable hinged mirrors, flip-up rotating grating, IR source
N. step_motor4	thermal actuated rotary stepper motor, rev. 4, some with gears
O. vertHeat2	vertical thermal actuator for initial lift of hinged plates

A.2.21 MUMPS12 Die Number 4

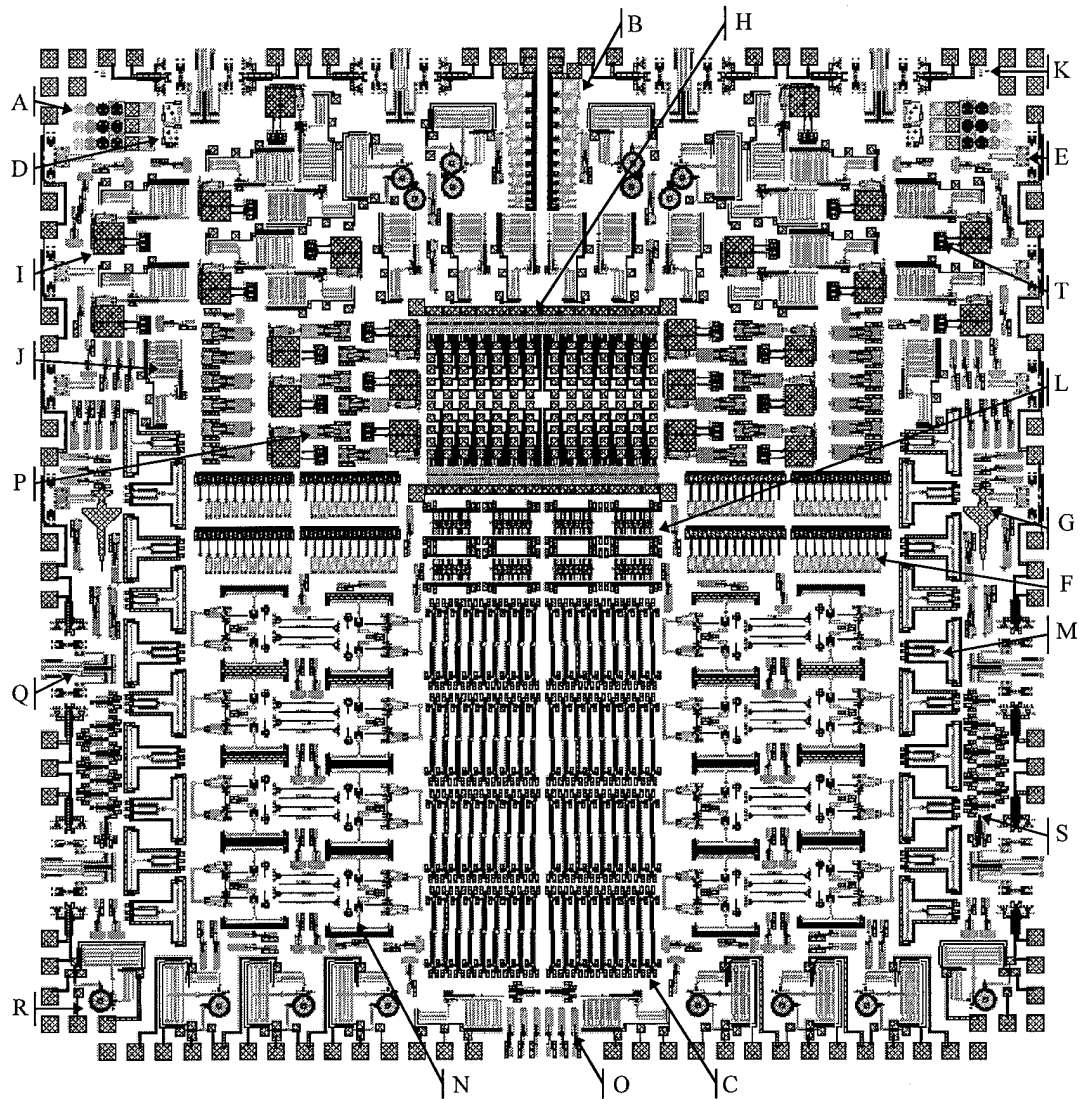


Figure A-27. MUMPS12 die number 4. This die contains only the author's devices. The upper middle contains dense linear arrays of thermally actuated vertical mirrors, connected to HDI pads.

A. AngleTestSm	smaller version of test cell with angled lines
B. EtchGaugeHt	etch gauge with thermal actuators built in closer to plates
C. LatchRelay	MUMPS version of LIGA latching relay
D. alignmentTest	layer alignment fabrication test
E. flip_grip2	version of flip-over thermal grippers with slide catches
F. hingeTest2	thermally actuated hinge pin width test for 0.75 μm thick <i>oxide2</i>
G. jet-logo	F-16 'AFIT MEMS' logo on break-off tethers
H. liftBridge	vertical thermal actuator for dense linear mirror arrays
I. lift_plate2	thermally actuated linear stepper motor set to lift hinged plate
J. linmot5	revision 5 of the thermally actuated linear stepper motor
K. overetch_test	test cell for SEM measurements of polysilicon sidewall etch
L. piston_tilt	rectangular electrostatically actuated piston/tilt mirror arrays
M. poly_relay1	thermally actuated ball-and-socket relay
N. powered_slide_catch	thermally positioned slide catch for hinged-wires
O. pull_store	pull-spring energy storage device, released by thermal fuse
P. pull_motor1	pull-spring energy storage device arranged to lift a hinged plate
Q. slide_grip2	second revision of thermal grippers that slide over the die edge
R. step_motor5	revision 5 of the thermally actuated rotary stepper motor
S. vert-poly2	vertical thermal actuator built in topologically formed <i>poly2</i>
T. vertHeat_150	150 μm long version of backbending vertical thermal actuator

A.3 LIGA Die Plots and Device Listings

The LIGA designs started with the second fabrication run offered by MCNC, and the LIGA die are numbered by fabrication run. Only the die from the second LIGA run have been fabricated as of this writing. MCNC offers two fabrication options, a 150 μm and a 30 μm tall run. Die for both fabrication options were submitted for the second run, but only a die for the shorter option was submitted for the third run. The devices on the two die for the second run are common to both die, so although the arrangement of the devices varies slightly, only the short die is shown.

A.3.1 LIGA2, Short Die

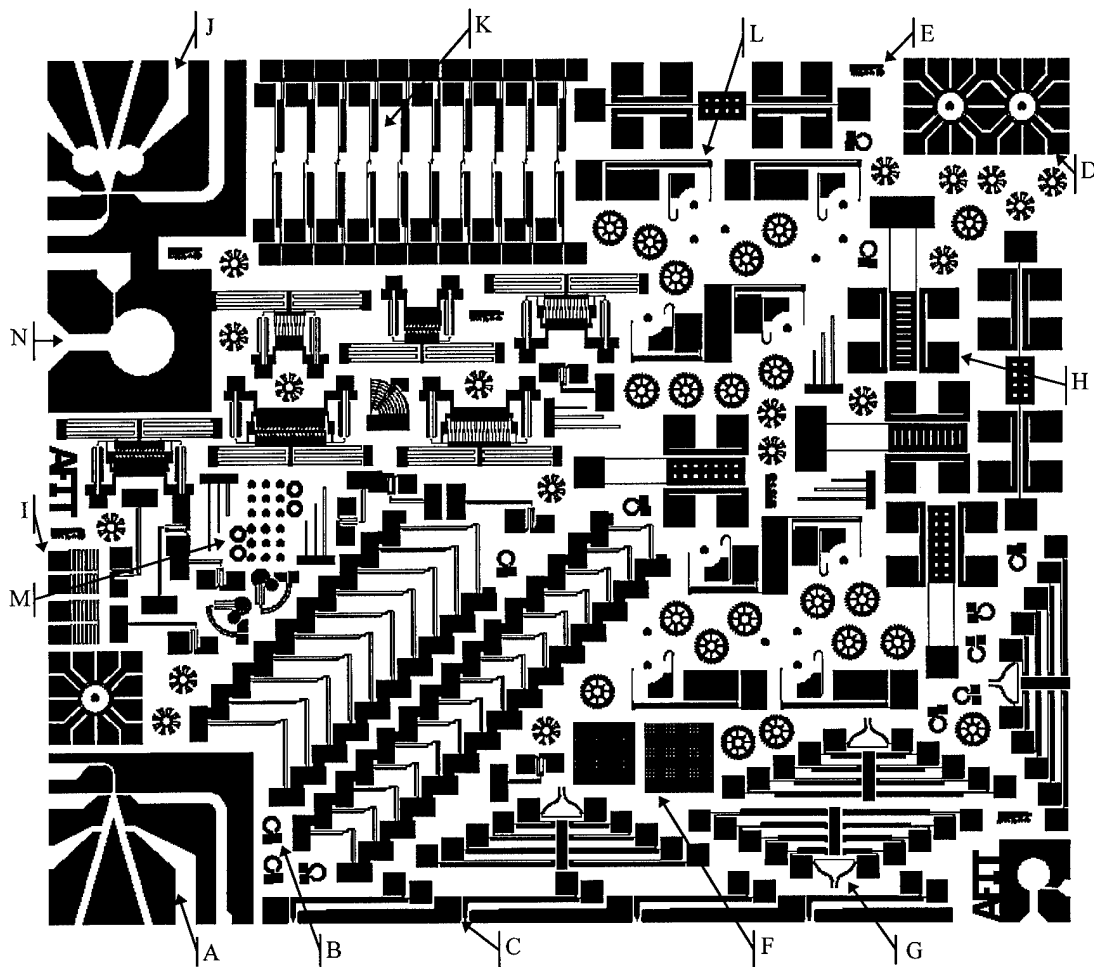


Figure A-28. LIGA2 die for 30 μm tall fabrication run. The die contains mostly the author's devices, with some comb driven relays and thermally actuated relays in diagonal arrays. The die for the 150 μm fabrication run contains a subset of these devices.

A. bistable_amp	bistable fluidic amplifier
B. circular_heatuator	round lateral thermal actuator
C. edge_tactstim	thermally actuated tactile stimulator
D. electrostatic_motor	electrostatic salient-pole rotary motor
E. etchgauge	square and round posts for partial undercut etch gauging
F. grid_cell	fabrication and etch test cell, grids of various sized holes
G. heatuator_array	various length lateral thermal actuators, and a gripper
H. lateral_accel	accelerometers with electrostatic or magnetic actuation
I. movespring	test actuator structure
J. proportional_amp	proportional fluidic amplifier
K. push_relay	latching relay with lateral thermal actuators
L. ratchet_motor	thermally actuated ratchet motor
M. test_axles	axle and wheel fit test cell, axles of various diameters
N. vortex_amp	vortex fluidic amplifier

A.3.2 LIGA3 Die

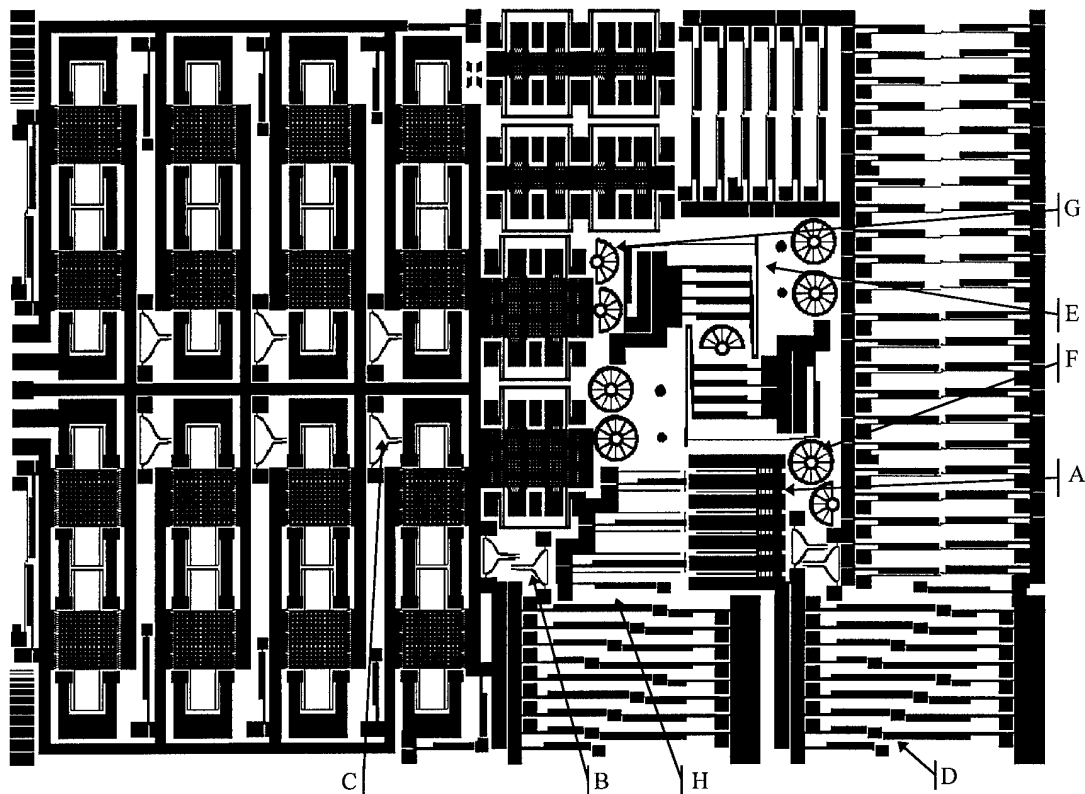


Figure A-29. LIGA3 die for 30 μm tall fabrication run. The right half of the die contains the author's devices, with some other devices worked into spaces on the left half also. Most of the author's devices are versions of the latching relay, the most promising device from the LIGA2 run.

- | | |
|--------------------|---|
| A. adj_force_test | adjustable force test beams, for forward and back-bend tests |
| B. grip2_half | variation of single thermally expanding beam gripper |
| C. grip3_half | variation of single thermally expanding beam gripper |
| D. latch_relay2 | latching relay from LIGA2 with latch tip spacing variations |
| E. motor2 | thermally actuated stepper motor similar to MUMPS motors |
| F. rotor400 | 400 μm diameter rotor for stepper motor |
| G. rotor400_sector | 400 μm diameter sector gear for stepper motor, fills in the layout |
| H. thermact | second revision of lateral thermal actuator, in various lengths. |

Appendix B

This appendix contains descriptions of the hardware and software that were created to design, etch and test MEMS at AFIT both for this dissertation research and for other AFIT MEMS research efforts. These items represent improvements in the MEMS research infrastructure at AFIT that were put in place for physical MEMS research on die designed in-house.

B.1 Computer Aided Design Layout Tools

Before any MEM devices or systems could be drawn, CAD tools had to be chosen and adapted to the technology specifications of the MEMS processes. This section contains the technology files for the Magic and Cadence layout tools. These two tools are typical of the tools available for MEMS layout, and are adaptations of existing VLSI layout tools. The Magic tool has been used at AFIT for VLSI design for over ten years, and was the tool that the author was most familiar with for CAD design of microelectronics. The Magic tool was adapted for drawing CMOS MEMS devices by the National Institute for Standards and Technology [1], and by the author for drawing MUMPS designs. The Cadence tool was made available for use by MEMS researchers early in this dissertation research and was adopted for MUMPS and LIGA design layout.

These drawing tools are adapted to different microelectronic or MEMS fabrication processes by 'technology files' that describe what color and style each

drawing layer should have, how those layers interact with each other, and how the layers are translated to and from the mask file format. The mask file is the end product which is sent electronically to the manufacturer when a design is to be fabricated. The format used at AFIT for transmitting mask files is the Caltech Intermediate Format, denoted with the '.CIF' file extension. With the MUMPS process, there is a one-to-one correspondence between the drawing and mask layers. In the LIGA process currently offered by MCNC, there is only one drawing and mask layer [2].

The CMOS MEMS process does not have a one-to-one correspondence between what is drawn and what is translated to the CIF file. This reflects the method used by Magic to display and manipulate the more complex CMOS microelectronic designs. In Magic, certain fabrication details are not displayed to make the drawing task easier. For example, in CMOS MEMS drawing, a via is a separate 'layer' with its own color and interaction with the other CMOS layers. When it is translated, however, it translates to three mask layers: the two aluminum metallization masks and the mask for the oxide between them. Similarly, when an *open* MEMS feature is drawn it appears as a single layer on the screen, but is translated to directly overlapping features on all the CMOS oxide masks. The result is that when the device is fabricated, the overlapping oxide cuts leave the silicon substrate exposed for anisotropic etching.

The Cadence tool can have similar interactions between the drawing and output representations, but with the MUMPS and LIGA processes, which have fewer masks,

it was not necessary to 'hide' fabrication details. The CMOS MEMS process has limited mechanical functionality, and the extra details would merely clutter the display; but the MUMPS process can produce complex mechanical structures, so every detail of oxide cuts and polysilicon layer interaction must be available and visible for the researcher to take maximum advantage of them [3].

One major difference between the Magic and Cadence CAD tools is in how the designs are stored and manipulated internally, which affects the types of objects which can be drawn. The Magic tool represents drawings internally on seven tiled planes. The basic tile shape is a square one generic unit on a side, and larger shapes are decomposed into rectangular, horizontal rows. Any features added to the drawing are automatically merged with the existing images.

The major limitation of Magic is that it can only represent rectangular polygons, a drawing style called 'Manhattan geometry'. Objects with curves or angular features must be painstakingly drawn in a stair-step fashion. The minimum feature step defined in the Magic MUMPS technology file is 1 μm , but the MUMPS process can define features in 0.25 μm steps, so the result is angled lines with a jagged appearance, as seen in the original hexagonal mirror design in Figure 5.31(b).

Cadence stores drawing objects as individual polygons, rectangles or circles. Objects are stored the way they are drawn, and overlapping features remain distinct objects in memory, unless specifically merged. This object representation allows circular and angular features to be much more precisely and quickly drawn in Cadence.

Other CAD tools were explored, specifically the L-Edit and AutoCAD tools which can be run on personal computers instead of Sun workstations. AutoCAD was found to be more complex than necessary for MEMS designs, with no advantage over Cadence for its added complexity. L-Edit has been specifically adapted by its creator, Tanner Research, Inc., for the MUMPS process, but it offers fewer features than Cadence, so has not been extensively used at AFIT. Its drawing capabilities fall between those of Magic and Cadence.

The following sections contain the technology files written by the author for Cadence and Magic. Magic is still used for CMOS MEMS layouts; but only the MUMPS 3, 4 and 5 layouts were done in Magic. Cadence is now the only tool used for MUMPS and LIGA, although any CAD tool with any technology file can be used for the LIGA designs, as long as a single mask layer is the final output. Cadence could be used for CMOS MEMS, but since rotating structures can not be designed in CMOS MEMS, there was no incentive to adapt Cadence for CMOS MEMS technology.

B.1.1 Magic Technology File for MUMPS

```
/*-----  
* mumps.tech    Multi-User MEMS Processs 29 Nov 93  
* Some of the characteristics of this technology are:  
*   2 releasable polysilicon layers  
*   1 non-releasable (base) poly layer  
*   1 base nitride layer  
*   1 aluminum metal layer  
*   2 layers of sacrificial PSG oxide  
*  
* For more information see MUMPS Process Specifications
```

```

*
* MCNC Electronic Technologies Division, August 20, 1993
*-----*/

```

```

tech
  mumps
end

```

```

planes
  nitride,n
  poly0,p0
  oxide1,ox1
  poly1,p1
  oxide2,ox2
  poly2,p2
  metal,m
end

```

```

types
  nitride  nitride,n
  poly0    poly0,p0
  oxide1   oxide1,ox1
  oxide1   dimple,d
  poly1    poly1,p1
  oxide2   oxide2thin,ox2thn,ox2n
  oxide2   oxide2thick,ox2thk,ox2k
  poly2    poly2,p2
  metal    metal,m
end

```

```

contact
end

```

```

styles
  styletype mos
  poly0      1
  poly1      20
  poly2      21
  metal      34
  nitride    13
  dimple     14
  oxide1     17
  oxide2thin 15
  oxide2thick 12
end

```

```

compose
end
connect
end

```

```

cifoutput

```

```

style lambda=1.0(gen)
  scalefactor 100
  layer CSN nitride
  or nitride
  layer CPZ poly0
  or poly0
  layer COF oxide1
  or oxide1
  layer COS dimple
  or dimple
  layer CPS poly1
  or poly1
  layer COT oxide2thin
  or oxide2thin
  layer COL oxide2thick
  or oxide2thick
  layer CPT poly2
  or poly2
  layer CCM metal
  or metal
end

```

```

cifinput
style lambda=1.0(gen)
  scalefactor 100
  layer nitride CSN
  labels CSN
  layer poly0 CPZ
  labels CPZ
  layer oxide1 COF
  labels COF
  layer dimple COS
  labels COS
  layer poly1 CPS
  labels CPS
  layer oxide2thin COT
  labels COT
  layer oxide2thick COL
  labels COL
  layer poly2 CPT
  labels CPT
  layer metal CCM
  labels CCM
end

```

/* The following features are not used. */

```

mzrouter
end

```

```

drc
end

```

extract
end

wiring
end

router
end

plowing
end

plot
end

B.1.3 Cadence Technology File for MUMPS

The following is an excerpt of the Cadence technology file for MUMPS; the complete file is too long to include here. What is shown here are the parts that were customized specifically for the MUMPS process, including the layer display definitions and ordering. Other sections are listed with just the start and end of their text for orientation purposes. Portions of the technology file that have been removed for this appendix are denoted with the message '<< text removed >>'.

MCNC has added mask definitions for holes in the *poly0* and metal layers, similar to those defined for the *poly1* and *poly2* layers. These changes have not yet been added to this technology file, as they have not been needed for the designs drawn to date at AFIT. More information about the technology file is available in the Cadence on-line manuals.

```
; Technology File for library jcomtois  
; Generated on Feb 23 10:12:31 1995  
; with layout version 4.3.2 Thu Aug 4 16:36:16 PDT 1994 (cmrd1)
```

```
tfcDefineDisplay(
```

```
tfcDefineColor(
;(DisplayName ColorName Index Red Green Blue)
(display white 0 1000 1000 1000)
(display silver 1 850 900 1000)
```

```
( display winColor4 30 800 800 800 )
( display winColor5 31 780 780 780 )
)
```

<< text removed >>

B-8

<< text removed >>

```
( display    smiley    21 ((000000000000000000)
                          (00000011111000000)
                          (00001110000110000)
                          (00010000000001000)
                          (0010001001000100)
                          (0010001001000100)
                          (0100001001000010)
                          (01000000000000010)
                          (01000000000000010)
                          (01001000000010010)
                          (0010010000100100)
                          (00100011111000100)
                          (00010000000001000)
                          (0000110000110000)
                          (0000001111100000)
                          (0000000000000000)))
)
```

```
tfcDefineLineStyle(
;( DisplayName LineStyle Index Size Pattern )
( display    solid    0    1  (1 1 1))
( display    dashed   1    1  (1 1 1 0 0))
```

<< text removed >>

```
( display    thickLine 7    3  (1 1 1))
)
```

```
tfcDefinePurpose(
;( PurposeName Purpose# )
( warning      234  )
( tool1        235  )
( tool0        236  )
( label        237  )
( flight       238  )
( error        239  )
( annotate     240  )
( drawing1     241  )
( drawing2     242  )
( drawing3     243  )
( drawing4     244  )
( drawing5     245  )
( drawing6     246  )
( drawing7     247  )
( drawing8     248  )
( drawing9     249  )
( boundary     250  )
( pin          251  )
( drawing      252  )
( net          253  )
```

```
( cell      254  )
( all      255  )
)
```

```
tfcDefineLayer(
;( LayerName      Purpose Layer# FillStyle  Priority Vis Sel Blink Valid)
( background      drawing 254  solid      0      t nil nil nil )
( grid            drawing 251  outlineStipple 1      t nil nil nil )
( grid            drawing1 251  outlineStipple 2      t nil nil nil )
```

<< text removed >>

```
( Unrouted      drawing8 200  outlineStipple 109  t t nil nil )
( Unrouted      drawing9 200  outlineStipple 110  t t nil nil )
( guide1        drawing 5   outlineStipple 111  t t nil t )
( line1         drawing 7   outlineStipple 112  t t nil t )
( poly0         drawing 9   solid      113  t t nil t )
( guide2        drawing 11  outlineStipple 114  t t nil t )
( line2         drawing 13  outlineStipple 115  t t nil t )
( poly1         drawing 15  outlineStipple 116  t t nil t )
( anchor1       drawing 17  outlineStipple 117  t t nil t )
( dimple        drawing 19  outlineStipple 118  t t nil t )
( hole1         drawing 21  X          119  t t nil t )
( poly2         drawing 23  outlineStipple 120  t t nil t )
( anchor2       drawing 25  outlineStipple 121  t t nil t )
( plp2via       drawing 27  outlineStipple 122  t t nil t )
( hole2         drawing 29  X          123  t t nil t )
( metal         drawing 31  outlineStipple 124  t t nil t )
( guide3        drawing 33  outlineStipple 125  t t nil t )
( line3         drawing 35  outlineStipple 126  t t nil t )
)
```

```
tfcDefineLayerDisplayInfo(
;( LayerName      Purpose DisplayName Stipple  LineStyle Fill  Bright Outline )
( background      drawing display  solid  solid  black  white  black )
( grid            drawing display  blank  solid  slate  white  slate )
```

<< text removed >>

```
( Unrouted      drawing8 display  blank  dashed  gold  white  gold )
( Unrouted      drawing9 display  blank  dashed  silver  white  silver )
( guide1        drawing display  hSlash  solid  forest  maroon  forest )
( line1         drawing display  blank  shortDash yellow  blue  yellow )
( poly0         drawing display  solid  solid  tan  chocolate tan )
( guide2        drawing display  vSlash  solid  purple  cream  purple )
( line2         drawing display  blank  dots  red  pink  red )
( poly1         drawing display  dense  solid  cadetBlue red  cadetBlue )
( anchor1       drawing display  hcurb  solid  blue  red  black )
( dimple        drawing display  triangle solid  cyan  magenta cyan )
( hole1         drawing display  blank  solid  blue  red  blue )
( poly2         drawing display  x      solid  pink  cyan  pink )
( anchor2       drawing display  vCurb  solid  magenta cyan  black )
```

```

( plp2via      drawing display grid      solid slate silver black )
( hole2        drawing display blank     solid magenta cyan  magenta )
( metal        drawing display M         solid gold  cadetBlue gold  )
( guide3       drawing display smiley    solid brown orange brown  )
( line3        drawing display blank     dots  slate  white  slate  )
)

```

```

tfcDefineLayerProp(
;( LayerName      Purpose  PropName      PropValue )
( background      drawing  dragEnable?    nil )
( background      drawing  contributesToChangedLayer? t )
( grid            drawing  dragEnable?    nil )
)

```

<< text removed >>

```

( Unrouted      drawing9 dragEnable?      t )
( Unrouted      drawing9 contributesToChangedLayer? t )
( guide1        drawing  dragEnable?      t )
( guide1        drawing  streamLayerNumber 0 )
( guide1        drawing  streamDatatypeNumber 0 )
( guide1        drawing  streamTranslateLayer? nil )
( guide1        drawing  contributesToChangedLayer? t )
( line1         drawing  dragEnable?      t )
( line1         drawing  streamLayerNumber 0 )
( line1         drawing  streamDatatypeNumber 0 )
( line1         drawing  streamTranslateLayer? nil )
( line1         drawing  contributesToChangedLayer? t )
( poly0         drawing  dragEnable?      t )
( poly0         drawing  streamLayerNumber 0 )
( poly0         drawing  streamDatatypeNumber 0 )
( poly0         drawing  streamTranslateLayer? nil )
( poly0         drawing  contributesToChangedLayer? t )
( guide2        drawing  dragEnable?      t )
( guide2        drawing  streamLayerNumber 0 )
( guide2        drawing  streamDatatypeNumber 0 )
( guide2        drawing  streamTranslateLayer? nil )
( guide2        drawing  contributesToChangedLayer? t )
( line2         drawing  dragEnable?      t )
( line2         drawing  streamLayerNumber 0 )
( line2         drawing  streamDatatypeNumber 0 )
( line2         drawing  streamTranslateLayer? nil )
( line2         drawing  contributesToChangedLayer? t )
( poly1         drawing  dragEnable?      t )
( poly1         drawing  streamLayerNumber 0 )
( poly1         drawing  streamDatatypeNumber 0 )
( poly1         drawing  streamTranslateLayer? nil )
( poly1         drawing  contributesToChangedLayer? t )
( anchor1       drawing  dragEnable?      t )
( anchor1       drawing  streamLayerNumber 0 )
( anchor1       drawing  streamDatatypeNumber 0 )
( anchor1       drawing  streamTranslateLayer? nil )
( anchor1       drawing  contributesToChangedLayer? t )

```



```

( dimple      drawing  dragEnable?      t )
( dimple      drawing  streamLayerNumber 0 )
( dimple      drawing  streamDatatypeNumber 0 )
( dimple      drawing  streamTranslateLayer? nil )
( dimple      drawing  contributesToChangedLayer? t )
( hole1       drawing  dragEnable?      t )
( hole1       drawing  streamLayerNumber 0 )
( hole1       drawing  streamDatatypeNumber 0 )
( hole1       drawing  streamTranslateLayer? nil )
( hole1       drawing  contributesToChangedLayer? t )
( poly2       drawing  dragEnable?      t )
( poly2       drawing  streamLayerNumber 0 )
( poly2       drawing  streamDatatypeNumber 0 )
( poly2       drawing  streamTranslateLayer? nil )
( poly2       drawing  contributesToChangedLayer? t )
( anchor2     drawing  dragEnable?      t )
( anchor2     drawing  streamLayerNumber 0 )
( anchor2     drawing  streamDatatypeNumber 0 )
( anchor2     drawing  streamTranslateLayer? nil )
( anchor2     drawing  contributesToChangedLayer? t )
( plp2via     drawing  dragEnable?      t )
( plp2via     drawing  streamLayerNumber 0 )
( plp2via     drawing  streamDatatypeNumber 0 )
( plp2via     drawing  streamTranslateLayer? nil )
( plp2via     drawing  contributesToChangedLayer? t )
( hole2       drawing  dragEnable?      t )
( hole2       drawing  streamLayerNumber 0 )
( hole2       drawing  streamDatatypeNumber 0 )
( hole2       drawing  streamTranslateLayer? nil )
( hole2       drawing  contributesToChangedLayer? t )
( metal       drawing  dragEnable?      t )
( metal       drawing  streamLayerNumber 0 )
( metal       drawing  streamDatatypeNumber 0 )
( metal       drawing  streamTranslateLayer? nil )
( metal       drawing  contributesToChangedLayer? t )
( guide3      drawing  dragEnable?      t )
( guide3      drawing  streamLayerNumber 0 )
( guide3      drawing  streamDatatypeNumber 0 )
( guide3      drawing  streamTranslateLayer? nil )
( guide3      drawing  contributesToChangedLayer? t )
( line3       drawing  dragEnable?      t )
( line3       drawing  streamLayerNumber 0 )
( line3       drawing  streamDatatypeNumber 0 )
( line3       drawing  streamTranslateLayer? nil )
( line3       drawing  contributesToChangedLayer? t )
)

tfcDefineTwoLayerProp(
;( Layer1Name Purpose1 Layer2Name Purpose2 Order PropName PropValue )
)

tfcDefineLibProp(

```

```

;( PropName      PropValue )
( artistVersion  "FALSE" )
)

tfcDefineView(
;( ViewName      ViewType    )
( layout        maskLayout   )
)

tfcDefineViewPropByViewType(
;( ViewType      PropName      PropValue )
( maskLayout     DBUPerUU      1000.000000 )
( maskLayout     userUnits      "micron" )
( maskLayout     minGridResolution 0.001000 )
( maskLayout     segSnapMode     "orthogonal" )
( maskLayout     snapMode        "L90XFirst" )
( maskLayout     ySnapSpacing    1.000000 )
( maskLayout     xSnapSpacing    1.000000 )
( maskLayout     gridMultiple    10 )
( maskLayout     gridSpacing     1.000000 )
( maskLayout     drawDottedGridOn t )
( maskLayout     drawGridOn      t )
( maskLayout     stopLevel       0 )
( maskLayout     startLevel      0 )
( maskLayout     instLabel        "master" )
( maskLayout     displayPinNames  t )
( maskLayout     textJustificationOn nil )
( maskLayout     drawSurroundingOn t )
( maskLayout     arrayDisplay     "Full" )
( maskLayout     iconsOn          nil )
( maskLayout     originMarkersOn  t )
( maskLayout     drawInstancePins nil )
( maskLayout     pathCL           "yes" )
( maskLayout     accessEdgesOn    nil )
( maskLayout     drawAxesOn       t )
( maskLayout     netsOn           nil )
( maskLayout     maxDragFig       100 )
( maskLayout     pathWidth        2.000000 )
)

tfcDefineViewProp(
;( ViewName      PropName      PropValue )
)
;
;
; Opus Pre-defined Class, Device and Wire Section
;
;
; no Opus pre-defined device classes
; no syEnhancement devices
; no syDepletion devices

```

```

; no syContact devices
; no syPin devices
; no syRectPin devices
; no symbolic wires

;
;
; Opus Symbolic Device Class Definition
;
;
;
; no other device classes
;
;
; Opus Symbolic Device Declaration
;
;
; no other devices
;
; Opus Symbolic Rules
;
;
; no symbolic rules
;

```

B.1.3 Cadence Technology File for LIGA

Cadence Default Technology File
 ; Generated on Apr 3 08:45:26 1991
 ; with opus2 version Fri Mar 29 10:03:28 PST 1991

```

tfcDefineDisplay(
;( DisplayName #Colors #Stipples #LineStyles )
( display 256 256 256 )
)

```

```

tfcDefineColor(
;( DisplayName ColorName Index Red Green Blue )
( display white 0 1000 1000 1000 )
( display silver 1 850 900 1000 )
)

```

<< text removed >>

```

( display winColor5 31 780 780 780 )

```

)

```
tfcDefineStipple(  
;( DisplayName StippleName Index Bitmap )  
( display blank 0 ((000000000000000000)  
 (000000000000000000)  
 (000000000000000000)  
 (000000000000000000)  
 (000000000000000000)  
 (000000000000000000)  
 (000000000000000000)  
 (000000000000000000)  
 (000000000000000000)  
 (000000000000000000)  
 (000000000000000000)  
 (000000000000000000)  
 (000000000000000000)  
 (000000000000000000)  
 (000000000000000000))
```

<< text removed >>

```
( display x 16 ((1000100010001000)  
 (0101010101010101)  
 (0010001000100010)  
 (0101010101010101)  
 (1000100010001000)  
 (0101010101010101)  
 (0010001000100010)  
 (0101010101010101)  
 (1000100010001000)  
 (0101010101010101)  
 (0010001000100010)  
 (0101010101010101)  
 (1000100010001000)  
 (0101010101010101)  
 (0010001000100010)  
 (0101010101010101)))
```

```
tfcDefineLineStyle(  
;( DisplayName LineStyle Index Size Pattern )  
( display solid 0 1 (111))  
( display dashed 1 1 (111100))  
( display dots 2 1 (100))  
( display dashDot 3 1 (11100100))  
( display shortDash 4 1 (1100))  
( display doubleDash 5 1 (1111001100))  
( display hidden 6 1 (1000))  
( display thickLine 7 3 (111)))
```

```
tfcDefinePurpose(  

```

```

;( PurposeName    Purpose# )
( warning        234    )
( tool1          235    )

<< text removed >>

( all            255    ))

tfcDefineLayer(
;( LayerName      Purpose Layer# FillStyle    Priority Vis Select Blink )
( metal          drawing 29   solid    _def_   t t nil t )
( open           drawing 30   solid    _def_   t t nil t )
( background     drawing 254  solid    _def_   t nil nil )
( grid           drawing 251  outlineStipple _def_   t nil nil )
( grid           drawing1 251  outlineStipple _def_   t nil nil )
( axis           drawing 252  outlineStipple _def_   t nil nil )

<< text removed >>

( Unrouted      drawing9 200  outlineStipple 110   t t nil ))

tfcDefineLayerDisplayInfo(
;( LayerName Purpose DisplayName Stipple LineStyle Fill Bright Outline )
( metal  drawing display  blank  solid  blue  blue  blue  )
( open  drawing display  blank  solid  winColor3 winColor3 winColor3 )
( background drawing display  solid  solid  black  white  black  )
( grid  drawing display  blank  solid  slate  white  slate  )
( grid  drawing1 display  blank  solid  white  white  white  )

<< text removed >>

( Unrouted  drawing9 display  blank  dashed  silver  white  silver ))

tfcDefineLayerProp(
;( LayerName      Purpose  PropName      PropValue ))

tfcDefineTwoLayerProp(
;(Layer1Name Purpose1 Layer2Name Purpose2 Order PropName      PropValue ))

tfcDefineLibProp(
;( PropName      PropValue ))

tfcDefineView(
;( ViewName      ViewType    )
( "moduleInfo"  schematicSymbol )
( _abel        "text.v"    )
( _minc        "text.v"    )

<< text removed >>

( vhdl          vhdl        )
( vhdl_config   vhdl        ))

```

```

tfcDefineViewPropByViewType(
;( ViewType      PropName      PropValue )
( maskLayout    minGridResolution  0.100000 )
( maskLayout    snapMode          "diagonal" )
( maskLayout    pathWidth         2.000000 )
( maskLayout    gridSpacing       1.000000 )

```

<< text removed >>

```

( package      DBUPerUU      160.0 )
( vhdl        enableDelta    t )
)

```

```

tfcDefineViewProp(
;( ViewName      PropName      PropValue )
( abstract      ySnapSpacing   0.100000 )

```

<< text removed >>

```

( layout      ySnapSpacing   0.100000 )
( layout      xSnapSpacing   0.100000 )

```

<< text removed >>

```

( tmxPicture   DBUPerUU      1000.0 )
( tmxPicture   userUnits     "millimeters" )
)

```

```

.....

```

```

;
; Opus Pre-defined Class, Device and Wire Section
;

```

```

.....

```

```

; no Opus pre-defined device classes
; no syEnhancement devices
; no syDepletion devices
; no syContact devices
; no syPin devices
; no syRectPin devices
; no symbolic wires
;

```

```

.....

```

```

;
; Opus Symbolic Device Class Definition
;

```

```

.....

```

```

;

```

```

; no other device classes
;

```

```

.....

```

```

;

```

```

; Opus Symbolic Device Declaration
;
;
; no other devices
;
;
; Opus Symbolic Rules
;
; no symbolic rules
;

```

B.2 Test Hardware

The following hardware was built by the author for both his own and other students' research. These items include die holders for the probe station and scanning electron microscope (SEM), test equipment for connecting and controlling power to MEMS devices on the probe station, chemical etching equipment, and a balance originally constructed for measuring the force of CMOS MEMS actuators.

B.2.1 Reflux Container for EDP Etching

A reflux reactor was constructed for anisotropically etching CMOS MEMS die in EDP. A reflux reactor was needed to keep the water in the solution. Evaporated water condenses on the reflux container lid and walls and falls back into the solution. A large glass reflux container was available, but it required too much EDP, roughly 800 ml, to immerse a wafer holder and stir bar. This made it uneconomical for etching a few die at a time.

The smaller reflux reactor, shown in Figure B-1, was fabricated from a 250-ml plastic beaker with a tight-fitting plastic cover. A spacer is placed inside to hold a two-inch fluoroware wafer holder above the stir bar. The tight cover has an access hole in the center to allow the insertion of a thermometer tube. The wafer holder is perforated to permit free flow of the etching solution, with holes small enough to prevent the test die from falling out. A reference used an EDP etch performed at a temperature of 115°C [1], but no suitable temperature-controlled heating apparatus was available, only basic laboratory hotplates. Instead, a double-boiler setup was adopted, which kept the EDP at a safe 90°C -95°C.

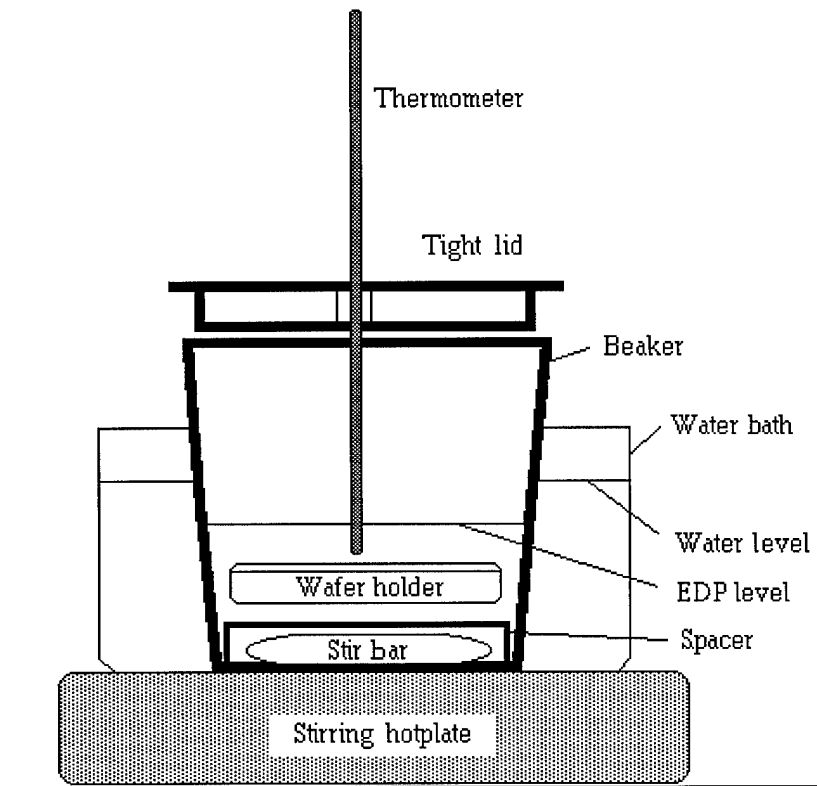


Figure B-1. Reflux reactor for anisotropic silicon etch using EDP. The water bath maintains a constant, safe temperature for the EDP. The wafer holder is perforated to allow the EDP to flow around the die being etched. Drawing is not to scale.

B.2.2 Patch Panel And Signal Generator Boost Amplifier

Several sources are used to drive the various types of MEMS devices. Electrostatic devices, especially comb drives, need high bias and drive voltages at low currents, thermal actuators need low voltages and small currents. Larger devices may have several actuators which need to be powered separately. The available power supplies include an electrometer for the high voltages, triple power supplies for the lower voltages, a signal generator, and a sequencing circuit, to be described below.

A patch panel was built to organize the many wires between the power supplies, meters, and probe station, and to make swapping power supplies quick and simple. Coaxial cables to the probe station are neatly routed to BNC connectors on the front of the panel, while the various power and signal supplies are routed to the back. The front face also contains columns of labeled holes for routing the power supplies to the probe station cables using mini-banana jacks. There is an unused set of 10 patch jacks for future expansion.

Incorporated into the patch panel is a pair of operational amplifiers arranged to take a single input from any signal generator, amplify it a fixed amount (gain = 1.8), and output normal and inverted versions. This is to boost the signal generator output to levels and polarities often needed by electrostatic actuators. The amplifiers are capable of boosting the signal to the level of their power supply, which is a maximum of $\pm 18\text{V}$. Thus the amplifiers can boost a signal generator output from 20V p-p to 36V p-p. The specific amplifier chips, Texas Instruments TL-082's, were chosen specifically because

they or their direct replacements can be purchased at electronics hobby stores. Figure B-2 shows the circuit diagrams for the amplifiers.

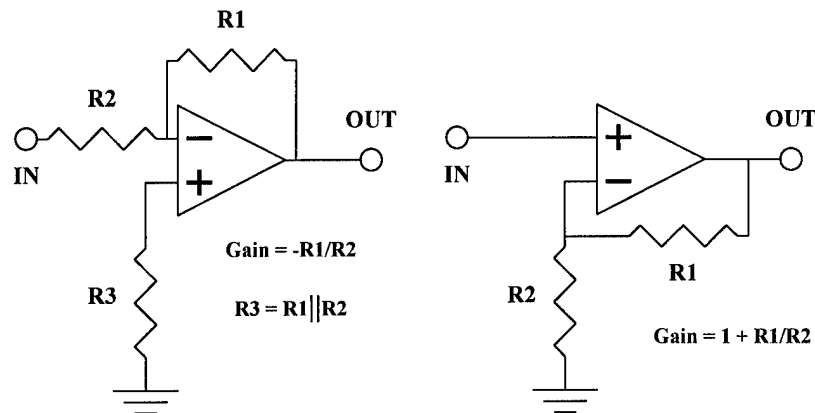


Figure B-2. Circuit diagrams for the signal generator amplifiers. The circuit on the left is the inverting amplifier, and the one on the right is the non-inverting amplifier.

B.2.3 Three Channel Power Interrupter/Sequencer

A sequencer circuit was designed and built to control the power to thermal actuator arrays for testing MUMPS stepper motors. A block diagram of the circuit is shown in Figure B-3. The circuit consists of an 8-bit counter fed by either an internal or external clock source. Comparators monitor the counter's output and drive latches when the count matches the count set for each comparator. The count set points for the comparators are set manually with a bank of switches. The latches in turn control reed relays. There are 6 comparators, two per channel, one to turn the latch on, and one to turn it off. Eight bits of counter resolution allow the start and stop points to be set at any of 256 time points in one full counter cycle, allowing fine control over the

sequencing of the actuators. Relays are used so the sequencer circuit is electrically isolated from the power supplies being controlled.

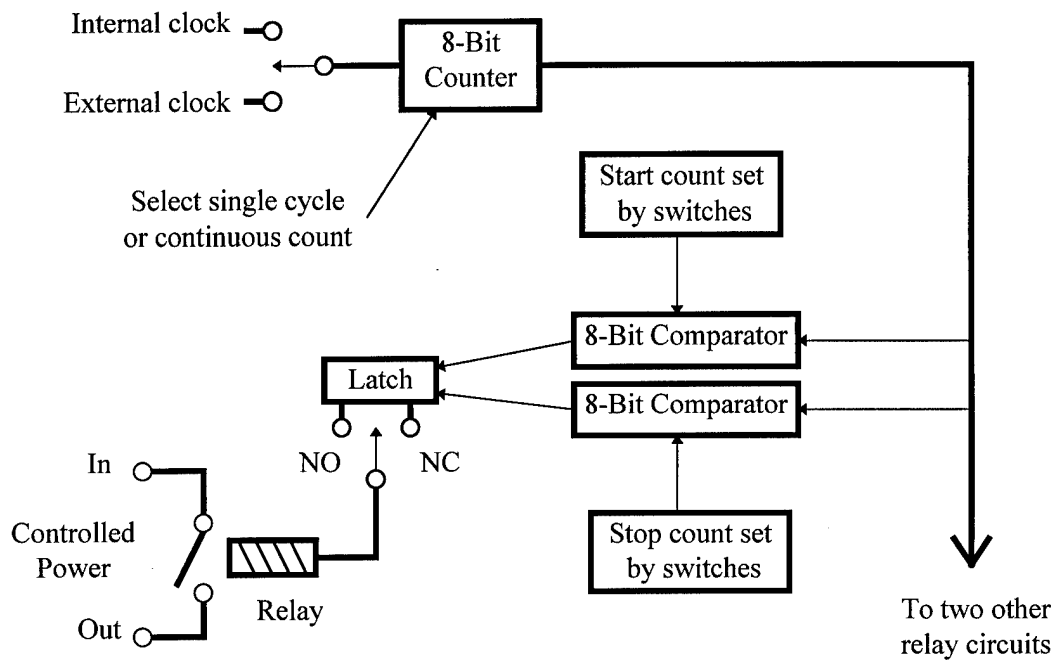


Figure B-3. Block diagram of the sequencer circuit. An internal or external clock source drives an 8-bit counter whose output is monitored by comparators, which turn relays on and off at the counts set by a bank of switches.

The state of the relay can be set to be normally closed (NC), normally open (NO), or it can be fixed in the open state (off), for test and setup purposes. The counter can be set to free-run for continuous operation, or it can be set to single-step, where it will run through only a single counter cycle each time a button is pressed. A plug-in remote control push-button is available so the researcher can move away from the sequencer panel to observe the operation in the microscope while stepping the counter circuit. A panel of mini-banana jacks allows connection to the power distribution patch panel.

Figure B-4 shows the drawing for the faceplate of the sequencer circuit. There are six sets of eight switches in the upper right for setting the turn on and turn off counts for the relays. The use of the switches is explained on the faceplate. The lower left has switches for selecting the clock source and counter operation. 5 volts DC must be fed into the counter circuit at the lower right. A potentiometer controls the frequency of the internal clock source, which can be monitored at one of the jacks on the patch panel.

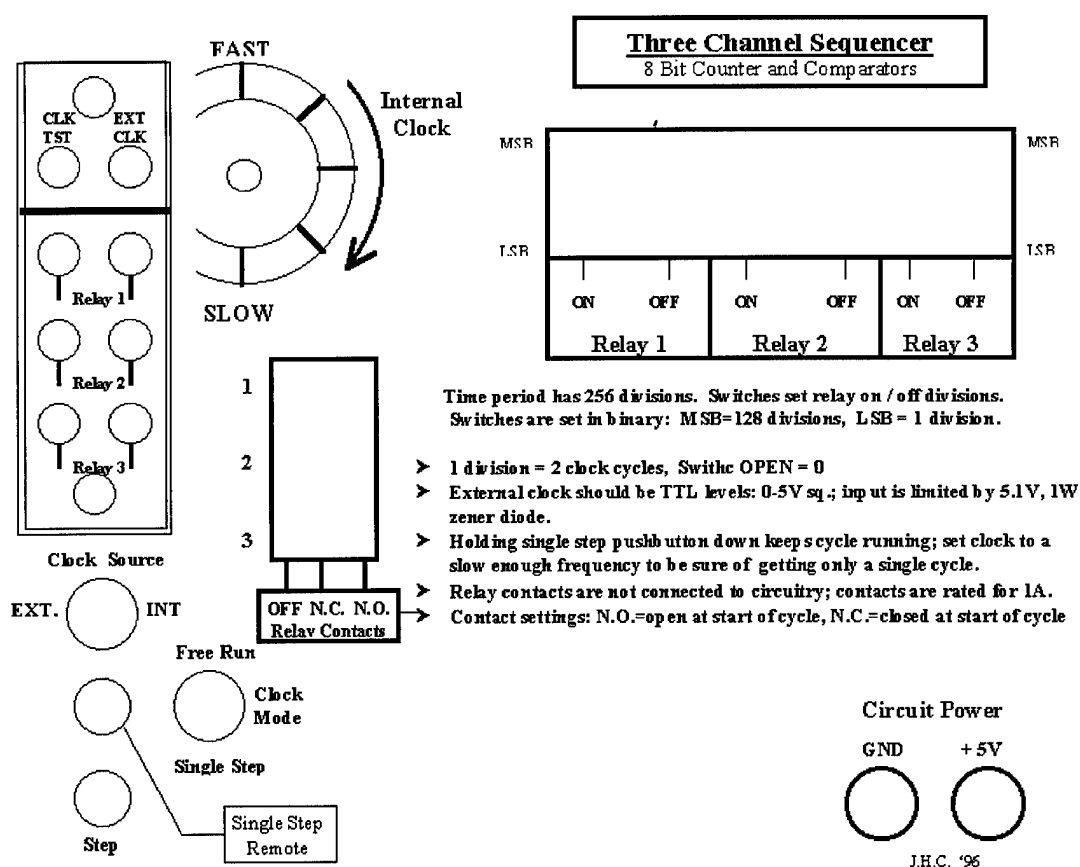


Figure B-4. Faceplate drawing for the three-channel sequencer. The blank rectangles are cut-out areas for slide switches. The blank circles are for toggle switches, screws, a push-button for single stepping in the extreme lower left, a jack for the remote push-button just above that, and banana jacks for power at the lower right.

B.2.4 Weight Balance Force Tester

A weight-balance force tester was designed and built to determine the force generated by vertically acting CMOS MEMS bimorph thermal actuators under loaded conditions [4]. The force tester, shown in Figure B-5, consists of a balance arm on knife-edge bearings, a counterweight, a replaceable probe tip, and a weight cup for adding weight on the probe tip side of the balance arm. The probe tip is the same type used for electrical probing, and has a diameter of approximately 5 μm . The device was fabricated from what are called 'found' parts; for example, the beam is machined from a solid aluminum #7 knitting needle, and the knife-edge bearings are tempered spring steel from a packing crate strap. Two previous models were built using a small ball bearing set and needle bearings, but these were found to be too stiff for the small weights and forces involved.

The tester arm is balanced by adjusting a counter-weight nut. The test weights are short lengths of stripped 40 gauge wire-wrap wire which are calibrated by placing the probe tip on a weight scale. The overall error associated with the weight-balance force tester is ± 2 mg, which was the accuracy of the scale used to calibrate the weights. During device testing, test weights are placed in the weight cup and the probe tip is placed on the actuating device using the probe table and tester base X-Y-Z controls.

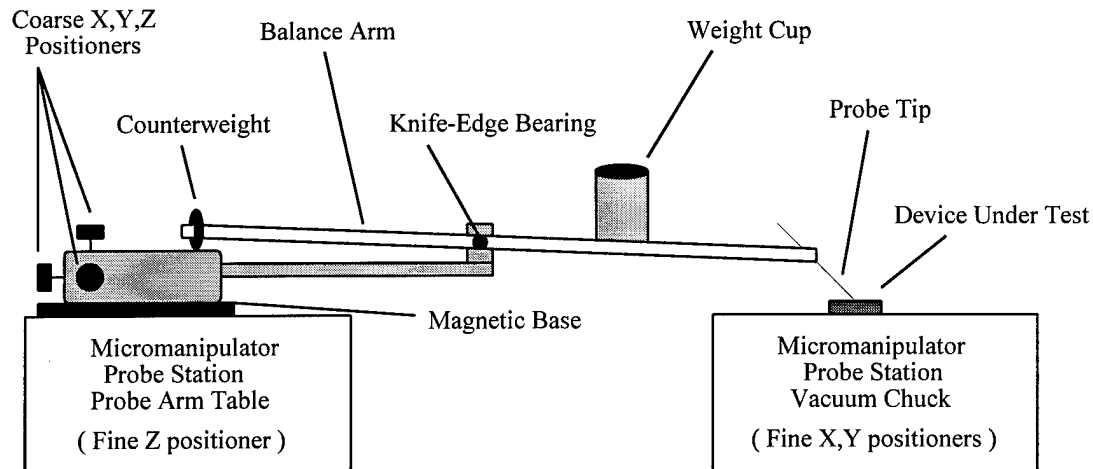


Figure B-5. Weight-balance force tester for vertically acting MEMS actuators. The balance beam rests on knife-edge bearings. Weights are short, calibrated sections of 40 gauge copper wire. The probe tip is one of the replaceable electrical probe tips.

B.2.5 Vacuum Pick

A vacuum pick was designed to pick up and place loose cover plates on the first hexagonal mirror array and hold them in place for gluing. Subsequent development of hinged cover plates made this application obsolete, but the tool has found a new application as a vacuum cleaner for removing small bits of debris from the surface of MEMS die, especially mirror arrays. This is a difficult task to perform with just a probe point, since the underlying device is often damaged while trying to spear the particles. The vacuum device is simply a nozzle tube clamped to the probe end of an X-Y-Z probe positioner, similar to the one shown in Figure B-5. The nozzle consists of nickel tubing with a 0.15 mm inside diameter and a 1 mm outside diameter. The nozzle is connected via clear rubber tubing to a valve manifold which allows connection to open air, an air pressure source, or a vacuum source.

B.2.6 Test Die Holders

Two clamps were built to hold individual die for viewing in the SEM and for probing on the probe station. The previously available SEM sample holders required the die to be glued onto the holder, a time consuming process which also makes it difficult to remove the die for post-SEM uses. The new clamp, shown schematically in Figure B-6, is adjustable to accept all of the different die sizes encountered during this research.

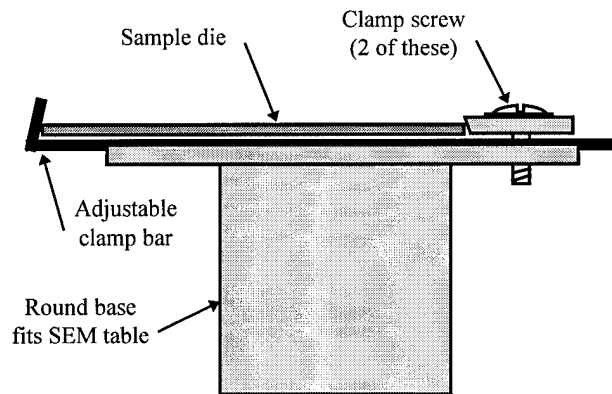


Figure B-6. Side view of the die clamp for holding samples in the scanning electron microscope. Samples are held in place against a stop by an 'L' shaped bar, which in turn is held in place by screws which tighten the stop onto the clamp bar.

The sample is placed on the clamp bar which presses the sample against the stop. Two screws tighten the stop down against the clamp bar to lock it in place. The clamp bar and stop have beveled edges to ensure a positive grip on die. The clamp is made of metal to provide a ground connection to the SEM frame. An SEM micrograph of the clamp holding a large sample can be seen in Figure 6-20.

A clamp was also built to hold die on the probe station table, which is perforated all over the top with many small holes for vacuum clamping. Individual die do not cover enough vacuum holes on the table top to provide a firm grip. The clamp, shown in Figure B-7, has a large base to generate sufficient vacuum grip, and an adjustable 'V' shaped clamp bar and stop hold the die in place. The base is $\frac{1}{4}$ inch thick Masonite and the clamp bar and stops are hardwood, roughly 2 mm thick.

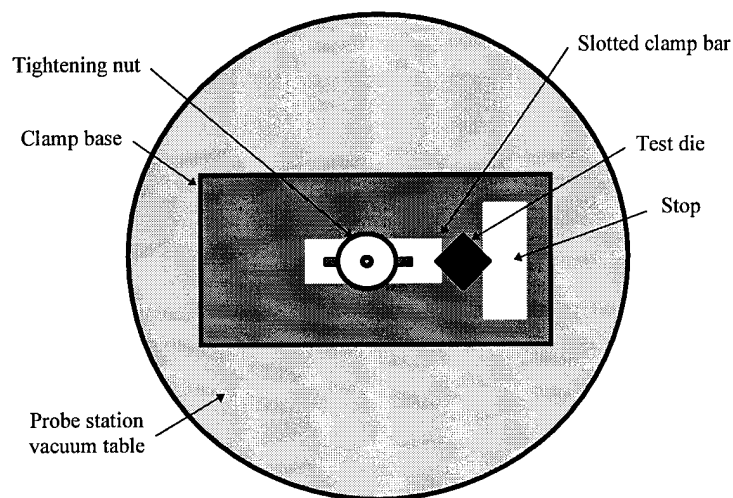


Figure B-7. Top view of the die clamp on the probe station vacuum table. Die clamp base covers more holes on the vacuum table than a bare die, so sufficient clamping force is generated to hold the die for probing.

REFERENCES

1. J. Marshall, M. Parameswaran, M. Zaghloul, and M. Gaitan, "High-level CAD melds micromachined devices with foundries," *Circuits and Devices*, pp. 10-17, Nov. 1992.
2. Information available from the MCNC World Wide Web home page, WWW url: <http://www.mcnc.org>.
3. J. Comtois and V. Bright, "Design techniques for surface-micromachining MEMS processes," *Proc. SPIE: Micromachining and Microfabrication Process Technology*, vol. 2639, pp. 211-222, 23-24 Oct. 1995.
4. B. Read, "Silicon based microactuators for telerobotic tactile stimulation," Master's Thesis, Air Force Institute of Technology, Wright-Patterson AFB, Ohio, AFIT/GE/ENG/94D-25, Dec 1994.

Appendix C

Vita: John H. Comtois, Major, USAF

Major John Comtois was born 7 February, 1961 in Hartford, Connecticut. He was commissioned into the Air Force in 1983 following his graduation from Carnegie-Mellon University with a Bachelor's Degree in Electrical Engineering. He was assigned as a computer programmer at the Command and Control Systems Office at Tinker AFB, Oklahoma, eventually becoming Chief of the Computer Maintenance Branch. His next assignment was to AFIT in 1987 to earn a Master's Degree in Electrical Engineering (MSEE), which he received in 1988. His MSEE research in Very Large Scale Integrated (VLSI) circuitry involved the design, layout and microprogramming of a 64 bit double precision floating point application specific microprocessor. He continued this project as an AFIT research associate in conjunction with the Air Force's Rome Laboratories, while assigned at the 84th Radar Evaluation Squadron at Hill AFB. There he was given funds, space and manning to create an electronics laboratory, where he designed, built, tested and programmed microcomputer-based radar data collection boards and telephone line interfaces for personal computers. These boards were subsequently mass-manufactured and are in use throughout the Air Force and Federal Aviation Administration to collect radar target data for evaluation and archiving. His current assignment as a PhD student in Electrical Engineering at AFIT began in June, 1993. Major Comtois is currently treasurer of AFIT's Eta Kappa Nu chapter and recently finished a year as president of AFIT's Tau Beta Pi chapter. He is also a student member of the IEEE.

Patent Applications and Invention Disclosures related to This Dissertation

1. S. Gustafson, G. Little, T. Rhoadarmer, V. Bright and J. Comtois, "Minimally Connected Piston Micromirror Light Modulator, Revision A," U.S. Patent Application No. 60/003,358 filed 7 September 1995.
2. M. Michalicek, V. Bright, J. Comtois, "Hidden-flexure axial-rotation micromirror device," Invention Disclosure, U.S. Air Force, Phillips Laboratory.
3. J. Comtois, V. Bright, D. Sene, "Method for mechanical connection of arrays of thermal microactuators," to be submitted.

Publications and Submissions Related to This Dissertation

1. T. Jenkins, J. Comtois and V. Bright, "Bulk etching of silicon for micromachining," *Proc. National Educator's Workshop: Update 94*, pp. 41-51, 7-9 Nov. 1994.
2. J. Comtois, T. Jenkins, and V. Bright, "Micromachining of Suspended Structures in Silicon," *Proc. National Educators' Workshop: Update 94*, pp. 53-65, 7-9 Nov. 1994.
3. T. Jenkins, J. Comtois and V. Bright, "Laboratory experiments in silicon micromachining," *Proc. ASEE 1995 Annual Conference*, vol. 2, pp. 2451-2459, Anaheim, CA, 1995.
4. M. Michalick, V. Bright and J. Comtois, "Design, fabrication, modeling, and testing of a surface-micromachined micromirror device," *Proc. 1995 ASME Dynamic Systems and Control Division*, DSC-vol. 57-2, pp. 981-985, International Mechanical Engineering Congress and Exposition, San Francisco, CA, 12-17 Nov. 1995.
5. J. Comtois, V. Bright, S. Gustafson and M. Michalick, "Implementation of hexagonal micromirror arrays as phase mostly spatial light modulators," *Proc. SPIE Microelectronic Structures and Microelectromechanical Devices for Optical Processing and Multimedia Applications*, vol. 2641, pp. 76-87, 23-24 Oct. 1995.
6. J. Comtois and V. Bright, "Design techniques for surface-micromachining MEMS processes," *Proc. SPIE: Micromachining and Microfabrication Process Technology*, vol. 2639, pp. 211-222, 23-24 Oct. 1995.
7. J. Comtois, V. Bright, M. Phipps, "Thermal microactuators for surface-micromachining processes," *Proc. SPIE: Micromachined Devices and Components*, vol. 2642, pp. 10-21, 23-24 Oct. 1995.
8. B. Read, V. Bright and J. Comtois, "Mechanical and optical characterization of thermal microactuators fabricated in a CMOS process," *Proc. SPIE: Micromachined Devices and Components*, vol. 2642, pp. 22-32, 23-24 Oct. 1995.
9. D. Sene, J. Grantham, V. Bright and J. Comtois, "Development and characterization of micro-mechanical gratings for optical modulation," *Proc. IEEE MEMS-96 Workshop*, San Diego, CA, pp. 222-227, 11-15 Feb. 1996.

10. V. Bright, J. Comtois, S. Gustafson and E. Watson, "Realizing micro-opto-electro-mechanical devices through a commercial surface micro-machining process," *Proc. SPIE: Miniaturized Systems With Micro-Optics and Micromechanics*, vol. 2687, pp. 34-46, 1996 International Symposium on Lasers and Integrated Optoelectronics, San Jose, CA, 27 Jan. - 2 Feb. 1996, Invited Paper.
11. J. Comtois and V. Bright, "Surface micromachined polysilicon thermal actuator arrays and applications," *to be published in Proc. 1996 Solid State Sensor and Actuator Workshop*, Hilton Head, SC, 2-6 June 1996.
12. J. Reid, J. Comtois and V. Bright, "Force measurement of polysilicon thermal microactuators," *submitted to SPIE: Micromachining and Microfabrication '96*, Austin, TX, 14-15 Oct. 1996.
13. S. Gustafson, V. Bright, J. Comtois and E. Watson, "Micromirrors for coherent beam steering and phase control," *submitted to SPIE: Micromachining and Microfabrication '96*, Austin, TX, 14-15 Oct. 1996.
14. V. Bright, J. Grantham, C. Christenson and J. Comtois, "Micromirror array control of a phased array laser diode," *submitted to SPIE: Micromachining and Microfabrication '96*, Austin, TX, 14-15 Oct. 1996.
15. J. Reid, V. Bright and J. Comtois, "A surface micromachined rotating micromirror normal to the substrate," *submitted to IEEE/LEOS Summer Topicals '96*, 1996.
16. J. Reid, V. Bright and J. Comtois, "Arrays of thermal microactuators coupled to micro-optical components," *submitted to SPIE International Symposium on Optical Science, Engineering, and Instrumentation*, Denver, CO, 4-9 Aug 1996.
17. D. Sene, J. Grantham, V. Bright and J. Comtois, "Development and characterization of polysilicon micro-mechanical gratings for optical modulation," *submitted to Sensors and Actuators A*.

REPORT DOCUMENTATION PAGE			Form Approved OMB No. 0704-0188	
Public reporting burden for this collection of information is estimated to average 1 hour per response, including the time for reviewing instructions, searching existing data sources, gathering and maintaining the data needed, and completing and reviewing the collection of information. Send comments regarding this burden estimate or any other aspect of this collection of information, including suggestions for reducing this burden, to Washington Headquarters Services, Directorate for Information Operations and Reports, 1215 Jefferson Davis Highway, Suite 1204, Arlington, VA 22202-4302, and to the Office of Management and Budget, Paperwork Reduction Project (0704-0188), Washington, DC 20503.				
1. AGENCY USE ONLY (Leave blank)	2. REPORT DATE June 1996	3. REPORT TYPE AND DATES COVERED Doctoral Dissertation		
4. TITLE AND SUBTITLE Structures and Techniques For Implementing and Packaging Complex, Large Scale Microelectromechanical Systems Using Foundry Fabrication Processes		5. FUNDING NUMBERS		
6. AUTHOR(S) John H. Comtois, Major, USAF				
7. PERFORMING ORGANIZATION NAME(S) AND ADDRESS(ES) Air Force Institute of Technology, WPAFB OH 45433-7765		8. PERFORMING ORGANIZATION REPORT NUMBER AFIT/DS/ENG/96-04		
9. SPONSORING / MONITORING AGENCY NAME(S) AND ADDRESS(ES) Mr. James Lyke, Phillips Laboratory (PL/VTEE) 3550 Aberdeen Ave. SE, Kirtland AFB, NM 87117-5776		10. SPONSORING / MONITORING AGENCY REPORT NUMBER		
11. SUPPLEMENTARY NOTES				
12a. DISTRIBUTION / AVAILABILITY STATEMENT Distribution Unlimited		12b. DISTRIBUTION CODE		
13. ABSTRACT (Maximum 200 words) Microelectromechanical Systems, or 'MEMS' is a broad new field of research into devices that range in size from a few microns to a few millimeters. Much of the technology supporting MEMS research is borrowed from the microelectronics industry; so MEMS holds out the promise of batch fabrication of micro-miniaturized machines that can be easily integrated with electronics. This dissertation research investigated structures and methods for implementing and packaging complex, large scale microelectromechanical devices and systems using commercially available foundry fabrication processes. It specifies methods for creating and packaging large, complex MEM systems, allowing the exploration of new MEMS architectures at a higher level than was previously possible at research institutions with minimal in-house fabrication capabilities. Completely new areas of research were created, including hinged wiring and a class of devices powered by arrays of low voltage, high force thermal actuators. Throughout this dissertation, example applications of these methods are presented, including stepper motors and large optical systems for high density holographic data storage and aberration correction in optical communication systems. The research culminates in the successful creation of the first commercially fabricated multichip module integrating foundry fabricated MEMS and electronic die.				
14. SUBJECT TERMS MEM, MEMS, MUMPS, micromirrors, micro-optics, micro-actuators, LIGA, MCM, HDI, packaging, microrelays, microhinges		15. NUMBER OF PAGES 475		
		16. PRICE CODE 475		
17. SECURITY CLASSIFICATION OF REPORT UNCLASSIFIED	18. SECURITY CLASSIFICATION OF THIS PAGE UNCLASSIFIED	19. SECURITY CLASSIFICATION OF ABSTRACT UNCLASSIFIED	20. LIMITATION OF ABSTRACT UL	